Investigation of the Mechanism of Multiple Cytochrome P450-catalysed Reactions

Matthew Podgorski

Submitted in fulfilment of the degree

Master of Philosophy

Supervisor: A/Prof Stephen G. Bell

THE UNIVERSITY of ADELAIDE

The University of Adelaide
School of Physical Sciences
Department of Chemistry

October 2019

Contents

List of Figures

List of Tables

Thesis declaration

I certify that this work contains no material which has been accepted for the award of any other degree or diploma in my name, in any university or other tertiary institution and, to the best of my knowledge and belief, contains no material previously published or written by another person, except where due reference has been made in the text. In addition, I certify that no part of this work will, in the future, be used in a submission in my name, for any other degree or diploma in any university or other tertiary institution without the prior approval of the University of Adelaide and where applicable, any partner institution responsible for the joint-award of this degree.

I give permission for the digital version of my thesis to be made available on the web, via the University's digital research repository, the Library Search and also through web search engines, unless permission has been granted by the University to restrict access for a period of time.

I acknowledge the support I have received for my research through the provision of an Australian Government Research Training Program Scholarship.

Matthew Podgorski, 25 Oct 2019

Acknowledgements

I thank my supervisor A/Prof Stephen G. Bell for his incredible effort in proofreading my thesis, his constant guidance and enthusiasm and for giving me the opportunity to attend the Cytochrome P450 conference in Brisbane. I would also like to thank the other members of the Bell group: Tom Coleman, Sherry Dezvarei, Md Raihan Sarkar, Saurabh Ahirwar, Joel Lee, Stella Child, Heba Mohamed, Amna Ghith, Daniel Doherty, Cameron Macintosh and Natasha Maddigan. I would like to especially thank Tom for teaching me how to produce and purify proteins, perform enzyme assays, crystallise proteins and solve X-ray crystal structures, Natasha for mentoring me when I did a lab placement with her as an undergraduate student, and I also thank Saurabh for his delicious curries and snacks. Thank you to Chris Sumby, John Bruning and members of the Bruning group: Jordan Pederick, Stephanie Nguyen, Andrew Marshall, Jia Truong, Andrew Thompson and Rebecca Frkic. I thank Jordan and Stephanie for showing me how to collect X-ray data at the Australian Synchrotron. I would also like to thank Josh Harbort and A/Prof. Jeffrey Harmer for performing the EPR experiments, Prof. James de Voss for chiral HPLC analysis of sulfoxide products, Luke Churchman for synthesis of a chiral epoxide, Prof. Paul Bernhardt for performing electrochemistry experiments, and Giang Nguyen and Dr William Donald for performing mass spectrometry experiments.

Abstract

The cytochrome P450 heme-thiolate enzymes catalyse a multitude of oxidation reactions and, in humans, carry out drug metabolism. P450s perform hydroxylation, epoxidation, *N*-, *O*- and *S*-dealkylation, sulfoxidation, alkyne oxidation and aldehyde oxidation of organic molecules (and many other reactions). These reactions are predominantly performed by the reactive intermediate Compound I, but other intermediates in the catalytic cycle may mediate some types of reactions. It would be appealing to exploit these enzymes as environmentally benign catalysts in the synthesis of fine chemicals. Their widespread use in industrial synthesis is, however, impractical given the high cost of the required cofactor NAD(P)H, but engineering P450s to instead use cheap H_2O_2 would overcome this problem.

CYP199A4 is a soluble bacterial P450 enzyme from *Rhodopseudomonas palustris* HaA2 that favours 4-methoxybenzoic acid and other *para*-substituted benzoic acids as substrates. It tightly binds these substrates and the *para*-substituent is rapidly oxidised. This enzyme has been used as a model system to study the mechanism of P450-catalysed reactions. While 4-methoxybenzoic acid is oxidatively demethylated at a rate of 1220 μM $(\mu M\text{-}P450)^{-1}$ min^{-1}, CYP199A4 displays no detectable activity towards the *meta* isomer, 3-methoxybenzoic acid. *In vitro* reactions were performed with a range of other *meta*-substituted benzoic acids (3-methylthio-, 3-methylamino-, 3-formyl-, 3-methyl-, 3-isopropyl-, 3-*tert*-butyl- and 3-ethoxy-benzoic acid) to assess whether CYP199A4 had activity towards these substrates. These *meta*-substituted substrates, except for 3-*tert*-butylbenzoic acid, were all metabolised by CYP199A4, but with low activity compared to the corresponding *para* isomers. Compared to the *para* isomers, the *meta* isomers had lower binding affinity and induced smaller type I spin-state shifts to high-spin. To rationalise CYP199A4's preference for *para*- over *meta*-substituted benzoic acid substrates and to investigate the requirements for efficient monooxygenase activity, crystal structures were solved of CYP199A4 in complex with 3-methoxy-, 3-methylamino-, 3-methylthio-, and 3- and 4-methyl-benzoic acid. These structures revealed that the heme-bound water ligand to the heme is retained when these substrates bind (water occupancy 21-90%) and is hydrogen-bonded to the heteroatom (N, S, O) of the substrate. The corresponding *para* isomers displace the iron-bound water. 3-Ethoxybenzoic acid, which has a bulkier *meta*-substituent, shifted the spin-state to 85% high-spin and in the crystal structure the iron-bound water was removed. The *meta*-substituent of each substrate is held in close proximity to the iron. 3-Methoxybenzoic acid is positioned near the iron but is not oxidised. This was attributed to the fact that the C-H bonds are oriented away from the heme, whereas those of 4-methoxybenzoic acid are ideally oriented for H-atom abstraction by Cpd I. These results emphasise that close proximity of the methyl carbon to the heme iron does not guarantee that hydroxylation will occur if the C-H bonds are not oriented appropriately for abstraction, and subtle modification of the substrate's position relative to the heme can abolish catalytic activity.

X-ray crystallography, CW and HYSCORE EPR and other experiments were performed to elucidate the binding modes of 4-pyridin-2-yl-, 4-pyridin-3-yl- and 4-imidazol-1-yl-benzoic acid in the CYP199A4 active site. These heterocyclic aromatic compounds are not metabolised and induce substantially different type II UV-Vis spectra. 4-Pyridin-3-yl- and 4-imidazol-1-yl-benzoic acid red-shifted the Soret band from 419 to 424 nm. They induced 'normal' type II spectra, characterised by a less intense α-band than β-band and an increase in δ-band intensity. The UV-Vis spectra of ferrous CYP199A4 in complex with these ligands indicated that 4-pyridin-3-ylbenzoic acid was directly ligated to the heme iron via the pyridine nitrogen, but the Fe-N bond between the iron and 4-imidazol-1-ylbenzoic acid was ruptured upon heme reduction. 4-Pyridin-2-ylbenzoic acid induced a smaller Soret band red-shift (to 422 nm) when added to the ferric enzyme. It produced an 'abnormal' type II spectrum, with no decrease in the α-band intensity. 4-Pyridin-2-ylbenzoic acid also induced a smaller Soret band trough in the difference spectrum than 4-pyridin-3-ylbenzoic acid. HYSCORE EPR and X-ray crystallography revealed that 4-pyridin-3-yl- and 4-imidazol-1-yl-benzoic acid were directly ligated to the ferric heme iron, but 4-pyridin-2-ylbenzoic acid was hydrogen-bonded to the heme-bound water. This study revealed that optical spectroscopy can distinguish between water-bridged and directly bound nitrogen donor ligands. 4-Pyridin-3-yl- and 4-imidazol-1-yl-benzoic acid-bound CYP199A4 were both reduced to the ferrous form by ferredoxin, ferredoxin reductase and NADH. On the other hand, binding of 4-pyridin-2-ylbenzoic acid to CYP199A4 lowered the reduction potential and prevented heme reduction by even the powerful reductant dithionite. This implies that water-bridged nitrogen ligands may in some instances be more effective P450 inhibitors than those that bind directly to the iron.

The T252E mutant of CYP199A4 was produced and characterised. This variant was no longer able to operate using NADH but was a more efficient peroxygenase (H_2O_2-utilising enzyme) than the wild-type (WT) enzyme. EPR indicated that the sixth axial ligand to the heme was a mixture of hydroxide and water. Crystal structures showed that this aqua/hydroxo ligand was tightly bound due to strong interactions with the carboxylate of E252. The axial aqua/hydroxo ligand was not displaced by substrates, even sterically bulky substrates, explaining the lack of substrate-induced spin-state shifts and the exceedingly slow rate of electron transfer from the ferredoxin to the P450. Because this ligand is not displaced by substrates, the active species could potentially be generated via light-driven oxidation of the water-bound ferric resting state to Compound I. Type II nitrogen ligands were also unable to displace the aqua/hydroxo ligand. 4-Pyridin-3-ylbenzoic acid, when added to the T252E mutant, induced an 'abnormal' type II spectrum, confirming that optical spectroscopy can distinguish between water-bridged and directly bound type II ligands. X-ray crystallography revealed that the T252 → E mutation only subtly altered the orientation of substrates in the CYP199A4 active site.

In the absence of substrate, the heme signal of the T252E mutant was rapidly bleached by 50 mM H_2O_2. When substrate was present, the T252E variant remained catalytically active for several hours. The T252E variant was able to perform a range of reactions using H_2O_2 (*O*-dealkylation,

hydroxylation/desaturation, epoxidation, sulfoxidation, alkyne oxidation and aldehyde oxidation). When the surrogate oxygen donor *tert*-butyl hydroperoxide was substituted for H_2O_2, the T252E mutant had negligible activity. *t*-BuOOH is presumably too bulky to access the heme iron in this P450. WT CYP199A4 and the T252A and D251N mutants also catalysed these reactions using H_2O_2 but afforded less product over a 4-hour period than the T252E mutant. H_2O_2- and NADH-driven epoxidation of 4-vinylbenzoic acid catalysed by WT and mutant CYP199A4 proceeded with high enantioselectivity, yielding almost exclusively the (*S*)-enantiomer.

In NADH-supported reactions, WT CYP199A4 catalysed *O*-demethylation of 4-methoxybenzoic acid more efficiently than sulfoxidation of 4-methylthiobenzoic acid. In H_2O_2-driven reactions, the T252E variant had higher activity towards sulfoxidation compared to *O*-demethylation, hydroxylation, epoxidation, aldehyde oxidation and alkyne oxidation. This may indicate the involvement of a second oxidant in sulfoxidation (e.g. the Fe^{III}–H_2O_2 species), allowing sulfoxidation to occur in the absence of Compound I as proposed by Shaik.

Abbreviations

4-AP	4-Aminoantipyrine
9-OHFlu	9-Hydroxyfluorene
AcCN	Acetonitrile
AMU	Atomic mass unit (1 AMU = 1.66×10^{-27} kg)
BA	Benzoic acid
BSTFA + TMCS	*N,O*-Bis(trimethylsilyl)trifluoroacetamide with trimethylsilyl chloride catalyst
Cpd 0	Compound 0, the electrophilic ferric-hydroperoxo intermediate (precursor to Cpd 1)
Cpd 1	Compound 1, the electrophilic oxy-ferryl porphyrin radical cation
CYP199A4	P450 enzyme from *Rhodopseudomonas palustris* HaA2
DMSO	Dimethyl sulfoxide
DTT	Dithiothreitol
E. coli	*Escherichia coli*
EtOAc	Ethyl acetate
EtOH	Ethanol
FAD	Flavin adenine dinucleotide
FMN	Flavin mononucleotide
GC-MS	Gas chromatography coupled with mass spectrometry
HaPuR	Ferredoxin reductase from *Rhodopseudomonas palustris* HaA2
HaPux	[2Fe2S] ferredoxin from *Rhodopseudomonas palustris* HaA2
HCl	Hydrochloric acid
HEPES	4-(2-Hydroxyethyl)-1-piperazineethanesulfonic acid
HPLC	High-performance liquid chromatography
HRP	Horseradish peroxidase
HS	High-spin
IPTG	Isopropyl β-D-1-thiogalactopyranoside
IS	Internal standard
LB	Lysogeny broth (or Luria-Bertani broth)
LS	Low-spin
MES	2-(*N*-morpholino)ethanesulfonic acid
NAD(P)H /	Reduced and oxidised forms of nicotinamide adenine dinucleotide
NMR	Nuclear magnetic resonance
P420	Inactive form of cytochrome P450
P450 or CYP	Cytochrome P450 enzyme
PDB	Protein Data Bank (www.rcsb.org)
PEG 3350	Polyethylene glycol (MW = 3350 g mol^{-1})
PFR	Product formation rate

RMSD	Root-mean-square deviation
RT	Retention time
RZ	Reinheitszahl (purity ratio): Abs_{419}/Abs_{280}
SB	Substrate-bound
SF	Substrate-free
SOB / SOC	Super optimal broth / super optimal broth with catabolite repression
***t*BuOOH / *t*BuOH**	*tert*-Butyl hydroperoxide / *tert*-butyl alcohol
TFA	Trifluoroacetic acid
TMS	Trimethylsilyl
Tris	Tris(hydroxymethyl)aminomethane
UV-Vis	Ultraviolet-visible spectroscopy
WT	Wild-type

Chapter 1

Introduction

1.1 Introduction to the cytochromes P450

Although nearly all organisms on Earth possess cytochrome P450 enzymes, this vast family of monooxygenases was not known to exist until 1958, when the first P450s were discovered by Klingenberg[1] and Garfinkel[2].[3-4] These enzymes contain an essential heme *b* unit embedded within the active site and are vivid red in colour (Figures 1.1 and 1.2). The name 'P450' references this red colouration, P being an abbreviation of pigment. The name also references the absorption band at 450 nm in the spectrum of the reduced CO-bound enzyme.[5-6] The characteristic absorption peak at 450 nm arises from ligation of the heme by a cysteine thiolate ligand, which links the heme to the polypeptide chain. P450s cannot perform their signature chemistry without this crucial thiolate ligand.[7-12]

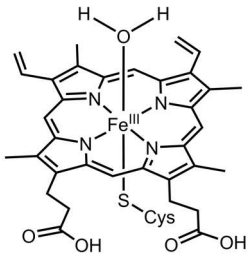

Figure 1.1. P450s contain an essential heme *b* prosthetic group in the active site.

The predominant role of these enzymes is to insert an oxygen atom into the unreactive C-H bonds of organic molecules, sourcing electrons from the nicotinamide cofactors NADH or NADPH and O_2 from the atmosphere to perform this hydroxylation reaction (Equation 1.1).[13]

$$\text{R-H} + O_2 + H^+ + \text{NAD(P)H} \rightarrow \text{R-OH} + H_2O + \text{NAD(P)}^+ \qquad (1.1)$$

P450s are exceptionally versatile enzymes which, in nature, catalyse a myriad of other oxidation and reduction reactions and can be engineered to perform unnatural reactions.[14-17] Additional reactions in the P450 repertoire include epoxidation, desaturation, *O*, *S*, *N*-dealkylation and sulfoxidation, among many others (Section 1.2).[18-20]

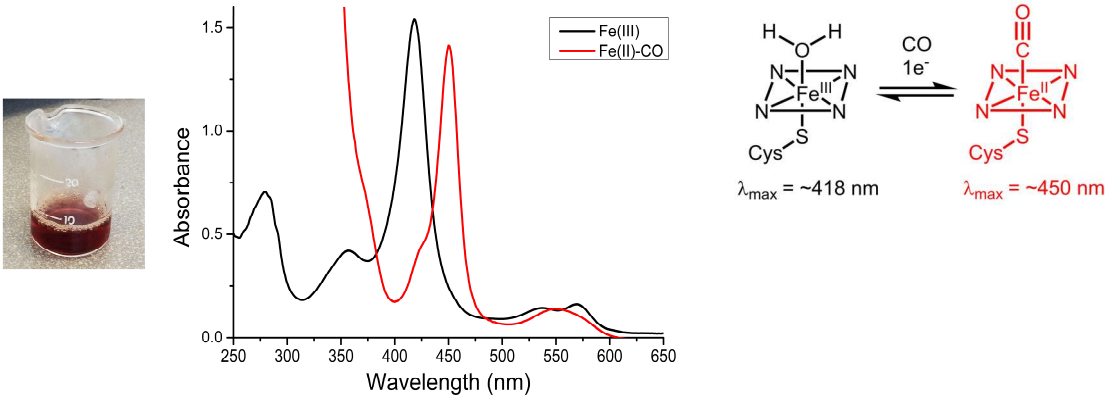

Figure 1.2. P450s are vivid red in colour and have a Soret absorbance peak at ~418 nm (black spectrum). The reduced, carbon monoxide-bound form has an intense absorption peak at ~450 nm (red spectrum).[5]

In total, a considerable number of P450s have been identified to date in archaea, bacteria, animals, plants, fungi and viruses[21], although certain species such as *Escherichia coli* lack any P450s.[22] *Homo sapiens* possess 57 P450s, rice (*Oryza sativa*) 356, the soybean 332, *Mycobacterium marinum* 47, the cannonball fungus (*Sphaerobolus stellatus*) 601 and baker's yeast three.[4, 22-25] By 2004 about 4000 P450s were known[26] and this number has since dramatically escalated. As of 2018, more than 300 000 P450 enzymes are known[22] and the expectation is that, by 2020, one million P450s will have been discovered.[22, 27] Of the >300 000 identified thus far, >41 000 have been assigned names by the Standardized Cytochrome P450 Nomenclature Committee.[22] This committee classifies each enzyme as a member of a family and subfamily, the assignment based predominantly on amino acid sequence similarities.[26] Each name begins with 'CYP', and the number after this prefix denotes the family. A letter then indicates the subfamily, followed by a number identifying the specific enzyme.[28] The enzyme named CYP199A4 is a member of family 199 and the fourth member of subfamily A (Figure 1.3).

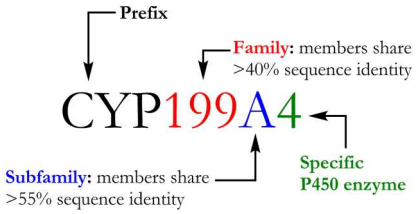

Figure 1.3. P450 nomenclature

Cytochrome P450 enzymes assigned to a specific family share ≥40% sequence identity, while inclusion in the same subfamily requires that the P450s share ≥55% sequence identity.[26] It can therefore be inferred that CYP199A4 and CYP199A2 have similar amino acid sequences (in fact, they share 86% sequence identity) and potentially have similar functions.[29] There are exceptions to this rule, however.[28] The CYP51 family encompasses P450s with low sequence similarity because they all catalyse an identical (and important) reaction.[30] Members of this family, referred to as sterol 14α-demethylases, all catalyse a critical demethylation step in the biosynthesis of sterol.[31] This family is significant, being the only P450 family whose members are found in every kingdom of life: bacteria, protists, plants, animals and fungi.[32] Trivial names exist for some P450s, some having

multiple names.[28] The intensely studied[33] camphor-hydroxylating P450 CYP101A1 from *Pseudomonas putida* is commonly referred to as $P450_{cam}$.[34] Although the amino acid sequences of different P450s may have little similarity, these enzymes share the same overall fold (Figure 1.4).[35]

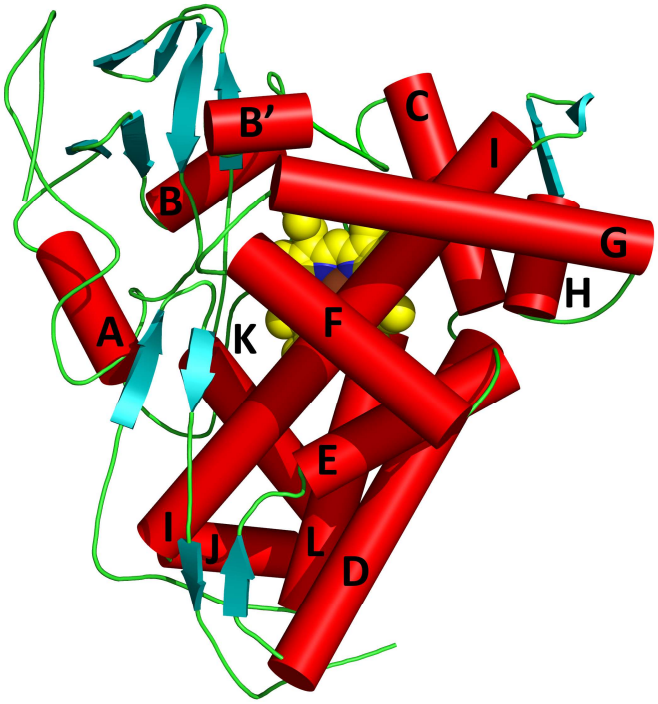

Figure 1.4. Structure of $P450_{cam}$ (PDB ID: 5CP4). Red cylinders represent α helices (labelled A-L), blue ribbons represent β sheets and the heme (yellow) is buried inside the enzyme.[36-37]

P450s have vital roles in humans and other organisms.[38] Human P450s are involved in steroid hormone biosynthesis and catalyse the metabolism of drugs in the liver, with the promiscuous P450 CYP3A4 responsible for metabolising ~50% of pharmaceuticals.[39-40] Another major drug-metabolising P450 is CYP2D6[41]; notably, it converts codeine into the active drug morphine.[42-43] P450 oxidation makes drugs more water soluble, aiding their excretion,[44] so inhibiting human P450s could be a means of reducing the dose of costly pharmaceuticals patients must take.[45] P450s may also unwittingly convert procarcinogens into carcinogens.[46] In plants, P450s participate in secondary metabolite biosynthesis, having major roles in the biosynthesis of the anti-cancer drug Taxol and anti-malarial drug artemisinin.[38, 47] Although mammalian P450s such as CYP3A4 can be highly promiscuous, bacterial P450s typically have narrow substrate ranges.[48]

P450s also have economic value. They can be exploited as biocatalysts in the synthesis of pharmaceuticals and other valuable chemicals, and in environmental remediation.[49] Interest in P450s stems from their ability to oxidise the usually unreactive C-H bonds of organic molecules at ambient temperature in water, and they are capable of carrying this out regio- and enantio-selectively.[47] This is an exceedingly difficult reaction to perform using chemicals. P450-catalysed reactions are thus environmentally benign, whereas chemical oxidation can require organic solvents and hazardous reagents such as toxic heavy metal catalysts and elevated temperatures and

pressures.[50-51] Notably, a P450 is employed in the synthesis of the cholesterol-lowering drug pravastatin, produced by hydroxylation of compactin (Figure 1.5a).[45, 52]

Although a particular P450 may accept only a limited range of substrates, P450s can be engineered to perform the desired oxidation of unnatural substrates.[50, 53-56] This can be achieved by rationally redesigning the enzyme's active site or by random mutagenesis (directed evolution).[53, 57] Protein engineering has yielded P450 mutants which are now used to generate commercial products.[58] Sowden *et al.* engineered $P450_{cam}$ and $P450_{BM3}$ to convert the inexpensive natural product valencene (from oranges) into nootkatone, a valuable natural product that has the flavour and aroma of grapefruit (Figure 1.5b).[55] Nootkatone commands a price of £3-4000 kg^{-1}.[55, 58] By employing an enzyme (CYP102A1) to accomplish this chemical transformation, the product can be labelled 'natural', satisfying public demand for food and drink to contain natural ingredients rather than synthetic chemicals.[58-59] Chemical methods of producing nootkatone rely on carcinogenic or corrosive reagents.[51, 59] A company, Oxford Biotrans, has been founded to produce nootkatone and other natural products using engineered P450s.[58]

P450s also have applications in the cut flower industry.[60] Because no natural roses are blue, roses of this colour are desired. By recruiting the P450 CYP75A (flavonoid 3,'5'-hydroxylase) from pansies that produces a blue pigment, genetically modified blue roses (which are in reality closer to lilac in colour) have been developed which sell for a high price ($40 per rose).[60-63] Given their ability to degrade pollutants, another proposed application of P450s is in environmental remediation. For example, the P450 enzyme XplA (CYP177A1) degrades the explosive hexahydro-1,3,5-trinitro-1,3,5-triazine, used extensively by the military.[64-65] P450s, therefore, can be exploited for a multitude of applications, including environmental remediation and the production of pharmaceuticals and fine chemicals.

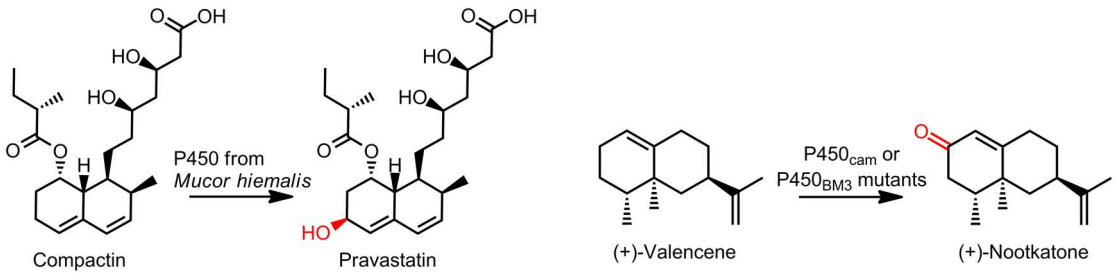

Figure 1.5. Commercial P450 applications include the production of **(a)** the pharmaceutical pravastatin and **(b)** the grapefruit fragrance and flavour molecule nootkatone.[45]

1.2 Diverse reactions catalysed by P450 enzymes

As mentioned, the main reaction catalysed by P450s is hydroxylation[13], but P450s also catalyse other reactions. Selected P450 reactions are shown in Figure 1.6.

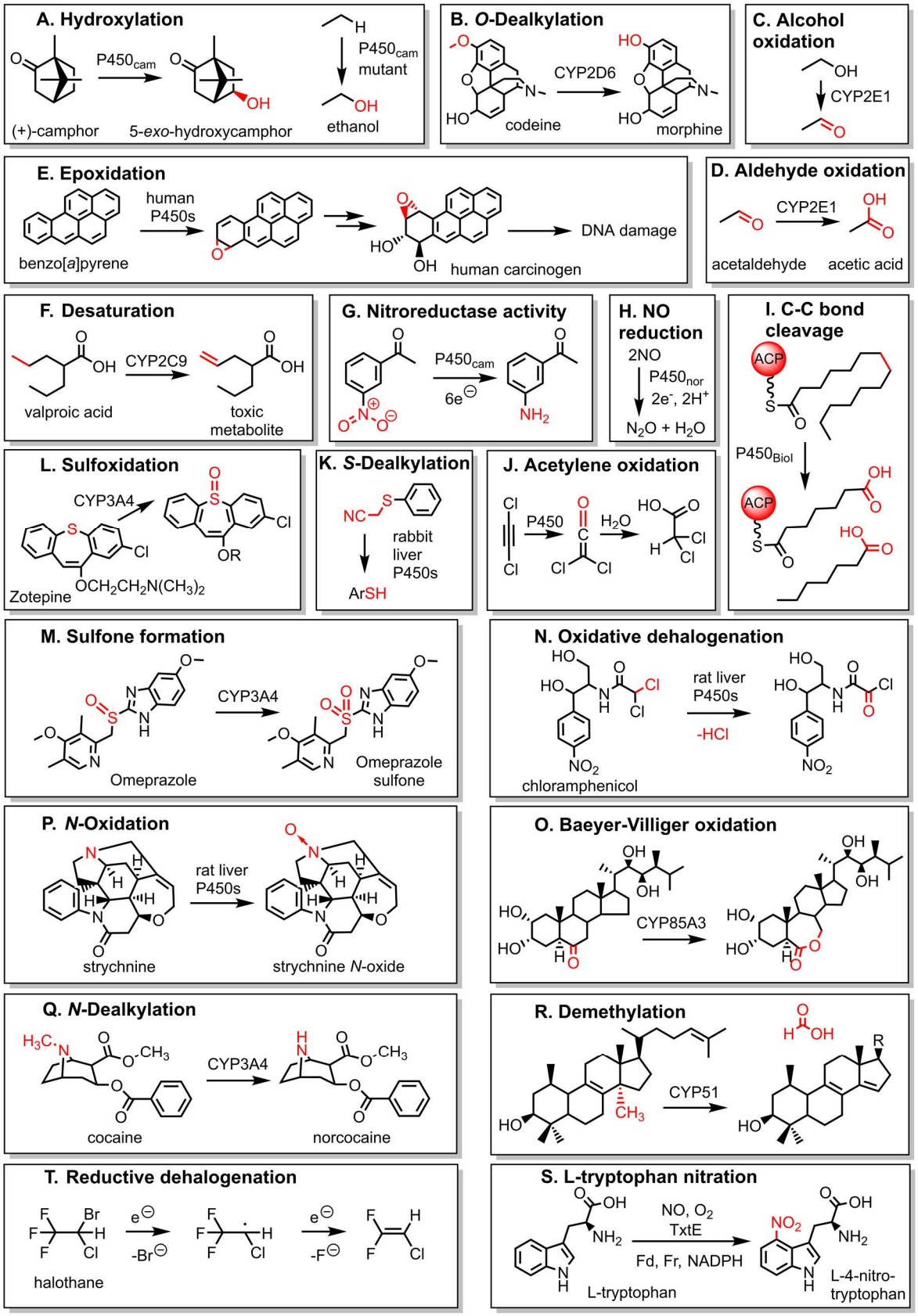

Figure 1.6. Selected P450 reactions are shown in white boxes. P450s also perform many other types of reactions. Non-natural reactions performed by P450 mutants, which are not technically P450 enzymes because they do not absorb at 450 nm, are shown in the blue box. *Figure continued on opposite page.*

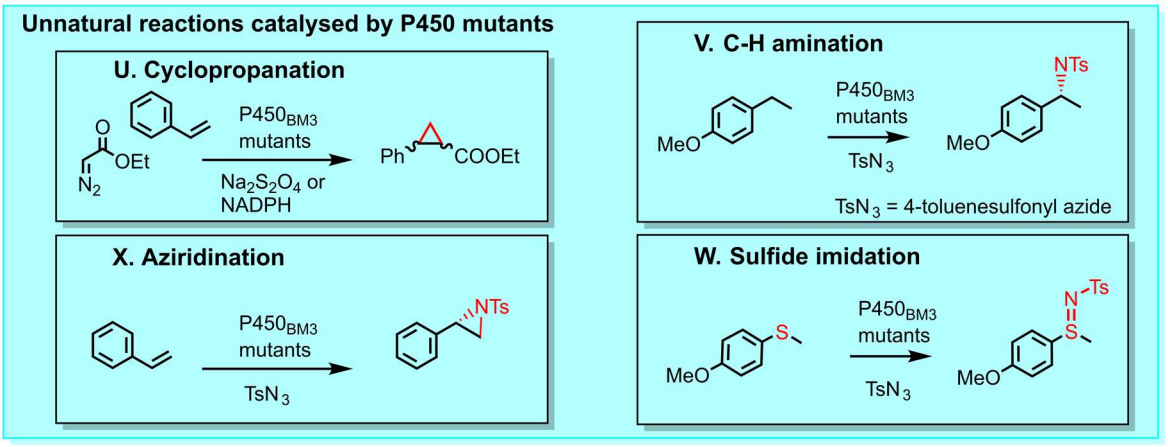

A. Hydroxylation: $P450_{cam}$ hydroxylates camphor[66] and was engineered to hydroxylate ethane.[56] **B. *O*-Dealkylation:** CYP2D6 converts ~15% of ingested codeine into morphine.[43, 67] **C. Alcohol oxidation:** CYP2E1 converts ethanol into acetaldehyde.[68] **D. Aldehyde oxidation:** CYP2E1 can further oxidise acetaldehyde to acetic acid.[68] **E. Epoxidation:** Benzo[*a*]pyrene from cigarette smoke is converted by human P450s into the carcinogen benzo[*a*]pyrene-7,8-diol-9,10-epoxide.[46, 69-71] **F. Desaturation:** Desaturation of valproic acid generates a toxic metabolite.[72-73] **G. Nitroreductase activity:** $P450_{cam}$ can reduce nitroaromatics to amines.[74] **H. Nitric oxide reduction:** Fungal $P450_{nor}$ reduces NO to N_2O.[19, 75-76] **I. C-C bond cleavage:** $P450_{BioI}$ catalyses C-C bond cleavage of tetradecanoic acid.[20, 77-78] **J. Acetylene oxidation:** P450s can oxidise acetylene compounds to ketenes, which react with water to generate the carboxylic acid.[79-81] **K. *S*-Dealkylation:** *S*-dealkylation is a rare P450 reaction.[82] **L. Sulfoxidation:** The sulfoxidation of the antipsychotic drug Zotepine is catalysed by CYP3A4.[83-84] **M. Sulfone formation:** Omeprazole, used to treat reflux, is oxidised to Omeprazole sulfone by CYP3A4.[83] **N. Oxidative dehalogenation:** Oxidative dehalogenation of the antibiotic chloramphenicol.[79, 85] **O. Baeyer-Villiger oxidation:** Tomato P450 CYP85A3 catalyses the Baeyer-Villiger oxidation of castasterone.[20] **P. *N*-Oxidation:** Rat liver P450s convert strychnine into the *N*-oxide.[79, 86] **Q. *N*-Dealkylation:** CYP3A4 converts a small portion of ingested cocaine into norcocaine.[83, 87] **R. Demethylation:** CYP51 demethylates lanosterol.[88] **S. L-tryptophan nitration:** The P450 TxtE catalyses the nitration of L-tryptophan.[89-90] **T. Reductive dehalogenation:** Under anaerobic conditions, CYP3A4 and CYP2A6 catalyse the reductive dehalogenation of the anaesthetic halothane.[91]

U, V, X, W. Cyclopropanation, C-H amination, aziridination and sulfide imidation: Arnold and co-workers engineered $P450_{BM3}$ to catalyse non-natural reactions.[8, 14-17, 92] The $P450_{BM3}$ mutants have serine or histidine as the heme ligand so the CO-bound forms do not absorb at 450 nm.[92-93]

1.3 The general P450 catalytic cycle

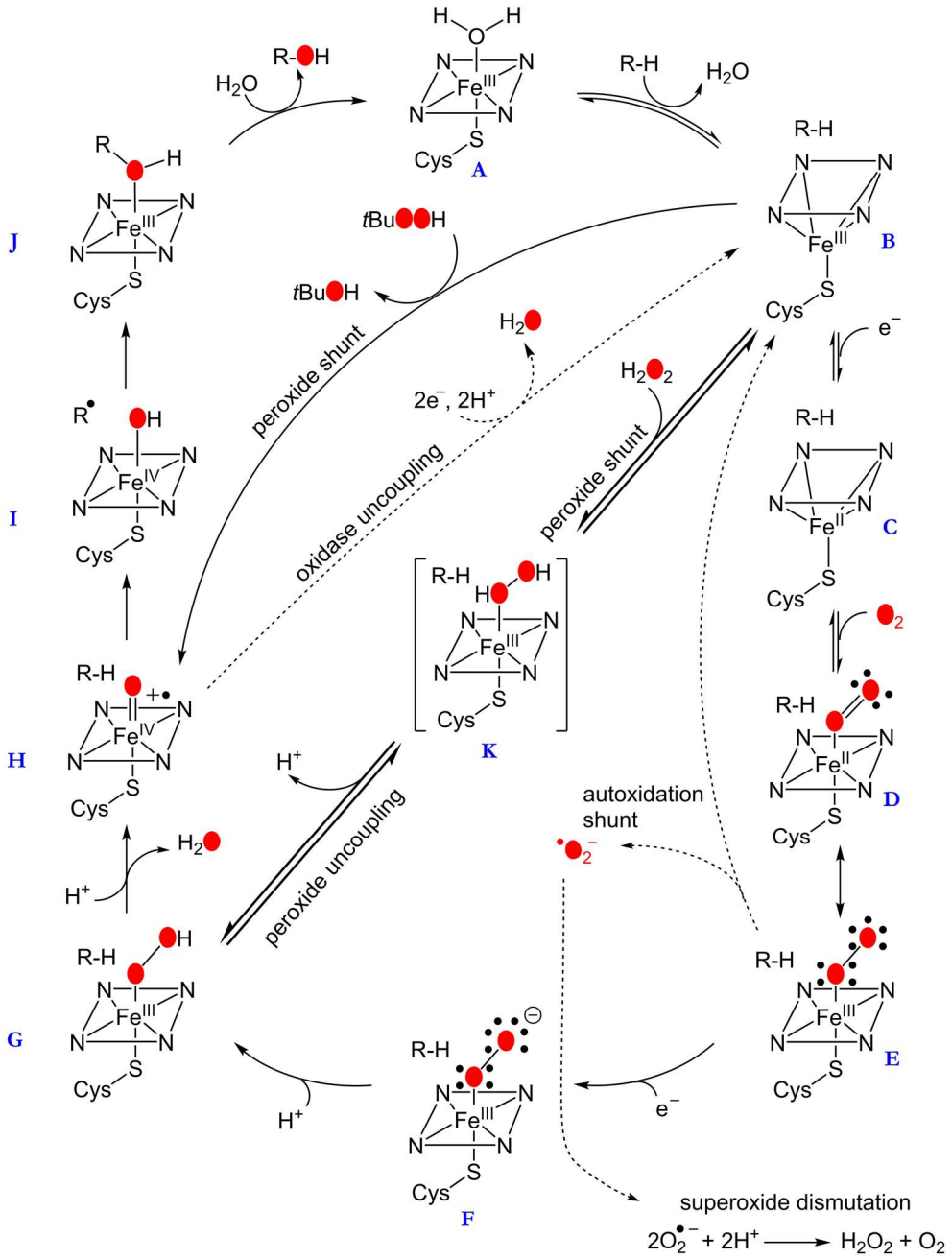

Figure 1.7. **(a)** The P450 catalytic cycle,[94-95] and **(b)**, Groves' radical rebound mechanism.[96] Red circles represent oxygen atoms from the oxidant.

Substrate oxidation requires the transfer of two protons and two electrons to the enzyme at precise moments in the catalytic cycle. The electrons are transferred individually to the heme cofactor via electron transfer proteins (Section 1.5). Figure 1.7a illustrates the P450 catalytic cycle. The steps in the cycle were established by studying $P450_{cam}$, the structure of which was solved in 1985.[97-99] Other P450s are thought to operate in the same fashion.[94] In its ferric resting state (**A**), the P450 has water loosely bound as the sixth axial ligand and is inactive until the aqua ligand is displaced by the binding of an appropriate substrate (**B**).[40] This weakens the ligand field, inducing a spin-state shift of the heme iron from low-spin (λ_{max} = 420 nm) to high-spin (λ_{max} = 390 nm) (Figure 1.8).[23, 40] There is also an upshift in the reduction potential which leads to transfer of the first electron from the electron transfer proteins to the P450, reducing the iron to Fe^{II} (**C**).[100]

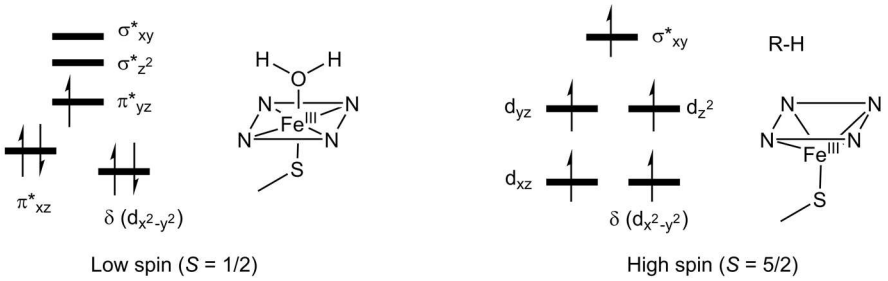

Figure 1.8. Binding of a substrate (R-H) to a P450 typically displaces the heme-bound aqua ligand and induces a spin-state shift from LS (S = 1/2) to HS (S = 5/2).[40, 101]

O_2 binds to the ferrous heme as the sixth ligand, yielding the ferrous dioxygen complex (Fe^{II}–O_2) (**D**). Binding of CO instead inhibits the enzyme.[102] Upon delivery of a second electron the nucleophilic ferric-peroxo anion (**F**) is generated. The ferric-hydroperoxo intermediate, Compound 0 (**G**), is then generated by delivery of a proton derived from the solvent to the distal oxygen. Protonation once again of the distal oxygen (to give Fe^{III}–OOH_2) induces heterolytic cleavage of the O–O bond with loss of water to yield Compound I (**H**), the ephemeral oxy-ferryl porphyrin radical cation species ($Por^{\bullet+}Fe^{IV}$=O). Cpd I is envisaged to be responsible for the majority of P450 oxidations and was finally observed in 2010 by Rittle and Green, who mixed *m*CPBA with purified CYP119 to generate Cpd I;[103] $P450_{cam}$ Cpd I has also been observed.[104] Cpd I then abstracts a proton from the substrate to give a substrate radical cation and an Fe(IV)-OH species (**I**). The substrate radical recombines with the hydroxyl radical attached to the iron via Groves' radical rebound mechanism[96] (Figure 1.7b) to yield the hydroxylated product (**J**). The P450 is converted back into its resting state **A** upon exit of the product.

The site of hydroxylation depends on the intrinsic reactivity of the substrate's C-H bonds and their proximity to the heme iron. If multiple C-H bonds are equally accessible, there will be a preference for hydrogen abstraction to occur at the weakest C-H bond. Benzylic, allylic, and tertiary C-H bonds are weaker than secondary and primary C-H bonds (Table 1.1). Thus, the order of reactivity of C-H bonds is:

Benzyl / allyl > tertiary > secondary > primary.[50, 79]

Table 1.1. Bond dissociation energies at 298 K for benzylic, allylic, tertiary, secondary and primary C-H bonds, and C-H bonds adjacent to heteroatoms[79, 105]

C-H bond type	Bond dissociation energy (kJ.mol^{-1})
Methane (CH_3-H)	439
Primary (CH_3CH_2-H)	423
Secondary ($(CH_3)_2CH$–H)	413
Tertiary ($(CH_3)_3C$–H)	404
Benzylic ($C_6H_5CH_2$–H)	376
Allylic (CH_2=$CHCH_2$–H)	372
Formaldehyde (O=HC–H)	369
C-H adjacent to oxygen ($HOCH_2$–H)	402
C-H adjacent to nitrogen (H_2NCH_2–H)	386

However, the positioning of the substrate in the active site has the most substantial influence over which site is oxidised; less reactive C-H bonds *will* react if in close proximity to the heme.[50] Thus, in some cases, P450s selectively attack the least reactive C-H bond of a substrate.[47]

The need for two electrons from NAD(P)H delivered by redox partners can be eliminated by instead driving catalysis using peroxides (Equation 1.2).[106] P450s and other enzymes which use H_2O_2 are known as peroxygenases.

$$R\text{-}H + H_2O_2 \rightarrow R\text{-}OH + H_2O \qquad (1.2)$$

Binding of H_2O_2 to the ferric heme iron, giving Fe^{III}–H_2O_2 (**K**), is thought to first generate Cpd 0 (**G**) and then Cpd I (**H**), bypassing much of the catalytic cycle.[107-108] This is known as the peroxide shunt pathway. Free H_2O_2 has a high pK_a (11.7)[109], so it would be fully protonated at neutral pH and hence H_2O_2, not ^-OOH, would be expected to bind to ferric heme.[108-110] Oxidants such as *tert*-butyl hydroperoxide (*t*BuOOH),[111] *m*CPBA and iodosylbenzene (PhIO) can also be used to drive catalysis.[94, 106] These generate Cpd I but not Cpd 0.[103, 107, 111] However, peroxides have low binding affinity, typically cause fast degradation of the heme (heme bleaching) and do not efficiently drive catalysis,[112] although it has been discovered that a very small minority of P450s can utilise H_2O_2 efficiently (such as $P450_{BS\beta}$ (CYP152A1), $P450_{SP\alpha}$ (CYP152B1), $P450_{CLA}$ (CYP152A2) and P450 $OleT_{JE}$ (CYP152L1)).[113]

In the oxidation of camphor by $P450_{cam}$, one molecule of product is generated for almost every molecule of NADH and O_2 consumed; the 'coupling efficiency' is nearly 100%[i].[66] This almost perfect coupling of reducing equivalents to product formation is unusual[70]; often a portion of the NAD(P)H/O_2 consumed is wasted through unproductive side-reactions, referred to as 'uncoupling'. NAD(P)H can be wasted through three major uncoupling pathways.[66] The first is the autoxidation shunt. In this pathway, the ferrous dioxygen species (**D**), which is unstable, decays with release of superoxide. Superoxide decomposes to H_2O_2.[70] Autoxidation can occur when timely delivery of the second electron fails to occur.[70, 114] The presence of substrate is known to extend the lifetime of the Fe–O_2 species.[70]

[i]Coupling efficiency = ([product generated]/[NAD(P)H consumed]) × 100%

In the second pathway, H_2O_2 is lost from the ferric-hydroperoxo species (**G**). H_2O_2 uncoupling is promoted by water in the active site.[114] A small substrate may permit access of water to the heme, resulting in incorrect protonation of the proximal oxygen to give Fe^{III}–H_2O_2 (**K**).[66] As H_2O_2 has low affinity for the heme iron, there is subsequent loss of H_2O_2.[115] H_2O_2 uncoupling can also occur if proton delivery is delayed.[66, 70]

Oxidase uncoupling is the third uncoupling pathway. In this pathway, Cpd I (**H**) is reduced to water by accepting two electrons (a second molecule of NAD(P)H is consumed) and two protons.[114] This pathway does not generate toxic reactive oxygen species (ROS) but does waste NAD(P)H. Oxidase uncoupling takes place when no C-H bond is near the heme iron. It has been demonstrated to occur with fluorinated compounds since C–F bonds are inert,[116-117] and when the substrate is not bound close enough to the heme iron.[66]

Although Cpd I is recognised as being the oxidant that probably mediates most P450 reactions, including hydroxylation, the participation of other intermediates has been postulated, yet remains to be proven (Table 1.2).[118]

Table 1.2. Intermediates proposed to participate in P450 reactions, discussed in Section 1.9[94]

Intermediate	Reactions proposed to possibly be mediated by each intermediate
Ferric-peroxo anion (nucleophilic)	Aldehyde oxidation[119]/deformylation[120]
Ferric-hydroperoxo (nucleophilic or electrophilic)	Deformylation, epoxidation[33, 121-122], sulfoxidation[123-124], hydroxylation (inserts OH^+)[125]
Cpd I (electrophilic)	Hydroxylation and most/all other P450 reactions[103, 126]
Fe^{III}–H_2O_2 complex	Sulfoxidation[118]

1.4 Role of the conserved acid-alcohol pair

Two protons are needed for conversion of the ferric-peroxo anion into Cpd I. In the majority of P450s, two residues in the I helix, referred to as the acid-alcohol pair, are vital for proper proton delivery. In both $P450_{cam}$ and CYP199A4, the acid-alcohol pair is T252 and D251, although some P450s possess serine (S) not threonine (T), and glutamate (E) not aspartate (D), and in some P450s, such as the P450 peroxygenases, these residues are absent altogether.[127] P450eryF (CYP107A), for example, lacks the threonine.[128] The role of the acid-alcohol pair has been interrogated using mutagenesis and X-ray crystallography.[98, 129-132]

As mentioned, $P450_{cam}$ hydroxylates camphor with ~100% coupling efficiency. Mutation of T252 in $P450_{cam}$ to alanine (A), resulted in almost all the O_2 consumed (~89%) being converted into H_2O_2 with negligible product formed, although the O_2 and NADH consumption rate remained high.[130-131] Mutation to valine or glycine also caused high levels of H_2O_2 uncoupling.[130-131] The T → S mutant, however, was still highly coupled, implying that the hydroxyl moiety is crucial. It was concluded that the role of the Thr252 hydroxyl was to directly donate a proton to Cpd 0 to form Cpd I.[130] This was disputed by a study involving a $P450_{cam}$ mutant in which the Thr252 hydroxyl

was replaced with a methoxy group, which cannot donate a proton.[131] No H_2O_2 was produced and the coupling efficiency of the OMe mutant was 100%.[131]

Crystal structures of the Fe^{II}–O_2 complex of WT $P450_{cam}$ and the T252A mutant have now been solved (Figure 1.9a,b).[98, 129] When dioxygen binds, two ordered water molecules (Wat354 and Wat443) appear close to the heme. These are thought to be the waters which protonate the oxygen.[98, 129] The conserved threonine is believed to stabilise Cpd 0, and the hydrogen bond between Cpd 0 and the threonine is thought to alter the pK_a of the distal oxygen (Figure 1.9c). This encourages protonation at the distal oxygen, not the proximal oxygen, so that Cpd I is formed.[110, 129]

Mutation of the conserved aspartate residue (D251) to asparagine (N) reduced the rate of camphor oxidation by a factor of 100.[133] It is believed the role of the aspartate is to shuttle protons into the active site.[110]

The threonine-to-alanine and aspartate-to-asparagine mutations have been used to investigate which intermediates mediate different P450 reactions.[124] The threonine-to-alanine mutation is expected to block Cpd I formation and increase the persistence of Cpd 0 (**G**),[33, 134] while the aspartate-to-asparagine mutation delays the protonation steps,[129] increasing the lifetime of the ferric-peroxo anion (**F**).[110, 133]

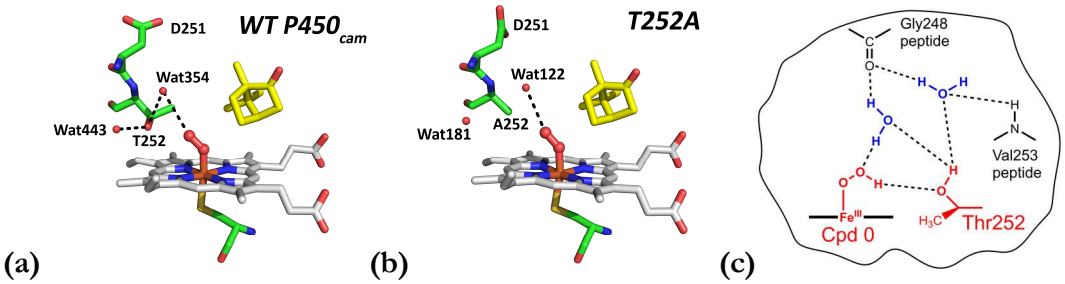

Figure 1.9. Crystal structures of the Fe^{II}–O_2 complex of WT $P450_{cam}$ **(a)** and the T252A mutant **(b)**. Camphor is depicted in yellow. **(c)** T252 stabilises the ferric-hydroperoxo species (Cpd 0).

1.5 P450 electron transfer partners

The electron transfer systems of P450s have been categorised into 10 classes[135] based on the partner proteins which supply the two electrons. The majority belong to Classes I and II, with the remaining classes representing less common systems (Figure 1.10).[135] Class I encompasses most bacterial and mitochondrial P450s,[136] and these systems consist of a FAD (flavin adenine dinucleotide)-containing ferredoxin reductase and an iron-sulfur cluster-containing ferredoxin. In the bacterial CYP199A4 enzyme system, for example, the transfer partners are HaPuR (a FAD-containing reductase) and HaPux (a [2Fe2S] ferredoxin).[137-138] The ferredoxin reductase is responsible for accepting two electrons from NAD(P)H, and single electrons are subsequently

ferried from the reductase to the P450 by the ferredoxin. Distinct differences exist between bacterial and mitochondrial P450 systems.[139] Bacterial Class I systems favour NADH as the electron source, whereas the mitochondrial partners source electrons from NADPH.[135, 140-141] In mitochondrial systems, only the [2Fe2S] ferredoxin adrenodoxin (Adx) is soluble while the P450 is membrane-bound. The reductase, adrenodoxin reductase (AdR), is also attached to the membrane. Contrastingly, in bacterial Class I systems, all proteins are soluble. Bacterial ferredoxins such as HaPux typically contain [2Fe2S] clusters but can alternatively contain various other cluster types.[135, 142]

Class II corresponds to the microsomal P450 system.[135, 142-143] Electrons are delivered to microsomal P450s (such as human CYP3A4) from NADPH via a single membrane-bound protein, cytochrome P450 reductase (CPR), without the involvement of an iron-sulfur ferredoxin.[143] CPR contains both FAD and FMN (flavin mononucleotide) cofactors; two electrons are initially transferred from NADPH to the FAD cofactor; these electrons are delivered one-at-a-time to the P450 via the FMN cofactor.[142]

Class IV contains the thermophilic P450 CYP119.[135] In contrast to most P450s, CYP119 operates at high temperatures and obtains its electrons not from NAD(P)H but from pyruvic acid.[136, 144] Classes VII-X correspond to self-sufficient P450s which function without any additional electron transfer proteins.[75] $P450_{BM3}$ is an example of a bacterial self-sufficient P450[145] belonging to Class VIII. Isolated from *Bacillus megaterium*, it consists of CPR fused to a P450 and is soluble.[135, 146] This enzyme is notable for its ability to oxidise arachidonic acid at a rate exceeding 17 000 μmol (μmol-P450)$^{-1}$ min^{-1} (abbreviated to min^{-1}).[147] The fungal membrane-bound CPR-P450 fusion protein $P450_{foxy}$ is another member of this class.[75, 148]

Class IX consists of the soluble self-sufficient fungal enzyme $P450_{nor}$ which converts NO into N_2O but is unable to catalyse hydroxylation reactions.[19, 75, 135, 149] $P450_{nor}$ is abnormal in that it is supplied with two electrons directly from NADH, rather than single electrons delivered by redox partners.[19]

Class X consists of self-sufficient P450s which function without redox partners and without NAD(P)H/O_2.[135] Allene oxide synthase (CYP74A), an enzyme that transforms fatty acid hydroperoxides into allene oxides, is an example of a Class X P450.[135, 150]

P450s classified as peroxygenases such as $P450_{SP\alpha}$ and $P450_{BS\beta}$ also have no requirement for redox partners nor NAD(P)H/O_2 because they instead utilise H_2O_2 to drive catalysis.[127, 142]

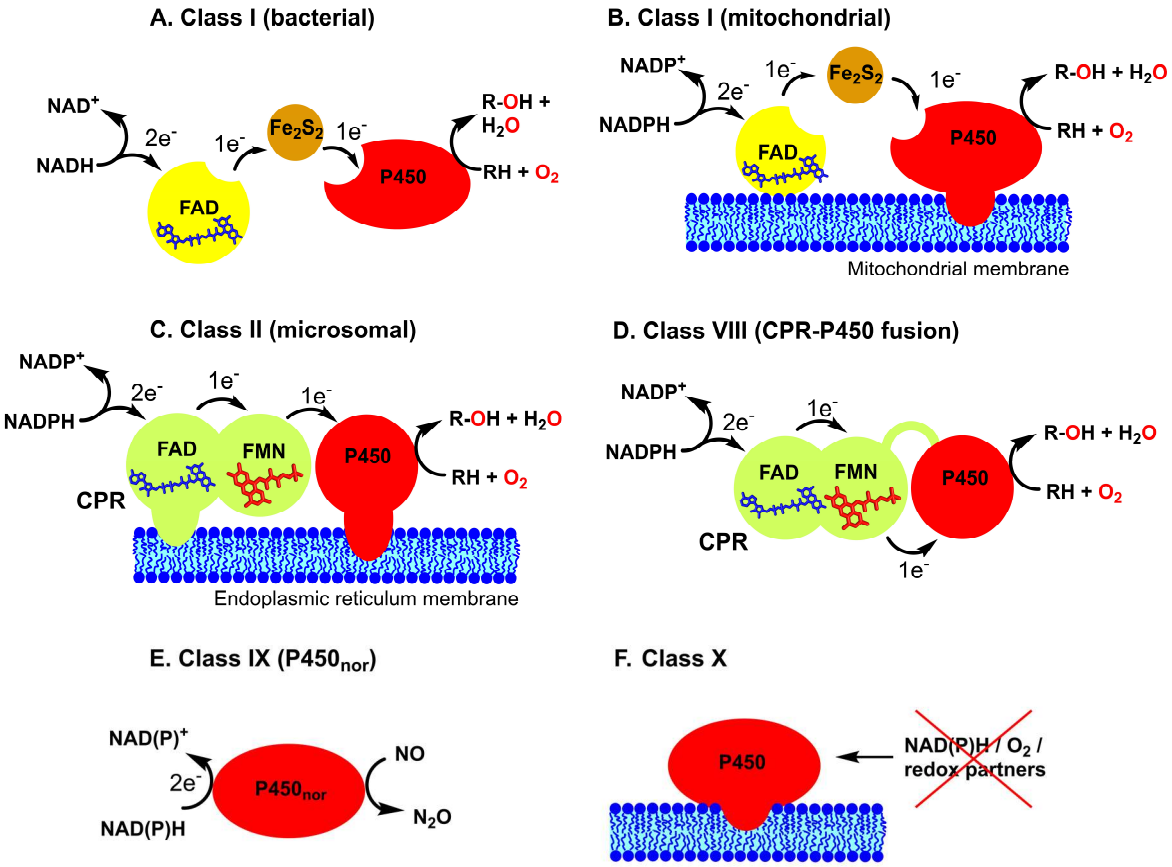

Figure 1.10. Selected P450 classes described in the text.

1.6 Gating of the P450 catalytic cycle

Commencement of the archetypal P450 catalytic cycle is gated to avoid NAD(P)H consumption when no substrate is bound.[74] Continuous NAD(P)H consumption would lead to formation of high levels of superoxide and H_2O_2.[151] When a substrate binds and removes the heme-bound water, it causes a shift in the reduction potential and allows the first electron to be transferred. This starts the catalytic cycle.[70, 151] When camphor binds to substrate-free $P450_{cam}$, for example, there is a shift in the reduction potential from -303 mV to -173 mV.[74] Before camphor binds, electron transfer from putidaredoxin, which has a reduction potential of -240 mV, to $P450_{cam}$ is thermodynamically unfavourable.[74] Once substrate binds, reduction becomes thermodynamically favourable. This shift in the redox potential is invoked as the reason why electron transfer is accelerated in the presence of substrate.[70, 152] Honeychurch *et al.* offered an alternative interpretation.[100] They claim that electron transfer to substrate-free $P450_{cam}$ is in fact probably thermodynamically favourable because ligand (O_2) binding to the reduced P450 should increase the reduction potential. According to Marcus theory, the driving force (ΔG°) for the reaction and the reorganisation energy (λ) influence the electron transfer rate (k_{et}). The reorganisation energy must be greater for the substrate-free enzyme since a water ligand is still bound and it has to convert from six- to five-coordinate.[100] They argue that the larger λ is the major reason why electron transfer to substrate-free P450s is slow.[100]

1.7 Ligand binding modes

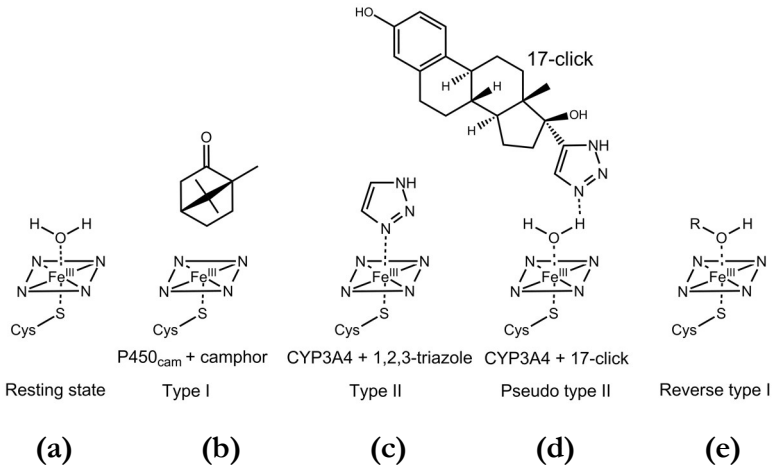

Figure 1.11. P450 resting state and ligand binding modes.[101, 153-154]

The way in which a ligand interacts with the P450 active site can be inferred from UV-Vis difference spectra. Type I difference spectra result from binding of a substrate with release of the water ligand (Figure 1.11a,b). A type I difference spectrum has a trough at roughly 420 nm and a peak at 390 nm.[153]

Nitrogen-containing molecules can potentially displace the water and directly bind to the heme iron (Figure 1.11c).[155-156] Coordination by a strong-field nitrogen ligand red-shifts the Soret band, resulting in a type II difference spectrum having a peak at 425-440 nm and trough at ≤415 nm.[153, 157] The usual interpretation is that a ligand inducing a type II spectrum must be coordinated to the heme.[158] It is now appreciated that this is sometimes incorrect.[154] Nitrogen ligands may alternatively form a hydrogen-bond to the heme-bound aqua ligand (Figures 1.11d and 1.12), modifying the ligand field strength and inducing a type II spectrum.[154, 159]

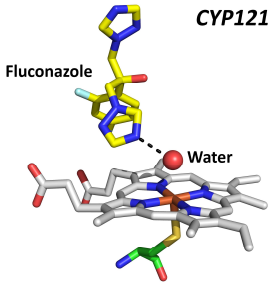

Figure 1.12. Fluconazole (yellow) bound to CYP121A1 (PDB: 2IJ7).[159]

Conner *et al.* recently studied the binding of '17-click' (Figure 1.11d), which incorporates a 1,2,3-triazole moiety, to CYP3A4.[154] Binding of this ligand induced a type II spectrum, implying direct nitrogen coordination to the heme. HYSCORE EPR unexpectedly revealed that the distal water was not displaced but instead remained *in situ* and was presumably hydrogen-bonded to the nitrogen. N-containing ligands can therefore induce a type II-like spectrum without coordinating to the iron.[154] Although type II ligands are expected to inhibit the enzyme, it was found that 17-click was oxidised by CYP3A4.[154] Consequently, if a type II spectrum is observed, it appears ill-

advised to assume that the nitrogen ligand must be coordinated to the heme iron without additional evidence.[153-154]

Reverse type I spectra are mirror images of type I spectra, having a peak at 420 nm and a trough at 390 nm[153] and arising from coordination of an alcohol or other weak ligand to the heme (Figure 1.11e).[160] For example, substrate-free CYP125A1 exists partly in the high-spin, five-coordinate state, but binding of the molecule LP10 promotes water coordination to the iron, thus inducing a reverse type I spectrum.[161]

1.8 Origin of the spin-state shift and relationship to catalytic activity

Measuring the spin-state shift induced by potential substrates identifies which compounds bind to the P450 and are likely to be efficiently metabolised. The explanation often given for a type I shift is displacement of the heme-bound water ligand.[117, 162-164] Crystal structures of substrate-bound P450s often show that the water ligand has been displaced.[165] However, large shifts to HS have been observed even when the water ligand remains *in situ*.[165] Adamantane induces a 99% shift from LS to HS when it binds to $P450_{cam}$, yet the water ligand is still *in situ* in the crystal structure, its occupancy 100%.[166] Norcamphor induces a spin-state shift of 46% but also fails to displace the water ligand.[166] To rationalise this, Poulos *et al.* proposed that when these substrates bind and expel other active-site waters, it changes the protonation state of the distal ligand. When the enzyme is substrate-free, the ligand is proposed to be more hydroxide-like; when a substrate binds and the cluster of water is displaced, the active site would become more hydrophobic and the ligand would be fully protonated. OH^- is a stronger-field ligand that would stabilise the low-spin state, whereas the iron should be high-spin with H_2O bound, a weak-field ligand.[167] Altering the amounts of OH^- and H_2O could therefore shift the heme to HS.[166] Models of the $P450_{cam}$ active site have been synthesised to investigate the factors that control the spin-state.[168-170] A model complex (Figure 1.13a) with water as the sixth ligand was found to be entirely high-spin.[168] A second complex was synthesised in which the water ligand was hydrogen-bonded to ether oxygens (Figure 1.13b). These interactions shifted the iron to LS. It was inferred that the $P450_{cam}$ resting state is LS due to the water ligand having hydroxide character resulting from hydrogen-bonding interactions with the water cluster.[168] However, EPR experiments indicated that the sixth ligand is water not hydroxide.[153, 171-172] Others have argued that changes in the conformation of the heme affect the spin-state.[74, 165]

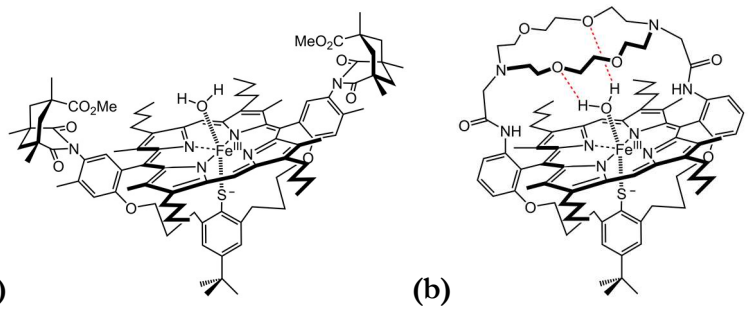

Figure 1.13. P450 model complex **(a)** is entirely HS, whereas the hydrogen bonding in **(b)** results in a shift to LS.

Spin-state shifts can be used to predict whether a ligand will be efficiently metabolised.[173-174] In general, for substrates which induce a large spin-state shift to the high-spin form, the NADH consumption and product formation rates are typically fast.[74, 117, 175-176] A strong correlation was found, for example, between the degree to which various benzphetamine analogues shift the spin-state to HS when they bind to rat liver P450s and the rate of substrate *N*-demethylation.[175] A large shift to HS, however, does not always mean that the catalytic activity towards a substrate will be high and some studies have failed to find any relationship between the spin-state shift, NADH consumption rate and coupling efficiency.[165, 177-178] α-Pinene induces a large (85%) shift to HS when it binds to $P450_{cam}$, yet the coupling efficiency is extremely low.[74, 177] Ortiz de Montellano also found that the rate of NADH consumption by $P450_{cam}$ was lower in some cases for substrates which induced a greater spin-state shift.[178]

A shift in the spin-state reveals that a substrate binds but fails to reveal the strength of binding.[162, 175, 177, 179] Often, substrates which bind with higher affinity induce larger spin-state shifts;[180] *d*-camphor, for example, binds tightly to $P450_{cam}$ (K_d = 0.84 μM)[179] and induces an essentially complete (~95%) shift to HS.[166] However, sometimes substrates bind tightly but fail to displace the heme-bound water or bind weakly yet efficiently displace the water.[178] 4-Methoxybenzamide and 4-methoxybenzoic acid both induce a ≥95% shift to HS when they bind to CYP199A4, yet 4-methoxybenzamide binds ~2000 times more weakly than 4-methoxybenzoic acid (K_d = 660 *vs.* 0.28 μM).[181] 4-Methoxyacetophenone binds reasonably tightly (K_d = 4.8 μM) yet induces less than a 5% shift to HS.[181]

1.9 P450 reaction mechanisms

1.9.1 Hydroxylation

There is extensive evidence that Cpd I mediates C-H hydroxylation.[103] Rittle and Green demonstrated that Cpd I of CYP119 hydroxylated lauric acid.[103] Additionally, the T252A mutant of $P450_{cam}$, which is hypothesised to form Cpd 0 but not Cpd I, does not hydroxylate camphor.[33] Groves' radical rebound mechanism, described earlier (Figure 1.7b), is the mechanism by which P450s are thought to perform substrate hydroxylation.

In the past, concerns arose that the radical rebound mechanism may not be valid from experiments involving 'radical clock' substrates.[125, 182] Researchers aimed to use radical clocks to ascertain the lifetime of the radical intermediate generated by H-atom abstraction from the substrate.[183] After H-atom abstraction, these radical clock substrates either undergo rebound to give the unrearranged alcohol, or first rearrange and then undergo radical rebound to yield a rearranged alcohol product (Figure 1.14a), depending on the relative rates of radical rebound and rearrangement.[182] The lifetime of the radical is deduced from the proportions of unrearranged and rearranged product, provided that the rearrangement rate of the radical is known.[182]

Studies on the lifetime of the radical intermediate using bicyclo[2.1.0]pentane as a radical clock substrate yielded a reasonable value for the lifetime of the radical intermediate (50 ps).[182-184] However, this result appeared to be contradicted by subsequent studies.[125, 185] Absurdly short radical lifetimes of τ = 70–200 fs, the lifetimes of transition states, not intermediates, were found using ultrafast radical clocks, and were used as an argument that radical intermediates were *not* formed.[182] Radical clock substrates designed to generate different products depending on whether radical or cationic intermediates were formed revealed that cationic intermediates were in some cases generated.[185] The assumption that Cpd I was the sole oxidant was thus questioned. To explain cationic rearrangement products, it was proposed that a second oxidant, Cpd 0, may mediate hydroxylation by 'OH$^+$' insertion (Figure 1.14b).[125] Calculations reveal, however, that Cpd 0 is a weak oxidant.[94] Cpd 0 has also been invoked as the oxidant in other P450 reactions, notably epoxidation and sulfoxidation.[94] Given the vast array of reactions catalysed by P450s, it appears reasonable that multiple active oxidants may exist mediating different reactions.[121] The theory that there is involvement of more than one oxidant in P450 reactions is known as the 'two-oxidant' theory.[94, 186-188]

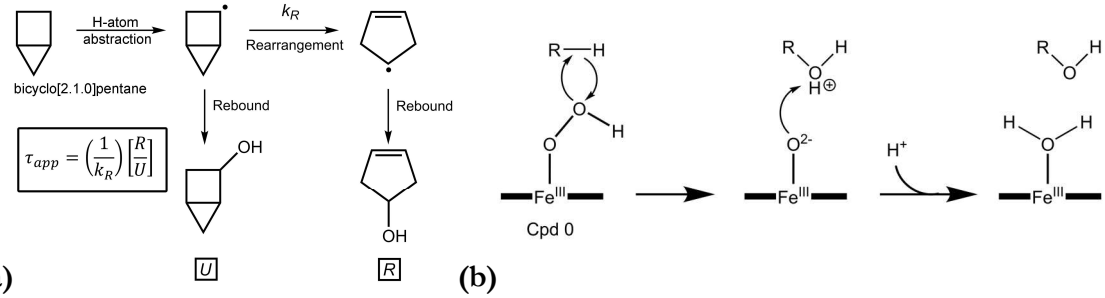

Figure 1.14. **(a)** Bicyclo[2.1.0]pentane was employed to measure the rate of radical recombination.[183] **(b)** It was hypothesised that Cpd 0 participates in hydroxylation by inserting 'OH$^+$'.[94]

Shaik's 'two-state reactivity' (TSR) theory was designed to explain these inconsistent experimental observations without invoking the participation of additional oxidants.[187, 189-190] Cpd I is believed to exist in two spin-states: a LS (doublet) state, $^2A_{2u}$, and a HS (quartet) state, $^4A_{2u}$ (Figure 1.15).[191] After H-atom abstraction, on the LS pathway radical rebound is barrier free, so discrete radical intermediates never form. In contrast, on the HS pathway the lifetime of the radical intermediates will be longer due to a barrier to radical rebound. Rearrangement products hence form on the HS, but not LS, pathway. The measured lifetime of the radical clocks thus depends on the proportions of LS and HS Cpd I, explaining the conflicting radical lifetimes measured. Cationic intermediates could form on the HS pathway by removal of an electron from the radical intermediate by Cpd II.[192]

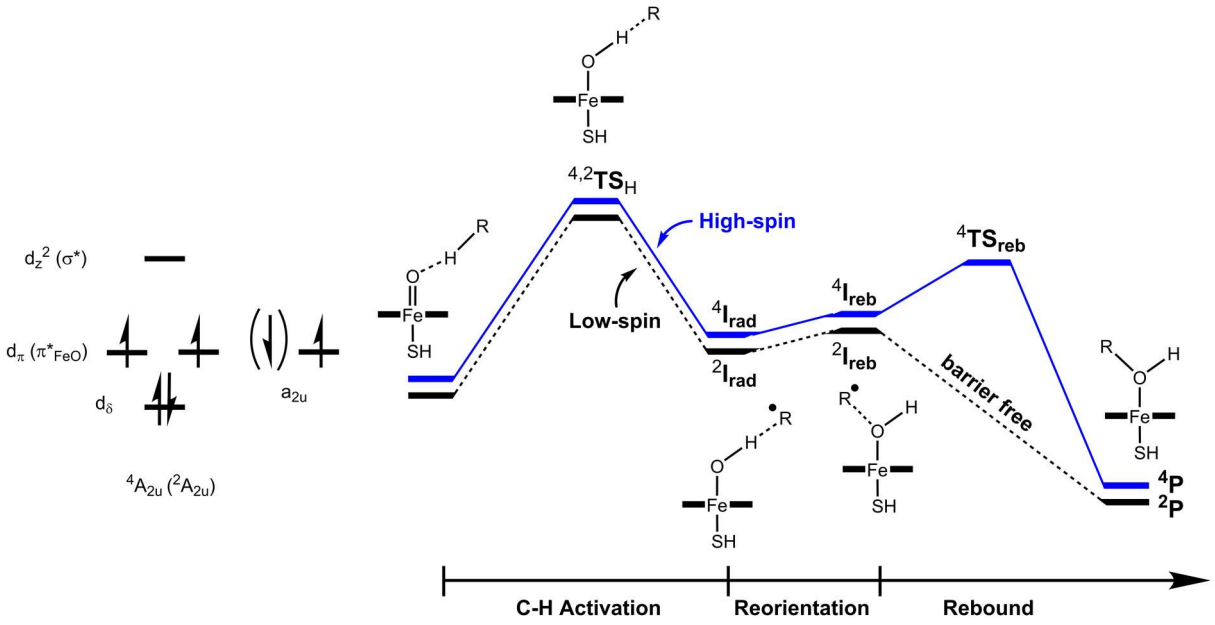

Figure 1.15. Mechanism of hydroxylation by LS and HS Cpd I. TS_H is the transition state for H-atom abstraction, I_{rad} is the radical intermediate, and $^4TS_{reb}$ is the transition state for radical rebound on the HS pathway. Contrastingly, on the LS pathway, radical rebound has no barrier. The electronic configuration of LS and HS Cpd I is shown on the left. Quartet ($S = 3/2$) and doublet ($S = 1/2$) states exist because the single electron in the porphyrin a_{2u} orbital can have the same spin, or opposite spin, to the two unpaired electrons in the π^*_{xz} and π^*_{yz} orbitals.[187, 191, 193]

Whereas the 'two-oxidant' theory assumes the participation of multiple oxidants in P450 reactions,[94, 123-125] the 'two-state reactivity' theory claims that Cpd I is the only oxidant. According to the TSR theory, if there appear to be multiple oxidants this arises from the differing reactivities of LS and HS Cpd I.[94, 126]

1.9.2 *N*, *O*, *S*-Dealkylation

If a carbon alpha to a heteroatom (nitrogen, oxygen or sulfur) is hydroxylated, it affords a hemiaminal, hemiacetal or thiohemiacetal.[18, 79, 192] This intermediate, being unstable, breaks down to give a dealkylated product. An aldehyde or ketone is liberated as a by-product; this by-product is formaldehyde in demethylation reactions[162]. Two mechanisms for these dealkylation reactions exist in the literature: the HAT (hydrogen atom transfer) and SET (single electron transfer) mechanisms.[79, 192] The consensus is that *O*-dealkylation occurs in a manner identical to alkane hydroxylation, first involving H-atom abstraction and then radical rebound to give the unstable hemiacetal.[79, 192] This is the HAT mechanism. *S*- and *N*-dealkylation could plausibly also occur via a HAT mechanism (Figure 1.16a).[194]

An electron can be more readily removed from N and S than the more electronegative oxygen, so *N*- and *S*-dealkylation could instead proceed via a SET mechanism (Figure 1.16b).[18, 79, 192, 194-195] In this mechanism, a sulfur or nitrogen radical cation is first formed via removal of a single electron from N or S by Cpd I. A proton (H^+) is then removed from the neighbouring carbon to give a substrate radical, followed by radical rebound yielding the unstable thiohemiacetal or hemiaminal.

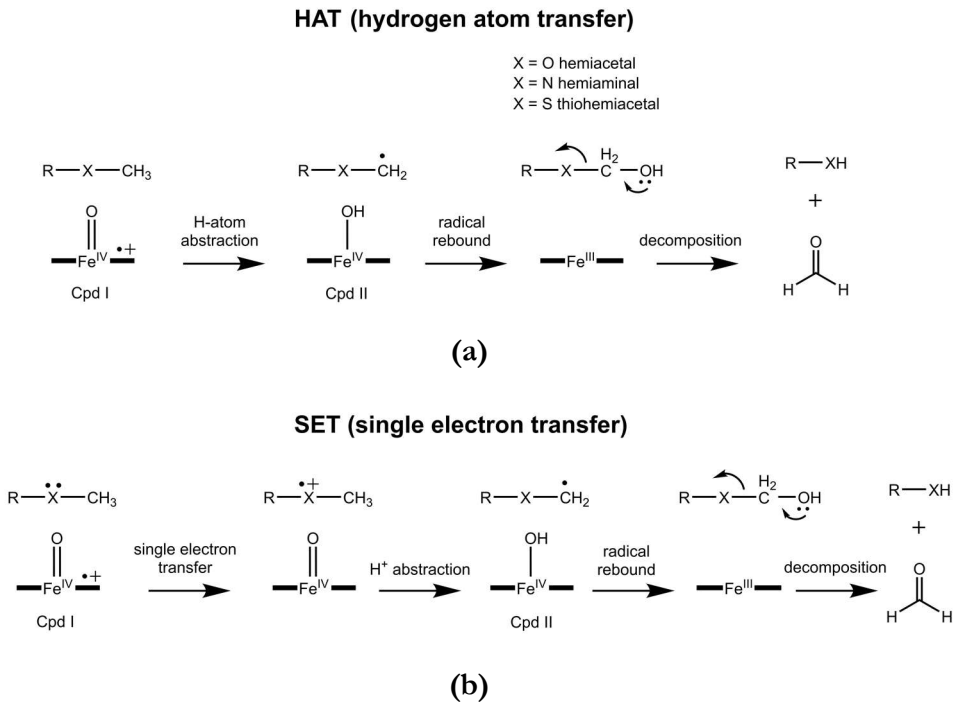

Figure 1.16. Proposed mechanisms of *N*, *O*, *S*-dealkylation (X = N, O, S).[18, 79, 192, 194, 196] **(a)** Dealkylation could be initiated by hydrogen abstraction (HAT mechanism). **(b)** Alternatively, a single electron transfer from the heteroatom to Cpd I could be the first step.

1.9.3 Sulfoxidation

N-dealkylation is a common reaction performed by P450s and *N*-oxidation is less common. *S*-dealkylation, on the other hand, is rare[82]; P450s prefer to convert sulfides into sulfoxides.[83, 117, 197-198] Multiple mechanisms for sulfoxidation have been proposed. Cpd I could abstract a single electron from the sulfur to give a sulfur radical cation; transfer of oxygen would then yield the sulfoxide. Alternatively, Cpd I could transfer the oxygen to the sulfur directly, as depicted in Figure 1.17.[18, 192]

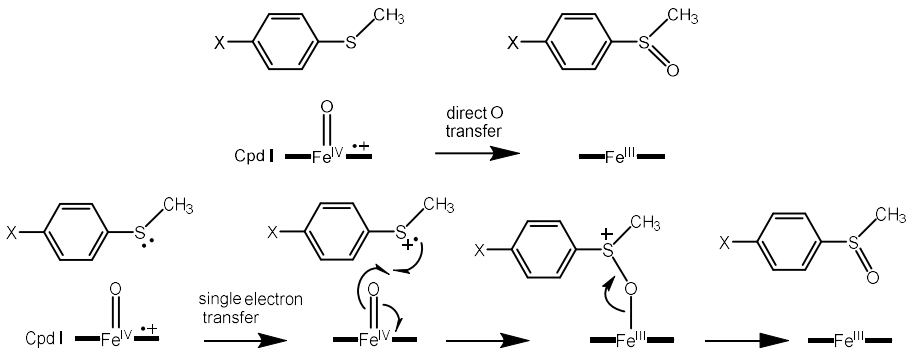

Figure 1.17. Proposed mechanisms of sulfoxidation mediated by Cpd I.[94, 118, 199]

It has been inferred that Cpd 0 may contribute to sulfoxidation or be entirely responsible for it.[123-124, 126, 192] *N*,*N*-dimethyl-4-(methylthio)aniline (Figure 1.18) can undergo sulfoxidation or *N*-dealkylation.[124] Volz *et al.* used this substrate to try to identify the active oxidant in sulfoxidation.[124] WT P450$_{BM3}$ gave a mixture of sulfoxidation and *N*-dealkylation products in a 15:1 ratio. The threonine-to-alanine mutation, expected to prevent Cpd I formation, strongly favoured sulfoxidation, increasing the ratio to 60:1.[124] This implied that the reactions were mediated by two oxidants. Cpd I presumably mediates *N*-dealkylation, while Cpd 0, which should be more abundant in the mutant enzyme, apparently mediates sulfoxidation.[124] However, calculations have indicated that Cpd 0 is a weak oxidant.[118, 126, 200] Shaik has offered multiple alternative explanations for the results of Volz *et al.*[118, 126, 134] The two different oxidants could be the two spin-states of Cpd I.[124, 126, 201] If LS and HS Cpd I mediate different reactions and the mutation altered the amounts of LS and HS Cpd I, this could lead to differing amounts of sulfoxidation and *N*-dealkylation. Another possibility is that structural changes in the enzyme's active site could have resulted in the sulfur being held closer to the heme, giving an altered ratio of sulfoxidation to *N*-dealkylation.[124, 134, 202]

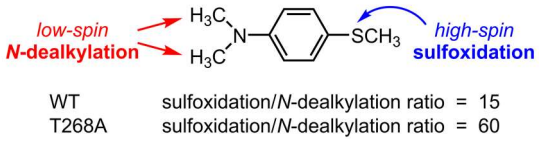

Figure 1.18. Volz *et al.* suggested that two different oxidants mediate *N*-dealkylation and sulfoxidation: Cpd 0 and Cpd I, or LS and HS Cpd I.[124]

Cryle and De Voss also propose that sulfoxidation is mediated by Cpd 0.[123] They investigated the sulfoxidation of thia fatty acids by $P450_{BM3}$ and found that the rate of sulfoxidation was not decreased whatsoever by the threonine-to-alanine mutation, implicating Cpd 0 in sulfoxidation.[123] $P450_{BM3}$ performed fatty acid hydroxylation and thia fatty acid sulfoxidation with opposite enantioselectivity, again hinting at the involvement of different oxidants (Figure 1.19).[123] However, Park *et al.* found that model ferric-hydroperoxo complexes were incapable of catalysing sulfoxidation.[203]

Shaik has subsequently proposed that the Fe^{III}–H_2O_2 complex may be the second oxidant in sulfoxidation, not Cpd 0.[118] DFT calculations revealed that the Fe^{III}–H_2O_2 species should be a competent sulfoxidation catalyst (Figure 1.20).[118] The ability of the Fe^{III}–H_2O_2 complex to mediate sulfoxidation would explain the results of Kerber *et al.*[204], who found that Fe^{III}–corrolazine together with H_2O_2 catalysed sulfoxidation, despite the authors concluding that Cpd I was not being formed.

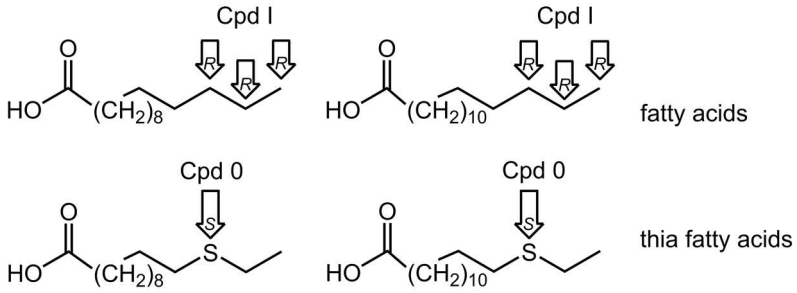

Figure 1.19. Cryle and De Voss found that $P450_{BM3}$ performed fatty acid hydroxylation and thia fatty acid sulfoxidation with opposite enantioselectivity.[123]

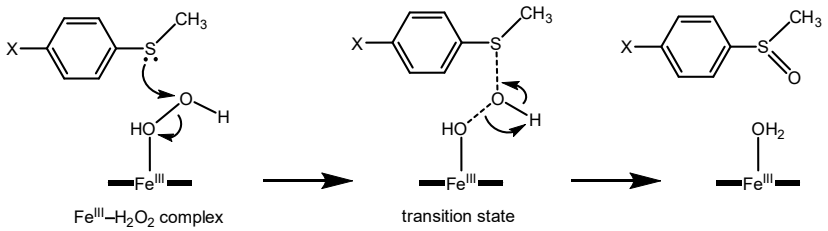

Figure 1.20. Shaik's proposed mechanism of sulfoxidation mediated by the Fe^{III}–H_2O_2 intermediate, which is a concerted asynchronous reaction.[94, 118]

1.9.4 Aldehyde oxidation

Cytochrome P450s can convert aldehydes into carboxylic acids.[205] It is debated whether this is mediated by the ferric-peroxo anion or Cpd I, and three mechanisms have been proposed.[206] As the aldehyde C-H bond is weaker than alkane C-H bonds (Table 1.1), aldehyde oxidation could proceed readily via the normal hydroxylation mechanism.[206] In this mechanism, Cpd I abstracts the aldehyde H, subsequent radical rebound then yielding the carboxylic acid (Figure 1.21a).[205-208] DFT studies have revealed that radical rebound is barrier-free for both the LS (doublet) and HS (quartet) states.[207, 209] Aldehydes react with water to form hydrates so there is the potential for the enzyme to react with this hydrate.[206] In this second mechanism, H-atom abstraction from the hydrate by Cpd I followed by radical rebound gives a geminal triol.[206] Dehydration then gives the carboxylic acid (Figure 1.21b).[206] A further proposal is that nucleophilic attack by the ferric-peroxo anion could lead to aldehyde oxidation to the acid (Figure 1.21c).[18, 119, 206]

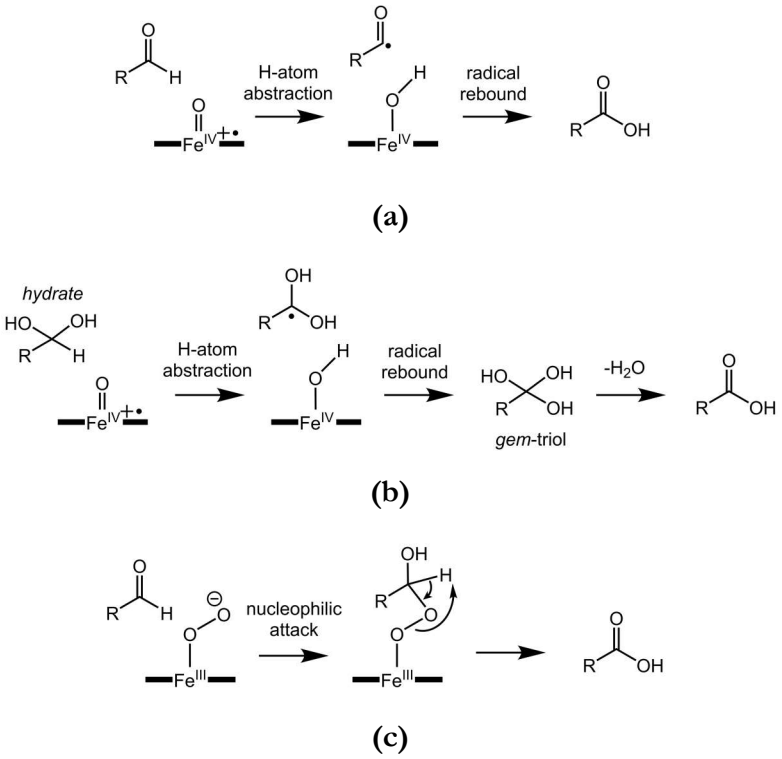

Figure 1.21. Three proposed mechanisms of aldehyde oxidation to the carboxylic acid involving Cpd I **(a, b)** or the ferric-peroxo anion **(c)**.[18, 206]

Experiments designed to identify the active oxidant in aldehyde oxidation yielded conflicting results. Raner *et al.* found that the threonine-to-alanine mutation strongly impaired CYP2B4's ability to convert aldehydes into carboxylic acids,[210] implicating Cpd I in aldehyde oxidation.[119] On the other hand, mutating the conserved threonine of CYP260B1 to alanine had minimal impact on the enzyme's ability to oxidise cinnamaldehyde to cinnamic acid, hinting at the involvement of the ferric-peroxo anion, not Cpd I.[119] Cytochromes P450 can also catalyse the deformylation of

aldehydes, a reaction believed to be mediated by the nucleophilic ferric-peroxo anion (Figure 1.22).[120, 211]

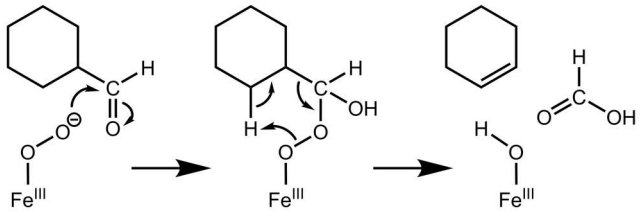

Figure 1.22. Proposed mechanism of aldehyde deformylation.[191]

1.9.5 Epoxidation

P450s metabolise olefins predominantly to epoxides, but are also known to form aldehyde rearrangement products and 'suicide complexes', in which the enzyme is permanently inactivated.[79, 193] That the epoxidation reaction is not concerted is inferred from the fact that these by-products are not generated by incubation of P450s with epoxides.[182] Figure 1.23a illustrates the proposed mechanism of epoxidation by Cpd I.[79]

According to the TSR theory, epoxidation via the doublet pathway occurs with barrierless ring closure, and therefore rearrangement products do not form. Conversely, on the quartet pathway, there *is* a barrier, enabling by-products to form.[79]

There is experimental evidence that implies that Cpd 0 is involved in epoxidation,[33, 121] though its involvement is unproven and controversial.[94] Figure 1.23b shows this mechanism.[121]

Vaz *et al.* inferred that Cpd 0 mediated epoxidation based on their observation that substituting the conserved threonine in CYP2E1 with alanine substantially *accelerated* the rate of alkene epoxidation.[121] More recently, Kim *et al.* argued that the epoxidation of 4,5-desepoxypimaricin by P450 PimD (CYP161A2) is mediated solely by Cpd 0, not Cpd I.[122] In the crystal structure of pimaricin-bound CYP161A2, the alkene is not suitably positioned to react with Cpd I but is appropriately placed to react with the distal oxygen of Cpd 0.[122] The enzyme was capable of utilising H_2O_2 to perform the epoxidation reaction, but no epoxidation occurred when iodosylbenzene or peracetic acid were used as oxygen donors, which are assumed to generate Cpd I but not Cpd 0. This was interpreted as evidence that Cpd 0 is the active epoxidising agent.[122]

Jin *et al.* found that the T252A variant of $P450_{cam}$ could still epoxidise the alkene group in 5-methylenylcamphor despite its inability to hydroxylate camphor (a Cpd I-mediated reaction), implying that Cpd 0 must mediate epoxidation.[33] However, it has been concluded from the results of DFT studies that Cpd 0 has high barriers to epoxidation so it is not expected to participate.[212] Shaik has argued that the above alkene, being bulky, can prevent loss of H_2O_2 from the active site of $P450_{cam}$, allowing formation of Cpd I via an alternative route.[213] Park *et al.* also demonstrated that model ferric-hydroperoxo complexes did not catalyse epoxidation.[203]

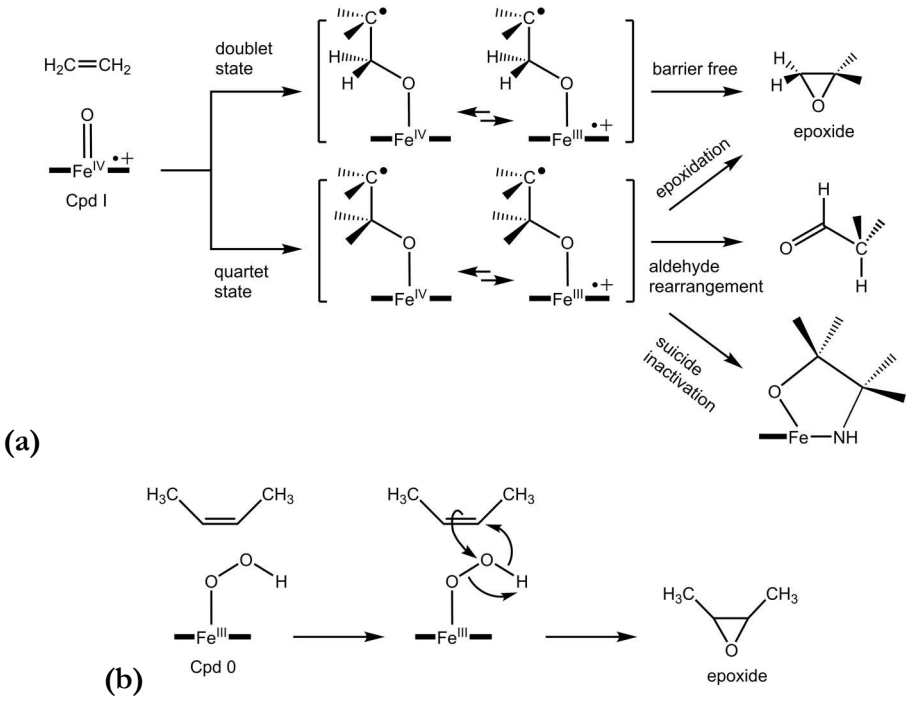

Figure 1.23. **(a)** Mechanism of olefin epoxidation by Cpd I.[79] **(b)** Concerted epoxidation mechanism involving Cpd 0.[121]

1.9.6 Alkyne oxidation

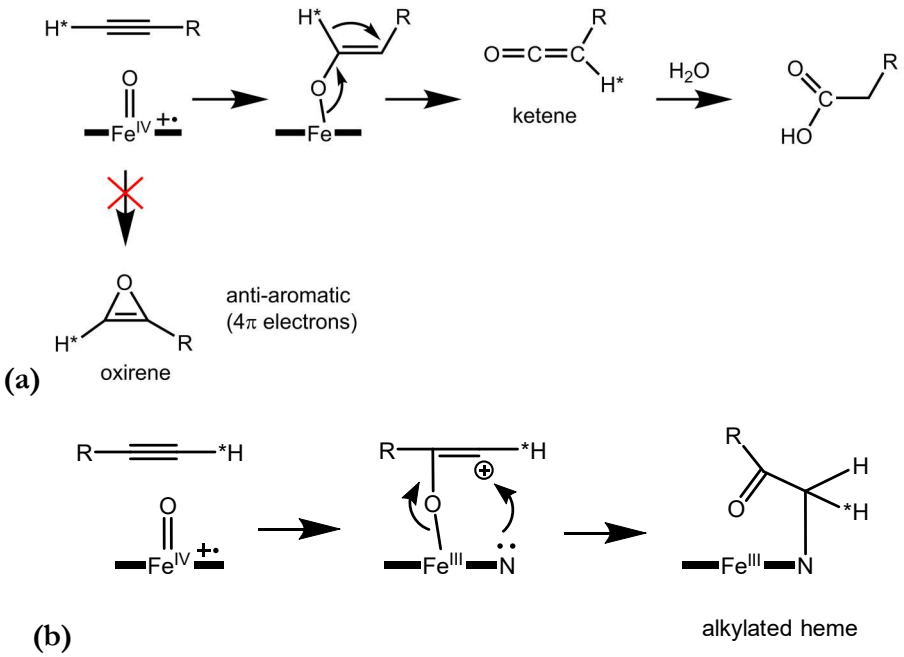

Figure 1.24. Mechanism of **(a)** alkyne oxidation and **(b)** P450 inactivation by terminal acetylenes.[214]

P450s convert terminal alkynes (acetylenes) into carboxylic acids. The proposed mechanism is shown in Figure 1.24a.[79] This involves initial formation of a ketene followed by hydrolysis giving the carboxylic acid.[79] Hypothetically, the enzyme could convert the alkyne into an oxirene, though this is thought not to occur as oxirenes are strained and anti-aromatic.[79, 215] Another reaction that can occur is alkylation of the heme which inactivates the P450 (Figure 1.24b).[79, 102, 214-215]

1.9.7 Desaturation

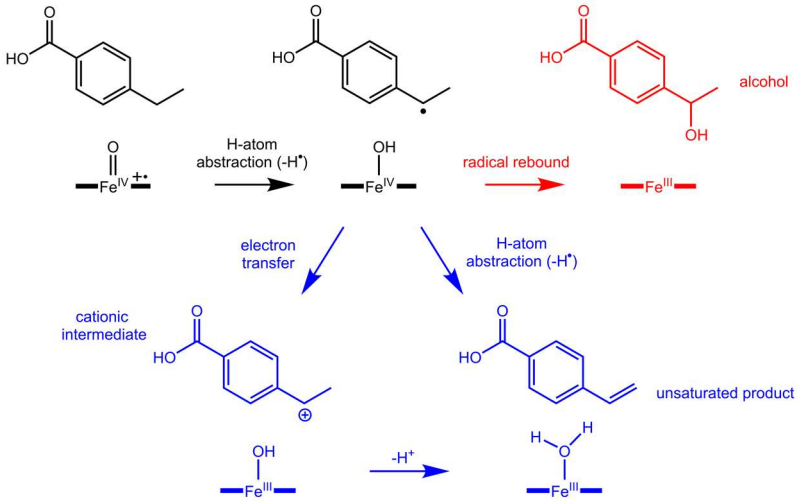

Figure 1.25. Proposed desaturation mechanisms (blue pathways)

P450s can catalyse the desaturation of alkanes[216], a reaction not as common as hydroxylation and first incorrectly thought to arise from dehydration of hydroxylated products. [217-218] When desaturation occurs, hydroxylated products are frequently also formed, these commonly being the major metabolites.[18, 217] There are some cases, though, where only the desaturated metabolite is formed; the Phe185Ile mutant of CYP199A4 converts 4-ethylbenzoic acid exclusively into the desaturation product 4-vinylbenzoic acid.[219] The proportions of hydroxylation and desaturation products can vary, with CYP4B1 and CYP2B1 both metabolising valproic acid but giving dramatically different ratios of hydroxylation to desaturation.[217]

Desaturation could occur by two possible mechanisms after H-atom abstraction by Cpd I, provided that radical rebound does not happen first to give the alcohol (Figure 1.25).[79, 219] One possibility is that Cpd II (Fe^{IV}–OH) abstracts a second hydrogen atom (H·), if two C-H bonds are close to the heme, to yield the desaturated product. If the substrate is oriented in the active site such that it hinders radical rebound[219], an electron could be removed from the substrate radical to yield a carbocation, followed by removal of a proton (H^+) by Fe^{III}–OH to give the desaturated product.

1.10 Converting P450s into peroxygenases through protein engineering

Although P450s are appealing catalysts, they have qualities that hinder their use in industrial applications,[62] such as their requirement for NAD(P)H and electron transfer proteins.[113] The exorbitant cost of NAD(P)H is a major obstacle to the use of P450s in industry.[62] NADPH costs 215 000 US dollars per mole (0.74 kg).[220-221] NADH is also expensive but less so than NADPH, costing 3000 US dollars per mole.[220] The cost makes it unfeasible to use NAD(P)H in stoichiometric amounts. If a whole-cell system is used, the cells supply the NAD(P)H.[62] However, there are disadvantages to using a whole-cell system.[222] The substrate may be toxic or not enter the cells, and undesirable side-products may be generated by other enzymes in the cells,[223-224] making it preferable to use the purified enzyme although this means that NAD(P)H must now be supplied. Methods of recycling NAD(P)H exist which can reduce the cost of using these cofactors.[220, 225] However, the use of an NAD(P)H regeneration method (such as an enzyme that converts $NAD(P)^+$ back into NAD(P)H) may be undesirable because it complicates the system, requires extra expense, produces waste products and product isolation may be problematic.[220, 225] A further limitation may be the poor stability/activity of the cofactor-regenerating enzyme.[220, 225]

As stated earlier, the requirement for NAD(P)H can be avoided by instead using H_2O_2. It has the advantage of being inexpensive, 50% H_2O_2 having a price of only 450 US dollars per tonne.[226] P450s could viably be used in the synthesis of commercial products if H_2O_2 was substituted for NAD(P)H.[227] P450s, however, are not efficient peroxygenases and H_2O_2 is destructive. It can destroy the heme and also oxidise the cysteine ligand, abolishing the enzyme's activity.[228] They can, however, be engineered to utilise H_2O_2 more effectively.[54, 227]

Mutation of Phe87 to Ala or Gly was found to enable $P450_{BM3}$ to utilise H_2O_2, whereas the WT enzyme could not.[229-230] For example, the rate of H_2O_2-driven oxidation of *p*-nitrophenoxydodecanoic acid (12-pNCA) catalysed by the F87A mutant was 162 min^{-1}, while WT $P450_{BM3}$ had negligible activity.[229] Cirino and Arnold found that the F87A mutant was also able to use H_2O_2 to oxidise myristic, lauric and capric acid with higher activity than the WT enzyme, although the product formation rates did not compare favourably to those of the NADPH-driven reactions.[230] Cirino and Arnold proceeded to develop mutants with further improved peroxygenase activity; the mutant dubbed '21B3' oxidised 12-pNCA at a rate of 800 min^{-1} and oxidised fatty acids more efficiently than the F87A mutant.[112] Nevertheless, it was highly susceptible to destruction by H_2O_2, failing to produce product beyond 5 minutes in 10 mM H_2O_2.[112] Directed evolution also improved the heat tolerance of the '21B3' mutant.[231] Additionally, Cirino *et al.* reported that the ability of $P450_{BM3}$ to use H_2O_2 could be enhanced by mutation of all methionine residues to norleucine, though the reason for this improvement remains unclear.[232] In 1999, Joo *et al.* reported that they had engineered $P450_{cam}$ by random mutagenesis to use H_2O_2 to oxidise naphthalene,[54] but doubt was cast over their results when the purified mutants were later shown to have negligible activity.[233]

Heme enzymes exist which *do* utilise H_2O_2 efficiently: chloroperoxidase (CPO), aromatic peroxygenase (APO), cytochrome *c* peroxidase (C*c*P), catalase, dye-decolourising peroxidase (*Aau*DyP) and others.[234] A characteristic feature of these H_2O_2-dependent heme proteins that is absent from P450s is the presence of an acid-base residue (histidine, aspartate or glutamate) above the heme (Figure 1.26).[234] This residue is thought to facilitate Cpd I generation using H_2O_2.[234-235] In HRP, this residue is His42 and in C*c*P it is His52, whereas in CPO the acid-base residue is Glu183. The essential role of these residues was emphasised by mutagenesis studies; when His52 in C*c*P was mutated to leucine, the rate of Cpd I formation decreased by a factor of 10^5.[236] Similarly, upon mutation of His42 in HRP to alanine, a 10^6-fold decrease in the rate of Cpd I formation was observed.[237] Such a substantial decrease in activity was not observed when His42 was replaced with glutamate, however, demonstrating that Glu also acts as an acid-base catalyst.[238-239] The mechanism by which the histidine, glutamate or aspartate residue facilitates Cpd I formation, offered by Poulos and Kraut,[240] is illustrated in Figure 1.26f. After H_2O_2 binds to the heme iron, becoming more acidic,[241-242] the acid-base residue is expected to first deprotonate the proximal oxygen to yield Cpd 0 (Fe^{III}–OOH).[235] This residue then protonates the distal oxygen to give Fe^{III}–O–OH_2^+, which converts into Cpd I.[235] As no acid-base residue exists in a suitable position in the active site of P450s, this explains their inability to utilise H_2O_2 efficiently.[234] The conserved threonine would not act as a general acid-base catalyst.[234]

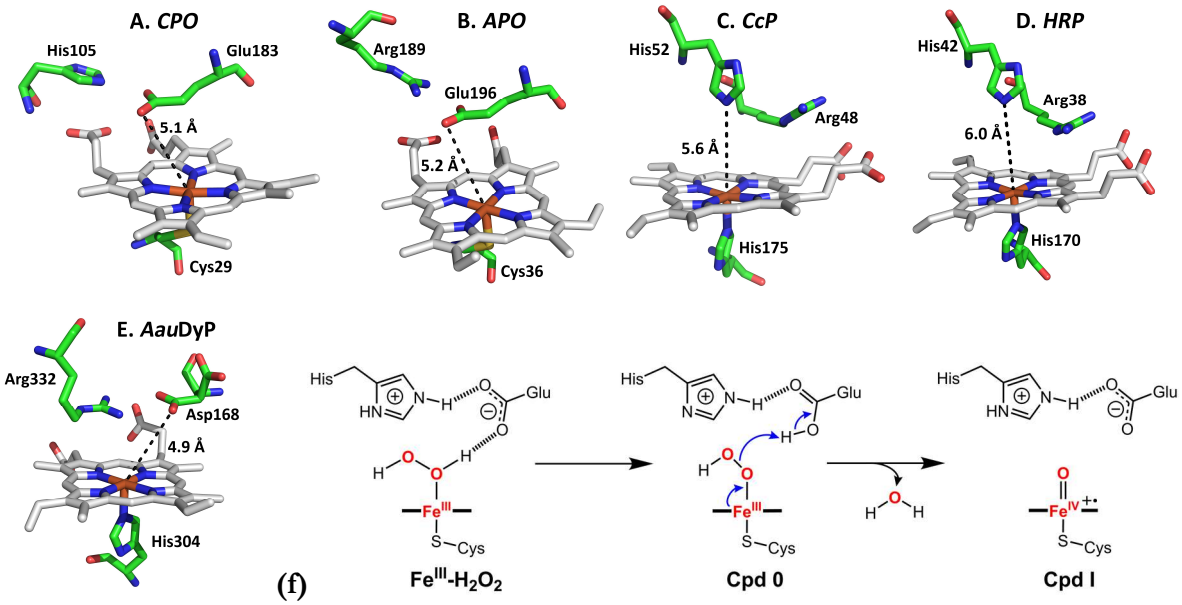

Figure 1.26. Crystal structures of H_2O_2-utilising enzymes: (**a**) chloroperoxidase (PDB ID: 1CPO), (**b**) aromatic peroxygenase (PDB: 2YPI), (**c**) cytochrome *c* peroxidase (PDB: 1CCA), (**d**) horseradish peroxidase (PDB: 1ATJ) and (**e**) dye-decolourising peroxidase (PDB: 4AU9).[234, 243] (**f**) Proposed mechanism of Cpd I generation in chloroperoxidase (CPO).[235]

Despite P450s having no acid-base residues suitably located in the active site, a minority of P450s, belonging to the CYP152 family, do effectively utilise H_2O_2.[234] $P450_{SP\alpha}$ (CYP152B1), $P450_{BS\beta}$ (CYP152A1), $P450_{CLA}$ (CYP152A2), CYP152K6, $P450_{Exa}$ (CYP152N1) and P450 $OleT_{JE}$

(CYP152L1), which metabolise fatty acids, are six P450 peroxygenases.[234, 244-246] $P450_{BS\beta}$, for example, metabolises myristic acid using H_2O_2 at a rate of 1400 min^{-1}.[247] Recently, Onoda *et al.* reported that $P450_{Ex\alpha}$ hydroxylates myristic acid at an even more rapid rate (k_{cat} = 1900 min^{-1}).[245] It has been argued that P450 peroxygenases may have predated O_2-consuming P450s given that hydrogen peroxide was abundant but O_2 scarce early in Earth's history.[54, 248-249] These P450 peroxygenases exhibit high affinity for H_2O_2 (for $P450_{BS\beta}$, the K_m value for binding of H_2O_2 is 21 μM while for $P450_{SP\alpha}$ the K_m value is 72 μM), and thus operate efficiently in the presence of low H_2O_2 concentrations.[234] This eliminates the need for high H_2O_2 concentrations which would more rapidly degrade the enzyme. In contrast, the F87A mutant of $P450_{BM3}$, an enzyme which evolved to utilise NADPH rather than H_2O_2, possesses weak affinity for H_2O_2 (K_m = 24 000 μM).[229]

From crystal structures of $P450_{BS\beta}$[250], $P450_{SP\alpha}$[247] and P450 $OleT_{JE}$[251], insight was gleaned into how these P450s utilise H_2O_2 effectively. As mentioned in Section 1.4, a characteristic feature of these peroxygenase P450s is that they lack the highly conserved acid-alcohol pair present in most P450s and in its place they instead all contain an arginine (Arg) and proline (Pro).[127, 249] Mutation of this conserved arginine to alanine was found to largely abolish the activity of $P450_{BS\beta}$, implying that it has a critical role.[252] The R242A mutant bound myristic acid less tightly, k_{cat} was reduced to only 0.83 min^{-1}, and the enzyme's affinity for H_2O_2 was also dramatically reduced (K_m = 4400 μM).[252] Crystal structures explain these observations. When these enzymes bind fatty acid substrates, the fatty acid carboxylate interacts via a salt bridge with the conserved arginine (Figure 1.27a–e).[234] These interactions position the fatty acid carboxylate directly above the heme. In fact, the fatty acid carboxylate is at a similar distance from the heme as the catalytic glutamate in APO and CPO.[234] This strongly implies that the substrate carboxylate also acts as an acid-base catalyst to generate Cpd I.[234] Figure 1.27f illustrates the proposed catalytic cycle of $P450_{BS\beta}$. Compelling evidence that the carboxylate has a vital role is that these P450s oxidise fatty acid substrates only (e.g. myristic acid), failing to metabolise compounds without a terminal carboxylate.[234]

Whereas $P450_{BS\beta}$ predominantly hydroxylates fatty acids, and $P450_{SP\alpha}$ solely hydroxylates fatty acids, P450 $OleT_{JE}$ chiefly *decarboxylates* fatty acids, transforming them into alkenes with release of CO_2.[249] Figure 1.28 illustrates one of the proposed mechanisms by which P450 $OleT_{JE}$ decarboxylates fatty acids.[245, 253] Decarboxylation is thought to proceed via initial H-atom abstraction, plausibly followed by single electron transfer from the substrate radical to Cpd II to yield a carbocation which subsequently decomposes, eliminating CO_2.[254] Although $OleT_{JE}$ predominantly decarboxylates, rather than hydroxylates, fatty acid substrates, Hsieh *et al.* found that $OleT_{JE}$ was capable of hydroxylating non-native substrates.[254] With the assistance of carboxylate-containing decoy molecules that facilitate Cpd I formation, $OleT_{JE}$ hydroxylated unnatural substrates such as the radical clock substrate norcarane.[254] Their explanation for $OleT_{JE}$'s tendency to decarboxylate rather than hydroxylate fatty acid substrates is that these substrates must be fixed rigidly in the active site, preventing the substrate from rearranging into a position appropriate for radical rebound to occur.[254]

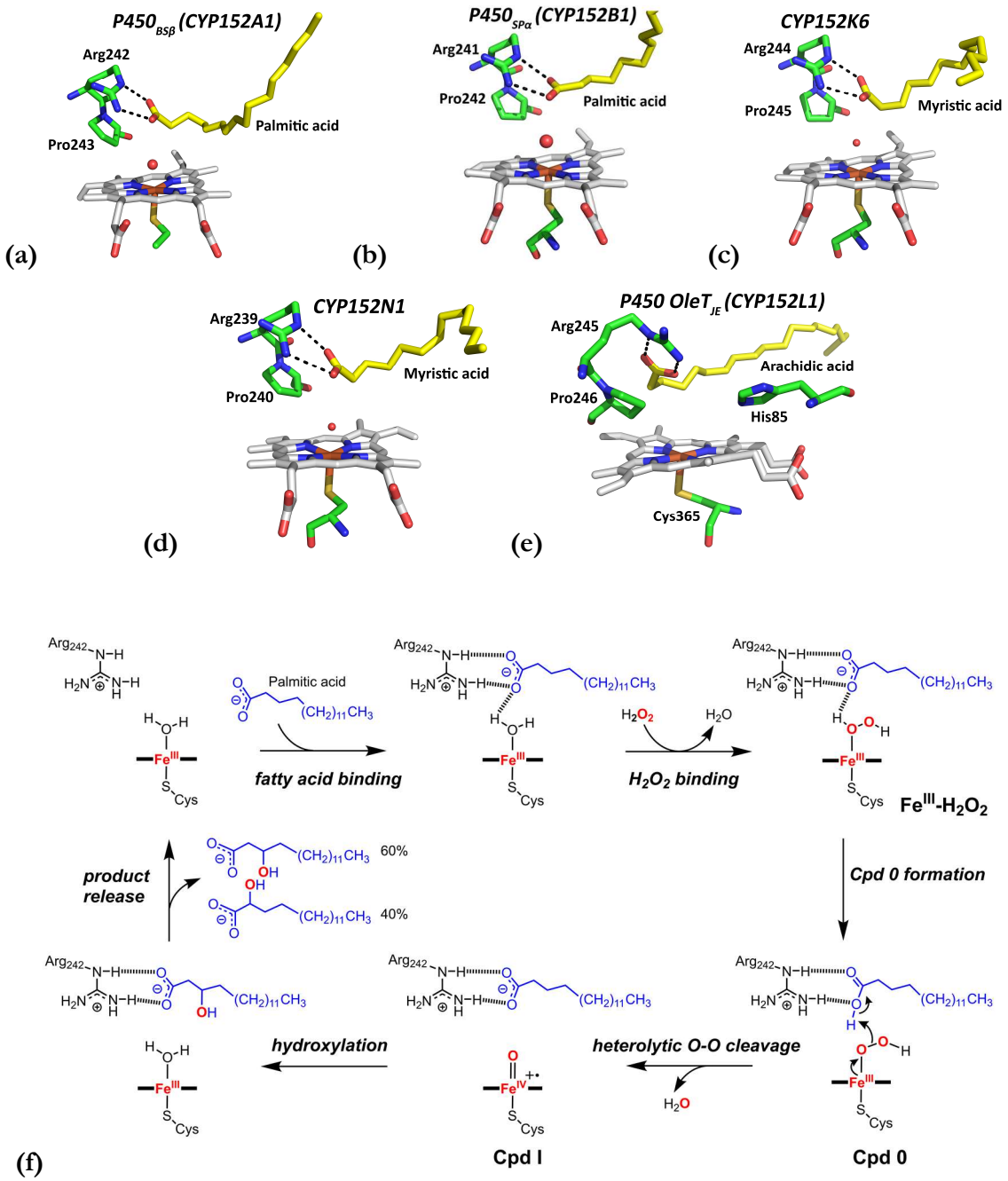

Figure 1.27. Crystal structures of **(a)** fatty acid-bound $P450_{BS\beta}$ (PDB: 1IZO), **(b)** $P450_{SP\alpha}$ (PDB: 3AWM), **(c)** CYP152K6 (PDB: 6FYJ), **(d)** CYP152N1 (PDB: 5YHJ) and **(e)** arachidic-acid bound P450 $OleT_{JE}$ (PDB: 4L40). The mechanism **(f)** by which Cpd I is assumed to be generated involves the fatty acid carboxylate as an acid-base catalyst.[255]

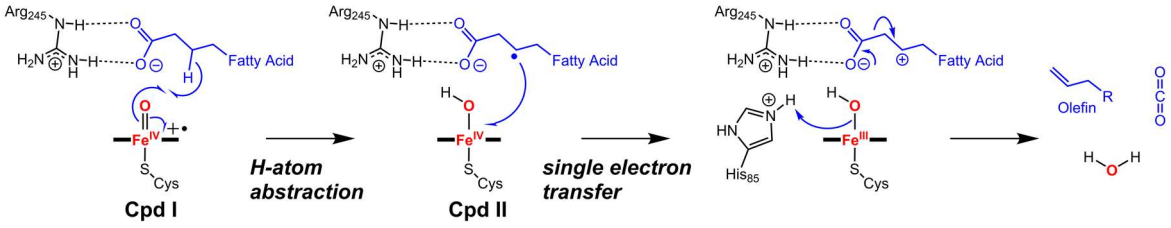

Figure 1.28. One of the proposed mechanisms by which P450 $OleT_{JE}$ decarboxylates fatty acid substrates.[245]

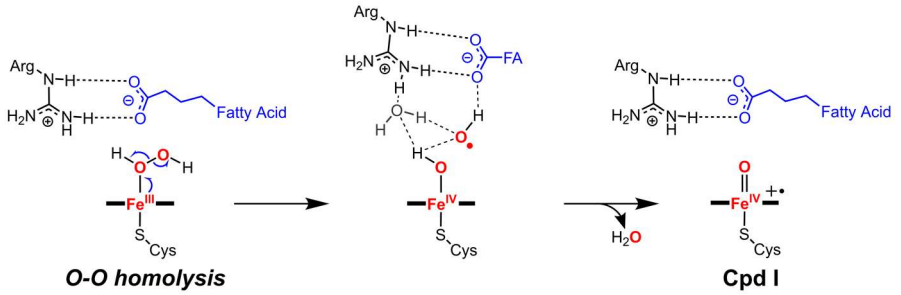

Figure 1.29. Role of the substrate carboxylate in $P450_{SP\alpha}$ Cpd I formation proposed by Shaik.[235] Others have proposed that it acts as an acid-base catalyst (Figure 1.27f).

While it has been inferred that the fatty acid carboxylate acts as a general acid-base catalyst to facilitate Cpd I formation, Shaik has proposed that Cpd I is formed via a different route.[213, 256] Rather than deprotonate the Fe^{III}–H_2O_2 complex to give Cpd 0, Shaik postulated that the fatty acid carboxylate instead stabilises the initial Fe^{III}–H_2O_2 complex. The O–O bond of this complex is then cleaved homolytically to generate a hydroxyl radical and Fe^{IV}–OH.[256] The role of the fatty acid carboxylate is to then trap the hydroxyl radical (via hydrogen bonding interactions) such that it is optimally positioned to abstract a proton from Fe^{IV}–OH to give Cpd I (Figure 1.29).[256] In this mechanism, Cpd 0 is bypassed.[256]

These P450s are not useful biocatalysts for organic synthesis given that they only oxidise fatty acids, accepting no other substrates.[227, 234, 257] Shoji *et al.* overcame this limitation by recruiting 'decoy molecules': small carboxylate-containing molecules with short carbon chains.[257] $P450_{SP\alpha}$ and $P450_{BS\beta}$ bind these decoy molecules in the active site, with the carboxylate interacting with the arginine, but do not oxidise them.[255] The decoy molecule carboxylate is thought to act as the acid-base catalyst needed for Cpd I generation.

Because these decoy molecules do not fully occupy the active site and are not themselves oxidised, unnatural substrates can enter the active site and are then oxidised.[255, 257-258] Using this approach, Shoji *et al.* were able to use $P450_{SP\alpha}$ and $P450_{BS\beta}$ to oxidise a range of non-native substrates lacking carboxylate groups such as styrene, ethylbenzene and thioanisole.[258-260] Without decoy molecules, the P450s did not oxidise these substrates. At high concentrations, acetic acid could also be used successfully as a decoy molecule.[261] Furthermore, chiral decoy molecules could be used to influence the stereochemistry of the product.[260] For example, chiral decoy molecules manipulated the enantioselectivity of styrene epoxidation by $P450_{SP\alpha}$ (Figure 1.30a,c). Using (*R*)-ibuprofen as the decoy molecule yielded (*S*)-styrene oxide in 63% ee, while use of (*S*)-ibuprofen gave a small excess of (*R*)-styrene oxide.[260]

Shoji *et al.* also succeeded in using $P450_{SP\alpha}$ to oxidise unnatural substrates *without* decoy molecules.[227] To do this, they placed a carboxylate above the heme by mutation of an alanine residue to glutamate (Figure 1.30b).[227] The A245E mutant efficiently catalysed styrene epoxidation using H_2O_2 (k_{cat} = 280 min^{-1}).[227] Shoji *et al.* also prepared mutants of $P450_{cam}$, $P450_{BM3}$ and CPY119 in which the conserved active-site threonine was replaced with glutamate.[227] The WT enzymes had essentially no peroxygenase activity but this mutation enabled the use of H_2O_2.[227] Notably, the

T268E mutant of $P450_{BM3}$ epoxidised styrene in the presence of 60 mM H_2O_2 at a rate of 110 min^{-1}.[227] Based on these results, Shoji *et al.* have predicted that introducing a carboxylate near the heme by mutation of the conserved threonine to glutamate should allow any P450 to operate using H_2O_2 instead of NAD(P)H/O_2.[227]

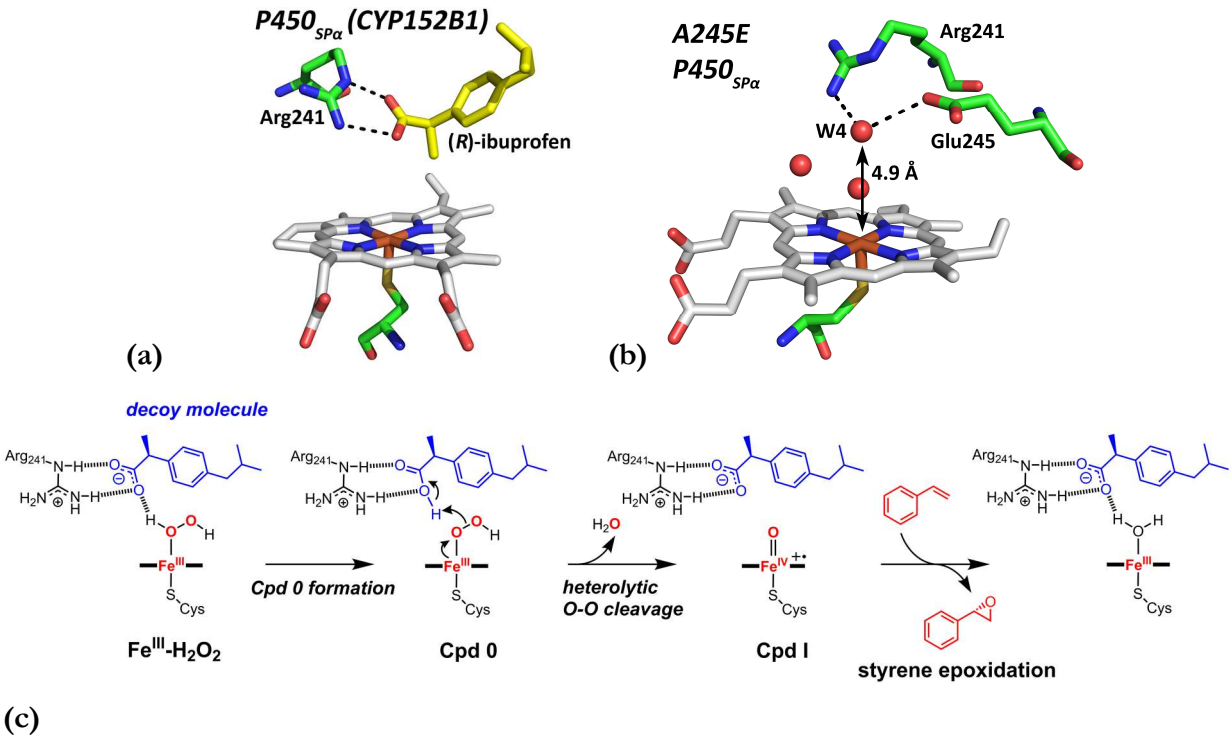

Figure 1.30. Crystal structures of **(a)** $P450_{SP\alpha}$ with the decoy molecule (*R*)-ibuprofen bound (PDB ID: 3VM4) and **(b)** the A245E mutant of $P450_{SP\alpha}$ (PDB ID: 3VOO). A water (W4) is thought to act as the general acid-base catalyst to facilitate Cpd I formation.[227] **(c)** Use of (*R*)-ibuprofen as a decoy molecule.[260]

To address the issue of fast P450 degradation by H_2O_2, P450s could be engineered by directed evolution to be less susceptible to inactivation when exposed to H_2O_2.[232] Cherry *et al.* succeeded in using directed evolution to improve the hydrogen peroxide stability of a fungal peroxidase by a factor of 100.[262] Because methionine oxidation may lead to loss of enzyme activity, Cirino *et al.* aimed to improve the H_2O_2 tolerance of $P450_{BM3}$ by replacing all methionine residues with norleucine.[232] This, however, failed to improve the H_2O_2 stability of $P450_{BM3}$.

Rapid destruction can be avoided by exposing the P450 biocatalyst to only low levels of H_2O_2. The enzyme would be inactivated less rapidly if small quantities of H_2O_2 were supplied and continuously replenished than if a large quantity of H_2O_2 were added all-at-once at the start of the reaction.[263-270] Seelbach *et al.* demonstrated that chloroperoxidase (CPO) remained active for longer (and the product yield was increased) when the H_2O_2 concentration was held at a steady, low level (50 μM) by using a sensor to monitor the H_2O_2 level and replenish it as required.[268, 271] Munro and co-workers used an alternate strategy to supply low levels of H_2O_2 to a P450: they fused a H_2O_2-generating enzyme (alditol oxidase) to P450 $OleT_{JE}$.[264] Gandomkar *et al.* similarly used a H_2O_2-

generating enzyme (α-hydroxyacid oxidase (α-HAO)) to continuously replenish the H_2O_2 consumed by $P450_{CLA}$ (Figure 1.31).[265]

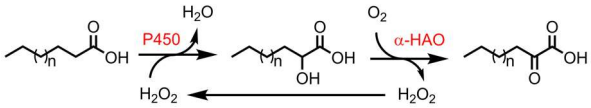

Figure 1.31. Gandomkar *et al.* used α-hydroxyacid oxidase (α-HAO) to replenish H_2O_2 consumed by $P450_{CLA}$ to maintain low H_2O_2 levels.[265]

Zhang *et al.* recently demonstrated that an Au-loaded TiO_2 photocatalyst could be used to supply a peroxygenase enzyme with low levels of H_2O_2.[263] This catalyst oxidises water and uses the electrons to reduce O_2 to H_2O_2.[263] FAD and FMN have also been used as photocatalysts to generate H_2O_2 *in situ* (Figure 1.32).[272-273] Following light excitation, flavin oxidises EDTA (ethylenediaminetetraacetic acid) and the reduced flavin converts O_2 into H_2O_2.[272]

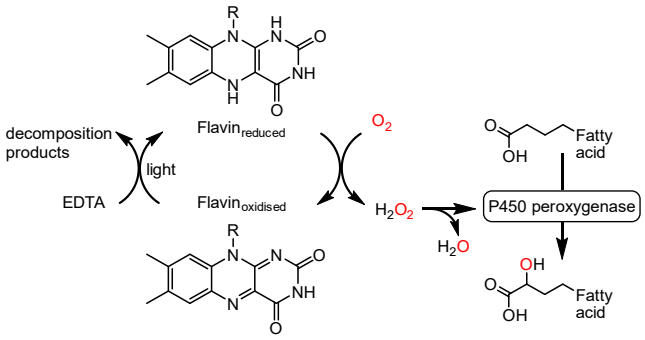

Figure 1.32. Urlacher *et al.* used FAD or FMN as photocatalysts to generate H_2O_2 to drive P450 reactions.[272]

In summary, P450s would be more widely embraced as industrial catalysts if they could be engineered to efficiently utilise H_2O_2 (without being rapidly inactivated by the peroxide).

1.11 CYP199A4 from *Rhodopseudomonas palustris* HaA2

CYP199A4 is a P450 from the bacterium *Rhodospeudomonas palustris* HaA2 that displays high catalytic activity. It has a narrow substrate range, preferring to oxidise *para*-substituted benzoic acids such as 4-methoxybenzoic acid, which it binds tightly (K_d = 0.28 μM).[117, 162, 219] This substrate induces a >95% spin-state shift and is converted by the enzyme into 4-hydroxybenzoic acid at the rapid rate of 1220 min^{-1}.[117] In nature, the role of CYP199A4 may be to degrade aromatic acids so that they can be used as a carbon source by *Rhodopseudomonas palustris* for growth.[274]

CYP199A4 could be exploited as a biocatalyst.[117] It can produce the flavouring vanillic acid by demethylating 3,4-dimethoxybenzoic acid at the *para* position,[137] and oxidises cinnamic acid derivatives which have medicinal properties.[275] This enzyme is readily crystallised and has been extensively studied by X-ray crystallography to elucidate the binding mode of substrates and rationalise its activity (Figure 1.33).[29, 117, 219]

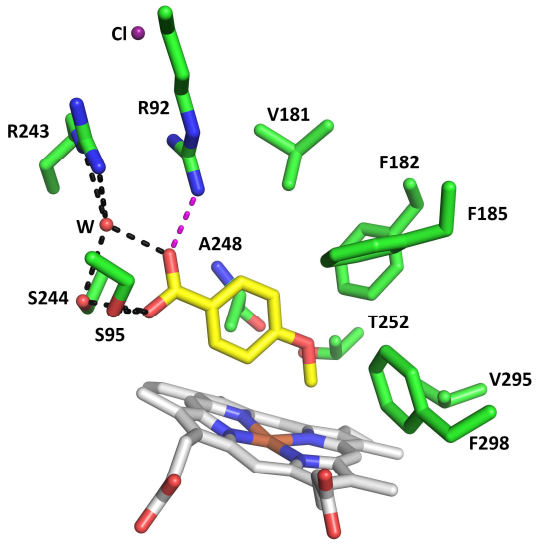

Figure 1.33. 4-Methoxybenzoic acid bound in the active site of CYP199A4 (PDB code: 4DO1). 4-Methoxybenzoic acid is in yellow and the chloride ion in purple. The water molecule interacting with 4-methoxybenzoic acid is shown as a red sphere. Hydrogen bonds are represented by black dashed lines and a salt bridge by a pink dashed line.

CYP199A4 has been studied as a model system to investigate the mechanism of P450 reactions.[276-277] The use of *para*-substituted benzoic acid substrates with different functional groups, such as ethyl, methoxy, methylthio, vinyl, ethynyl and formyl groups, allows a variety of P450 reactions to be studied. These reactions are hydroxylation, *O*-dealkylation, sulfoxidation, epoxidation, acetylene oxidation and aldehyde oxidation (Section 1.9). By comparing the activity of WT CYP199A4 to that of the acid-alcohol pair mutants (the T252A and D251N mutants), the involvement of more than one oxidant in P450 reactions can be investigated.[276]

1.12 Thesis aims

Initially, the substrate range of CYP199A4 will be explored. CYP199A4 is known to oxidise *para*-substituted benzoic acid substrates, such as 4-methoxy-, 4-methylthio- and 4-methylamino-benzoic acid, but not 3-methoxybenzoic acid. The activity of CYP199A4 towards *meta*-substituted benzoic acids other than 3-methoxybenzoic acid has never been tested and will be explored in Chapter 3. Docking and X-ray crystallography will be used to identify the binding mode of these *meta*-substituted benzoic acids. This will allow the enzyme's strong preference for *para*- over *meta*-substituted benzoic acid substrates to be rationalised. These results will yield insight into the requirements for efficient catalysis to occur.

In Chapter 4, the binding modes of three nitrogen ligands which induce different type II spectra will be investigated. X-ray crystal structures of CYP199A4 in complex with these inhibitors will be solved and other experiments, including CW and HYSCORE EPR, will be performed to rationalise the different optical spectra that these ligands induce. This chapter will seek to determine whether optical spectroscopy can distinguish between type II ligands that form a direct Fe-N bond with the heme iron and those which have alternative binding modes.

In Chapter 5, the structure of the T252E mutant of CYP199A4 in complex with 4-methoxybenzoic acid will be elucidated by X-ray crystallography. Enzyme activity assays will be performed to assess whether the T252E mutant retains any ability to use NADH/O_2 to drive catalysis. Its tolerance towards H_2O_2 and its ability to utilise H_2O_2 to drive 4-methoxybenzoic acid *O*-demethylation will then be explored to establish whether this mutant is an efficient peroxygenase. Its peroxygenase activity will be compared to that of the WT enzyme and its substrate binding properties will be investigated.

In Chapter 6, the activity of the T252E mutant towards different P450 reaction types (sulfoxidation, aldehyde oxidation, olefin epoxidation, alkyne oxidation, *O*-dealkylation and hydroxylation/desaturation) will be studied. Both NADH- and H_2O_2-supported reactions will be performed with the T252E mutant, WT enzyme and D251N and T252A mutants, and the enantioselectivity will be measured. By comparing the activity of the T252E mutant, WT enzyme and T252A and D251N mutants towards these different reaction types, we can explore whether multiple oxidants participate in P450 reactions. For example, Shaik has postulated based on theoretical calculations that the Fe^{III}–H_2O_2 complex should be capable of rapidly mediating sulfoxidation.[118]

Chapter 2

Experimental

2.1 General

2.1.1 Materials

Substrates, inhibitors, reagents and derivatisation agents were purchased from Sigma-Aldrich, Tokyo Chemical Industry Co, Ltd, Fluorochem Ltd, Maybridge, Alfa Aesar, Merck Millipore, and Enamine Ltd.[ii] HPLC grade solvents, TFA and salts were from Sigma-Aldrich, Ajax Finechem and Chem-Supply. Hydrogen peroxide (30% w/w) was purchased from Chem-Supply and *t*BuOOH (70% w/w) from Sigma-Aldrich. Bovine liver catalase and HRP were supplied by Sigma-Aldrich and Astral Scientific. NADH disodium salt trihydrate was purchased from VWR International, LLC. Antibiotics (chloramphenicol, kanamycin and ampicillin) were from Gold Biotechnology (GoldBio.com) and Astral Scientific. Tris, dithiothreitol (DTT), Tween 20, lysozyme and isopropyl β-D-1-thiogalactopyranoside (IPTG) were from Astral Scientific. Crystallisation reagents and Paratone-N oil were from Hampton Research and MicroMounts, MicroLoops and MicroTools were purchased from MiTeGen, LCC. *E. coli* BL21 (DE3) competent cells were from New England Biolabs. pET28a, pETDuet and pACYCDuet vectors were from Novagen (Merck). The composition of the *E. coli* growth media and buffers is described in Table 2.1. Substrate, product and IS (internal standard) stock solutions were prepared in DMSO or EtOH. Ferredoxin reductase (HaPuR) was supplied by Associate Professor Stephen Bell.[137] HaPuR was quantified using A_{454} = 10.0 mM^{-1} cm^{-1}. WT CYP101B1 and CYP101A1 ($P450_{cam}$) were supplied by Md Raihan Sarkar and A/Prof Bell.

2.1.2 Instruments

Cells were lysed using a Vibra-Cell VC 505 ultrasonic processor (Sonics & Materials, USA) with a CV334 probe at 70% amplitude. A Cary 60 UV-Vis spectrophotometer (Agilent Technologies) coupled to a Peltier unit was used to record UV-Vis spectra and kinetic traces at 30 ± 0.5 °C; a quartz cuvette was used with a path length of 10 mm. ^{1}H NMR spectra were recorded in DMSO-d_6 at 500 MHz or 600 MHz using an Agilent Technologies 500/54 Premium Shielded spectrometer or an Oxford 600 MHz spectrometer. Analytical high-performance liquid chromatography was performed using a Kinetex XB-C18 reversed-phase liquid chromatography column (100 Å pore size, 250 × 4.6 mm, 5 μm; Phenomenex). A gradient of 0-50% or 20-95% AcCN in water (with 0.1% TFA) over 20 minutes was used to elute the samples at a rate of 1 mL

[ii]Substrates and products were all at least 95% pure.

min^{-1} and the eluate was monitored at 254 nm. The instrument used was either a Shimadzu Prominence HPLC system or an Agilent 1260 Infinity system. Preparative-scale HPLC was performed using a Kinetex EVO C18 reversed-phase column (100 Å pore size, 150 × 21.2 mm, 5 μm; Phenomenex) using a flow rate of 5 mL min^{-1}. A Lux Cellulose-1 chiral column (1000 Å pore size, 100 × 4.6 mm, 3 μm; Phenomenex) was used for enantioselective separation of chiral products. Separation was achieved by isocratic elution (15% or 20% AcCN in Milli-Q water containing 0.1% TFA) at a flow rate of 0.4-0.8 mL min^{-1}. Gas chromatography-mass spectrometry (GC-MS) was performed using a Shimadzu GC-17A gas chromatograph with a GCMS-QP5050A mass spectrometer detector in electron ionisation (EI) mode; the column used was a DB-5MS column (30 m × 0.25 mm, 0.25 μm; Agilent). The interface and injection port temperatures were set to 280 and 250 °C. For the first 3 min the column temperature was held at 120 °C and then increased to 200 °C at a rate of 5 °C min^{-1}. The column was held at this temperature for 2 min, and the temperature was then increased to 250 °C at a rate of 20 °C min^{-1}. Analysis was also performed using a Shimadzu GC-2010 gas chromatograph equipped with an autoinjector and a GCMS-QP2010S detector; the column used was again a DB-5MS UI column. The interface and injection port temperatures were held at 280 and 250 °C. The column was held at 120 °C for 3 min, and the temperature was then increased to 240 °C at a rate of 7.5 °C min^{-1} and held at 240 °C for 6 min.

2.2 Protein production and purification

Table 2.1. Composition of *E. coli* growth media and buffers

Medium or buffer	Constituents (L^{-1})
LB broth (Lennox)	Sodium chloride (5 g), Bacto yeast extract (5 g), Bacto tryptone (10 g)
Trace elements	Na_2EDTA (20.1 g), $FeCl_3.6H_2O$ (16.7 g), $CaCl_2.H_2O$ (0.74 g), $CoCl_2.6H_2O$ (0.25 g), $ZnSO_4.7H_2O$ (0.18 g), $MnSO_4.4H_2O$ (0.132 g), $CuSO_4.5H_2O$ (0.10 g)
Super optimal broth (SOB)[278]	Tryptone (20 g), yeast extract (5 g), NaCl (0.584 g), KCl (0.186 g), $MgCl_2$ (0.952 g), $MgSO_4$ (1.204 g)
Super optimal broth with catabolite repression (SOC)[278]	SOB with 20 mM glucose
LB agar	Sodium chloride (5 g), Bacto yeast extract (5 g), Bacto tryptone (10 g), Agar No. 1 (15 g)
Buffer T	50 mM Tris-HCl buffer, pH 7.4, 1 mM DTT (dithiothreitol)

2.2.1 Expression and purification of the T252E mutant and other variants of CYP199A4

pET28a plasmid DNA containing the T252E$_{CYP199A4}$ gene (100 ng) and pACYCDuet plasmid DNA containing the ferrochelatase gene (100 ng) were added to *E. coli* BL21 (DE3) competent cells (50 µL) on ice. Co-expression of ferrochelatase has been shown to improve heme incorporation into P450 proteins (Figure 2.1).[279-280] The mixture was incubated on ice for 50 min and then subjected to heat shock at 42 °C for 45 s before it was cooled on ice for 2 min. Sterilised SOC medium (200 µL) was added and the mixture was incubated at 37 °C and 180 rpm for 1 h. The bacteria were then plated on an LB agar plate containing chloramphenicol (34 mg L^{-1}) and kanamycin (30 mg L^{-1}) and incubated at 37 °C overnight (for ~20 h). The pET28a plasmid harbours a kanamycin resistance gene and the pACYCDuet plasmid a chloramphenicol resistance gene.

Colonies of the bacteria were introduced into six 750 mL volumes of LB broth containing kanamycin (30 mg L^{-1}) and chloramphenicol (34 mg L^{-1}) ($LB_{kan/cm}$) and the bacteria were incubated for ~16 h at 37 °C and 95 rpm, followed by incubation for 30 min at a reduced temperature (18 °C). Subsequently, 2% v/v EtOH and 0.02% v/v benzyl alcohol were added to induce the expression of chaperones which improve protein folding.[281-282] The medium was also supplemented with iron required for heme synthesis: 2 mM ferric ammonium citrate and 2 mL of trace elements solution (Table 2.1). The culture continued to be incubated for 30 minutes at 18 °C, after which ~30 µM IPTG (isopropyl β-D-1-thiogalactopyranoside) was added to induce protein expression. After incubating the culture for ~72 hours at 18 °C and 95 rpm, it was centrifuged (5000 *g*, 10 min, 4 °C) to collect the cell pellet (Figure 2.1), which was stored frozen at -20 °C.

Before cell lysis, the frozen cell pellet was first thawed at 30 °C and suspended in 200 mL of buffer T (Table 2.1). To extract the P450, the cells were lysed by sonication (sixty 20 s pulses) on ice with manual stirring. Between each 20 s pulse was a 40 s interval to prevent overheating. The lysate was centrifuged (35 000 *g*, 30 min, 4 °C) to separate the protein-containing supernatant from the cellular debris, which was discarded. The P450 was then isolated by precipitation with ammonium sulfate. Precipitated protein was collected by centrifugation (20 400 *g*, 15 min, 4 °C). The 0-30% fraction was discarded and the 30-60% ammonium sulfate fraction, which contained the P450, was retained and dissolved in buffer T. Ammonium sulfate was removed from the protein using a Sephadex G-25 coarse grain column (250 mm × 40 mm; GE Healthcare), with buffer T used as the eluent. The protein solution was then purified by ion-exchange chromatography using a DEAE Fast Flow Sepharose column (XK 50, 200 × 40 mm; GE Healthcare) (flow rate: 6 mL min^{-1}). A gradient elution (100-400 mM KCl in buffer T) was performed. Fractions containing the P450 were pooled and concentrated by ultrafiltration using a Vivacell 100 centrifugal concentrator with a 10 kDa molecular weight cut-off membrane (Sartorius). Salt removal was achieved using a Sephadex G-25 medium grain size-exclusion column (250 mm × 40 mm; GE Healthcare), with buffer T used as the eluent. The protein solution was concentrated to ~10 mL and ion-exchange chromatography using a Source Q column (XK26, 80 x 30 mm; GE Healthcare) was performed to

further purify the protein. A gradient of 0-160 mM KCl in buffer T was used to elute the protein at a rate of 6 mL min^{-1}. The purity of the fractions was assessed by measuring the Reinheitszahl, RZ = $Abs_{420\ nm}/Abs_{280\ nm}$, and fractions with a RZ value >1.8 were combined and concentrated to >40 μM.[iii] If the protein was still not sufficiently pure (when RZ <1.8), it was passed down a HiPrep Sephacryl S-200 HR size-exclusion column (60 cm x 16 mm; GE Healthcare). The protein was eluted using buffer T (flow rate: 1 mL min^{-1}). The concentrated protein was centrifuged at 7000 rpm for 10 min to remove particulate matter and autoclaved glycerol was added to a final concentration of 40-50% v/v. The purified protein was stored at -20 ˚C following filtration through a 0.2 μm filter to sterilise the solution. WT CYP199A4 and the T252A and D251N variants were produced by the same method except that they were not co-expressed with ferrochelatase and no ammonium ferric citrate was added to the LB medium (only trace elements). The final RZ value was >1.9 for all CYP199A4 variants. Before use, glycerol was first removed from the purified protein using a PD-10 desalting column (GE Healthcare). The extinction coefficients used to quantify the CYP199A4 isoforms are given in Section 2.3.2.

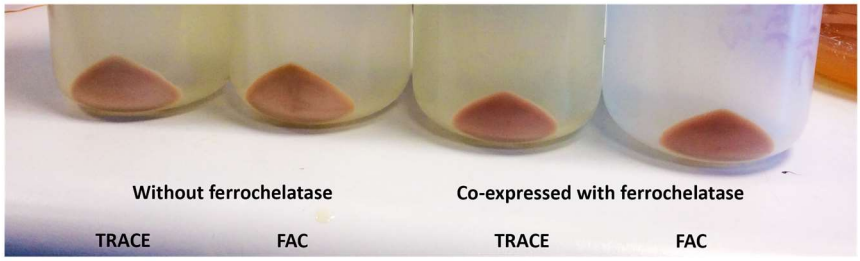

Figure 2.1. Heme incorporation into P450s can be improved by co-expression of ferrochelatase.[279] The cell pellets were noticeably redder when $T252E_{CYP199A4}$ was co-expressed with ferrochelatase (right) than when the P450 was expressed without ferrochelatase (left). In this experiment, the growth medium was supplemented with either 2 mL of trace elements (TRACE) or 2 mM ferric ammonium citrate (FAC). After this initial experiment, the $T252E_{CYP199A4}$ mutant was always co-expressed with ferrochelatase and the growth medium was supplemented with both trace elements and FAC.

2.2.2 Production and purification of HaPux ([2Fe2S] ferredoxin)

A pETDuet plasmid containing the HaPux gene (and an ampicillin resistance gene) was transformed into *E. coli* BL21 (DE3) competent cells (New England Biolabs) and the bacteria were incubated overnight at 37 ˚C on an LB agar plate containing 100 mg L^{-1} ampicillin. Colonies of the *E. coli* were introduced into seven 750 mL volumes of LB medium containing ampicillin (100 mg L^{-1}) and the bacteria were incubated for ~8 hours at 37 ˚C and 120 rpm. Subsequently, the temperature and speed of rotation were reduced to 18 ˚C and 105 rpm. After 30 minutes, 2% v/v EtOH, 0.02% v/v benzyl alcohol, 2.25 mL of trace elements solution and 1 mM ferric ammonium citrate were added. The culture was incubated for an additional 30 minutes and protein expression

[iii]Aromatic amino acids in proteins are responsible for the absorption peak at 280 nm. If the 280 nm peak is large relative to the P450 Soret peak it therefore indicates the presence of contaminating protein.[283]

was then induced by ~30 μM IPTG. The culture was incubated for 40 hours at 18 °C and 105 rpm before the bacteria were collected by centrifugation (8000 rpm, 10 min, 4 °C) and stored at -20 °C.

To extract the ferredoxin, the cell pellet was first thawed and resuspended in 200 mL of a mixture consisting of Tris-HCl buffer (10 mM, pH 7.4), 20% v/v glycerol and 2 mM DTT. To the stirred cell mixture were added 1 mg mL^{-1} lysozyme, 1% v/v Tween 20 (detergent) and 1% v/v β-mercaptoethanol and, after mixing for a 60-min period, the cells were lysed by sonication on ice for 1 h (20 s on, 40 s off). After centrifugation (40 000 *g*, 35 min, 4 °C), the cell debris was discarded and the protein solution was purified by ion-exchange chromatography using a DEAE Fast Flow Sepharose column (XK 50, 200 × 40 mm; GE Healthcare). A gradient of 200-450 mM KCl in buffer T was used to elute the ferredoxin at a rate of 6 mL min^{-1}. The pooled fractions containing HaPux were concentrated and salt was removed using a Sephadex G-25 medium grain size-exclusion column (250 mm × 40 mm; GE Healthcare), using buffer T as the eluent. The solution was again concentrated and further purified on a Source Q column (XK26, 80 x 30 mm; GE Healthcare), eluting the protein at a rate of 6 mL min^{-1} using a gradient of 0-0.5 M KCl in buffer T. Fractions containing HaPux were combined, concentrated and further purified on a HiPrep 16/60 Sephacryl S-200 HR column (GE Healthcare), using buffer T as the eluent and a flow rate of 1 mL min^{-1}. The purity was assessed by measuring the Abs_{325}/Abs_{280} ratio. Fractions with a ratio >0.49 were combined and concentrated. Autoclaved glycerol (~40-50% v/v) was added (to prevent freezing when the solution was stored at -20 °C) and the ferredoxin solution was filter-sterilised using a 0.2 μm filter. HaPux was quantified using ε_{416} = 11.2 mM^{-1} cm^{-1}.[137]

2.3 *In vitro* assays

2.3.1 CO binding assay[284-285]

The UV-Vis spectrum of a ~10-15 μM solution of the P450 (500 μL) in Tris-HCl buffer (50 mM, pH 7.4) was recorded from 250 to 700 nm. A few grains of sodium dithionite were added and the spectrum of the reduced P450 was recorded. To form the P450-CO adduct (Figure 2.2), Tris-HCl buffer (50 mM, pH 7.4; 350 μL) through which CO had been bubbled for ~10 s was added and the spectrum was recorded. If necessary, more dithionite was added to reduce the P450. If the Soret peak shifted completely to 450 nm, P450 concentration could be determined from the Fe(II)-CO versus Fe(II) difference spectrum using $\varepsilon_{450\text{-}490}$ = 91 mM^{-1} cm^{-1}.[286] The assay was repeated with 0.2 mM 4-methoxybenzoic acid added to the P450 solution.[287]

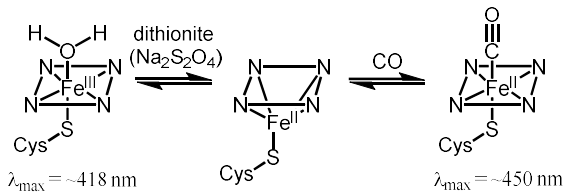

Figure 2.2. Coordination of CO to the P450 after reduction with dithionite shifts the Soret peak to ~450 nm. Inactive P450 instead absorbs at 420 nm.[284]

2.3.2 Pyridine hemochromogen assay

When the T252E$_{CYP199A4}$ enzyme was reduced with dithionite under CO, the Soret peak failed to shift completely to 450 nm. The CYP199A4 variants were therefore also quantified by the hemochromogen method.[288-289] A ~10 µM P450 solution was prepared in Tris-HCl buffer (50 mM, pH 7.4) and the UV-Vis spectrum was recorded from 250 to 700 nm. A baseline was then recorded of a 1:1 mixture of Tris-HCl buffer and a solution containing 40% pyridine, 0.2 M NaOH and 500 µM $K_3[Fe(CN)_6]$. To 500 µL of the P450 solution was then added 500 µL of the solution containing 40% pyridine, 0.2 M NaOH and 500 µM $K_3[Fe(CN)_6]$ and the UV-Vis spectrum was recorded. To form reduced pyridine hemochromogen, 10 µL of 0.5 M $Na_2S_2O_4$ in 0.5 M aqueous NaOH was then added (Figure 2.3). Spectra were recorded until the intensity of the peak at 557 nm failed to increase further and heme was then quantified using ε_{557} = 34.7 mM^{-1} cm^{-1} (Figure 2.4). Once the P450 concentration was known, the extinction coefficient of the Soret band (ε_{419}) was calculated for the native P450 using Beer's law. The extinction coefficient was measured eight times for each CYP199A4 isoform and is reported in Table 2.2.

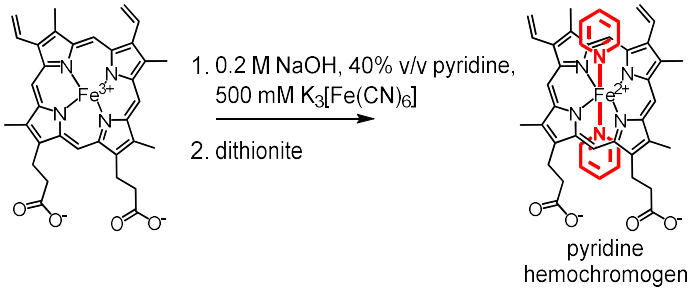

Figure 2.3. Formation of pyridine hemochromogen by treating dithionite-reduced P450s with alkaline pyridine.

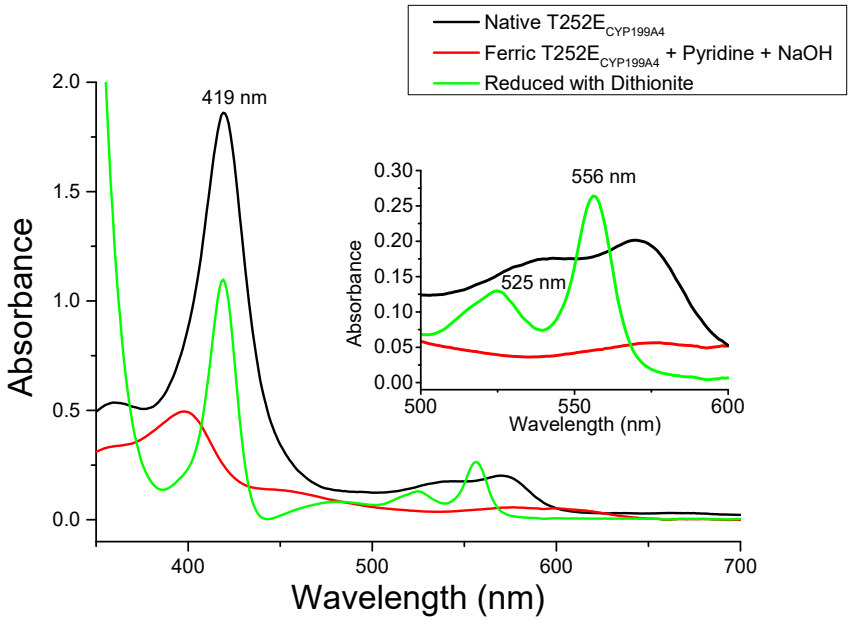

Figure 2.4. UV-Vis spectra of native T252E$_{CYP199A4}$ in Tris-HCl buffer (black), oxidised pyridine hemochromogen (red) and reduced pyridine hemochromogen (green). [Heme] was determined from the intensity of the peak at ~557 nm in the spectrum of reduced pyridine hemochromogen using ε_{557} = 34.7 mM^{-1} cm^{-1}.

Table 2.2. Extinction coefficients of CYP199A4 isoforms determined by the hemochromogen method. Values given are the mean ± SD, with n = 8.

CYP199A4 variant	Extinction coefficient (ε_{419} / mM^{-1} cm^{-1})
WT†	125 ± 3
T252E	119 ± 2
T252A	120 ± 4
D251N	122.8 ± 0.6

†The extinction coefficient determined from the CO binding assay (Section 2.3.1) was 122.6 mM^{-1} cm^{-1} and the literature value for WT CYP199A4 is 119 mM^{-1} cm^{-1}.[137]

2.3.3 Spin-state shifts

Binding of a substrate typically displaces the heme-bound water shifting the heme iron from LS (λ_{max} = ~418 nm) to HS (λ_{max} = ~390 nm).[74, 101, 173] Some substrates shift the spin-state fully to HS, whereas others only induce a partial shift.[101] To measure the spin-state shift, 1 µL aliquots of a 100 mM substrate stock solution in EtOH or DMSO were successively added to 500 µL of ~1 µM P450 in Tris-HCl buffer (50 mM, pH 7.4), recording the UV-Vis spectrum after each addition, until there was no further shift. The fraction of the P450 enzyme in the high-spin state (% HS) was estimated by visually comparing the spectrum of the substrate-bound enzyme to a series of spectra of $P450_{cam}$ which show varying percentages of HS and LS enzyme (Figure 2.5).[219]

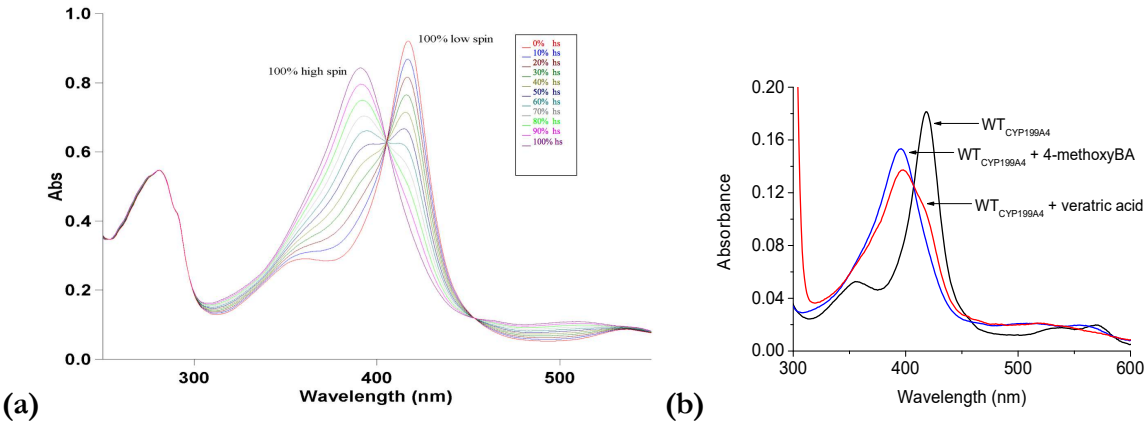

Figure 2.5. **(a)** Spectra of $P450_{cam}$. The spectrum of ~100% HS $P450_{cam}$ is that of camphor-bound $P450_{cam}$ and the ~0% HS spectrum is that of substrate-free $P450_{cam}$, the other spectra being sums of different percentages of these two spectra.[219] **(b)** Examples of substrate-induced spin-state shifts. 4-Methoxybenzoic acid induces a ≥95% spin-state shift when it binds to CYP199A4 (blue), while veratric acid induces a 70% spin-state shift (red).[137]

2.3.4 Binding constant analysis

Titrations were performed to determine substrate binding affinity (K_d) (Figure 2.6).[283] Using a UV-Vis spectrophotometer, a baseline was recorded of 2.5 mL of ~2 μM P450 in Tris-HCl buffer (50 mM, pH 7.4). Aliquots (0.5-5 μL) of 1, 10, or 100 mM substrate stock solutions in EtOH/DMSO were then added using a 5 μL Hamilton syringe. After each addition of substrate, the difference spectrum was recorded from 300 to 600 nm. Binding of a substrate induces a type I difference spectrum with a peak at ~390 nm and trough at ~420 nm (or, for inhibitors, a type II difference spectrum with a peak at 425–440 and trough at <415 nm).[153] Aliquots were added until no further spectral shift occurred and no more than 10 μL of each stock was added to avoid diluting the enzyme. Titrations were performed in triplicate. The peak-to-trough absorbance difference, ΔA (A_{peak} minus A_{trough}), was then plotted against substrate concentration. For coloured substrates whose absorption interfered with the peak at ~390 nm, only the decrease in absorbance at ~420 nm was used to determine the binding constant (ΔA = Abs_{460nm}-Abs_{420nm}).

For tight-binding ligands (ligands with $K_d \leq 5 \times$ P450 concentration) the data were fitted to the Morrison (tight-binding) equation (Equation 2.1).[290]

$$\frac{\Delta A}{\Delta A_{max}} = \frac{([E] + [S] + K_d) - \sqrt{([E] + [S] + K_d)^2 - 4[E][S]}}{2[E]} \quad (2.1)$$

In this equation, ΔA is the peak-to-trough absorbance difference, ΔA_{max} is the ΔA at infinite substrate concentration, [E] is the P450 concentration and [S] is the concentration of substrate added to the P450. K_d is the dissociation constant of the P450-ligand complex. For all other substrates, the data were fitted to the hyperbolic (Michaelis-Menten) equation (Equation 2.2).[iv]

$$\Delta A = \frac{\Delta A_{max} \times [S]}{K_d + [S]} \quad (2.2)$$

If binding of a ligand failed to induce any appreciable spin-state shift, K_d could not be accurately determined by this method. In these cases, purified enzyme was sent to the University of New South Wales (UNSW) where Giang T. H. Nguyen and Dr William A. Donald determined K_d values using a mass spectrometry method.[291]

[iv] The hyperbolic equation is not valid for tight-binding ligands.

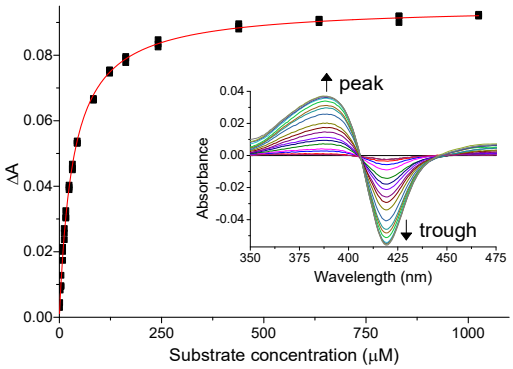

Figure 2.6. UV-Vis spectral changes induced by binding of the substrate 3-methylthiobenzoic acid to CYP199A4 (inset) and the plot of ΔA against [substrate]. ΔA is defined as $A_{peak} - A_{trough} = A_{389nm} - A_{419nm}$.

2.3.5 *In vitro* NADH activity assays

In vitro NADH turnovers[117] were performed at 30 °C and contained 0.5 μM CYP199A4 (WT or mutant), 5 μM HaPux, 0.25 μM HaPuR and 100 ng μL^{-1} bovine liver catalase in oxygenated Tris-HCl buffer (50 mM, pH 7.4) in a total volume of 1.2 mL. Catalase was added to remove H_2O_2 generated via uncoupling which could oxidise reactive substrates such as thioethers.[292] The absorbance at 340 nm was set to zero and the mixture was incubated at 30 °C for 2 min before NADH was added to a concentration of ~320 μM, corresponding to an absorbance of ~2.0. The rate of NADH background oxidation (the 'leak' rate) was measured before initiating the reaction. To start the reaction, 1 mM substrate was added from a 100 mM stock in EtOH/DMSO and NADH depletion was monitored at 340 nm (Figure 2.7a). (NADH absorbs strongly at 340 nm while NAD^+ has no absorption at the same wavelength.[293]) The rate of NADH consumption (N) by the P450 enzyme in units of (μM-NADH) $(\mu M\text{-P450})^{-1}$ min^{-1} was calculated from the slope of the graph of Abs_{340} versus time using an extinction coefficient of ε_{340} = 6.22 mM^{-1} cm^{-1} (Equation 2.3). The units are abbreviated to min^{-1}.

$$N = \frac{\frac{\Delta Abs_{340}}{\Delta time} \times 1000 \times 2}{6.22} \qquad (2.3)$$

All experiments were performed at least three times and the mean and standard deviation reported. Control reactions were also performed in which either the P450 or NADH was omitted from the turnover mixture (replaced with the same volume of buffer).

A modified method was used for the T252E mutant. The rate of NADH consumption by the T252E mutant was exceedingly slow (Figure 2.7b) and therefore half the amount of NADH (~160 μM rather than 320 μM) was added to each reaction. After substrate was added, NADH consumption was monitored by UV-Vis spectroscopy at 30 °C for the first ~15 min. The reaction mixture was then left at room temperature until all NADH had been consumed. NADH consumption rates reported for the T252E mutant are the initial rates over the first 10 min.

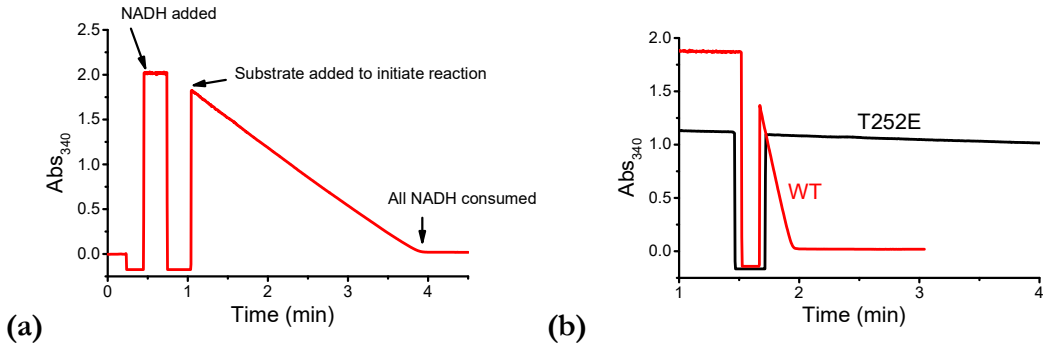

Figure 2.7. **(a)** *In vitro* reactions were initiated by addition of 1 mM substrate and the rate of NADH consumption was monitored at 340 nm. **(b)** Comparison of the rate of NADH consumption by WT CYP199A4 (**red**; N = 1340 ± 28 min^{-1})[117] and the T252E variant (**black**; N = 8.6 ± 0.5 min^{-1}), with 4-methoxybenzoic acid as the substrate. Note that the NADH leak rate (~9 min^{-1}) was not subtracted from the NADH consumption rates.

2.3.6 *In vitro* H_2O_2-driven turnovers

Reaction mixtures contained 3 µM CYP199A4 (WT, D251N, T252E or T252A isoform), 1 mM substrate from a 100 mM stock in EtOH or DMSO and 6 or 50 mM H_2O_2 in Tris-HCl buffer (50 mM, pH 7.4) in a total volume of 600 µL. Thioethers can be oxidised to sulfoxides with H_2O_2.[294] Therefore, a reduced concentration of H_2O_2 (6 mM instead of 50 mM) was used when the substrate was a thioether to minimise background oxidation. For all other substrates, a H_2O_2 concentration of 50 mM was used. Reaction mixtures were incubated for 2 minutes at 30 °C prior to addition of the appropriate concentration of H_2O_2 to initiate the reaction.[v] Each reaction was performed in triplicate or duplicate at 30 °C. At time points of 0, 20, 60 and 240 minutes, aliquots of the reaction mixture (132 µL) were removed and immediately quenched by mixing with 10 µL of 10 mg mL^{-1} catalase to rapidly decompose any remaining H_2O_2 (Equation 2.4)[296-297] and 66 µL of AcCN to denature the enzyme.[vi]

$$2H_2O_2\,(aq) \xrightarrow{Catalase} 2H_2O\,(l) + O_2\,(g) \qquad (2.4)$$

After quenching the reaction, IS was added (2 µL of 10 mM 9-hydroxyfluorene (9-OHFlu)) and the mixture was centrifuged at 13000 rpm for 3 minutes to remove particulate matter prior to analysis by HPLC. Control reactions performed without P450 were used to assess whether any background oxidation was occurring when the substrate was exposed to H_2O_2. If product was detected in these controls, it was subtracted from that in the turnover mixtures when quantifying the amount of product generated by the P450 enzyme. In the absence of enzyme, 4-vinyl-, 4-ethyl-, 4-methoxy- and 4-ethynyl-benzoic acid were not oxidised by H_2O_2,[298] and minimal background oxidation of 4-formylbenzoic acid occurred.

[v] H_2O_2 was added from a 200 mM stock freshly prepared before each experiment from a 30% w/w stock. The concentration of the 30% w/w stock was measured spectrophotometrically using ε_{240} = 43.6 M^{-1} cm^{-1}.[295]

[vi] Negligible amounts of product were detected in reactions that were quenched immediately after H_2O_2 was added to initiate the reaction, confirming the effectiveness of the quenching method.

Control reactions were performed to confirm that the substrate was not being oxidised by reactive oxygen species (ROS) generated by a Fenton-type reaction arising from free iron or free heme from degraded protein. The first control reaction contained an equivalent amount of denatured T252E$_{CYP199A4}$, which had first been heated at 80 °C for 45 minutes (Figure 2.8). A second control reaction was performed with CYP101B1: a P450 from *Novosphingobium aromaticivorans* DSM12444 which does not bind *para*-substituted benzoic acids. CYP101B1 was quantified using ε_{417} = 113 mM^{-1} cm^{-1}.[299]

Figure 2.8. Heat-denatured T252E$_{CYP199A4}$

2.3.7 *In vitro* *t*BuOOH-driven turnovers

Reaction mixtures contained 3 μM P450, 50 mM *t*BuOOH and 1 mM substrate in Tris-HCl buffer (50 mM, pH 7.4) in a total volume of 990 μL. Reactions were performed at 30 °C and were initiated by addition of substrate. After 1 hour, 20 μL of 3 M HCl and 15 μL of 10 mM 9-OHFlu were added, followed by extraction with EtOAc (2 × 400 μL). Samples were evaporated under N_2 and the residue redissolved in 500 μL of AcCN and 1000 μL of Tris-HCl buffer and analysed by HPLC.

2.3.8 Analysis of metabolites

Products were identified and quantitated by HPLC and GC-MS. To prepare turnover mixtures for HPLC, 132 μL of the *in vitro* turnover mixture was mixed with 66 μL of AcCN and 2 μL of internal standard (10 mM 9-OHFlu in EtOH) and centrifuged to remove particulate matter. HPLC analysis was performed as described in Section 2.1.2. Products were identified by co-elution with pure authentic samples of the expected oxidation products. Calibration curves were constructed to quantify the product (Figure 2.9). Solutions of product with concentrations of 20, 50, 100, 200 and 500 μM were prepared for HPLC analysis in the same way as the turnovers. For minor products, a 5 μM solution was also prepared. A plot of product peak area/IS peak area *vs.* product concentration was then constructed. The calibration factor is the slope of this graph and has units of μM^{-1}. If authentic samples of the oxidation products were unavailable, calibration curves were constructed using structurally similar compounds to estimate the amount of product. Pure authentic 4-oxiran-2-ylbenzoic acid and 4-ethylsulfinylbenzoic acid were unavailable so these products were quantified using 4-(1-hydroxyethyl)benzoic acid and 4-methylsulfinylbenzoic acid, respectively. 3-Hydroxymethylbenzoic acid was quantified using the substrate, 3-methylbenzoic acid. 4-Oxiran-2-ylbenzoic acid and the aldehyde rearrangement product were also calibrated by GC-MS using TMS-derivatised 4-vinylbenzoic acid.[276] Table 2.3 lists the HPLC and GC calibration factors.

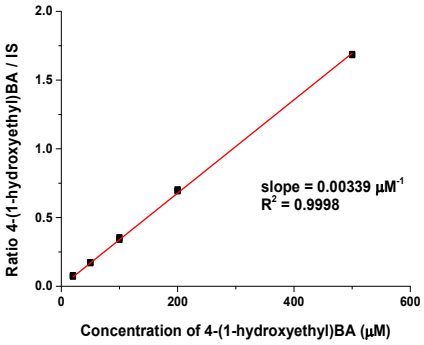

Figure 2.9. Calibration curve for quantifying 4-(1-hydroxyethyl)benzoic acid

Samples were prepared for GC-MS analysis by first adding 10 μL of internal standard (10 mM 9-OHFlu) and 3 μL of 3 M HCl to 990 μL of the turnover mixture. After extraction with EtOAc (3 × 400 μL), the organic extracts were pooled, dried over anhydrous $MgSO_4$ and solvent was evaporated under N_2. The residue was redissolved in anhydrous AcCN (150 μL) and the substrate, product(s) and internal standard were converted into TMS derivatives by treatment with excess derivatisation reagent (>35 μL BSTFA + TMCS, 99:1) (Figure 2.10). The mixtures were left for 2 hours at 37˚C prior to analysis by GC-MS. GC-MS analysis was performed using the instruments and methods described in Section 2.1.2. TMS derivatives decompose upon exposure to moisture and hence were analysed after formation without storage.[300] Calibration curves were constructed to quantify reaction products.

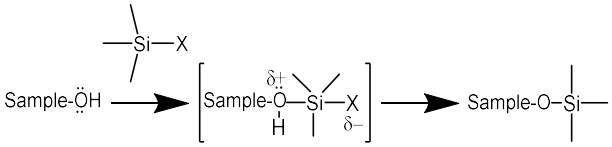

Figure 2.10. Mechanism of derivatisation of an alcohol by BSTFA. Alcohols, carboxylic acids and amines (among other functional groups) react with BSTFA to generate TMS derivatives, which are more volatile, thermally stable and less polar than the underivatised compound leading to improved peak shape.[300-301] Mass spectra of TMS derivatives exhibit a prominent $[M - 15]^+$ peak corresponding to loss of a $-CH_3$ group from the TMS group.[302]

For the 3-methylaminobenzoic acid turnovers, a modified method was used. After extraction, the dry samples were redissolved in anhydrous EtOAc (300 μL) and 45 μL of derivatisation reagent (BSTFA + TMCS, 99:1) was added and the samples left for 36 h to fully convert 3-aminobenzoic acid into the doubly derivatised form. Samples were then analysed by GC-MS. The column was held at 120 ˚C for 3 min, and the temperature was then increased to 140 ˚C at a rate of 5 ˚C min^{-1} and held at 140 ˚C for 9 min. The temperature was then raised to 240 ˚C at 5 ˚C min^{-1}.

Table 2.3. HPLC and GC calibration factors used to quantify P450 oxidation products†

Analysis method	Compound	Calibration factor (μM^{-1})
HPLC	4-Hydroxybenzoic acid	0.0110
	4-(1-Hydroxyethyl)benzoic acid[a]	0.00339
	4-(2-Hydroxyethyl)benzoic acid	0.00452
	4-Vinylbenzoic acid	0.0117
	4-Acetylbenzoic acid	0.0150
	4-Methylsulfinylbenzoic acid[b]	0.00559
	Terephthalic acid	0.00807
	Vanillic acid (4-hydroxy-3-methoxybenzoic acid)	0.00746
	Isovanillic acid (4-methoxy-3-hydroxybenzoic acid)	0.00761
	4-Carboxyphenylacetic acid	0.00298
	3-Hydroxybenzoic acid	0.00105
	Isophthalic acid	0.000742
	3-Methylsulfinylbenzoic acid	0.00153
	3-Methylbenzoic acid[c]	0.000602
GC-MS	4-Vinylbenzoic acid (singly derivatised)[d]	0.00627
	3-Aminobenzoic acid (doubly derivatised)	0.00120

† With only one exception, the R^2 value for all calibration plots was >0.99. [a] 4-(Oxiran-2-yl)benzoic acid was quantified using 4-(1-hydroxyethyl)benzoic acid. [b] 4-Ethylsulfinylbenzoic acid was quantified using 4-methylsulfinylbenzoic acid. [c] 3-Methylbenzoic acid was used to quantify 3-hydroxymethylbenzoic acid. [d] 4-Vinylbenzoic acid (singly derivatised) was used to quantify 4-oxiran-2-ylbenzoic acid and the aldehyde rearrangement product.

2.3.9 Enantioselective HPLC analysis

Chiral products generated by WT and mutant forms of CYP199A4 were analysed using enantioselective HPLC as described in Section 2.1.2 (using a Lux Cellulose-1 chiral column and eluting the samples with 15% or 20% AcCN in Milli-Q water containing 0.1% TFA at a flow rate of 0.4-0.8 mL min^{-1}). Turnover mixtures were prepared for HPLC analysis by mixing 132 µL of the turnover mixture with 66 µL of acetonitrile. The enantiomers of 4-ethylsulfinylbenzoic acid could not be separated satisfactorily using this method. Instead, the 4-ethylthiobenzoic acid turnovers were extracted with EtOAc (3 × 400 µL), evaporated to dryness and sent to Professor James de Voss at the University of Queensland (UQ) for chiral analysis. Chiral analysis was performed by de Voss after conversion of the compounds into the methyl esters with diazomethane. The column used was a cellulose carbamate coated silica column (OD-H, 10 µm, 250 × 4.6 mm, CHIRALCEL®). The enantiomers were eluted with 5% isopropyl alcohol in hexane at 0.8 mL min^{-1}. The eluate was monitored at 270 nm.

2.3.10 Analysis of catalytic activity

Coupling efficiency (C) is the percentage of NADH consumed that was channelled into substrate oxidation (Equation 2.5).

$$C = \frac{[product]}{[NADH\ consumed]} \times 100\% \quad (2.5)$$

The product formation rate (PFR) was calculated from the NADH consumption rate (*N*) and the coupling efficiency (C) (Equation 2.6). When the coupling efficiency is 100%, the PFR is equal to the rate of NADH consumption.[303] If high levels of uncoupling occur, the rate of product formation is substantially slower than NADH consumption. The PFR has units of (μM-product) (μM-P450)$^{-1}$ min^{-1} (abbreviated to min^{-1}).

$$PFR = N \times \frac{C}{100} \quad (2.6)$$

2.3.11 Quantification of H_2O_2

Hydrogen peroxide formation during *in vitro* NADH turnovers was quantitated using the HRP/phenol/4-AP assay.[117, 304] This assay detects H_2O_2 at levels as low as 1 μM.[304] *In vitro* NADH activity assays were performed without catalase and H_2O_2 was quantified immediately after all NADH had been consumed. The turnover mixture (400 μL) was mixed with 200 μL of 50 mM phenol and 200 μL of 5 mM 4-AP in Tris-HCl buffer (50 mM, pH 7.4). After the absorbance of the mixture at 510 nm had been set to zero, 1 μL of 20 mg mL^{-1} HRP in Milli-Q water was added. The concentration of H_2O_2 was calculated from the absorbance of the resulting mixture at 510 nm.

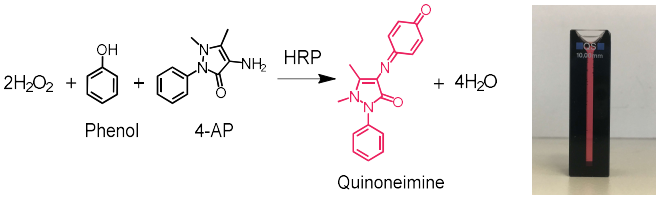

Figure 2.11. HRP catalyses the formation of quinoneimine, a vivid pink dye, from H_2O_2, phenol and 4-aminoantipyrine.[305-306] HRP first catalyses the oxidation of phenol to quinone, which then reacts with 4-AP.[305] Quinoneimine is quantified using ε_{510} = 6580 M^{-1} cm^{-1}.[117]

If H_2O_2 is present, it reacts rapidly with phenol and 4-aminoantipyrine to generate pink-coloured quinoneimine dye, catalysed by HRP (Figure 2.11).[305] Quinoneimine was quantified using ε_{510} = 6580 M^{-1} cm^{-1} (Equation 2.7).[117]

$$[Quinoneimine\ dye] = \frac{A_{510} \times 10^6}{6580} \mu M \quad (2.7)$$

The formation of one quinoneimine molecule requires two molecules of H_2O_2. The concentration of H_2O_2 in the original (undiluted) turnover mixture is therefore given by four times the calculated quinonimine concentration (Equation 2.8).

$$[H_2O_2] = 4 \times [Quinoneimine\ dye]_{\text{diluted mixture}} = \frac{A_{510} \times 10^3}{1.645} \mu M \quad (2.8)$$

2.3.12 Detection of H_2O_2 after incubation with turnover components

If NADH consumption by the P450 is slow, H_2O_2 generated via uncoupling may be lost before the reaction is complete. To investigate how rapidly H_2O_2 is lost, ~300 μM H_2O_2 was added to a control turnover mixture (1.2 mL) containing 5 μM HaPux, 0.25 μM HaPuR and 0.5 μM CYP199A4 in Tris-HCl buffer (but no NADH, substrate or catalase) and the mixture was incubated at 30 °C for 60 min. H_2O_2 levels were measured (as already described) at time points of 2, 10, 20, 40 and 60 minutes. Measurements were made in triplicate. H_2O_2 was also incubated with the individual components of the turnover mixture in Tris-HCl buffer.

2.3.13 Heme bleaching assay[264]

A 600 μL aliquot of $T252E_{CYP199A4}$ or $WT_{CYP199A4}$ solution (3 μM) in Tris-HCl buffer (50 mM, pH 7.4) was used to baseline the spectrophotometer. H_2O_2 (1, 10, 20, 40, or 60 mM) was added and the UV-Vis spectrum was recorded after 1 min. Heme prosthetic group destruction was monitored by recording UV-Vis spectra at 2 min intervals. The assay was repeated in the presence of 1 mM 4-methoxybenzoic acid using 60 mM H_2O_2.

2.4 Product synthesis

If authentic samples of expected oxidation products could not be obtained from a commercial source, where possible they were chemically synthesised. The chemically synthesised compounds were then used to confirm the identity of the P450 oxidation products by co-elution.

Synthesis of 4-oxiran-2-ylbenzoic acid: Racemic epoxide was synthesised using the method of Lane and Burgess (Scheme 2.1).[307] To a stirred mixture of 4-vinylbenzoic acid (0.148 g, 1 mmol) and $MnSO_4.4H_2O$ (2.23 mg, 0.01 mmol) in *t*BuOH (23 mL) at 20 °C was added dropwise a $H_2O_2/NaHCO_3$ buffer solution at 1 °C over 4 h. The solution consisted of H_2O_2 (1.05 mL, 9.57 M, 10 mmol) in 0.2 M $NaHCO_3$-HCl buffer, pH 8 (17 mL). Reaction progress was monitored by GC-MS. The reaction mixture was then diluted with water (10 mL), acidified to pH 3 with HCl and extracted with hexane (5 × 30 mL). The organic extracts were washed with brine (2 × 20 mL), dried over anhydrous Na_2SO_4 and filtered. Solvent was removed under reduced pressure to yield a white solid. The mass of the TMS-derivatised product agreed with the calculated mass of derivatised 4-oxiran-2-ylbenzoic acid (m/z of 236.15 AMU *vs.* calculated m/z of 236.09 AMU). The crude epoxide (estimated by GC-MS to be ~78% pure) was used to confirm the identity of the P450 oxidation product by co-elution. Attempts to purify the epoxide by semi-prep HPLC, using 20% AcCN in H_2O with 0.1 TFA as the eluent, resulted in partial ring-opening of the epoxide to give the corresponding diol (m/z of 398.2 AMU). The epoxide could therefore not be used for calibration.

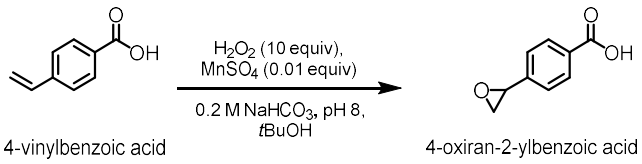

Scheme 2.1. Synthesis of racemic 4-oxiran-2-ylbenzoic acid

Synthesis of 3-methylsulfinylbenzoic acid: *m*CPBA (0.59 mmol) in chloroform (60 mL) was added portionwise to 3-methylthiobenzoic acid (0.59 mmol) in chloroform (60 mL) (Scheme 2.2). The mixture was stirred for 10 min at room temperature.[308] The solvent was removed under reduced pressure and the crude product purified by semi-prep HPLC and freeze-dried to yield a white solid. The mass of the TMS-derivatised product agreed with the expected mass (m/z of 256.10 AMU *vs.* calculated m/z of 256.06 AMU).

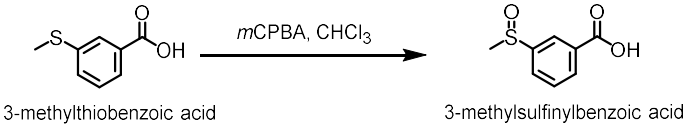

Scheme 2.2. Synthesis of 3-methylsulfinylbenzoic acid

Synthesis of 4-ethylsulfinylbenzoic acid: To 4-ethylthiobenzoic acid (1 mM) in Tris-HCl buffer (50 mM, pH 7.4) was added 200 mM H_2O_2 (Scheme 2.3).[294] After 2 h the reaction was quenched with catalase.

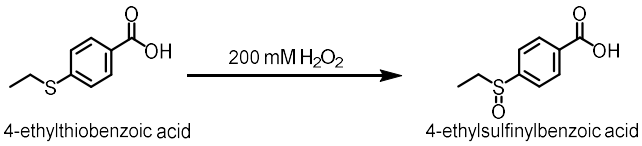

Scheme 2.3. Synthesis of 4-ethylsulfinylbenzoic acid

2.5 Docking of ligands into CYP199A4

To identify the likely binding mode of 3-methylaminobenzoic acid in the binding pocket of CYP199A4, the ligand was docked into a crystal structure of CYP199A4 (PDB ID: 5U6W) using ICM-Pro software, version 3.8-6a (Molsoft LLC, San Diego CA).[309] First, the CYP199A4 crystal structure from the PDB was converted into an ICM object; this resulted in automatic addition of hydrogens to the crystal structure and optimisation of their orientation. Charges were also automatically assigned to residues which should be protonated/deprotonated at neutral pH and the orientation of histidine, proline, asparagine, glutamine and cysteine residues was also optimised.[310-311] The general guideline is that waters should be deleted from the crystal structure before docking ligands unless they are involved in ligand binding.[310] An active-site water molecule was retained which is known to interact via a H-bond with the carboxylate of bound benzoic acid substrates.[29, 117, 219] The co-crystal ligand (4-methylaminobenzoic acid) was then removed from the active site of the enzyme. Next, the binding site was defined by selecting the option to 'Make Box Around Existing Ligand' or by using ICMPocketFinder. After defining the ligand binding pocket,

the 4-methylaminobenzoic acid ligand was modified to 3-methylaminobenzoic acid using the ICM 3D Fully Interactive Ligand Editor. When the modified ligand was re-docked into the binding pocket (using the 'Redock Ligand in Current Receptor' function), the top scoring (lowest-energy) pose had the 3-methylamino substituent pointing down towards the heme. A positional restraint was imposed on the nitrogen atom in order to dock the ligand in an alternative configuration with the 3-methylamino moiety pointing away from the heme. The docking 'score' was then used to evaluate the docked poses.[310, 312] A docking score is deemed to be 'good' if it is more negative than -32.[313] Several other ligands were docked into CYP199A4 using the same method.

2.6 X-ray crystallography

A HiPrep Sephacryl S-200 HR size-exclusion column (60 cm x 16 mm; GE Healthcare) was used to purify the protein (T252E or WT CYP199A4) for crystallisation. The protein was eluted using Tris-HCl buffer (50 mM, pH 7.4) at a flow rate of 1 mL min^{-1}. The purified protein (RZ >2) was concentrated to 40 mg mL^{-1} (900 μM) in 50 mM Tris-HCl buffer (pH 7.4) by ultrafiltration using a Microsep Advance centrifugal device (10 kDa MWCO, Pall Corporation). Substrate was then added to a concentration of 1-4 mM from a 100 mM stock in DMSO or EtOH. 4-1*H*-Imidazol-1-ylbenzoic acid was insoluble in these solvents but could be dissolved in Tris-HCl buffer (50 mM, pH 9.5). For poorly soluble ligands, a co-concentration method was used instead of adding the ligand directly to concentrated protein.[283, 314] These ligands (4-pyridin-2-yl- and 4-pyridin-3-yl-benzoic acid) were added to dilute protein (~10 μM) to a concentration of ~3 mM from a 100 mM stock solution in DMSO. The mixture was incubated at 4 °C for 2 hours, and the protein-ligand complex was then concentrated to 30-40 mg mL^{-1}.

Crystallisation screening trials were first performed using the Hampton Research Crystal Screen HT kit to identify favourable crystallisation conditions for the SF and SB forms of the T252E mutant. Screening was performed using a 96-well sitting-drop Intelli-Plate (Art Robbins Instruments, USA), and the crystal tray was set up using an Art Robbins Phoenix crystallisation robot. Sitting drops of 1 μL of crystallisation reagent mixed with 1 μL of T252E protein (with or without 2 mM 4-methoxybenzoic acid) were equilibrated with a 75 μL reservoir of crystallisation reagent at 16 °C. Most conditions yielded no crystals but three conditions gave crystals (Figure 2.12) which appeared to be small or of poor quality so these were not used for X-ray crystallography. The conditions that produced crystals were condition No. 10 (0.2 M ammonium acetate, 0.1 M sodium acetate trihydrate buffer (pH 4.6) and 30% w/v polyethylene glycol 4000), condition No. 23 (0.2 M magnesium chloride hexahydrate, 0.1 M HEPES sodium buffer (pH 7.5) and 30% v/v polyethylene glycol 400), and condition No. 74 (0.2 M ammonium sulfate, 0.1 M MES monohydrate (pH 6.5) and 30% w/v polyethylene glycol monomethyl ether 5000).

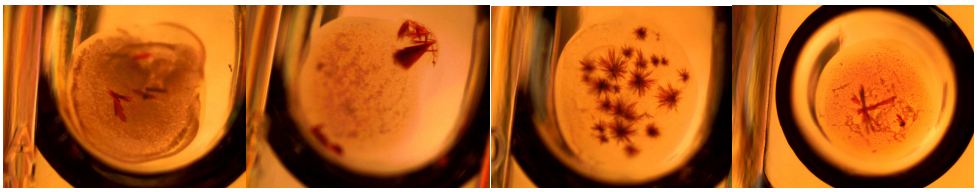

Figure 2.12. Crystals of substrate-free and 4-methoxybenzoate-bound T252E$_{CYP199A4}$ obtained using crystallisation reagents No. 10, 23 and 74 in the Hampton Research Crystal Screen HT kit.

Good quality crystals (Figure 2.13) were subsequently obtained using optimised conditions for the WT enzyme reported by Coleman *et al.*: 0.2 M magnesium acetate, 100 mM Bis-Tris buffer (adjusted with acetic acid to pH 5.0-5.75) and 20-32% w/v polyethylene glycol (PEG) 3350.[117, 277] Crystallisation of the protein was accomplished using the hanging-drop vapour-diffusion method using a 24-well crystallisation tray. Hanging drops of 1.2-2 µL of protein mixed with an equal volume of crystallisation reagent were equilibrated with a 500 µL reservoir of the crystallisation reagent at a temperature of 16 ˚C. Under these conditions, clusters of red plate-like crystals appeared within half a day to one week.

Figure 2.13. Magnified images of crystals of 4-methoxybenzoate-bound T252E$_{CYP199A4}$ grown under optimised conditions. Refer to Appendix E for crystal dimensions.

Single crystals were mounted onto MicroMounts or MicroLoops (MiTeGen LLC, New York, USA) and dragged through Parabar 10312 oil (Paratone-N, Hampton Research, California, USA) before they were flash-frozen in liquid N_2. High-resolution X-ray diffraction data (360 images per crystal) were obtained at 100 K at the Australian Synchrotron, beamlines MX1 or MX2, in Melbourne, Australia.[315-316] The exposure time was 1 s, oscillation angle 1˚ and wavelength 0.9537 or 0.7108 Å. iMosflm[317] was used to index and integrate the data, and the data were then scaled and merged using Aimless[318] (part of the CCP4 suite of programs).[319] PhaserMR in the CCP4 suite of programs was used to solve the structure by the molecular replacement method.[320] A high-resolution (1.54-Å resolution) structure of CYP199A4 (PDB: 5UVB, with the heme, chloride, 4-cyclopropylbenzoate substrate and waters deleted) was used as the search model.[277] Positive density in the difference map revealed the position of the Glu252 side-chain and the ligand in the active site. Coordinates and restraints for the ligand were generated using Phenix eLBOW[321] and the protein model was manually rebuilt in Coot.[322] Refinement was performed using phenix.refine,[323-324] and this was followed by multiple rounds of manual rebuilding in Coot and refinement to improve the model. Solvent was added automatically using phenix.refine and positive density in

the anion binding site of CYP199A4 was modelled as a chloride ion.[29] The Fe-S(Cys) and Fe-OH_2 bond lengths were not restrained during refinement. The occupancy of the substrate and water ligand, if present, was refined using phenix.refine. In the final stages of refinement, waters were manually deleted if they were in low electron density or unrealistically close to other waters or residues.[325-326] Composite omit maps[327] and feature-enhanced maps[328] were generated using Phenix to verify the presence of the ligand in the enzyme's active site. The validation tool *MolProbity* was used to assess the quality of the model before the structure was deposited into the Protein Data Bank (www.rcsb.org).[329] Fully refined structures should satisfy the following quality criteria: R_{work} <25%, R_{free} <25%, Ramachandran favoured >98%, poor rotamers <1%, RMSD bond lengths <0.02 Å, RMSD bond angles <2 °.[329-331] Images of the refined crystal structures were generated using PyMOL.[332]

Chapter 3

Investigation of CYP199A4's preference for *para*- over *meta*-substituted benzoic acid substrates

3.1 Introduction

Investigations into the substrate range of CYP199A4 revealed that the enzyme avidly binds and rapidly oxidises *para*-substituted benzoic acid substrates.[29, 117, 137, 162, 181, 219, 275, 333] The fastest reaction catalysed by CYP199A4 is *O*-demethylation of 4-methoxybenzoic acid, performed at a rate of 1220 min^{-1} with a coupling efficiency of 91%.[117, 162] CYP199A4 is also able to bind and oxidise the bulkier substrate 3,4-dimethoxybenzoic acid (veratric acid). Demethylation occurs only at the *para* position, affording 4-hydroxy-3-methoxybenzoic acid; the *meta* substituent is not attacked.[137] CYP199A4 does not hydroxylate the aromatic ring of these substrates and also fails to oxidise benzoic acid itself.[162]

Crystal structures of substrate-bound CYP199A4 have been solved to elucidate the orientation of substrates in the binding pocket and explain CYP199A4's tendency to attack only the *para* substituent (Figure 3.1).[29, 117, 219] These crystal structures revealed that the benzoate moiety, held perpendicular to the heme, forms hydrogen-bonding interactions with residues in the binding pocket.[29] The substrate carboxylate interacts with the hydroxyl groups of S95 and S244 and forms a salt bridge with the guanidinium of R92.[29] Additionally, it interacts with a water which is hydrogen-bonded to S244 and R243.[29] If the substrate carboxylate is replaced with alternate functional groups, it abolishes the enzyme's ability to tightly bind the substrate.[181, 333] Van der Waals interactions exist between the benzene ring and L98, A248, V181, and F185 and also between the *para* substituent and F182 and F298.[29] Consistent with the ≥95% shift to high-spin observed when 4-methoxybenzoic acid binds, the crystal structure (PDB ID: 4DO1) revealed that the iron-bound water is completely displaced by this substrate (Figure 3.1, cyan). The *para* methoxy group is held in close proximity to the heme iron (the methyl carbon is 4.1 Å from the iron) and thus hydroxylation occurs at this position.[29] When veratric acid binds (PDB: 4EGN), its benzoate moiety and *para* methoxy group occupy virtually identical positions to those of 4-methoxybenzoic acid (Figure 3.1, yellow).[219] While the *para* methoxy group is close to the heme, the *meta* methoxy group of veratric acid is oriented away from the heme and is too far (8.1 Å) from the iron to react.[219] Hydrogen atoms must be close to the Cpd I ferryl oxygen to be abstracted so oxidation is not expected to occur at sites further than 6 Å from the heme iron.[334-335]

CYP199A4's activity towards multiple other substituted benzoic acid substrates has been investigated (Figure 3.2).[117, 137, 162, 181, 219, 275, 333] 2,4-Dimethoxybenzoic acid was again solely oxidised at the *para* position.[162] On the other hand, 2- and 3-methoxybenzoic acid were not oxidised at all.[162] The NADH consumption rate with 3-methoxybenzoic acid was reasonably fast (498 min^{-1}) but

virtually all the reducing equivalents were lost via uncoupling.[162] As only minute quantities of H_2O_2 were formed, it was inferred that the reducing equivalents were predominantly channelled into oxidase uncoupling.[162] 3-Methoxybenzoic acid binds substantially less tightly than 4-methoxybenzoic acid (K_d = 69 μM *vs.* 0.22 μM) and induces only a small spin-state shift to high-spin (40%), implying that the substrate is not bound close enough to the heme to efficiently displace the water.[162] Other 3-substituted benzoic acids also fail to induce large shifts in the spin-state when they bind to CYP199A2, which shares 86% sequence identity with CYP199A4.[29, 336] As an example, 3-chlorobenzoic acid induces a substantially smaller spin-state shift than the *para* isomer 4-chlorobenzoic acid (10% *vs.* 80%).[336] A crystal structure of 3-methoxybenzoate-bound CYP199A4 is not available. Based on these results, Coleman proposed that 3-methoxybenzoic acid binds in the active site with the *meta* substituent pointing away from the heme iron, as is the case when veratric acid binds, rather than towards the heme.[162] The *meta* substituent would be held too far from the iron to react.[162] 3,5-Dimethoxybenzoic acid, which must bind with one *meta* methoxy group pointing away from the heme and one methoxy group pointing towards it, was oxidised with low efficiency (the product formation rate was 7 min^{-1}).[162]

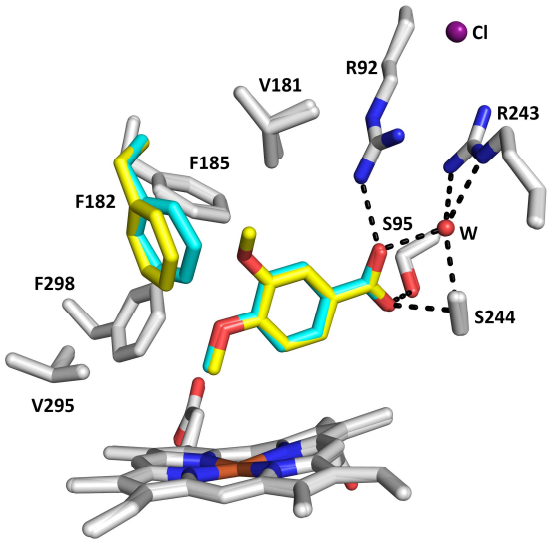

Figure 3.1. Binding modes of 4-methoxybenzoic acid (cyan; 4DO1) and veratric acid (yellow; 4EGN) in the binding pocket of CYP199A4. F182 rotates to accommodate the *meta* methoxy group of veratric acid, which points away from the heme. When substrate binds to CYP199A4, a chloride ion (purple sphere) binds at the entrance to the active site.[29] This chloride is thought to prevent excess water entering the active site.[29] Hydrogen bonds are represented by dashed lines and the donor-acceptor distances are 2.5-3.1 Å.

CYP199A4 also catalyses reactions other than *O*-dealkylation such as sulfoxidation of 4-methylthiobenzoic acid (PDB ID: 5KT1), *N*-dealkylation of 4-methylaminobenzoic acid (PDB ID: 5U6W), hydroxylation of 4-methylbenzoic acid, and oxidation of 4-formylbenzoic acid to the corresponding carboxylic acid (terephthalic acid).[117, 276-277] It also oxidises bulkier substrates such as 4-ethoxy- (PDB ID: 5U6T), 4-*tert*-butyl- and 4-isopropyl-benzoic acid (PDB ID: 5KDB).[117, 277]

To date, 3-methoxybenzoic acid is the only monosubstituted benzoic acid substrate with a substituent at the *meta* position that has been tested with CYP199A4. We will therefore investigate CYP199A4's activity towards benzoic acid substrates with alternative substituents at the *meta*

position to assess whether 3-substituted benzoic acids all bind with the *meta* substituent pointing away from the heme. The substrates tested will be 3-methylamino-, 3-methylthio-, 3-methyl-, 3-formyl-, 3-ethoxy-, 3-isopropyl- and 3-*tert*-butyl-benzoic acid (Figure 3.3). Docking and X-ray crystallography will be used to clarify the binding mode of these substrates and rationalise CYP199A4's preference for *para*-substituted compared to *meta*-substituted benzoic acids. These experiments should lead to greater understanding of the substrate range of this enzyme and the factors that determine whether efficient monooxygenation will occur.

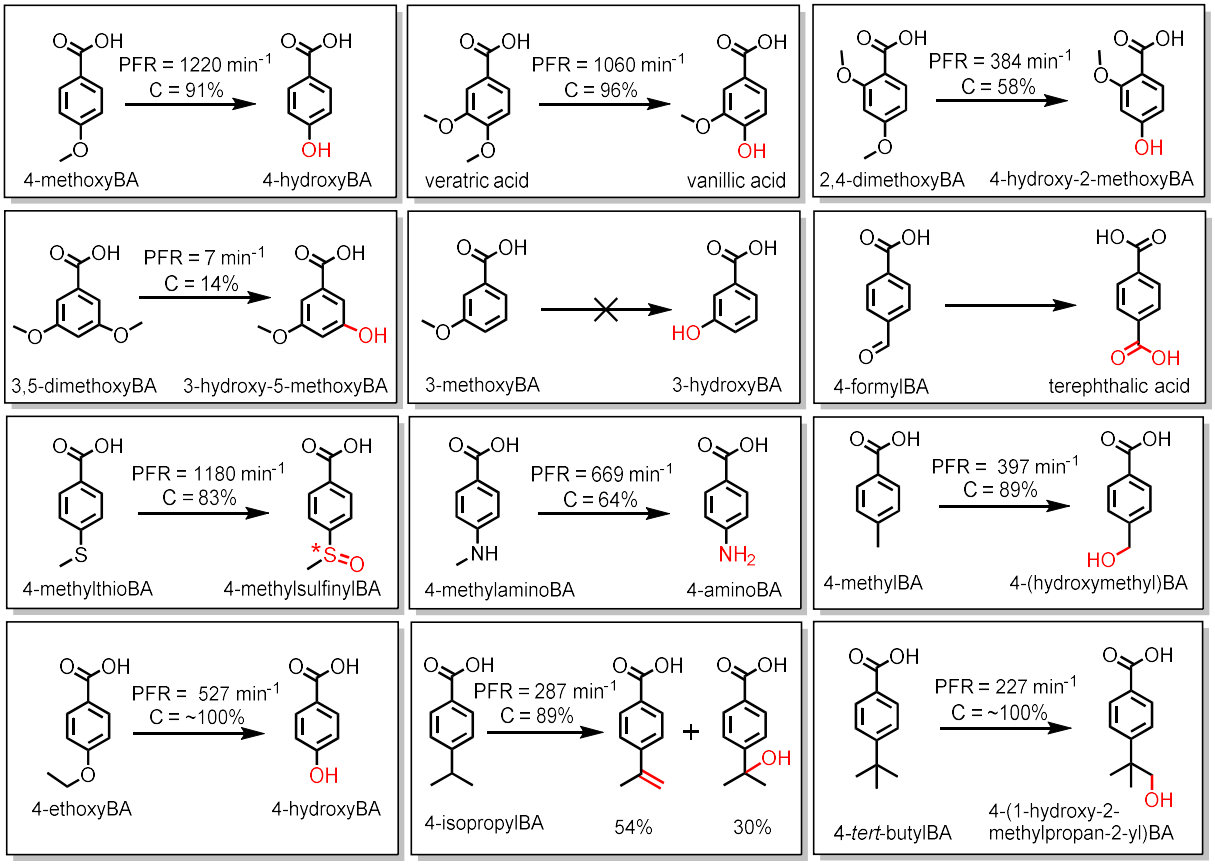

Figure 3.2. Selected reactions catalysed by CYP199A4.[117, 137, 162, 181, 219, 275, 277] Product formation rates (PFR) and coupling efficiencies (C) are given.

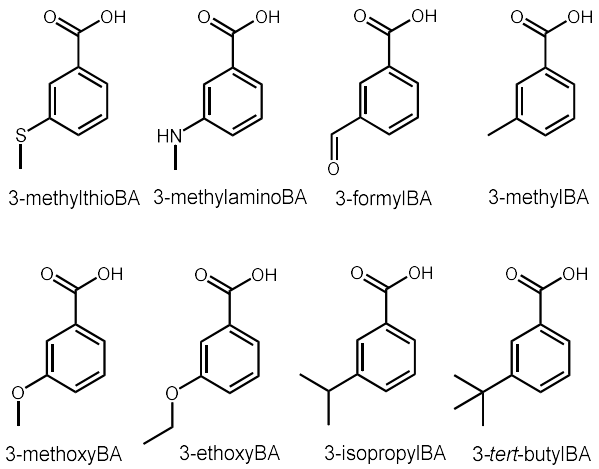

Figure 3.3. New substrates investigated with CYP199A4 in this study

3.2 Results

3.2.1 Catalytic activity of CYP199A4 towards 3-methylamino-, 3-methylthio-, 3-methyl- and 3-formyl-benzoic acid

Initially, the catalytic activity of CYP199A4 towards 3-methylamino-, 3-methylthio-, 3-methyl- and 3-formyl-benzoic acid was explored. Compared to 3-methoxybenzoic acid, which induces a 40% spin-state shift upon binding to CYP199A4[162] (Figure 3.4a), 3-methylamino-, 3-methylthio-, 3-methyl- and 3-formyl-benzoic acid all induced smaller type I shifts: 10%, 30%, 30% and 10%, respectively (Table 3.1, Figure 3.4b–e). These spin-state shifts are drastically smaller than those reported for the corresponding *para* isomers. 4-Methylamino-, 4-methylthio- and 4-methyl-benzoic acid all induce 70% shifts to high-spin[117], consistent with the *para* substituent being held in close proximity to the heme and removing the iron-bound water. By way of contrast, 4-formylbenzoic acid induces a smaller spin-state shift (25%)[276], though this is still larger than that induced by 3-formylbenzoic acid. Note that binding of 3-methylaminobenzoic acid and 3-formylbenzoic acid induced a small (0.5 nm) red-shift in the position of the Soret band (Figure A1, Table A1).

Table 3.1. Binding data and catalytic activity of CYP199A4 towards *meta*-substituted benzoic acids. Turnover data for *para*-substituted benzoic acid substrates is included for comparison; this data was published by others and is referenced. Values given are the mean ± SD, with $n \geq 3$. The NADH consumption rate (N) and product formation rate (PFR) are given in units of μM (μM-P450)$^{-1}$ min^{-1}. C is the coupling efficiency. The NADH leak rate was ~9 min^{-1}. This leak rate was not subtracted from the NADH consumption rates.

Substrate	% HS	K_d (μM)	N (min^{-1})	PFR (min^{-1})	C (%)	H_2O_2 (%)
3-methoxyBA [117]	40%	69 ± 2	498 ± 5	–[a]	–[a]	2 ± 0.7
4-methoxyBA [117]	≥95%	0.22 ± 0.02	1340 ± 28	1220 ± 120	91 ± 2	2 ± 0.2
3-methylaminoBA	10%	31 ± 1	255 ± 2	175 ± 1	69 ± 1	3.9 ± 0.2
4-methylaminoBA [117]	70%	1.6 ± 0.07	923 ± 200	669 ± 15	64 ± 2	3 ± 0.6
3-methylthioBA	30%	33 ± 0.5	56 ± 0.2	37 ± 1	66 ± 2	~1
4-methylthioBA [117]	70%	2.3 ± 0.3	1430 ± 180	1180 ± 130	83 ± 3	2 ± 0.4
3-methylBA [b]	30%	89 ± 3	78 ± 1	38 ± 1	48 ± 1	1.1 ± 0.5
4-methylBA [219]	70%	0.66 ± 0.05	444 ± 8	397 ± 22	89 ± 4	–[c]
3-formylBA	10%	420 ± 30	11 ± 0.2[d]	0.9 ± 0.1	8 ± 1	–[c]
4-formylBA	25% [276]	48 ± 2 [276]	134 ± 1	110 ± 2	83 ± 1	1.5 ± 0.3 [276]

[a] Coleman *et al.* reported that no product was formed. [b] 2-Methylbenzoic acid induced only a 5% spin-state shift and displayed low binding affinity (K_d = 610 ± 70 μM); the NADH consumption rate was only 13.1 ± 0.3 min^{-1} and no product was detected by either HPLC or GC-MS analysis of the turnover mixture. [c] Not measured. [d] The NADH consumption rate reported is the average rate over the first 15 minutes.

The small spin-state shifts induced by these *meta*-substituted benzoic acids imply that the substrate is not bound in a suitable orientation relative to the heme to efficiently displace the iron-bound water. If the *meta* substituent was oriented towards the heme, we might expect to observe

larger spin-state shifts due to steric displacement of the water. The small spin-state shifts additionally suggest that NADH consumption by CYP199A4 in the presence of these substrates will be slow because electron transfer is gated by displacement of the water.[100, 117, 152, 337] If these substrates bind exclusively with the *meta* substituent pointing away from the heme, we would also expect no product to be formed.

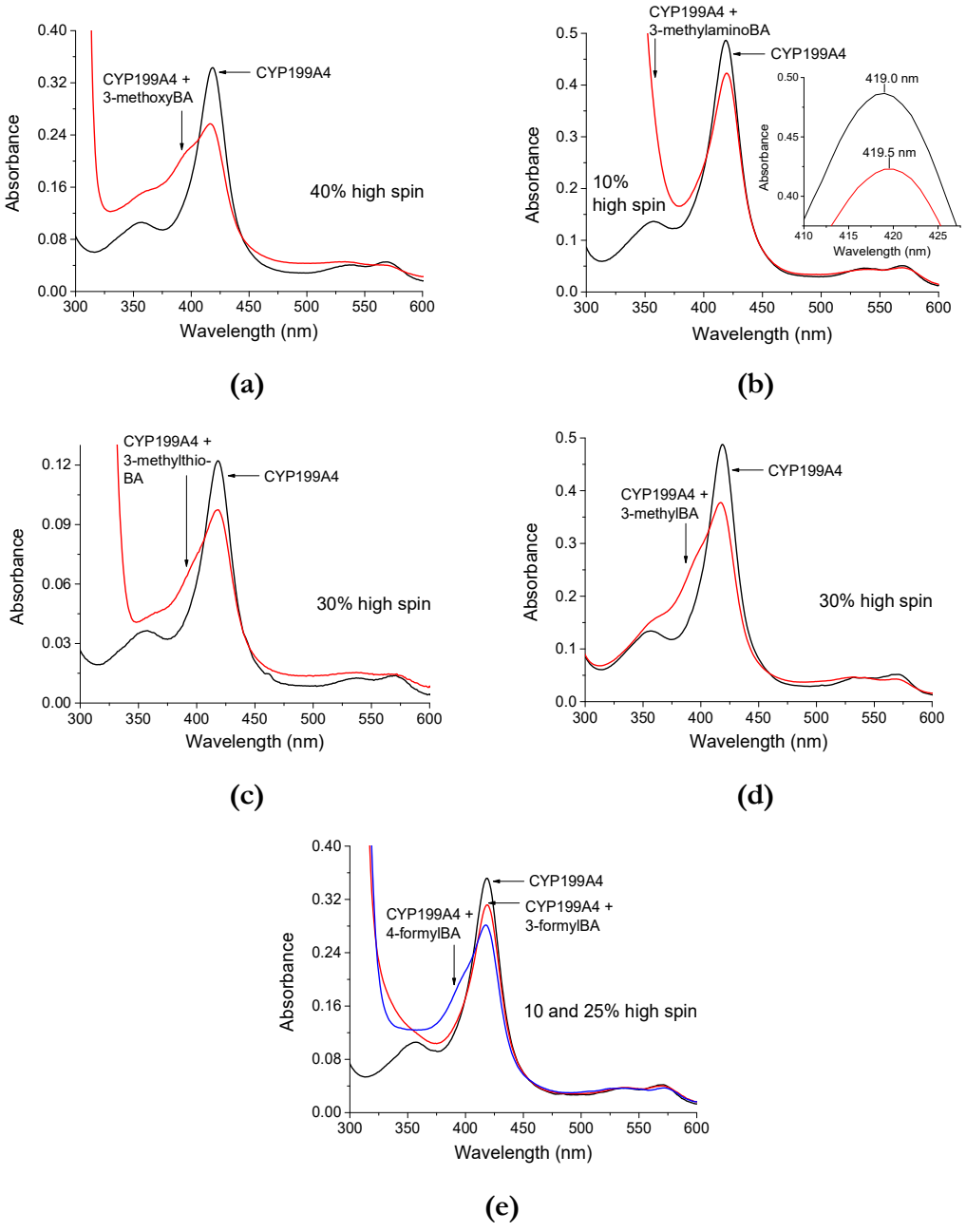

Figure 3.4. Spin-state shifts of CYP199A4 induced by **(a)** 3-methoxybenzoic acid[162], **(b)** 3-methylaminobenzoic acid, **(c)** 3-methylthiobenzoic acid, **(d)** 3-methylbenzoic acid and **(e)** 3-formylbenzoic acid. In **black** is the substrate-free form and in **red** is the substrate-bound enzyme. In **blue** is 4-formylbenzoic acid-bound CYP199A4 for comparison.

Based on the weak binding reported for 3-methoxybenzoic acid, the substrates investigated here were predicted to bind weakly to CYP199A4. 3-Methylaminobenzoic acid was found to have 20-fold lower affinity for CYP199A4 than the corresponding *para* isomer (K_d = 31 μM *vs.* 1.6 μM,[117] Figure 3.5a) and 3-methylthiobenzoic acid binds 14-fold less tightly than the corresponding *para*

isomer (K_d = 33 *vs.* 2.3 μM, Figure 3.5b). 3-Methylbenzoic acid has lower affinity than 3-methylamino- and 3-methylthio-benzoic acid (K_d = 89 μM, Figure 3.5c), and binds more than 100-fold less tightly than 4-methylbenzoic acid. 3-Formylbenzoic acid binds even more weakly than the other *meta*-substituted benzoic acids studied (K_d = 420 μM, Figure 3.5d) and it has ~9-fold lower affinity than the corresponding *para* isomer. This data indicates that the *meta*-substituted benzoic acids fit poorly in the CYP199A4 active site compared to the corresponding *para* isomers. It has been proposed that this weaker binding is due to steric clashes between the *meta* substituent and active site residues.[162]

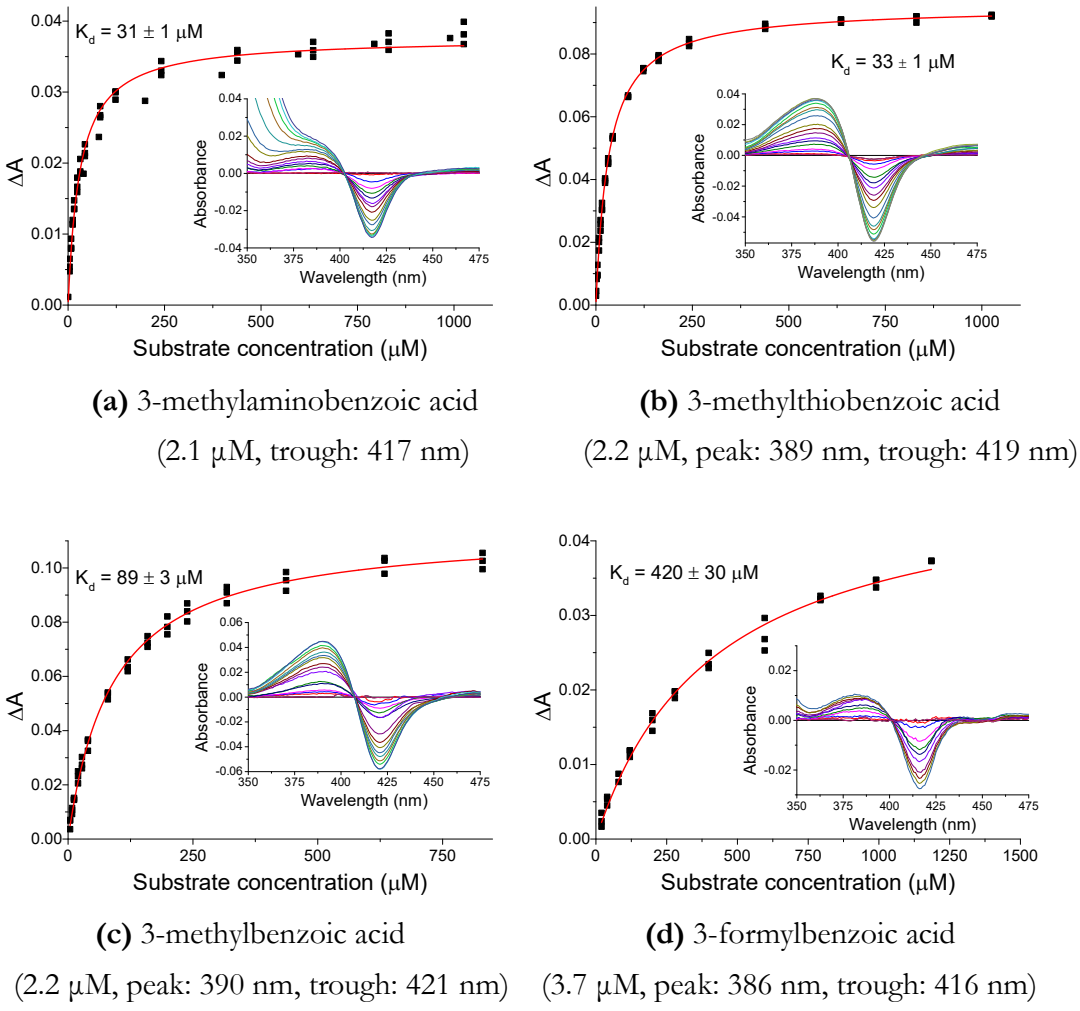

(a) 3-methylaminobenzoic acid (2.1 μM, trough: 417 nm)

(b) 3-methylthiobenzoic acid (2.2 μM, peak: 389 nm, trough: 419 nm)

(c) 3-methylbenzoic acid (2.2 μM, peak: 390 nm, trough: 421 nm)

(d) 3-formylbenzoic acid (3.7 μM, peak: 386 nm, trough: 416 nm)

Figure 3.5. UV-Vis titrations to determine the dissociation constant of CYP199A4 with benzoic acid substrates. The concentration of enzyme used and the peak and trough wavelengths are given under each graph. ΔA is defined as A_{peak} minus A_{trough}. Due to 3-methylaminobenzoic acid's interfering absorption **(a)**, the peak height at 390 nm could not be accurately measured. Only the decrease at 417 nm was used to calculate the dissociation constant. These substrates all induce type I difference spectra even though 3-methylamino- and 3-formyl-benzoic acid red-shift the Soret band.

In vitro NADH activity assays were performed to evaluate whether these substrates are metabolised by CYP199A4 (Table 3.1). The rate of NADH consumption by CYP199A4 with 3-methylaminobenzoic acid was substantially slower than the NADH consumption rate reported for the *para* isomer (255 *vs.* 923 min^{-1}) (Figure A2). However, HPLC analysis of the turnover mixture

unexpectedly revealed the presence of a metabolite, consistent with 3-aminobenzoic acid, which would arise from *N*-dealkylation of the substrate. As this compound was resolved poorly by HPLC under standard conditions (Figure 3.6), its identity was confirmed by GC-MS analysis of the TMS-derivatised turnover mixture (Figure 3.7). Both the retention time and mass of the product were identical to those of authentic 3-aminobenzoic acid. The mass spectrum of the TMS-derivatised product exhibited a molecular ion peak at m/z = 281.20, consistent with the calculated mass of doubly derivatised 3-aminobenzoic acid (m/z = 281.1267) (Figure A3). The coupling efficiency and product formation rate were calculated to be 69% and 175 min^{-1}, respectively. *N*-Dealkylation of 3-methylaminobenzoic acid by CYP199A4 thus occurs at a four-fold lower rate than *N*-dealkylation of 4-methylaminobenzoic acid (Table 3.1). Minimal levels of H_2O_2 were detected in the turnover mixtures; only 3.9% of the NADH was wasted via H_2O_2 uncoupling.

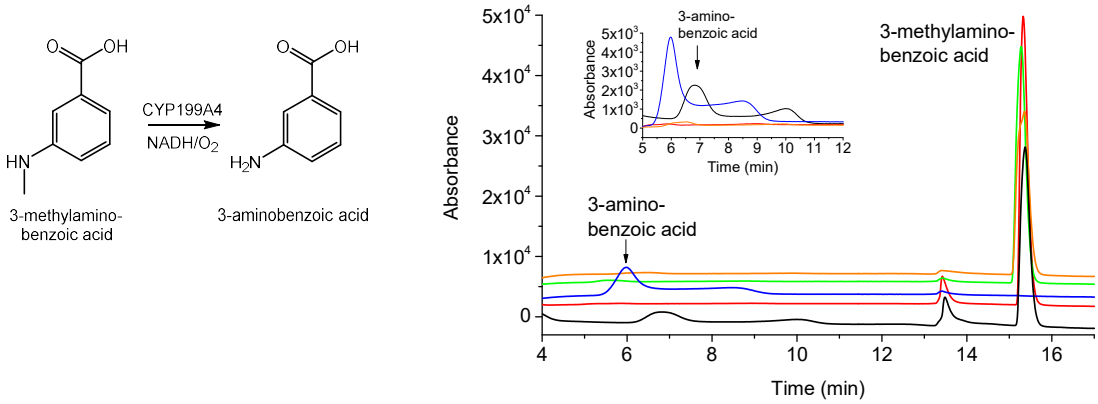

Figure 3.6. HPLC analysis of the CYP199A4 reaction with 3-methylaminobenzoic acid. In **black** is the *in vitro* turnover, in **red** and **orange** are control reactions omitting the P450 or NADH, in **blue** is authentic 3-aminobenzoic acid (broad bulge between 5.5 and 9.5 min) and in **green** is the 3-methylaminobenzoic acid (substrate) control (RT = 15.3 min). The eluate was monitored at 254 nm and elution was performed using a 0-50% gradient of AcCN in H_2O with 0.1% TFA. Absorbance is given in milli-Absorbance Units (mAU) in all HPLC chromatograms in this thesis.

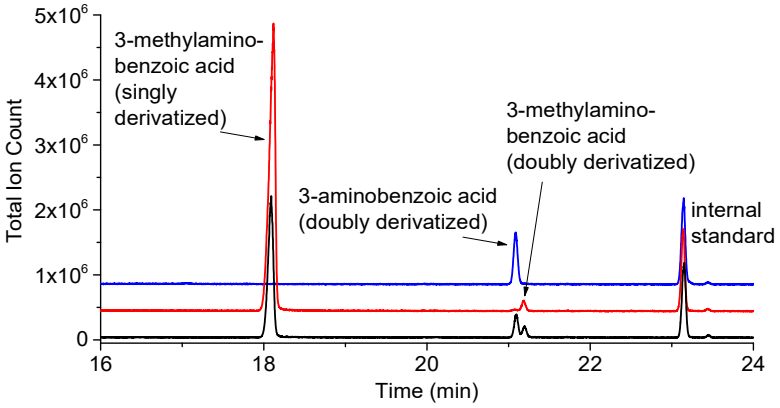

Figure 3.7. GC-MS analysis of the CYP199A4 reaction with 3-methylaminobenzoic acid after TMS derivatisation. In **black** is the *in vitro* turnover, in **red** is the substrate control (singly derivatised substrate has a RT of 18.1 min and doubly derivatised substrate a RT of 21.2 min), and in **blue** is the 3-aminobenzoic acid product control (doubly derivatised, RT = 21.1 min).

Although 3-methylthiobenzoic acid induced a 3-fold larger spin-state shift than 3-methylaminobenzoic acid, the NADH consumption rate with 3-methylthiobenzoic acid was substantially slower. CYP199A4 consumed NADH at a rate of only 56 min^{-1} with 3-methylthiobenzoic acid (Figure A2). This is ~25-fold slower than the NADH consumption rate with 4-methylthiobenzoic acid.[117] Again, a metabolite was unexpectedly detected via HPLC and GC-MS analysis of the turnover mixture and was identified as the sulfoxide by co-elution with chemically synthesised 3-methylsulfinylbenzoic acid (Figure 3.8, Figure A4, Scheme 2.2). No other peaks which might correspond to the sulfone or dealkylation product were detected. This is consistent with reports that sulfoxidation is a common P450 reaction but *S*-dealkylation is rare.[197] Presumably the sulfoxide does not preferentially bind to the P450 given that there was no further oxidation to the sulfone. We were unable to separate the enantiomers of 3-methylsulfinylbenzoic acid by chiral HPLC, so the enantioselectivity of the reaction is unknown. 3-Methylsulfinylbenzoic acid from a commercial source was used for calibration and the coupling efficiency and product formation rate were calculated to be 66% and 37 min^{-1}, respectively. Thus, CYP199A4 oxidises 3-methylthiobenzoic acid at a ~30-fold slower rate than it oxidises 4-methylthiobenzoic acid (Table 3.1). Only minor amounts of H_2O_2 generated via uncoupling were detected in the reaction mixture (~3 μM).

However, we reasoned that when the rate of NADH consumption is slow, as it is here, H_2O_2 generated via uncoupling may be lost before the reaction is complete. Indeed, we found that when ~300 μM H_2O_2 was incubated with a control turnover mixture containing HaPux, HaPuR and CYP199A4 in Tris-HCl buffer (but no NADH, substrate or catalase), almost all H_2O_2 was lost over a 60-minute period (Figure A5a). It appeared that the [2Fe-2S] ferredoxin HaPux was consuming the H_2O_2 (Figure A5b). Therefore, the amount of H_2O_2 detected at the end of a slow reaction is likely to be an underestimate of the actual amount of H_2O_2 generated.

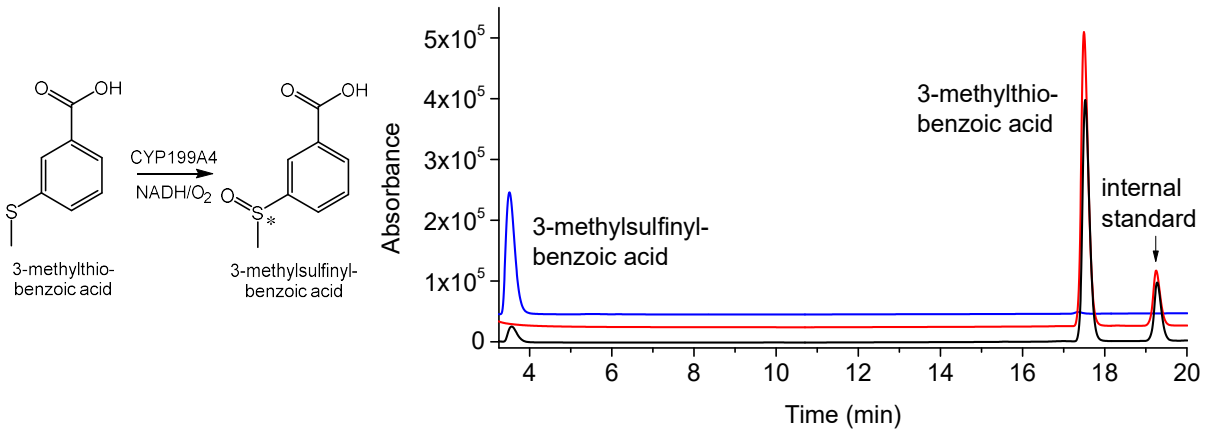

Figure 3.8. HPLC analysis of the CYP199A4 reaction with 3-methylthiobenzoic acid. In **black** is the *in vitro* turnover, in **red** is a control reaction performed without P450, and in **blue** is chemically synthesised 3-methylsulfinylbenzoic acid (RT = 3.5 min). The 3-methylthiobenzoic acid substrate appears at RT = 17.5 min. The eluate was monitored at 254 nm and elution was performed using a 20-95% gradient of AcCN in H_2O with 0.1% TFA.

NADH was consumed at a rate of 78 min^{-1} by CYP199A4 with 3-methylbenzoic acid, compared to a rate of 444 min^{-1} with the *para* isomer (Figure A2).[219] CYP199A4 has previously been reported to convert the *para* isomer exclusively into 4-hydroxymethylbenzoic acid.[219] CYP199A4 similarly converted 3-methylbenzoic acid into a single product (Figure 3.9, Figure A6). The mass of the TMS-derivatised product (m/z = 296.10) is consistent with the calculated mass of doubly derivatised 3-hydroxymethylbenzoic acid (m/z = 296.1264) (Figure A7). The product could also conceivably be 4-hydroxy-3-methylbenzoic acid, arising from hydroxylation of the benzene ring (Figure A8). However, the retention time of authentic 4-hydroxy-3-methylbenzoic acid was substantially different to that of the P450 product, discounting the possibility that the substrate was hydroxylated at the *para* position of the aromatic ring (Figure A9). The product of the P450 reaction was subsequently confirmed to be 3-hydroxymethylbenzoic acid via co-elution with synthesised 3-hydroxymethylbenzoic acid, which was obtained by reduction of 3-formylbenzoic acid with sodium borohydride (Figures A10, A11). As a pure sample of 3-hydroxymethylbenzoic acid was not available for calibration, the substrate was instead used. The estimated coupling efficiency for this reaction was 48%, and the product formation rate 38 min^{-1}. CYP199A4 therefore oxidises 3-methylbenzoic acid at a ~10-fold slower rate than it hydroxylates 4-methylbenzoic acid (Table 3.1). We further investigated whether CYP199A4 had any activity towards the *ortho* isomer (Table A2). CYP199A4 displayed weak affinity for 2-methylbenzoic acid (K_d = 611 μM) and only a small spin-state shift (~5%) was observed (Figure A12). In line with the small spin-state shift induced by this substrate, the NADH consumption rate was only 13 min^{-1}, barely faster than the leak rate (~9 min^{-1}). No product was detected by GC-MS or HPLC analysis of the turnover mixture (Figures A13–A15). This result reaffirms that CYP199A4 does not oxidise *ortho*-substituted benzoic acids.

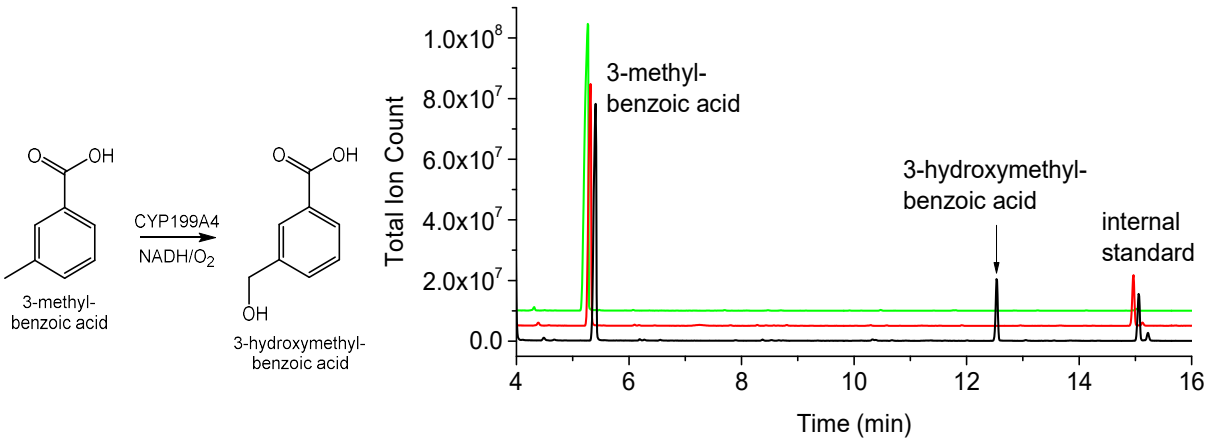

Figure 3.9. GC-MS analysis of the CYP199A4 *in vitro* reaction with 3-methylbenzoic acid. In **black** is the *in vitro* turnover, in **red** is a control reaction omitting the P450 and in **green** is the derivatised 3-methylbenzoic acid substrate control (RT = 5.1 min). The product, presumed to be 3-hydroxymethylbenzoic acid, appears at 12.3 min.

CYP199A4 consumed NADH with 3-formylbenzoic acid at a rate (11 min^{-1}) roughly equal to the leak rate and only minor amounts of product (isophthalic acid) were detected (Figures 3.10 and

A2). No product was detected when the P450 was omitted from the reaction mixture, so it does not appear that the product arose simply from air oxidation of the aldehyde.[338-339] The coupling efficiency and product formation rate were only 8% and 0.9 min^{-1}, respectively. For comparison, CYP199A4 converts 4-formylbenzoic acid into terephthalic acid at a rate of 110 min^{-1} with a coupling efficiency of ~83% (Figure 3.11). CYP199A4's activity towards 4-formylbenzoic acid has been previously investigated.[276] This again demonstrates CYP199A4's preference for *para*- over *meta*-substituted benzoic acid substrates.

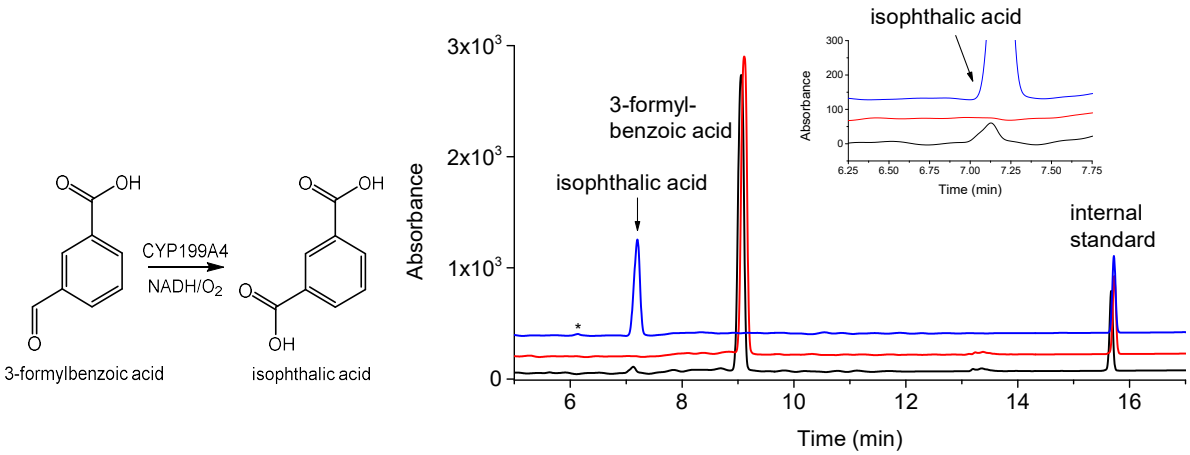

Figure 3.10. HPLC analysis of the CYP199A4 *in vitro* reaction with 3-formylbenzoic acid. In **black** is the *in vitro* turnover, in **red** is a control reaction performed without P450, and in **blue** is authentic isophthalic acid (RT = 7.1 min). The substrate appears at RT = 9.1 min. Gradient: 20-95% AcCN in H_2O with 0.1% TFA. Detection wavelength: 220 nm. * The sample of authentic isophthalic acid was contaminated with 6% terephthalic acid (RT = 6.1 min).

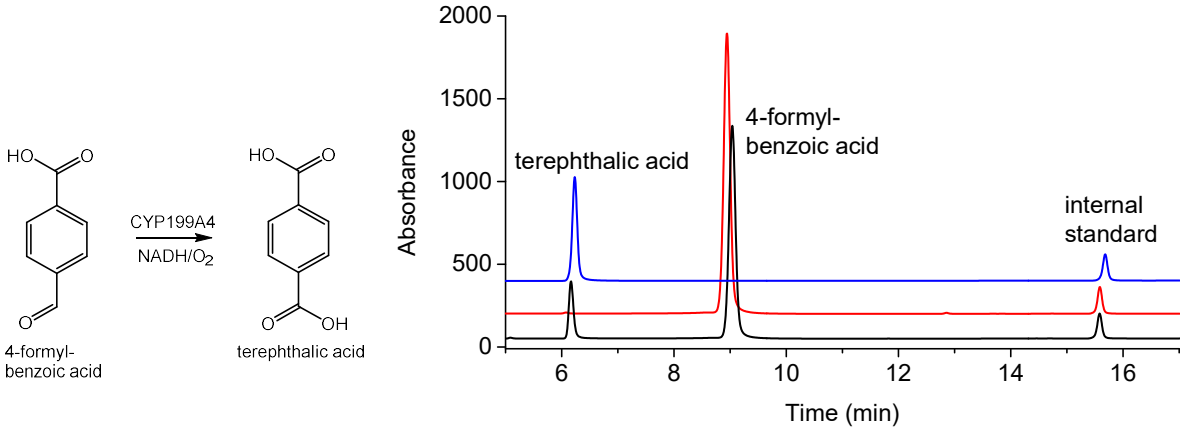

Figure 3.11. HPLC analysis of the CYP199A4 *in vitro* reaction with 4-formylbenzoic acid. In **black** is the *in vitro* turnover, in **red** is a control reaction performed without P450, and in **blue** is authentic terephthalic acid (RT = 6.1 min). The substrate appears at RT = 8.9 min. Gradient: 20-9% AcCN in H_2O with 0.1% TFA. Detection wavelength: 254 nm.

3.2.2 Docking substrates into the active site of CYP199A4

The finding that CYP199A4 oxidises 3-methylamino-, 3-methylthio-, and 3-methyl-benzoic acid was unexpected. This result led us to speculate that the orientation of these substrates in the

binding pocket of CYP199A4 may differ from that of 3-methoxybenzoic acid. We therefore decided to dock 3-methylaminobenzoic acid into the active site of CYP199A4 to predict the likely binding mode of this substrate. The methylamino moiety must spend some portion of time at a suitable distance from the heme to be oxidised.

ICM-Pro software (Molsoft)[309] was used to dock 3-methylaminobenzoic acid into CYP199A4 (PDB: 5U6W). The top-scoring pose had the 3-methylamino moiety pointing down towards the heme, with the methyl carbon only 4.1 Å from the iron (Figure 3.12, Table A3). This binding mode could rationalise why the substrate was hydroxylated at this position. An alternative, poorer-scoring pose had the *meta* substituent pointing away from the heme. Docking scores are given in Table A4.

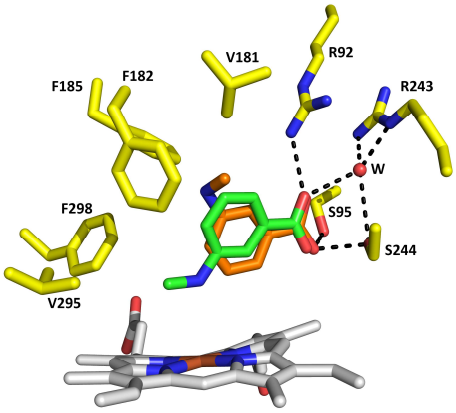

Figure 3.12. 3-Methylaminobenzoic acid docked into the active site of CYP199A4 (PDB ID: 5U6W). The top-scoring pose is depicted in **green** and a higher-energy (lower-scoring) pose is shown in **orange**.

3-Methylthio- and 3-methyl-benzoic acid were also docked into the binding pocket of CYP199A4, and again the top-scoring poses had the *meta* substituent pointing towards the heme (Figure 3.13a,b, Tables A5, A6). The position of the benzene ring was shifted relative to that of the *para* isomers (Figure A16). The sulfur of 3-methylthiobenzoic acid and methyl group of 3-methylbenzoic acid were 4.2 Å and 4.0 Å from the heme iron, respectively. On the other hand, when veratric acid was docked into the active site, the top-scoring poses had the *meta* substituent pointing away from the heme, consistent with the crystal structure orientation (Figures 3.13c and A17, Table A7). Thus, ICM-Pro software correctly predicted the binding mode of veratric acid. For comparison, we docked 2- and 3-methoxybenzoic acid into the active site with the expectation that these substrates would bind with the methoxy substituent oriented away from the heme. 2-Methoxybenzoic acid did prefer to bind with the *ortho* methoxy group pointing away from the heme (Figure A18, Table A8). However, the top-scoring pose of 3-methoxybenzoic acid had the *meta* substituent pointing towards the heme, with the methyl group 4.0 Å from the iron (Figure 3.13d, Table A9). This result was unexpected given that CYP199A4 does not metabolise 3-methoxybenzoic acid.[162] To more satisfactorily answer the question of how these different *meta*-substituted benzoic acids bind, we decided to solve the crystal structures of these substrates bound to CYP199A4 (Section 3.2.3).

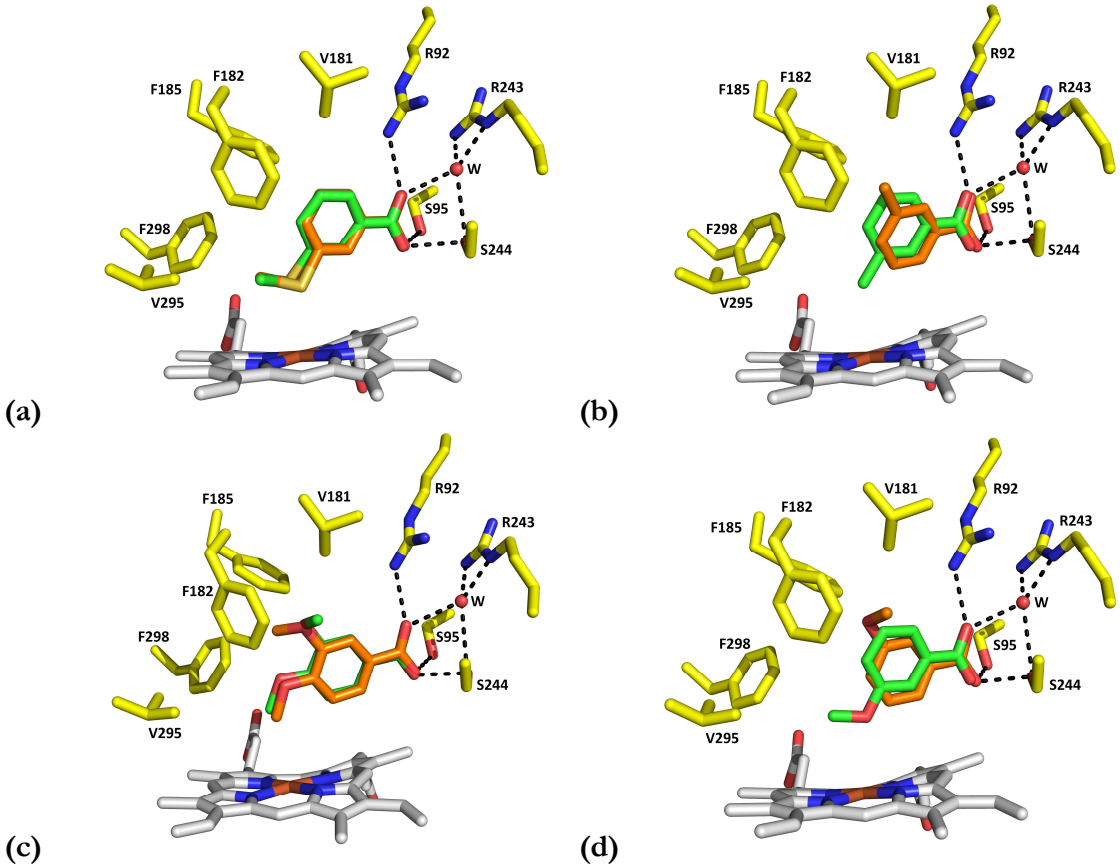

Figure 3.13. Benzoic acids docked into CYP199A4 (PDB ID: 5U6W). The docked substrates are **(a)** 3-methylthiobenzoic acid, **(b)** 3-methylbenzoic acid, **(c)**, veratric acid and **(d)** 3-methoxybenzoic acid. The top-scoring pose is shown in **green**, and lower-scoring poses in **orange**.

3.2.3 X-ray crystal structures of 3-methoxy-, 3-methylthio-, 3-methylamino-, 3-methyl- and 4-methyl-benzoic acid-bound CYP199A4

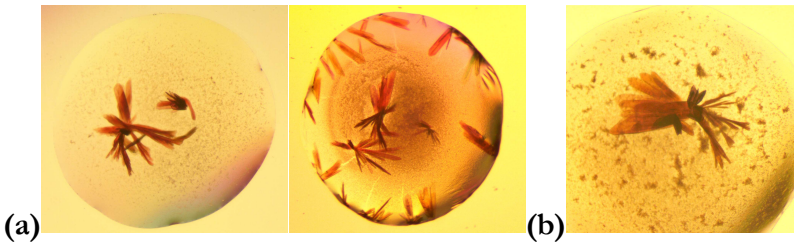

Figure 3.14. **(a)** 3-Methylthio- and **(b)** 3-methoxy-benzoate-bound CYP199A4 crystals under magnification. Refer to Appendix E for crystal dimensions.

CYP199A4 was co-crystallised with 3-methoxy-, 3-methylthio-, 3-methylamino-, and 3-methyl-benzoic acid (Figure 3.14) and X-ray diffraction data were collected at the MX1 and MX2 beamlines at the Australian Synchrotron[315-316] at 100 K. CYP199A4 was also co-crystallised with 4-methylbenzoic acid since the crystal structure of this complex had not previously been solved. Crystal structures of CYP199A4 in complex with the other *para* isomers have been reported in the literature.[29, 117] High-resolution crystal structures of these protein-ligand complexes were solved at resolutions of 1.60-1.89 Å (Figure 3.15) and deposited into the PDB. Data collection and refinement statistics and PDB accession codes are presented in Table A10.

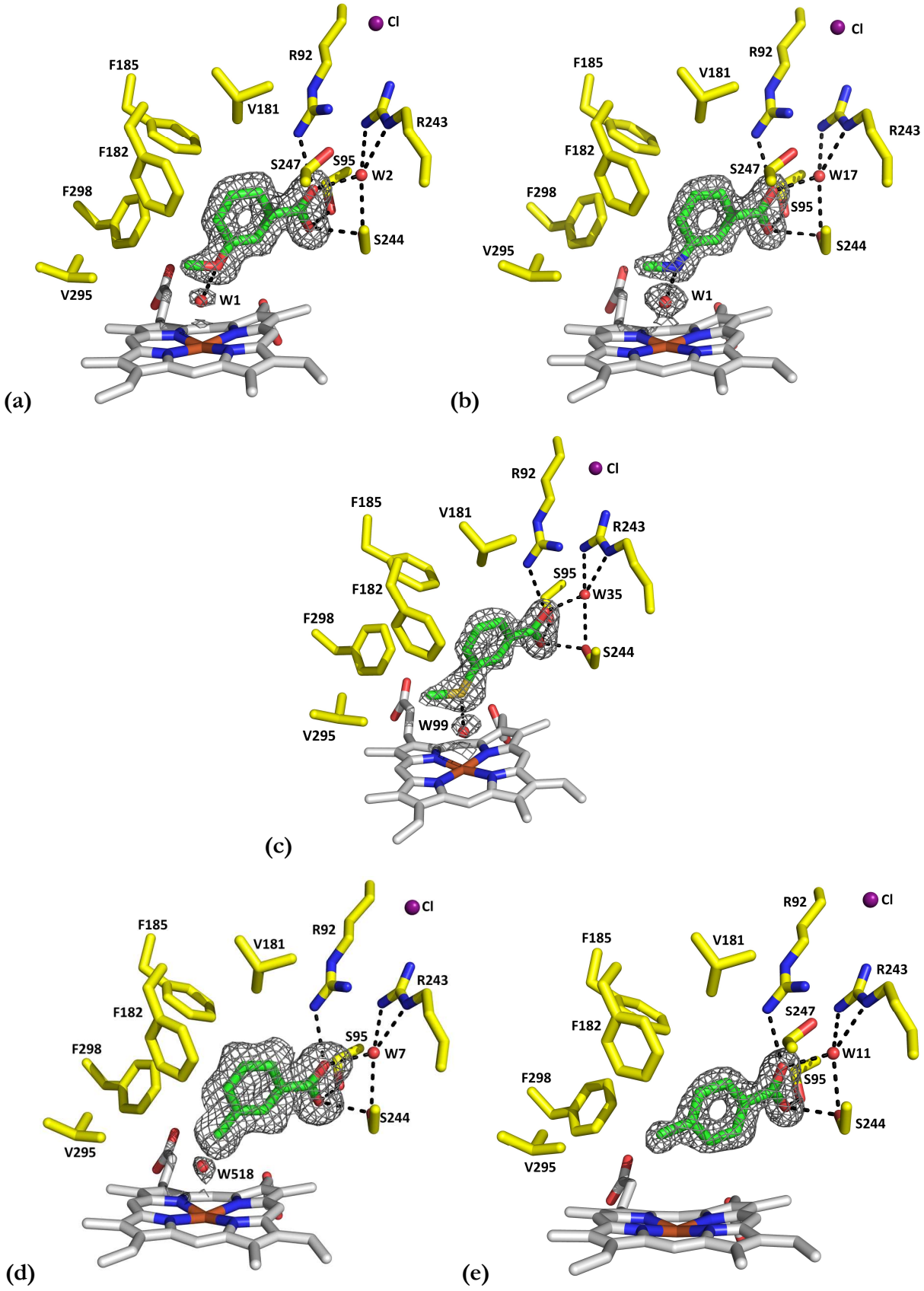

Figure 3.15. Crystal structures of **(a)** 3-methoxy-, **(b)** 3-methylamino-, **(c)** 3-methylthio-, **(d)** 3-methyl- and **(e)** 4-methyl-benzoate-bound CYP199A4. The *2mFo-DFc* electron density of the substrate and iron-bound water ligand is shown as grey mesh. The electron density map is either a composite omit map[327] or a polder omit map[340]. The contour level is given in Table A10. Hydrogen bonds are represented by black dashed lines. In grey is the heme, active-site residues are yellow, the substrate is green, waters are represented by red spheres, and the chloride ion is purple.

The RMSD between Cα atoms of the superimposed structures is ≤0.178 Å, indicating that the overall protein fold is virtually identical for all five complexes. These crystal structures also had a highly similar fold to previously reported structures of CYP199A4 (Figure A19). The crystallographic poses of 3-methoxy-, 3-methylthio-, 3-methylamino-, and 3-methyl-benzoic acid agree with the top-scoring docked poses (Figure A20); the RMSD between the crystal structure poses and docked poses was <0.54 Å. These substrates bind with the *meta* substituent close to the heme. Despite not being oxidised, the *meta* substituent of 3-methoxybenzoic acid also points down towards the heme (Figure 3.15a).

Consistent with the small spin-state shifts induced by 3-methoxy-, 3-methylamino-, and 3-methylthio-benzoic acid, the crystal structures show that a partial-occupancy water ligand is present in the sixth coordination position of the heme (Figure 3.15, Table 3.2). P450 crystal structures in which the iron-bound water has partial occupancy have previously been reported.[159, 166] A hydrogen bond potentially exists between the water ligand and the heteroatom (N, S, or O) of the *meta* substituent. This hydrogen bond between the nitrogen of 3-methylaminobenzoic acid and the heme-bound aqua ligand (3.1 Å) explains the small (0.5 nm) Soret band red-shift that is observed when this substrate binds to CYP199A4.[154] The occupancy of the water ligand in these crystal structures approximately matches the measured fraction of low-spin heme (Table 3.2). The 3-methylaminobenzoate-CYP199A4 complex is 90% low-spin and the occupancy of the water ligand in the crystal structure is also 90% (Figure 3.15b). The 3-methylthiobenzoate-CYP199A4 complex is 70% low-spin and the refined water occupancy is 77% (Figure 3.15c), while the 3-methoxybenzoate-CYP199A4 complex is 60% low-spin and the water ligand occupancy is 50%. 4-Methylbenzoic acid, on the other hand, induces a large spin-state shift to high-spin (70%) and a water ligand is not observed in the crystal structure (Figure 3.15e). In the 3-methylbenzoic acid crystal structure, the occupancy of the water ligand is low (21%) even though this substrate induces only a small shift to high-spin. 3-Methylbenzoic acid has a hydrophobic substituent, so it cannot form a hydrogen bond with the water ligand (Figure 3.15d).

Table 3.2. Refined occupancies of the heme-bound water ligand

Crystal structure	Occupancy of iron-bound water ligand	Spin-state shift (% HS)
3-methoxybenzoic acid	50%	40%
3-methylthiobenzoic acid	77%	30%
3-methylaminobenzoic acid	90%	10%
3-methylbenzoic acid	21%	30%
4-methylbenzoic acid	no sixth ligand	70%

Figure 3.16 shows the active site of 3-methylthiobenzoate-bound CYP199A4 superimposed with the 4-methylthiobenzoic acid crystal structure solved by Coleman.[117] Only subtle differences in the positions of active-site residues are observed. While the methylthio moiety of 3-methylthiobenzoic acid is rotated out of the plane of the benzene ring by 13°, that of 4-

methylthiobenzoic acid is rotated 34° out of the benzene plane (Table 3.3). The benzene ring of 3-methylthiobenzoic acid is shifted up away from the heme relative to the benzene ring of 4-methylthiobenzoic acid, as was predicted by the docking software (Figure A16). This avoids a steric clash between the *meta* substituent and the heme (Figure A21). In both structures, the methylthio moiety is held close to the heme, though the sulfur of 3-methylthiobenzoic acid is nearer to the iron than that of 4-methylthiobenzoic acid (4.3 *vs.* 5.0 Å). The methyl group of 3-methylthiobenzoic acid is also held in close proximity to the heme iron (4.4 Å), yet no *S*-dealkylation was observed in the *in vitro* turnovers.

In the crystal structure of 4-methylthiobenzoate-bound CYP199A4, the heme iron is five-coordinate.[117] As mentioned, in the 3-methylthiobenzoate-CYP199A4 structure, a 0.77-occupancy water ligand is present (Fe–O distance 2.3 Å). The sulfur of 3-methylthiobenzoic acid is 3.3 Å from the water and the water ligand must be stabilised by an interaction with the sulfur. In the 3-methylthiobenzoic acid structure, there is more space above the heme than in the 4-methylthiobenzoic acid structure, allowing the heme iron to remain hexacoordinate (Figure 3.16).

Computational chemists have calculated that the Fe=O bond length of Cpd I is 1.62 Å[341-342]. The Cpd I Fe=O bond length of several P450s has also been measured using EXAFS (Extended X-Ray Absorption Fine Structure) and found to be 1.67 Å.[343] To estimate distances between the ferryl oxygen of Cpd I and the bound substrate, an oxygen atom was introduced 1.62 Å above the heme iron opposite and aligned with the Fe-S bond. The measured distance between the Cpd I oxygen and the sulfur of 3-methylthiobenzoic acid is 3.2 Å (Table 3.3). This is slightly shorter than the distance between the Cpd I oxygen and the sulfur of 4-methylthiobenzoic acid (3.4 Å). For the *meta* isomer the Fe^{IV}=O–S angle is 126.2°, whereas for the *para* isomer the angle is larger (162.5°).

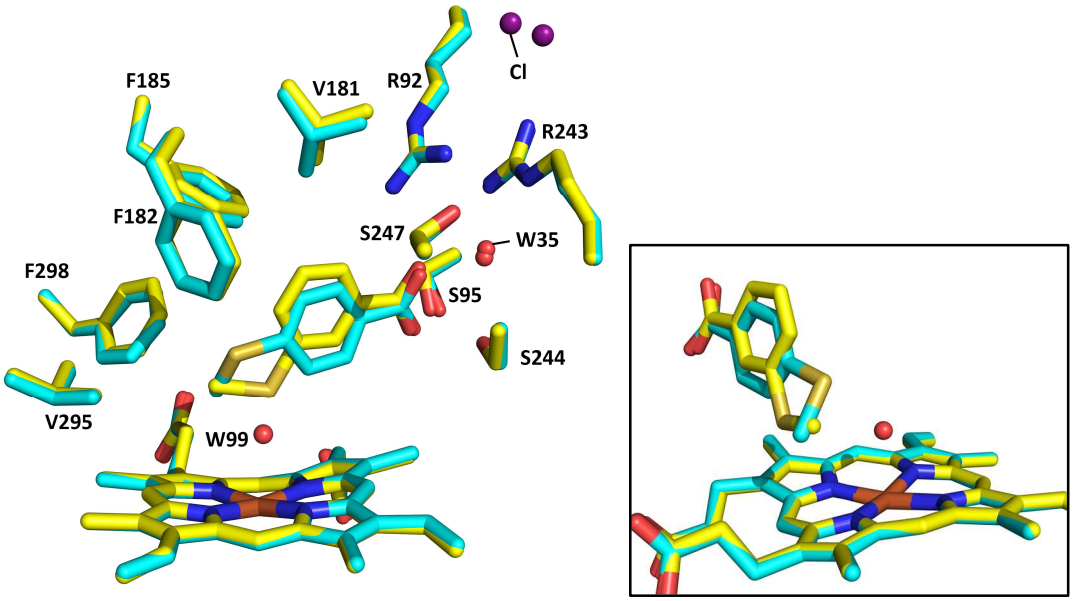

Figure 3.16. Overlaid crystal structures of 4-methylthio- (cyan) and 3-methylthio-benzoate-bound CYP199A4 (yellow). The waters and chloride in the 3-methylthiobenzoic acid structure are labelled.

In Figure 3.17, the active site of 3-methylaminobenzoate-bound CYP199A4 is overlaid with the 4-methylaminobenzoate-CYP199A4 structure. A water ligand to the heme is present in the 3-methylaminobenzoate-CYP199A4 structure at 90% occupancy (Fe–O distance 2.2 Å), and this water interacts with the substrate nitrogen (3.1 Å). The nitrogen and methyl group of 3-methylaminobenzoic acid are 4.2 and 4.4 Å from the heme iron, respectively. Distances were also measured between the substrate and the Cpd I oxygen. The distance between the Cpd I oxygen and methyl carbon of 3-methylaminobenzoic acid is 3.1 Å. This distance is similar to that between the Cpd I oxygen and methyl carbon of 4-methylaminobenzoic acid (3.0 Å). The Fe^{IV}=O–C_{Me} angle is similar for both the *meta* and *para* isomers (129.9 *vs.* 124.6°). Even though the nitrogen is also close to the Cpd I oxygen (3.0 Å), no *N*-oxidation of 3-methylaminobenzoic acid occurred.

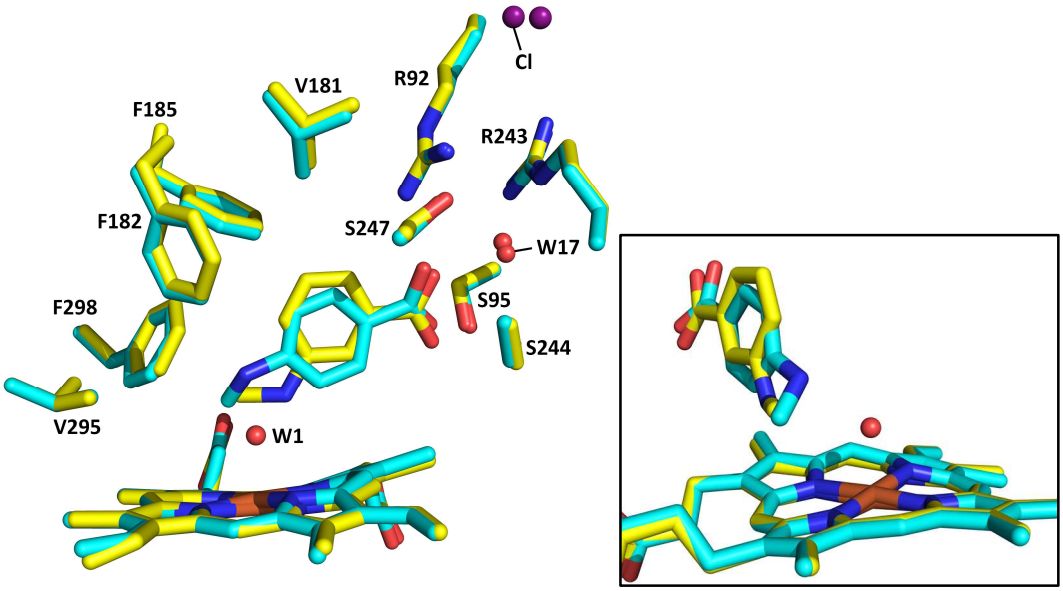

Figure 3.17. Overlaid crystal structures of 4-methylamino- (cyan) and 3-methylamino-benzoate-bound CYP199A4 (yellow). The waters and chloride in the 3-methylaminobenzoic acid structure are labelled.

The 3-methoxybenzoate- and 4-methoxybenzoate-bound CYP199A4 crystal structures are overlaid in Figure 3.18. In both structures, the methoxy group is held above the heme. The O and C_{Me} of 3-methoxybenzoic acid are equidistant from the heme iron (4.4 Å), and the methoxy group is rotated 20° out of the plane of the benzene ring. In contrast, the methoxy group of 4-methoxybenzoic acid lies almost in the plane of the benzene ring, and the C_{Me} is closer to the iron (4.1 Å) than that of 3-methoxybenzoic acid, preventing the heme iron from remaining hexacoordinate.

Distances were also measured between the substrate and ferryl oxygen of Cpd I. The C_{Me} and O of 3-methoxybenzoic acid are both 3.1 Å from the Cpd I oxygen, whereas the C_{Me} and O of 4-methoxybenzoic acid are 2.7 and 3.6 Å from the ferryl oxygen. The Fe^{IV}=O–C_{Me} angle is roughly the same for both 3-methoxy- and 4-methoxy-benzoic acid (136.3 *vs.* 140.7°).

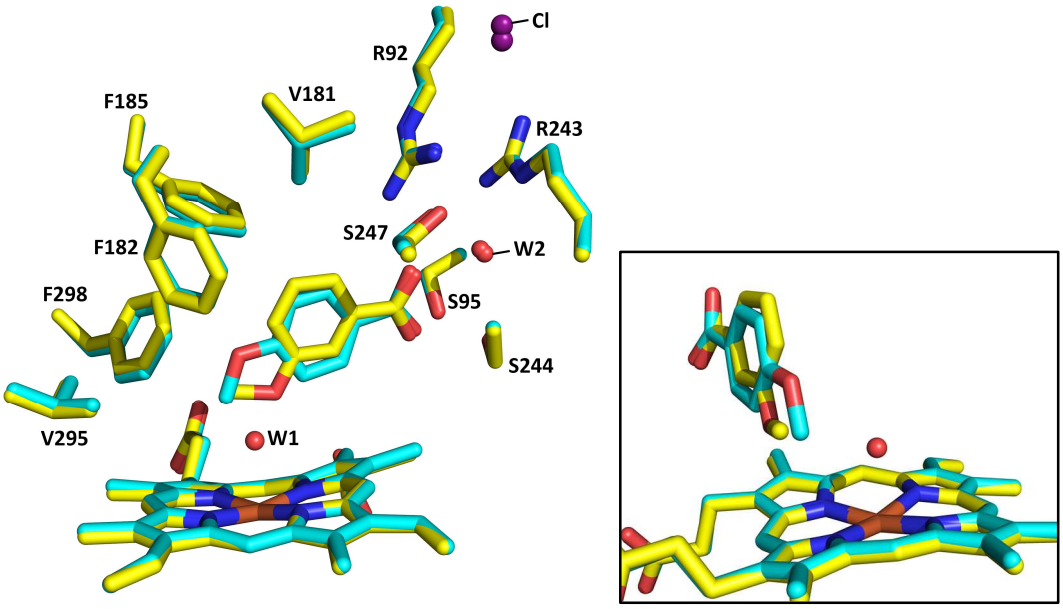

Figure 3.18. Overlaid crystal structures of 4-methoxy- (cyan) and 3-methoxy-benzoate-bound CYP199A4 (yellow). The waters and chloride in the 3-methoxybenzoic acid structure are labelled.

The methyl group of both 3-methyl- and 4-methyl-benzoic acid is held close to the heme iron (4.4 *vs.* 4.5 Å) and hydroxylation accordingly occurs at this position (Figure 3.19). A low-occupancy water ligand is present in the 3-methylbenzoate-CYP199A4 structure with an Fe–O distance of 2.5 Å, but no water ligand was detected in the 4-methylbenzoic acid structure (Figure 3.15d,e). Again, the benzene ring of 3-methylbenzoic acid is shifted away from the heme relative to that of 4-methylbenzoic acid, though the carboxylate groups are held in similar positions. The methyl of 3-methylbenzoic acid is held slightly further from the ferryl oxygen than that of 4-methylbenzoic acid (3.2 *vs.* 3.0 Å). The Fe^{IV}=O–C_{Me} angle is larger for 4-methylbenzoic acid than for 3-methylbenzoic acid (154.4 *vs.* 130.4°) (Table 3.3).

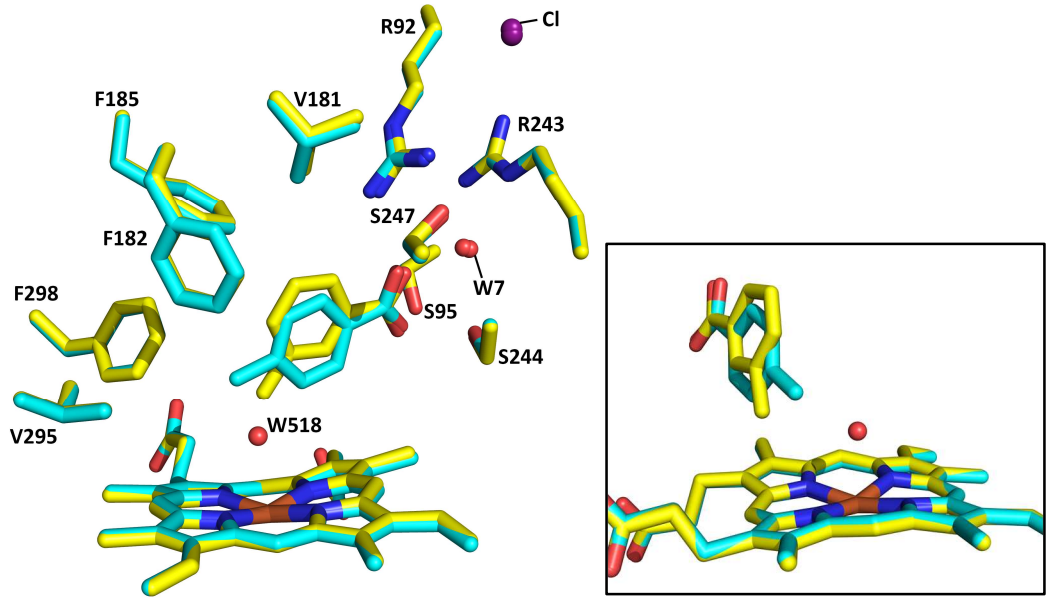

Figure 3.19. Overlaid crystal structures of 4-methyl- (cyan) and 3-methyl-benzoate-bound CYP199A4 (yellow). The waters and chloride in the 3-methylbenzoic acid structure are labelled.

Table 3.3. Distances between the heme iron and *meta*-substituted benzoic acid substrates. Values are also given for the corresponding *para* isomers for comparison.[277] Angles and distances were measured between the substrate and the hypothetical position[117] of the Cpd I oxygen (inserted 1.62 Å above the heme iron). Substrate names are abbreviated: **3-S** = 3-methylthioBA; **4-S** = 4-methylthioBA; **3-N** = 3-methylaminoBA; **4-N** = 4-methylaminoBA; **3-O** = 3-methoxyBA; **4-O** = 4-methoxyBA; **3-Me** = 3-methylBA; **4-Me** = 4-methylBA.

Distance (Å) (X = S, N, or O)	**3-S**	**4-S**	**3-N**	**4-N**	**3-O**	**4-O**	**3-Me**	**4-Me**
C_{Me} - Fe	4.4	4.5	4.4	4.1	4.4	4.1	4.4	4.5
C_{Me} - O=Fe^{IV}	3.1	3.3	3.1	3.0	3.1	2.7	3.2	3.0
X - Fe	4.3	5.0	4.2	4.2	4.4	5.2	-	-
X - O=Fe^{IV}	3.2	3.4	3.0	2.8	3.1	3.6	-	-
Fe - OH_2 ligand	2.3	-	2.2	-	2.4	-	2.5	-
X - OH_2 ligand	3.3	-	3.1	-	3.2	-	-	-
C_{Me} - OH_2 ligand	3.2	-	3.2	-	3.1	-	3.1	-
Angle (°)								
Fe^{IV}=O-C_{Me}	136.8	131.9	129.9	124.6	136.3	140.7	130.4	154.4
Fe^{IV}=O-X	126.2	162.5	126.8	148.6	130.0	158.3	-	-
Dihedral angle C_{Me}-X-C_3-C_4	13.1	33.9	32.7	50.0	20.0	2.1	-	-

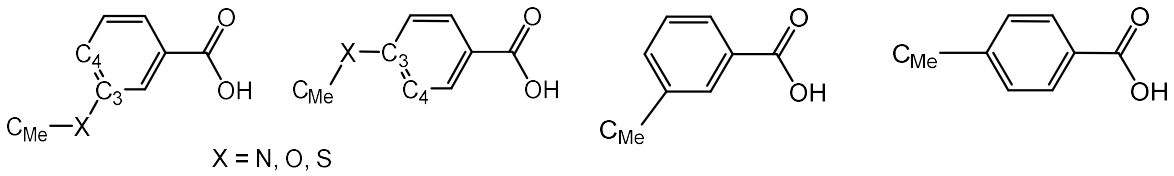

Refer to Figure A22 and Tables A11–A13 for measurements of the Fe-S distance and displacement of the iron out of the heme plane. The heme iron is displaced further below the porphyrin plane in structures lacking a heme-bound water ligand.

3.2.4 Spin-state shifts induced by bulky *meta*-substituted benzoic acids and turnover data

The crystal structures of 3-methoxy-, 3-methylamino-, and 3-methylthio-benzoate-bound CYP199A4 revealed that although the *meta* substituent is positioned close to the heme, the water ligand is not displaced. We therefore hypothesised that substrates with bulkier *meta* substituents would be more likely to efficiently displace the water ligand and that CYP199A4 would display higher activity towards these substrates. Various bulky substrates (3-ethoxybenzoic acid, 3-isopropylbenzoic acid, and 3-*tert*-butylbenzoic acid) were docked into the active site of CYP199A4 (Figure 3.20, Tables A14–A16). The top-scoring poses have the *meta* substituent positioned close to the heme (Table 3.4). However, docking 3-*tert*-butylbenzoic acid into CYP199A4 resulted in a steric clash between the *tert*-butyl group and a heme nitrogen (Figure 3.20c). This indicates that this substrate may be too bulky to fit into the active site. We subsequently measured the spin-state shifts induced by these substrates. The minimal spin-state shift (<5%) induced by 3-*tert*-butylbenzoic acid implies that the bulky *tert*-butyl group hinders binding (Figure 3.21a). In contrast, 3-ethoxybenzoic acid induced an almost complete shift to HS (85%), indicating efficient removal of the water

(Figure 3.21b). A crystal structure of this complex was later solved which confirmed the water had been expelled (*vide infra*). 3-Isopropylbenzoic acid induced a smaller spin-state shift (40%) (Figure 3.21c). The binding affinity of 3-ethoxybenzoic acid and 3-isopropylbenzoic acid was measured (Figure 3.22). 3-Ethoxybenzoic acid was found to bind substantially less tightly than the *para* isomer (K_d = 82 ± 2 *vs.* 0.17 μM). 3-Isopropylbenzoic acid binds even more weakly than 3-ethoxybenzoic acid (K_d = 411 μM), indicating a poor fit to the binding pocket.

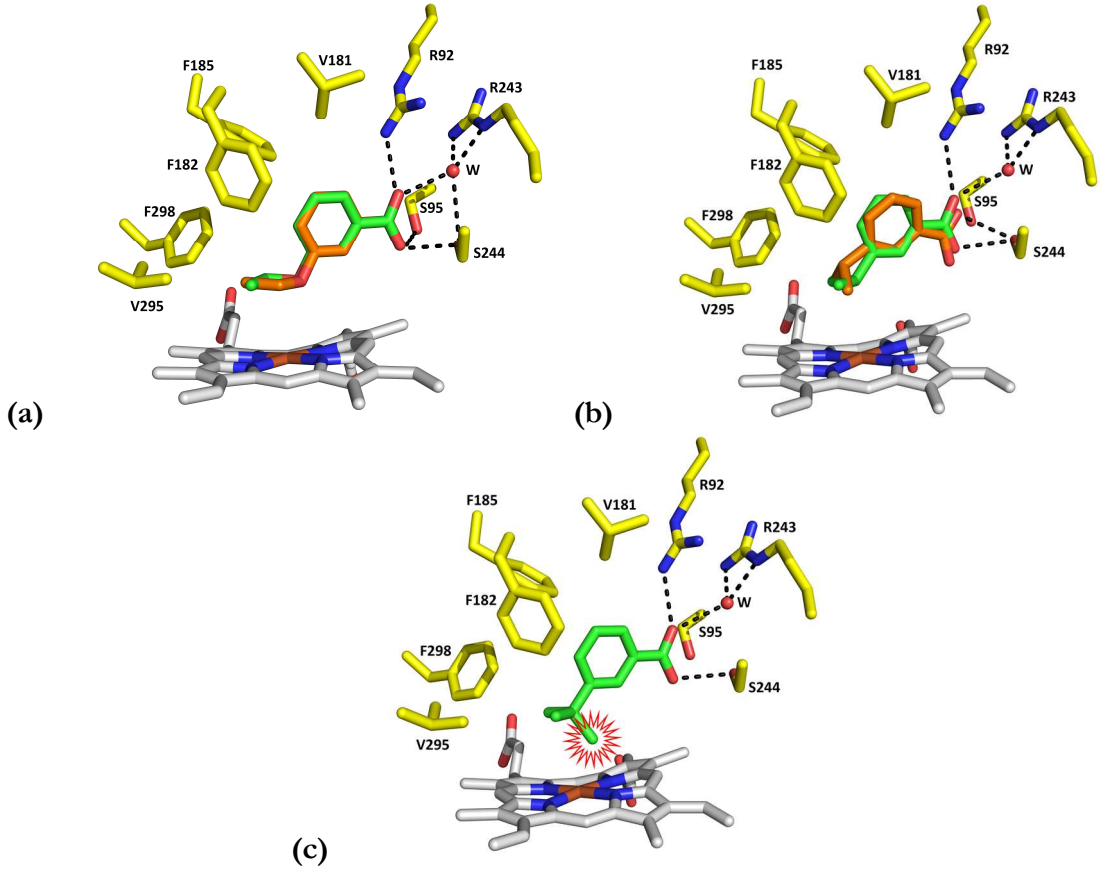

Figure 3.20. Bulky *meta*-substituted benzoic acids docked into CYP199A4 (PDB ID: 5U6W). The docked substrates are **(a)** 3-ethoxybenzoic acid, **(b)** 3-isopropylbenzoic acid, and **(c)** 3-*tert*-butylbenzoic acid. The top scoring pose is shown in **green**, and lower scoring poses in **orange**. A significant steric clash is indicated by a red star.

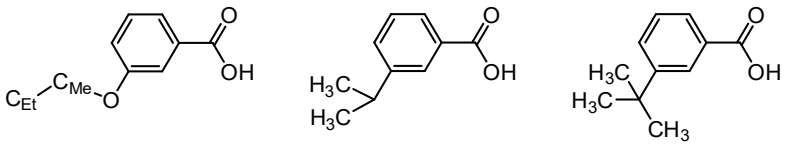

Table 3.4. Selected distances in Å between the docked ligands and active-site residues/heme.

Docked ligand	Distance (Å)	
3-ethoxyBA	C_{Me} - Fe	4.2
	C_{Et} - Fe	3.6
3-isopropylBA	CH_3 - Fe	3.3, 4.5
	$(CH_3)_2HC$ - Fe	3.8
3-*tert*-butylBA	CH_3 - Fe	3.0, 3.4, 4.7
	CH_3 - closest heme N	2.1

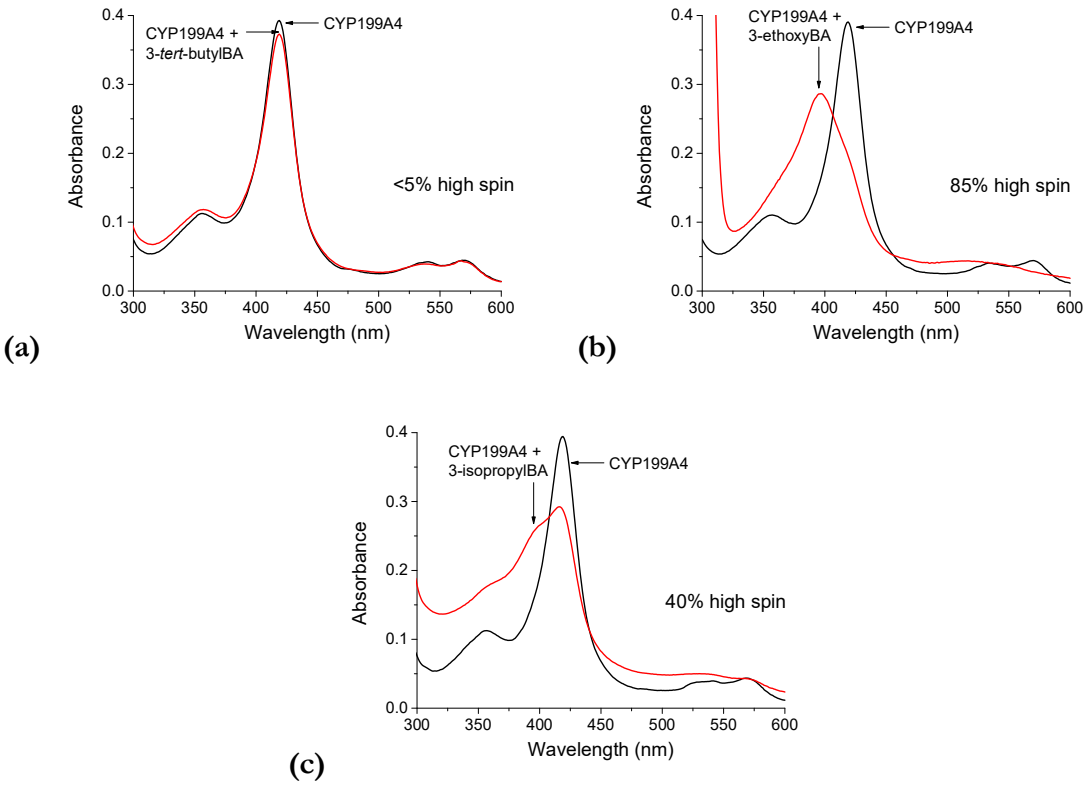

Figure 3.21. Spin-state shifts of CYP199A4 induced by **(a)** 3-*tert*-butylbenzoic acid, **(b)** 3-ethoxybenzoic acid, and **(c)** 3-isopropylbenzoic acid.

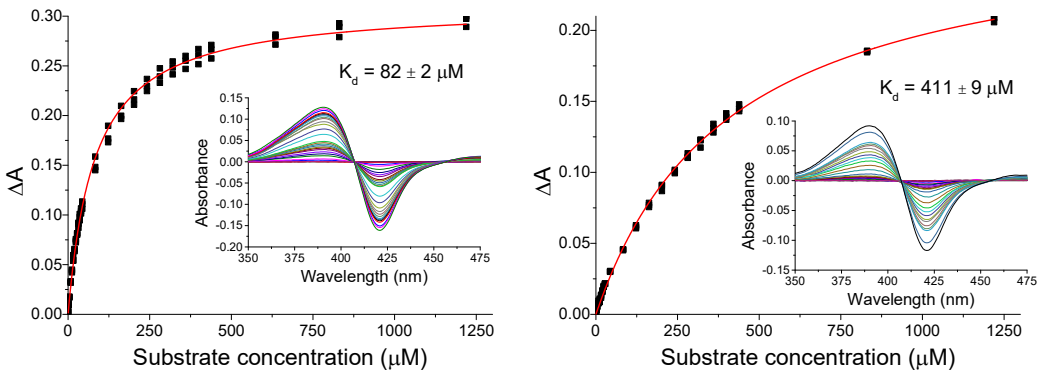

(a) 3-ethoxybenzoic acid (2.9 µM, peak: 391 nm, trough: 421 nm)

(b) 3-isopropylbenzoic acid (3.9 µM, peak: 390, trough: 421 nm)

Figure 3.22. UV-Vis titrations to determine the dissociation constant of CYP199A4 with **(a)** 3-ethoxybenzoic acid and **(b)** 3-isopropylbenzoic acid.

In vitro NADH turnovers were performed (Table 3.5). The NADH consumption rate was not increased above the leak rate in the presence of 3-*tert*-butylbenzoic acid and no product was detected by HPLC analysis of the reaction mixture (Figure 3.23). Apparently 3-*tert*-butylbenzoic acid does not bind to CYP199A4. The reducing equivalents were presumably lost via air oxidation of the ferredoxin.[303, 344] It was previously reported that the corresponding *para* isomer, 4-*tert*-butylbenzoic acid, is hydroxylated by CYP199A4 at a methyl carbon at a rate of 227 min^{-1}; the coupling efficiency is 100%.[277] This again demonstrates that CYP199A4 prefers to oxidise *para*- over *meta*-substituted benzoic acids.

On the other hand, CYP199A4 consumed NADH with 3-ethoxybenzoic acid at a moderately fast rate (208 min^{-1}). Whereas CYP199A4 is unable to oxidise 3-methoxybenzoic acid, the enzyme did catalyse the *O*-demethylation of 3-ethoxybenzoic acid (Figure 3.24). The coupling efficiency and product formation rate were calculated to be 66% and 138 min^{-1}, and 7% of the NADH consumed was channelled into H_2O_2 production. Incorrect protonation of the proximal oxygen of the Fe^{III}–OOH species is thought to be responsible for H_2O_2 production.[114] A single product, 3-hydroxybenzoic acid, was detected, indicating that no hydroxylation occurred at the less reactive terminal CH_3 group. Coleman previously reported that CYP199A4 converts the *para* isomer, 4-ethoxybenzoic acid, into 4-hydroxybenzoic acid at a rate of 527 min^{-1} with ~100% coupling efficiency.[117] CYP199A4 therefore exhibits substantially higher activity towards 4-ethoxybenzoic acid than 3-ethoxybenzoic acid.

CYP199A4 consumed NADH with 3-isopropylbenzoic acid at a slower rate (94 min^{-1}). Product was observed in the 3-isopropylbenzoic acid turnover, but the metabolites have not yet been quantified (Figure A23). These products are expected to be a hydroxylation product and the desaturation product, 3-(prop-1-en-2-yl)benzoic acid, based on the HPLC retention times and mass spectra (Figures A23, A24).

Table 3.5. *In vitro* turnover data for WT CYP199A4 with bulky *meta*-substituted benzoic acid substrates. Turnover data for CYP199A4 with the corresponding *para* isomers, previously reported by others, is included for comparison.

Substrate	% HS	K_d (μM)	N (min^{-1})	PFR (min^{-1})	C (%)	H_2O_2 (%)
3-ethoxyBA	85	82 ± 2	208 ± 5	138 ± 6	66 ± 1	7 ± 0.4
4-ethoxyBA [117]	95	0.17 ± 0.02	527 ± 10	527 ± 10	100 ± 8	≤1
3-isopropylBA	40	411 ± 9	94 ± 2			
4-isopropylBA [219]	≥95	0.29 ± 0.1	321 ± 24	287 ± 18	89 ± 2	1.5 ± 0.2 [277]
3-*tert*-butylBA	<5%	–[a]	8 ± 1[b]	–[c]	–[c]	–[d]
4-*tert*-butylBA [277]	90	39 ± 2	227 ± 4	227 ± 32	100 ± 13	–[d]

[a] The lack of any appreciable spin-state shift prevented measurement of binding affinity. [b] The NADH consumption rate reported is the average rate over the first 15 minutes. [c] No product detected. [d] Not measured or not reported.[277]

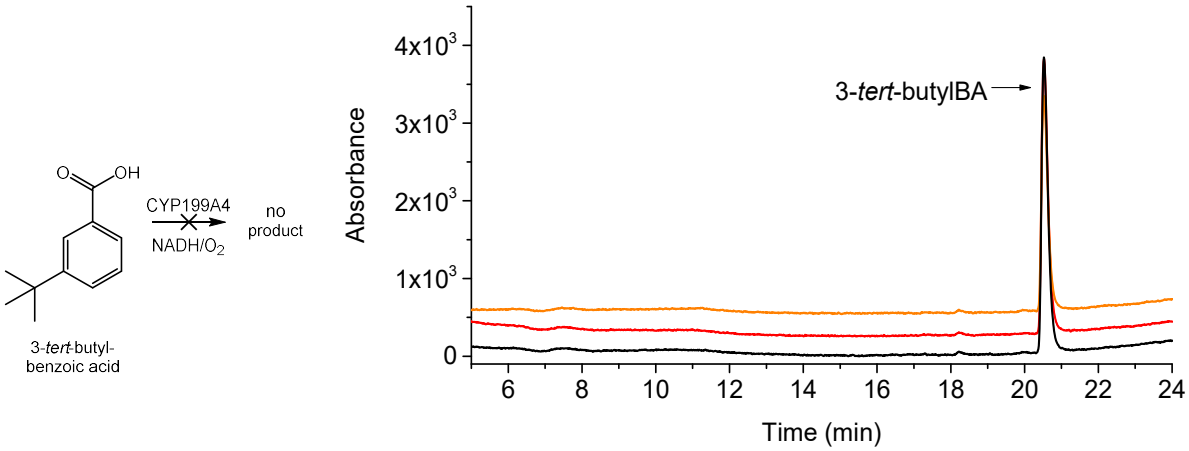

Figure 3.23. HPLC analysis of the CYP199A4 *in vitro* reaction with 3-*tert*-butylbenzoic acid, which yielded no product. In **black** is the turnover, and in **red** and **orange** are control reactions without P450 or NADH. The substrate appears at RT = 20.5 min. Gradient: 20-9% AcCN in H_2O with 0.1% TFA. Detection wavelength: 254 nm.

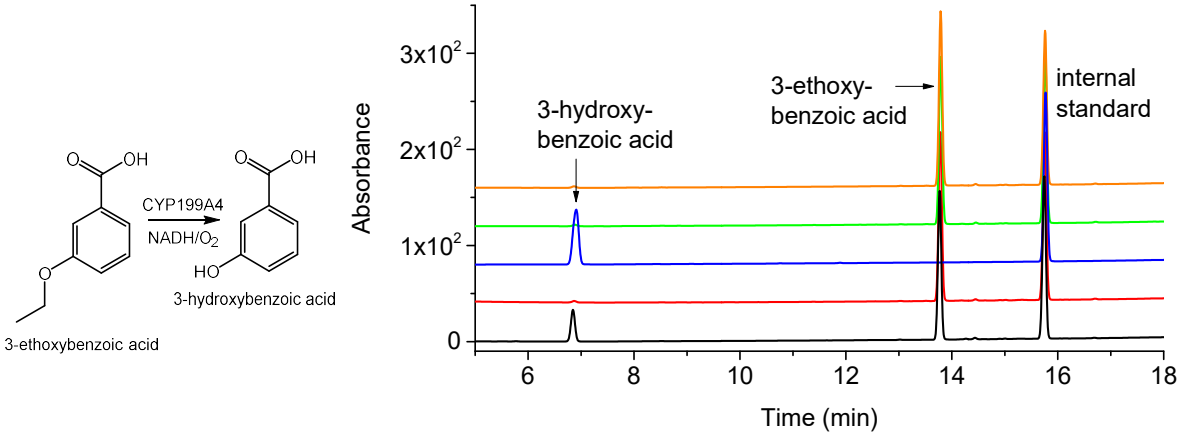

Figure 3.24. HPLC analysis of the CYP199A4 *in vitro* reaction with 3-ethoxybenzoic acid. In **black** is the *in vitro* reaction mixture, in **red** is a control reaction without P450, in **blue** is authentic 3-hydroxybenzoic acid (RT = 6.9 min), in **green** is the 3-ethoxybenzoic acid substrate control (RT = 13.8 min), and in **orange** is a control reaction without NADH. Gradient: 20-9% AcCN in H_2O with 0.1% TFA. Detection wavelength: 254 nm.

3.2.5 Crystal structure of 3-ethoxybenzoate-bound CYP199A4

We attempted to obtain crystal structures of 3-ethoxybenzoate- and 3-isopropylbenzoate-bound CYP199A4. 3-Isopropylbenzoate-bound CYP199A4 failed to crystallise. 3-Ethoxybenzoate-bound CYP199A4 did crystallise and the crystal structure was solved at medium (2.37-Å) resolution (Figures 3.25a and A25, Table A17) (PDB ID: 6PRS). In agreement with the docked poses (Figure A26), the *meta* substituent points down towards the heme. The crystal structure confirms that the water ligand is displaced, consistent with the 85% shift to HS. This reveals that certain *meta*-substituted benzoic acid substrates efficiently remove the water ligand; a *para* substituent is not essential.

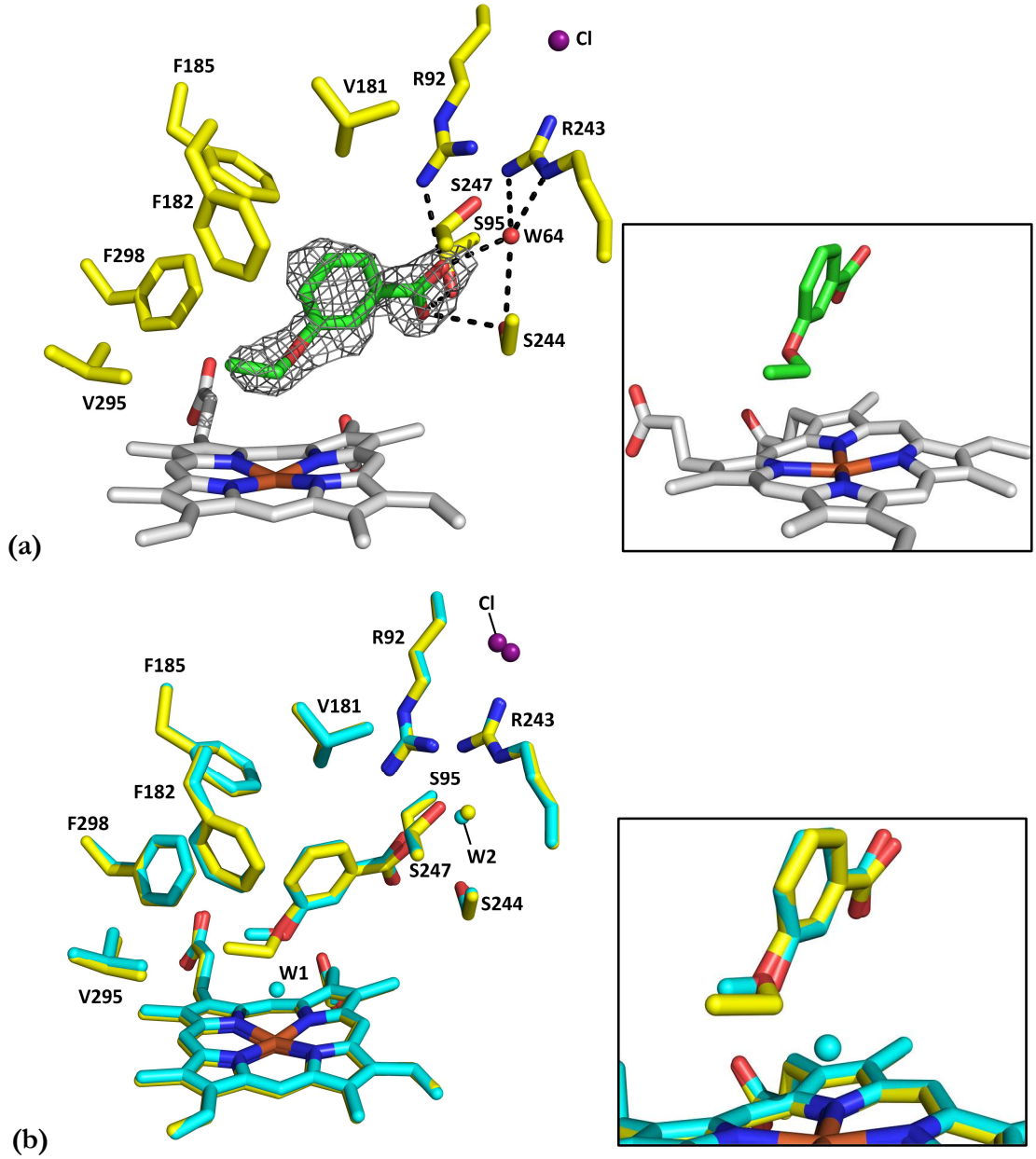

Figure 3.25. **(a)** Crystal structure of 3-ethoxybenzoic acid-bound CYP199A4. A feature-enhanced map of the substrate is shown as grey mesh contoured at 1.0 σ (1.5 Å carve). **(b)** Overlaid structures of 3-methoxy- (cyan) and 3-ethoxy-benzoate-bound CYP199A4 (yellow). The waters and chloride in the 3-methoxybenzoic acid structure are labelled.

This crystal structure is superimposed with the 3-methoxybenzoic acid structutre in Figure 3.25b. In the 3-methoxybenzoic acid structure, the C_{Me}-O-C_3-C_4 dihedral angle is +20°, while in the 3-ethoxybenzoic acid structure the CH_2-O-C_3-C_4 dihedral angle is -52° (Table 3.6). The altered dihedral angle results in the methylene carbon of 3-ethoxybenzoic acid being held considerably closer to the iron than the methyl carbon of 3-methoxybenzoic acid. Consequently, 3-ethoxybenzoic acid is able to sterically displace the water whereas when 3-methoxybenzoic acid binds to CYP199A4 there remains enough space above the heme for a water ligand to remain *in situ*.

Both the CH_2 and CH_3 carbons of 3-ethoxybenzoic acid are held in close proximity to the heme iron (3.6 and 4.2 Å, respectively) (Table 3.6). Distances were measured between the substrate and the hypothetical position of the Cpd I oxygen. The methylene carbon (CH_2) is held closer to the ferryl oxygen than the CH_3 carbon (2.1 *vs.* 2.7 Å). The Fe^{IV}=O−CH_2 and Fe^{IV}=O–CH_3 angles are 155.3 and 147.7°, respectively. CYP199A4 exclusively abstracts a hydrogen from the methylene carbon, with no hydroxylation occurring at the CH_3 carbon. This is explained by the weaker strength of secondary C-H bonds, especially those adjacent to oxygen,[79] compared to the primary C-H bonds of the terminal methyl group (Figure 3.26), as well as the methylene carbon being the closest carbon to the iron.

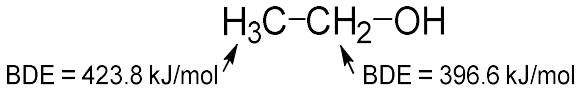

Figure 3.26. Bond dissociation energies of the C-H bonds in ethanol. The terminal methyl C-H bonds are stronger (BDE = 423.8 kJ/mol) than the secondary C-H bonds adjacent to oxygen (BDE = 396.6 kJ/mol).[345-347]

Table 3.6. Angles and distances between the heme iron and 3-ethoxybenzoic acid. Values are also given for the corresponding *para* isomer for comparison. Distances between the substrate and the hypothetical position of the Cpd I oxygen are also given. Abbreviations used are: **3-OEt** = 3-ethoxyBA; **4-OEt** = 4-ethoxyBA.

Distance (Å)	**3-OEt**	**4-OEt**[117]
CH_2 - Fe	3.6	4.2
CH_2 - O=Fe^{IV}	2.1	2.8
CH_3 - Fe	4.2	4.3
CH_3 - O=Fe^{IV}	2.7	3.0
O - Fe	4.6	5.1
O - O=Fe^{IV}	3.3	3.6
Angle (°)		
Fe^{IV}=O-CH_2	155.3	143.1
Fe^{IV}=O-CH_3	147.7	138.1
Fe^{IV}=O-O	139.2	160.8
Dihedral angle CH_2-O-C_3-C_4	-52.4	-9.2

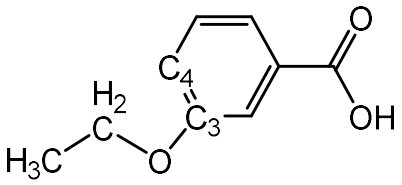

3-OEt

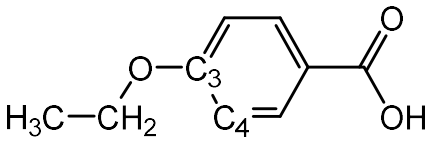

4-OEt

3.3 Discussion

This study reaffirms that CYP199A4's activity is highest towards substrates possessing a *para* substituent. Despite having no activity towards 3-methoxybenzoic acid and 3-*tert*-butylbenzoic acid, this enzyme nevertheless *does* oxidise certain *meta*-substituted benzoic acids. The binding mode of *meta*-substituted benzoic acids revealed by the crystal structures has the *meta* substituent positioned close to the heme, as predicted by the docking software, not directed away from the heme as previously believed.[162] This rationalises why CYP199A4 was able to oxidise the *meta* substituent (albeit with low activity). All *meta*-substituted benzoic acid substrates studied here bind with the benzene ring and carboxylate held in highly similar positions (Figure 3.27a). Likewise, the

benzene ring and carboxylate of the *para* isomers all occupy similar positions (Figure 3.27b). However, the position of the benzene moiety of the *meta* isomers is altered compared to that of the *para* isomers. While only a single binding mode is observed in these crystal structures, in solution the *meta* isomers may have multiple binding modes.

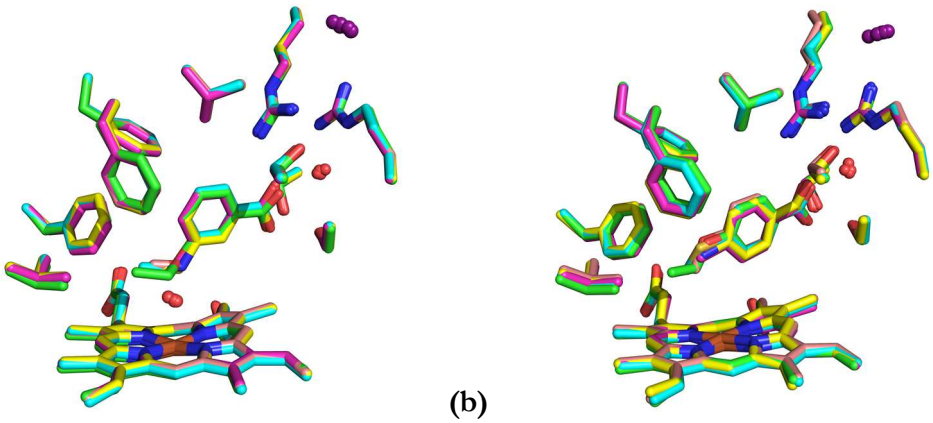

Figure 3.27. **(a)** Superimposed crystal structures of CYP199A4 in complex with 3-methoxy- (salmon), 3-methylamino- (yellow), 3-methylthio- (cyan), 3-methyl- (magenta), and 3-ethoxy-benzoic acid (green). In all of these structures, the active-site residues and benzoic acid moiety are held in virtually identical positions. **(b)** Superimposed crystal structures of CYP199A4 in complex with *para*-substituted benzoic acids. The *para* isomers are depicted in the same colours as the corresponding *meta* isomers.

Among the substrates tested, there is no clear relationship between the binding affinity and magnitude of the spin-state shift the substrate induces. The spin-state shift induced by 3-ethoxybenzoic acid (85%) is larger even than that induced by some *para*-substituted substrates (e.g. 4-methylthio-, 4-methylamino- and 4-methyl-benzoic acid), which bind considerably more tightly. Previously, only benzoic acid substrates possessing a *para* substituent were thought to be capable of inducing large spin-state shifts with CYP199A4.[162]

Within each pair of *meta* and *para* isomers, the extent of the spin-state shift is correlated with the NADH consumption rate. This is because the first electron transfer step is gated by displacement of the iron-bound water.[100, 117, 337] The *para*-substituted benzoic acid substrates induce large spin-state shifts and efficiently displace the water. In contrast, a partial-occupancy water ligand to the heme is present in the crystal structures of 3-methyl-, 3-methylamino-, 3-methoxy- and 3-methylthio-benzoate-bound CYP199A4. The presence of this water would hamper heme reduction and hinder oxygen binding, thus slowing down the catalytic cycle. More space for a water exists above the heme when the *meta* isomers are bound than when the corresponding *para* isomers are bound. The water ligand is potentially hydrogen-bonded to the N or O of the substrate and interacting with the S, and these interactions would stabilise the water ligand. This would explain why the occupancy of the water in the 3-methoxy-, 3-methylthio- and 3-methylamino-benzoic acid crystal structures is higher than in the 3-methylbenzoic acid structure. We note, however, that the extent of the spin-state shift is not perfectly correlated to the NADH consumption rate for all substrates investigated here. 3-Methylaminobenzoic acid induces only a 10% spin-state shift, yet the NADH consumption rate with this substrate is faster than the rate with 3-ethoxybenzoic acid,

which induces an 85% shift to HS. Furthermore, the extent of the spin-state shift does not always correlate with the catalytic activity of CYP199A4 towards the substrate. 3-Methoxybenzoic acid induces a 4-fold greater spin-state shift than 3-methylaminobenzoic acid, yet CYP199A4 does not oxidise 3-methoxybenzoic acid at all but oxidises the latter.

The fact that 3-methoxybenzoic acid is not oxidised and the reducing equivalents appear to be lost via oxidase uncoupling indicates that it must be inappropriately positioned in the active site. Factors that would affect whether Cpd I can abstract a hydrogen are the distance of the C-H bond from the ferryl oxygen and the angle of approach of the substrate.[79, 348-349] It has been proposed that the optimal angle for the substrate to approach the Fe^{IV}=O species is ~130° (Fe-O-C angle),[348] and that a linear C-H-O angle is ideal for hydrogen abstraction (Figure 3.28).[349-352] In addition, the heteroatom may be positioned in such a manner that it interferes with hydrogen abstraction. In the 4-methoxybenzoic acid structure, the methyl group is held significantly closer to the heme than the oxygen, so the heteroatom would be less likely to interfere. In contrast, in the 3-methoxybenzoic acid structure, the methyl group and oxygen are held at equal distances from the iron and we speculated that this oxygen could be interfering with the reaction. Whereas 3-methoxybenzoic acid is not oxidised, CYP199A4 is able to demethylate 3-ethoxybenzoic acid. The methylene carbon of 3-ethoxybenzoic acid is held significantly closer to the heme than the oxygen, enabling efficient C-H abstraction.

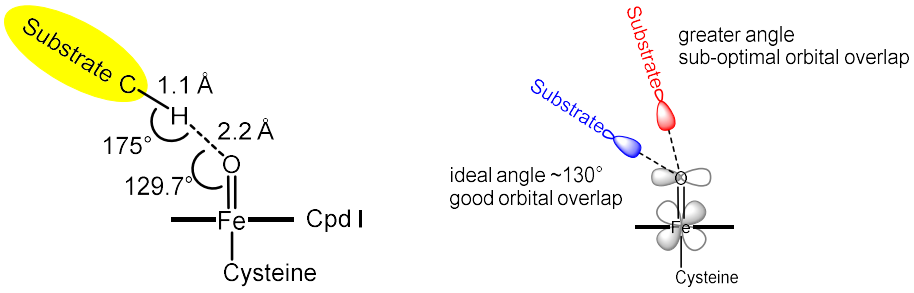

Figure 3.28. It has been proposed that a linear C-H-O angle is ideal for hydrogen abstraction[350, 352] and the optimal approach angle of the substrate to the Fe^{IV}=O species is postulated to be ~130°.[348] Larger angles of approach are suggested to result in higher energy barriers.[348]

In the 4-methoxybenzoic acid crystal structure, the methoxy group is oriented such that the hydrogens point towards the heme (Figure 3.29a). On the other hand, the methoxy group of 3-methoxybenzoic acid is oriented such that the hydrogens instead point away from the heme (Figure 3.29b). This may explain why this substrate is not oxidised. However, it is plausible that the binding mode of 3-methoxybenzoic acid observed in the crystal structure is not the same as in solution, and its position may be altered once oxygen binds to the iron.[349] In the 3-ethoxybenzoic acid structure, the terminal methyl group hydrogens still point away from the heme, but a methylene C-H bond points towards the heme iron, rationalising why the methylene carbon is hydroxylated (Figure 3.29c).

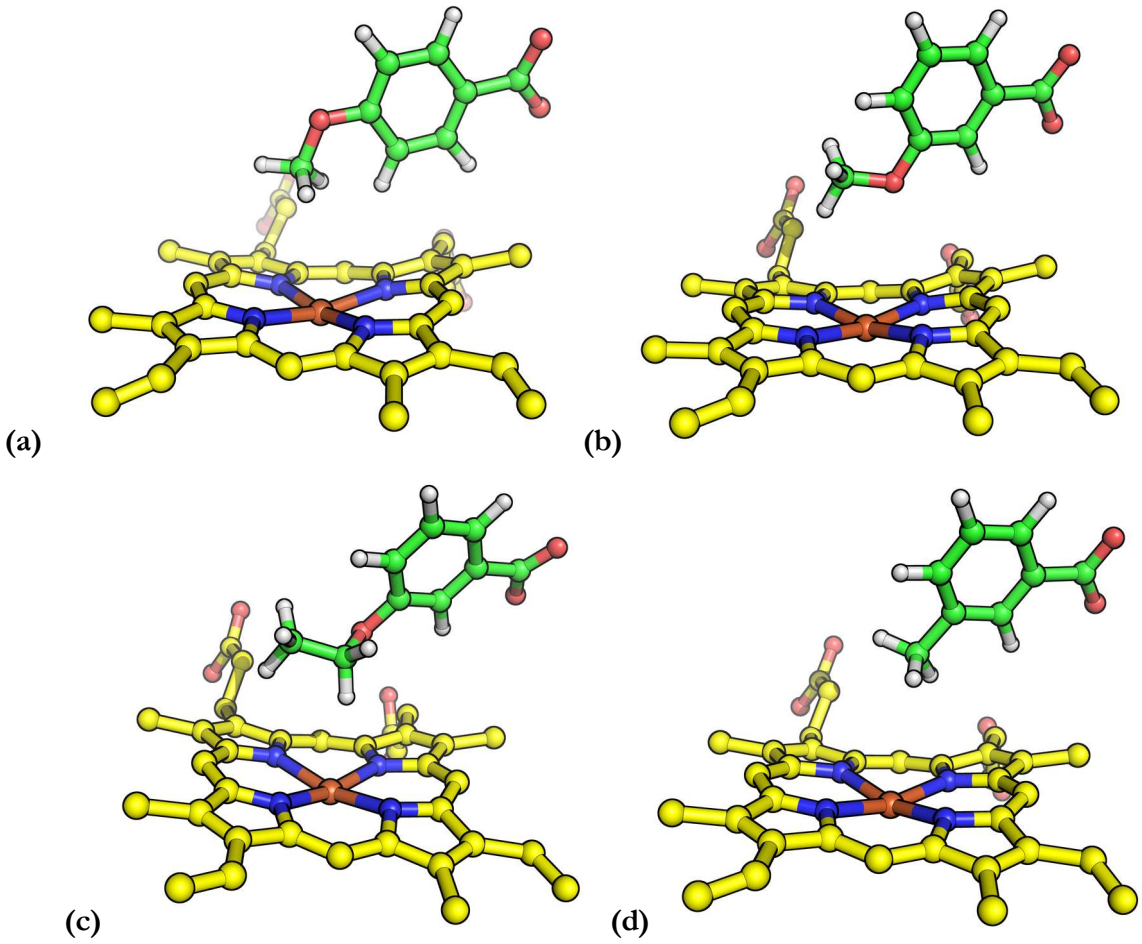

Figure 3.29. Crystal structures of **(a)** 4-methoxy-, **(b)** 3-methoxy-, **(c)** 3-ethoxy- and **(d)** 3-methyl-benzoate-bound CYP199A4 with modelled hydrogens. Hydrogens were added using ICM-Pro (MolSoft).[311]

Although the crystallographic binding mode of 3-methylaminobenzoic acid is highly similar to that of 3-methoxybenzoic acid (Figure A27a), this substrate, unlike 3-methoxybenzoic acid, was metabolised by CYP199A4. The difference in CYP199A4's activity towards 3-methylaminobenzoic acid compared to 3-methoxybenzoic acid may be due to the reactions proceeding via different mechanisms. *O*-demethylation must occur via hydrogen abstraction, whereas *N*-demethylation could occur via a SET mechanism involving initial reaction with the nitrogen. Unlike 3-methoxybenzoic acid, 3-methylbenzoic acid must be appropriately positioned to allow Cpd I to abstract a hydrogen from the methyl group (Figure 3.29d). The methyl group of 3-methylbenzoic acid is held slightly further from the Cpd I oxygen than that of 4-methylbenzoic acid, which may explain why the coupling efficiency is lower for the *meta* isomer. It is plausible that 3-methylbenzoic acid may have multiple binding modes in solution and may also bind with the methyl group pointing away from the heme, resulting in loss of NADH via oxidase uncoupling.

With 3-methylthiobenzoic acid, Cpd I reacts with the heteroatom rather than abstracting a hydrogen from the methyl group. Sulfoxidation could occur via direct oxygen transfer, or via single electron transfer followed by oxygen rebound.[18, 199] The crystal structure revealed that the sulfur of 3-methylthiobenzoic acid is positioned even closer to the heme iron than that of 4-methylthiobenzoic acid. It has been previously reported that CYP199A4-catalysed sulfoxidation of

4-ethylthiobenzoic acid is highly enantioselective, generating almost exclusively a single enantiomer.[117] However, as we were unable to separate the enantiomers of 3-methylsulfinylbenzoic acid, the enantioselectivity of this reaction could not be determined.

In summary, this study reveals that CYP199A4 does oxidise certain *meta*-substituted benzoic acids, though its activity towards these substrates is substantially lower than its activity towards the *para* isomers. CYP199A4 was previously believed to be unable to oxidise this type of compound. The fact that 4-methoxybenzoic acid is rapidly demethylated but 3-methoxybenzoic acid is not oxidised emphasises that minor variations in the orientation of the substrate relative to the heme can result in substantially diminished catalytic activity (Figure 3.30). Even if a substrate is in close proximity to the heme iron, hydroxylation may not occur if the C-H bonds are not oriented favourably for hydrogen abstraction by Cpd I.

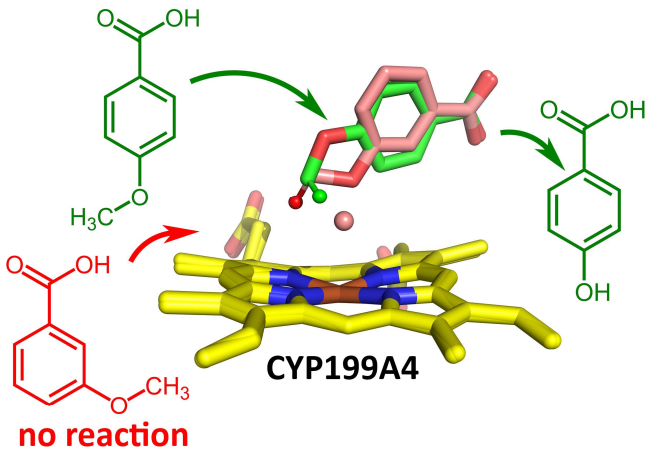

Figure 3.30. Both 4-methoxy- and 3-methoxy-benzoic acid bind with the methoxy moiety in close proximity to the heme iron, yet only 4-methoxybenzoic acid is oxidised. This emphasises that the orientation of the C-H bonds relative to the heme iron is important in determining whether efficient monooxygenation will occur.

Chapter 4

Exploring the different binding modes of type II ligands using CYP199A4

4.1 Introduction

CYP199A4 is capable of binding a variety of *para*-substituted benzoic acid substrates.[277] Coleman[277] previously investigated the catalytic activity of WT CYP199A4 towards various benzoic acid substrates with heterocyclic aromatic substituents. 4-Pyridin-2-yl-, 4-pyridin-3-yl- and 4-1*H*-imidazol-1-yl-benzoic acid (Figure 4.1) displayed high affinity for CYP199A4 (K_d = 1.0, 2.3 and 1.6 μM, respectively) and engendered type II spin-state shifts.[277] A type II shift induced by a nitrogen compound is traditionally assumed to mean that it has formed a direct Fe-N bond with the heme iron, replacing the weak-field water ligand as the sixth axial ligand.[154-155, 158, 353] For other P450 enzymes, type II nitrogen ligands have been found to bind more tightly than structurally similar substrates which do not coordinate to the iron[157, 354-355] and are used as drugs due to their ability to inhibit P450s.[356] For example, azole drugs such as fluconazole can inhibit fungal CYP51 enzymes and are commonly used as antifungals.[154, 159, 357] Another example is ritonavir, which inhibits human CYP3A4 via nitrogen ligation to the heme iron, blocking oxidation by this enzyme of administered anti-HIV drugs.[358-359] Electron transfer from the redox partners to the P450 heme is not expected to occur efficiently when a strong-field nitrogen ligand binds to the iron because six-coordinate low-spin heme is not readily reduced.[160, 360] Additionally, coordination of a type II ligand to the heme iron obstructs binding of dioxygen and substrates.[159-160, 353, 361] 4-Pyridin-2-yl-, 4-pyridin-3-yl- and 4-1*H*-imidazol-1-yl-benzoic acid were not metabolised by CYP199A4 and the NADH consumption rate was sluggish (ranging from 10 to 41 min^{-1}),[277] indicating that they may inhibit CYP199A4. Crystal structures of these inhibitors in complex with CYP199A4 are not yet available so their binding modes are not known.

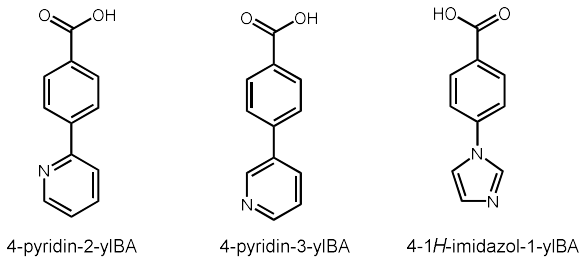

Figure 4.1. Heteroaromatic type II ligands investigated with CYP199A4 in this chapter.

In drug development, UV-Vis spectroscopy is used to identify compounds which could potentially serve as P450 inhibitors by ligating to the heme iron.[155, 355] Although compounds which induce type II spectra are expected to coordinate to the heme, it has been revealed that in some instances alternative binding modes can occur (Figure 1.11).[154, 156, 159] Hydrogen-bonding of the

nitrogen ligand to the heme-bound water can also induce a type II shift.[154] This hydrogen bonding interaction is proposed to result in the aqua ligand becoming a stronger field ligand.[154] Conner *et al.* found that the 1,2,3-triazole-containing molecule '17-click' failed to displace the water ligand in CYP3A4 (Figure 1.11d).[154] Nevertheless, it induced a type II difference spectrum by hydrogen-bonding to the heme-bound water.[154] 17-Click did not inhibit the P450 as anticipated but was instead readily metabolised.[154] It has been reported that some type II ligands are in fact oxidised readily (in some cases more rapidly than type I substrates), rather than inhibiting the P450 catalytic cycle.[154, 353-354, 361] Conner *et al.* found that the spectra induced by these 'pseudo' type II ligands are deceptive because they so convincingly resemble genuine type II spectra.[154-155, 360] Hence, although a type II shift has often been used as evidence that the nitrogen compound is directly bound to the heme, this may not be correct in all cases. They advised that UV-Vis spectroscopy could not be relied upon to decide whether drug molecules bind directly to the heme iron.[153-155, 360] X-ray crystallography and EPR were proposed to be more reliable techniques for identifying whether the water ligand has been replaced by the type II inhibitor.[153, 155, 360] In another study, Munro *et al.* reported that binding of fluconazole to CYP121 induced a smaller red-shift of the Soret band than expected for a coordinated azole derivative.[159] The crystal structure revealed that the predominant binding mode had fluconazole hydrogen-bonded to the heme-bound water ligand, which remained *in situ*.[159] Only in a small proportion of molecules in the crystal was fluconazole directly bound to the iron.[159] The small red-shift was attributed to the fact that fluconazole was only ligated to the heme in a fraction of enzyme molecules.[159] The size of the Soret red-shift induced by a type II ligand is thought to depend on multiple factors.[157] It has been proposed that a smaller-than-expected Soret red-shift may arise because the nitrogen ligand is unable to form an 'optimal' Fe-N bond with the heme iron due to steric constraints,[101, 154, 156] or because it has multiple binding modes.[157] It has also been proposed that the planarity of the heme may affect the Soret peak position.[157] In type II difference spectra, the maximum peak-to-trough absorbance difference (ΔA_{max}) induced by a type II ligand can vary for different ligands; it is thought that different ΔA_{max} values may arise because the Fe-N bond is strained or there is a mixture of type II and type I binding modes.[154, 157] The appearance of a type II spectrum can also vary depending on whether the ligand-free enzyme is predominantly in the high-spin or low-spin state.[157, 362] A type IIa difference spectrum arises when the P450 is in the high-spin state and is converted into the low-spin state by binding of a type II ligand, leading to a trough at ~390 nm.[157] In contrast, a type IIb difference spectrum with a trough at 410 nm is generated when a type II ligand binds to a P450 in the low-spin state.[157] Thus, there are many factors that may affect the appearance of a type II spectrum.[157]

The changes to the absolute UV-Vis spectrum that arise when nitrogen ligands bind to the heme iron have been investigated by Dawson and Sono, who studied the binding of various oxygen and nitrogen donor ligands to $P450_{cam}$.[363] They divided the nitrogen donor ligands that they tested into two classes, referred to as 'normal' and 'abnormal' nitrogen donors (Figure B1).[363] When

oxygen donor ligands (e.g. water) were bound to $P450_{cam}$, the Soret band was centred at ~417 nm and the α-band was more intense than the β-band.[363] Binding of a 'normal' nitrogen donor ligand red-shifted the Soret band to ~424 nm. The intensity of the α-band was also reduced such that the α-band was now markedly less intense than the β-band.[155, 363] For oxygen donor ligands, the α-band had an extinction coefficient of 11-13 mM cm^{-1}, but when 'normal' nitrogen donor ligands were bound the extinction coefficient decreased to 8-9.5 mM cm^{-1}.[363] Binding of these 'normal' nitrogen donor ligands also led to an increase in the intensity of the δ-band. The bulky nitrogen donor ligands 2-phenylimidazole, indole and benzimidazole were classified as 'abnormal'.[363-364] The spectra of these 'abnormal' complexes of $P450_{cam}$ were more resemblant of the spectra of complexes of $P450_{cam}$ with oxygen donor ligands.[155, 363-365] The 'abnormal' nitrogen donor ligands indole and benzimidazole induced smaller Soret red-shifts than the 'normal' nitrogen ligands and did not substantially reduce the intensity of the α-band.[363]

In the CYP199A4 system, Coleman found that the magnitude of the red-shift induced by 4-pyridin-3-ylbenzoic acid was larger than that induced by 4-pyridin-2-ylbenzoic acid (Table 4.1, Figure 4.2a).[277] Addition of 4-pyridin-2-ylbenzoic acid to CYP199A4 produced a 3 nm red-shift of the Soret peak (from 419 to 422 nm).[277] 4-Pyridin-3-ylbenzoic acid, on the other hand, induced a 5 nm red-shift (to 424 nm).[277] The difference spectra induced by these two pyridine-containing ligands also differed (Figure 4.2b). The fact that the two pyridine-containing compounds induce different optical spectra implies that their binding modes may differ. If both compounds were coordinated to the heme iron via the pyridine moiety, their UV-Vis spectra would not be expected to differ so substantially. The difference spectrum induced by 4-1*H*-imidazol-1-ylbenzoic acid closely resembled the 4-pyridin-3-ylbenzoic acid spectrum (Figure 4.2c,d).[277] The objective of this chapter is to solve crystal structures of CYP199A4 in complex with 4-pyridin-2-yl-, 4-pyridin-3-yl- and 4-1*H*-imidazol-1-yl-benzoic acid and to perform other experiments to rationalise the different type II spectra induced by these inhibitors.

Table 4.1. Binding and *in vitro* turnover data for CYP199A4 with 4-pyridin-2-yl-, 4-pyridin-3-yl- and 4-1*H*-imidazol-1-yl-benzoic acid reported by Coleman.[277] No product was detected and the amount of H_2O_2 generated was negligible.[277] *N* is the rate of NADH consumption, given in units of μM (μM-P450)$^{-1}$ min^{-1}.

Substrate	Spin-state shift	K_d (μM)	*N* (min^{-1})
4-Pyridin-2-ylBA	Type II (419 → 422)	1.0 ± 0.1	10 ± 2
4-Pyridin-3-ylBA	Type II (419 → 424)	2.3 ± 0.1	30 ± 3
4-1*H*-Imidazol-1-ylBA	Type II (419 → 424)	1.6 ± 0.2	41 ± 1

4.2 Results

4.2.1 Analysis of different type II spectra induced by pyridine, imidazole, 4-pyridin-2-yl-, 4-pyridin-3-yl- and 4-1*H*-imidazol-1-yl-benzoic acid

To confirm the previous results[277], absolute and difference spectra were recorded for CYP199A4 with 4-pyridin-2-yl- and 4-pyridin-3-yl-benzoic acid, using the same P450 concentration for both ligands. The spectra induced by 4-pyridin-2-yl- and 4-pyridin-3-yl-benzoic acid are overlaid in Figure 4.2a,b to highlight their differences. As noted by Coleman, 4-pyridin-3-ylbenzoic acid induces a larger Soret (γ) band red-shift than 4-pyridin-2-ylbenzoic acid (5 *vs.* 3 nm). Additionally, 4-pyridin-3-ylbenzoic acid-bound CYP199A4 has a less intense Soret band than 4-pyridin-2-ylbenzoic acid-bound CYP199A4 (ε_{424} = 106 *vs.* ε_{422} = 115 mM^{-1} cm^{-1}; Table 4.2).

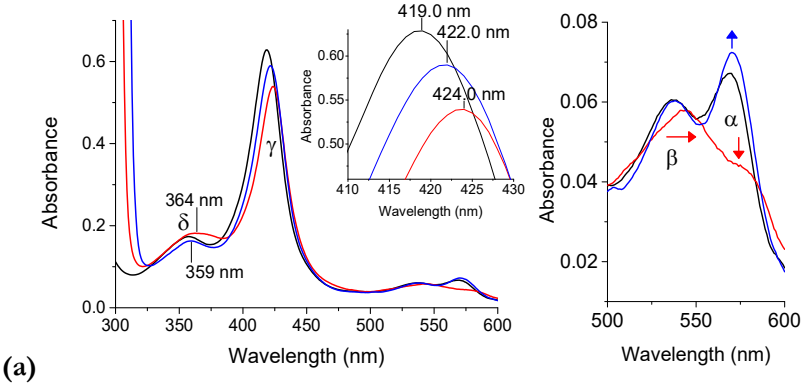

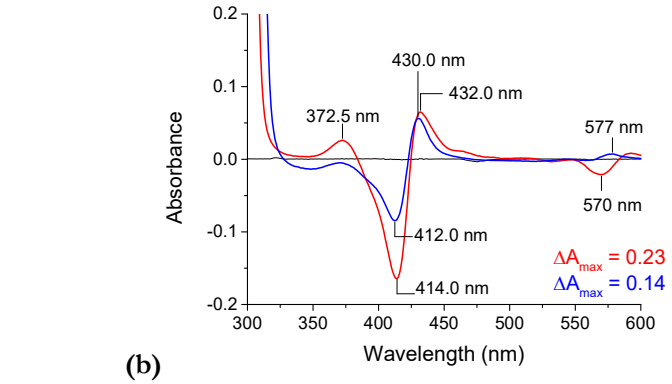

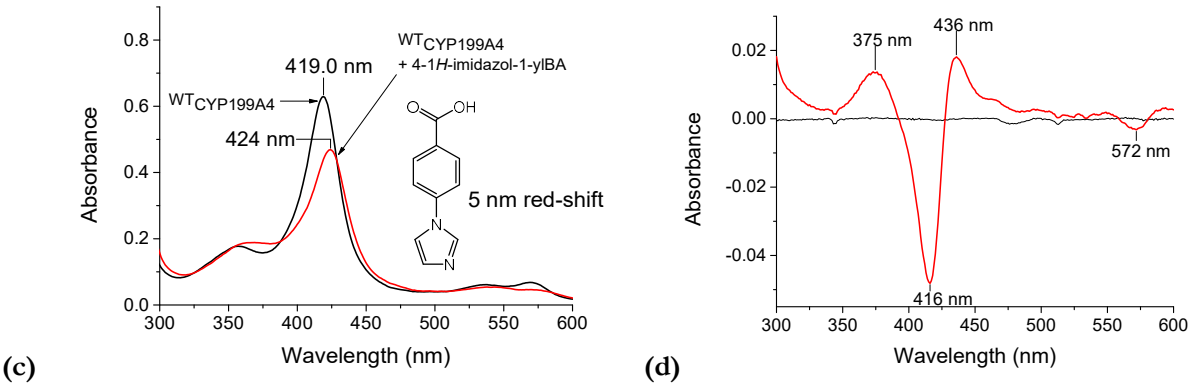

Figure 4.2. **(a)** Spin-state shifts of CYP199A4 with 4-pyridin-3-ylbenzoic acid (red) and 4-pyridin-2-ylbenzoic acid (blue). **(b)** Overlaid difference spectra of CYP199A4 with 4-pyridin-3-ylbenzoic acid (red) and 4-pyridin-2-ylbenzoic acid (blue). The enzyme concentration was 5.2 μM and ligand concentration 3.8 mM. **(c)** Spin-state shift induced by 4-1*H*-imidazol-1-ylbenzoic acid. **(d)** Difference spectrum of CYP199A4 with 4-1*H*-imidazol-1-ylbenzoic acid.

Table 4.2. Extinction coefficients of ferric and ferrous CYP199A4 in complex with 4-pyridin-2-yl-, 4-pyridin-3-yl- and 4-1*H*-imidazol-1-yl-benzoic acid. Refer to Appendix B (Figures B2–B8) for spectra and calculations.

Complex	δ		Soret band		β		α		α:β ratio
	λ_{max} (nm)	ε (mM^{-1} cm^{-1})	λ_{max} (nm)	ε (mM^{-1} cm^{-1})	λ_{max} (nm)	ε (mM^{-1} cm^{-1})	λ_{max} (nm)	ε (mM^{-1} cm^{-1})	
ferric CYP199A4	357	32.6	419	119 [162]	537	11.0	569	12.3	1.1
ferric CYP199A4 + 4-pyridin-2-ylBA	359	31.6	422	115	540	11.3	571	13.6	1.2
ferric CYP199A4 + 4-pyridin-3-ylBA	364	35.7	424	106	541	10.8	shoulder at ~570	8.4	0.78
ferric CYP199A4 + 4-imidazol-1-ylBA	366	39.0	424	94.6	541	11.5	571	9.6	0.83
ferrous CYP199A4 + 4-pyridin-3-ylBA	-	-	447	118	542	18.6	571	19.6	-
ferrous CYP199A4 + 4-imidazol-1-ylBA	-	-	414	81.7	merged α/β bands λ_{max} = 548 nm, ε_{548} = 17.4 mM^{-1} cm^{-1}				-

In the 4-pyridin-2-ylbenzoic acid difference spectrum, the peak and trough appear at 430 and 412 nm, whereas the difference spectrum induced by 4-pyridin-3-ylbenzoic acid has a peak and trough at 432 nm and 414 nm. 4-Pyridin-3-ylbenzoic acid induces a substantially larger Soret band trough than 4-pyridin-2-ylbenzoic acid. Consequently, the ΔA_{max} induced by 4-pyridin-2-ylbenzoic acid is only ~60% of that induced by 4-pyridin-3-ylbenzoic acid. The 4-pyridin-3-ylbenzoic acid spectrum is also distinguished by an additional peak at 372.5 nm which is absent from the 4-pyridin-2-ylbenzoic acid spectrum. This peak arises because the δ-band at 357 nm increases in intensity and is red-shifted to ~364 nm. The δ-band extinction coefficient increases from 32.6 mM^{-1} cm^{-1} to 35.7 mM^{-1} cm^{-1}. In contrast, the intensity of the δ-band decreases subtly when 4-pyridin-2-ylbenzoic acid binds (ε_{359} = 31.6 mM^{-1} cm^{-1}). Further differences are observed in the α/β band region (500-600 nm) (Figure 4.2a). For substrate-free CYP199A4, as for other ligand-free P450s[363], the α-band (at 570 nm) is more intense than the β-band (at 537 nm) (α:β ratio: 1.1). Binding of 4-pyridin-3-ylbenzoic acid to CYP199A4 dramatically reduces the intensity of the α-band such that the β-band is now more intense than the α-band (α:β ratio: 0.78). For substrate-free CYP199A4 the α-band extinction coefficient (ε_{569}) is 12.3 mM^{-1} cm^{-1} but this value decreases to 8.4 mM^{-1} cm^{-1} when 4-pyridin-3-ylbenzoic acid binds. As a result, there is a prominent trough at 570 nm in the 4-pyridin-3-ylbenzoic acid difference spectrum. The β-band is also red-shifted. These changes to the α/β band region are consistent with those induced by Dawson's 'normal' nitrogen donor ligands.[154, 363]

The absolute and difference spectra of CYP199A4 with 4-1*H*-imidazol-1-ylbenzoic acid have similar characteristics to the 4-pyridin-3-ylbenzoic acid spectra (Figure 4.2c,d). Note that when 4-1*H*-imidazol-1-ylbenzoic acid binds, the Soret band shifts to 424 nm and decreases substantially in intensity (ε_{424} = 94.6 mM^{-1} cm^{-1}), and the α-band intensity is diminished. In contrast, when 4-pyridin-2-ylbenzoic acid binds to CYP199A4 there is instead a subtle increase in the intensity of the α-band region (ε_{571} = 13.6 mM^{-1} cm^{-1}), resulting in a peak at 577 nm in the difference spectrum.

For this complex, the α-band is more intense than the β-band (α:β ratio: 1.2). Dawson reported that this was characteristic of P450 complexes with oxygen donor ligands.[363]

The type II difference spectra of CYP199A4 with the small molecules pyridine and imidazole were also recorded (Figure B9a–d). Type II shifts were observed only when high concentrations of pyridine or imidazole were added to CYP199A4, implying that these compounds, which lack the benzoic acid moiety known to be critical for tight binding to CYP199A4[181, 219], have low binding affinity. The K_d for binding of the polar molecule imidazole to CYP199A4 was measured to be ~81 mM. Pyridine displayed lower affinity (K_d >370 mM) but the high concentration of pyridine required to achieve binding may have denatured the enzyme so we could not obtain enough data points to determine the K_d value (Figure 4.3). Addition of imidazole shifted the Soret peak to 425 nm, which is similar to the shift induced by 4-1*H*-imidazol-1-ylbenzoic acid (424 nm). However, the Soret peak only shifted to 421 nm when pyridine was added, with further addition of pyridine appearing to denature the enzyme. The difference spectra resemble closely the spectra of CYP199A4 with 4-pyridin-3-ylbenzoic acid and 4-1*H*-imidazol-1-ylbenzoic acid, having troughs at 570 nm due to decreases in the intensity of the α-band (Figure B9c,d).

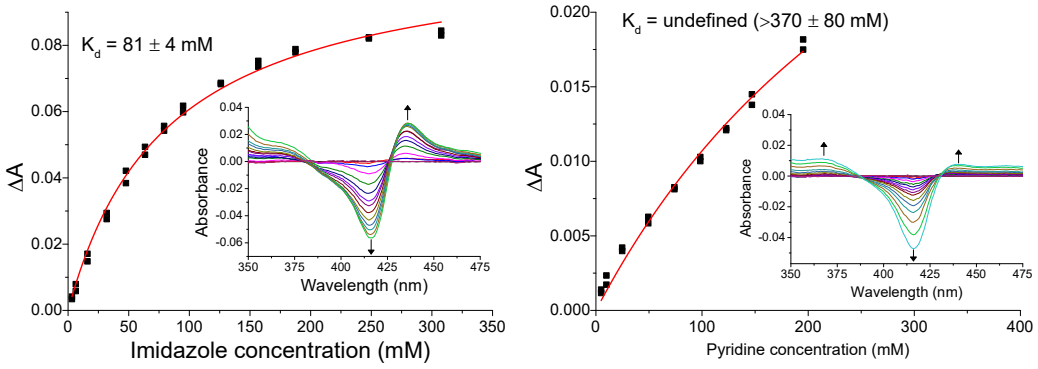

(a) imidazole
(1.6 μM, peak: 436 nm, trough: 416 nm)

(b) pyridine
(2.2 μM, peak: 440, trough: 416 nm)

Figure 4.3. Dissociation constant (K_d) analysis of imidazole and pyridine with CYP199A4. The enzyme concentration and peak/trough wavelengths are given below each figure.

In summary, the spectra induced by 4-pyridin-3-ylbenzoic acid and 4-1*H*-imidazol-1-ylbenzoic acid are consistent with the spectra reported by Dawson of $P450_{cam}$ in complex with 'normal' nitrogen donors, whereas 4-pyridin-2-ylbenzoic acid would be classified as an 'abnormal' nitrogen donor ligand. We note that the 'abnormal' spectrum induced by 4-pyridin-2-ylbenzoic acid does not appear to arise from a mixture of type I and 'normal' type II binding modes (Figures B10, B11).

4.2.2 UV-Vis spectra of reduced (ferrous) CYP199A4 in complex with 4-pyridin-2-yl-, 4-pyridin-3-yl- and 4-1*H*-imidazol-1-yl-benzoic acid

To investigate the binding modes of these type II ligands, UV-Vis spectra were recorded of the CYP199A4-ligand complexes after reduction with dithionite. The reduced spectra can

potentially give insight into whether the nitrogen ligands are directly coordinated to the iron.[358] Dawson *et al.* reported that when σ-donor nitrogen ligands (pyridine, metyrapone and *N*-phenylimidazole) are coordinated to the iron of $P450_{cam}$ and the iron is reduced, there is a shift in the position of the Soret band to 442-445 nm.[366] These spectra were also characterised by intense α and β bands.[366] Sevrioukova and Poulos[358] reported the same observations for ferrous CYP3A4 in complex with ritonavir, which ligates to the heme iron via the thiazole nitrogen, and pyridine and oxazole analogues of desoxyritonavir.[359]

Reduction of the 4-pyridin-3-ylbenzoate-CYP199A4 complex with dithionite resulted in a shift in the Soret band position (λ_{max}) to 447 nm. The Soret band intensity also increased compared to the oxidised form (ε_{447} = 118 mM^{-1} cm^{-1}) (Table 4.2, Figure 4.4a). Prominent β and α peaks appeared at 542 and 571 nm (ε_{542} and ε_{571} = 18.6 and 19.6 mM^{-1} cm^{-1}). This spectrum is consistent with the spectra reported by Dawson[366] and indicates direct coordination of the pyridine moiety to the heme iron. We were also able to reduce 4-pyridin-3-ylbenzoic acid-bound CYP1994 to the ferrous form using ferredoxin (HaPux), ferredoxin reductase (HaPuR) and NADH (Figure B12a). On the other hand, addition of dithionite to the 4-pyridin-2-ylbenzoate-CYP199A4 complex failed to shift the Soret band, and no changes were observed in the α/β-band region (Figure 4.4b). This may indicate that the heme was not being reduced.[358-359, 361] This complex was also not reduced by ferredoxin (HaPux), ferredoxin reductase (HaPuR) and NADH (Figure B12b). In case the interaction of the ligand with the active site was hindering heme reduction[359], substrate-free CYP199A4 was first reduced with dithionite before it was complexed with 4-pyridin-2-ylbenzoic acid (Figure B13). When substrate-free CYP199A4 was reduced with dithionite, the α- and β-bands merged, the Soret peak shifted to ~417 nm and its intensity diminished. Addition of 4-pyridin-2-ylbenzoic acid then resulted in a small red-shift of the Soret band to 419 nm, but again the Soret peak failed to shift to 440-450 nm (Figure B13b). This implied that the pyridine moiety was not directly ligated to the iron.

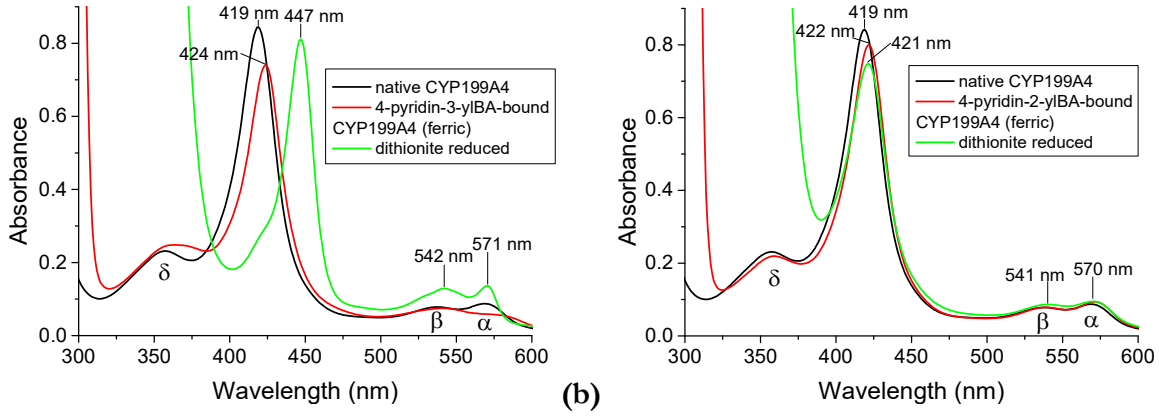

Figure 4.4. UV-Vis spectra of substrate-free ferric WT CYP199A4 (**black**) and ferric (**red**) and ferrous (**green**) CYP199A4 in complex with **(a)** 4-pyridin-3-ylbenzoic acid and **(b)** 4-pyridin-2-ylbenzoic acid. The ligand concentration was 2 mM and P450 concentration was 7.1 μM.

When the 4-1*H*-imidazol-1-ylbenzoic acid-CYP199A4 complex was reduced with dithionite, the Soret band also failed to shift to 440-450 nm. Instead, the Soret band was blue-shifted to ~416

nm and the α- and β-bands merged (Figure 4.5a). The same spectrum was obtained when 4-1*H*-imidazol-1-ylbenzoic acid was added to CYP199A4 after it had already been reduced (Figure B13d). This spectrum strongly resembles that of reduced substrate-free CYP199A4 and other reduced P450s.[25] We found that we could also reduce this complex using HaPux, HaPuR and NADH (Figure B12c).

For comparison, the UV-Vis spectra of ferrous CYP199A4 in complex with the type I substrates 4-vinyl-, 4-methoxy- and 4-phenyl-benzoic acid were obtained (Figure 4.5b and B14). These spectra of ferrous, five-coordinate[367-368] CYP199A4 had a Soret band that was blue-shifted to ~415 nm and all had a single peak at ~548 nm resulting from merging of the α- and β-bands. These spectra are virtually identical to the spectrum of reduced 4-1*H*-imidazol-1-ylbenzoic acid-bound CYP199A4. Assuming that the imidazole moiety is directly coordinated to the heme iron in the ferric state, this appears to imply that when the heme is reduced, the Fe-N bond breaks and the heme becomes five-coordinate.

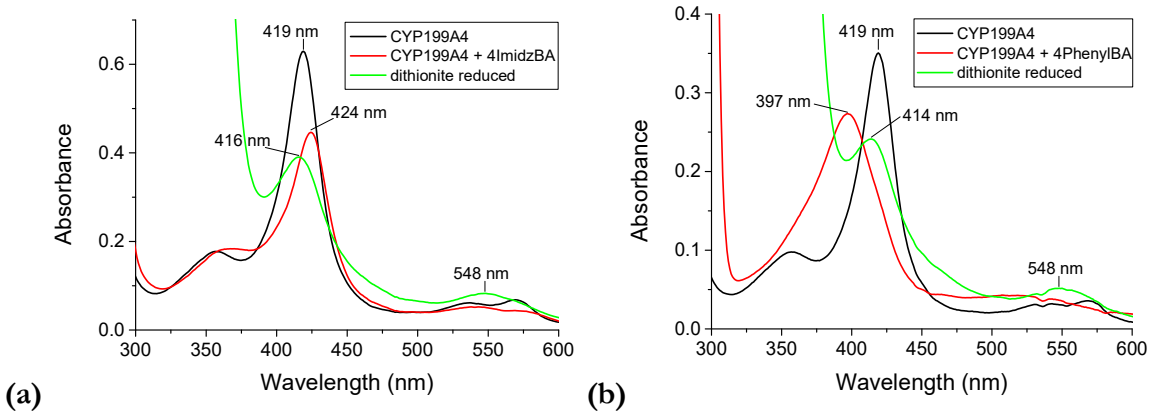

Figure 4.5. UV-Vis spectra of ferrous CYP199A4 in complex with **(a)** the type II ligand 4-1*H*-imidazol-1-ylbenzoic acid (4ImidzBA) and **(b)** the type I ligand 4-phenylbenzoic acid (4PhenylBA). In **black** is ferric substrate-free CYP199A4, in **red** is ferric substrate-bound CYP199A4 and in **green** is the reduced complex.

In case the Fe-N bond was breaking due to protonation of the basic imidazole nitrogen at pH 7.4,[369] the experiment was repeated at higher pH (Figure B15). However, the spectra at pH 8.5 and 9.3 were identical to those at lower pH.

We also recorded the spectrum of reduced CYP199A4 in complex with imidazole itself (Figure B16a). Upon reduction of CYP199A4 in the presence of saturating amounts of imidazole, spectral changes were observed; the Soret band shifted to 423 nm and prominent bands appeared at 528 and 558 nm. However, the Soret peak failed to shift to ~447 nm. The reduced CYP199A4-imdiazole spectrum strongly resembled that of reduced cytochrome b_5,[366, 370] which has peaks at 423, 528 and 558 nm. In cytochrome b_5, the heme iron has two histidine (imidazole) ligands in the axial positions.[370] The high concentration of imidazole required to achieve binding may partially denature the enzyme, with two molecules of imidazole coordinating to the heme in the two axial positions. Another possibility is that this is the spectrum of ferrous heme with imidazole and a neutral cysteine thiol ligand bound, arising from protonation of the proximal cysteine thiolate

ligand. We note that our reduced CYP199A4-imidazole spectrum also resembles that of reduced cytochrome *c*, in which the heme has a histidine and a methionine (neutral sulfur) ligand.[371] In agreement with this hypothesis, when we subsequently added 4-pyridin-3-ylbenzoic acid to the cuvette, the Soret band only partially shifted to 447 nm, indicating that a portion of the enzyme had been denatured by the high concentration of imidazole (Figure B17a). Furthermore, when imidazole and dithionite were added to denatured CYP199A4 (which had been heated at 65˚C for 30 min), this yielded essentially the same spectrum with peaks at ~425, ~527 and ~559 nm (Figure B18a).

When we added dithionite to the CYP199A4-pyridine complex, we similarly found that the resulting spectrum resembled that of ferrous heme with two axial pyridine ligands (pyridine hemochromogen)[288] (Figures B16b, B17b, B18b).

In summary, the UV-Vis spectra of the ferrous CYP199A4-ligand complexes indicate that 4-pyridin-3-ylbenzoic acid ligates directly to the heme iron, but further work is needed to elucidate the binding modes of 4-pyridin-2-ylbenzoic acid and 4-1*H*-imidazol-1-ylbenzoic acid.

4.2.3 Crystal structures of 4-pyridin-2-yl-, 4-pyridin-3-yl- and 4-1*H*-imidazol-1-yl-benzoic acid in complex with CYP199A4

To prepare the ligand-CYP199A4 complexes, dilute protein was incubated with the 3 mM 4-pyridin-2-yl- or 4-pyridin-3-yl-benzoic acid and subsequently concentrated to 30-35 mg/mL. Crystals formed readily under the standard conditions (Figure B19). To prepare the CYP199A4 complex with 4-1*H*-imidazol-1-ylbenzoic acid, 3 mM substrate was added to 40 mg/mL protein from a 25 mM stock solution in 50 mM Tris-HCl buffer (pH 9.5). Crystal structures of CYP199A4 in complex with 4-pyridin-2-yl-, 4-pyridin-3-yl- and 4-1*H*-imidazol-1-yl-benzoic acid were solved by the molecular replacement method, using the CYP199A4 crystal structure 5UVB as the search model. The crystal structures were solved at resolutions of 1.80, 1.66 and 1.58 Å, respectively. Data collection and refinement statistics are presented in Table B1. These structures were deposited into the PDB (codes: 6U3K, 6U30, 6U31). The overall fold of CYP199A4 in complex with these type II ligands is highly similar to previously solved structures (Figure B20). The RMSD between the Cα atoms of the superimposed structures of CYP199A4 in complex with 4-pyridin-2-yl- and 4-pyridin-3-yl-benzoic acid is 0.262 Å over all 393 residues. In each structure, a sphere of electron density was located in the anion binding site[29] and modelled as chloride (Figure B21).

In agreement with the type II shift induced by 4-pyridin-3-ylbenzoic acid, the crystal structure revealed that the pyridine moiety ligates directly to the iron (Figure 4.6). The Fe-N bond distance was refined to 2.2 Å. This is longer than the Fe-N bond length in $[Fe(bipy)_3]^{2+}$ (1.97 Å)[372], but comparable to the Fe-N bond lengths in crystal structures of P450s with directly bound pyridine derivatives (~2.1-2.4 Å) (Table B2).[359, 364, 373-374] There is an almost linear arrangement of the Cys358

sulfur, iron and pyridine nitrogen (S_{Cys}-Fe-N angle = 176.9°). The pyridine ring is at an 18° angle to the iron-sulfur bond axis.

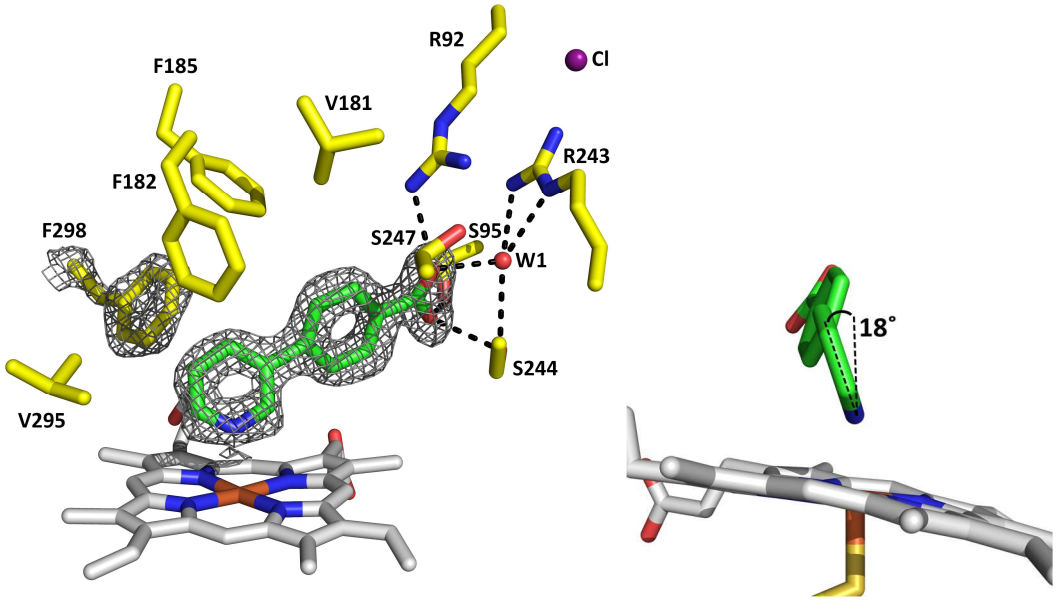

Figure 4.6. Crystal structure of 4-pyridin-3-ylbenzoic acid-bound CYP199A4. A composite omit map of the 4-pyridin-3-ylbenzoic acid ligand and F298 residue is shown as grey mesh contoured at 1.5 σ (1.2 Å carve). The heme is grey, active site residues are yellow and 4-pyridin-3-ylbenzoic acid is green. The pyridine ring is not perpendicular to the heme; it is held an 18° angle to the Fe-S axis (measured using UCSF Chimera[375]).

In contrast, the heme-bound water ligand remains *in situ* in the crystal structure of CYP199A4 in complex with the isomer 4-pyridin-2-ylbenzoic acid (Figure 4.7). The pyridine moiety, which is at an angle of 42° to the Fe-S bond axis, hydrogen-bonds to the distal water ligand (with a donor-acceptor distance of 2.9 Å) rather than replacing it as the sixth axial ligand. The occupancy of the water ligand was refined to 76%[vii]. The Fe-O distance is 2.2 Å and S_{Cys}-Fe-O angle is 163.4°. The side-chain phenyl ring of F298 is displaced to accommodate the pyridine moiety of 4-pyridin-2-ylbenzoic acid, which is positioned above pyrrole ring A. F298 must shift when 4-pyridin-2-ylbenzoic acid binds because the distance between the pyridine ring and phenyl ring would otherwise be 0.76 Å (a steric clash). Displacement of F298 by bulky substrates has previously been observed in the crystal structures of CYP199A4 in complex with 4-ethylthiobenzoic acid (PDB ID: 5U6U) (Figure B22) and 4-thiophen-3-ylbenzoic acid (PDB ID: 6C3J).[117, 277] On the other hand, F298 is not displaced when 4-pyridin-3-ylbenzoic acid binds. This is because the pyridine moiety is positioned directly above the heme iron and is not close enough to interact with F298.

[vii] By way of contrast, the refined occupancy of the water molecule which bridges between the substrate carboxylate and R243 was 100%.

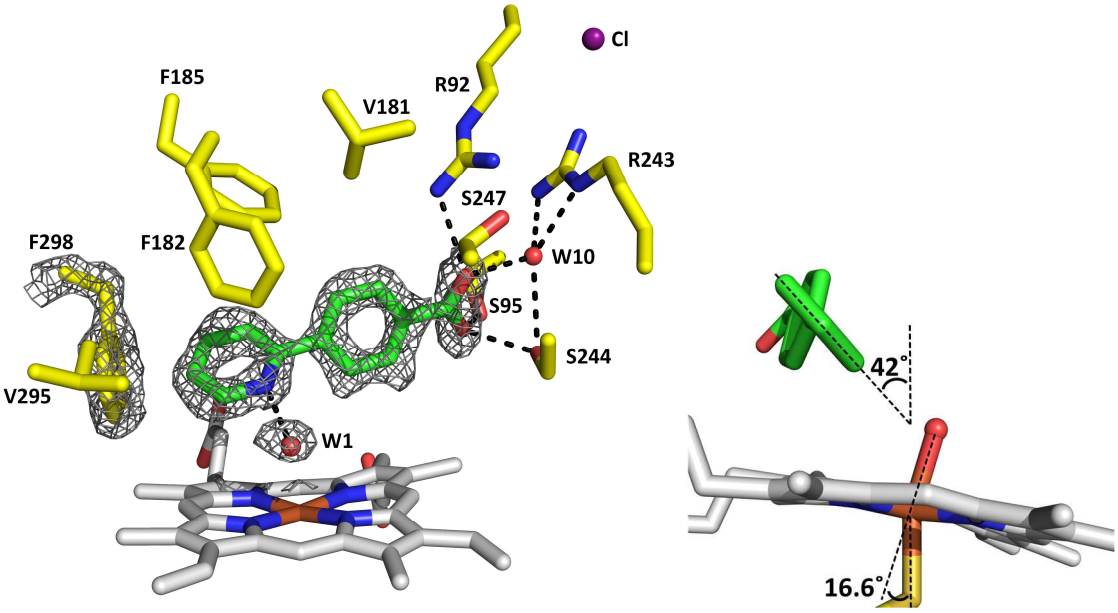

Figure 4.7. Crystal structure of 4-pyridin-2-ylbenzoic acid-bound CYP199A4. A feature-enhanced map of the 4-pyridin-2-ylbenzoic acid ligand, F298 residue and heme-bound water ligand is shown as grey mesh contoured at 1.5 σ (1.5 Å carve). The heme is grey, active site residues are yellow and 4-pyridin-2-ylbenzoic acid is green. The refined occupancy of the heme-bound water ligand (W1) is 76%. The Fe-O bond is at an angle of 16.6° to the Fe-S bond. The pyridine ring is at an angle of 42° to the Fe-S bond.

As mentioned, the refined occupancy of the iron-bound water ligand was 76%, not 100%. It is plausible that in the X-ray beam the heme iron was partially reduced to the ferrous form.[376] Water is a poor ligand for ferrous heme[367, 377-378], so it may be that the water partially dissociates due to reduction in the X-ray beam.[376, 379] Others have previously reported that the X-ray beam can generate ferrous heme and the occupancy of the heme-bound water ligand may be reduced.[376, 379] There is also a possibility that 4-pyridin-2-ylbenzoic acid may bind in an alternative orientation. If there was a second binding mode in which the pyridine ring was flipped, it would no longer be able to hydrogen-bond to the water and the water would be displaced. However, we see no evidence of a contribution from a low-spin to high-spin shift in the UV-Vis spectrum when 4-pyridin-2-ylbenzoic acid binds to CYP199A4.

The 4-pyridin-2-yl- and 4-pyridin-3-yl-benzoic acid structures are overlaid in Figure 4.8. Table B3 gives distances between equivalent atoms of the two inhibitors. The pyridine ring of 4-pyridin-3-ylbenzoic acid is rotated out of the plane of the benzene ring by 40.2°, whereas that of 4-pyridin-2-ylbenzoic acid is rotated out of the benzene plane by 60.6° (Table 4.3). The pyridine ring of 4-pyridin-2-ylbenzoic acid is oriented such that the α-carbon and β-nitrogen are held in roughly similar positions to the α- and β-carbons of 4-ethylbenzoic acid (Figure B23), though the ethyl group is closer to the iron. The N of 4-pyridin-2-ylbenzoic acid is 4.2 Å from the iron, compared to 3.5 Å between the iron and C_β of 4-ethylbenzoic acid. The benzoic acid moiety of 4-pyridin-2-ylbenzoic acid occupies a similar position to that of 4-methoxybenzoic acid and 4-ethylbenzoic acid, whereas the benzoic acid moiety of 4-pyridin-3-ylbenzoic acid is more substantially shifted (Figure 4.9a,b). As a result of the altered position of the 4-pyridin-3-ylbenzoic acid benzoic acid

moiety, the position of the water molecule which bridges between the carboxylate and R243 is also shifted (by 0.3 Å) (Figures 4.8 and 4.9a). Although most of the amino acid residues have similar positions in the two structures, multiple active-site residues, including V295, F185 and F182, have altered positions (Figure 4.8). The phenyl ring of F182, for example, is shifted away from the pyridine moiety of 4-pyridin-3-ylbenzoic acid. The phenyl ring atoms of F182 are shifted by 0.8-0.9 Å relative to their position in the 4-pyridin-2-ylbenzoic acid structure (Table B3).

4-Pyridin-3-ylbenzoic acid is positioned closer to the oxygen-binding groove than 4-pyridin-2-ylbenzoic acid and the residues in the groove are consequently shifted away from 4-pyridin-3-ylbenzoic acid (Figure 4.8). The C^{β} atom of A248 is displaced by 1 Å and the T252 side-chain atoms are shifted by 0.9-1.0 Å relative to the positions of the equivalent atoms in the 4-pyridin-2-ylbenzoic acid structure (Figure 4.8, Table B3). Other amino acids flanking the active site also have altered orientations, including N255, P294 and T395 (Figure 4.8).

Table 4.3. Distances (in angstroms) of key structural features of 4-pyridin-3-ylbenzoic acid- and 4-pyridin-2-ylbenzoic acid-bound CYP199A4.

Distance (Å)	**4-pyridin-3-yl**	**Distance (Å)**	**4-pyridin-2-yl**
Fe - N_5	2.2	Fe - W1	2.2
Fe - C_4	3.0	Fe - N_4	4.2
Fe - C_6	3.1	N_4 - W1	2.9
C_2 - closest F298 C	3.6	C_1- closest F298 C	3.8
C_2 - closest F185 C	4.8	C_2 - closest F185 C	3.7
C_2 - closest F182 C	3.4	C_2 - closest F182 C	3.6
N_5 - closest T252 C	3.7	Fe - C_5	4.4
N_5 - closest F182 C	5.0	N_4 - closest F182 C	3.6
O_{15} - W1 (bridging water)	2.5	O_{15} - W10 (bridging water)	2.6
O_{15} - closest R92 N	2.9	O_{15} - closest R92 N	3.0
C_7 - closest A248 C	3.4	C_5 - W1	3.3
C_7 - closest L98 C	4.1	C_7 - closest L98 C	3.7
Angle (°)		**Angle (°)**	
(C358)S-Fe-N(pyridine)	176.9	(C358)S-Fe-(W1)	163.4
Dihedral C_4-C_3-C_7-C_8	40.21	Dihedral N_4-C_3-C_7-C_8	60.62
Refined occupancy (%)		**Refined occupancy (%)**	
4-pyridin-3-ylbenzoic acid ligand	99	4-pyridin-2-ylbenzoic acid ligand	100
		W1 (water ligand to heme)	76

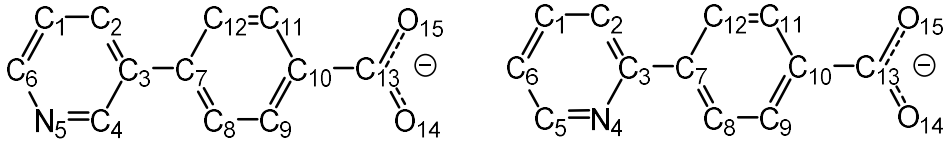

Atom numbers in 4-pyridin-3-ylbenzoic acid were assigned by Phenix eLBOW.[321] 4-Pyridin-2-ylbenzoic acid is labelled with matching numbers.

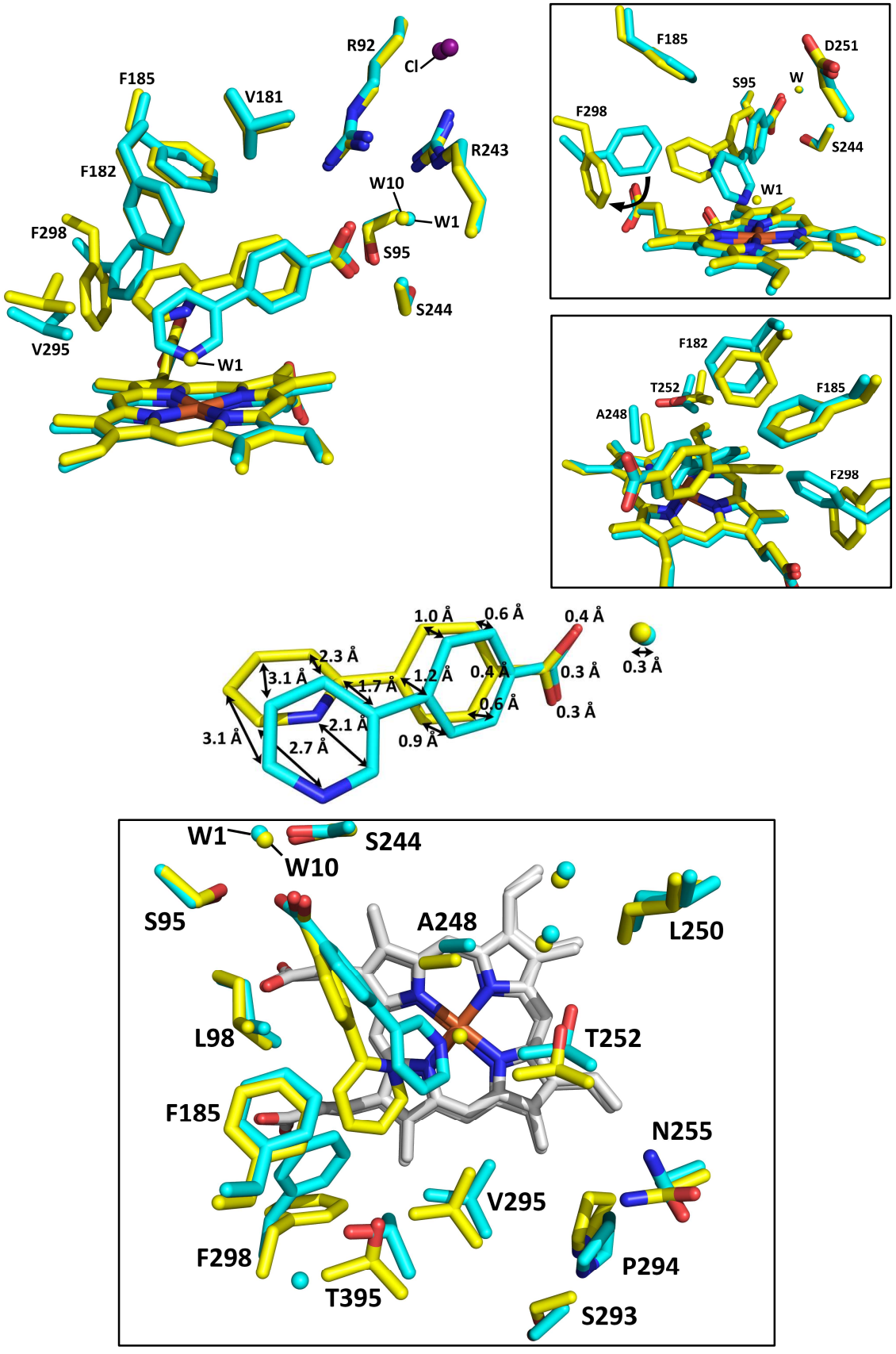

Figure 4.8. Overlaid structures of 4-pyridin-3-yl- (cyan) and 4-pyridin-2-yl-benzoic acid-bound CYP199A4 (yellow). An active site water (W1, yellow sphere) is bound to the iron in the 4-pyridin-2-ylbenzoic acid structure, whereas 4-pyridin-3-ylbenzoic acid displaces the heme-bound water and the nitrogen coordinates to the iron. F298 shifts to accommodate 4-pyridin-2-ylbenzoic acid (movement described by the black arrow) but not when 4-pyridin-3-ylbenzoic acid binds.

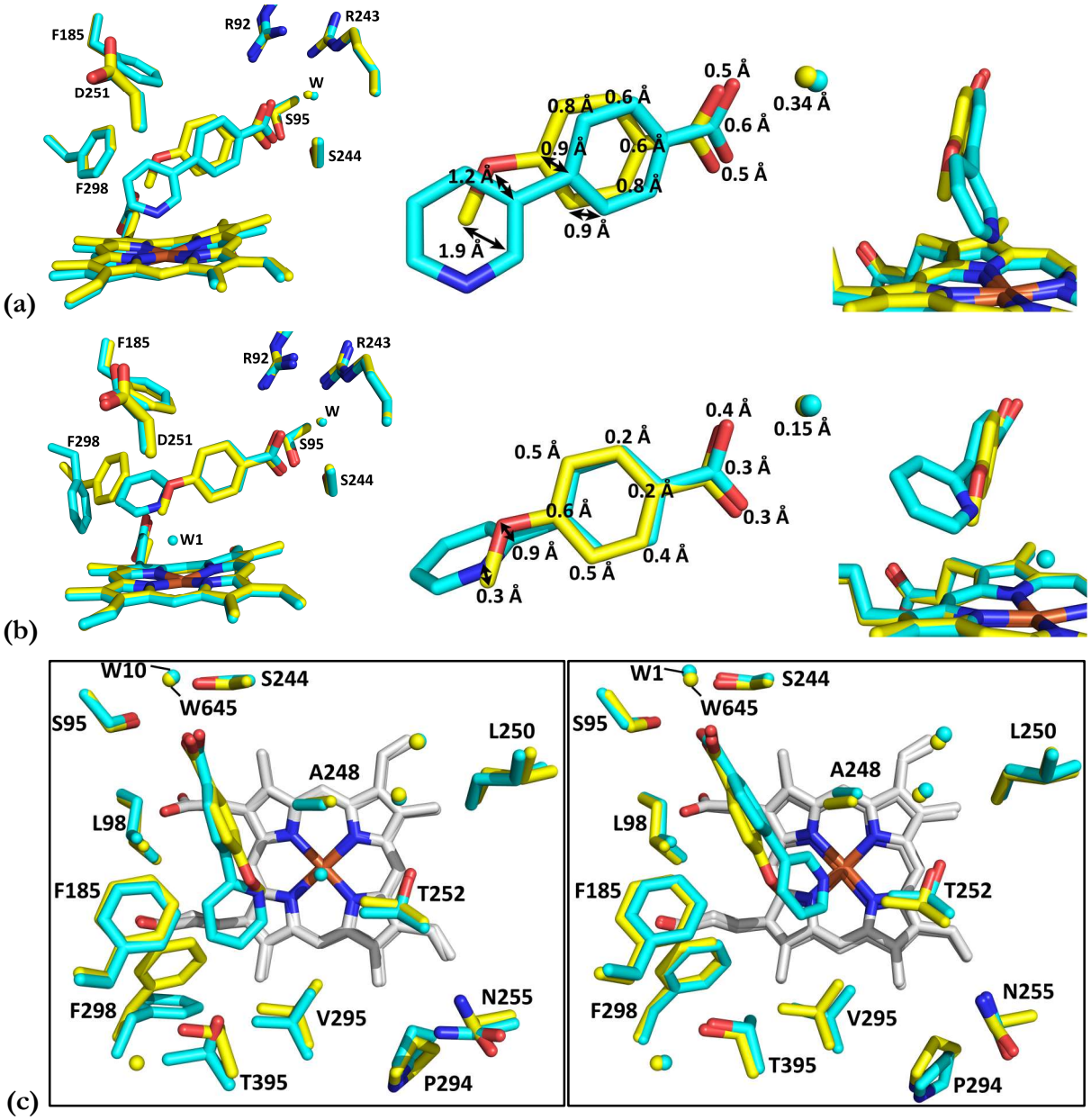

Figure 4.9. **(a)** Overlaid structures of 4-pyridin-3-ylbenzoic acid-bound CYP199A4 (cyan) and 4-methoxybenzoic acid-bound CYP199A4 (yellow, PDB: 4DO1). Distances between equivalent atoms of the benzoic acid moiety are given in Å. In **(b)** the 4-pyridin-2-ylbenzoic acid structure (cyan) and 4-methoxybenzoic acid structure (yellow) are overlaid. In **(c)** is a view of the active site looking down on the heme. **Left**: the 4-pyridin-2-ylbenzoic acid structure (cyan) overlaid with the 4-methoxybenzoic acid structure (yellow). **Right**: the 4-pyridin-3-ylbenzoic acid structure (cyan) overlaid with the 4-methoxybenzoic acid structure.

The crystal structure of 4-1*H*-imidazol-1-ylbenzoate-bound CYP199A4 revealed that this inhibitor coordinates to the heme iron via the imidazole nitrogen, replacing water as the sixth axial ligand (Figure 4.10). The Fe-N bond length is 2.2 Å and the S_{Cys}-Fe-N angle is approximately linear (176°) (Table 4.4). This bond length is comparable to the Fe-N bond length in the crystal structures of $P450_{cam}$ in complex with 1- and 4-phenylimidazole (2.2 and 2.3 Å)[364, 380] (Table B2). The imidazole ring is rotated out of the plane of the benzene ring by 43°. Ideally the azole ring should be perpendicular to the heme as observed in other crystal structures of inhibitor-bound P450s (Figure B24, Tables B4, B5),[156, 159, 380] but the imidazole ring of 4-1*H*-imidazol-1-ylbenzoic acid is noticeably

tilted (it is at an angle of 26° to the iron-sulfur axis) (Figure 4.10). The angle between the imidazole ring and heme plane is 56.8° (Table B6). The bulky benzoic acid substituent may prevent the imidazole ring from binding perpendicular to the heme. Both the imidazole ring and the benzoic acid moiety occupy highly similar positions to the pyridine ring and benzoic acid moiety of 4-pyridin-3-ylbenzoic acid (Figure 4.11). In both the 4-1*H*-imidazole-1-ylbenzoic acid and 4-pyridin-3-ylbenzoic acid structures, the active-site residues have essentially the same positions, and the RMSD between the Cα atoms of the superimposed structures is only 0.107 Å (over all 393 residues).

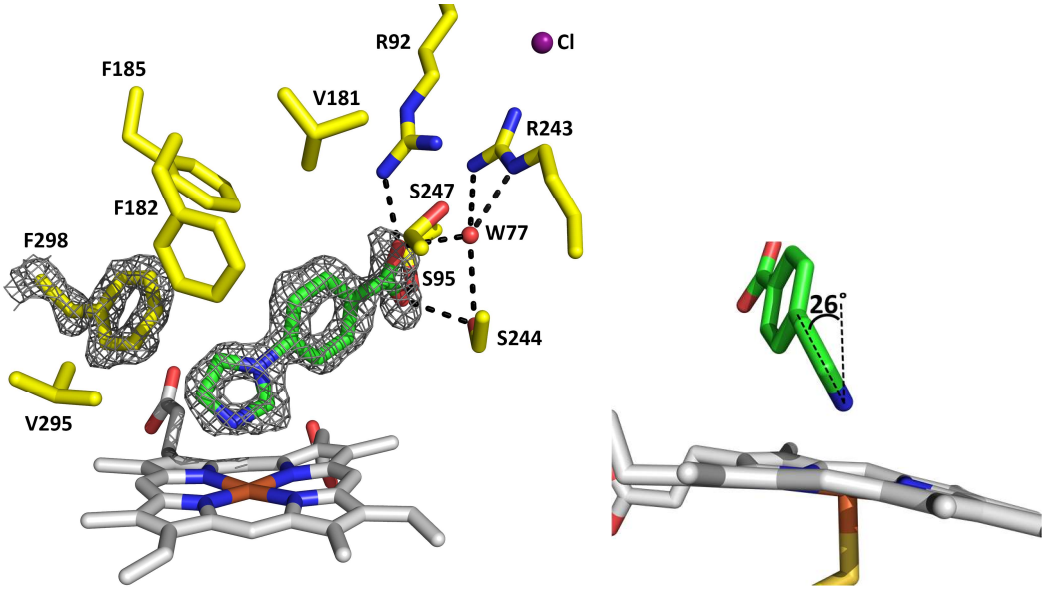

Figure 4.10. Crystal structure of 4-(1*H*-imidazol-1-yl)benzoic acid-bound CYP199A4. A feature-enhanced map of the substrate and F298 residue is shown as grey mesh contoured at 1.5 σ (1.5 Å carve).

Table 4.4. Distances (in angstroms) in 4-1*H*-imidazol-1-ylbenzoate-bound CYP199A4.

Distance (Å)	**4-1*H*-imidazol-1-yl**
Fe - N_{11}	2.2
Fe - C_{10}	3.3
Fe - C_{12}	3.0
C_9 - closest F298 C	3.7
N_{11} - closest T252 C	3.7
O_1 - W77 (bridging water)	2.6
O_1 - closest R92N	2.7
C_7 - closest A248 C	3.3
C_{12} - closest A248 C	3.1
C_7 - closest L98 C	4.2
C_9 - closest F182	3.5
C_9 - closest F185	5.4
Angle (°)	
(C358)S-Fe-N(imidazole)	176.6
Dihedral C_{13}-C_7-N_8-C_{12}	42.5
Refined occupancy (%)	
4-1*H*-imidazol-1-ylbenzoic acid ligand	87

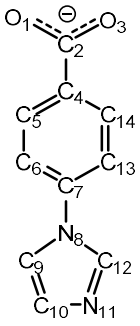

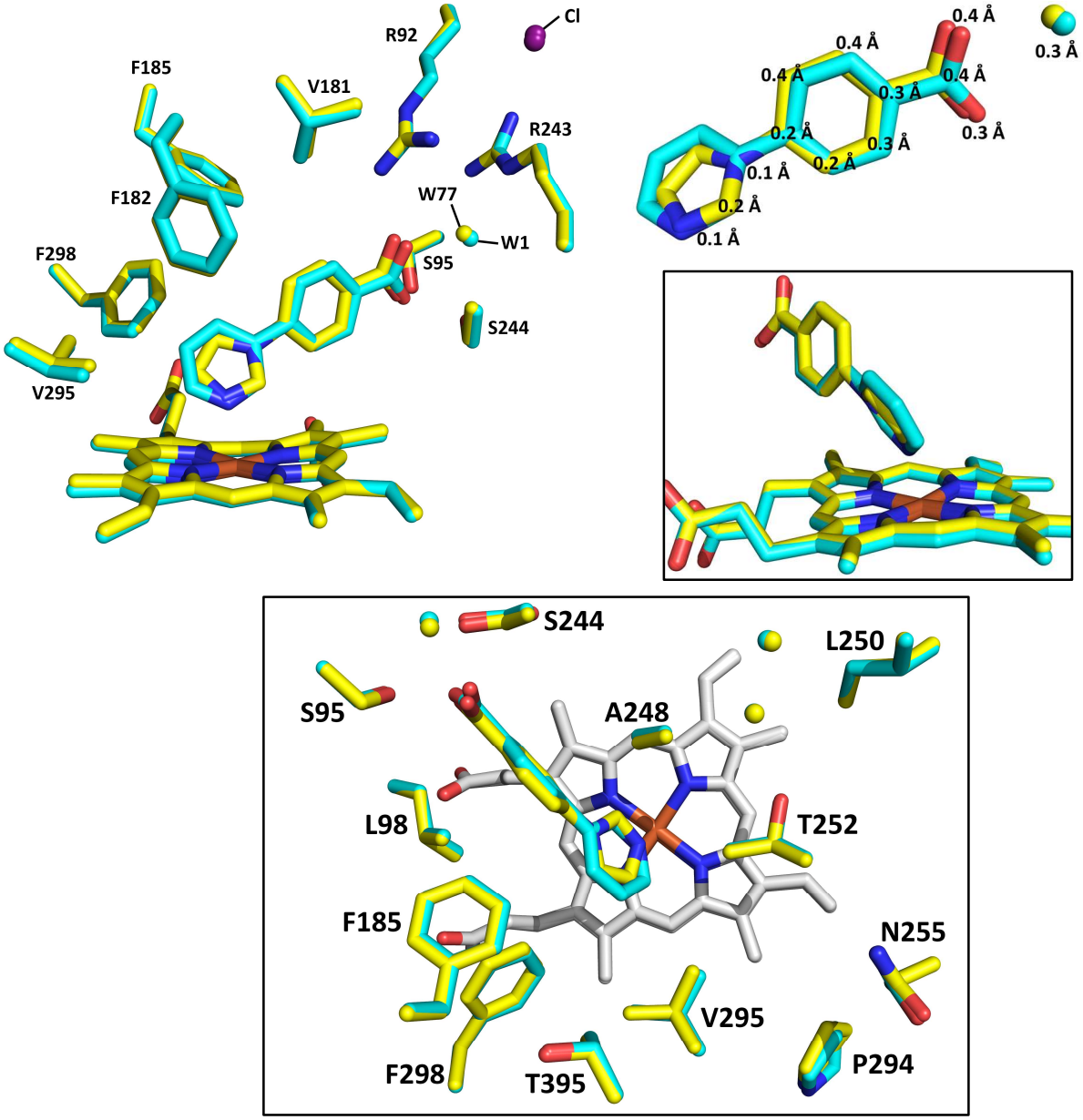

Figure 4.11. Overlaid structures of WT CYP199A4 in complex with 4-pyridin-3-yl- and 4-1*H*-imidazol-1-yl-benzoic acid (cyan and yellow, respectively).

In these three inhibitor-bound CYP199A4 crystal structures, in which the iron is hexacoordinate and low-spin, the iron is predominantly in the plane of the porphyrin ring (Figure 4.12a–d).[356] In the 4-pyridin-3-ylbenzoic acid structure, the iron is displaced by only 0.05 Å out of the plane defined by the four pyrrole nitrogens (Figure 4.12b, Table 4.5). In contrast, when a substrate removes the water ligand without coordinating to the heme to yield pentacoordinate, high-spin iron, the iron, now having a larger ionic radius,[173] moves below the porphyrin plane.[101, 356, 381] In structures of HS ferric CYP1994 in complex with substrates which expel the water such as 4-methyl- and 4-cyclopropyl-benzoic acid (PDB ID: 5UVB), the iron is ~0.3 Å below the plane of the four pyrrole nitrogens (Figure 4.12e–g, Table 4.5). In camphor-bound $P450_{cam}$, the iron is also displaced 0.3 Å out of the plane of the heme.[98] The Fe-S distance is ~2.3 Å in the inhibitor-

bound CYP199A4 structures and the Fe-N(porphyrin) distances range from 2.01-2.08 Å (Tables B7, B8).

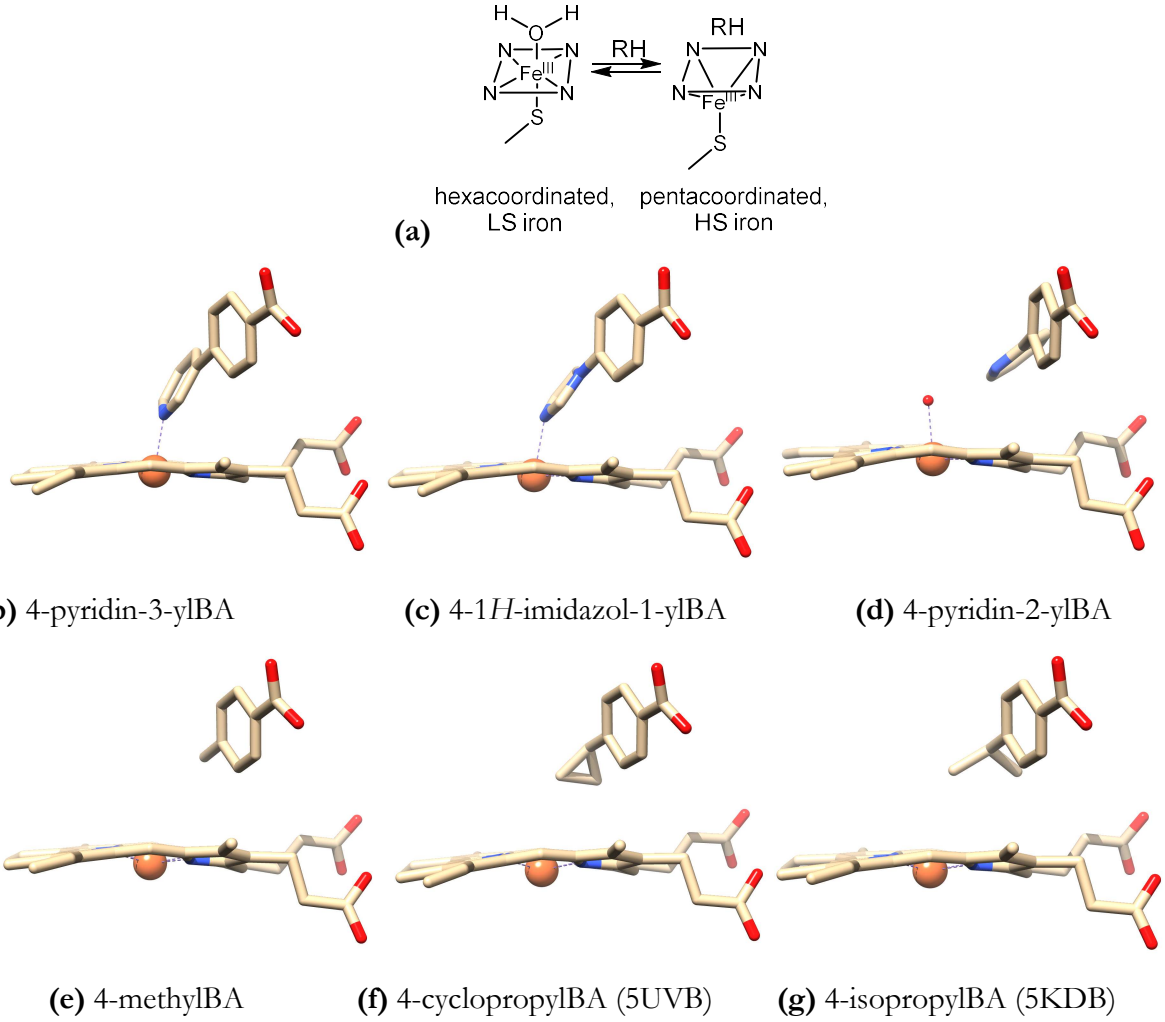

Figure 4.12. **(a)** Geometry of five- and six-coordinate ferric heme.[101, 381] In the hexacoordinate, low-spin state, the heme iron is more or less in the plane of the heme. High-spin pentacoordinate iron moves below the plane.[356] In the inhibitor-bound CYP199A4 complexes, the iron is approximately in the plane of the heme **(b–d)**.[356] In pentacoordinate, high-spin CYP199A4 complexes, the iron is displaced ~0.3 Å out of the heme plane **(e–g)**.

Table 4.5. Displacement of the heme iron below the porphyrin plane in CYP199A4 crystal structures

Ligand bound to WT CYP199A4		**Iron displacement below porphyrin plane**	
		Plane defined by the four pyrrole nitrogens	**Plane defined by the 24 atoms of the porphyrin macrocycle**
4-Pyridin-3-ylBA	Hexacoordinated, low-spin iron	0.053 Å	0.042 Å
4-Pyridin-2-ylBA		0.131 Å	0.096 Å
4-Imidazol-1-ylBA		0.100 Å	0.086 Å
4-MethylBA	Pentacoordinated, high-spin iron	0.309 Å	0.287 Å
4-CyclopropylBA (5UVB)		0.351 Å	0.335 Å
4-MethoxyBA (4DO1)		0.204 Å	0.234 Å
4-EthoxyBA (5U6T)		0.280 Å	0.256 Å
4-IsopropylBA (5KDB)		0.309 Å	0.309 Å

In the CYP199A4 crystal structures, the Fe-S bond appears to be marginally shorter when the iron is hexacoordinate and low-spin than when it is pentacoordinate and high-spin (Table B7). This agrees with high-resolution structures of ligand-free and camphor-bound $P450_{cam}$ (PDB ID: 1PHC and 1DZ4). In the crystal structure of ligand-free $P450_{cam}$, where the iron is hexacoordinate and LS, the Fe-S distance is 2.25 Å, but in the camphor-bound, pentacoordinate HS form the bond distance is 2.37 Å.[98, 382] However, it has also been suggested that a shift from LS to HS may shorten the Fe-S bond length.[101]

4.2.4 HYSCORE EPR data for binding of type II inhibitors to CYP199A4

EPR (electron paramagnetic resonance) is a valuable technique for studying the P450 heme structure and environment.[153] Continuous wave EPR can establish whether the Fe^{III} iron is in the low-spin or high-spin state[viii], and the *g*-values give insight into the type of ligand coordinated to the heme iron, with larger g_z values being associated with nitrogen donor ligands.[153, 158, 360] Coordination of an imidazole/histidine ligand to the heme iron often yields g_z values of around 2.65 to 2.5,[159, 363] whereas P450s with water bound usually have g_z values of ≤2.45.[159, 363, 383] HYSCORE (HYperfine Sublevel CORrElation) EPR is a technique that can be used to determine whether the water ligand to the heme is displaced by substrate or remains *in situ*. The interaction that is detected is that between the unpaired electron on the iron and ^1H nuclei.[153-154, 158, 360] If the water is expelled by the substrate, the proton signals (Figure 4.13a) corresponding to the aqua ligand in the HYSCORE spectrum vanish.[158] HYSCORE EPR experiments were performed by Josh Harbort and Jeffrey Harmer at the University of Queensland. The HYSCORE spectra (Figure 4.13b) show that the proton peaks of the axial water ligand disappear when 4-pyridin-3-ylbenzoic acid binds, with peaks appearing which correspond to the pyridine nitrogen coordinated to the heme iron. When 4-pyridin-2-ylbenzoic acid binds, the water proton peaks do not disappear (Figure 4.13c). As a control, HYSCORE EPR showed that when 4-methoxybenzoic acid binds to CYP199A4, the water proton peaks almost entirely disappear (Figure B25a).

[viii] Low-spin P450s are characterised by *g*-values of ~[1.92, 2.25, 2.42], whereas for the high-spin state the *g*-values are ~[1.8, 4.3, 7].[360]

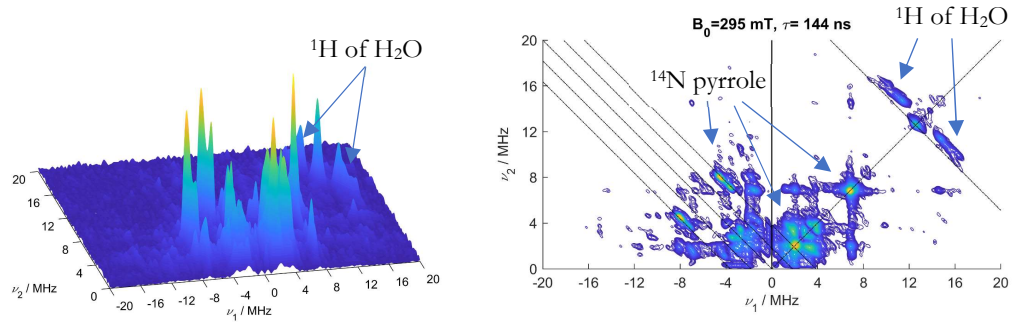

(a) substrate-free CYP199A4

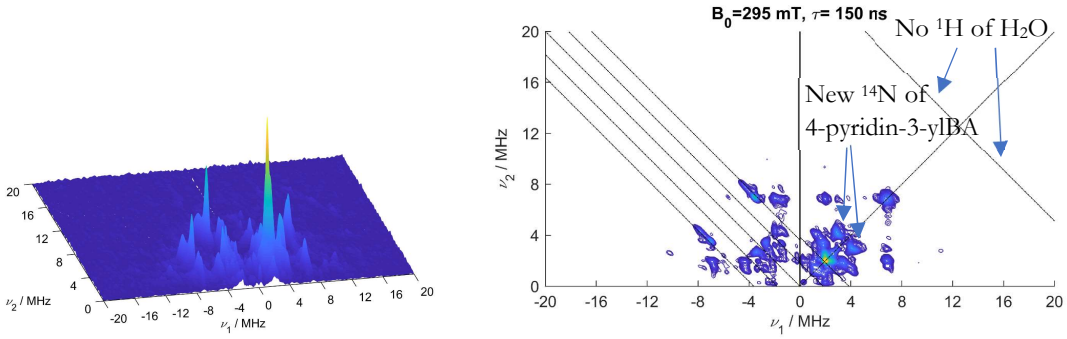

(b) 4-pyridin-3-ylbenzoic acid-bound CYP199A4

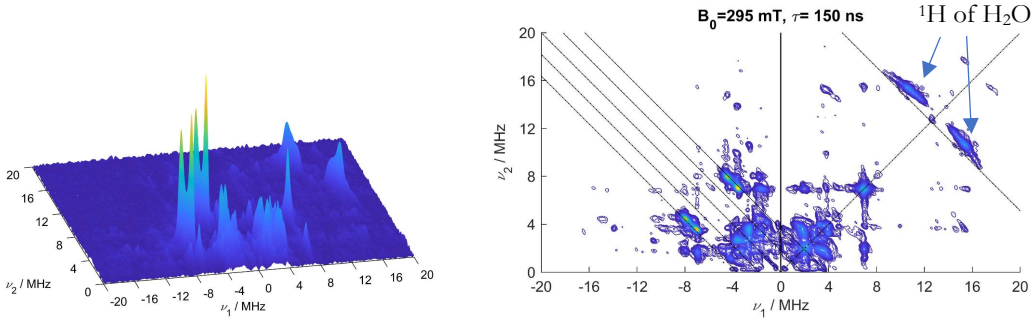

(c) 4-pyridin-2-ylbenzoic acid-bound CYP199A4

Figure 4.13. HYSCORE spectra of CYP199A4 **(a)** without substrate and in complex with the type II inhibitors 4-pyridin-3-ylbenzoic acid **(b)** and 4-pyridin-2-ylbenzoic acid **(c)**. Binding of 4-pyridin-3-ylbenzoic acid resulted in the disappearance of the peaks corresponding to the distal water ligand protons; binding of 4-pyridin-2-ylbenzoic acid did not. This figure was supplied by Josh Harbort and Jeffrey Harmer at the University of Queensland, who performed the EPR experiments.

The CW EPR spectrum of CYP199A4 in complex with the two pyridine inhibitors showed that both complexes were low spin (Figure B25b, Table B9). However, the CW EPR spectrum of 4-pyridin-2-ylbenzoic acid-bound CYP199A4 differs from that of 4-pyridin-3-ylbenzoic acid-bound CYP199A4. The CW EPR spectrum of the 4-pyridin-3-ylbenzoic acid-CYP199A4 complex, which has a g_z value that is considerably greater than that of native CYP199A4 (g_z = 2.526 *vs.* 2.433), is consistent with the sixth axial ligand being a nitrogen donor (Table B9).[159, 363, 384] It has been reported that when a nitrogen ligand displaces the heme-bound water and directly coordinates to the iron, the g_z value becomes larger by ~0.04.[360] For 4-pyridin-2-ylbenzoic acid, the EPR spectrum is only subtly altered compared to that of the water-bound substrate-free resting state and is

consistent with water being retained as the sixth ligand (g_z = 2.439). Conner *et al.* previously found that CYP3A4 in complex with 17-click, which hydrogen-bonds to the water ligand rather than coordinating to the iron, also had an EPR spectrum which was only subtly different to that of substrate-free CYP3A4.[154] Substrate-free CYP3A4 had a g_z value of 2.421 and 17-click-bound CYP3A4 a similar g_z value of 2.415.[154] In contrast, the complex of CYP3A4 with the *bona fide* type II ligand 1,2,3-triazole had g_z values of 2.505 and 2.459.[154]

Although CYP199A4 in complex with 4-methoxybenzoic acid is ≥95% high-spin at room temperature, low-temperature CW EPR revealed that a considerable portion of the enzyme was in the LS state (Table B9). This is in line with previous EPR results for other P450s, where the LS state was found to be more abundant at lower temperatures.[153, 173, 337, 385] Camphor-bound $P450_{cam}$ is only 45% HS at 4.2 K, but 77% HS at 200 K.[385]

4.3 Discussion

The crystal structures of CYP199A4 in complex with the three inhibitors revealed that 4-pyridin-3-ylbenzoic acid and 4-1*H*-imidazol-1-ylbenzoic acid coordinate via the nitrogen lone pair to the heme iron. On the other hand, 4-pyridin-2-ylbenzoic acid, which induces a smaller red-shift than 4-pyridin-3-ylbenzoic acid, instead forms a hydrogen bond to the iron-bound aqua ligand. Only a small number of P450 crystal structures displaying this water-bridged binding mode have been reported[360], but Atkins *et al.* hypothesised that this binding mode may in reality occur more frequently.[158] 4-Pyridin-2-ylbenzoic acid is not metabolised even though some ligands (e.g. 17-click) which hydrogen-bond to the axial water ligand are known to be readily metabolised instead of inhibiting the P450 catalytic cycle.[154-155]

Jones *et al.* have previously observed that type II ligands which form direct Fe-N bonds with the heme iron bind with substantially higher affinity than analogues which bind in a type I fashion.[353, 384] They prepared quinoline-4-carboxamide analogues incorporating a pyridine moiety in which the pyridine nitrogen location was varied.[384] Those compounds with the nitrogen in the *para* position were capable of forming direct Fe-N bonds, but not those with the nitrogen in the *ortho* or *meta* positions.[384] Analogues which formed direct Fe-N bonds with the heme iron were found to bind with up to 4200-fold greater affinity than those which did not coordinate to the iron.[384] Despite forming a direct Fe-N bond with the heme iron, 4-pyridin-3-ylbenzoic acid displays lower affinity for CYP199A4 than 4-pyridin-2-ylbenzoic acid (K_d = 2.3 μM *vs.* 1.0 μM). It also binds more weakly than 4-phenylbenzoic acid (K_d = 1.7 μM)[277], which binds in a type I fashion. The crystal structures reveal that the orientations of 4-phenylbenzoic acid and 4-pyridin-2-ylbenzoic acid in the active site are virtually identical but differ substantially from the orientation of 4-pyridin-3-ylbenzoic acid (Figure B26). The benzoic acid moiety of 4-pyridin-3-ylbenzoic acid is shifted compared to that of 4-methoxybenzoic acid, 4-pyridin-2-ylbenzoic acid and 4-phenylbenzoic acid, and active-site residues are also shifted. The water molecule which bridges between the substrate carboxylate and R243 is also shifted from its usual position in the 4-pyridin-3-ylbenoic acid-

CYP199A4 structure. This indicates that in order for 4-pyridin-3-ylbenzoic acid to directly coordinate to the heme iron, it must adopt a less favourable orientation in the active site. Because it must bind in a less favourable orientation, this must counteract the gain in affinity resulting from formation of the direct Fe-N bond. 4-Pyridin-3-ylbenzoic acid could be readily displaced from the binding pocket of ferric and ferrous CYP199A4 by the high-affinity type I substrate 4-methoxybenzoic acid (Figure B27a,b). It could also be displaced by 4-pyridin-2-ylbenzoic acid (Figure F28). 4-1*H*-imidazol-1-ylbenzoic acid could also easily be displaced by 4-methoxybenzoic acid, but a larger concentration of 4-methoxybenzoic acid was required to displace 4-pyridin-2-ylbenzoic acid from the CYP199A4 active site (Figure B29a,b).

HYSCORE EPR experiments confirmed that in solution 4-pyridin-3-ylbenzoic acid is directly ligated to the heme iron, but 4-pyridin-2-ylbenzoic acid fails to displace the heme-bound water ligand. The binding modes of these inhibitors in the crystal structures appear to explain the different type II spectra that they induce. Others have suggested that nitrogen donor ligands which are directly coordinated to the iron and those which interact with the iron-bound water are difficult to distinguish based on UV-Vis spectra.[154-155] In this instance, though, the difference spectra do appear to discriminate between these two binding modes. The changes induced by 4-pyridin-3-ylbenzoic acid and 4-1*H*-imidazol-1-ylbenzoic acid (directly coordinating ligands) are consistent with those described by Dawson and Sono for 'normal' nitrogen donor ligands.[363] For these complexes there is larger Soret band red-shift and a substantial decrease in the intensity of the α-band. The β-band is also red-shifted. In contrast, the optical spectrum of the 4-pyridin-2-ylbenzoic acid-CYP199A4 complex resembles the spectra of 'abnormal' nitrogen donor ligands. One feature of the optical spectrum of 4-pyridin-2-ylbenzoic acid-bound CYP199A4 is that it has an α-band which is more intense than the β-band. Dawson and Sono found that this was a characteristic of complexes of $P450_{cam}$ with oxygen donor ligands. $P450_{cam}$ in complex with the 'abnormal' nitrogen donor ligand 2-phenylimidazole also had a more intense α-band than β-band.[363, 365] Poulos later solved the X-ray crystal structure of $P450_{cam}$ in complex with this 'abnormal' nitrogen donor ligand (Figure B30).[364] It was found that 2-phenylimidazole did not coordinate to the heme iron and failed to displace the heme-bound water ligand, explaining the 'abnormal' spectrum.[364] Unlike 4-pyridin-2-ylbenzoic acid, however, 2-phenylimidazole did not form a hydrogen bond to the heme-bound water and did not red-shift the Soret band.[363-364]

Another difference between the spectrum induced by 4-pyridin-3-ylbenzoic acid and that induced by 4-pyridin-2-ylbenzoic acid is that the intensity of the δ-band is increased when 4-pyridin-3-ylbenzoic acid binds to CYP199A4, but not when 4-pyridin-2-ylbenzoic acid binds. A red-shift in the position of the δ-band and an increase in intensity was also induced by 4-1*H*-imidazol-1-ylbenzoic acid. This is consistent with the observations of Dawson *et al.*, who reported that binding of nitrogen donor ligands to $P450_{cam}$ red-shifted the δ-band and increased its intensity.[363, 386]

Conner[154] reported that the 1,2,3-triazole-containing molecule 17-click induced a type II spectrum when it bound to CYP3A4 even though it did not form a direct Fe-N bond. Instead, it formed a hydrogen-bond to the heme-bound water ligand. Although this 'fake' type II spectrum strongly resembled genuine type II spectra, they did notice that 17-click induced a smaller Soret band red-shift than 1,2,3-triazole itself (2 nm *vs.* 6 nm), which did form a direct Fe-N bond. Additionally, the maximum peak-to-trough intensity difference (ΔA_{max}) induced by 17-click was smaller than that induced by 1,2,3-triazole. We noticed the same differences when we compared the spectra induced by 4-pyridin-2-ylbenzoic acid and 4-pyridin-3-ylbenzoic acid. 4-Pyridin-2-ylbenzoic acid induced a smaller Soret red-shift and a smaller ΔA_{max} than 4-pyridin-3-ylbenzoic acid.

The UV-Vis spectra of the reduced CYP199A4-ligand complexes were also informative. Reduction of the 4-pyridin-3-ylbenzoic acid complex shifted the Soret band to 447 nm, indicative of direct nitrogen coordination to the heme iron, whereas addition of dithionite to the 4-pyridin-2-ylbenzoic acid complex did not. Despite 4-1*H*-imidazol-1-ylbenzoic acid directly ligating to the ferric iron, the spectrum of the reduced 4-1*H*-imidazol-1-ylbenzoic acid-CYP199A4 complex instead resembled that of five-coordinate ferrous CYP199A4, with the Soret band blue-shifted to ~416 nm. We speculate that the Fe-N bond dissociates when the iron is reduced, with 4-1*H*-imidazol-1-ylbenzoic acid adopting an alternative orientation in the active site. Others have reported that imidazole binds less tightly to ferrous porphyrins than ferric porphyrins.[387-389] The crystal structure of dithionite-reduced CYP199A4 in complex with 4-1*H*-imidazol-1-ylbenzoic acid could be obtained to confirm this. Yoshida[365] previously reported that reduction of $P450_{SG1}$, an inactive variant of lanosterol 14-demethylase (from a mutant of *Saccharomyces cerevisiae*) that has a histidine residue as the sixth axial ligand to the heme[390], also failed to shift the Soret band to 440-450 nm. Instead, the Soret peak blue-shifted to 407 nm.[365] They also concluded that upon reduction the sixth ligand may be dissociating.[365] Haines *et al.* similarly observed no shift to 440-450 nm when they reduced $P450_{BM3}$ in complex with an imidazole inhibitor, concluding that the Fe-N bond must break when the iron is reduced, potentially due to changes in active-site conformation.[391] Dawson previously reported that *N*-phenylimidazole remained bound to the heme iron of $P450_{cam}$ when it was reduced, with the Soret band shifting to 445 nm.[366]

When dithionite was added to the 4-pyridin-2-ylbenzoate-CYP199A4 complex, the UV-Vis spectrum was not appreciably altered; the Soret band did not shift from its position at ~422 nm. This may indicate that the complex was not reduced under the experimental conditions. If the P450 was reduced to the ferrous state, it is unclear whether the water ligand hydrogen-bonded to 4-pyridin-2-ylbenzoic acid would be retained as the sixth axial ligand to the heme. Water is a poor ligand for ferrous heme and it is unusual for six-coordinate ferrous heme to possess water as an axial ligand.[368, 376-378, 392-394] According to Egawa *et al.*, an axial water ligand coordinated to ferrous heme has not been observed, with the exception that when aqua-metmyoglobin is reduced at cryogenic temperatures (77 K) the water ligand is retained.[377] Upon warming to >190 K, however,

the water dissociates from the ferrous heme.[377] Consequently, we do not expect that the spectrum recorded after addition of dithionite to the 4-pyridin-2-ylbenzoic acid-CYP199A4 complex is that of ferrous P450 with water as the sixth ligand. After this chapter had been written, reduction potentials of the CYP199A4 complexes were measured by Professor Paul V. Bernhardt at the University of Queensland (Table B10). It was found that 4-pyridin-2-ylbenzoate-bound CYP199A4 had a more negative reduction potential than the substrate-free enzyme ($E_{m,8}$ = -462 *vs.* -438 mV), which may rationalise why I was unable to reduce this complex, even with dithionite. He found that the spectrum of the reduced complex had peaks at 412 nm (Soret) and 544 nm (merged α/β bands), resembling that of ferrous substrate-free CYP199A4 (Figure B31). Therefore, the spectrum that I recorded after addition of dithionite to the 4-pyridin-2-ylbenzoate-CYP199A4 complex does not appear to be the reduced spectrum. The finding that CYP199A4 could not be successfully reduced with dithionite when 4-pyridin-2-ylbenzoic acid was bound is not unprecedented. Sevrioukova and Poulos[359] reported that binding of imidazole-substituted desoxyritonavir to CYP3A4 induced a large decrease in the reduction potential (it became more negative by >70 mV), and they found that they were unable to reduce this complex with dithionite.

Even though direct coordination of a nitrogen ligand to the iron has been reported by others to shift the reduction potential to more negative values[358-359, 361], Bernhardt found that the CYP199A4 complexes with 4-pyridin-3-ylbenzoic acid and 4-1*H*-imidazol-1-ylbenzoic acid had less negative redox potentials than the ligand-free enzyme (-321 and -278 mV) (Table B10, Figure B32). These redox potentials are in harmony with the NADH consumption rates by CYP199A4 in complex with these ligands. The rates of NADH consumption by CYP199A4 in complex with 4-pyridin-3-yl- and 4-1*H*-imidazol-1-yl-benzoic acid (30 and 41 min^{-1}) were faster than the rate with 4-pyridin-2-ylbenzoic acid, which was equivalent to the leak rate (10 min^{-1}).[277] Given that 4-pyridin-2-ylbenzoic acid binds more tightly to CYP199A4 and prevents heme reduction by the electron transfer partners (and even by the powerful reducing agent dithionite[395]), it is likely that 4-pyridin-2-ylbenzoic acid would be a more effective inhibitor of CYP199A4 than the directly coordinating ligands 4-pyridin-3-ylbenzoic acid and 4-1*H*-imidazol-1-ylbenzoic acid.

In summary, the binding modes of 4-pyridin-3-yl- and 4-pyridin-2-yl-benzoic acid in the crystal structures agree with the different type II spectra observed. When Conner and Atkins[154] reported that the type II spectrum induced by 17-click, which hydrogen-bonds to the water ligand instead of coordinating to the iron, closely resembled genuine type II spectra, they only reported the Soret band region of the spectrum. Our study indicates that close examination of the α/β-band region and δ-band may enable directly bound nitrogen ligands to be distinguished from those that bind via a bridging water ligand. We speculate that the difficulty that others have had in identifying the binding mode of an inhibitor based on optical spectra[155] could have arisen because they had a mixture of directly bound and water-bridged binding modes.

In conclusion, the UV-Vis spectra reported here could potentially be used by other researchers to diagnose whether a nitrogen ligand which elicits a type II spectrum is directly bound to the iron, is hydrogen-bonded to the heme-bound water or displays a mixture of these two binding modes.

Chapter 5

Characterisation of the T252E mutant of CYP199A4

5.1 Introduction

It has been predicted that mutation of the conserved active-site threonine (T252 in $P450_{cam}$ and CYP199A4) to glutamate should enable any P450 to use H_2O_2 to oxidise substrates.[227, 234] The reasoning is that heme enzymes which use H_2O_2 possess an acid-base residue (glutamate, histidine or aspartate) above the heme iron (Figure 1.26)[234]. This essential residue is believed to facilitate formation of the active species, Compound I, by transferring the proton on the proximal oxygen of the Fe(III)–H_2O_2 species to the distal oxygen, thus triggering O–O bond rupture to yield Cpd I (Figure 1.26f).[234]

The objective of this chapter is to assess whether the T → E mutation can convert CYP199A4 into an efficient peroxygenase. The T252E mutant of CYP199A4 will be prepared and its peroxygenase activity will be compared to that of the WT enzyme. It has been proposed that CYP199A4 could be exploited as a biocatalyst for the synthesis of valuable flavour compounds or medicinal chemicals[137, 275-276, 333], and it would be more economical to drive the reactions using H_2O_2 than costly NADH. Using H_2O_2 also eliminates the requirement for electron transfer proteins. The effect of the T → E mutation on the structure of CYP199A4 and its activity towards different substrates (4-methoxy-, 3-4-dimethoxy- and 4-ethyl-benzoic acid) will be investigated. X-ray crystal structures will be solved of the T252E mutant in complex with various substrates and type II ligands. The aim is to understand the properties of this mutant so that it can potentially be exploited as a biocatalyst and used to probe the mechanism of different P450 reactions.

5.2 Results

5.2.1 UV-Vis spectra of the T252E mutant of CYP199A4 and CO binding assay

The gene of the T252E mutant of CYP199A4 was co-expressed with that of ferrochelatase[279] in *E. coli* and the P450 was purified by the same method used for the WT enzyme. The UV-Vis spectrum of this variant was found to differ subtly from that of the WT enzyme (Figure 5.1). WT CYP199A4 displays a peak at 419.0 nm, whereas the T252E mutant has a maximum at 419.5 nm. Differences were also observed in the α/β band region (500-600 nm). WT CYP199A4 has α- and β-bands at ~570 and ~537 nm; the T252E mutant has α- and β-bands at ~571 and ~543 nm. The δ-band intensity at ~360 nm is also increased in the T252E mutant and this band is red-shifted.

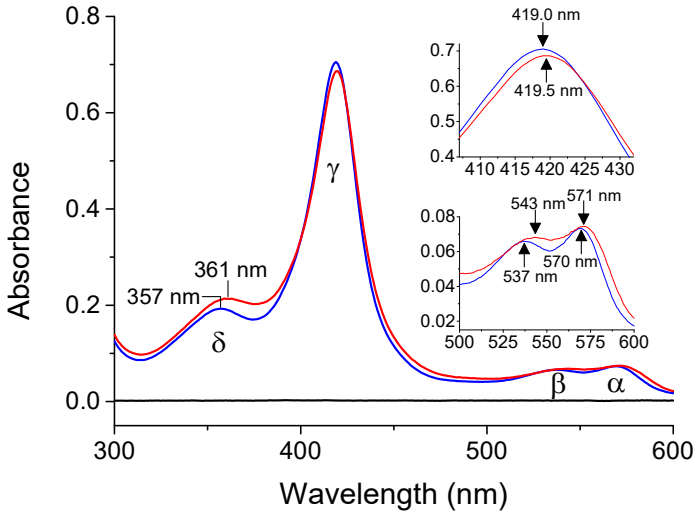

Figure 5.1. Overlaid UV-Vis spectra of substrate-free WT CYP199A4 (**blue**) and the T252E mutant (**red**). The concentrations used of the WT and T252E enzymes were similar (5.6 and 5.8 μM, respectively).

The carbon monoxide binding assay[283-284] was performed to assess whether the purified protein was correctly folded. Reduced P450s bind CO as the sixth axial ligand to the heme.[102] A complete shift of the Soret band to ~450 nm upon complexation of the reduced P450 with CO is evidence that the P450 is properly folded and functional.[285] On the other hand, if the P450 is in an inactive form, the Soret peak will shift to ~420 nm.[284] The conversion of active P450 into inactive 'P420' is thought to be due to protonation of the thiolate ligand yielding a neutral thiol ligand[287, 396-397] (or replacement of the thiolate ligand by a histidine ligand[398]). High pressure[399], heat[400], proteases[401], altering the pH[397], or treatment with organic solvents such as acetone[402] can all convert active P450 into the inactive 'P420' form.

Reduction of purified WT CYP199A4 with dithionite and binding of CO resulted in an almost complete shift of the Soret band to ~450 nm, verifying that the enzyme was active (Figure 5.2a). Conversely, treatment of the T252E mutant with $Na_2S_2O_4$ in the presence of CO yielded two peaks: one at ~420.5 nm and the other at 451.5 nm (Figure 5.2b). It does not appear that the large peak at ~420 nm was due to denatured enzyme, however, because further additions of dithionite led to a decrease in the intensity of the ~420 nm peak and an increase in the ~450 nm peak intensity. However, the Soret peak failed to shift completely to ~450 nm. We note that reduction of WT CYP199A4 by dithionite (in the absence of CO) resulted in a shift of the Soret band from ~418.5 nm to ~414.0 nm, but treatment of the T252E mutant with dithionite did not result in any shift in the position of the Soret band (Figure 5.2, red spectra).

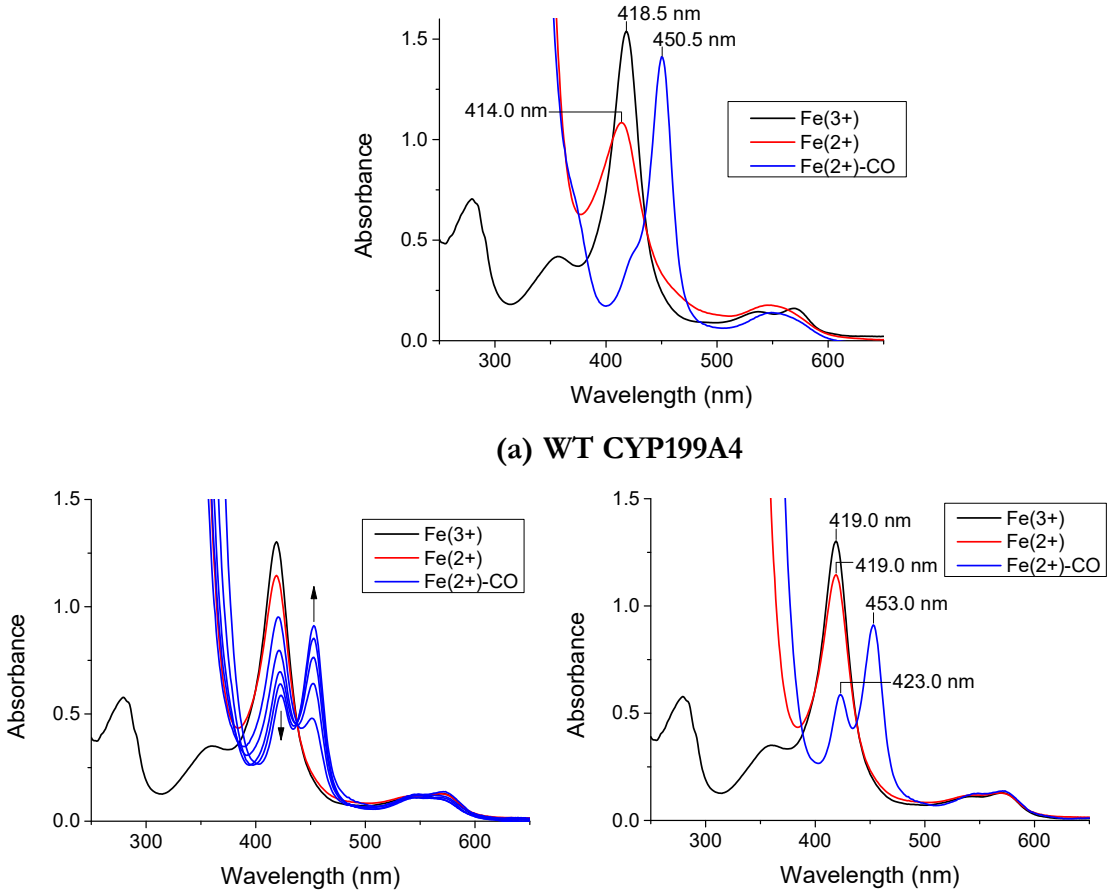

Figure 5.2. CO binding assay with **(a)** WT CYP199A4 and **(b)** the T252E variant. The spectrum of oxidised (Fe^{3+}) P450 is in **black**, reduced (Fe^{2+}) P450 is in **red**, and the Fe^{2+}–CO spectrum is in **blue**. The Soret peak of the WT enzyme **(a)** shifted almost completely to 450 nm. The T252E mutant **(b)** failed to shift completely to 450 nm, but further addition of dithionite increased the intensity of the 450 nm peak (**blue** spectra). The figure to the right shows the largest observed shift to 450 nm.

For some P450s, the P450–CO complex is unstable and produces a peak at 420 nm, but the P420 form can sometimes be converted back into the P450 form by binding native substrates to the P450.[283, 287] Munro *et al.* reported that when the Fe^{II}–CO complex of CYP142 was formed, there was a substantial peak at 420 nm, but the inactive P420 form could be almost entirely converted into the P450 form by addition of the substrate cholest-4-en-3-one.[396] Therefore, the CO binding assay was repeated in the presence of 0.2 mM substrate (4-methoxybenzoic acid) (Figure 5.3a,b). However, when 4-methoxybenzoic acid-bound $T252E_{CYP199A4}$ was reduced with dithionite in the presence of CO, we found that again the Soret peak only partially shifted to 450 nm (Figure 5.3b).

Another important observation is that addition of substrate to ferric $T252E_{CYP199A4}$ did not shift the Soret peak to ~390 nm characteristic of high-spin substrate-bound P450s (Figure 5.3b, green spectrum). The results above indicate that the sixth axial ligand to the heme in the T252E mutant is not displaced when substrate binds and that this variant is less readily reduced than the WT enzyme.

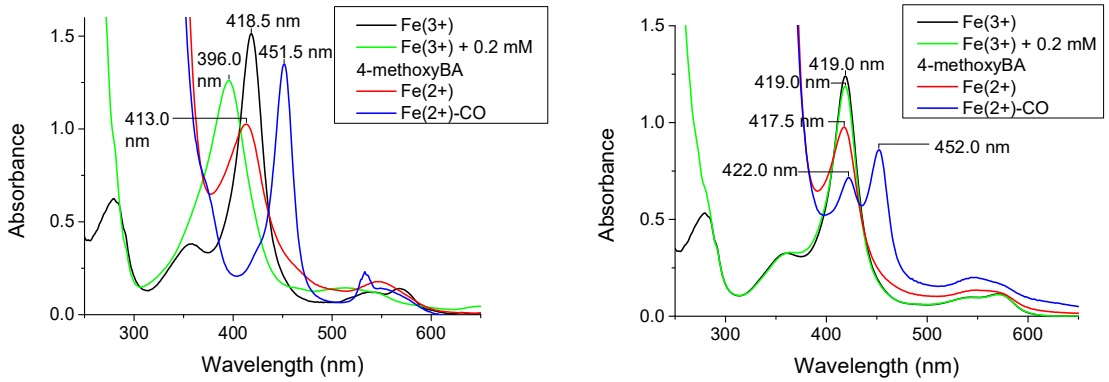

(a) WT CYP199A4 **(b) T252E**

Figure 5.3. Spectra of the CO complexes of WT CYP199A4 **(a)** and the T252E variant **(b)** in the presence of 0.2 mM 4-methoxybenzoic acid. The spectrum of the oxidised P450 is in **black**, the 4-methoxybenzoic acid-bound form is in **green**, the reduced spectrum is in **red**, and the Fe^{2+}–CO complex is in **blue**.

If reduction of the P450 in the presence of CO results in a complete shift of the Soret band to 450 nm, the P450 can be quantified from the Fe^{II}–CO versus Fe^{II} difference spectrum using an extinction coefficient of $\varepsilon_{450\text{-}490}$ = 91 mM^{-1} cm^{-1}.[286] Using this method (Figure C1), the extinction coefficient of the Soret band for WT CYP199A4 was determined to be 122 mM^{-1} cm^{-1}, which is comparable to the previously reported literature value (119 mM^{-1} cm^{-1}).[29] The extinction coefficient of the T252E mutant was instead determined by the pyridine hemochromogen method[288-289], which yielded a value of 119 ± 2 mM^{-1} cm^{-1} (Table C1, Figure C2). Using the same method, a value of 125 ± 3 mM^{-1} cm^{-1} was obtained for the extinction coefficient of WT CYP199A4 (Table C1). It appears that the extinction coefficient of the T252E mutant is comparable to that of the WT enzyme.

5.2.2 Binding of *para*-substituted benzoic acid substrates to $T252E_{CYP199A4}$

The spin-state shifts induced by binding various *para*-substituted benzoic acid substrates to $T252E_{CYP199A4}$ were measured (Table 5.1). The extent of the spin-state shift indicates whether the substrate binds sufficiently close to the heme to displace the 6th water ligand. 4-Methoxy-, 4-vinyl-, 4-methylthio-, 4-ethyl-, 4-ethynyl-, 4-isopropyl-benzoic acid and veratric acid are reported to all induce large (≥70%) type I shifts when they bind to WT CYP199A4[162, 219, 276-277]; 4-formyl- and 4-ethylthio-benzoic acid induce smaller type I shifts (25 and 10%) (Table 5.1, Figure 5.4).[117, 276] When a type I substrate binds and induces a large shift to HS, the Soret band shifts to ~396 nm and spectral changes occur in the α/β-band region (the α-band at 570 nm is lost) (Figure 5.4).[403-404]

Binding of 4-methoxybenzoic acid to the WT enzyme shifts the spin-state to ≥95% HS[219], yet addition of this substrate to the T252E mutant effected only a ~5% shift to HS (Table 5.1, Figure 5.5a). In case the mutation had substantially altered the active-site structure and the enzyme was now unable to bind benzoic acid derivatives, we tested substrates with alternative functional groups *para* to the methoxy group (4-methoxybenzamide, methyl *p*-anisate and 4-nitroanisole). All these substrates also failed to induce any appreciable spin-state shift (Figure 5.5b–d). 4-Ethylbenzoic

acid, which has a more hydrophobic substituent and may be more likely to displace the heme-bound aqua ligand, also induced only a minor type I shift (<5%) (Figure 5.5e). No changes occurred in the α/β band region. On the other hand, several substrates induced red-shifts of the Soret band (as observed with type II substrates). Type II spectra can result when a stronger field ligand than water coordinates to the heme iron.[405] The heteroatom-containing substrates 4-formyl-, 4-methylthio- and 4-ethylthio-benzoic acid red-shifted the Soret band by ~2.5, ~1.5 and ~2.0 nm, respectively (Figures C3 and C4). 4-Vinylbenzoic acid and veratric acid induced smaller (~0.5 nm) red-shifts (Figures 5.5f, C3 and C4).

Table 5.1. Spin-state shifts induced by binding of various substrates to the T252E mutant of CYP199A4. Shifts for the WT enzyme, previously reported by others, are included for comparison.[117, 162, 181, 276-277] Several substrates induced red-shifts of the Soret band maximum (λ_{max}) of T252E$_{CYP199A4}$; these red-shifts are shown in Figure C4.

Substrate	Spin-state shift (% HS)	
	T252E	WT
4-methoxyBA	5%	≥95% [162]
veratric acid	~0.5 nm red-shift	70% [162]
4-formylBA	~2.5 nm red-shift	25% [276]
4-vinylBA	~0.5 nm red-shift	80% [276]
4-methylthioBA	~1.5 nm red-shift	70% [117]
4-ethylBA	<5%	≥95% [117]
4-ethylthioBA	~2 nm red-shift	10% [117]
4-ethynylBA	-[a]	70% [276]
4-methoxybenzamide	5%	≥95% [181]
methyl *p*-anisate	<5%	<5% [181]
4-nitroanisole	-[a]	<5% [181]

[a] Spin-state shifts could not be determined due to interfering absorption by the substrate.

At the time, we speculated that the lack of a spin-state shift may be due to the side-chain carboxylate of Glu252 being bound to the heme iron. If the glutamate carboxylate was tightly bound to the iron, substrate may be unable to displace this ligand. Munro and co-workers reported that binding of fatty acid substrates to the A264H and A264K variants of P450$_{BM3}$ failed to induce any spin-state shift because the side-chains of Lys264 or His264 were tightly bound to the heme iron as the 6th ligand and substrate failed to displace these ligands.[405] Munro also prepared the A264E mutant in which the iron was ligated by glutamate.[406] However, the glutamate in our CYP199A4 mutant is not in an equivalent position to the glutamate, lysine or histidine in these P450$_{BM3}$ mutants and may not be close enough to coordinate to the iron. (The equivalent threonine in P450$_{BM3}$ is T268.)

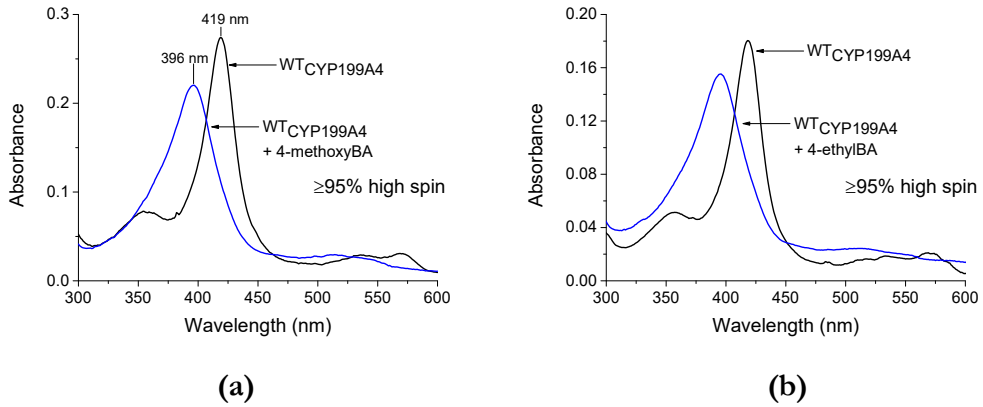

Figure 5.4. Spin-state shifts of WT CYP199A4 induced by **(a)** 4-methoxybenzoic acid and **(b)** 4-ethylbenzoic acid.

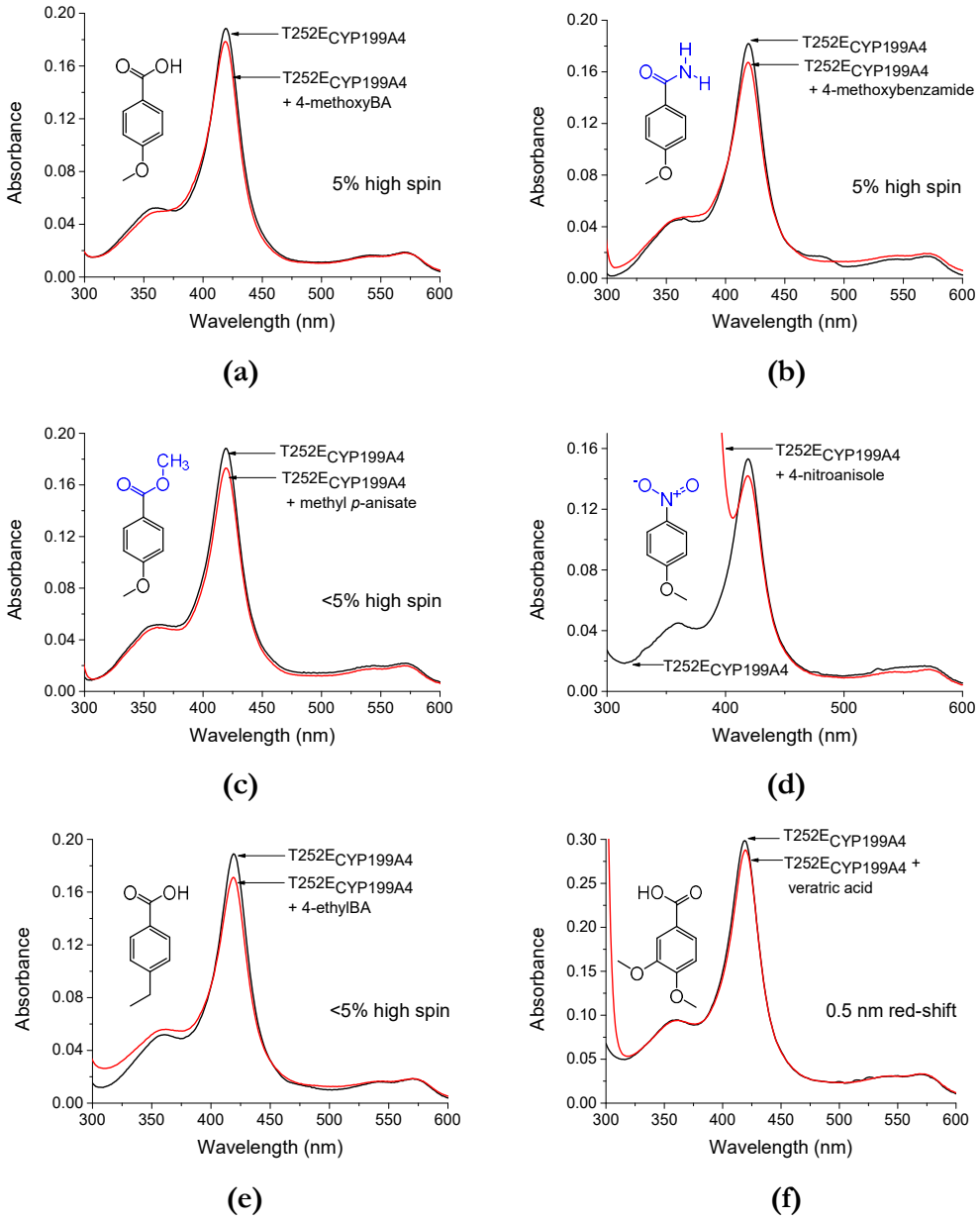

Figure 5.5. Spin-state shifts of the T252E mutant of CYP199A4 induced by **(a)** 4-methoxybenzoic acid, **(b)** 4-methoxybenzamide, **(c)** methyl *p*-anisate, **(d)** 4-nitroanisole, **(e)** 4-ethylbenzoic acid and **(f)** veratric acid.

Due to the minimal spin-state shift induced by substrate binding to the T252E mutant, only crude values for the substrate binding affinity (K_d) could be obtained by performing UV-Vis titrations (Figures 5.6 and C5). These values are presented in Table 5.2 and reveal that the T252E mutant retains the ability to bind *para*-substituted benzoic acid substrates tightly. While 4-methoxybenzoic acid induced a type I difference spectrum (Figure 5.6a), 4-formylbenzoic acid and 4-ethylthiobenzoic acid induced type II difference spectra (Figures 5.6b and C5c) in agreement with the red-shifted Soret band. As the lack of any significant spin-state shift prevented accurate measurement of binding affinity, a mass spectrometry method[291] was instead used to obtain accurate K_d values. These K_d values, obtained by Giang T. H. Nguyen at the University of New South Wales, are presented in Table 5.2 alongside literature K_d values for the WT enzyme. While the T252E variant displays lower affinity for 4-methoxybenzoic acid than the WT enzyme (1.11 μM *vs.* 0.22 μM), the mutant binds 4-methylthio-, 4-ethylthio- and 4-ethynyl-benzoic acid more tightly than WT CYP199A4. The T252E mutant also displays substantially higher affinity towards 4-formylbenzoic acid than the WT enzyme (1.03 μM *vs.* 48 μM). Evidently, the Thr → Glu mutation has not impaired the enzyme's ability to tightly bind *para*-substituted benzoic acids.

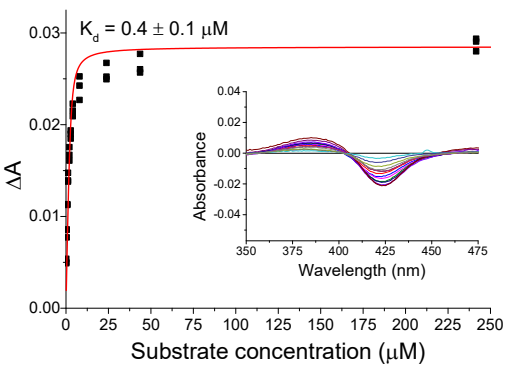

(a) 4-methoxybenzoic acid
(2.5 μM, peak: 385 nm, trough: 425 nm)

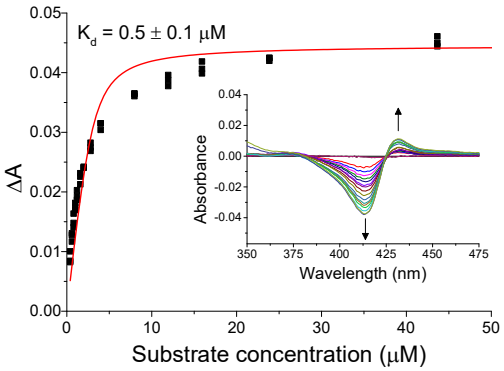

(b) 4-formylbenzoic acid
(3.0 μM, peak: 431 nm, trough: 413 nm)

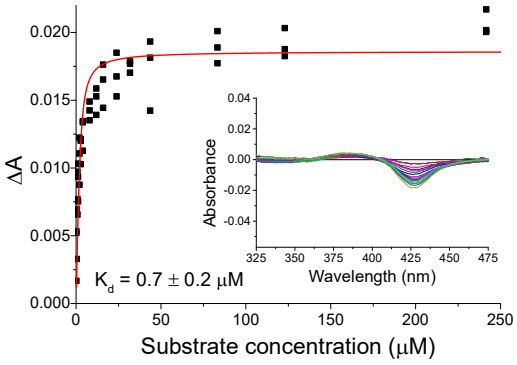

(c) 4-ethylbenzoic acid
(2.3 μM, peak: 387 nm, trough: 426 nm)

Figure 5.6. UV-Vis titrations to determine the dissociation constant of $T252E_{CYP199A4}$ with *para*-substituted benzoic acid substrates. The enzyme concentration used and the peak and trough wavelengths are provided under each graph. The data were fitted to the Morrison tight-binding equation, but the fits are poor so the K_d values are given to only one significant figure.

Table 5.2. Binding affinity of the T252E variant of CYP199A4 for *para*-substituted benzoic acid substrates. Crude K_d values were determined by performing UV-Vis titrations. More accurate values were obtained by Giang T. H. Nguyen and Dr Alex Donald (University of New South Wales) using a mass spectrometry method.[291] Literature K_d values for WT CYP199A4 are provided for comparison.

		T252E		WT
Substrate	**Method**	K_d (μM) UV-Vis titration[a]	K_d (μM) Mass spectrometry	K_d (μM) UV-Vis titration
4-methoxyBA		0.4 ± 0.1	1.11 ± 0.04	0.22 ± 0.02 [117]
4-formylBA		0.5 ± 0.1	1.03 ± 0.09	48 ± 2 [276]
4-vinylBA		0.02 ± 0.07	0.58 ± 0.02	0.46 ± 0.03 [276]
4-methylthioBA		0.1 ± 0.1	0.84 ± 0.08	2.3 ± 0.3 [117]
4-ethylBA		0.7 ± 0.2	2.3 ± 0.2	0.34 ± 0.02 [117]
4-ethylthioBA		0.02 ± 0.06	0.21 ± 0.01	0.99 ± 0.05 [117]
4-ethynylBA		-[b]	0.88 ± 0.1	1.2 ± 0.3 [276]

[a] UV-Vis titrations were performed in triplicate. [b] Not measured due to interfering absorption by the substrate.

5.2.3 Catalytic activity of T252E$_{CYP199A4}$ towards *para*-substituted benzoic acid substrates

In vitro NADH turnovers were subsequently performed to evaluate whether the T252E mutant retained any ability to utilise NADH/O_2 to oxidise substrates. Mutation of the catalytically important threonine residue may impair the enzyme's normal catalytic cycle and ability to generate the active oxidant.[130] The lack of any significant substrate-induced spin-state shift to HS implies that the mutant may have low activity.[100]

The rate of NADH consumption by the T252E mutant with *para*-substituted benzoic acid substrates was exceedingly slow, equivalent to the NADH leak rate (~9 min^{-1}) (Table 5.3, Figure 2.7b). For comparison, data for the WT enzyme is also given (the values are similar to those previously published by others).[117, 137, 276-277] HPLC analysis of the T252E$_{CYP199A4}$ reaction with 4-methoxybenzoic acid revealed the presence of minor levels of 4-hydroxybenzoic acid arising from *O*-demethylation of the substrate (Figures 5.7 and C6). The coupling efficiency and product formation rate were calculated to be 10% and 0.8 min^{-1}, respectively. This product formation rate is ~2000-fold slower than the rate of WT$_{CYP199A4}$-catalysed oxidation of 4-methoxybenzoic acid (1440 min^{-1}) and the coupling efficiency is reduced by a factor of >9. Thus, the Thr → Glu mutation has largely abolished the enzyme's ability to utilise NADH/O_2 to perform monooxygenation reactions. The reducing equivalents may have been lost via competing air oxidation of the ferredoxin, generating the superoxide radical which would dismutate to hydrogen peroxide.[303, 344] Minimal H_2O_2 was detected in reactions performed without catalase, but, as discussed in Chapter 3, if NADH consumption is slow the H_2O_2 will be lost before the reaction is complete (Figure A5).

Table 5.3. NADH activity assay data for the T252E mutant and WT CYP199A4 with various *para*-substituted benzoic acid substrates. Values given are the mean ± SD, with $n \geq 3$. The reported NADH consumption rate (N) for the T252E mutant is the initial rate over the first 10 minutes. NADH consumption and product formation rates (PFR) are given in units of μM (μM-P450)$^{-1}$ min^{-1}. The NADH leak rate was ~9 min^{-1}. The concentration of NADH used in the T252E assays was ~160 μM while ~320 μM NADH was used in the WT assays.

Substrate	N (min^{-1})	PFR (min^{-1})	C (%)	H_2O_2 (%)
4-methoxyBA$_{T252E}$	9 ± 0.5	0.8 ± 0.1	10 ± 1	2 ± 1
4-methoxyBA$_{WT}$	1580 ± 20	1440 ± 30	91 ± 1	-[a]
veratric acid$_{T252E}$	11 ± 0.5	1.6 ± 0.03	14 ± 1	2 ± 1
veratric acid$_{WT}$	1078 ± 7	1010 ± 20	93 ± 1	-[a]
4-ethylBA$_{T252E}$	8 ± 0.2	0.5 ± 0.03	6 ± 0.3	1 ± 0.6
4-ethylBA$_{WT}$	911 ± 9	810 ± 50	89 ± 4	-[a]

[a] It has previously been reported that WT CYP199A4 channels only ~2% of the reducing equivalents into H_2O_2 production with the substrates 4-methoxyBA and 4-ethylBA.[117]

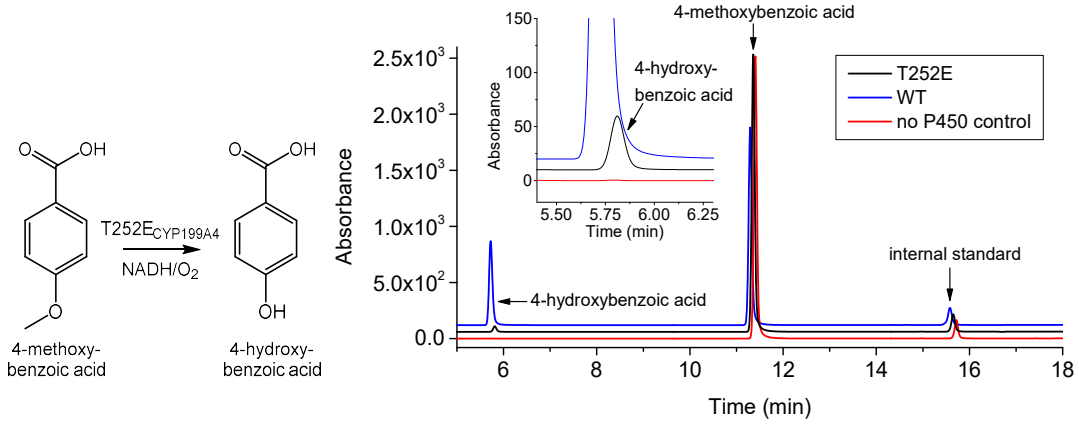

Figure 5.7. HPLC analysis of the NADH/O_2-driven oxidation of 4-methoxybenzoic acid by T252E$_{CYP199A4}$ (**black**) and WT CYP199A4 (**blue**). In **red** is a control reaction omitting the P450. 4-Hydroxybenzoic acid elutes at 5.8 min and the substrate appears at 11.4 min. Gradient: 20-95% AcCN in H_2O with 0.1% TFA. Detection wavelength: 254 nm.

In vitro assays were also performed using veratric acid (3,4-dimethoxybenzoic acid) as the substrate. This experiment explored whether the regioselectivity of the mutant remained the same as that of the WT enzyme, which exclusively demethylates the *para* substituent. It was plausible that the Thr → Glu mutation had altered the substrate orientation in the active site. HPLC analysis of the reaction mixture showed that vanillic acid (4-hydroxy-3-methoxybenzoic acid) was the sole product and that no isovanillic acid (4-methoxy-3-hydroxybenzoic acid) had been generated (Figures 5.8 and C7). Thus, both the WT and T252E isoforms display the same regioselectivity. Again, the coupling efficiency was low (14%) and product was formed at a sluggish rate (1.6 min^{-1}).

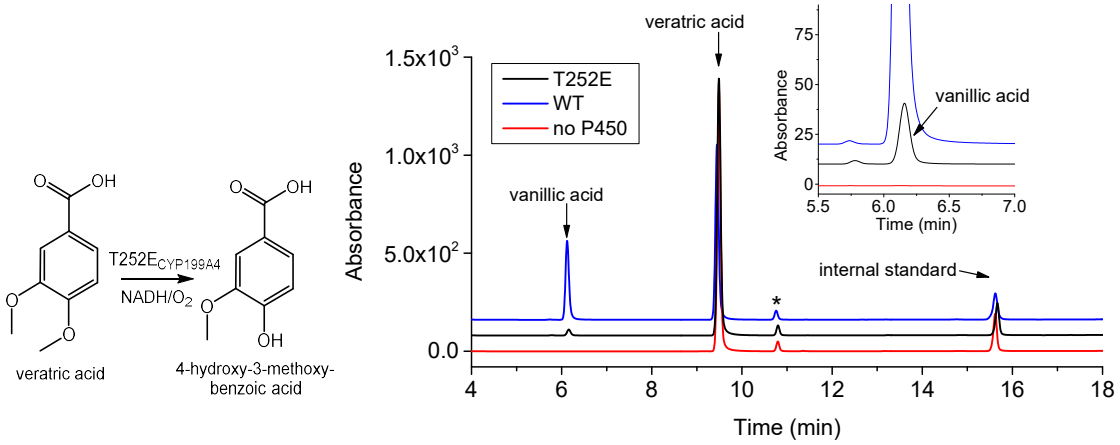

Figure 5.8. HPLC analysis of the NADH/O_2-driven oxidation of veratric acid by T252E$_{CYP199A4}$ (**black**) and WT CYP199A4 (**blue**). In **red** is a control reaction omitting the P450. Vanillic acid elutes at 6.1 min. Isovanillic acid (RT = 6.4 min) and 3,4-dihydroxybenzoic acid (RT = 4.5 min) are not observed. The substrate appears at 9.4 min. Gradient: 20-95% AcCN in H_2O with 0.1% TFA. Detection wavelength: 254 nm. * Impurity in substrate.

T252E$_{CYP199A4}$ consumed NADH with 4-ethylbenzoic acid at a rate equivalent to the leak rate (8 min^{-1}) and the coupling efficiency was only 6% (compared to 89% for the WT enzyme). The major metabolites were 4-vinylbenzoic acid (~60%) and 4-(1-hydroxyethyl)benzoic acid (~30%), arising from hydroxylation at the more reactive benzylic carbon (Figures 5.9 and C8). Lower levels of 4-(2-hydroxyethyl)benzoic acid (~6%), 4-acetylbenzoic acid (~0.3%) and 4-oxiran-2-ylbenzoic acid (3%) were detected. These products are the same as those generated by the WT enzyme, but the T252E variant generated a higher proportion of 4-vinylbenzoic acid and a lower proportion of epoxide than the WT enzyme (Table 5.4). Note that for both WT CYP199A4 and the T252E mutant, 4-vinylbenzoic acid and the epoxide represent ~60% of the product.

Table 5.4. Product distribution for NADH/O_2-driven oxidation of 4-ethylbenzoic acid by WT CYP199A4 and the T252E variant

Isoform	**Product distribution (%)**				
	4-vinylBA	**4-(1-hydroxyethyl)BA**	**4-(2-hydroxyethyl)BA**	**4-acetylBA**	**4-oxiran-2-ylBA**
WT	40 ± 0.3	40 ± 0.1	~4	<0.5	16 ± 0.4
T252E	60 ± 0.6	30 ± 0.6	6 ± 0.2	<0.5	3.5 ± 0.5

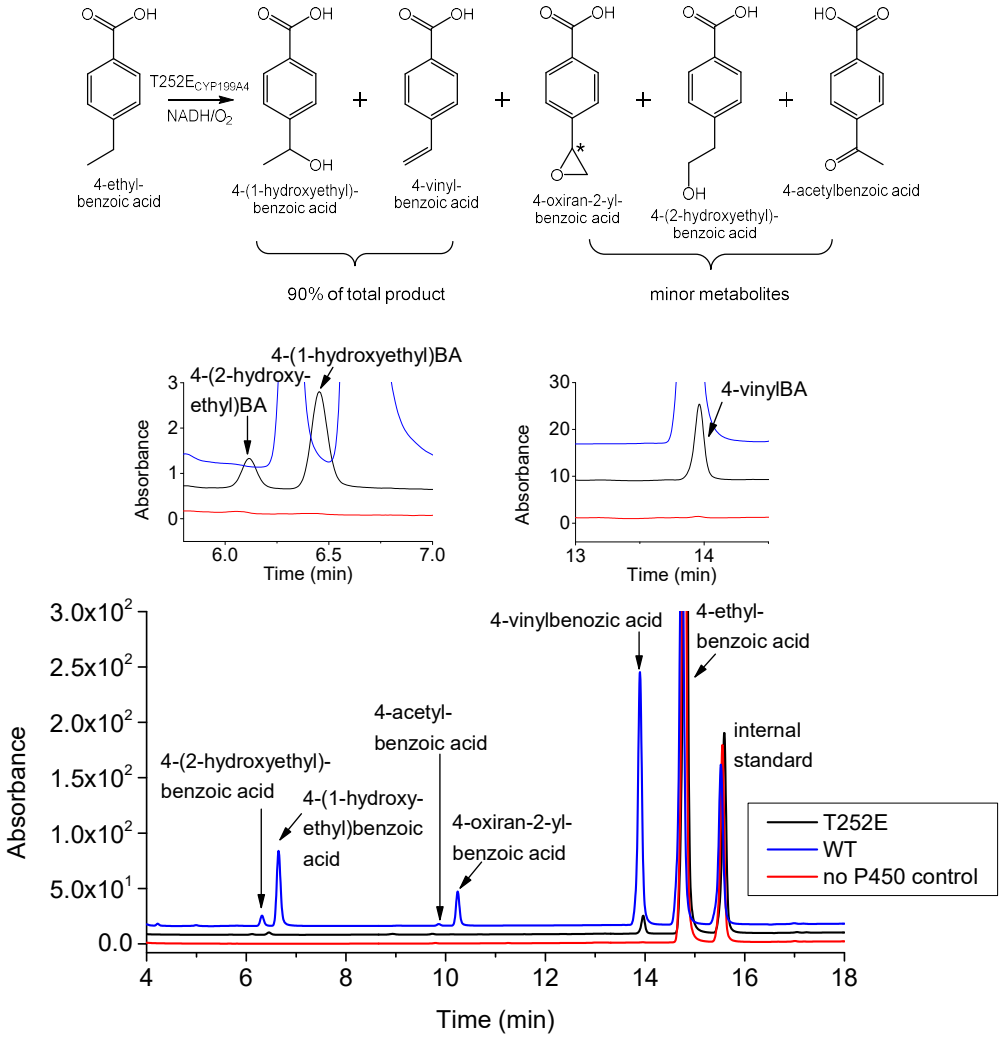

Figure 5.9. HPLC analysis of the NADH/O_2-driven oxidation of 4-ethylbenzoic acid by T252E$_{CYP199A4}$ (**black**) and WT CYP199A4 (**blue**). In **red** is a control reaction omitting the P450. Retention times are: 4-vinylbenzoic acid, 14.1 min; 4-(2-hydroxyethyl)benzoic acid, 6.2 min; 4-(1-hydroxyethyl)benzoic acid, 6.6 min; 4-acetylbenzoic acid, 9.9 min; epoxide, 10.4 min. The substrate appears at 14.9 min. Gradient: 20-95% AcCN in H_2O with 0.1% TFA. Detection wavelength: 254 nm.

The insets show enlarged views of the peaks corresponding to the major products in the T252E reaction mixture (**black** chromatogram).

5.2.4 H_2O_2-driven oxidation of 4-methoxybenzoic acid and veratric acid

After establishing that the T252E mutant of CYP199A4 is unable to efficiently use NADH/O_2 to perform monooxygenation, we investigated whether the mutation conferred peroxygenase activity to CYP199A4. *In vitro* H_2O_2-driven reactions were performed at 30 °C and contained 3 μM P450, 1 mM 4-methoxybenzoic acid as the substrate, and 50 mM H_2O_2 in Tris-HCl buffer (pH 7.4). Reactions were terminated after 4 hours because it was found that negligible product was generated after this time (Figure C9). HPLC analysis of the reaction mixtures revealed that both the T252E variant and WT enzyme were able to utilise H_2O_2 to demethylate 4-methoxybenzoic acid (Figure 5.10). The amount of product generated by the T252E mutant (379 ± 7 μM) was more than 2-fold greater than that generated by WT CYP199A4 (156 ± 2 μM) over the four-hour period. No product was detected in control reactions omitting the P450. The T252E variant was also able to generate substantially more vanillic acid from veratric acid (158 ± 2 μM) than WT CYP199A4 (~27 μM) during a four-hour reaction (Figure 5.11).

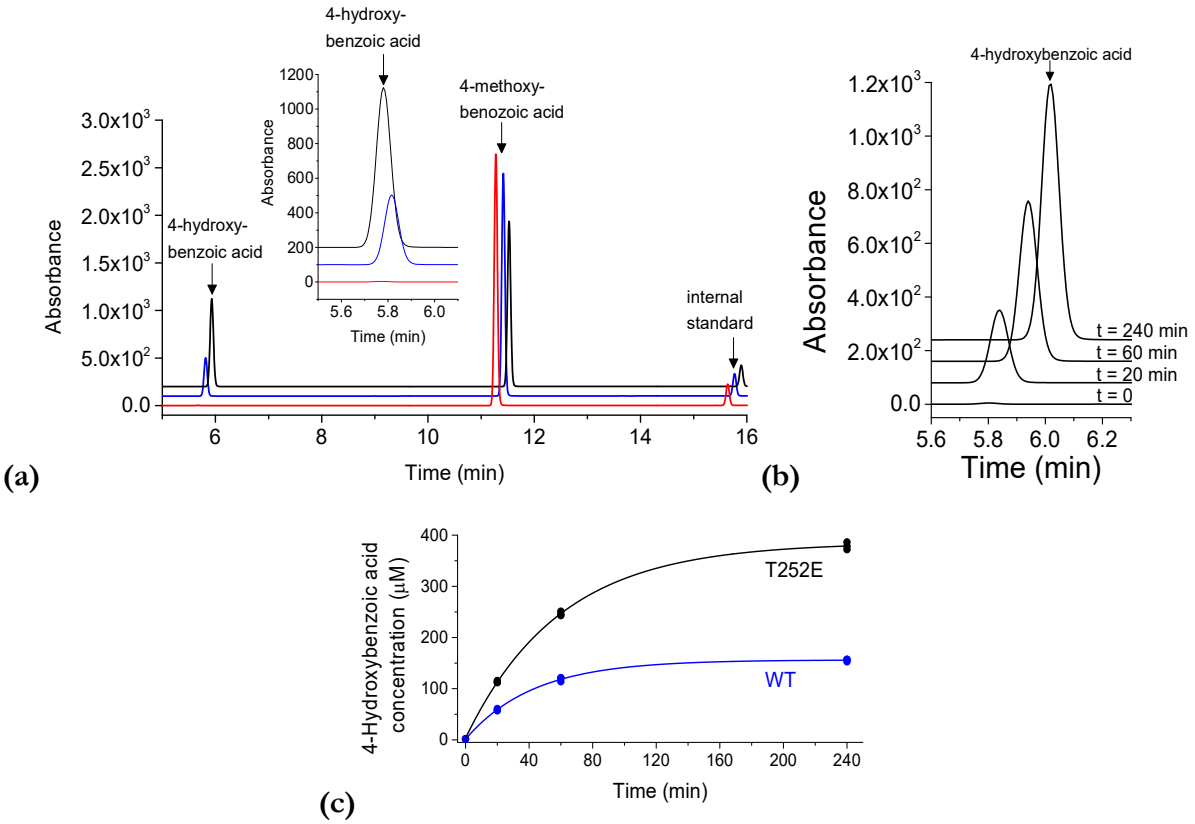

Figure 5.10. HPLC analysis of the amount of 4-hydroxybenzoic acid produced from 4-methoxybenzoic acid by WT CYP199A4 (**blue**) and the T252E mutant (**black**) during a 4-hour reaction driven by H_2O_2. The conditions were: 3 μM P450, 1 mM substrate and 50 mM H_2O_2 in 50 mM Tris-HCl buffer at 30 °C. In **red** is a control reaction omitting the P450. Gradient: 20-95% AcCN in H_2O with 0.1% TFA. Detection wavelength: 254 nm. **(b)** Amount of product generated by the T252E mutant at various time points. **(c)** Time course of product formation. Reactions were performed in triplicate and product concentration was measured at time points of 0, 20, 60 and 240 min. A trendline was added.

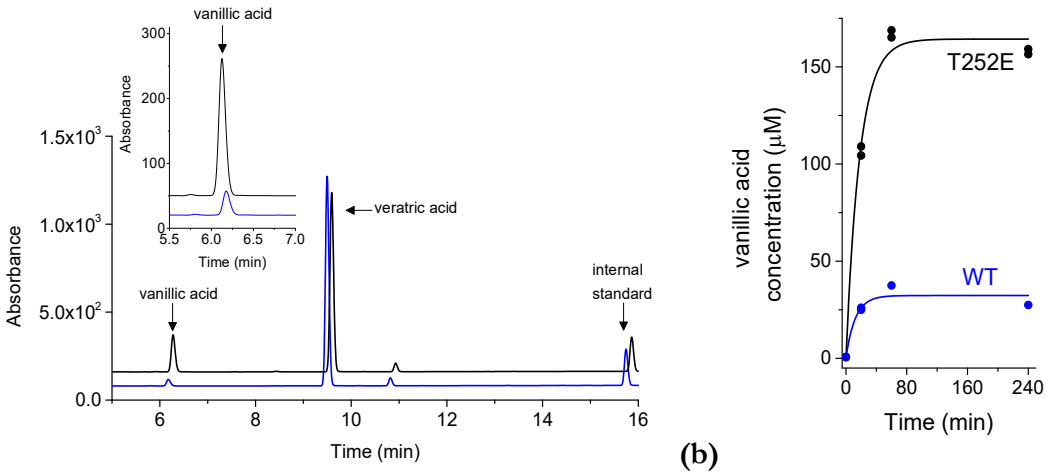

Figure 5.11. (a) HPLC analysis of the amount of vanillic acid generated from veratric acid by WT CYP199A4 (**blue**) and the T252E mutant (**black**) during a 4-hour reaction driven by H_2O_2. The conditions were: 3 μM P450, 1 mM substrate and 50 mM H_2O_2 in 50 mM Tris-HCl buffer at 30 °C. Gradient: 20-95% AcCN in H_2O with 0.1% TFA. Detection wavelength: 254 nm. **(b)** Time course of product formation.

Iron(II) and H_2O_2 (known as Fenton's reagent) react to generate the hydroxyl radical (HO•), a potent oxidant which oxidises organic compounds (Equation 5.1).[407-412] Benzene, for example, can be oxidised to phenol and biphenyl by Fenton's reagent (Figure 5.12).[407, 413-415]

$$Fe(II) + H_2O_2 \longrightarrow Fe(III) + OH^- + HO^{\cdot} \qquad (5.1)$$

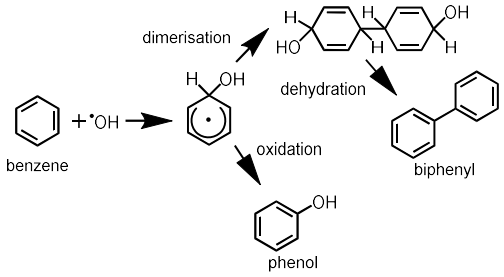

Figure 5.12. Benzene can be converted into phenol and biphenyl by Fenton's reagent (H_2O_2 and Fe(II)).[407, 414-415]

To confirm that the substrate had been oxidised by the P450 enzyme, not by a Fenton-type reaction arising from free iron or free heme from degraded protein, control reactions were performed with an equivalent amount of denatured $T252E_{CYP199A4}$ instead of functional enzyme (Figures C10 and C11). To denature the enzyme, it was heated at 80 °C for 45 minutes. A second control reaction was performed with CYP101B1, a P450 which does not bind *para*-substituted benzoic acids (Figures C10–C12). No product was detected in either of these reactions, demonstrating that a Fenton-type reaction was not responsible for product formation.

We additionally investigated whether the $T252E_{CYP199A4}$ enzyme exhibited any activity towards 4-nitroanisole, which is a substrate of WT CYP199A4, albeit a poor one which binds weakly and is oxidised at a rate of only 14 min^{-1}.[181, 333] The vivid yellow demethylation product, 4-nitrophenolate, absorbs strongly at 410 nm (ε_{410} = 18.3 mM^{-1} cm^{-1}), which enables product formation to be conveniently monitored by UV-Vis spectrophotometry (Figure C13a).[181, 333] However, when reactions containing 3 μM $T252E_{CYP199A4}$, 1 mM 4-nitroanisole and 60 mM H_2O_2

were performed, we could detect no yellow colour. Instead, we observed a rapid decrease in absorbance at 410 nm due to bleaching of the P450 heme by H_2O_2 (Figure C13b). This prompted us to investigate how rapidly various concentrations of H_2O_2 destroy the $T252E_{CYP199A4}$ enzyme.

In the presence of ≥10 mM H_2O_2, the $T252E_{CYP199A4}$ enzyme appeared to be almost completely bleached within ~10 min (Figure 5.13). Higher H_2O_2 concentrations (e.g. 60 mM H_2O_2) resulted in faster bleaching and the bleached enzyme was completely inactive (Figures C14 and C15). The presence of 4-methoxybenzoic acid or other benzoic acid substrates, however, was found to protect the T252E mutant from rapid bleaching (Figures 5.14 and C16). The rate of heme bleaching was substantially reduced when 4-methoxybenzoic acid was bound. This is in contrast to the results of Cirino[230, 416] and Li[229], who found that the presence of substrate resulted in more rapid bleaching/inactivation of $P450_{BM3}$ by H_2O_2. Substrate-free $WT_{CYP199A4}$ was bleached more slowly than substrate-free $T252E_{CYP199A4}$ when exposed to 60 mM H_2O_2 (Figure 5.15).

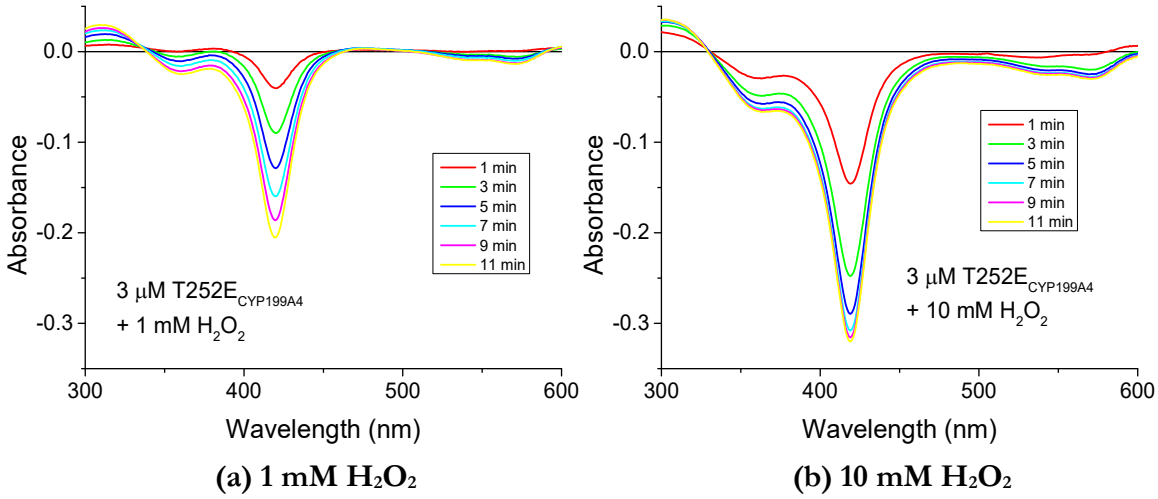

Figure 5.13. Rate of heme bleaching of **substrate-free $T252E_{CYP199A4}$** (3 µM) when exposed to **(a) 1 mM H_2O_2** and **(b) 10 mM H_2O_2**. Difference spectra were recorded at 2-minute intervals to monitor the loss of the Soret absorbance band.

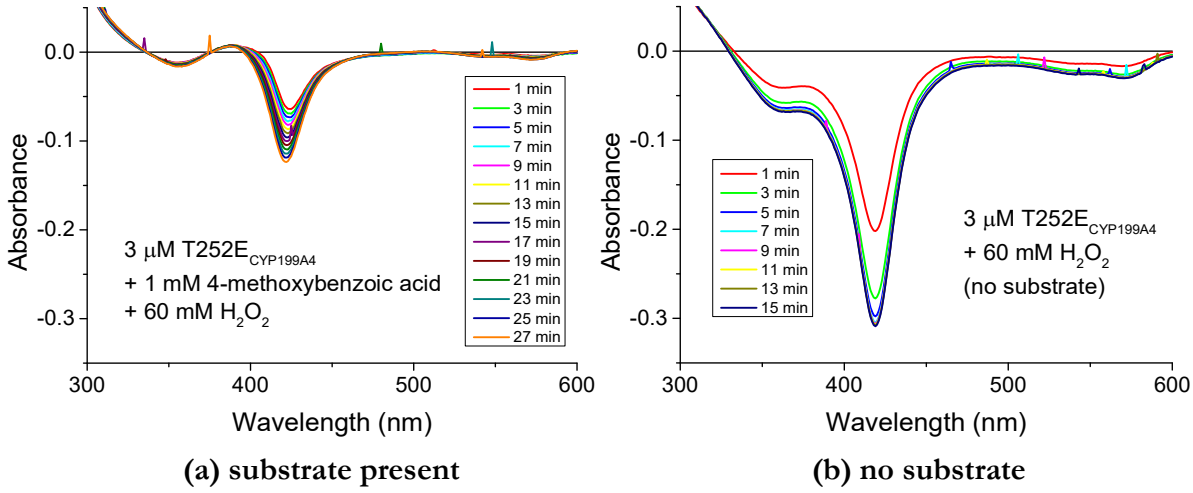

Figure 5.14. Rate of heme bleaching of the $T252E_{CYP199A4}$ enzyme (3 µM) exposed to **60 mM H_2O_2** in **(a)** the presence of **1 mM 4-methoxybenzoic acid** and **(b)** in **the absence of substrate**. Spectra were recorded at 2 min intervals to monitor bleaching.

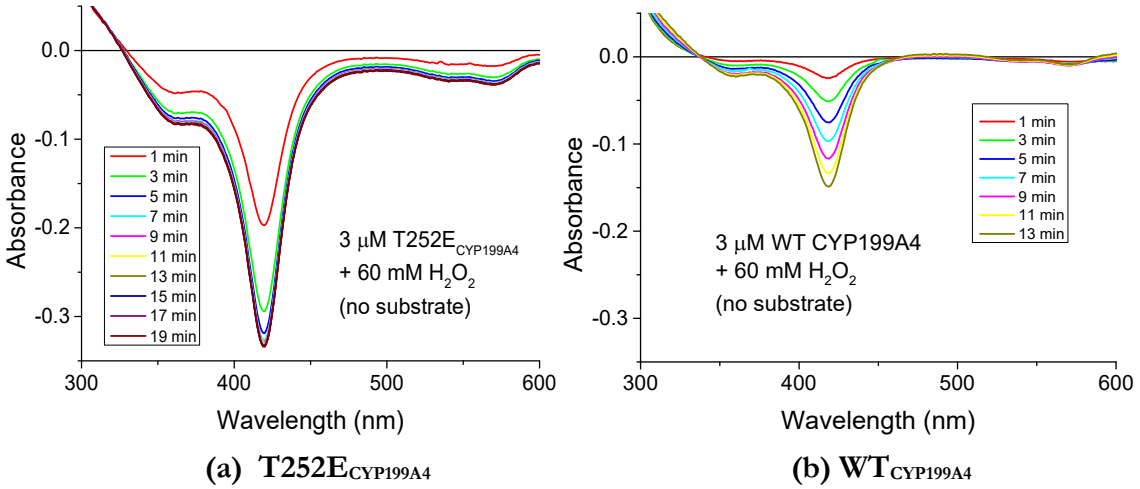

Figure 5.15. Comparison of the rate of heme bleaching of **(a) substrate-free T252E$_{CYP199A4}$** enzyme (3 μM) exposed to 60 mM H_2O_2, and **(b) substrate-free WT CYP199A4** exposed to 60 mM H_2O_2.

5.2.5 Crystal structure of T252E$_{CYP199A4}$ in complex with 4-methoxybenzoic acid

To rationalise the properties of the T252E mutant, we solved crystal structures of the substrate-bound enzyme, though we were unable to obtain a structure of the substrate-free form (Figure C17). We obtained crystals of the 4-methoxybenzoate-T252E$_{CYP199A4}$ complex using the hanging-drop vapour-diffusion method. Crystallisation screening trials using the Hampton Research Crystal Screen HT kit were initially performed to identify favourable crystallisation conditions (Figure 2.12), but we found that higher-quality crystals could be obtained using conditions previously optimised for the WT enzyme (0.2 M magnesium acetate, 100 mM Bis-Tris (pH 5.0-5.75) and 20-32 % PEG-3350)[117] (Figure 2.13). X-ray diffraction data for 4-methoxbenzoate-T252E$_{CYP199A4}$ crystals were obtained at the Australian Synchrotron[316], beamline MX1, and the crystal structure was solved at 1.55-Å resolution. Data collection and refinement statistics are presented in Table C2.

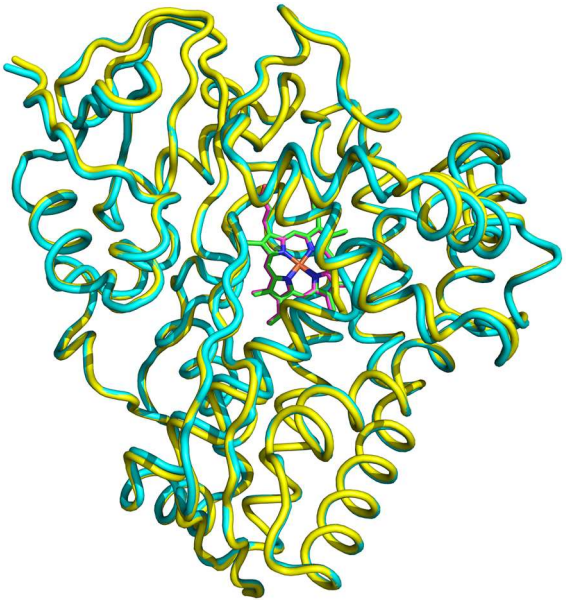

Figure 5.16. Overlaid structures of the T252E mutant (yellow cartoon, magenta heme) and WT CYP199A4 (blue cartoon, green heme) with 4-methoxybenzoate bound. The RMSD between the Cα atoms is 0.579 Å (over 393 pairs).

The overall structure of the T252E variant was found to be highly similar to that of the WT enzyme. Figure 5.16 shows superimposed Cα traces of the T252E variant and WT enzyme in complex with 4-methoxybenzoate, illustrating that the single-point mutation in the active site has not significantly altered the overall fold of the enzyme. The RMSD between the Cα atoms of the superimposed structures is 0.579 Å over all 393 pairs. WT CYP199A4 is known to bind a chloride ion in its anion binding site[29], and a sphere of electron density located in a similar position in the T252E mutant was also modelled as a chloride ion (Figure C18). In the *mFo-DFc* difference electron density map, positive density unambiguously revealed the location of the substrate in the substrate binding pocket, the position of the Glu252 side-chain and the presence of a 0.92-occupancy aqua/hydroxo ligand (W17) to the heme (Fe–O distance 2.1 Å) (Figure 5.17). Retention of the sixth axial ligand indicates that it must be more tightly bound in the T252E mutant than in the WT enzyme and is consistent with the observation that substrate binding induced only minimal perturbation of the spin-state equilibrium. It is also consistent with the difficulty in reducing the T252E mutant and low catalytic activity.[100] Hydrogens are invisible in the electron density map and therefore we cannot identify whether the axial ligand to the heme is water or hydroxide.[330] Rather than directly ligate the heme, the Glu252 side-chain carboxylate interacts with the H_2O/OH^- ligand via a hydrogen bond, with a donor-acceptor distance of 2.6 Å. This interaction must stabilise the water ligand, preventing displacement when substrate binds. In the WT enzyme, the aqua ligand is only loosely bound and is readily displaced by *para*-substituted benzoic acids[117], vacating the sixth axial site and allowing dioxygen to bind.

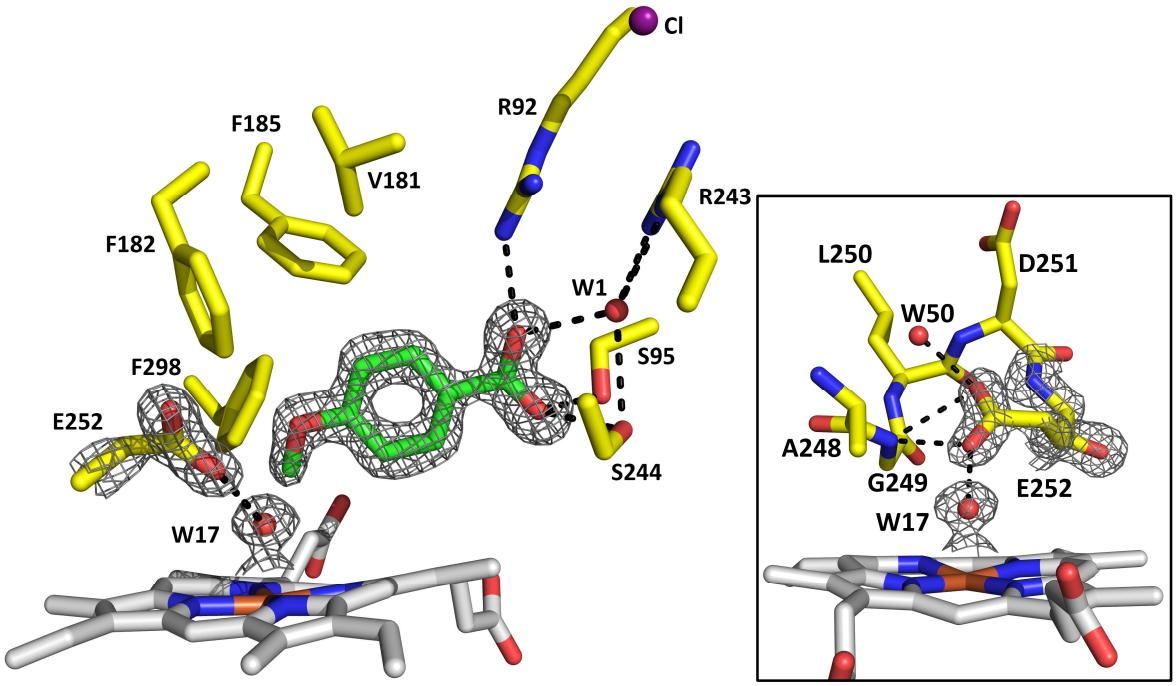

Figure 5.17. Crystal structure of the T252E mutant of CYP199A4 in complex with 4-methoxybenzoate. A composite omit map of the substrate, water ligand (W17) and E252 side-chain is shown as grey mesh contoured at 2.0 σ (1.5 Å carve). The image on the right depicts the oxygen-binding groove. The carboxylate of E252 is hydrogen-bonded to the water/hydroxide ligand (W17), the amide N of G249 and to a second water (W50). The proximal cysteine ligand, iron and the water/hydroxide ligand are linearly arranged (S-Fe-O angle = 172.7°).

The position of the benzoic acid moiety of 4-methoxybenzoic acid is almost identical in both the T252E mutant and WT enzyme. However, the orientation of the methoxy group differs (Figure 5.18 and Table 5.5). In the WT enzyme, the *para*-methoxy substituent lies almost in the same plane as the benzene ring. In the T252E mutant, on the other hand, the methoxy moiety is rotated out of the plane of the benzene ring by 18° to avoid a steric clash with the H_2O/OH^- ligand (Figure 5.18, black arrow, and Figure C19). This rotation results in the methyl carbon being held 0.3 Å further from the heme iron than in the WT enzyme. The distance between the H_2O/OH^- ligand and the methyl carbon is 3.2 Å.

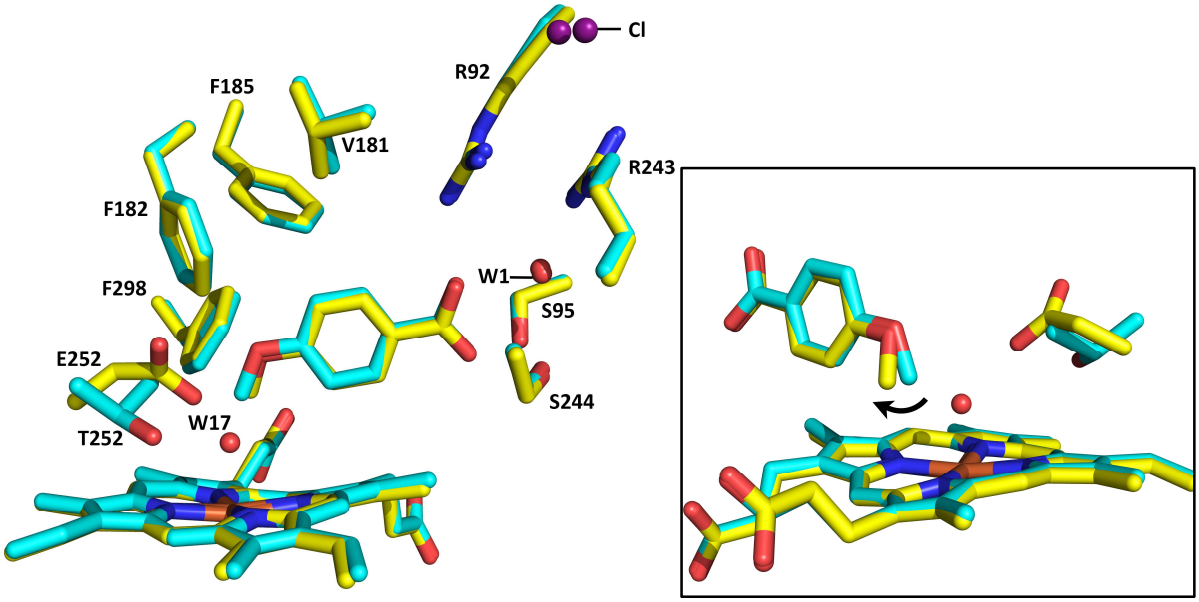

Figure 5.18. Overlaid structures of WT (cyan) and T252E CYP199A4 (yellow) with 4-methoxybenzoate bound. The waters and chloride in the T252E structure are labelled.

Mutation of Thr252 to Glu resulted in alterations in the structure of the oxygen-binding groove in the I-helix (Figures 5.19 and 5.20). In WT CYP199A4, the backbone carbonyl of Ala248 is hydrogen-bonded to the hydroxyl of Thr252 (Figure 5.20a). In the T252E variant, however, the amide bond linking Ala248 and Gly249 is flipped by ~180° (Figure 5.19b, black arrow). This results in the carbonyl of Ala248 instead pointing away from residue 252 and the amide NH of Gly249 pointing towards Glu252. This peptide flip allows the amide NH of Gly249 to hydrogen-bond to the two carboxylate oxygens of Glu252 (2.7 Å and 3.1 Å) (Figure 5.17). The Glu252 side-chain carboxylate is also hydrogen-bonded to the amide NH of Glu252 (2.5 Å) and to an ordered water molecule (W50) (2.4 Å). In the structure of the WT enzyme there is no water at this position, but there is an ordered water located nearby (W1063) (Figure 5.19a). The closest carboxylate oxygen of Glu252 is located 4.2 Å from the heme iron. The orientation of the catalytic residue D251 is also altered in the T252E mutant (Figure 5.19a).

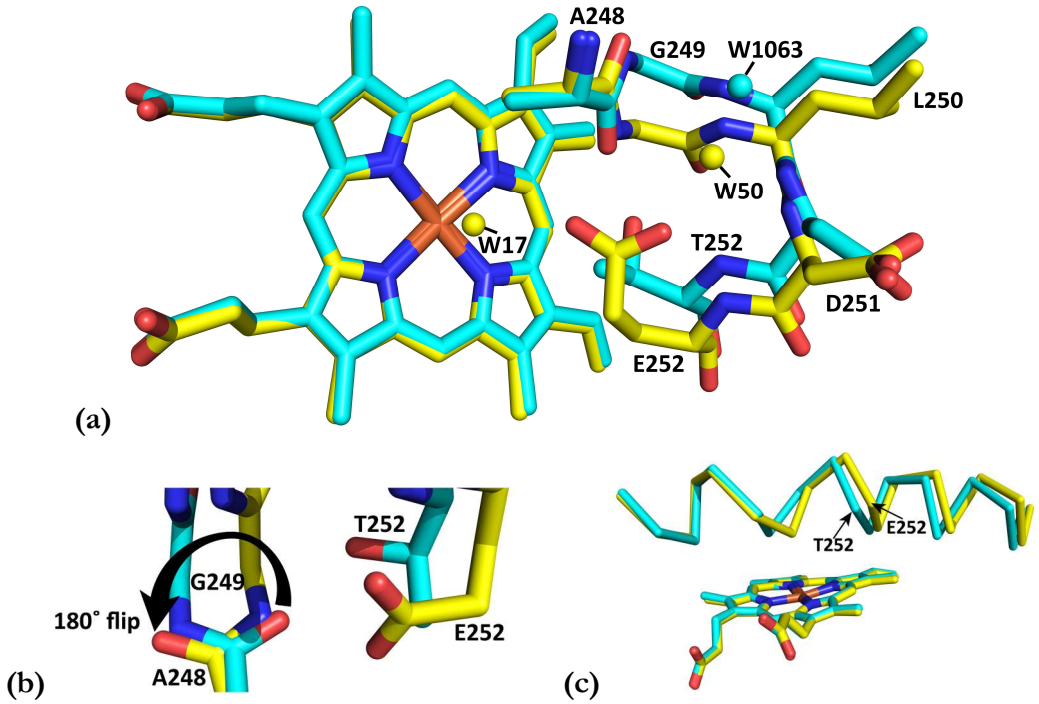

Figure 5.19. **(a)** Overlaid oxygen-binding grooves of WT CYP199A4 (cyan) and the T252E variant (yellow). Waters are represented by yellow and cyan spheres. **(b)** In the T252E variant the amide bond linking Ala248 and Gly249 is flipped by ~180˚ (black arrow). **(c)** Comparison of the I-helix structure of WT CYP199A4 (cyan Cα trace) and the T252E variant (yellow Cα trace).

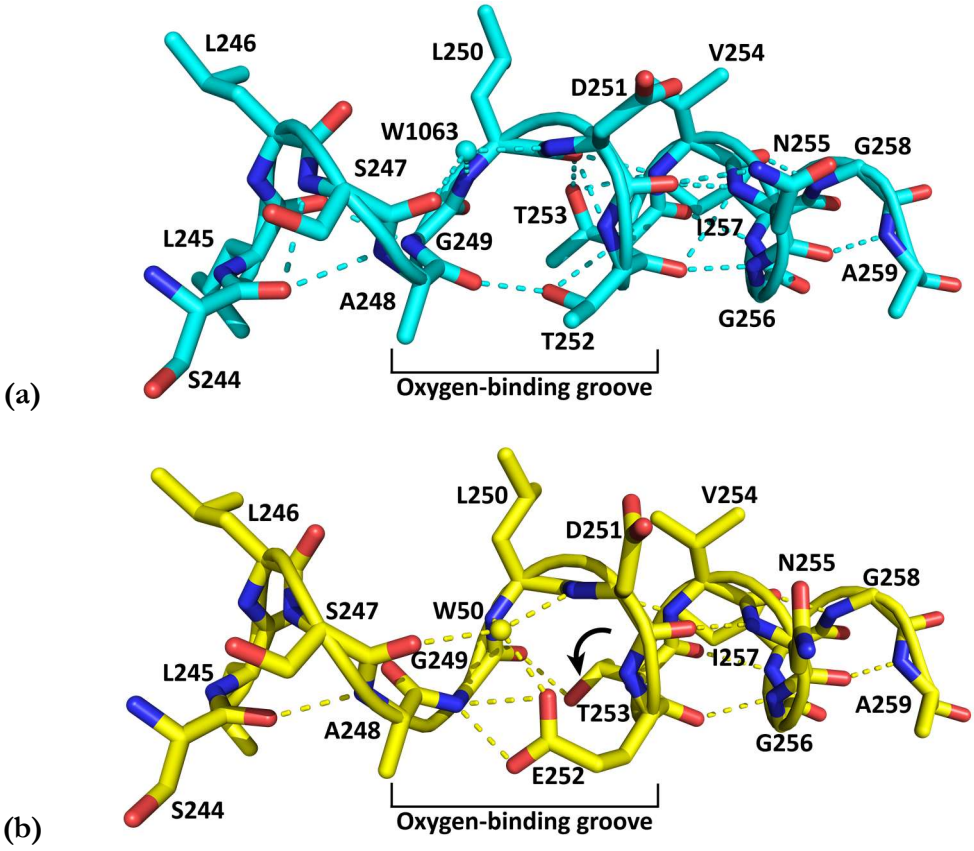

Figure 5.20. Hydrogen bonding interactions in the I-helix of **(a)** WT CYP199A4 (cyan) and **(b)** the T252E variant (yellow). The T252 → E mutation alters the structure of the I-helix and the hydrogen bonding network. In this mutant the side chain of T253 is rotated (movement described by the black arrow) to allow the hydroxyl to form a hydrogen bond to the carbonyl of G249.

The T252 → E mutation modified the hydrogen bonding network in the I-helix (Figure 5.20). In the WT enzyme, the side chain hydroxyl of T253 is hydrogen-bonded to the carbonyl of L250 and peptide NH of V254 (Figure 5.20a). In the T252E mutant, the side chain of this threonine is rotated (Figure 5.20b, black arrow). This allows the T253 hydroxyl to instead form a hydrogen bond to the carbonyl of G249. In the WT enzyme, the hydroxyl of T253 is too far (3.9 Å) from G249 to form a hydrogen bond. The orientation of the T253 side chain in the T252E mutant resembles the orientation of the equivalent threonine in $P450_{terp}$, $P450_{cin}$, and $P450_{BM3}$ (Figure C20).

Table 5.5. Distances and angles between notable features of the 4-methoxybenzoate-T252E crystal structure. Values are also given for WT CYP199A4 (PDB ID: 4DO1) in complex with 4-methoxybenzoic acid for comparison.

Species 1	Species 2	Distance (Å)	
		T252E	WT (PDB: 4DO1)
Fe	OH_2/OH^- ligand	2.1	-
Fe	C358 Sγ	2.3	2.4
Fe	C_{Me}	4.4	4.1
Fe	O_{Me}	5.0	5.2
Fe	closest O of E252	4.2	-
OH_2/OH^- ligand	closest O of E252	2.6	-
OH_2/OH^- ligand	C_{Me}	3.2	-
OH_2/OH^- ligand	O_{Me}	3.4	-
amide NH of G249	closest O of E252	2.7	-
amide NH of G249	furthest O of E252	3.1	-
amide NH of E252	closest O of E252	2.5	-
amide carbonyl O of A248	hydroxyl O of T252	-	2.6
WAT50	closest O of E252	2.4	-
C_{Me}	closest C of F298 (Cζ)	3.4	3.8
Angle (˚)			
dihedral angle C_{Me}-O-C_3-C_4		-18.3	2.1
Occupancies			
OH_2/OH^- ligand		92%	-

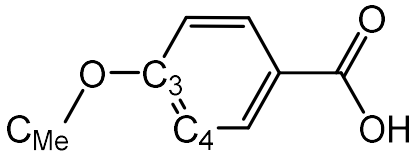

5.2.6 Crystal structures of $T252E_{CYP199A4}$ in complex with 4-methylthio- and 4-ethylthio-benzoic acid

Crystal structures were also solved of the T252E mutant in complex with 4-methylthiobenzoic acid and the bulkier substrate 4-ethylthiobenzoic acid (Figures 5.21 and 5.22) to explain the Soret band red-shifts induced by these substrates. The turnover of these substrates will be investigated with $T252E_{CYP199A4}$ in more detail in Chapter 6. The structures were both solved at 1.66-Å resolution (Table C2). Again, the fold of the T252E mutant in complex with these substrates was highly similar to that of the WT enzyme (RMSD ~0.4 Å, Figure C21). Neither substrate displaced

the heme-bound H_2O/OH^- ligand. In the 4-ethylthiobenzoic acid structure, the refined occupancy of the H_2O/OH^- ligand was 100%, while in the 4-methylthiobenzoic acid structure the occupancy was 80%. The Fe–O distance was similar in both structures (2.1 *vs.* 2.2 Å). In each structure, the substrate sulfur is in proximity to the heme-bound oxygen ligand and would be interacting with this ligand. This interaction would explain the Soret band red-shift. In the 4-methylthiobenzoic acid structure, the sulfur is 3.3 Å from the H_2O/OH^- ligand, while in the 4-ethylthiobenzoic acid structure the sulfur is closer to the aqua/hydroxo ligand (3.1 Å) (Table 5.6).

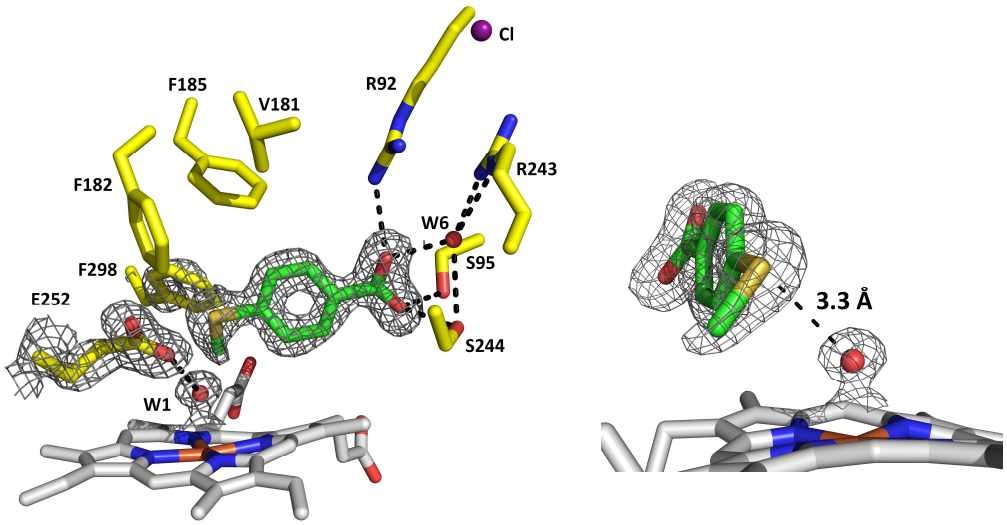

Figure 5.21. Crystal structure of the T252E mutant of CYP199A4 in complex with 4-methylthiobenzoate. A composite omit map of the substrate, water ligand (W1) and E252 side-chain is shown as grey mesh contoured at 1.5 σ (1.5 Å carve). The 4-methylthiobenzoic acid sulfur could be interacting with the iron-bound oxygen ligand (3.3 Å).

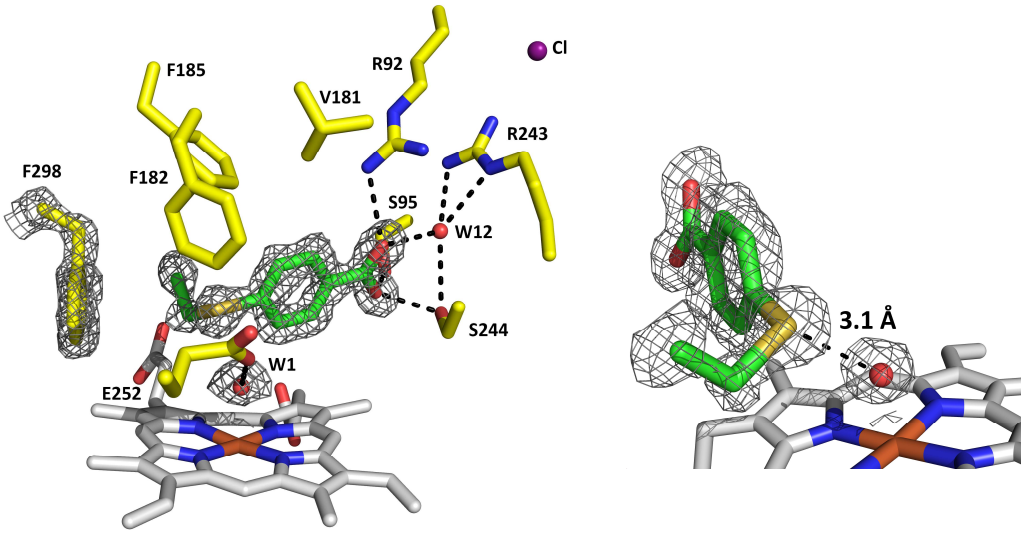

Figure 5.22. Crystal structure of the T252E mutant of CYP199A4 in complex with 4-ethylthiobenzoate. A feature-enhanced map of the substrate, F298 and water ligand (W1) is shown as grey mesh contoured at 1.0 σ (1.5 Å carve). There is an interaction between the 4-ethylthiobenzoic acid sulfur and the iron-bound aqua/hydroxo ligand (3.1 Å).

Again, we found that the positioning of these substrates in the active site of the T252E mutant was only subtly different to their positioning in the WT enzyme (Table 5.6). Figures 5.23 and 5.24 show the overlaid structures of WT CYP199A4 and the T252E mutant in complex with 4-methylthio- and 4-ethylthio-benzoic acid. In the T252E structures, the substrates are shifted further

away from the heme due to the presence of the aqua/hydroxo ligand. Because of this shift, the methylthio moiety of 4-methylthiobenzoic acid is nearer to residue 298 in the T252E structure than in the WT structure and consequently the phenyl ring of F298 has rotated away to accommodate the methylthio moiety (Figure 5.23). When 4-ethylthiobenzoic acid binds to both WT CYP199A4 and the T252E mutant, the bulky ethylthio moiety displaces the side-chain of F298.

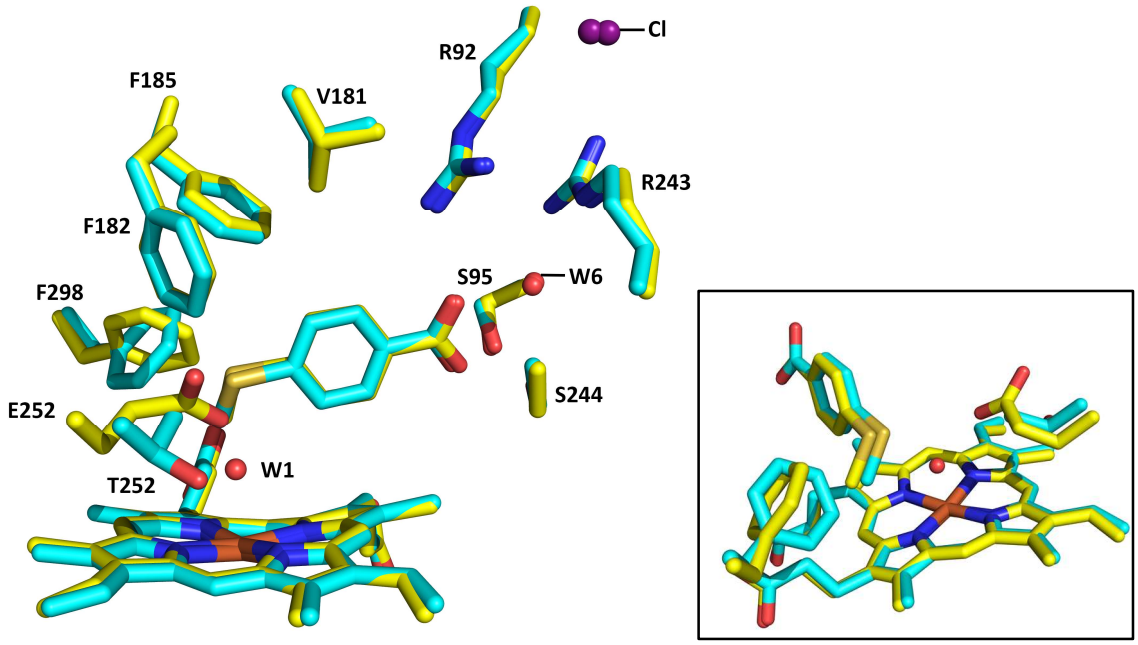

Figure 5.23. Overlaid structures of WT (cyan; PDB ID: 5KT1)[117] and T252E CYP199A4 (yellow) with 4-methylthiobenzoate bound. The waters and chloride in the T252E structure are labelled.

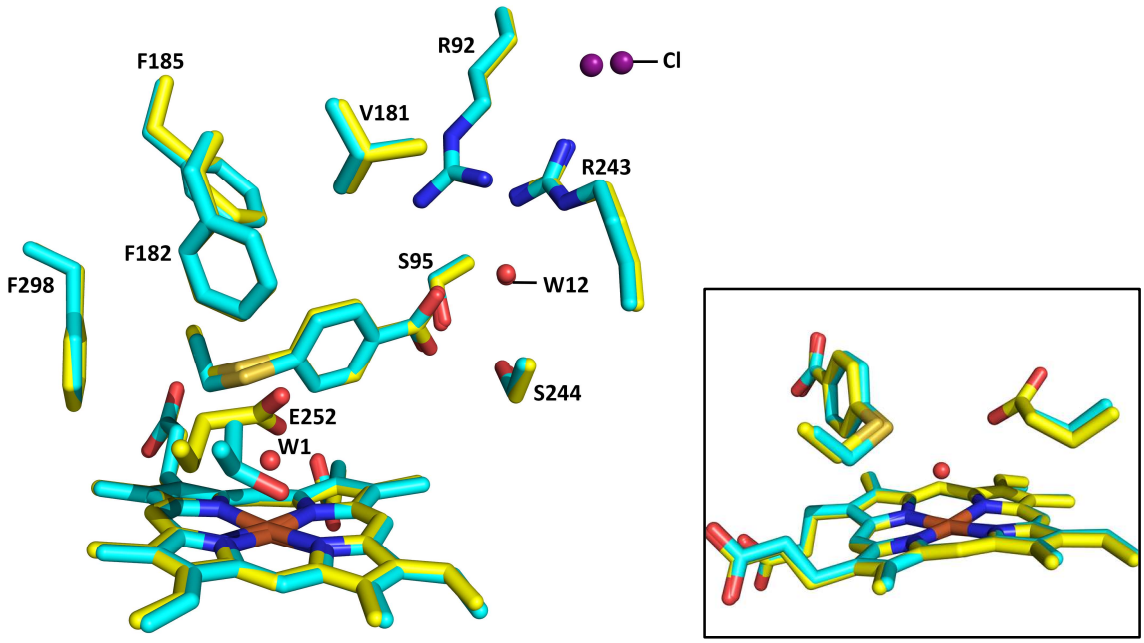

Figure 5.24. Overlaid structures of WT (cyan; PDB ID: 5U6U)[117] and T252E CYP199A4 (yellow) with 4-ethylthiobenzoate bound. The waters and chloride in the T252E structure are labelled.

Table 5.6. Distances and angles between notable features of the 4-methylthio- and 4-ethylthio-benzoate-bound T252E crystal structures. Values are also given for the WT structures for comparison.[117]

Distance	**4-Methylthio-T252E**	**4-Methylthio-WT (PDB: 5KT1)[117]**	**4-Ethylthio-T252E**	**4-Ethylthio-WT (PDB: 5U6U)[117]**
Fe - OH_2/OH^- ligand	2.2	-	2.1	-
Fe - C358 Sγ	2.3	2.5	2.3	2.4
Fe - C_{Me}/CH_2	4.8	4.5	5.4	5.2
Fe - CH_3	-	-	6.9	6.7
Fe - S	5.1	5.0	4.9	4.8
Fe - closest O of E252	4.4	-	4.3	-
OH_2/OH^- ligand - closest O of E252	2.7	-	2.7	-
OH_2/OH^- ligand - C_{Me}/CH_2	3.6	-	4.2	-
OH_2/OH^- ligand - S	3.3	-	3.1	-
Angle (˚)				
dihedral angle C_{Me}-S-C_3-C_4	-31.8	-33.9	-59.4	-55.2
Occupancies				
OH_2/OH^- ligand	80%	-	100%	-

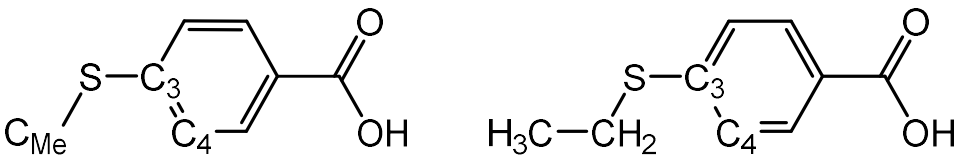

5.2.7 Binding bulky hydrophobic ligands to the T252E mutant to attempt to displace the iron-bound aqua/hydroxo ligand

The $T252E_{CYP199A4}$ crystal structures revealed that 4-methoxy-, 4-methylthio- and 4-ethylthio-benzoic acid are unable to displace the heme-bound H_2O/OH^- ligand in this mutant. To probe how tightly the oxygen ligand is bound to the iron, we attempted to displace it using various bulky hydrophobic substrates (4-thiophen-3-ylbenzoic acid, 4-benzylbenzoic acid, 4-cyclohexylbenzoic acid, 4-phenylbenzoic acid, 4-isopropylbenzoic acid and 4-*t*-butylbenzoic acid). We reasoned that these substrates, due to their steric bulk, would have greater likelihood of removing the ligand. When added to WT CYP199A4, they all induce large shifts to high-spin (≥90% HS).[219, 277] The spin-state shift of the T252E mutant induced by each of these substrates was measured, but again the lack of any substantial shift to HS implied that the aqua ligand had not been displaced (Figures 5.25 and C22, Table 5.7). The sulfur-containing ligand 4-thiophen-3-ylbenzoic acid induced a 1.0 nm red-shift in the Soret band position, whereas 4-phenyl- and 4-benzyl-benzoic acid induced 0.5 nm red-shifts (Figure C23). 4-Cyclohexylbenzoic acid appeared to induce a ~10% shift to HS and bound more weakly to the T252E variant than to the WT enzyme (1.46 ± 0.08 *vs.* 0.45 ± 0.05 μM) (Figure C22, Table C3).[277] 4-*t*-Butylbenzoic acid also induced a ~10% shift to HS (Figure C22c). Crystal structures of the T252E mutant in complex with 4-benzylbenzoic acid and 4-thiophen-3-ylbenzoic acid confirmed that these bulky ligands had not displaced the water (Figures 5.26 and

5.27), but we were unable to obtain the crystal structure of the mutant in complex with 4-*t*-butylbenzoic acid or 4-cyclohexylbenzoic acid (Figure C24). The crystals of 4-*t*-butylbenzoate-T252E$_{CYP199A4}$ diffracted poorly. We also attempted to solve the crystal structure of T252E$_{CYP199A4}$ in complex with the bulky substrate 4-isopropylbenzoic acid, which induces a ~10% shift to HS, but the isopropyl methyl groups were not visible in the electron density map (Figure C25).

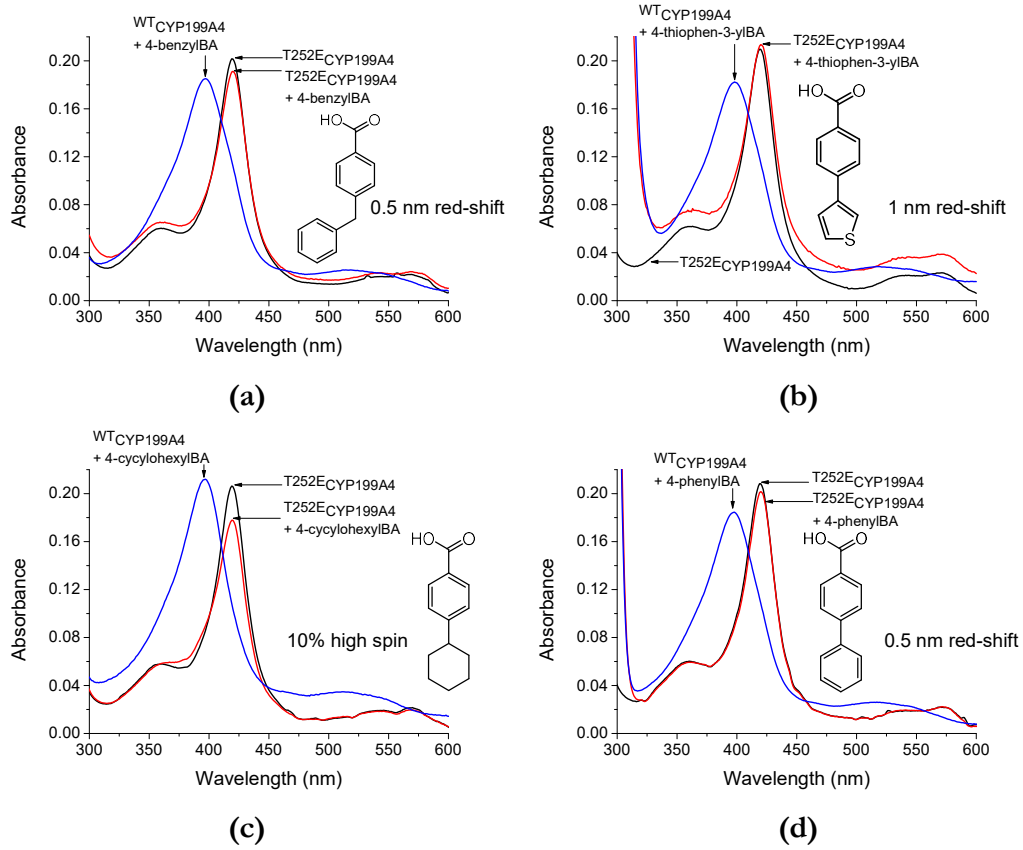

Figure 5.25. Spin-state shifts of the T252E mutant of CYP199A4 induced by **(a)** 4-benzylbenzoic acid, **(b)** 4-thiophen-3-ylbenzoic acid, **(c)** 4-cyclohexylbenzoic acid, and **(d)** 4-phenylbenzoic acid. Substrate-free T252E$_{CYP199A4}$ is in black and substrate-bound T252E$_{CYP199A4}$ in red. For comparison, the spin-state shift of WT CYP199A4 is given in blue.

Table 5.7. Spin-state shifts induced by binding of various bulky substrates to the T252E mutant of CYP199A4. Shifts for the WT enzyme, previously reported by others, are included for comparison. 4-Benzyl-, 4-thiophen-3-yl- and 4-phenyl-benzoic acid induced small Soret band red-shifts from 419.5 → 420.0 or 420.5 nm upon binding to T252E$_{CYP199A4}$ (Figure C23).

Substrate	**Spin-state shift (% HS)**	
	T252E	**WT**
4-benzylBA	~0.5 nm red-shift	90% [277]
4-thiophen-3-ylBA	~1.0 nm red-shift	90% [277]
4-cyclohexylBA	~10%	≥95% [277]
4-phenylBA	~0.5 nm red-shift	90% [277]
4-isopropylBA	~10%	≥95%
4-*t*-butylBA	~10%	90% [277]

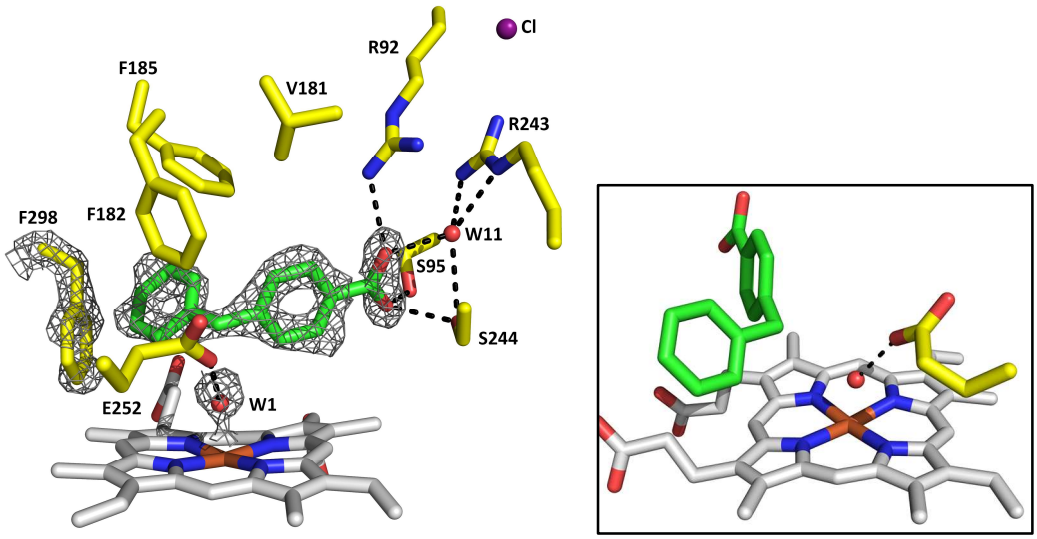

Figure 5.26. Crystal structure of the T252E mutant of CYP199A4 in complex with 4-benzylbenzoate. A feature-enhanced map of the substrate, F298 and water ligand (W1) is shown as grey mesh contoured at 1.5 σ (1.5 Å carve).

Table 5.8. Distances and angles between notable features of the 4-benzylbenzoic acid-bound T252E$_{CYP199A4}$ structure.

Distance	**4-benzylBA T252E**
Fe - OH_2/OH^- ligand	2.0
Fe - C358 Sγ	2.3
Fe - closest O of E252	4.1
OH_2/OH^- ligand - closest O of E252	2.3
C_7 - OH_2/OH^- ligand	3.3
Fe - C_7	4.8
Fe - C_3	5.5
Fe - C_{13}	5.1
C_2 - closest carbon of F298	3.2
Angle (˚)	
dihedral angle C_{13}-C_8-C_7-C_4	-91.1
Occupancies	
OH_2/OH^- ligand	92%
4-Benzylbenzoic acid	82%

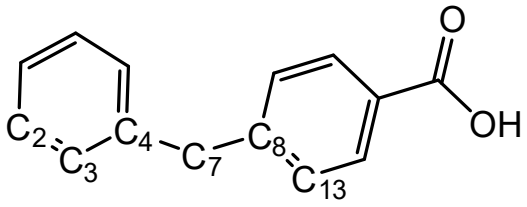

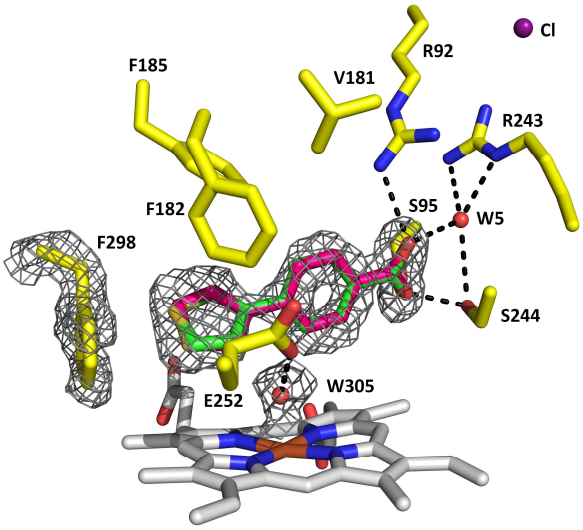

Figure 5.27. Crystal structure of the T252E mutant of CYP199A4 in complex with 4-thiophen-3-ylbenzoate. A feature-enhanced map of the substrate, F298, and water ligand (W305) is shown as grey mesh contoured at 1.0 σ (1.5 Å carve). The two orientations of the 4-thiophen-3-ylbenzoic acid ligand are shown in green (sulfur pointing 'up' away from heme) and pink (sulfur pointing 'down' towards heme).

The crystal structures of 4-benzyl- and 4-thiophen-3-yl-benzoate-bound T252E$_{CYP199A4}$ were solved at resolutions of 1.77 and 2.02 Å (Table C2). The refined occupancy of the H_2O/OH^- ligand was 92% in the 4-benzylbenzoate-T252E crystal structure, and 100% in the 4-thiophen-3-ylbenzoate-T252E structure. The Fe–O distances are 2.0 and 2.1 Å, respectively. In the 4-benzylbenzoate-T252E$_{CYP199A4}$ structure, the *para*-benzyl group points away from the heme and occupies the space vacated by F298 (Figure 5.26). The crystal structure of the WT enzyme in complex with 4-benzylbenzoic acid has not been reported. The *B*-factors are higher for the atoms of the *para*-benzyl group than those of the benzoic acid moiety, indicating that the benzyl group has greater mobility in the active site (Table C4).[314, 417] The closest carbon atom of 4-benzylbenzoic acid to the heme iron is the benzylic carbon (4.8 Å), and this is the position at which the substrate is hydroxylated by WT CYP199A4 (Table 5.8).[277] WT CYP199A4 is known to convert this substrate in *in vivo* turnovers into both 4-(hydroxy(phenyl)methyl)benzoic acid and the further oxidation product 4-benzoylbenzoic acid.[277]

We investigated whether the T252E mutant also displayed activity towards this substrate, using H_2O_2 instead of NADH/O_2 to drive catalysis. We found that the T252E could indeed utilise H_2O_2 to convert 4-benzylbenzoic acid into the same two oxidation products (Figure 5.28).

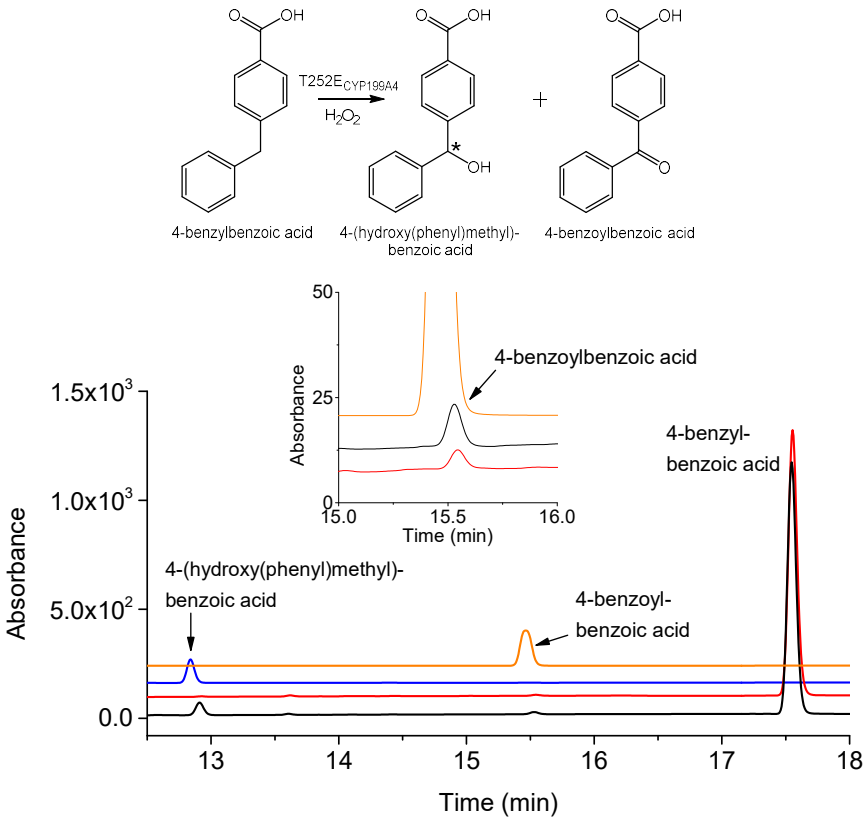

Figure 5.28. HPLC analysis of the H_2O_2-driven oxidation of 4-benzylbenzoic acid by $T252E_{CYP199A4}$. In **black** is the *in vitro* reaction, in **red** is a control reaction performed with heat-denatured T252E enzyme, in **blue** is authentic 4-(hydroxy(phenyl)methyl)benzoic acid (RT = 12.8 min) synthesised and purified by Tom Coleman (using a CYP199A4 whole-cell system)[277] and in **orange** is authentic 4-benzoylbenzoic acid (RT = 15.5 min). The substrate appears at 17.6 min. Conditions: 3 µM P450, 50 mM H_2O_2, reaction time = 240 min, T = 30°C. Gradient: 20-95% AcCN in H_2O with 0.1% TFA. Detection wavelength: 254 nm.

Figure 5.29 shows the overlaid structures of WT CYP199A4 and the T252E mutant in complex with 4-thiophen-3-ylbenzoic acid. This comparison reveals that the position of the substrate is highly similar in both structures, but the substrate appears to be subtly shifted away from the heme in the T252E structure. The thiophene ring of 4-thiophen-3-ylbenzoic acid could either be oriented with the sulfur pointing 'down' towards the heme or pointing 'up' away from the heme (Figure C26). Both orientations of the ligand were modelled, and the refined occupancies of these alternative conformations were 36% 'down' and 45% 'up' in the T252E structure (Tables C5 and C6); the overall occupancy of the substrate was 81%. In the 'down' orientation the distance between the aqua ligand and sulfur is 4.3 Å (Table 5.9). An interaction between the sulfur and aqua ligand would explain the 1.0 nm Soret band red-shift induced by this substrate.[154] In the WT structure, the ligand is oriented with the sulfur pointing 'down' towards the heme, and the water is displaced by this bulky ligand.[277]

In the crystal structures of $T252E_{CYP199A4}$ in complex with 4-methoxy-, 4-methylthio-, 4-ethylthio- and 4-pyridin-2-yl-benzoic acid, the cysteine sulfur ligand, iron and H_2O/OH^- ligand are linearly arranged (S-Fe-O angle ≈180°) (Table C7). We noticed that when the bulky hydrophobic substrates 4-benzylbenzoic acid and 4-thiophen-3-ylbenzoic acid are bound, the S-Fe-O angle is

bent because the aqua/hydroxo ligand is shifted away from the sterically bulky substrate (Figure 5.30). In the 4-thiophen-3-ylbenzoic acid structure, the Fe-O bond is at a 20.7° angle to the Fe-S bond. In the 4-benzylbenzoic acid structure, the Fe-O bond is at a 15.9° angle to the Fe-S bond. In summary, this study reveals that even sterically bulky ligands are unable to displace the aqua/hydroxo ligand in the T252E mutant, which must be tightly bound.

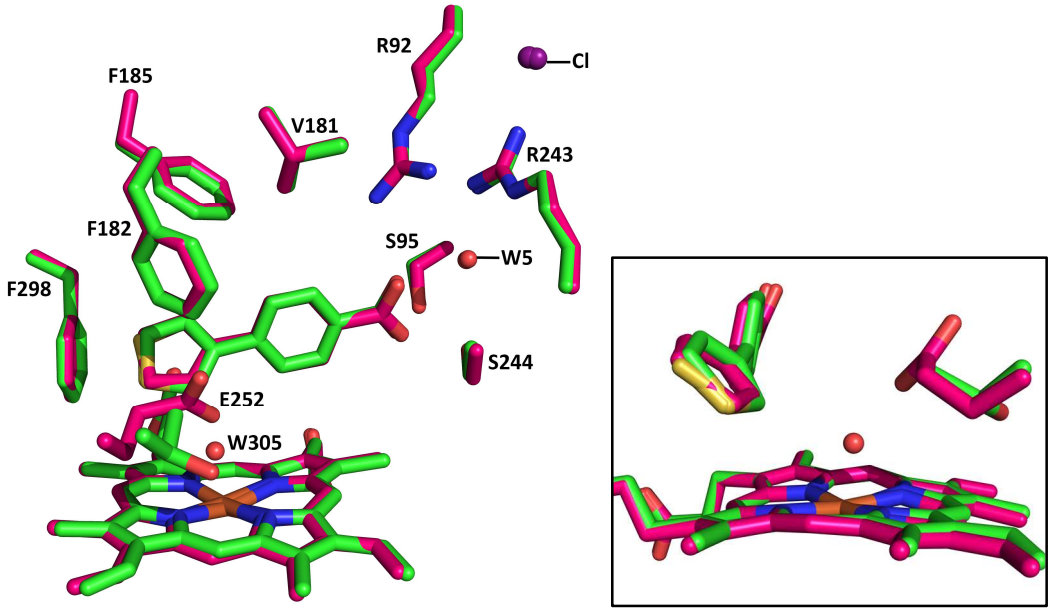

Figure 5.29. Overlaid structures of WT (green; PDB: 6C3J) and T252E CYP199A4 (pink) with 4-thiophen-3-ylbenzoate bound. The waters and chloride in the T252E structure are labelled.

Table 5.9. Distances and angles between notable features of the 4-thiophen-3-ylbenzoate-bound T252E and WT CYP199A4 crystal structures. Note that distances are given for the conformation in which the sulfur of the ligand is pointing 'down' towards the heme. Distances for the alternative conformation are given in Table C5.

Distance	**4-thiophen-3-yl-T252E**	**4-thiophen-3-yl-WT (PDB: 6C3J)[277]**
Fe - OH_2/OH^- ligand	2.1	-
Fe - C358 Sγ	2.3	2.4
Fe - C_8	4.2	4.2
Fe - S_9	5.1	5.2
Fe - closest O of E252	4.2	-
OH_2/OH^- ligand - closest O of E252	2.2	-
OH_2/OH^- ligand - C_8	3.3	-
OH_2/OH^- ligand - S_9	4.3	-
Angle (°)		
dihedral angle C_8-C_7-C_6-C_5	54.6	50.0
Occupancies		
OH_2/OH^- ligand	100%	-
4-Thiophen-3-ylbenzoic acid	81%	-

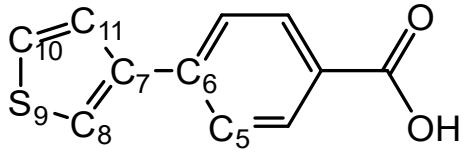

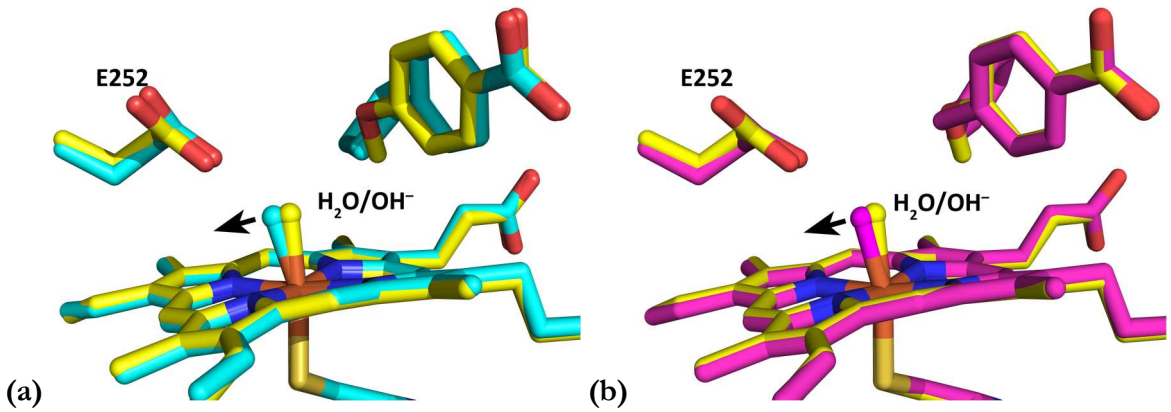

Figure 5.30. The active-site structure of 4-methoxybenzoic acid-bound T252E$_{CYP199A4}$ (yellow) overlaid with **(a)** the 4-thiophen-3-ylbenzoic acid structure (blue) and **(b)** the 4-benzylbenzoic acid structure (magenta). When bulky hydrophobic substrates are bound, the S-Fe-O angle is bent because the H_2O/OH^- ligand is shifted away from the sterically bulky substrate (black arrow).

5.2.8 Binding type II ligands to the T252E mutant to attempt to displace the iron-bound water ligand

As we were unable to displace the heme-bound H_2O/OH^- ligand using various sterically bulky substrates, we next used type II ligands to attempt to displace the water. These ligands contain N and O heteroatoms that could replace the water as the sixth axial ligand to the heme. 4-Propionylbenzoic acid, 4-pyridin-2-ylbenzoic acid and 4-pyridin-3-ylbenzoic acid all induce type II shifts when they bind to WT CYP199A4.[277] These substrates were also found to induce red-shifts of the Soret band when they were added to the T252E mutant (Figures 5.31 and C27, Table C8). 4-Propionylbenzoic acid (and its isomer 4-2-oxopropylbenzoic acid) both induced a ~2.5 nm red-shift, while the pyridine compounds induced greater shifts. 4-Pyridin-2-ylbenzoic acid induced a ~3 nm shift and 4-pyridin-3-ylbenzoic acid a ~3.5 nm shift. 4-Pyridin-2-ylbenzoic acid was found to bind more tightly to the T252E mutant than to WT CYP199A4 (0.10 ± 0.01 *vs.* 1.0 ± 0.1 μM[277]) (Figure C28, Table C9). On the other hand, 4-pyridin-3-ylbenzoic acid displayed lower affinity for the T252E mutant than for the WT enzyme (7.9 ± 0.1 *vs.* 2.3 ± 0.1 μM[277]).

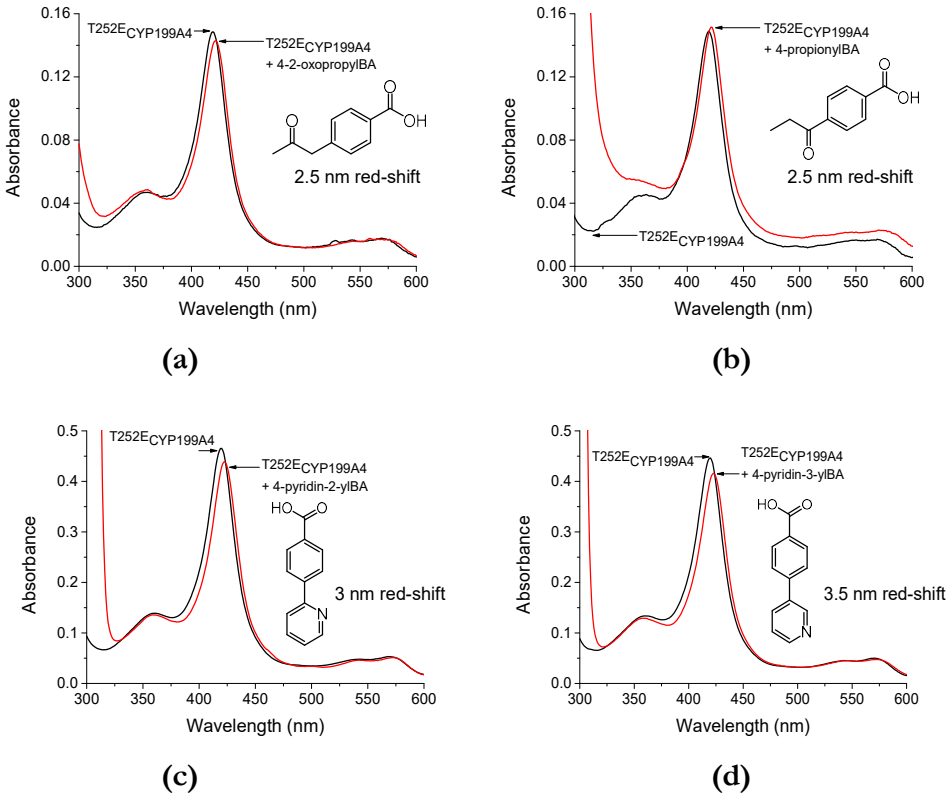

Figure 5.31. Spin-state shifts of the T252E mutant of CYP199A4 induced by **(a)** 4-2-oxopropylbenzoic acid, **(b)** 4-propionylbenzoic acid, **(c)** 4-pyridin-2-ylbenzoic acid, and **(d)** 4-pyridin-3-ylbenzoic acid.

I previously demonstrated that 4-pyridin-3-ylbenzoic acid directly coordinates to the heme iron in WT CYP199A4, but 4-pyridin-2-ylbenzoic acid instead hydrogen-bonds to the heme-bound water. 4-Pyridin-3-ylbenzoic acid was therefore the obvious compound to use to try to displace the heme-bound aqua ligand in the T252E mutant. Although we obtained crystals of the 4-pyridin-3-ylbenzoate-T252E$_{CYP199A4}$ complex, we were unable to solve the crystal structure (Figure C24). The crystal structure of 4-pyridin-2-ylbenzoate-bound T252E$_{CYP199A4}$, on the other hand, was readily solved (at 1.73-Å resolution) (Table C2). This crystal structure revealed that the binding mode of 4-pyridin-2-ylbenzoic acid in T252E$_{CYP199A4}$ is almost identical to its binding mode in WT CYP199A4 (Figure 5.32). The nitrogen of the pyridine moiety hydrogen-bonds to the heme-bound H_2O/OH^- ligand, the occupancy of which is 100% (Figure C29). The Fe–O distance is 2.3 Å and the donor-acceptor distance between the H_2O/OH^- ligand and pyridine N is 2.7 Å. This hydrogen bond is slightly shorter than in the WT enzyme (2.9 Å). Figure 5.33 and Table 5.10 compare the structures of WT CYP199A4 and the T252E mutant with 4-pyridin-2-ylbenzoic acid bound.

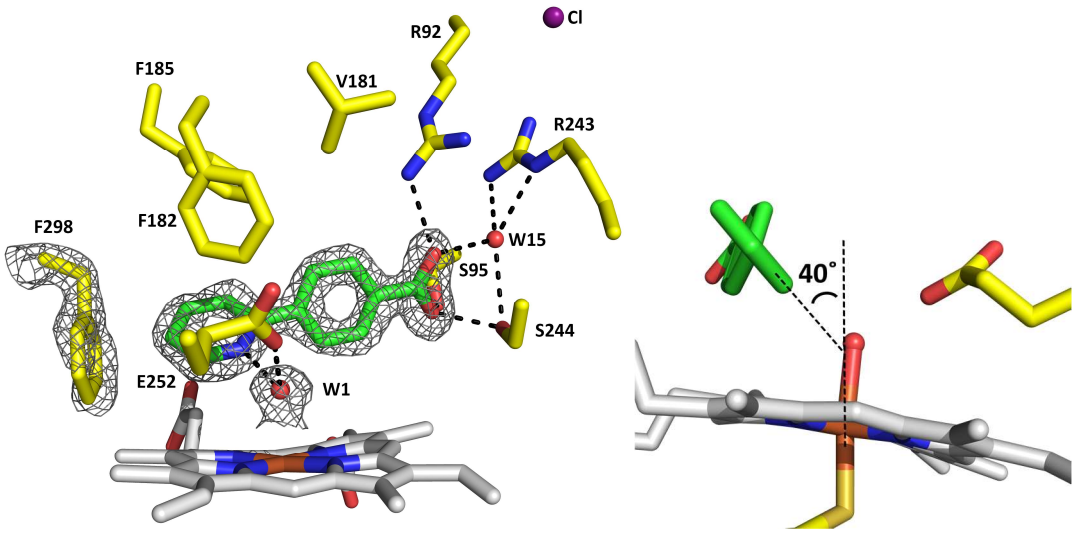

Figure 5.32. Crystal structure of the T252E mutant of CYP199A4 in complex with 4-pyridin-2-ylbenzoate. A feature-enhanced map of the substrate, F298, and water ligand (W1) is shown as grey mesh contoured at 2.0 σ (1.5 Å carve). The pyridine ring is at a 40° angle to the Fe-S bond.

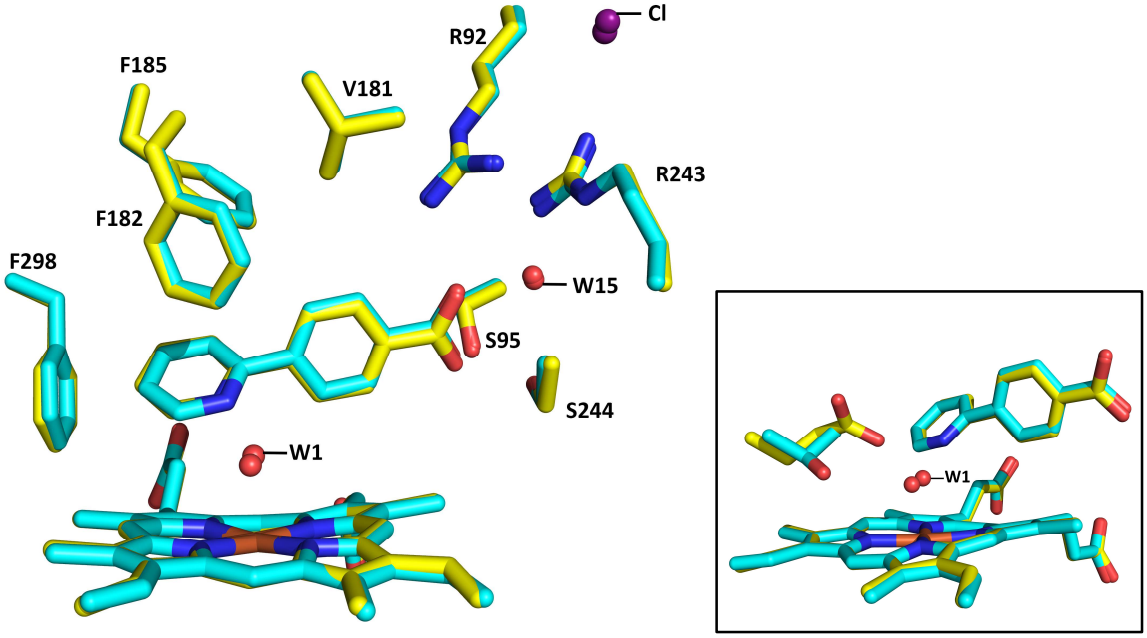

Figure 5.33. Overlaid structures of WT (cyan) and T252E CYP199A4 (yellow) with 4-pyridin-2-ylbenzoate bound. The waters and chloride in the T252E structure are labelled.

Table 5.10. Distances and angles between notable features of the 4-pyridin-2-ylbenzoate-bound T252E and WT CYP199A4 crystal structures.

Distance	**4-pyridin-2-yl-T252E**	**4-pyridin-2-yl-WT**
Fe - OH_2/OH^- ligand	2.3	2.2
Fe - C358 Sγ	2.3	2.3
Fe - closest O of E252	4.3	-
OH_2/OH^- ligand - closest O of E252	2.4	-
OH_2/OH^- ligand - pyridine N_4	2.7	2.9
OH_2/OH^- ligand - C_5	3.3	3.3
Angle (˚)		
dihedral angle N_4-C_3-C_7-C_8	63.1	60.6
Occupancies		
OH_2/OH^- ligand	100%	76%
4-Pyridin-2-ylbenzoic acid	100%	100%

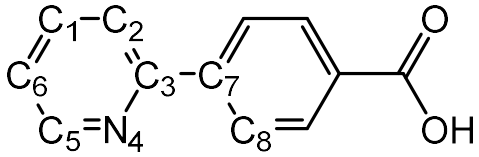

When 4-pyridin-3-ylbenzoic acid binds to WT CYP199A4, it coordinates directly to the heme iron and induces a larger red-shift of the Soret band than 4-pyridin-2-ylbenzoic acid, which does not displace the water (Chapter 4). 4-Pyridin-3-ylbenzoic acid induces a 5 nm red-shift of the Soret peak (from 419 to 424 nm), whereas 4-pyridin-2-ylbenzoic acid only shifts the Soret peak by 3 nm to 422 nm. As discussed in Chapter 4, the difference spectra induced by these two ligands when they bind to WT CYP199A4 are also noticeably different (Figure 5.34a). 4-Pyridin-3-ylbenzoic acid induces a larger Soret band trough, and additionally induces a trough at 570 nm which does not appear in the 4-pyridin-2-ylbenzoic acid spectrum. This trough at 570 nm arises from a decrease in intensity of the α band. A prominent peak also appears at 372.5 nm in the 4-pyridin-3-ylbenzoic acid spectrum which is absent from the 4-pyridin-2-ylbenzoic acid spectrum (Tables 5.11 and 5.12).

For the T252E mutant, the difference spectra induced by 4-pyridin-2-ylbenzoic acid and 4-pyridin-3-ylbenzoic acid are almost indistinguishable (Figure 5.34c). They do not resemble the spectrum of WT CYP199A4 with 4-pyridin-3-ylbenzoic acid bound but instead both closely resemble the spectrum induced by 4-pyridin-2-ylbenzoic acid. The magnitude of the red-shift is almost the same for both ligands (3 *vs.* 3.5 nm), and the α-band remains more intense than the β-band (a characteristic of P450s in complex with oxygen donor ligands[363, 365]) (Figure 5.34b). There is also no increase in the intensity of the δ-band. This is evidence that 4-pyridin-3-ylbenzoic acid does not displace the water in the T252E mutant. Similar results were obtained with the type II ligand 4-1*H*-imidazol-1-ylbenzoic acid, suggesting retention of the oxygen donor ligand in the T252E variant (Figure C30).

As discussed in Chapter 4, ferrous P450s with directly bound σ-donor nitrogen ligands display red-shifted Soret peaks at 440-450 nm. To confirm that the nitrogen ligands were not directly bound to the heme iron in the T252E variant, I attempted to reduce the T252E mutant in the

presence of the N-donor substrates but, as reported earlier, this variant did not seem to be fully reduced by dithionite (Figures C31–C33).

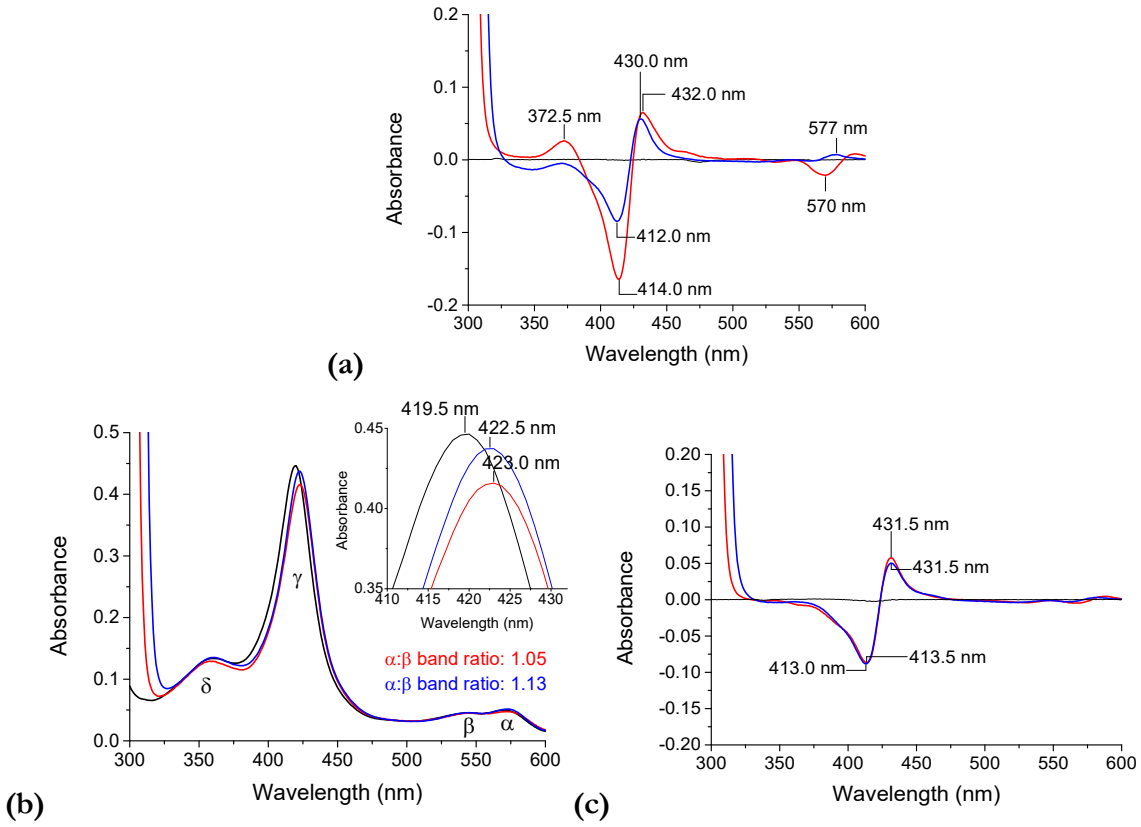

Figure 5.34. **(a)** Difference spectra of WT CYP199A4 with 4-pyridin-3-ylbenzoic acid (**red**) and 4-pyridin-2-ylbenzoic acid (**blue**). The enzyme concentration was 5.2 μM. **(b)** Spin-state shift of T252E$_{CYP199A4}$ with 4-pyridin-3-ylbenzoic acid (**red**) and 4-pyridin-2-ylbenzoic acid (**blue**). In **black** is substrate-free enzyme. **(c)** Difference spectra of T252E$_{CYP199A4}$ with 4-pyridin-3-ylbenzoic acid (**red**) and 4-pyridin-2-ylbenzoic acid (**blue**). The enzyme concentration was 3.7 μM.

Table 5.11. Difference spectra peaks and troughs for 4-pyridin-2-yl- and 4-pyridin-3-yl-benzoic acid-bound T252E$_{CYP199A4}$ and WT CYP199A4.

WT CYP199A4	**λ_{trough} (nm)**	**λ_{peak} (nm)**
4-pyridin-2-ylbenzoic acid	412	430
4-pyridin-3-ylbenzoic acid	414 (prominent trough)	432
T252E CYP199A4	**λ_{trough} (nm)**	**λ_{peak} (nm)**
4-pyridin-2-ylbenzoic acid	413	431.5
4-pyridin-3-ylbenzoic acid	413.5	431.5

Table 5.12. Additional peaks and troughs in the difference spectra of 4-pyridin-2-yl- and 4-pyridin-3-yl-benzoic acid-bound WT CYP199A4.

WT CYP199A4	**λ_{trough} (nm)**	**λ_{peak} (nm)**
4-pyridin-2-ylbenzoic acid	-	577 (α/β band region)
4-pyridin-3-ylbenzoic acid	570 (α band)	372.5

5.2.9 Electron paramagnetic resonance (EPR) data for the T252E$_{CYP199A4}$ mutant

EPR experiments were performed to evaluate whether binding of substrates to the T252E mutant induces any shift to HS and to investigate the identity of the sixth axial ligand to the heme. In the low-spin state, ferric P450s have *g*-values of ~2.45, 2.26, and 1.91, but in the high-spin state they have *g*-values of ~8, 4, and 1.7.[173] Continuous-wave EPR experiments were performed by Josh Harbort at the University of Queensland using T252E$_{CYP199A4}$ protein that I prepared and purified.

Substrate-free WT CYP199A4 is low-spin, but there is a shift to high-spin when 4-methoxybenzoic acid binds (Figure 5.35a,c). In contrast, there were no HS heme signals in the CW EPR spectrum of 4-methoxybenzoic acid-bound T252E$_{CYP199A4}$. A new signal set is present in the substrate-free and substrate-bound T252E$_{CYP199A4}$ spectra that is absent from the spectra of WT CYP199A4 ($g \approx$ [2.52, 2.24, 1.86]) (Table 5.13, Figure 5.35b,d).

For P450s with water bound as the sixth ligand, the g_z value is generally ≤2.45, whereas larger g_z values are associated with low-spin ferric P450s with anionic ligands bound, such as formate.[164, 383, 418] Sono and Dawson reported that the complex of P450$_{cam}$ with formate exhibited a signal set with *g*-values of 2.55, 2.25 and 1.88 (Figure C34a).[164] Additionally, they reported that raising the pH of substrate-free P450$_{cam}$ to 10 resulted in the appearance of a new unstable signal set with *g*-values of 2.54, 2.24, and 1.86, postulated to correspond to an OH^- complex.[164] Hayakawa *et al.* reported that raising the pH of the thermophilic enzyme P450st to 10 also resulted in the appearance of a signal set with *g*-values of 2.49, 2.24, and 1.90 (Figure C34b) which they attributed to a hydroxide complex.[418] This EPR spectrum closely resembles that of T252E$_{CYP199A4}$. Based on comparison of these spectra to the T252E$_{CYP199A4}$ spectra, we speculate that a proportion of the T252E$_{CYP199A4}$ molecules have hydroxide bound.

Table 5.13. CW EPR *g*-values for substrate-free and 4-methoxybenzoic acid-bound T252E$_{CYP199A4}$. The proportion of each species is also given. Analysis was performed by Josh Harbort at the University of Queensland.

Species	g_z	g_y	g_x	Proportion
T252E CYP199A4 + 4-methoxybenzoic acid	2.528	2.243	1.865	55%
	2.413	2.240	1.902	45%
Substrate-free T252E CYP199A4	2.443	2.244	1.897	53%
	2.519	2.247	1.866	47%

Using HYSCORE EPR, our collaborators at the University of Queensland measured Fe^{III}–H distances for 4-methoxybenzoic acid-bound T252E$_{CYP199A4}$ of 2.5 Å and 2.35 Å. The distance of 2.5 Å would be expected for an axial water ligand[153], and the distance of 2.35 Å may correspond to a hydroxide ligand, though further work is required to confirm this.

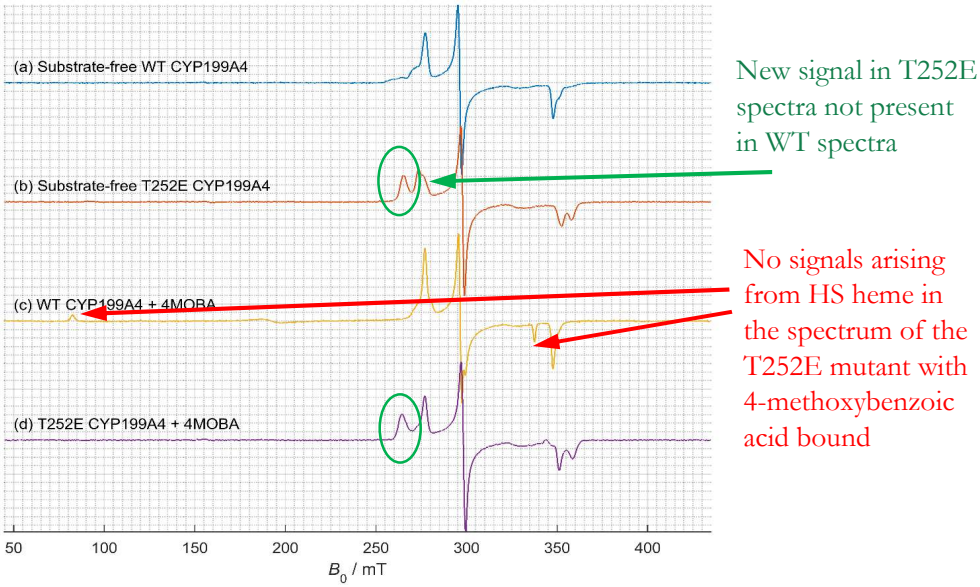

Figure 5.35. Continuous-wave EPR spectra for substrate-free and 4-methoxybenzoate-bound WT CYP199A4 and the T252E mutant. EPR experiments and analysis were performed by Josh Harbort and Jeffrey Harmer at the University of Queensland. The temperature was 15 K, the microwave frequency was 9.38 GHz and the microwave power was 1.257 mW.

5.3 Discussion

Shoji *et al.* previously prepared mutants of $P450_{cam}$, P450 BM3 and CYP119 in which the highly conserved threonine (T) was replaced with glutamate (E)[227]. However, this is the first investigation to report crystal structures of a substrate-bound T → E mutant and substrate binding and turnover data with NADH/O_2. This study reveals that the properties of the T252E mutant of CYP199A4 differ substantially from those of the WT enzyme. This mutation was found to almost entirely abolish CYP199A4's ability to utilise NADH/O_2 to oxidise substrates via the normal catalytic cycle. The activity of the T252E mutant is dramatically lower than that of the T252A mutant, in which the catalytically important threonine residue has been substituted with alanine.[276] The T252A mutant demethylates 4-methoxybenzoic acid at a rate of 570 ± 56 min^{-1} and the reaction is 68% coupled[276], whereas the T252E mutant performs the same reaction at a rate of ~0.8 min^{-1} and is 90% uncoupled. The activity of the T252E mutant is also lower than that of the D251N mutant studied by Chao[276] and Coleman[277]; the D251N mutant demethylates 4-methoxybenzoic acid at a >4-fold faster rate (3.5 min^{-1}) and the coupling efficiency is 59%.[276] The lack of any significant spin-state shift to HS upon addition of substrates, the exceedingly slow NADH consumption rate and the low coupling efficiency could be explained by the fact that the H_2O/OH^- ligand to the heme is tightly bound and is not displaced by substrate. This is also in agreement with the reduced ability of the T252E mutant to bind CO in the presence of dithionite. Crystal structures of the T252E mutant in complex with 4-methoxybenzoic acid, 4-methylthiobenzoic acid, 4-ethylthiobenzoic acid and various other sterically bulky ligands show that the H_2O/OH^- ligand interacts strongly with the side-chain carboxylate of Glu252 (Table 5.14). The Glu252 carboxylate occupies essentially the

same position in all solved crystal structures (Figure 5.36). The closest oxygen of the Glu252 carboxylate is ~4.2 Å from the heme iron. This is closer than the iron-carboxylate distance in chloroperoxidase (5.1 Å).[234] The occupancy of the aqua/hydroxo ligand is close to 100% even when bulky substrates are bound (Table 5.14). Because the iron is six-coordinate and low-spin even when substrate is bound, the iron is predominantly in the plane of the porphyrin ring, whereas it is displaced further out of the porphyrin plane in the crystal structures of high-spin, five-coordinate WT CYP199A4 (Tables C10 and C11, Figure C35). The iron-sulfur distance in these T252E crystal structures was 2.25-2.31 Å, which is slightly shorter than the Fe-S distance in crystal structures of high-spin, five-coordinate WT CYP199A4 (Tables C12 and C13). The Fe-S bond length in the T252E crystal structures is similar to that in crystal structures of six-coordinate low-spin WT CYP199A4. Due to the presence of this aqua/hydroxo ligand, the orientation of these substrates in the T252E active site is subtly altered compared to their orientation in the active site of the WT enzyme. The substrates are shifted away from the aqua/hydroxo ligand. As the structure of the substrate-binding pocket is largely unchanged by the mutation, most substrates have similar affinity for the T252E mutant and WT enzyme. We were unable to solve crystal structures of the T252E mutant in complex with the bulky ligands 4-*tert*-butyl-, 4-cyclohexyl-benzoic acid, and 4-pyridin-3-ylbenzoic acid, but the UV-Vis spectra suggest that the H_2O/OH^- ligand has not been displaced. HYSCORE EPR could be performed to provide additional evidence that the aqua/hydroxo ligand is not displaced when 4-pyridin-3-ylbenzoic acid is bound.

Although the T252E mutant is unable to efficiently utilise $NADH/O_2$ to drive catalysis, the peroxygenase activity of CYP199A4 was enhanced by this mutation. This agrees with the prediction made by Shoji *et al.* that this single-point mutation should enable P450s to utilise H_2O_2 more efficiently.[227] The glutamate could deprotonate the proximal oxygen of the Fe^{III}–H_2O_2 complex and transfer the proton to the distal oxygen, triggering cleavage of the O–O bond and generation of the active oxidant, Cpd I.[227] Importantly, we demonstrated that product formation was not due to a Fenton-type reaction.

Table 5.14. Refined occupancy of the heme-bound water ligand in the $T252E_{CYP199A4}$ crystal structures and distance between the glutamate carboxylate and iron-bound H_2O/OH^- ligand

Crystal structure	Occupancy of iron-bound water/hydroxo ligand (%)	Distance between glutamate and H_2O/OH^- (Å)
4-methoxyBA	92	2.6
4-methylthioBA	80	2.7
4-ethylthioBA	100	2.7
4-benzylBA	92	2.3
4-thiophen-3-ylBA	100	2.2
4-pyridin-2-ylBA	100	2.4

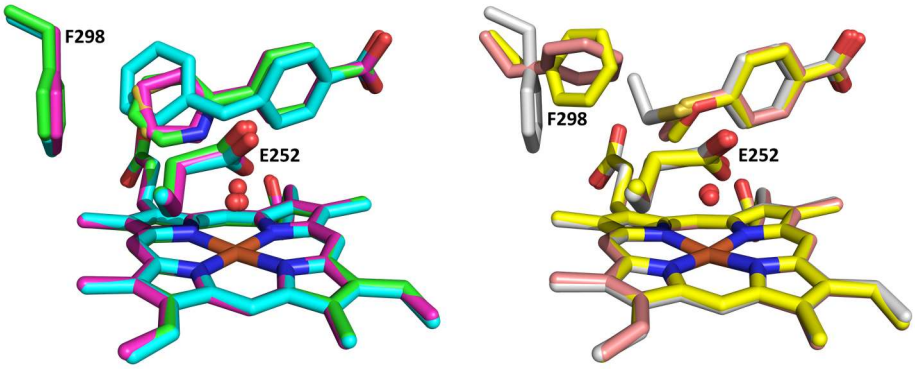

Figure 5.36. Overlaid structures of T252E$_{CYP199A4}$ in complex with 4-pyridin-2-yl- (green), 4-thiophen-3-yl- (magenta), 4-benzyl- (cyan), 4-methoxy- (yellow), 4-methylthio- (salmon), and 4-ethylthio-benzoate (grey). In all structures, the E252 carboxylate and H_2O/OH^- ligand are in similar positions.

Differences were observed in the EPR spectra of the T252E mutant and WT CYP199A4. We speculate that the new set of signals in the EPR spectrum of the T252E mutant is due to a fraction of the P450 molecules having OH^- as the sixth axial ligand. We propose that the hydroxide ligand may arise from deprotonation of the water ligand by the side-chain carboxylate of E252 (Figure 5.37). The side-chain of glutamic acid has a low pK_a (4.5)[419] and would not be expected to be able to deprotonate water (pK_a = 14). However, glutamate side-chains in hydrophobic environments can have higher pK_a values than normal (e.g. 5.2–9.4[419]), and water bound to ferric heme is more acidic than free water (the pK_a can be around 8 or 9).[420-421] For example, the pK_a value for the aqua ligand of sperm whale metmyoglobin is 8.95 and Hayakawa *et al.* reported that the pK_a value for P450st is 8.7.[418, 422]

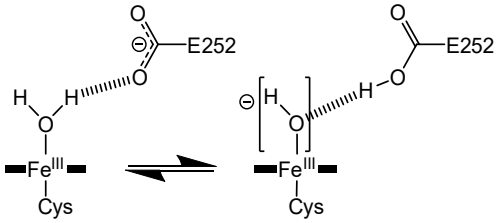

Figure 5.37. Water- and hydroxide-bound forms of the T252E mutant may exist in equilibrium.

Differences were also noticed in the UV-Vis spectra of the T252E mutant and WT enzyme. The Soret band of the substrate-free T252E mutant is red-shifted by 0.5 nm relative to that of the WT enzyme, and its intensity is reduced. The δ-band intensity at ~360 nm also appears to be increased. This red-shift may be due to the T252E mutant potentially having hydroxide as a ligand in a proportion of molecules, which is a stronger field ligand than water.[167] Hayakawa *et al.* reported that elevating the pH of P450st to 10, which they propose generated a hydroxide complex, similarly resulted in a red-shift of the Soret peak and diminished its intensity.[418] It also resulted in an increase in the intensity of the δ-band at 363 nm.[418]

Addition of 4-formyl-, 4-thiophen-3-yl, 4-methylthio-, and 4-ethylthio-benzoic acid to the T252E mutant induced a red-shift of the Soret peak. 4-Formylbenzoic acid red-shifted the Soret

peak by ~2.5 nm, 4-ethylthiobenzoic acid by ~2 nm, 4-methylthiobenzoic acid by ~1.5 nm and 4-thiophen-3-ylbenzoic acid by ~1.0 nm. These substrates induce type I shifts when they bind to WT CYP199A4.[117, 276] These red-shifts may be due to interactions between the substrate heteroatom and the sixth axial ligand to the heme in the T252E mutant, which may alter the ligand field strength.[154] The crystal structures reveal that there is a stronger interaction between the sulfur of 4-ethylthiobenzoic acid and the oxygen ligand than there is between the oxygen ligand and sulfur of 4-methylthiobenzoic acid or 4-thiophen-3-ylbenzoic acid. (The sulfur-oxygen distances are 3.1, 3.3 and 4.3 Å, respectively.) This may rationalise the larger red-shift induced by 4-ethylthiobenzoic acid. Veratric acid, 4-vinyl-, 4-benzyl- and 4-phenyl-benzoic acid induced small (0.5 nm) red-shifts. This red-shift may be due to the H_2O/OH^- ratio or Fe–O interactions being altered by substrate binding.

Substrate-free T252E$_{CYP199A4}$ was found to be rapidly bleached by exposure to H_2O_2, while 4-methoxybenzoate-bound T252E$_{CYP199A4}$ was bleached at a slower rate. It has been proposed that heme bleaching in peroxygenases, for example *Aae*UPO, occurs via reaction of Cpd I with hydrogen peroxide to generate Cpd III (Figure 5.38).[416, 423-424] Cpd III is then thought to react with H_2O_2 to generate the destructive hydroxyl radical, which may oxidise heme to yield α-meso-hydroxyheme.[424] This can subsequently be converted into verdoheme and biliverdin, releasing iron.[423-424] This mechanism, which involves reactions with multiple H_2O_2 molecules, explains why bleaching occurs more rapidly when the P450 is exposed to high concentrations of H_2O_2.[416] When substrate was present, the rate of heme bleaching of the T252E$_{CYP199A4}$ mutant was dramatically reduced compared to when no substrate was present. Substrate presumably protects the heme from bleaching by excluding excess H_2O_2 from the active site and by reacting with Cpd I before other reactions can destroy the heme. We also noticed that heme bleaching was faster for substrate-free T252E$_{CYP199A4}$ than for substrate-free WT CYP199A4. It may be that the T252E mutant is bleached more rapidly because it generates Cpd I more efficiently than the WT enzyme. During H_2O_2-driven reactions, inactivation of the P450 may also be caused by oxidation of the crucial cysteine ligand to the heme.[425]

When a large excess of H_2O_2 (50 mM) was added to the T252E mutant at the start of the reaction, the P450 remained active for up to ~4 h. Supplying low levels of H_2O_2 to the T252E mutant and replenishing the H_2O_2 as it is consumed would be expected to extend the lifetime of the enzyme and lead to greater product yields.[264-265, 426] This could be accomplished by fusing the T252E$_{CYP199A4}$ enzyme to a H_2O_2-generating enzyme such as alditol oxidase.[264] Freakley *et al.*[426] demonstrated that peroxygenase reactions could be driven by the low levels of H_2O_2 produced *in situ* by an AuPd catalyst from H_2 and O_2, and other methods of *in situ* H_2O_2 production have been described.[263, 265-266, 270, 272-273, 427-428]

The identity of the active oxidant or oxidants which participate in different P450 reactions (e.g. sulfoxidation and epoxidation) could be investigated using the T252E mutant (Chapter 6). *O*-Dealkylation and hydroxylation are believed to be mediated by Cpd I, but Cpd 0 has been proposed

to mediate epoxidation and sulfoxidation.[94] The Fe^{III}–H_2O_2 species is also postulated to participate in sulfoxidation.[118, 429] The reaction which WT CYP199A4 performs at the fastest rate is *O*-demethylation of 4-methoxybenzoic acid. It performs sulfoxidation less rapidly, and epoxidation and aldehyde oxidation at a significantly slower rate. If the T252E mutant were to exhibit higher activity towards sulfoxidation or epoxidation, it would imply that alternative oxidants may be involved as they would be more prevalent in the T252E catalytic cycle than in the natural catalytic cycle (e.g. the Fe^{III}–H_2O_2 species). If differences are observed between the activities of the T252E mutant and the WT enzyme, we would not expect these to simply be due to the substrates having different orientations in the active site of the mutant as the crystal structures showed that the substrate orientation is only minimally altered by the mutation.

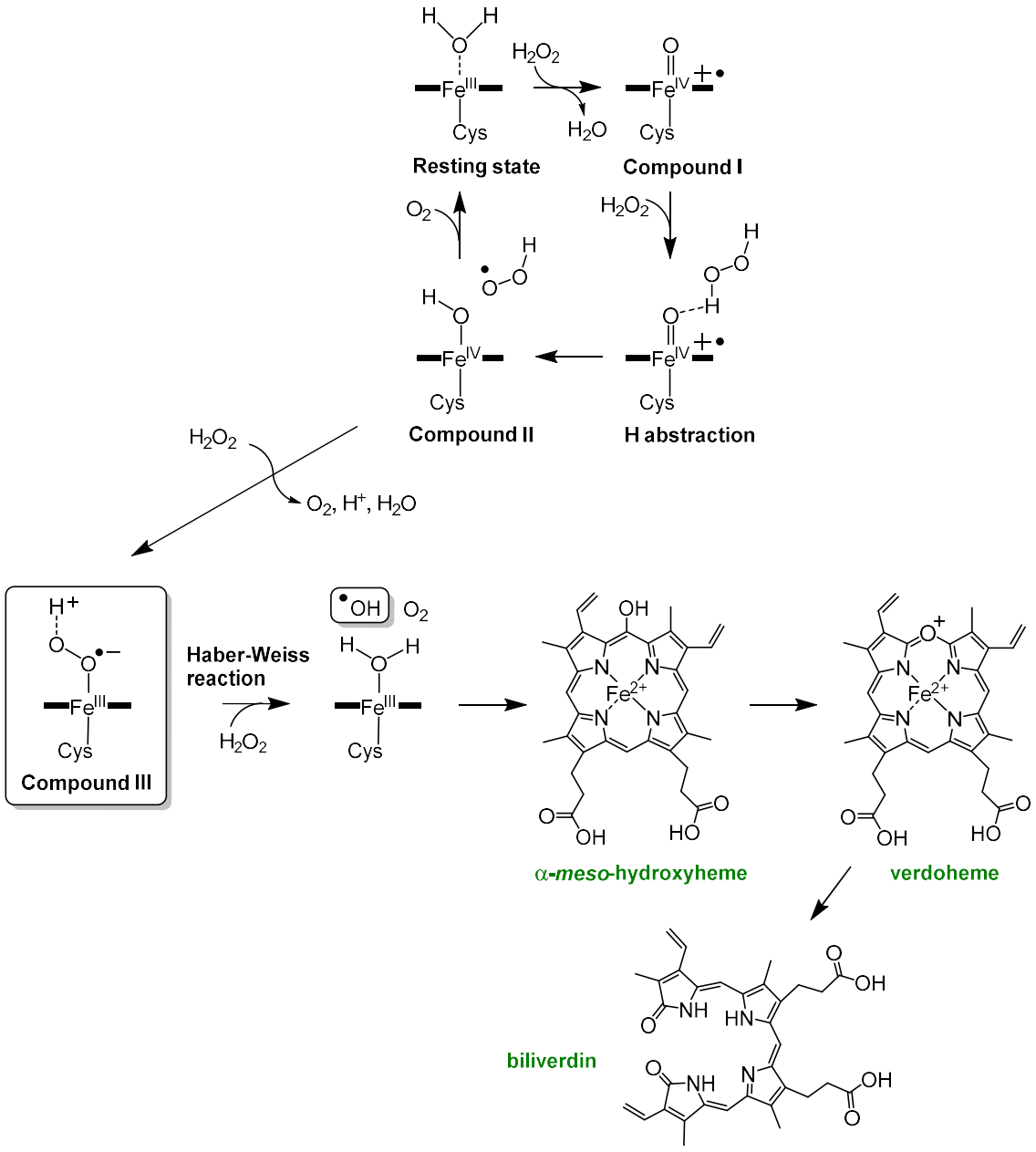

Figure 5.38. Proposed mechanism for heme bleaching by H_2O_2.[423-424]

Chapter 6

Investigation into the active oxidants in sulfoxidation, aldehyde oxidation, epoxidation and alkyne oxidation

6.1 Introduction

In the native (NADH/O_2-driven) P450 catalytic cycle, two protons sourced from the surrounding solvent are needed to generate the active species Cpd I.[98] After O_2 binds to the reduced heme, a second electron is transferred. The resulting ferric-peroxo anion is protonated on the distal oxygen, giving the ferric-hydroperoxo intermediate (Cpd 0).[98] Protonation again on the distal oxygen ruptures the O–O bond, generating Cpd I.[98] Correct, timely delivery of these two protons is controlled by a conserved acid-alcohol pair of residues: T252 and D251 in $P450_{cam}$ and CYP199A4.[129] Mutation of the conserved acid-alcohol pair impairs the enzyme's ability to form Cpd I. $P450_{cam}$ hydroxylates camphor to give 5-*exo*-hydroxycamphor with ~100% coupling efficiency, but the T252 → A mutant instead almost exclusively generates H_2O_2.[130] Although the T252A mutant is nearly completely uncoupled, the NADH consumption rate is only slightly diminished.[129-131, 430] It has been inferred that the hydrogen bond between Cpd 0 and the conserved threonine in the WT enzyme (Figure 6.1a) encourages protonation on the distal oxygen by increasing its proton affinity.[110, 129] If T252 is mutated to alanine, conversion of Cpd 0 into Cpd I is interrupted, leading to accumulation of Cpd 0 and ultimately incorrect protonation on the proximal oxygen with release of H_2O_2.[134] Accelerated epoxidation by the T → A mutant of CYP2E1 relative to the WT enzyme was interpreted as evidence that Cpd 0 is active in olefin epoxidation.[33, 121] It was also found that the T252A mutant of $P450_{cam}$ catalysed epoxidation (albeit less efficiently than the WT enzyme), strengthening the argument that Cpd 0 can mediate epoxidation.[33] Despite this, Cpd 0's involvement in epoxidation is disputed.[203, 212-213]

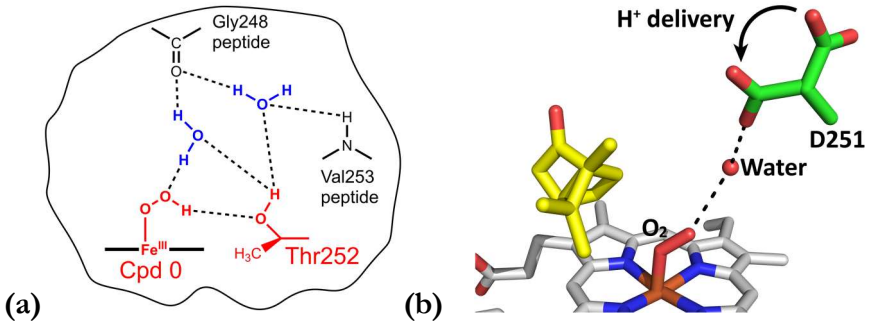

Figure 6.1. **(a)** Thr252 accepts a hydrogen bond from Cpd 0, which encourages protonation on the distal oxygen to generate Cpd I.[110] **(b)** Asp251 is believed to rotate in and out of the active site, delivering protons into the active site.[110]

On the other hand, mutation of the conserved aspartate residue (D251) of $P450_{cam}$ to asparagine (N) reduced the rate of camphor oxidation by a factor of 100 without reducing the

coupling efficiency.[133] Equivalent results were reported for the D → N mutant of $P450_{cin}$.[430] The role of this acidic residue is to deliver the protons required for oxygen activation (Figure 6.1b).[110] Thus, mutation of D251 severely reduces the rate of the protonation steps, extending the lifetime of the ferric-peroxo anion.[430-432]

The threonine-to-alanine and aspartate-to-asparagine mutants can in theory be used to probe whether alternative oxidants to Cpd I participate in P450 reactions.[94, 123-124, 430] The threonine-to-alanine mutation is assumed to inhibit Cpd I formation and increase the persistence of Cpd 0,[33, 134] while the aspartate-to-asparagine mutation delays the protonation steps,[129] increasing the lifetime of the nucleophilic ferric-peroxo anion.[110, 133, 430] Thus, the WT enzyme, in which Cpd I is rapidly generated[123], catalyses Cpd I-mediated reactions such as C-H hydroxylation[103] efficiently. In contrast, the T252A mutant would be expected to have low activity towards reactions mediated solely by Cpd I.[123] However, it may display *increased* activity towards Cpd 0-mediated reactions, given that Cpd 0 is now more abundant.[33, 123] Similarly, the D251N mutant would be predicted to efficiently catalyse reactions mediated by the nucleophilic ferric-peroxo anion.[430] Aldehyde oxidation to the corresponding carboxylic acid is one reaction that is plausibly mediated by the ferric-peroxo anion.[206]

Chao[276] employed this strategy to investigate the identity of the active oxidant(s) involved in different CYP199A4-catalysed reactions (Figure 6.2). Whereas the T252A mutant of $P450_{cam}$ generates negligible amounts of 5-*exo*-hydroxycamphor and converts the majority of O_2 consumed (83%) into H_2O_2,[130] the T252A mutant of CYP199A4 displayed higher coupling efficiency than $P450_{cam}$ and produced less H_2O_2. The T252A mutant of CYP199A4 demethylated 4-methoxybenzoic acid at a rate of 570 min^{-1} (half that of the WT enzyme) with a coupling efficiency of 68%; only 31% of the reducing equivalents were channelled into H_2O_2 formation.[276] Thus, mutation of the conserved threonine must have less of a deleterious effect on CYP199A4's ability to form Cpd I than $P450_{cam}$'s.[276-277] $T252A_{CYP199A4}$ must still generate Cpd I, although less efficiently than the WT enzyme. If the T → A mutant generated no Cpd I, this would be preferable because it would allow us to more readily distinguish between reactions mediated by Cpd I and those mediated by Cpd 0. The reduced ability of the T252A mutant to catalyse *O*-demethylation is consistent with Cpd I mediating this reaction.[276] Note that the T252A mutant of CYP199A4 generally had lower coupling efficiency than the WT enzyme.

As expected, the D251N mutant of CYP199A4 had dramatically reduced NADH consumption and product formation rates (and low coupling efficiency), attributed to slow proton transfer.[277] Its low activity towards reactions such as hydroxylation, *O*-demethylation of 4-methoxybenzoic acid and epoxidation of 4-vinylbenzoic acid implies a lack of reactivity of the ferric-peroxo anion in these types of reactions, but its high activity towards aldehyde oxidation suggested the ferric-peroxo anion's involvement in this reaction.[276] Oxidation of 4-formylbenzoic acid to the corresponding carboxylic acid by the D251N mutant proceeded with high coupling efficiency (72%).[276]

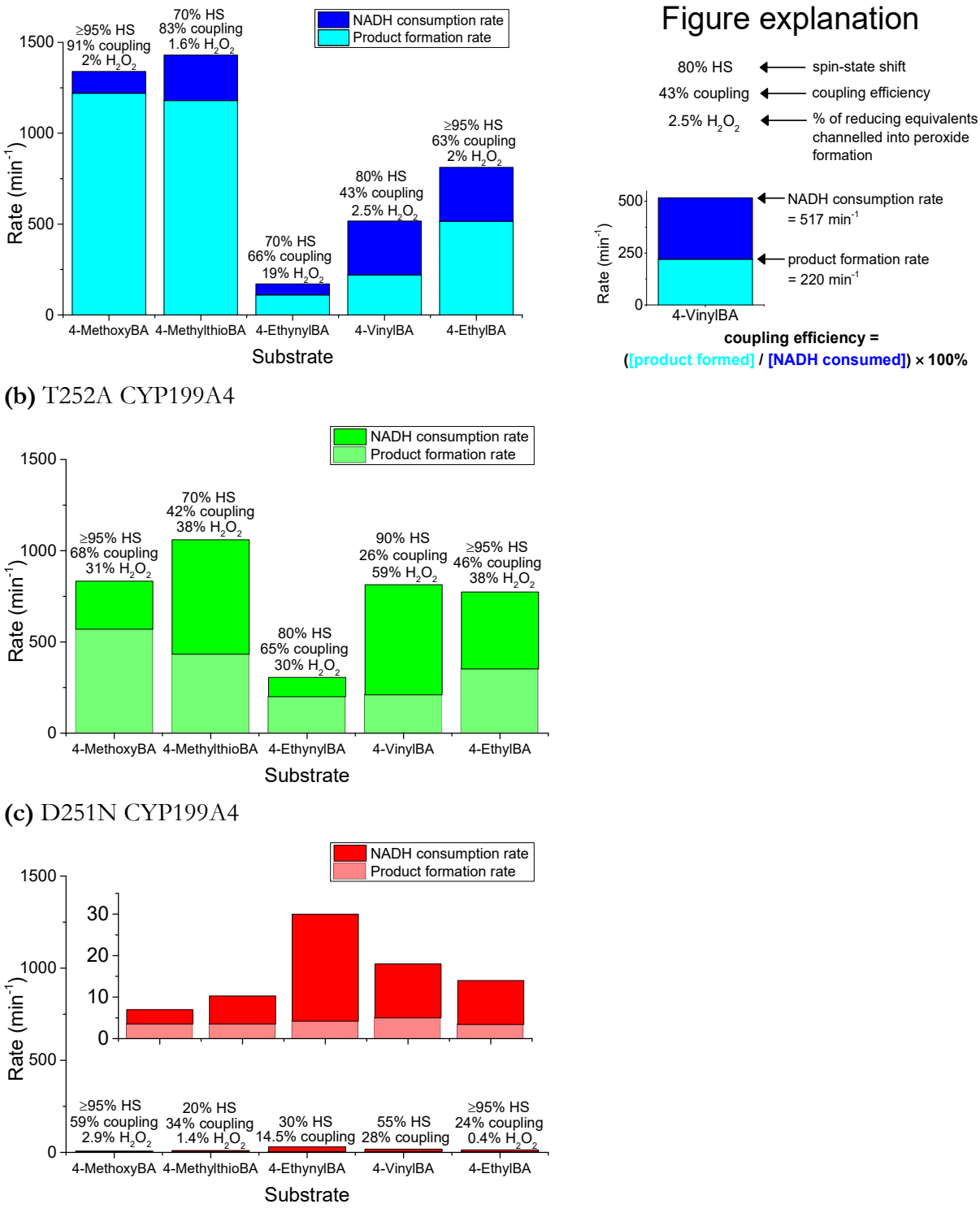

Figure 6.2. Activity of **(a)** WT CYP199A4 and the **(b)** T252A and **(c)** D251N mutants towards different P450 reactions. These figures were adapted from Coleman and Chao.[276-277] For each substrate, the spin-state shift (% HS), coupling efficiency (%) and percentage of reducing equivalents that were channelled into H_2O_2 production are given. The bar graphs give the product formation rate and NADH consumption rate.

The coupling efficiency is the percentage of NADH consumed by the P450 that was channelled into product formation (not wasted through unproductive side reactions such as H_2O_2 formation). When the coupling efficiency is 100%, the product formation rate is equal to the NADH consumption rate. When the coupling efficiency is less than 100%, product formation is slower than NADH consumption. Note that the T252A mutant has generally lower coupling efficiency, whereas the D251N mutant has both lower NADH consumption rates and lower coupling efficiency.

The Fe(III)–H_2O_2 complex is an additional intermediate that has been proposed to mediate certain P450 reactions.[94, 118] Shaik has reported that the Fe(III)–H_2O_2 complex would be a sluggish C-H hydroxylation catalyst[433] but should be eminently capable of catalysing sulfoxidation.[118] In fact, it should catalyse sulfoxidation more rapidly than it can transform into Cpd I.[118] Cpd 0, proposed by some to be the second oxidant in sulfoxidation, was calculated to be a weak oxidant.[94, 118, 123-124, 203, 429] The Fe(III)–H_2O_2 intermediate must be generated during H_2O_2-driven reactions (by binding of H_2O_2 to ferric iron)[256, 434] but could only be formed during the native NADH/O_2-driven catalytic cycle by mistake (when incorrect protonation on the proximal oxygen of Cpd 0 instead of the distal oxygen occurs). By performing H_2O_2-driven reactions with the T252E mutant, we can assess whether the Fe(III)–H_2O_2 intermediate is likely to participate in certain P450 reactions. Our assumption is that reactions which can be effectively mediated by the Fe(III)–H_2O_2 species may be more efficiently catalysed by the T252E mutant than those requiring Cpd I. (The T252E mutant is an unnatural enzyme that has not evolved to rapidly generate Cpd I.)

The reactions that will be investigated are *O*-demethylation of 4-methoxybenzoic acid, hydroxylation/desaturation of 4-ethylbenzoic acid, epoxidation of 4-vinylbenzoic acid, sulfoxidation of 4-(m)ethylthiobenzoic acid, and oxidation of 4-formyl- and 4-ethynyl-benzoic acid (Figure 6.3). By comparing the activity of WT CYP199A4 and the T252E, D251N and T252A mutants towards these different substrates in NADH-supported and H_2O_2-driven reactions, we can evaluate whether multiple oxidants participate in P450 reactions.

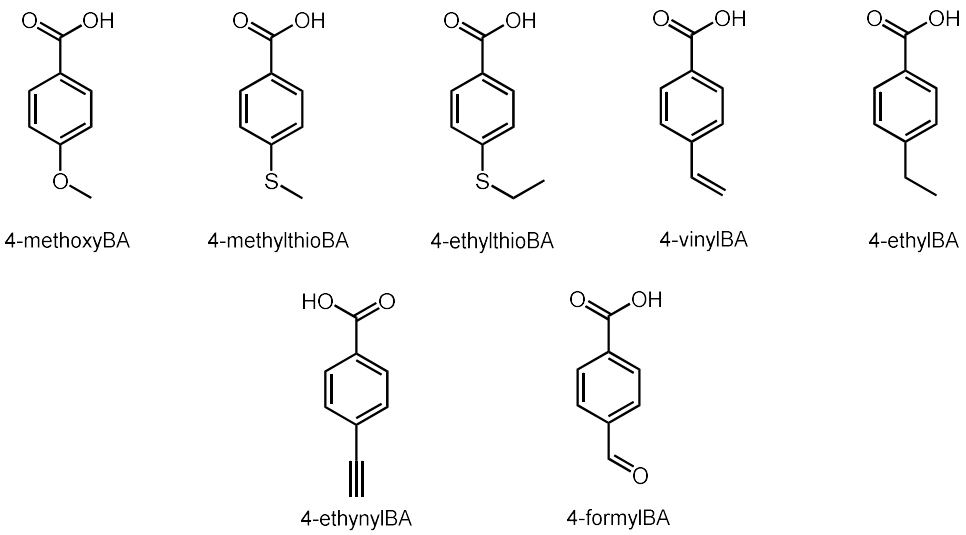

Figure 6.3. *Para*-substituted benzoic acid substrates investigated with WT CYP199A4 and the T252E, D251N and T252A variants in this chapter in NADH- and H_2O_2-supported reactions.

6.2 Results

6.2.1 NADH-supported reactions of the T252E mutant with *para*-substituted benzoic acids with alternative functional groups

We investigated the T252E mutant's ability to perform reactions other than hydroxylation/*O*-demethylation using NADH/O_2 and compared its activity to that of the WT enzyme and T252A and D251N mutants (Table 6.1). The rate of NADH consumption by the T252E mutant with each *para*-substituted benzoic acid tested was comparable to the leak rate (Figure D1).

The T252E mutant displayed marginally higher activity towards 4-methylthiobenzoic acid than towards 4-methoxybenzoic acid; the coupling efficiency was 15% and the product formation rate 1 min^{-1}. By way of contrast, the rate of product formation by WT CYP199A4 is ~1260 min^{-1}. 4-Methylsulfinylbenzoic acid was the sole product; the levels of dealkylation product (4-mercaptobenzoic acid) were negligible and no further oxidation metabolites were detected (Figures 6.4 and D2, Table D1). The T252E mutant's activity towards 4-ethylthiobenzoic acid was lower. The reaction was 96% uncoupled and only minor quantities of 4-ethylsulfinylbenzoic acid were generated at a rate of 0.2 min^{-1} (Figures 6.5 and D3). For comparison, the product formation rate by the WT enzyme is 138 ± 0.9 min^{-1}.

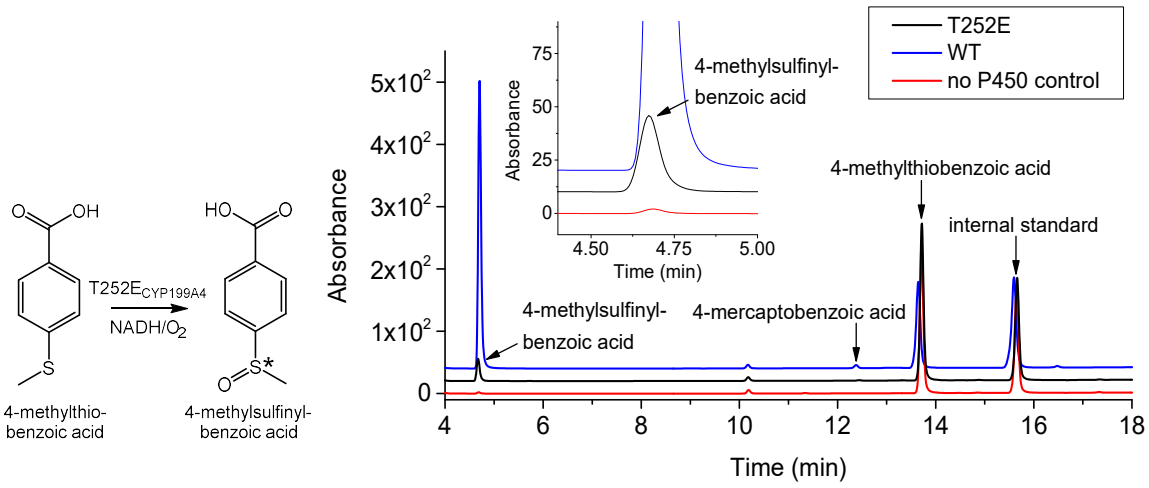

Figure 6.4. HPLC analysis of the NADH/O_2-driven oxidation of 4-methylthiobenzoic acid by T252E$_{CYP199A4}$ (**black**) and WT CYP199A4 (**blue**). In **red** is a control reaction omitting the P450. 4-Methylsulfinylbenzoic acid elutes at 4.7 min and 4-mercaptobenzoic acid at 12.5 min. The substrate appears at 13.6 min. Negligible levels of 4-mercaptobenzoic acid were detected. No sulfone was detected.
Gradient: 20-95% AcCN in H_2O with 0.1% TFA. Detection wavelength: 254 nm.

Table 6.1. Binding and *in vitro* NADH turnover data for T252E CYP199A4 with benzoic acid substrates. For comparison, data for the WT CYP199A4 and the D251N and T252A mutants is also given. Data for the WT enzyme is similar to that previously reported by Chao[276] and Coleman[277]. Data taken from others[276-277] is shaded, while my data appears in unshaded squares.

Substrate	% HS	K_d (μM)	NADH (min^{-1})	PFR (min^{-1})	Coupling (%)	% H_2O_2
4-methoxyBA$_{WT}$	>95	0.28 ± 0.01	1580 ± 20	1440 ± 30	91 ± 1	2 ± 0.2
4-methoxyBA$_{T252A}$	>95	0.22 ± 0.02	833 ± 8	570 ± 56	68 ± 5	31 ± 4
4-methoxyBA$_{D251N}$	>95	0.17 ± 0.01	7 ± 0.8	3.5 ± 0.9	59 ± 3	-
4-methoxyBA$_{T252E}$	5%	0.4 ± 0.1	9 ± 0.5	0.8 ± 0.1	10 ± 1	2 ± 1
4-methylthioBA$_{WT}$	70	2.3 ± 0.3	1260 ± 20	~1260	~100	1.6 ± 0.4
4-methylthioBA$_{T252A}$	70	1.4 ± 0.1	1060 ± 18	433 ± 29	42 ± 2	38 ± 1
4-methylthioBA$_{D251N}$	20	0.83 ± 0.08	10.3 ± 0.3	3.5 ± 0.1	34 ± 2	1.4 ± 0.1
4-methylthioBA$_{T252E}$	419→420.5 nm	0.1 ± 0.1	7 ± 0.4	1 ± 0.1	15 ± 1	2 ± 1
4-ethylBA$_{WT}$	≥95	0.34 ± 0.02	911 ± 9	810 ± 50	89 ± 4	2.0 ± 0.1
4-ethylBA$_{T252A}$	≥95	0.15 ± 0.01	774 ± 12	352 ± 52	46 ± 7	38 ± 1
4-ethylBA$_{D251N}$	≥95	0.08 ± 0.03	14 ± 4	3.4 ± 0.7	24 ± 1	0.4 ± 0.1
4-ethylBA$_{T252E}$	<5%	0.7 ± 0.2	8 ± 0.2	0.5 ± 0.03	6 ± 0.3	1 ± 0.6
4-vinylBA$_{WT}$	80	0.46 ± 0.03	550 ± 10	370 ± 60	66 ± 9	2.5 ± 0.4
4-vinylBA$_{T252A}$	90	0.30 ± 0.02	590 ± 20	180 ± 10	30 ± 1	60 ± 2
4-vinylBA$_{D251N}$	55	0.06 ± 0.01	16.5 ± 0.5	6.1 ± 0.1	37 ± 1	-
4-vinylBA$_{T252E}$	419.5→420 nm	0.02 ± 0.07	5 ± 0.2	0.3 ± 0.03	5 ± 1	2 ± 1
4-formylBA$_{WT}$	25	48 ± 2	134 ± 1	110 ± 2	83 ± 0.5	1.5 ± 0.3
4-formylBA$_{T252A}$	25	54 ± 2	56.3 ± 0.3	31 ± 2	54 ± 3	4.5 ± 0.3
4-formylBA$_{D251N}$	10	10.8 ± 0.4	25 ± 0.8	18 ± 1	72 ± 4	-
4-formylBA$_{T252E}$	419→421.5	0.5 ± 0.1	6 ± 0.2	0.06 ± 0.02	1 ± 0.2	2 ± 0.1
4-ethynylBA$_{WT}$	70	1.2 ± 0.3	230 ± 10	194 ± 7	83 ± 2	19 ± 2
4-ethynylBA$_{T252A}$	80	1.5 ± 0.1	306 ± 5	200 ± 15	65 ± 4	30 ± 2
4-ethynylBA$_{D251N}$	30	0.7 ± 0.1	30 ± 0.7	4.2 ± 0.2	14.5 ± 0.1	-
4-ethynylBA$_{T252E}$	-	-	16 ± 1[a]	0	0	42 ± 4
4-ethylthioBA$_{WT}$	10% [b]	0.99 ± 0.05	139 ± 0.4	138 ± 0.9	99.5 ± 0.3	-
4-ethylthioBA$_{T252A}$	35%	0.25 ± 0.05	441 ± 8	164 ± 7	37 ± 1	-
4-ethylthioBA$_{D251N}$	*	0.12 ± 0.25	7.2 ± 0.2	1.1 ± 0.1	15.3 ± 0.3	-
4-ethylthioBA$_{T252E}$	419→421 nm	0.02 ± 0.06	6 ± 1	0.2 ± 0.02	4 ± 1	1 ± 0.1

[a] The NADH consumption rate with 4-ethynylbenzoic acid was the same both in the presence and absence of the T252E enzyme.

[b] Addition of 4-ethylthiobenzoic acid to WT CYP199A4 induced a 10% type I shift to HS but also red-shifted the Soret band from 418 → 419 nm.[117]

* Addition of 4-ethylthiobenzoic acid to D251N$_{CYP199A4}$ failed to induce any spin-state shift to HS (~0% HS). However, this substrate red-shifted the Soret band from 420 → 421 nm and induced an unusual difference spectrum which may be due to an interaction between the sulfur and heme iron.

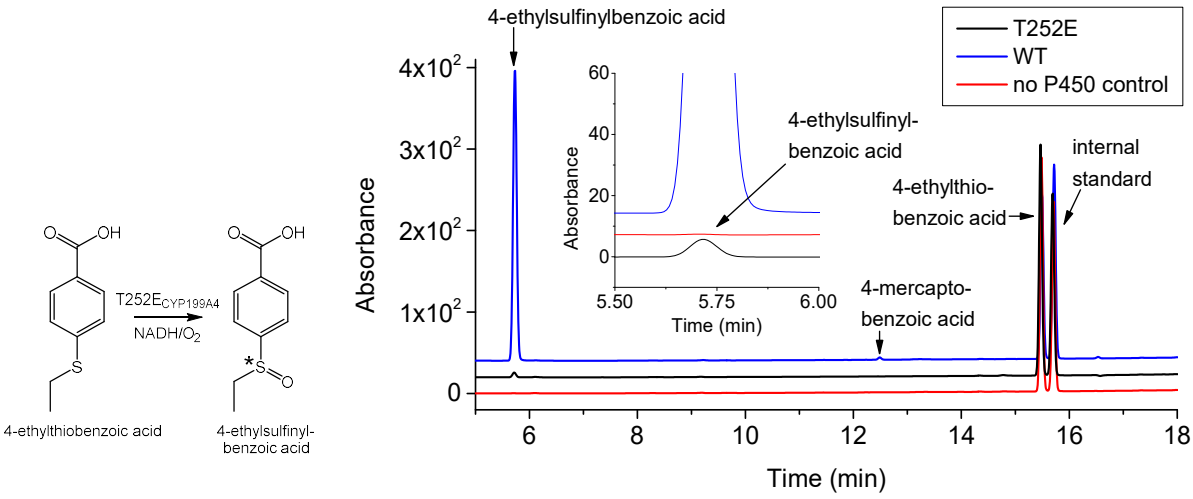

Figure 6.5. HPLC analysis of the NADH/O_2-driven oxidation of 4-ethylthiobenzoic acid by T252E$_{CYP199A4}$ (**black**) and WT CYP199A4 (**blue**). In **red** is a control reaction omitting the P450. 4-Ethylsulfinylbenzoic acid appears at 5.7 min and the substrate at 15.5 min. Gradient: 20-95% AcCN in H_2O with 0.1% TFA. Detection wavelength: 254 nm. No 4-mercaptobenzoic acid was detected in the T252E turnover. In the absence of an authentic sample of 4-ethylsulfinylbenzoic acid for calibration, 4-methylsulfinylbenzoic acid was used.

Although *in vitro* NADH turnover data for WT CYP199A4 with 4-ethylthiobenzoic acid has been previously reported by Coleman,[117] the activity of the T252A and D251N mutants towards this substrate has not. We therefore performed binding studies and NADH turnovers with these mutants. Binding of 4-ethylthiobenzoic acid to D251N$_{CYP199A4}$ did not induce any discernible shift to HS but resulted in a small red-shift of the Soret peak (from 420 nm to 421 nm) (Figure 6.6a). On the other hand, binding of the same substrate to the T252A mutant induced a 35% shift to HS and there was no red-shift in the Soret band position (Figure 6.6b). By way of contrast, 4-ethylthiobenzoic acid is reported to only induce a 10% shift to HS when it binds to the WT enzyme.[117] 4-Ethylthiobenzoic acid was found to bind more tightly to the T252A mutant than to the WT enzyme (K_d = 0.25 ± 0.05 μM *vs.* 0.99 μM[117]) (Figure 6.6). It also bound tightly to D251N$_{CYP199A4}$, but due to the minimal spin-state shift the binding constant could not be accurately determined (K_d ≈ 0.12 ± 0.25 μM). The unusual difference spectrum that resulted when 4-ethylthiobenzoic acid was added to the D251N mutant (Figure 6.6c) may be due to an interaction between the sulfur of the substrate and the heme iron[435] and resembles the spectrum obtained by addition of thioanisole to P450$_{cam}$ (Figures D4 and D5, Table D2). Our observation that 4-ethylthiobenzoic acid interacts differently with the D251N active site is in line with previous observations that the D251 → N mutation affects substrate binding.[276-277, 436]

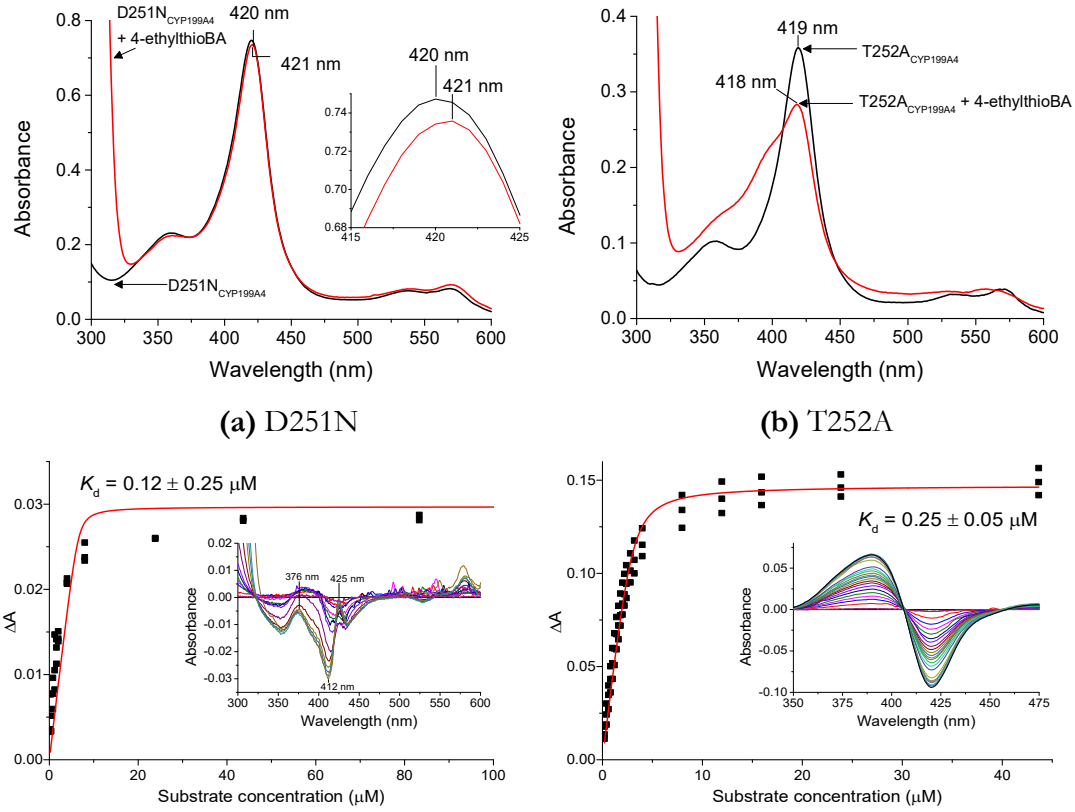

Figure 6.6. Spin-state shifts of **(a)** D251N$_{CYP199A4}$ and **(b)** T252A$_{CYP199A4}$ induced by 4-ethylthiobenzoic acid. UV-Vis titrations to determine the dissociation constant of **(c)** D251N$_{CYP199A4}$ and **(d)** T252A$_{CYP199A4}$ with 4-ethylthiobenzoic acid. The enzyme concentration used and the peak and trough wavelengths are provided under each graph. The data were fitted to the Morrison tight-binding equation. As there is no prominent peak at 390 nm in the D251N difference spectrum, ΔA was taken to be A_{490}-A_{412} (baseline - trough).

In line with the greater spin-state shift induced by binding of 4-ethylthiobenzoic acid to T252A$_{CYP199A4}$ compared to the WT enzyme (35 *vs.* 10%), the NADH consumption rate was ~3-fold faster for the T252A mutant (441 *vs.* 139 min^{-1}) (Figure D6). Although the coupling efficiency was substantially lower for the T252A mutant than for the WT enzyme (37 *vs.* 99.5%), the T252A mutant performed sulfoxidation of 4-ethylthiobenzoic acid faster (164 *vs.* 138 min^{-1}) (Figure D7). Minimal 4-mercaptobenzoic acid was detected (~2% of the product in the T252A turnover and ~0.7% of the product in the WT turnover). Contrastingly, the NADH consumption rate by the D251N mutant was only 7.2 min^{-1} and coupling efficiency 15.3%, resulting in slow formation of the sulfoxide (PFR = 1.1 min^{-1}). No dealkylation product was detected in the D251N reaction. The sulfoxide product was subsequently sent to James de Voss at the University of Queensland for determination of the enantioselectivity of these reactions (Section 6.2.4).

T252E$_{CYP199A4}$ exhibited even lower activity towards 4-formylbenzoic acid; the reaction was ~99% uncoupled (Figures 6.7 and D8). No product was generated by T252E$_{CYP199A4}$ with 4-ethynylbenzoic acid (Figures 6.8 and D9).

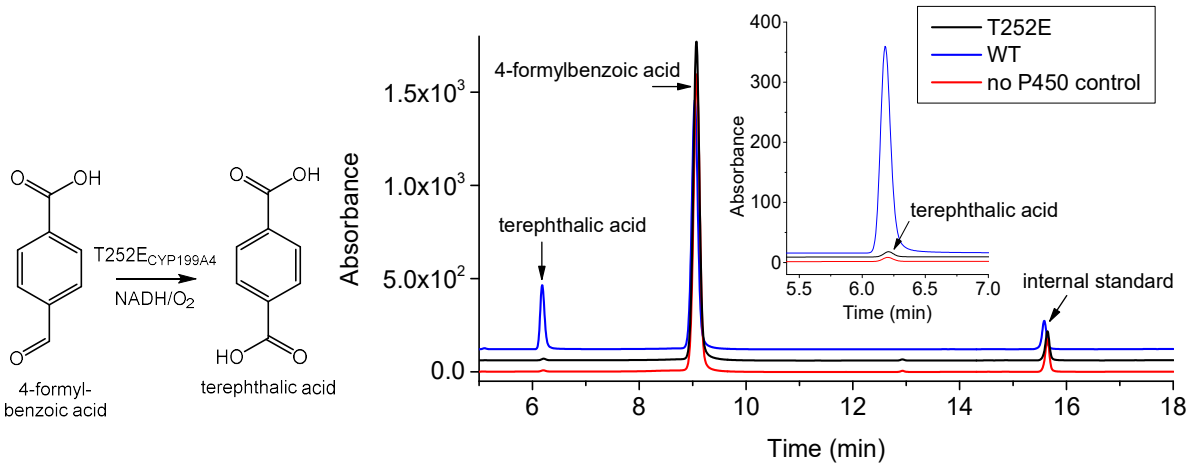

Figure 6.7. HPLC analysis of the NADH/O_2-driven oxidation of 4-formylbenzoic acid by T252E$_{CYP199A4}$ (**black**) and WT CYP199A4 (**blue**). In **red** is a control reaction omitting the P450. Terephthalic acid elutes at 6.2 min while the substrate appears at 9.1 min. Gradient: 20-95% AcCN in H_2O with 0.1% TFA. Detection wavelength: 254 nm.

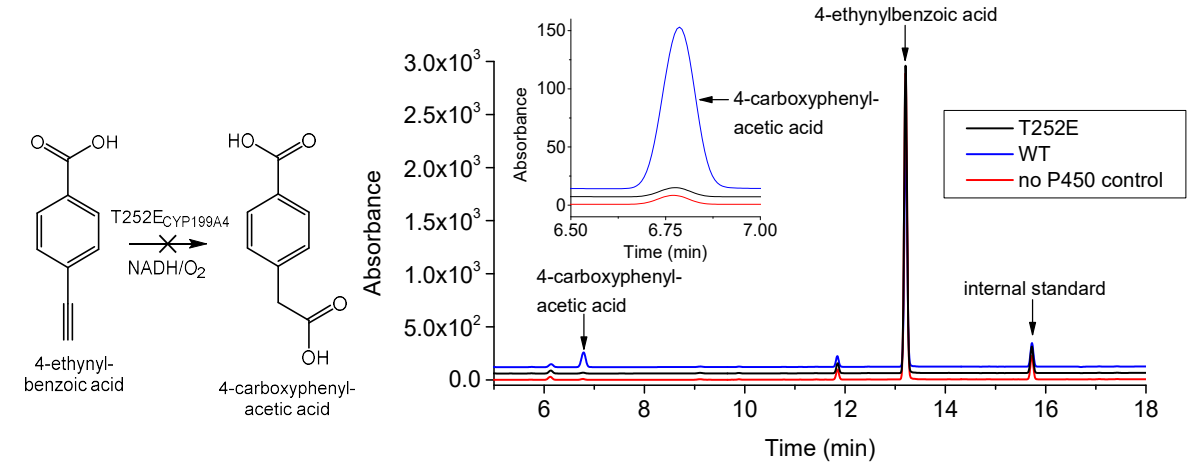

Figure 6.8. HPLC analysis of the NADH/O_2-driven oxidation of 4-ethynylbenzoic acid by T252E$_{CYP199A4}$ (**black**) and WT CYP199A4 (**blue**). In **red** is a control reaction omitting the P450. 4-Carboxyphenylacetic acid elutes at 6.8 min and the substrate appears at 13.2 min. Gradient: 20-95% AcCN in H_2O with 0.1% TFA. Detection wavelength: 254 nm.

The T252E variant did, however, afford low levels of product with 4-vinylbenzoic acid (Figures 6.9 and D10). Chao[276] showed that the WT enzyme converts 4-vinylbenzoic acid into predominantly 4-oxiran-2-ylbenzoic acid. Minor amounts of the aldehyde side product 4-(2-oxoethyl)benzoic acid are also observed (Figure D11). This aldehyde rearrangement product is thought to arise from a cationic intermediate (Figure D12).[437] The T252E$_{CYP199A4}$ reaction with 4-vinylbenzoic acid gave small amounts of a single detectable product, which was confirmed to be the epoxide by co-elution with chemically synthesised 4-oxiran-2-ylbenzoic acid (Figures D10 and D13). The coupling efficiency was estimated to be 5%, and the product formation rate 0.3 min^{-1}. Thus, the data for the T252E mutant reaffirms that this mutant is essentially incapable of utilising NADH/O_2 to perform catalysis.

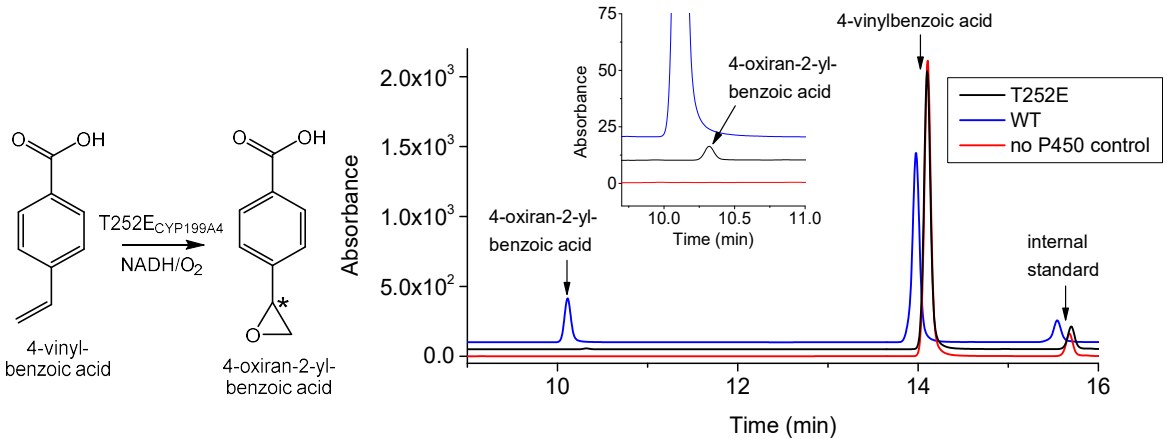

Figure 6.9. HPLC analysis of the NADH/O_2-driven oxidation of 4-vinylbenzoic acid by T252E$_{CYP199A4}$ (**black**) and WT CYP199A4 (**blue**). In **red** is a control reaction omitting the P450. 4-Oxiran-2-ylbenzoic acid elutes at 10.4 min while the substrate appears at 14.1 min. Gradient: 20-95% AcCN in H_2O with 0.1% TFA. Detection wavelength: 254 nm. The identity of the product was confirmed by co-elution with chemically synthesised epoxide. We attempted to obtain 100% pure epoxide for calibration by using preparative-scale HPLC to purify the synthesised epoxide. However, this failed due to partial ring-opening of the epoxide in the acidic solvent (Figure D14). As pure 4-oxiran-2-ylbenzoic acid could not be obtained, the closest available compound, 4-(1-hydroxyethyl)benzoic acid, was instead used for calibration.

Although Chao[276] reported *in vitro* NADH turnover data for WT CYP199A4 and the D251N and T252A mutants with 4-vinylbenzoic acid, the exact proportions of the epoxide and aldehyde side product were not reported. Reactions with these mutants were repeated and comparable NADH consumption and product formation rates to those previously reported were obtained (Table 6.1, Figure 6.10). WT CYP199A4 displayed the highest product formation rate, 370 min^{-1}. Although the T252A mutant consumed NADH more rapidly than the WT enzyme, the T252A mutant channelled most of the reducing equivalents (60 ± 2%) into H_2O_2 production. The faster NADH consumption rate by the T252A mutant may be explained by the larger spin-state shift induced by 4-vinylbenzoic acid when it binds to T252A$_{CYP199A4}$ than to the WT enzyme.[276] The T252A mutant had the lowest coupling efficiency (30 ± 1%), contrary to what might be expected if Cpd 0 was highly active towards olefin epoxidation. The D251N mutant and WT enzyme displayed higher coupling efficiency (37 ± 1 and 66 ± 9%), in agreement with Chao's data.[276] If more than a single intermediate in the P450 catalytic cycle was involved in epoxidation, we might expect the product distribution to vary for the D251N, T252A and WT isoforms. Thus, we determined the relative proportions of epoxide and aldehyde side products (Table D3 and Figure 6.11). It was assumed that the GC-MS detector response was identical for both compounds. For all three isoforms, the measured product distribution was similar: WT, 96% epoxide, 4% aldehyde; D251N, 95% epoxide, 5% aldehyde; T252A, 95% epoxide, 5% aldehyde. This may imply the involvement of a single active oxidant.

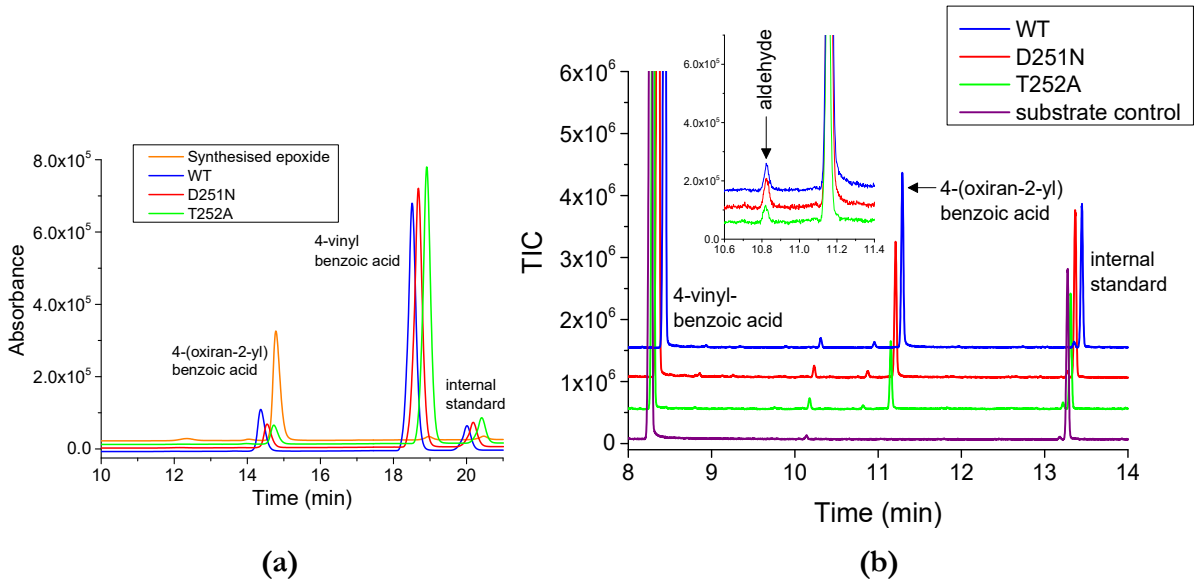

(a) **(b)**

Figure 6.10. **(a)** HPLC and **(b)** GC-MS analysis of the 4-vinylbenzoic acid reactions. The WT turnover is in **blue**, the D251N turnover is in **red**, the T252A turnover is in **green** and the substrate control is in **purple**. GC retention times are: 4-vinylbenzoic acid, 8.3 min; aldehyde rearrangement product, 10.8 min; epoxide, 11.2 min; internal standard, 13.3 min. GC-MS analysis was performed using a Shimadzu GCMS-QP2010S gas chromatograph-mass spectrometer.

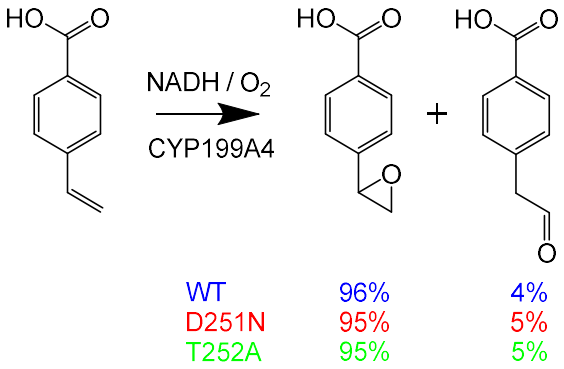

Figure 6.11. CYP199A4 converts 4-vinylbenzoic acid into the corresponding epoxide and minor amounts of the aldehyde rearrangement product.

In summary, in NADH-supported reactions, T252E$_{CYP199A4}$ had minimal or no activity towards *para*-substituted benzoic acids with formyl, (m)ethylthio, vinyl or ethynyl functional groups. Its activity was marginally higher towards 4-methylthiobenzoic acid than 4-methoxybenzoic acid, whereas it had no detectable activity towards 4-ethynylbenzoic acid. Our results for the T252A variant do no provide clear evidence that Cpd 0 contributes significantly to epoxidation or sulfoxidation. The T → A mutation reduced the coupling efficiency of these reactions by more than a factor of 2. Cpd I appears to be the most active oxidant in these reactions.

6.2.2 Comparison of the T252E mutant's activity towards different P450 oxidation reactions utilising the H_2O_2-shunt pathway

In Chapter 5, $T252E_{CYP199A4}$ was shown to catalyse *O*-demethylation using H_2O_2 as a surrogate oxygen donor, but its activity towards other P450 reaction types (epoxidation, sulfoxidation, alkyne oxidation and aldehyde oxidation) was not explored. Initially, 20-minute reactions were performed to assess the T252E mutant's ability to catalyse these different types of P450 reactions using H_2O_2 (50 mM) as a surrogate oxygen donor (Table 6.2). Cpd I would be required for hydroxylation/desaturation and *O*-demethylation to occur, but other intermediates which may be more prevalent in these H_2O_2-driven reactions (e.g. Cpd 0 or the Fe(III)–H_2O_2 species) may oxidise more reactive functional groups such as alkenes or sulfides.[33, 118, 123] The T252E mutant may therefore have higher activity towards sulfoxidation and epoxidation than *O*-demethylation in these H_2O_2-supported reactions.[429]

Table 6.2. Product generated by the T252E mutant utilising the H_2O_2-shunt pathway during **20-min** reactions. The values given are mean ± SD, with $n \geq 2$. Reaction volumes were 600 µL and contained 1 mM substrate, 3 µM P450 and **50 mM H_2O_2** in 50 mM Tris-HCl buffer (pH 7.4). Reactions were performed at **30 °C** and 132 µL aliquots were quenched after 20 min by addition of 10 µL of 10 mg mL^{-1} bovine liver catalase and 66 µL of acetonitrile. Note that the amount of product detected in the no P450 control reactions has been subtracted from the amount of product in the T52E turnovers.

Substrate	Product concentration (µM)	Average product formation rate over 20-min period (µM (µM-P450)$^{-1}$ min^{-1})
4-methoxyBA	114 ± 2	1.9
veratric acid	107 ± 3	1.8
4-formylBA	64 ± 6	1.1
4-vinylBA	78 ± 1 [b]	1.3
4-methylthioBA	245 ± 2 [a]	4.1
4-ethylBA	104 ± 3	1.7
4-ethynylBA	9 ± 0.5	0.2

[a] The 4-methylsulfinylbenzoic acid concentration in the reaction mixture was 311 ± 2 µM and the product concentration in the no P450 control was 66 ± 1. [b] The epoxide and unidentified minor products were quantified using the calibration curve for 4-1-hydroxyethylbenzoic acid (Table D4).

Over a 20-minute period, the T252E enzyme converted 114 µM of 4-methoxybenzoic acid and 107 µM of veratric acid into 4-hydroxybenzoic acid and vanillic acid, respectively. Lower levels of terephthalic acid (64 µM) were generated from 4-formylbenzoic acid over the same time period, while reactions with 4-ethynylbenzoic acid yielded minimal 4-carboxyphenylacetic acid (9 µM). Oxidation of 4-ethylbenzoic acid gave a mixture of products (Table 6.3). In total, 104 µM product was generated, composed predominantly of 4-(1-hydroxyethyl)benzoic acid (29%), 4-vinylbenzoic acid (43%) and the corresponding epoxide (22%). Minor levels of 4-(2-hydroxyethyl)benzoic acid (5%) and the ketone 4-acetylbenzoic acid (1%) were observed. This product distribution is similar

to that reported for NADH-driven oxidation of 4-ethylbenzoic acid by WT CYP199A4.[277] It is also similar to the product distribution for NADH-supported 4-ethylbenzoic acid oxidation by T252E$_{CYP199A4}$, except that in these H_2O_2-supported reactions a larger percentage of the product was the epoxide (~22% *vs.* 3%).

Table 6.3. Product distribution for H_2O_2-driven oxidation of 4-ethylbenzoic acid by T252E CYP199A4 (20-min reaction)

Product distribution (%)				
4-vinylBA	**4-(1-hydroxyethyl)BA**	**4-(2-hydroxyethyl)BA**	**4-acetylBA**	**4-oxiran-2-ylBA**
43 ± 1	~29	~5	~1	~22

Oxidation of 4-vinylbenzoic acid by the T252E mutant yielded ~78 μM of product, consisting predominantly of the epoxide 4-oxiran-2-ylbenzoic acid (~70% of the total product). Additional product peaks were detected by HPLC with retention times of 5.1, 4.3 and 4.1 minutes (Table D4). The epoxide may be further metabolised by the T252E enzyme (Figure D15). Plausibly, one of the products may be the diol arising from epoxide ring opening. We attempt to identify these products in Section 6.2.3.

The T252E mutant displayed markedly higher activity towards sulfoxidation of 4-methylthiobenzoic acid. The quantity of 4-methylsulfinylbenzoic acid detected after a 20-minute reaction was 311 ± 2 μM. However, the thioether can be converted into the sulfoxide by H_2O_2 alone. When the P450 was omitted from the reaction, 66 μM sulfoxide was formed in the same time period (Figure D16, Table D5). Thus, we estimate that the amount of sulfoxide generated by the T252E mutant over this time period was ~245 μM.

In the NADH/O_2-supported reactions, WT CYP199A4 has the highest activity towards *O*-demethylation of 4-methoxybenzoic acid and lower activity towards other reaction types:

O-demethylation > sulfoxidation > hydroxylation/desaturation > epoxidation > alkyne oxidation > aldehyde oxidation.

Notably, in the H_2O_2-driven reactions the T252E mutant had substantially higher activity towards sulfoxidation than the other reaction types:

sulfoxidation > *O*-demethylation ≈ hydroxylation/desaturation > epoxidation > aldehyde oxidation > alkyne oxidation.

This may imply the existence of second oxidant capable of catalysing sulfoxidation that is more abundant in these H_2O_2-driven reactions. This may be the Fe(III)–H_2O_2 complex.[118]

6.2.3 Comparison of the activity of WT CYP199A4 and the T252E, T252A and D251N mutants utilising the H_2O_2-shunt pathway

To investigate the role of the T252 → E mutation and to gain additional insight into potential oxidants responsible for certain P450 reactions, H_2O_2-driven reactions were performed with the WT, T252E, D251N and T252A isoforms of CYP199A4. Their activity towards different reaction types was compared (Table 6.4). If a reaction was catalysed by Cpd 0 rather than Cpd I, the T252A mutant may display enhanced ability to catalyse that reaction. Product formation was monitored over a 4-hour period and a time course of product formation was constructed for each isoform. Each reaction contained 3 μM P450 and was driven by 50 mM H_2O_2, except where the substrate was a thioether, in which case 6 mM H_2O_2 was used to minimise background oxidation to the sulfoxide.

All CYP199A4 isoforms tested were able to perform the different P450 reactions using H_2O_2 but with varying efficiency. Control reactions were performed in which CYP101B1 or heat-denatured T252E (sources of heme or free iron) were substituted for functional T252E enzyme. Only low levels of product (or no product) were detected in these control reactions and in control reactions omitting the P450. This confirmed that a Fenton-type reaction did not generate the product in the hydrogen peroxide turnovers (Figure D17, Table D6).

Table 6.4. Product generated by WT CYP199A4 and the T252E, D251N and T252A mutants utilising the H_2O_2-shunt pathway during **240-min** reactions. The values given are mean ± SD, with $n \geq 2$. Reaction volumes were 600 μL and contained 1 mM substrate, 3 μM P450 and **50 mM H_2O_2** in 50 mM Tris-HCl buffer (pH 7.4). * For the thioethers, **6 mM H_2O_2** was used instead of 50 mM to minimise background oxidation. Reactions were performed at **30 °C** and 132 μL aliquots were quenched by addition of 10 μL of 10 mg mL^{-1} bovine liver catalase and 66 μL of acetonitrile. Note that the amount of product detected in the no P450 control reactions has been subtracted from the amount of product in the enzyme turnovers.

Substrate	Product concentration (μM)			
	T252E	WT	T252A	D251N
4-methoxyBA	379 ± 7	156 ± 2	89 ± 3	55 ± 1
4-formylBA	246 ± 16	209 ± 15	42 ± 1	40 ± 0.2
4-vinylBA	293 ± 22	125 ± 2	74 ± 5	81 ± 4
4-methylthioBA *	417 ± 17	40 ± 3	83 ± 1	7 ± 8
4-ethylthioBA *	107 ± 4	1 ± 8	38 ± 11	~0
4-ethylBA	155 ± 1	94 ± 0.3	41 ± 0.1	49 ± 0.1
4-ethynylBA	34 ± 1	9 ± 1	8 ± 1	8 ± 1

As reported in Chapter 5, the T252E mutant converted >2-fold more 4-methoxybenzoic acid into 4-hydroxybenzoic acid than the WT enzyme over a 4-hour period (379 *vs.* 156 μM). In contrast, the T252A and D251N mutants gave considerably less product (89 and 55 μM, respectively) (Table 6.4). While the T252E mutant was active for ~4 hours, the T252A and D251N mutants were readily

inactivated and produced little additional product after the first 20 minutes of the reaction (Figures 6.12 and D18).

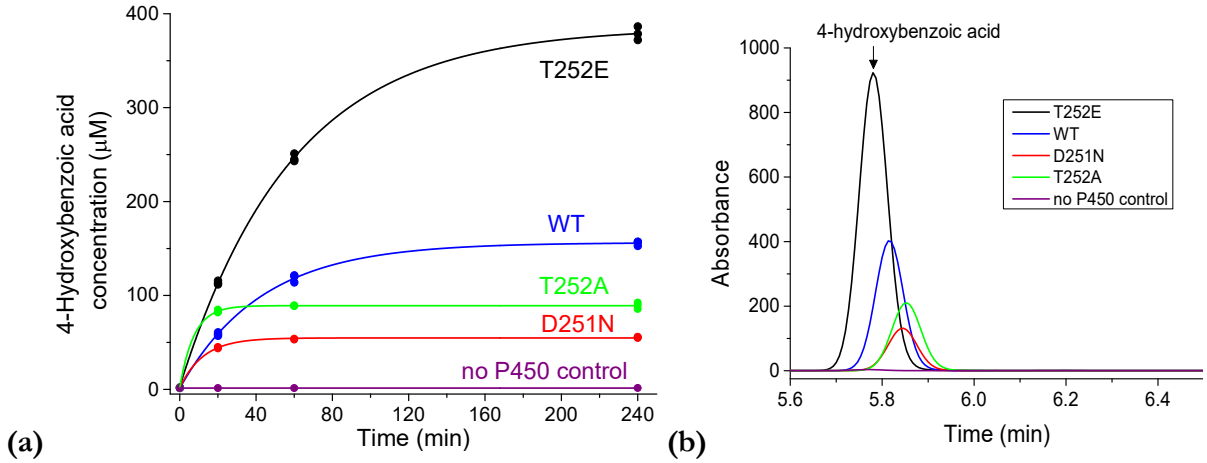

Figure 6.12. **(a)** Time course of 4-methoxybenzoic acid conversion into 4-hydroxybenzoic acid by CYP199A4 isoforms. **(b)** HPLC analysis of the amount of 4-hydroxybenzoic acid product (RT = 5.8 min) generated by the CYP199A4 isoforms over 240 minutes. For clarity, the internal standard and substrate peaks are not shown.

A single product, terephthalic acid, was generated in the H_2O_2-driven CYP199A4 reactions with 4-formylbenzoic acid (Figures 6.13 and D19). Over a four-hour period, the T252E mutant produced more terephthalic acid than the other CYP199A4 isoforms tested. Initially, the WT enzyme converted 4-formylbenzoic acid into product faster than the T252E mutant but was more rapidly inactivated than the T252E mutant (Figure 6.13), and consequently more product was ultimately produced by the T252E mutant (246 *vs.* 209 μM). It has been reported that aldehydes can inactivate P450s and perhaps this is occurring here.[7, 438-439] Again, the T252A and D251N mutants yielded low levels of product (42 and 40 μM), and were inactive after the first 20 min.

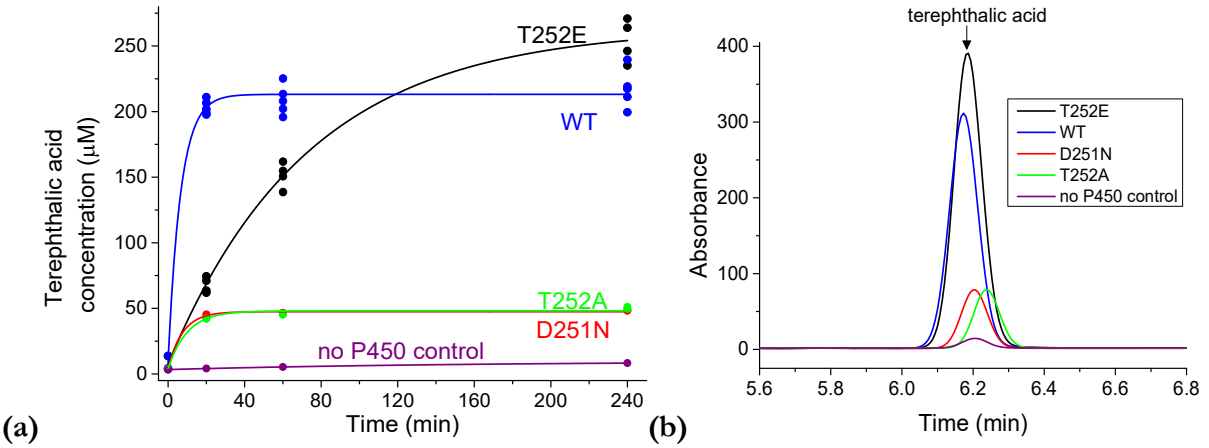

Figure 6.13. **(a)** Time course of 4-formybenzoic acid conversion into terephthalic acid by CYP199A4 isoforms. **(b)** HPLC analysis of the amount of the terephthalic acid product (RT = 6.2 min) generated by the CYP199A4 isoforms over 240 minutes. Only a single product was detected by HPLC. Further investigation is required to understand why WT CYP199A4 was able to initially oxidise 4-formylbenzoic acid faster than the T252E mutant.

The CYP199A4 isoforms were less active towards oxidation of 4-ethynylbenzoic acid than they were towards other reaction types (Table 6.4). After a 4-hour reaction, the amount of 4-carboxyphenylacetic acid, the sole product, detected in the T252E reactions was ~34 μM, while

the WT, T252A and D251N reactions contained only 8-9 μM (Figures 6.14, D20 and D21). Future work would be to clarify why the oxidation of 4-ethynylbenzoic acid is so inefficient in these H_2O_2-supported reactions. We note that terminal alkynes can inactive P450s by alkylating the heme.[215] Another possibility is that the inflexible linear alkyne group may be positioned such that it interferes with binding of H_2O_2 to the heme iron.

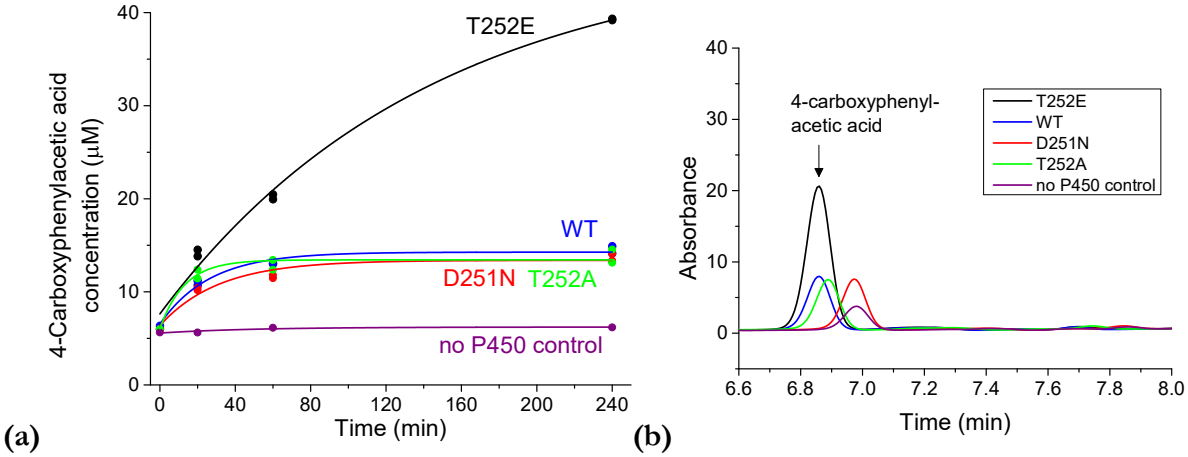

Figure 6.14. **(a)** Time course of 4-ethynylbenzoic acid conversion into 4-carboxyphenylacetic acid by CYP199A4 isoforms. **(b)** HPLC analysis of the amount of the 4-carboxyphenylacetic acid product (RT = 6.8 min) generated by the CYP199A4 isoforms over 240 minutes. Note that the initial product concentration in the reactions is not zero because the substrate was contaminated with minor amounts of product.

Analysis of the 4-vinylbenzoic acid reactions was complex because multiple unknown minor products were generated (Figures 6.15 and D22). In addition to the epoxide, which was the major product, peaks in the chromatogram were observed which may correspond to the aldehyde side product, 4-(2-oxoethyl)benzoic acid, and further oxidation products. We speculate that the peak at 9.3 min in the D251N, T252A, WT and T252E reaction mixtures corresponds to this aldehyde based on its retention time. This product represents ~8% of the product in the T252E turnover, and ~10%, 23% and ~20% of the product in the WT, D251N and T252A turnovers (Table D7).

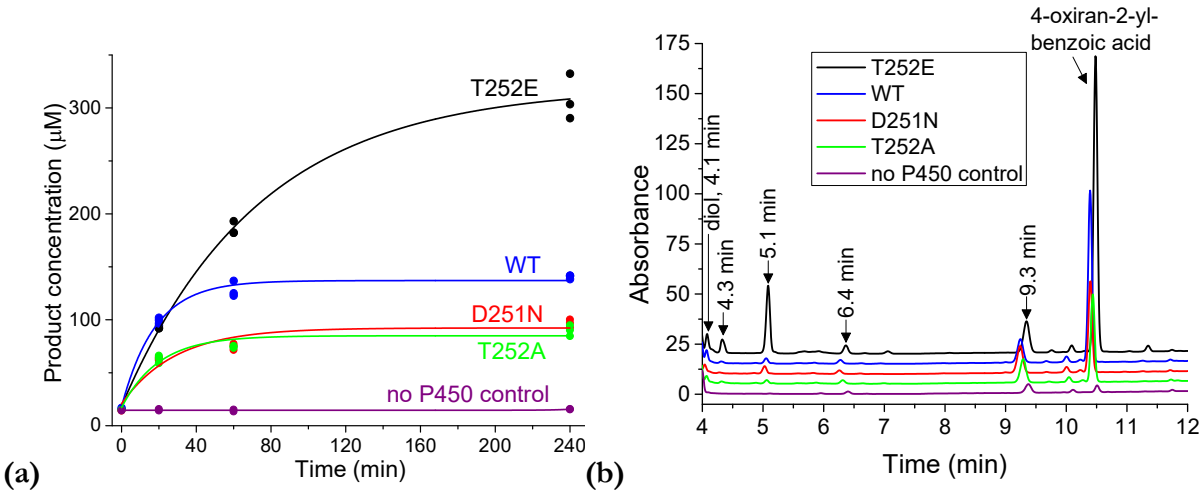

Figure 6.15. **(a)** Time course of 4-vinylbenzoic acid conversion into the corresponding epoxide by CYP199A4 isoforms. **(b)** HPLC analysis of the amount of the epoxide product (RT = 10.3 min) generated by the CYP199A4 isoforms over 240 minutes. Additional minor products have retention times of 4.1, 4.3, 5.1, 6.4 and 9.3 min.

Future work would be to synthesise 4-(2-oxoethyl)benzoic acid, which would allow us to confirm that the peak at 9.3 min is the aldehyde via a co-elution experiment. Other products were detected in the T252E reaction mixture that were not formed by the WT, D251N and T252A isoforms. A prominent peak is observed at 5.1 min in the T252E turnover (~16% of the total product). Based on its retention time we speculated that this peak may correspond to the diol arising from ring-opening of the epoxide. Negligible amounts of this product were generated by the other CYP199A4 isoforms. Additional minor peaks in the T252E reaction mixture are seen at 4.1, 4.3 and 6.4 min. Co-elution experiments with an authentic sample of the diol, 4-1,2-dihydroxyethylbenzoic acid, synthesised by Luke Churchman and James de Voss at the University of Queensland revealed that the minor peak at 4.1 min is the diol (Figure D23). We also considered the possibility that the unidentified peak at 5.1 min arises from a bond cleavage reaction. Plausibly, Baeyer-Villiger oxidation of the aldehyde rearrangement product followed by ester hydrolysis could give 4-hydroxymethylbenzoic acid (Figure D24a). However, authentic 4-hydroxymethylbenzoic acid did not co-elute with the product at 5.06 min (Figure D24b). (The retention time of authentic 4-hydroxymethylbenzoic acid was 5.16 min.)

We did establish that this unknown product arises from further metabolism of the epoxide by $T252E_{CYP199A4}$. When H_2O_2-driven reactions were performed using 50 μM chemically synthesised 4-oxiran-2-ylbenzoic acid as the substrate, the T252E enzyme converted the epoxide into the product at 5.1 min. H_2O_2 alone failed to convert the epoxide into this product. This confirms that the epoxide was further metabolised by the T252E enzyme (Figures D25 and D26). We attempted to identify the mass of this additional product by GC-MS. We extracted the reaction mixture with ethyl acetate, evaporated the solvent, redissolved the residue in anhydrous AcCN and derivatised it using BSTFA/TMCS, but were unable to detect the unknown product. Further work is needed to identify this product.

The total concentration of product formed by each CYP199A4 isoform was estimated by assuming that the detector response was similar for all products. Again, the T252E mutant yielded more product than the WT enzyme over a 4-hour period (293 *vs.* 125 μM). Although comparable levels of product were produced by the two isoforms over the first 20 min of the reaction, the T252E mutant remained catalytically active for a longer time period (Figure 6.15). $D251N_{CYP199A4}$ and $T252A_{CYP199A4}$ yielded lower levels of product (81 and 74 μM), even though Cpd 0, which is proposed to catalyse epoxidation, may be more abundant in the T252A mutant.

The T252E mutant exhibited substantially higher activity towards sulfoxidation of 4-methylthiobenzoic acid than the WT enzyme using 6 mM H_2O_2 (Figures 6.16 and D27). In control reactions omitting the P450, the presence of 6 mM H_2O_2 resulted in slow sulfoxidation of 4-methylthiobenzoic acid. The quantity of sulfoxide in control reactions omitting the P450 (Table D6) was subtracted from that in the CYP199A4 reactions to estimate the amount formed by the P450. Over a 4-hour period, the T252E mutant generated an estimated 417 μM of sulfoxide, whereas the WT enzyme only formed 40 μM. The sulfoxide concentration in the D251N reaction

mixture was comparable to that in control reactions omitting the enzyme. Thus, it appears that the D251N mutant generated minimal product (~7 μM). The T252A mutant, on the other hand, displayed elevated activity towards sulfoxidation compared to the WT enzyme, yielding 83 μM sulfoxide. Recall that for the other substrates, the T252A mutant had lower activity than the WT enzyme. No sulfone was detected in these reactions.

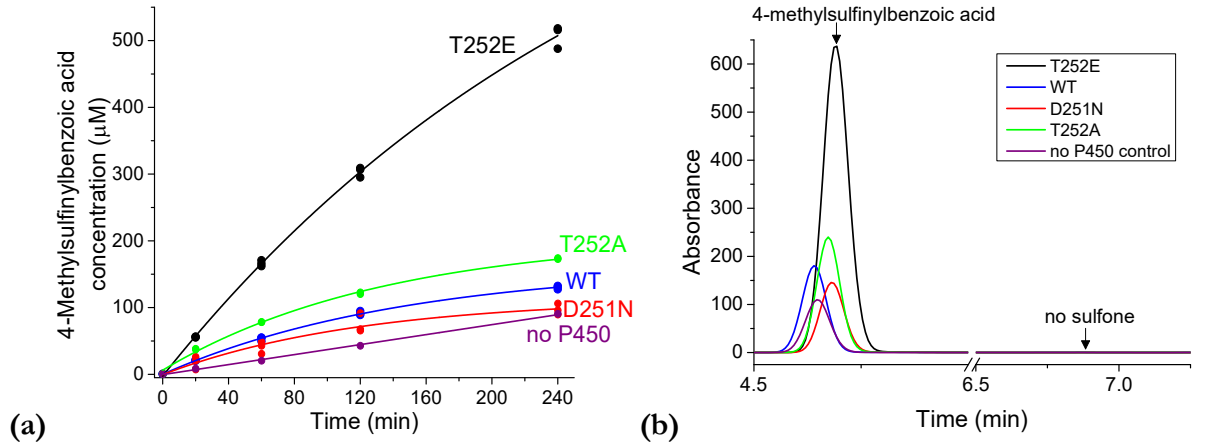

Figure 6.16. **(a)** Time course of 4-methylthiobenzoic acid conversion into the corresponding sulfoxide by CYP199A4 isoforms. **(b)** HPLC analysis of the amount of the 4-methylsulfinylbenzoic acid product (RT = 4.7 min) generated by the CYP199A4 isoforms over 240 minutes. No sulfone (RT = 6.9 min) was detected.

Similar results were obtained when 4-ethylthiobenzoic acid was used as the substrate (Figures 6.17 and D28). Again, the substrate was slowly converted into the sulfoxide when exposed to 6 mM H_2O_2. The amount of sulfoxide formed in control reactions lacking the P450 was subtracted from that in the CYP199A4 reactions to estimate the sulfoxide concentration generated by each CYP199A4 isoform.

The T252E mutant formed the most product (107 μM), while the T252A mutant generated less (38 μM sulfoxide) but was again more active towards sulfoxidation than the WT enzyme. The concentration of sulfoxide in the WT and D251N reaction mixtures was roughly equal to that in control reactions lacking the P450; therefore, the product formed by these isoforms is reported as ~1 μM and 0 μM, respectively. All CYP199A4 isoforms tested were less active towards oxidation of 4-ethylthiobenzoic acid than 4-methylthiobenzoic acid using H_2O_2.

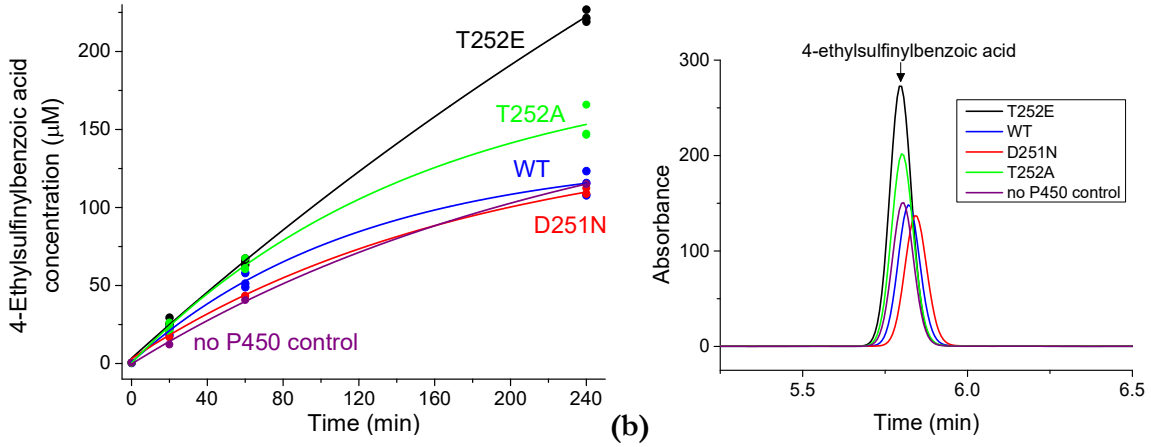

Figure 6.17. **(a)** Time course of 4-ethylthiobenzoic acid conversion into the corresponding sulfoxide by CYP199A4 isoforms. **(b)** HPLC analysis of the amount of the 4-ethylsulfinylbenzoic acid product (RT = 5.8 min) generated by the CYP199A4 isoforms over 240 minutes.

The order of activity of the CYP199A4 isoforms towards oxidation of 4-ethylbenzoic acid was: T252E > WT > D251N > T252A (Figure 6.18 and D29). The T252E mutant yielded 155 μM product over 4 hours, the WT enzyme gave 94 μM, and the D251N and T252A mutants 49 and 41 μM. For all isoforms, the dominant products were 4-(1-hydroxyethyl)benzoic acid and 4-vinylbenzoic acid; these are also the major products of the NADH-supported reactions.[277] The product distributions were similar for the different isoforms, but not identical (Table 6.5).

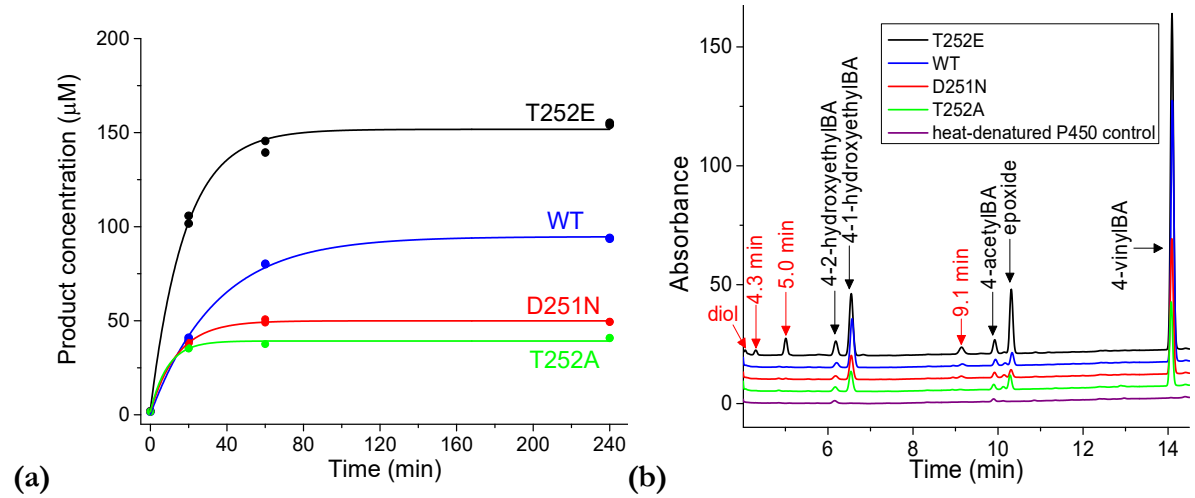

Figure 6.18. **(a)** Time course of 4-ethylbenzoic acid conversion into various products by CYP199A4 mutants. **(b)** HPLC analysis of the amount of product generated by the CYP199A4 isoforms over 240 minutes. Additional minor unidentified products appear in the T252E reaction with retention times of 9.1, 5.0, and 4.3 min (red arrows).

Table 6.5. Product distribution for H_2O_2-driven oxidation of 4-ethylbenzoic acid by CYP199A4 isoforms (240-min reactions)

	Product distribution (%)				
	4-vinylBA	**4-(1-hydroxyethyl)BA**	**4-(2-hydroxyethyl)BA**	**4-acetylBA**	**4-oxiran-2-ylBA**
T252E	38	30	5	1	26
WT	49	39	3	1	8
D251N	48	36	4	2	10
T252A	34	35	7	2	23

The product of the T252E reaction consisted of 38% 4-vinylbenzoic acid, 30% 4-(1-hydroxyethyl)benzoic acid, 5% 4-(2-hydroxyethyl)benzoic acid, 1% 4-acetylbenzoic acid and 26% epoxide. In contrast, the D251N and WT reactions yielded a higher proportion of 4-(1-hydroxyethyl)benzoic acid and 4-vinylbenzoic acid, but a lower proportion of the epoxide than the T252E mutant (8 and 10 *vs.* 26%). The epoxide accounted for 23% of the product generated by the T252A mutant. Compared to the other isoforms, the T252A mutant generated a larger proportion of 4-(2-hydroxyethyl)benzoic acid (7%). Notice that for all the isoforms, 4-vinylbenzoic acid and its further oxidation product, 4-oxiran-2-ylbenzoic acid, accounted for roughly the same percentage of the total product (57-64%). In the chromatogram of the T252E reaction, additional minor unidentified products are observed with retention times of 9.1, 5.0, and 4.3 min (Figure D30). The other CYP199A4 isoforms did not form these products. Products with these retention times were also detected in the T252E reaction with 4-vinylbenzoic acid. They are believed to arise from further oxidation of 4-vinylbenzoic acid and the epoxide formed from this metabolite. These minor products were not considered when calculating the total concentration of product generated by the T252E mutant. Consequently, the amount of product generated by the $T252E_{CYP199A4}$ enzyme is an underestimate. We estimate the concentration of these additional products formed by the T252E mutant to be 27 ± 1 μM (Table D8). These unidentified minor products represent ~15% of the total product.

6.2.4 Enantioselectivity of NADH/O_2- and H_2O_2-driven sulfoxidation of 4-ethylthiobenzoic acid, α-hydroxylation of 4-ethylbenzoic acid and epoxidation of 4-vinylbenzoic acid by CYP199A4 isoforms

If a second oxidant other than Cpd I can mediate certain reactions such as sulfoxidation and epoxidation (e.g. Fe(III)–H_2O_2 or Fe(III)–OOH)[118, 121, 123], we might expect that the D251N, T252A and T252E mutants would display different enantioselectivity than the WT enzyme. This is because the different active oxidants would be positioned differently relative to the substrate.[123] To assess whether multiple oxidants are involved in CYP199A4-catalysed reactions, we measured the enantioselectivity of NADH-supported and H_2O_2-driven sulfoxidation, epoxidation and hydroxylation reactions catalysed by these isoforms. Crystal structures of these mutants[277] revealed that the active site structure is minimally altered by these mutations, so we do not expect the substrate binding mode to differ across the mutants (Figure D31). Therefore, changes in enantioselectivity could be due to a change in the identity of the active oxidant.

Although WT CYP199A4 was previously shown to convert 4-vinylbenzoic acid into the corresponding epoxide by Chao[276], the enantioselectivity of the reaction was not determined. The enantioselectivity has been reported of NADH-supported α-hydroxylation of 4-ethylbenzoic acid and sulfoxidation of 4-ethylthiobenzoic acid by WT CYP199A4.[117] WT CYP199A4 generates 4-(1-hydroxyethyl)benzoic acid in 74% ee and 4-ethylsulfinylbenzoic acid in 82% ee.[117] The major enantiomer of 4-(1-hydroxyethyl)benzoic acid generated by WT CYP199A4 was identified by

Coleman *et al.* as the (*S*)-enantiomer, but the absolute configuration of the sulfoxide was not reported.[117]

The enantiomers of the 4-vinylbenzoic acid epoxide were successfully separated by enantioselective HPLC. CYP199A4-catalysed epoxidation of 4-vinylbenzoic acid was found to proceed with even higher enantioselectivity than the sulfoxidation and hydroxylation reactions (Tables 6.6 and D9). In NADH-supported reactions, WT CYP199A4 generated almost exclusively a single enantiomer of 4-oxiran-2-ylbenzoic acid; the enantioselectivity of the reaction was ~99% (Figure 6.19a). The T252A mutant had equivalent enantioselectivity (~99%), while the T252E and D251N mutants were marginally less enantioselective (97.5 and 93.5%, respectively).

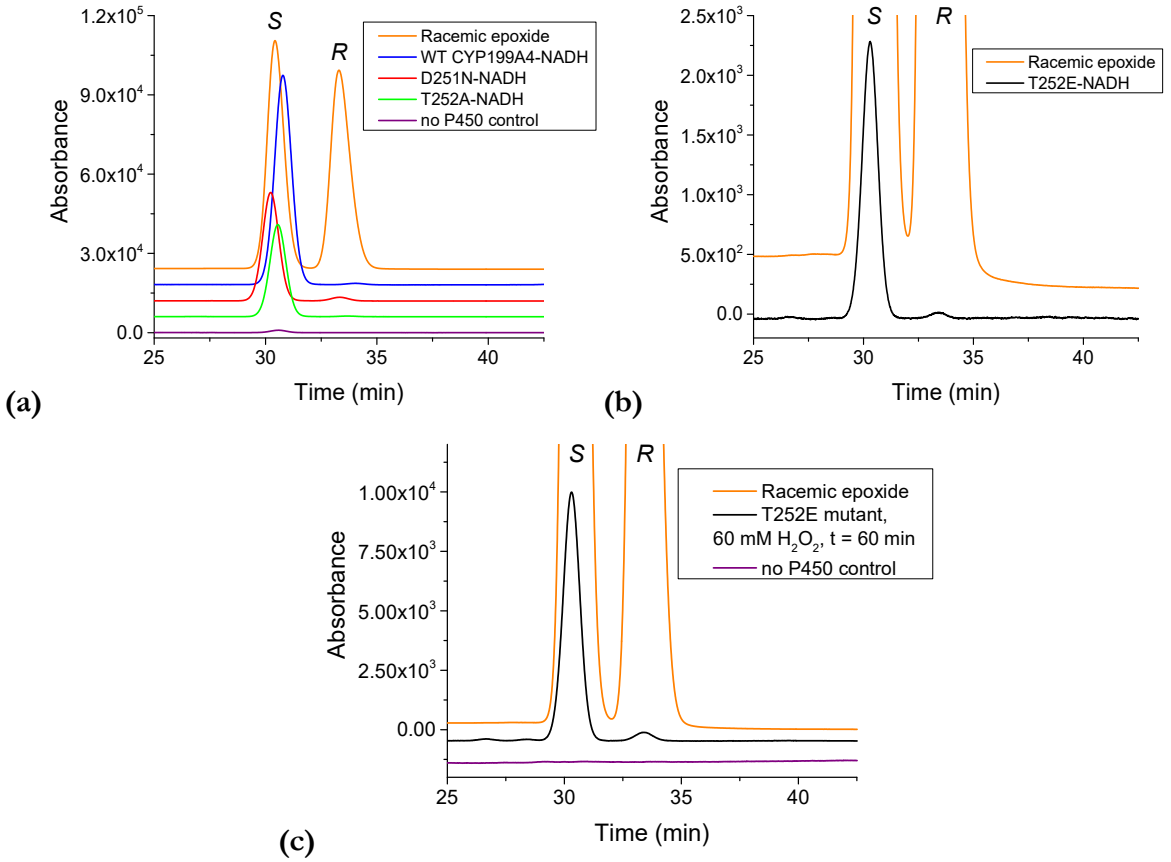

Figure 6.19. **(a)** Chiral HPLC analysis of the **NADH-driven** epoxidation of 4-vinylbenzoic acid by WT CYP199A4 (**blue**), the D251N mutant (**red**) and the T252A mutant (**green**). In **purple** is a control reaction omitting the P450. In **orange** are the separated enantiomers of chemically synthesised racemic 4-oxiran-2-ylbenzoic acid.
(b) Chiral HPLC analysis of the **NADH-driven** epoxidation of 4-vinylbenzoic acid by the T252E mutant (**black**).
(c) Chiral HPCL analysis of the epoxide generated by the T252E mutant in a **H_2O_2-driven reaction** (60 mM H_2O_2) over a 60-minute period (**black**). In **purple** is a control reaction omitting the P450. Chiral analysis was performed using a Lux Cellulose-1 column (100 × 4.6 mm, 3 µm, 1000 Å pore size; Phenomenex). The epoxide was eluted using 20% AcCN in H_2O (0.1% TFA) (flow rate: 0.4 mL min^{-1}). The retention times of the enantiomers are 31 and 33.9 min.

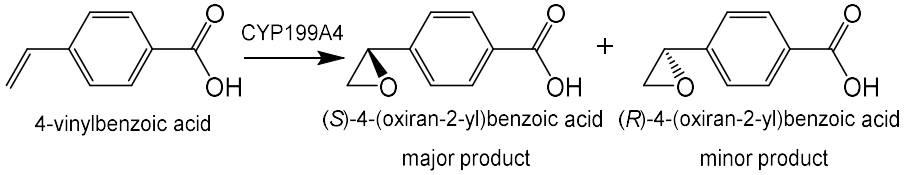

Figure 6.20. The CYP199A4 isoforms convert 4-vinylbenzoic acid predominantly into the (*S*)-epoxide; only minor amounts of the (*R*)-epoxide are formed.

The enantioselectivity of the T252E mutant was similar in both H_2O_2-driven and NADH-supported reactions (~94 *vs.* 97.5% ee) (Figure 6.19b,c). In H_2O_2-driven reactions the WT enzyme was also highly enantioselective (~93% ee) (Figure D32). In all cases, the major enantiomer was the (*S*)-enantiomer (Figure 6.20). The absolute configuration was assigned via HPLC co-elution with an authentic sample of the (*S*)-enantiomer synthesised by Luke Churchman and James de Voss at the University of Queensland (Figure D33). The enantioselectivity of 4-vinylbenzoic acid epoxidation by CYP199A4 is higher than that reported by Jacobsen[440], who generated 4-oxiran-2-ylbenzoic acid in 72% ee using a (salen)Mn(III) complex as the catalyst. CYP199A4's high enantioselectivity implies that this enzyme could have applications in the synthesis of chiral chemicals.[182]

Table 6.6. Enantioselectivity of NADH- or H_2O_2-driven epoxidation of 4-vinylbenzoic acid catalysed by CYP199A4 isoforms. In all cases, the major enantiomer is the (*S*)-enantiomer.

CYP199A4 isoform	enantiomeric excess (%ee)	ratio of enantiomers (*S* : *R*)
WT-NADH	99 ± 0.2	99.5 : 0.5
D251N-NADH	93.5 ± 0.3	97 : 3
T252A-NADH	99 ± 0.1	99.5 : 0.5
T252E-NADH	97.5	99 : 1
T252E-60 mM H_2O_2 (60-min reaction)	~94	~97 : ~3
WT-60 mM H_2O_2 (60-min reaction)	93 ± 1	96 : 4

The enantioselectivity of α-hydroxylation of 4-ethylbenzoic acid by the CYP199A4 mutants was also investigated. The D251N and T252A mutants were found to yield predominantly the (*S*)-enantiomer in NADH-driven reactions (Tables 6.7 and D10). D251N$_{CYP199A4}$ displayed higher enantioselectivity than the WT enzyme (87.5% *vs.* 76% ee), whereas the enantioselectivity of the T252A mutant was lower (60% ee) (Figure 6.21a). The measured enantioselectivity of the WT enzyme is comparable to that reported in the literature. In 60-min, H_2O_2-driven reactions, the WT enzyme also gave predominantly the (*S*)-enantiomer (~59% ee) (Figure D34).

NADH-supported reactions with the T252E mutant were also performed, but the measured enantioselectivity for this mutant was lower (~6% ee) (Figure 6.21b). Note that product peaks appeared in a control reaction omitting the P450 and the areas of these peaks were subtracted from those in the T252E turnovers when calculating the enantioselectivity. For this mutant, the (*R*)-enantiomer appeared to be the major enantiomer. A caveat is that the low yield of product may limit our ability to measure the enantioselectivity accurately. In 60-min H_2O_2-driven reactions performed with the T252E mutant, the major peak corresponded to the (*R*)-enantiomer, and the reaction again had low enantioselectivity (13%) (Figure 6.21c). Future work would be to solve a crystal structure of the T252E mutant in complex with 4-ethylbenzoic acid to rationalise the altered enantioselectivity.

Table 6.7. Enantioselectivity of NADH- or H_2O_2-driven α-hydroxylation of 4-ethylbenzoic acid catalysed by CYP199A4 isoforms. The major enantiomer generated by WT CYP199A4 was established to be the (*S*)-enantiomer by Coleman *et al.*[117]

CYP199A4 isoform	enantiomeric excess (%ee)	ratio of enantiomers (*S* : *R*)
WT-NADH	76 ± 1	88 : 12
D251N-NADH	87.5 ± 0.4	94 : 6
T252A-NADH	60 ± 0.4	80 : 20
T252E-NADH	6 ± 5	47 : 53
T252E-60 mM H_2O_2 (60-min reaction)	13	44 : 57
WT-60 mM H_2O_2 (60-min reaction)	59 ± 7	79 : 21

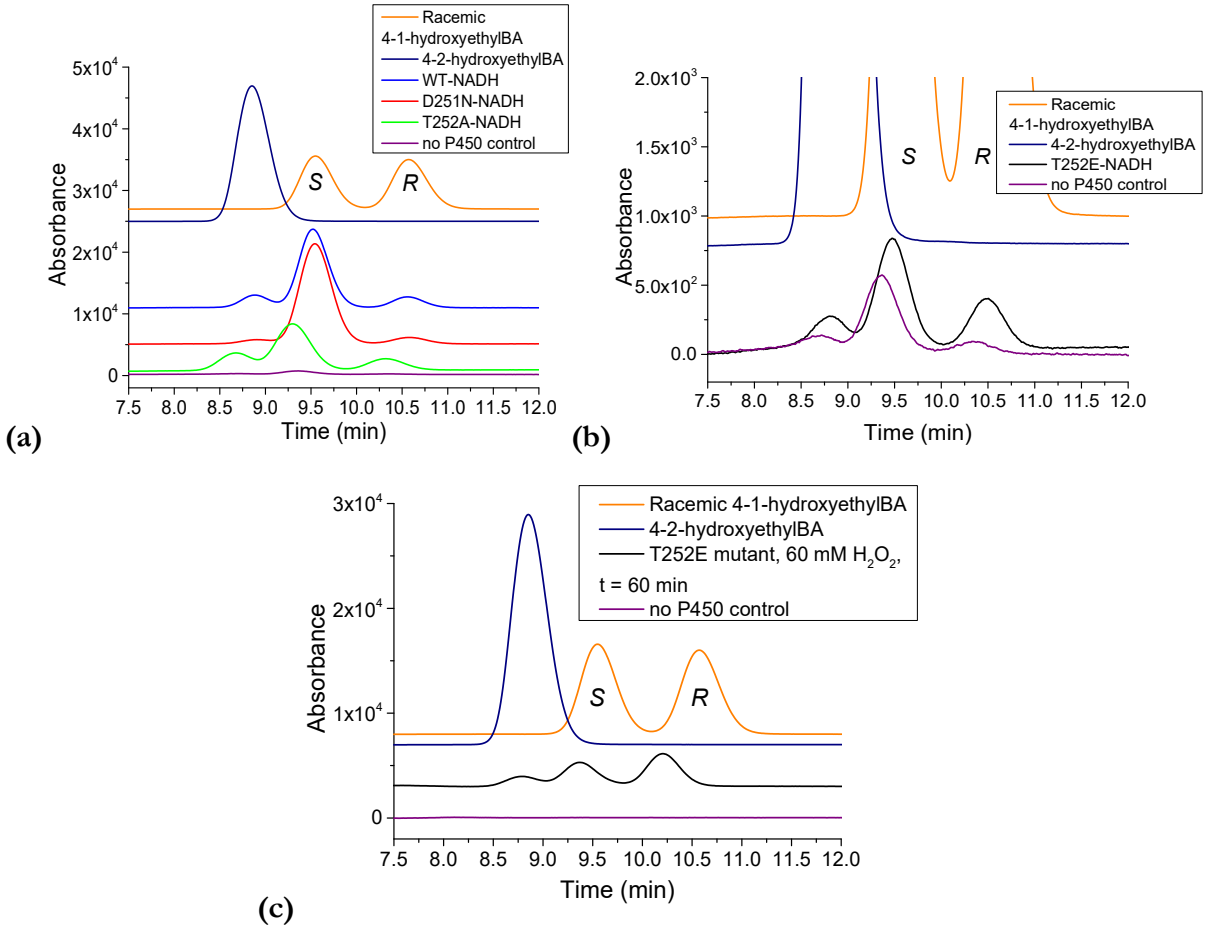

Figure 6.21. **(a)** Chiral HPLC analysis of the **NADH-driven** hydroxylation of 4-ethylbenzoic acid catalysed by WT CYP199A4 (**blue**) and the D251N (**red**) and T252A (**green**) isoforms. In **orange** are the separated enantiomers of racemic 4-(1-hydroxyethyl)benzoic acid (labelled *S* and *R*[117]), and in **navy blue** is the achiral isomer 4-(2-hydroxyethyl)benzoic acid. In **purple** is a no P450 control reaction.

(b) Chiral analysis of the **NADH-driven** hydroxylation of 4-ethylbenzoic acid by the T252E mutant (**black**).

(c) Chiral analysis of the **H_2O_2-driven** hydroxylation of 4-ethylbenzoic acid by the T252E mutant (**black**). The H_2O_2 concentration was 60 mM and reaction time 60 minutes. In **purple** is a control reaction omitting the P450. Chiral analysis was performed using a Lux Cellulose-1 column (100 × 4.6 mm, 3 µm, 1000 Å pore size; Phenomenex). The enantiomers were separated using 15% AcCN in H_2O (0.1% TFA) (flow rate: 0.8 mL min^{-1}). The retention times of the 4-(1-hydroxyethyl)benzoic acid enantiomers were 9.6 and 10.6 min. 4-(2-Hydroxyethyl)benzoic acid had a retention time of 8.9 min.

As mentioned, NADH-supported sulfoxidation of 4-ethylsulfinylbenzoic acid catalysed by WT CYP199A4 proceeds with high enantioselectivity (82% ee)[117], but the absolute configuration of the major enantiomer is unknown. The enantioselectivity of CYP199A4-catalysed sulfoxidation of 4-methylthiobenzoic acid has not been determined because Coleman *et al.* could not separate the enantiomers.[117] We investigated the enantioselectivity of NADH- and H_2O_2-supported sulfoxidation of 4-ethylthiobenzoic acid by the CYP199A4 mutants (Tables 6.8 and D11). H_2O_2-driven reactions were performed over a period of 2 hours and were initiated by addition of 6 mM H_2O_2 (Figures D35 and D36). Chiral analysis was performed by James de Voss at the University of Queensland.

In harmony with the previously published value[117], the measured enantioselectivity of NADH-supported sulfoxidation of 4-ethylthiobenzoic acid by the WT enzyme was 83%. The enantioselectivity of the T252A reaction was comparable to that of the WT enzyme (82% ee), while that of the D251N and T252E mutants was lower (38 and 68% ee, respectively). All these CYP199A4 isoforms generated an excess of the same enantiomer. Accurate measurement of the enantioselectivity of the H_2O_2-driven reactions was not possible due to background oxidation of the sulfide by H_2O_2 giving racemic sulfoxide (Figure D35). The measured enantioselectivities were 18% (T252E), 27% (WT), 18% (T252A) and 15% ee (D251N), but these values would underestimate the true enantioselectivity of the enzyme-catalysed reactions. The major enantiomer was always the same for both the H_2O_2-driven and NADH-supported reactions. A strategy to minimise uncatalysed background oxidation of the sulfide would be to continuously generate low levels of H_2O_2 *in situ* instead of adding H_2O_2 directly to the solution.[266] If background oxidation of the sulfide could be avoided, we could achieve a higher enantiomeric excess.[266]

Table 6.8. Enantioselectivity of **H_2O_2-driven** sulfoxidation of 4-ethylthiobenzoic acid by WT CYP199A4 and the T252E, D251N and T252A mutants. The H_2O_2 concentration was 6 mM and reaction time 2 hours. Note that due to background oxidation of the thioether by H_2O_2 the true enantioselectivity of the P450 reactions is unknown. The enantioselectivity of **NADH/O_2-driven** reaction is also given.

	CYP199A4 isoform			
% ee of 4-ethylsulfinylBA product	**T252E**	**WT**	**T252A**	**D251N**
6 mM H_2O_2 (2-hour reaction)	18%	27%	18%	15%
NADH/O_2-driven reaction	68%	83%	82%	38%

In crystal structures of 4-ethylthiobenzoic acid-bound $WT_{CYP199A4}$ and $T252E_{CYP199A4}$, the orientation of the ethylthio moiety is highly similar (Figure 6.22). This is in agreement with the similar enantioselectivity of both isoforms (although the enantioselectivity of the T252E mutant is slightly reduced).

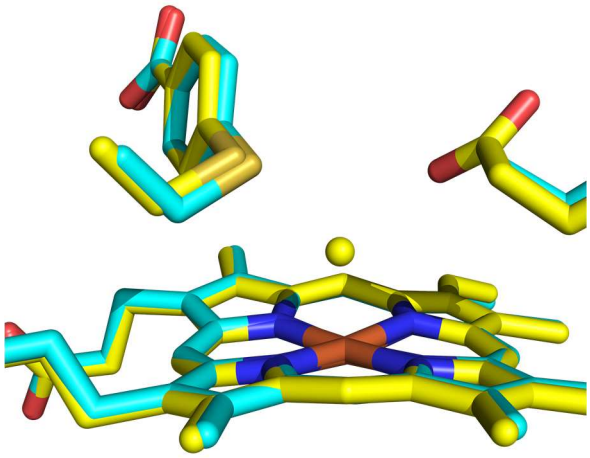

Figure 6.22. Binding orientation of 4-ethylthiobenzoic acid in the active site of WT CYP199A4 (cyan; PDB ID: 5U6U)[117] and T252E$_{CYP199A4}$ (yellow).

6.2.5 Utilising *t*-BuOOH as the oxygen donor to probe the active intermediate in different P450 reactions

We sought to further investigate the identity of the active oxidant involved in different P450 reactions by using *tert*-butyl hydroperoxide as the oxygen atom donor instead of H_2O_2. Reacting P450s with H_2O_2 is hypothesised to yield Cpd I via Cpd 0 and Fe(III)–H_2O_2.[107, 246, 264, 441] On the other hand, formation of Cpd 0 is circumvented when organic peroxides such as *t*-BuOOH are used (Figure 6.23).[111, 122] Consequently, *t*-BuOOH can in theory be used to probe whether a particular P450 reaction is mediated predominantly by Cpd I or Cpd 0.[111, 122, 211] If a reaction is catalysed by Cpd 0, the reaction would not be expected to proceed efficiently using the surrogate oxygen donors *t*-BuOOH, cumene hydroperoxide[196], *m*CPBA (*meta*-chloroperoxybenzoic acid) or iodosobenzene but H_2O_2 would be expected to support the reaction.[122] Vaz *et al.* demonstrated that CYP2B4 catalysed the deformylation of cyclohexanecarboxaldehyde in the presence of NADPH/O_2 and H_2O_2, but not in the presence of iodosobenzene, *m*CPBA or cumene hydroperoxide.[211] They interpreted this to mean that Cpd I was not the active oxidant, but rather iron-bound peroxide was the active species.[211] Kells *et al.* proposed that the epoxidation of 4,5-desepoxypimaricin by the P450 enzyme PimD is mediated exclusively by Cpd 0, finding that the reaction occurred in the presence of H_2O_2, but not in the presence of iodosobenzene or peracetic acid.[122] Hutzler *et al.* showed that *O*-demethylation of dextromethorphan by CYP2D6 occurred at the same rate when CuOOH was substituted for NADPH/O_2, indicating that Cpd I was the active oxidant in *O*-dealkylation.[196, 442]

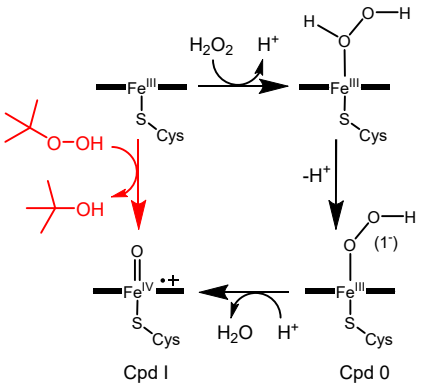

Figure 6.23. Utilising H_2O_2 as the oxygen donor is hypothesised to yield Cpd I via Cpd 0. Organic peroxides (e.g. *t*-BuOOH) and iodosobenzene, on the other hand, cannot generate Cpd 0.[111, 122, 211] Organic peroxides can therefore be used to probe whether a particular P450 reaction is mediated by Cpd I or Cpd 0.[111, 122]

Initially, we investigated whether WT CYP199A4 and the T252E mutant could use *t*-BuOOH to catalyse the *O*-demethylation of 4-methoxybenzoic acid (a Cpd I-mediated reaction) to assess whether *t*-BuOOH could access the heme iron in CYP199A4 and generate Cpd I. Recall that in the presence of 50 mM H_2O_2, the T252E mutant generated ~380 μM 4-hydroxybenzoic acid over a 4-hour period. We found that in the presence of 50 mM *t*-BuOOH, minimal product (~5 μM) was generated by the T252E mutant over the same time period, while WT CYP199A4 failed to produce any product (Figure 6.24).

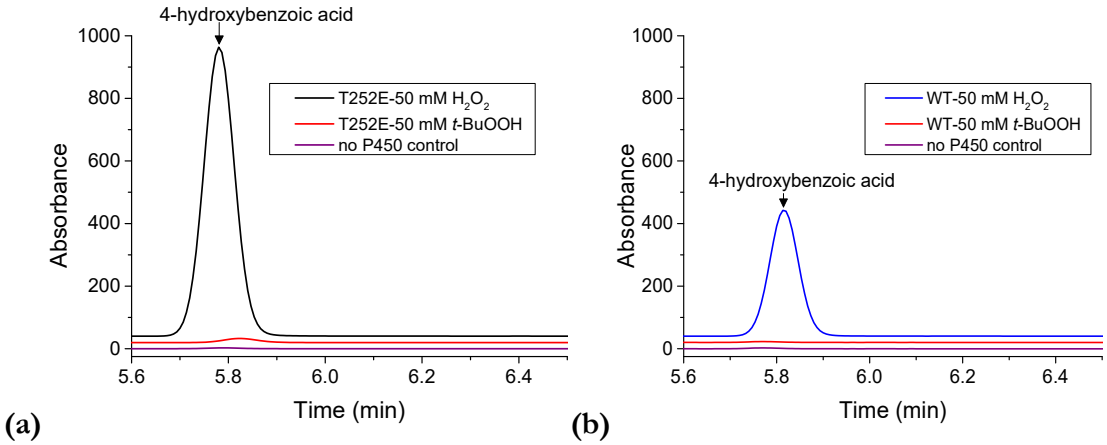

Figure 6.24. HPLC analysis of the *t*-BuOOH-driven *O*-demethylation of 4-methoxybenzoic acid. The reaction time was **4 hours** at 30 °C and *t*-BuOOH concentration 50 mM. In **(a)** the amount of product generated by the T252E mutant using *t*-BuOOH as the oxygen donor (**red**) is compared to the amount produced using H_2O_2 (**black**). In **(b)** the amount of 4-hydroxbenzoic acid produced by WT CYP199A4 using either 50 mM *t*-BuOOH (**red**) or H_2O_2 (**blue**) is compared.

There is compelling evidence that Cpd I is responsible for C-H hydroxylation[103] and therefore we do not interpret these results as evidence that *O*-demethylation is mediated by Cpd 0. Due to its steric bulk, *t*-BuOOH is presumably not accommodated within the confined active site of CYP199A4 when substrate is bound and therefore cannot react with the ferric heme iron to generate Cpd I. Reactions were also performed using alternative substrates (4-formyl- and 4-vinyl-

benzoic acid), but again the T252E mutant failed to generate any significant levels of product. The amount of product generated by the T252E mutant in 1 hour in the presence of 50 mM *t*-BuOOH was 6 ± 1 μM epoxide and 11 ± 1 μM terephthalic acid (Table D12, Figure D37). In the same time period, the T252E mutant could generate 122 μM epoxide and 146 μM terephthalic acid using H_2O_2.

We additionally investigated whether the T252A mutant was capable of utilising *t*-BuOOH as a surrogate oxygen atom donor. Replacement of threonine-252 with alanine creates more free space above the heme, potentially allowing *t*-BuOOH to bind to the heme iron. While threonine has a polar side chain, the side chain of alanine is hydrophobic. This substitution may make binding of the hydrophobic *t*-butyl group of *t*-BuOOH in the active site more favourable. However, the T252A mutant failed to convert any 4-methoxybenzoic acid into 4-hydroxybenzoic acid during a 1-hour reaction in the presence of 50 mM *t*-BuOOH. The D251N mutant was also unable to use *t*-BuOOH (Table D12, Figure D38). Due to the failure of CYP199A4 to utilise *t*-BuOOH as a surrogate oxygen donor, we were unable to use this oxidant to probe whether Cpd I or Cpd 0 is the active species in different P450 reactions.

6.3 Discussion

In NADH-supported reactions, $T252E_{CYP199A4}$ had minimal activity towards *para*-substituted benzoic acid substrates with (m)ethylthio, vinyl, formyl and ethynyl functional groups. The product formation rate ranged from 0 to ~1 min^{-1}. This confirms that the T252E variant is unable to operate efficiently via the normal catalytic cycle.

NADH-supported reactions were also performed to investigate the activity of $D251N_{CYP199A4}$ and $T252A_{CYP199A4}$ towards sulfoxidation of 4-ethylthiobenzoic acid. Cryle and de Voss[123] reported that the T → A mutant of $P450_{BM3}$ was able to perform the sulfoxidation of thiafatty acids at the same rate and with the same coupling efficiency as the WT enzyme. As Cpd 0 should be more abundant in the T → A mutant and Cpd I formation should be hindered, this implied that sulfoxidation was mediated by Cpd 0 (not Cpd I).[123] They also found that the sulfoxidation of thiafatty acids by $P450_{BM3}$ occurred with opposite enantioselectivity to the hydroxylation of fatty acids, again suggesting that an oxidant other than Cpd I mediated sulfoxidation.[123] In contrast, the T252A mutant of CYP199A4 performed sulfoxidation of 4-ethylthiobenzoic acid with substantially lower coupling efficiency compared to the WT enzyme (37 *vs.* 99.5%). These results do not indicate that Cpd 0 is a highly efficient oxidant for sulfoxidation but are consistent with DFT studies which suggested that Cpd 0 is a weak oxidant.[118, 200]

Cpd 0 has also been proposed to mediate epoxidation.[33, 121-122] Vaz and Coon[121] found that the T → A mutant of CYP2E1 catalysed epoxidation of olefins (e.g. styrene) more efficiently than the WT enzyme, implying that Cpd 0 mediated epoxidation. In NADH-supported reactions, $T252A_{CYP199A4}$ performed epoxidation of 4-vinylbenzoic acid at a slower rate and with lower coupling efficiency than the WT enzyme (30 *vs.* 66%).[276] $T252A_{CYP199A4}$ predominantly produced

H_2O_2, implying that Cpd 0 accumulated (with subsequent loss of H_2O_2) rather than rapidly reacting with the alkene. If Cpd 0 were highly active towards epoxidation, we would expect *enhanced* epoxidation from the T252A mutant. This result agrees with Shaik's proposal that Cpd 0 is a poor oxidant.[7, 212] If there were multiple active oxidants, we might expect the product distribution to differ for the WT, D251N and T252A isoforms. However, these isoforms all gave the same product distribution (95-96% epoxide and 4-5% aldehyde side product). The enantioselectivity of epoxidation was virtually the same for these isoforms, which may again imply that a single oxidant was responsible.

Hydrogen peroxide-driven reactions were performed with the T252E mutant of CYP199A4. These demonstrated that it could perform a variety of P450 oxidation reactions using H_2O_2. Note that these H_2O_2-driven reactions are slow compared to the rate of NADH-supported reactions performed by WT CYP199A4. In $T252E_{CYP199A4}$, Cpd I may not be efficiently formed, and further mutations may be required to improve its ability to generate Cpd I.

It is hypothesised that H_2O_2 binds to the heme iron to give Fe(III)–H_2O_2, which can convert into Cpd I via Cpd 0 (Figure 6.25). We assume that the ferric-peroxo anion intermediate would be bypassed in H_2O_2-driven reactions.[111] Shaik has also proposed that the Fe(III)–H_2O_2 complex can convert into Cpd I via an O-O homolysis/H-abstraction mechanism (Figure 6.26).[213] Shaik suggested that this is the mechanism by which Cpd I is generated by the peroxygenase $P450_{SP\alpha}$ (and WT $P450_{cam}$ when it is shunted with H_2O_2).[213, 256] Cpd I is required for hydroxylation and *O*-dealkylation, but other functional groups (e.g. alkenes and thioethers) may be oxidised by earlier intermediates that may be more abundant in the peroxide-driven reactions.[33, 94, 121-122]

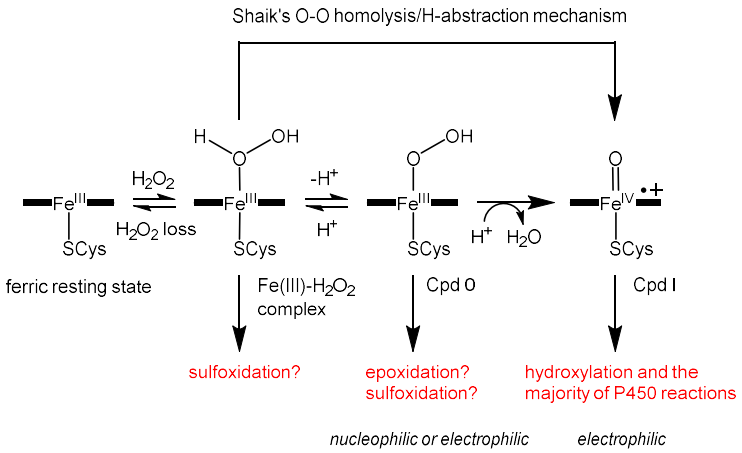

Figure 6.25. Possible active oxidants formed during H_2O_2-driven CYP199A4 turnovers.[33, 94, 103, 111, 118, 121, 123-124, 203, 213, 429, 443-445]

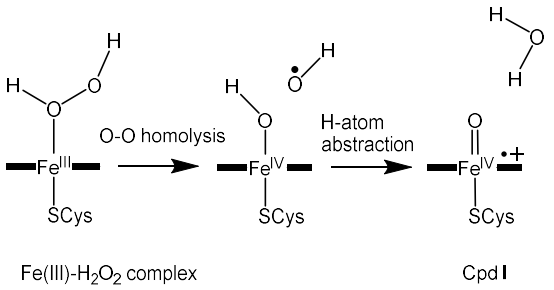

Figure 6.26. Shaik proposed that Cpd I could be formed from the Fe(III)–H_2O_2 species in hydrogen peroxide-driven reactions via an O-O homolysis/H-atom abstraction mechanism.[213] This mechanism involves formation of an •OH radical by homolytic cleavage of the O–O bond, which gives Cpd II (Fe^{IV}–OH).[213] This is followed by H-abstraction from Cpd II by •OH to give Cpd I.[213] Shaik suggested that this is the mechanism by which Cpd I is formed in the peroxygenase $P450_{SPα}$ and in WT $P450_{cam}$ when H_2O_2 is used to drive camphor hydroxylation.[213, 256]

In NADH-supported reactions, WT CYP199A4 is more active towards *O*-demethylation of 4-methoxybenzoic acid than sulfoxidation of 4-methylthiobenzoic acid, which is performed faster than epoxidation, aldehyde oxidation and alkyne oxidation:

O-demethylation > sulfoxidation > hydroxylation/desaturation > epoxidation > alkyne oxidation > aldehyde oxidation.

In NADH-supported reactions the T252E mutant had low activity towards all substrates but performed *O*-demethylation and sulfoxidation more efficiently than the other reactions. In H_2O_2-driven reactions, the T252E variant performed sulfoxidation considerably more efficiently than *O*-demethylation:

sulfoxidation > *O*-demethylation ≈ hydroxylation/desaturation > epoxidation > aldehyde oxidation > alkyne oxidation.

The consensus is that *O*-demethylation and hydroxylation require Cpd I.[33, 94] If sulfoxidation was solely mediated by Cpd I, we would not expect this reaction to have occurred more efficiently than *O*-demethylation and hydroxylation. A plausible explanation for this is that there is a second oxidant capable of catalysing sulfoxidation that is more abundant in these H_2O_2-driven reactions. Shaik proposed that the Fe(III)–H_2O_2 complex should be capable of mediating sulfoxidation with high efficiency so that sulfoxidation can still readily occur in the absence of Cpd I (Figure 1.20).[118] Our results agree with those of Dezvarei *et al.*, who also found that in H_2O_2-driven reactions the T → E mutant of $P450_{BM3}$ performed sulfoxidation faster than epoxidation and C-H hydroxylation.[429]

If the T252E mutant had had substantially higher activity towards epoxidation than *O*-demethylation in these hydrogen peroxide-driven reactions, this may have been evidence that an alternative oxidant to Cpd I can carry out epoxidation (e.g. Cpd 0 or Fe(III)–H_2O_2[33, 121]). However, the T252E mutant was less active towards epoxidation than *O*-demethylation. The enantioselectivity of H_2O_2-driven epoxidation catalysed by $T252E_{CYP199A4}$ was essentially the same as that of NADH-supported epoxidation catalysed by $WT_{CYP199A4}$. If the enantioselectivity had differed, this could have been other evidence of the involvement of a second oxidant.

Four-hour H_2O_2-driven reactions were performed with WT CYP199A4 and the T252A and D251N mutants to compare their activity to that of the T252E mutant. All CYP199A4 isoforms tested catalysed the different reactions using H_2O_2, which appears to imply that they could all generate Cpd I to some extent. WT CYP199A4 and the T252A and D251N mutants were all less active than the T252E mutant. In H_2O_2-driven reactions, the T252A mutant, which is assumed to have impaired ability to convert Cpd 0 into Cpd I, was less active towards 4-vinylbenzoic acid epoxidation than the WT enzyme. This may imply that Cpd 0 is not a potent enough oxidant to efficiently mediate epoxidation. The T252A mutant was also less active than the WT enzyme towards *O*-demethylation, 4-formylbenzoic acid oxidation, 4-ethynylbenzoic acid oxidation, and 4-ethylbenzoic acid hydroxylation/desaturation. The T252A mutant was, however, more active towards sulfoxidation of 4-methylthio- and 4-ethylthio-benzoic acid than the WT enzyme, which may suggest the involvement of a second oxidant in sulfoxidation (Fe(III)–H_2O_2 or Cpd 0).

The T252A and D251N mutants of CYP199A4 had reduced peroxygenase activity compared to the WT enzyme with most substrates. This implies that when the WT enzyme is shunted with H_2O_2, the conserved acid-alcohol pair still has an important role in generating the active species. The reduced activity of the D251N mutant suggests that delivery of protons to the active site may still be important. The low activity of the T252A mutant indicates that the threonine OH facilitates catalysis. This agrees with previous studies that found that substitution of the conserved threonine in WT $P450_{cam}$ and $P450_{BM3}$ with aliphatic residues severely reduced their peroxygenase activity.[113, 416, 446-447]

In H_2O_2-supported reactions, WT $P450_{cam}$ was capable of efficiency hydroxylating camphor, whereas the T252A mutant had minimal activity.[446] Shaik's explanation for the greater peroxygenase activity of WT $P450_{cam}$ is that in the T252A mutant, the Fe(III)–H_2O_2 complex is unstable and H_2O_2 would dissociate, whereas in the WT enzyme the threonine stabilises the Fe(III)–H_2O_2 species by hydrogen bonding to this species, so that it can convert into Cpd I.[213] Ma *et al.*[113] similarly found that substitution of the conserved threonine with valine in the F87A mutant of $P450_{BM3}$ abolished this enzyme's ability to epoxidise styrene using H_2O_2. These results and ours emphasise that the conserved acid-alcohol pair is important when WT P450s are shunted using H_2O_2. When H_2O_2 binds to the iron, the Fe(III)–H_2O_2 species may lose a proton to give Cpd 0. The conserved threonine would then be required to stabilise Cpd 0. The conserved aspartate would also be needed to shuttle protons into the active site to protonate Cpd 0 on the distal oxygen, which leads to O–O bond rupture and formation of the active species (Figure 6.27).

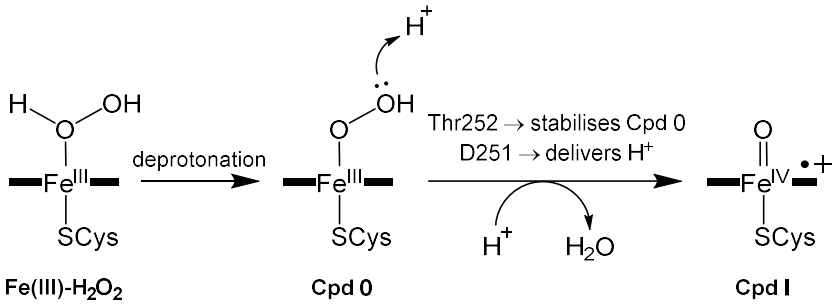

Figure 6.27. When WT CYP199A4 is shunted with H_2O_2, the conserved acid-alcohol pair still appears to have an important role in generating the active species. Loss of a proton from Fe(III)–H_2O_2 would generate Cpd 0. To convert Cpd 0 into Cpd I, Asp251 would be required to deliver H^+ into the active site to protonate Cpd 0 and Thr252 would be required to stabilise Cpd 0.

In conclusion, in H_2O_2-driven reactions, T252E$_{CYP199A4}$ displayed higher activity towards sulfoxidation than C-H hydroxylation, *O*-demethylation and epoxidation. This could imply that the Fe(III)–H_2O_2 complex can carry out sulfoxidation.

Chapter 7

Future directions and conclusions

Chapter 3

In Chapter 3, the substrate range of CYP199A4 was investigated and the requirements for efficient P450 catalytic activity were explored. By solving crystal structures of CYP199A4 in complex with *meta*-substituted benzoic acids, it was established that these substrates bind with the *meta* substituent held close to the heme iron. Despite the proximity of the methoxy group of 3-methoxybenzoic acid to the heme iron, it is not oxidised by CYP199A4. We postulated that the reason for the lack of detectable activity is that the C-H bonds are not correctly oriented for abstraction by Cpd I even though the methyl group is near the iron. We cannot, however, discount the possibility that the orientation of the substrate in the CYP199A4 active site is modified upon heme reduction and dioxygen binding. To assess whether the substrate binding geometry is altered during the catalytic cycle, crystal structures of the O_2-bound ferrous form of the enzyme (or the CN^--bound form[448]) could be solved. However, these complexes are more difficult to obtain due to the limited stability of the ferrous dioxy complex[98] and because the use of KCN presents safety issues. Future work could also involve exploring whether CYP199A4 displays activity towards alternative heterocyclic substrates containing a carboxylic acid moiety, such as 4- or 5-methylfuran carboxylic acid, 5-methylpicolinic acid and 6-methylnicotinic acid (Figure 7.1).

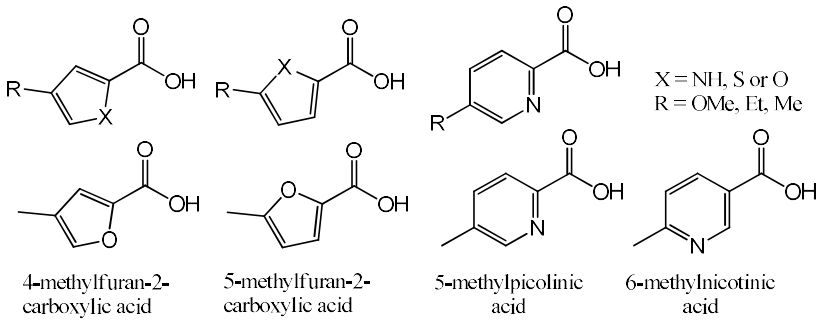

Figure 7.1. Alternative heterocyclic aromatic substrates containing a carboxylic acid moiety that could be investigated with CYP199A4.

To further explore the substrate range of CYP199A4, we could investigate whether CYP199A4 performs more unusual reactions, such as the reduction of nitroaromatics to amines.[18] Pochapsky *et al.* recently reported that $P450_{cam}$ catalyses the six-electron reduction of 3-nitroacetophenone to 3-aminoacetophenone (Figure 7.2), considered an uncommon P450 reaction.[74] We could likewise investigate whether CYP199A4 reduces nitroaromatics, such as 4-nitrobenzoic acid or 4-nitroacetophenone, to the corresponding amines.

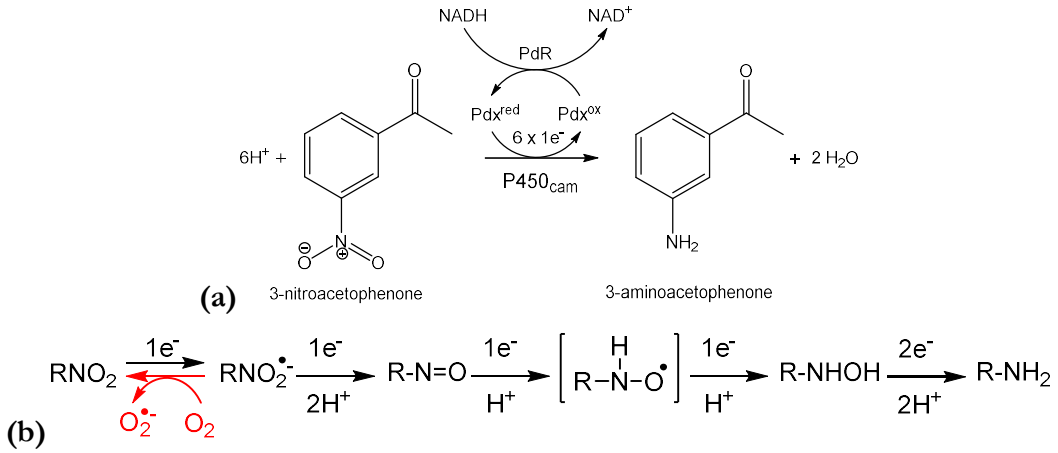

Figure 7.2. **(a)** $P450_{cam}$ reduces 3-nitroacetophenone to the corresponding amine, an uncommon P450 reaction.[18, 74] **(b)** Proposed mechanism for the conversion of nitroaromatics to amines by P450s, requiring six electrons.[18, 74, 449]

I solved a crystal structure of 4-nitrobenzoate-bound CYP199A4 at 1.67-Å resolution, confirming that 4-nitrobenzoic acid binds to CYP199A4 (Table 7.1, Figure 7.3). The dissociation constant (K_d) was estimated to be ~150 ± 10 μM (Table 7.2). A high-occupancy (0.76-occupancy) water ligand to the heme is present in the crystal structure, in harmony with the small spin-state shift (~35%) induced by this substrate. This implies that electron transfer to the heme may be sluggish. Hydrogen-bonding interactions between the nitro moiety and water ligand (3.0 and 3.1 Å) explain why this water ligand is retained, not displaced. 4-Nitrobenzoic acid was modelled in the active site with the nitro group held over the heme and the carboxylate interacting with polar active-site residues, as per other crystal structures of CYP199A4 with benzoic acid derivatives bound (Figure 7.3).

Future work would be to investigate whether CYP199A4 catalyses the reduction of 4-nitrobenzoic acid and other nitroaromatic compounds under anaerobic conditions. Preliminary experiments indicated that CYP199A4 is not able to reduce 4-nitrobenzoic acid to 4-aminobenzoic acid under aerobic conditions (Table 7.2). In the presence of O_2, the nitro anion radical intermediate may be re-oxidised to the starting material (Figure 7.2b) or the ferrous iron heme of the enzyme may bind dioxygen.[18, 449-450] This reaction may therefore occur only under anaerobic conditions.

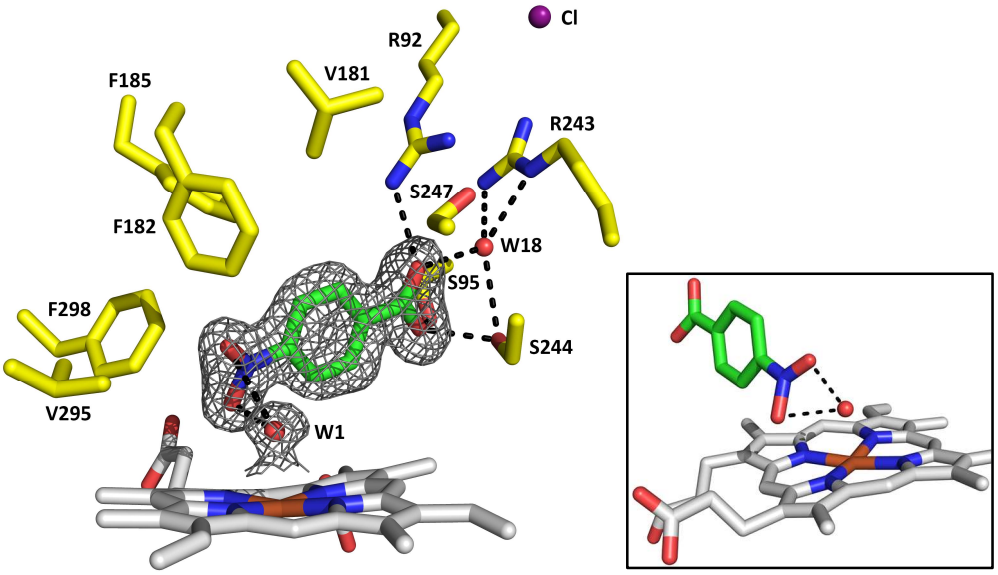

Figure 7.3. Crystal structure of 4-nitrobenzoate-bound CYP199A4; the *2DFo-mFc* electron density of the substrate and heme-bound water (W1) is shown as grey mesh. The map is a composite omit map contoured at 1.0 σ.

Table 7.1. Angles and distances between the heme iron and 4-nitrobenzoic acid.

Distance (Å)	
Fe - N_{nitro}	4.7
Fe - O_{nitro}	4.2, 5.0
Fe - OH_2 ligand	2.2
O_{nitro} - OH_2 ligand	3.0, 3.1
Refined occupancies	
Iron-bound H_2O ligand	76%

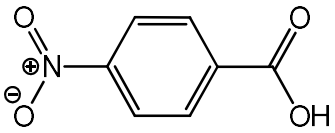

Table 7.2. Binding and *in vitro* turnover data for CYP199A4 with 4-nitrobenzoic acid (under aerobic conditions).

Substrate	**% HS**	**K_d (μM)**	***N*** **(min^{-1})**	**PFR (min^{-1})**	**C (%)**
4-nitrobenzoic acid	~35[a]	150 ± 10[a]	65 ± 2[b]	–[c]	–[c]

[a] Interfering absorption by the substrate prevented accurate measurement of the spin-state shift and binding constant [b] In control reactions omitting the P450, the NADH consumption rate was accelerated by addition of substrate (rate = 34 ± 3 min^{-1}). [c] No product was detected by HPLC analysis of the turnover mixture.

Chapter 4

In Chapter 4, we proposed that optical spectra can distinguish between type II nitrogen ligands which hydrogen-bond to the heme-bound aqua ligand and those which coordinate directly to the heme iron. Future work would be to assess whether the differences we report in the UV-Vis spectra of directly bound and water-bridged complexes can be used to reliably diagnose whether other CYP199A4-drug complexes are water-bridged or have a directly coordinated nitrogen ligand.

We postulated that water-bridged ligands can in some instances be more effective P450 inhibitors than directly coordinated nitrogen ligands.

When the 4-1*H*-imidazol-1-ylbenzoic acid-CYP199A4 complex was reduced with dithionite or NADH/HaPux/HaPuR, the UV-Vis spectrum was identical to that of five-coordinate ferrous CYP199A4. This implied that the Fe-N bond was breaking upon iron reduction. To confirm this, the crystal structure of the ferrous complex could be solved by soaking the crystals in dithionite. Future work would also be to measure the dissociation constant of 4-pyridin-3-ylbenzoic acid with ferrous CYP199A4. Reduction of the 4-pyridin-3-ylbenzoic acid-CYP199A4 complex results in a shift of the Soret band from 424 to 447 nm, and this spectral shift would allow the dissociation constant to be determined by performing a UV-Vis titration. We could also solve the crystal structure of 4-pyridin-3-ylbenzoic acid in complex with ferrous CYP199A4.

Chapters 5 and 6

Mutation of the conserved active-site threonine (T252) of CYP199A4 to glutamate was shown to enhance the peroxygenase activity of this enzyme. Future work is to assess whether the peroxygenase activity of CYP199A4 would be higher if T252 was instead replaced with aspartate (D) or histidine (H), residues which also function as acid-base catalysts in H_2O_2-utilising heme enzymes.[227] Future work could also be to improve the peroxygenase activity of $T252E_{CYP199A4}$ by directed evolution (random mutagenesis).[54] Ideally, variants would be developed with the ability to operate efficiently in the presence of low concentrations of H_2O_2 (variants with low K_m values). The lifetime of the P450 would be extended if it were exposed to lower H_2O_2 concentrations.[264] A rapid screening strategy is required to identify mutants with enhanced peroxygenase activity. The S244D mutant of CYP199A4 is known to bind and oxidise 4-nitroanisole.[333] *O*-Dealkylation of this substrate affords 4-nitrophenolate, a vivid yellow product (Figure 7.4). Directed evolution could be performed using the CYP199A4 S244D T252E double mutant as the starting enzyme, and this colorimetric assay could be used to rapidly identify mutants with enhanced peroxygenase activity.

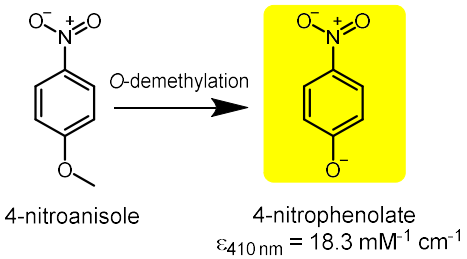

Figure 7.4. CYP199A4 mutants with enhanced peroxygenase activity could be identified using a colorimetric assay.[333] *O*-Demethylation of 4-nitroanisole yields a vivid yellow product (4-nitrophenolate); therefore, mutants with improved peroxygenase activity could be identified based on the intensity of the yellow colour that results when H_2O_2 is added.[333]

Another objective would be to engineer the P450 to be more resistant to inactivation when exposed to H_2O_2.[232] Cirino and Arnold aimed to improve the H_2O_2 tolerance of $P450_{BM3}$ by replacing methionine residues, which are susceptible to oxidation, with norleucine in case enzyme inactivation was arising from methionine oxidatation.[232] This failed to improve its tolerance towards H_2O_2 but did inexplicably enhance its peroxygenase activity.[232] An attempt could be made to improve the hydrogen peroxide stability of CYP199A4 by random mutagenesis.

In the presence of H_2O_2, oxidation of the proximal cysteine thiolate ligand to a sulfenic acid (Cys-SOH) may occur.[228, 425, 451] This inactivates the enzyme but reducing agents (e.g. dithionite and dithiothreitol) can convert the sulfenic acid back into thiolate.[228, 425] If inactivation of $T252E_{CYP199A4}$ is occurring due to oxidation of the proximal thiolate ligand by H_2O_2, this could be addressed by immobilising the enzyme so that it can be readily recovered and regenerated by treatment with a mild reducing agent such as dithiothreitol. The reactivated enzyme could then be re-used. Enzyme immobilisation could be accomplished by encapsulation in a MOF (metal organic framework) such as ZIF-8 (zeolitic imidazolate framework-8) or a HOF (hydrogen-bonded organic framework).[452-453]

Once a variant of the $T252E_{CYP199A4}$ enzyme with enhanced peroxygenase activity has been developed, it could be fused to an H_2O_2-generating enzyme (e.g. alditol oxidase or choline oxidase) (Figure 7.5).[264, 454-455] Supplying low levels of H_2O_2 and replenishing it as it is consumed by the P450 is less destructive than exposure to high H_2O_2 concentrations.[270-271]

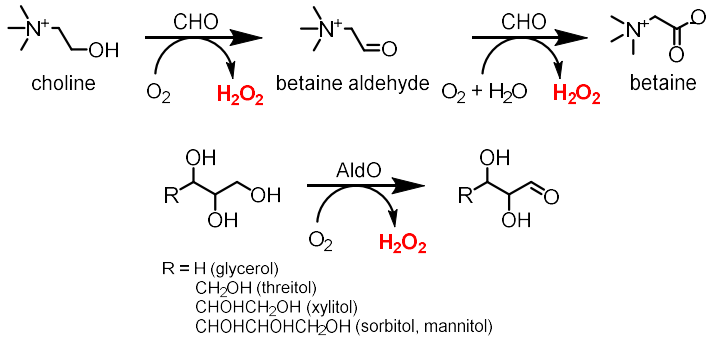

Figure 7.5. Choline oxidase (CHO) and alditol oxidase (AldO) are H_2O_2-generating enzymes that could be fused to the P450 to supply low levels of H_2O_2 required for catalysis. Substrates oxidised by CHO and AldO are given in the figure.[454-455]

Another future project could be to obtain crystal structures of substrate-bound $T252E_{CYP199A4}$ after soaking the crystals in H_2O_2 for various time periods. This would potentially allow us to observe heme degradation and conversion of the substrate into product.

In the T252E mutant, the distal heme-bound aqua/hydroxo ligand is tightly bound and was not displaced by substrates or type II ligands. This property could allow us to drive catalysis by using visible light to oxidise the water- or hydroxide-bound resting state to Cpd II and subsequently to Cpd I (Figure 7.6). This avoids the requirement for expensive NADH or destructive peroxides. Photooxidation of the ferric resting state to Cpd I could be achieved using the photocatalyst

$[Ru(bpy)_3]^{2+}$, as proposed by Cheruzel and co-workers.[456-459] Cheruzel *et al.*[456] succeeded in oxidising ferric $P450_{BM3}$ to Cpd II using $[Ru(bpy)_3]^{2+}$ as the photocatalyst, which they covalently attached to the surface of the enzyme.[456, 459] Irradiation of $[Ru(bpy)_3]^{2+}$ with blue light generates an excited state, $*[Ru(bpy)_3]^{2+}$, which reacts with a quencher to give the powerful oxidant $[Ru(bpy)_3]^{3+}$ (Figure 7.7), that can oxidise heme enzymes to Cpd II and Cpd I.[456, 458-459]

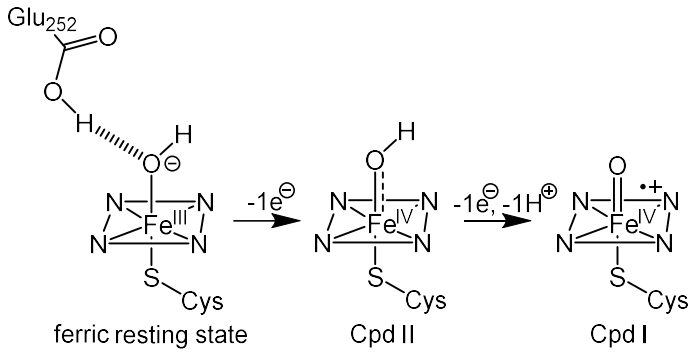

Figure 7.6. Oxidation of the ferric resting state of the T252E mutant could generate Cpd I.

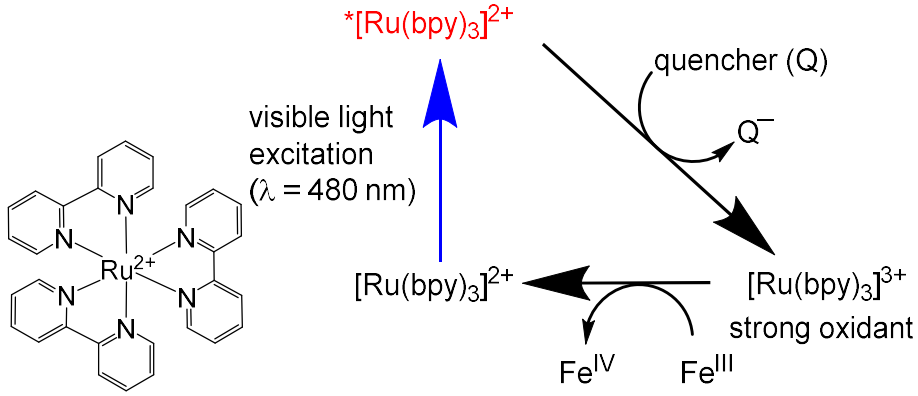

Figure 7.7. Structure of the photocatalyst $[Ru(bpy)_3]^{2+}$. Irradiation of this complex with blue light yields an excited state, which is quenched to give the strong oxidant $[Ru(bpy)_3]^{3+}$ which oxidises ferric $P450_{BM3}$ to give Cpd II.[456, 459]

In Chapter 6, we aimed to identify the active oxidant(s) in P450 reactions. In H_2O_2-driven reactions, the T252E mutant displayed the highest activity towards sulfoxidation of 4-methylthiobenzoic acid, and lower activity towards hydroxylation and epoxidation reactions.

The surrogate oxygen donor H_2O_2 is thought to generate Cpd I via Cpd 0, but *tert*-butyl hydroperoxide should generate Cpd I without formation of Cpd 0. We expected that we could use *tert*-butyl hydroperoxide to identify whether certain P450 reactions were mediated by Cpd I or Cpd 0. We found that CYP199A4, however, was unable to utilise *tert*-butyl hydroperoxide as a surrogate oxygen donor. We speculated that this was because the bulky tertiary butyl group prevented it from accessing the heme iron when substrate was bound in the CYP199A4 active site. We could instead attempt to generate Cpd I with methyl hydroperoxide, which is less bulky and may be able to access the heme (Figure 7.8). This would allow us to probe whether Cpd 0 or Cpd I was predominantly

responsible for certain P450 reactions. Methyl hydroperoxide can be synthesised but care would need to be exercised because it is a hazardous chemical (potentially explosive).[460-461]

tert-butyl hydroperoxide methyl hydroperoxide

Figure 7.8. Methyl hydroperoxide is less bulky than *tert*-butyl hydroperoxide and may be able to access the heme when substrate is bound in the CYP199A4 active site.

In conclusion, CYP199A4 was utilised as a model system to investigate the mechanism of various cytochrome P450-catalysed reactions, to understand the requirements for efficient C-H hydroxylation and to assess whether different type II inhibitor binding modes can be distinguished by UV-Vis spectroscopy.

Appendix A: Supplementary Information for Chapter 3

Spin-state shift data for CYP199A4 with *meta*-substituted benzoic acid substrates

Table A1. Shift in Soret band position upon binding of substrates to CYP199A4

Substrate	Position of Soret band (λ_{max} / nm)		Shift
	Substrate-free CYP199A4	Substrate-bound CYP199A4	
3-methoxyBA	418.5	416.0	2.5 nm blue shift
3-methylaminoBA	419.0	419.5	**0.5 nm red shift**
3-methylthioBA	418.5	418.0	0.5 nm blue shift
3-methylBA	419.0	417.0	2 nm blue shift
3-formylBA	418.5	419.0	**0.5 nm red shift**
4-formylBA	418.5	418.0	0.5 nm blue shift
3-ethoxyBA	419.0	397.0	22 nm blue shift
3-*tert*-butylBA	419.0	419.0	no shift
3-isopropylBA	419.0	416.0	3 nm blue shift

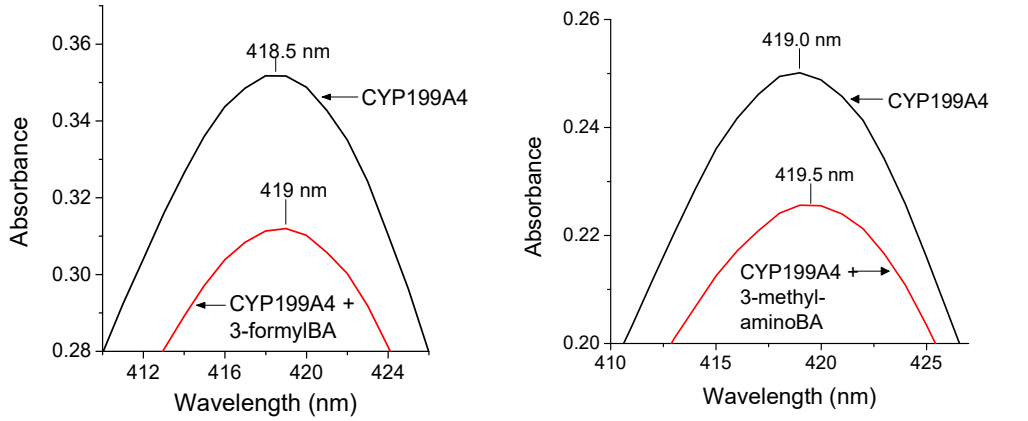

(a) 3-formylbenzoic acid **(b)** 3-methylaminobenzoic acid

Figure A1. Soret band red shifts induced by binding of **(a)** 3-formylbenzoic acid and **(b)** 3-methylaminobenzoic acid to CYP199A4. This 0.5-nm red shift may indicate that the heteroatoms of the benzoic acid substrates are interacting with the iron-bound water ligand.

In vitro NADH turnover data

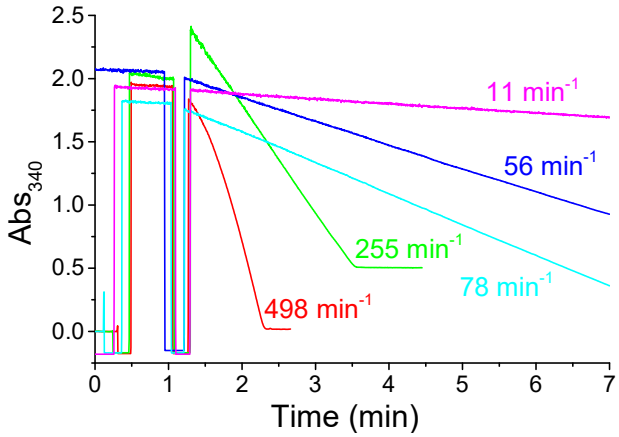

Figure A2. Rates of NADH consumption by CYP199A4 with 3-methoxybenzoic acid (**red**), 3-methylaminobenzoic acid (**green**), 3-methylthiobenzoic acid (**dark blue**), 3-methylbenzoic acid (**cyan**), and 3-formylbenzoic acid (**magenta**).

GC-MS data for 3-methylamino- and 3-methylthio-benzoic acid turnovers

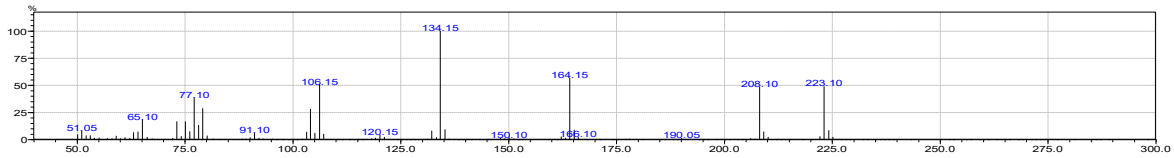

3-Methylaminobenzoic acid substrate (singly derivatized): m/z = 223.10 (expected m/z = 223.1029), RT = 18.1 min

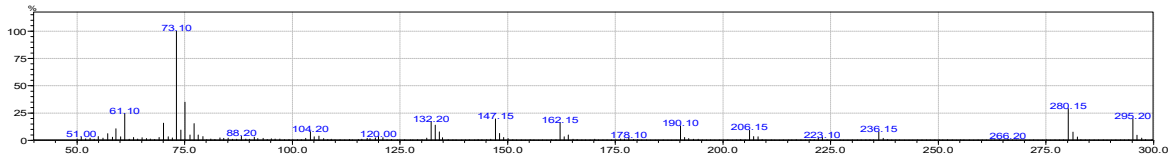

3-Methylaminobenzoic acid substrate (doubly derivatized): m/z = 295.20 (exp. m/z = 295.1424), RT = 21.19 min

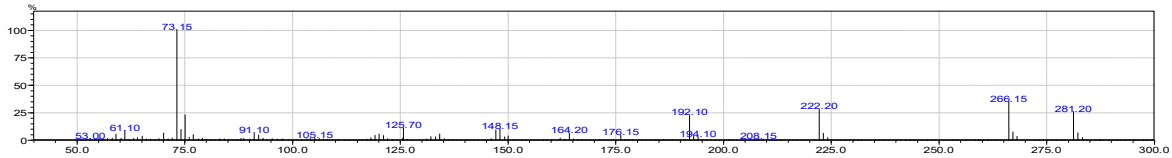

3-Aminobenzoic acid product (doubly derivatized): m/z = 281.20 (exp. m/z = 281.1267), RT = 21.09 min

Figure A3. Mass spectral data for the CYP199A4 *in vitro* reaction with 3-methylaminobenzoic acid.

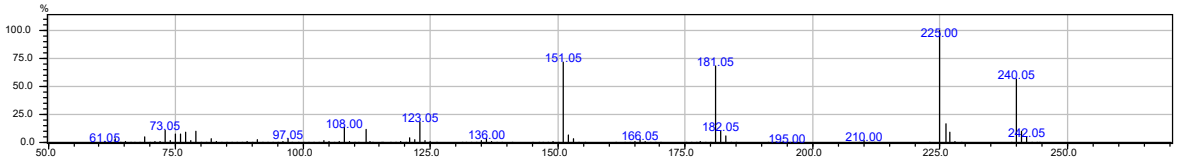

3-Methylthiobenzoic acid substrate (singly derivatised): m/z = 240.05 (exp. m/z = 240.0640), RT = 12.2 min.

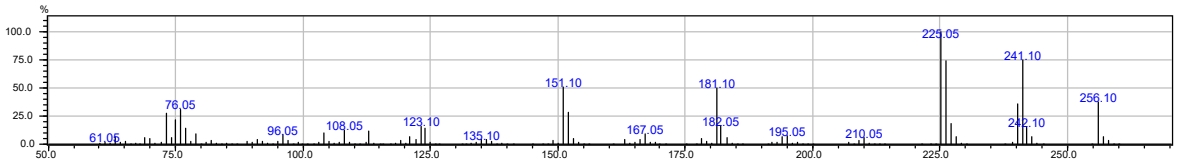

3-Methylsulfinylbenzoic acid (singly derivatised): m/z = 256.10 (exp. m/z = 256.0589), RT = 17.0 min.

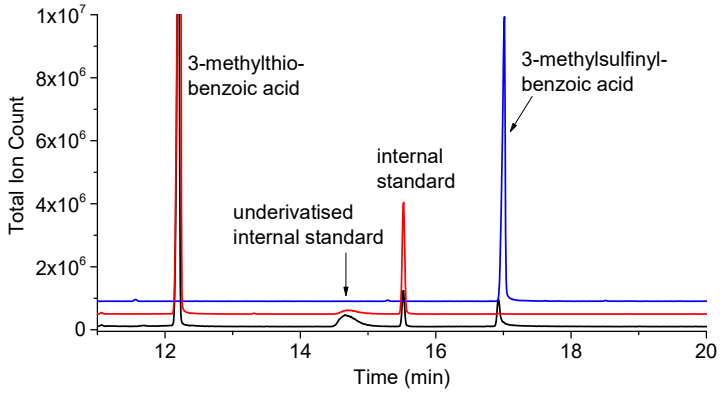

Figure A4. Mass spectral data for the CYP199A4 *in vitro* reaction with 3-methylthiobenzoic acid. The **black** chromatogram is the TMS-derivatised turnover, and in **blue** is chemically synthesised 3-methylsulfinylbenzoic acid. In **red** is a control reaction omitting the P450.

Rate of disappearance of H_2O_2 added to a control turnover mixture

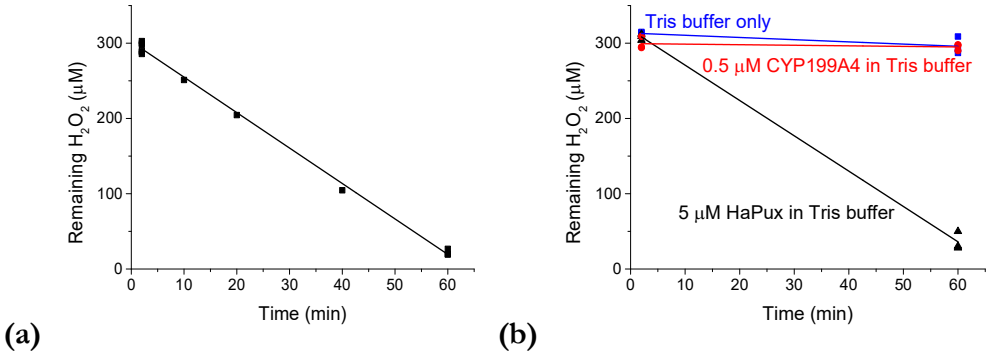

Figure A5. **(a)** Rate of disappearance of 300 μM H_2O_2 incubated in a control turnover mixture containing 5 μM HaPux, 0.25 μM HaPuR and 0.5 μM CYP199A4 in Tris-HCl buffer (but no NADH, substrate or catalase) at 30 °C. **(b)** Rate of disappearance of H_2O_2 incubated with the individual components of the turnover mixture in Tris-HCl buffer (**blue** = Tris-HCl buffer only, **red** = 0.5 μM CYP199A4 in Tris buffer, **black** = 5 μM HaPux in Tris buffer).

When the rate of NADH consumption by the P450 is slow, a portion of the H_2O_2 generated via uncoupling may be lost before the H_2O_2 concentration is measured at the end of the reaction. We would therefore be underestimating the amount of H_2O_2 generated.

To assess whether any loss of H_2O_2 occurs over time, 300 μM H_2O_2 was incubated in a control turnover mixture containing 5 μM HaPux, 0.25 μM HaPuR and 0.5 μM CYP199A4 in Tris-HCl buffer (but no NADH, substrate or catalase) at 30 °C for 1 h. The H_2O_2 concentration was measured at intervals using the horseradish peroxidase/phenol/4-aminoantipyrine assay. Substantial decreases in H_2O_2 concentration were observed over the sixty-minute period (Figure A5a). No significant loss of H_2O_2 occurred, however, when H_2O_2 was incubated in Tris buffer, or Tris buffer containing only 0.5 μM CYP199A4 (Figure A5b, **blue**, **red**). Either the ferredoxin or some component of its solution appeared to be responsible for the loss of H_2O_2 (Figure A5b, **black**). Accurate measurement of H_2O_2 is therefore only possible for reactions which are completed in less than 10 minutes, requiring the NADH consumption rate by the P450 to be at least 64 μM $(\mu M\text{-}P450)^{-1}$ min^{-1}.

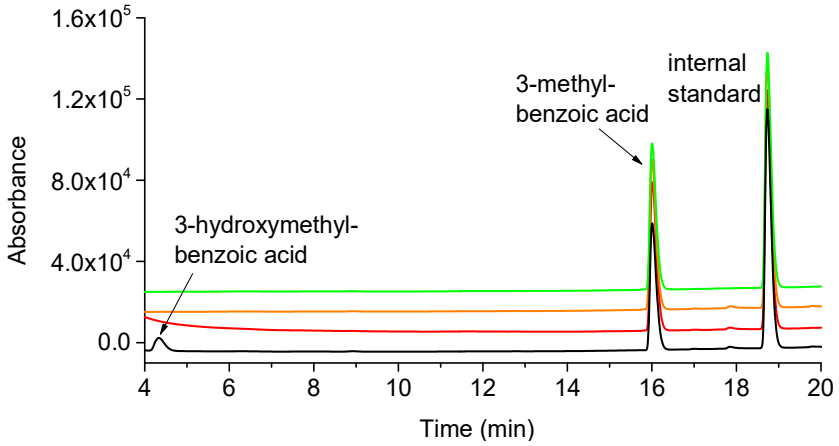

Figure A6. HPLC analysis of the reaction with 3-methylbenzoic acid. In **black** is the *in vitro* turnover, in **red** and **orange** are control reactions omitting the P450 and NADH, and in **green** is the substrate control (RT = 16 min). Product appears at RT = 4.3 min. Gradient: 20-95% AcCN in H_2O_2 with 0.1% TFA. Detection wavelength: 254 nm.

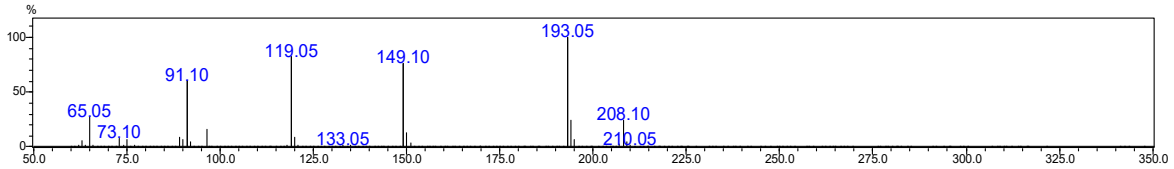

3-Methylbenzoic acid substrate (singly derivatised): m/z = 208.10 (exp. m/z = 208.0920), RT = 5.1 min.

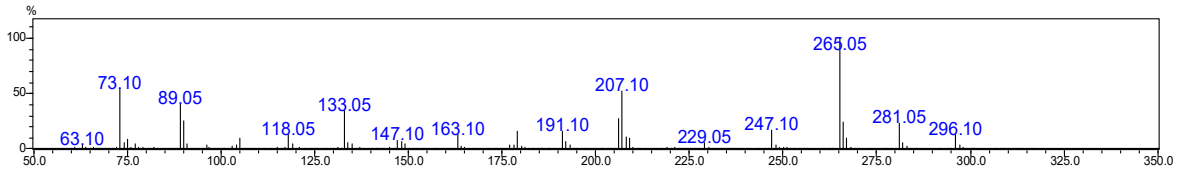

Oxidation product, presumed to be 3-hydroxymethylbenzoic acid (doubly derivatized): m/z = 296.10 (exp. m/z = 296.1264), RT = 12.3 min.

Figure A7. Mass spectral data for the CYP199A4 *in vitro* reaction with 3-methylbenzoic acid.

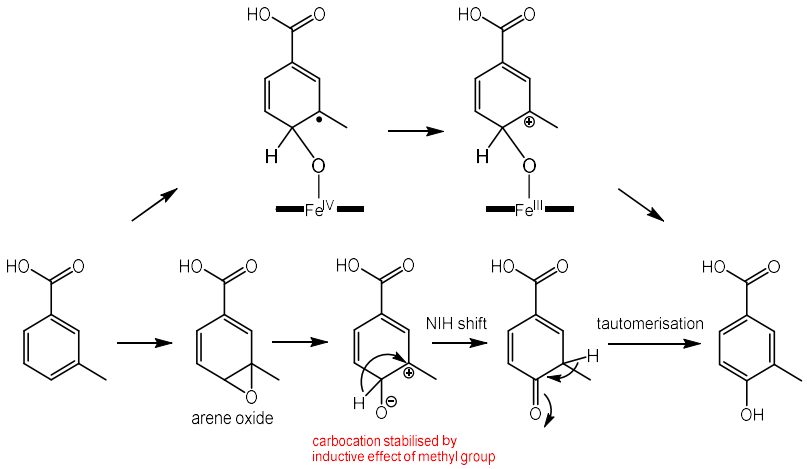

Figure A8. CYP199A4 could conceivably convert 3-methylbenzoic acid into 4-hydroxy-3-methylbenzoic acid via hydroxylation of the aromatic ring. However, authentic 4-hydroxy-3-methylbenzoic acid did not co-elute with the oxidation product (Figure A9).

Identification of the product of the 3-methylbenzoic acid turnover

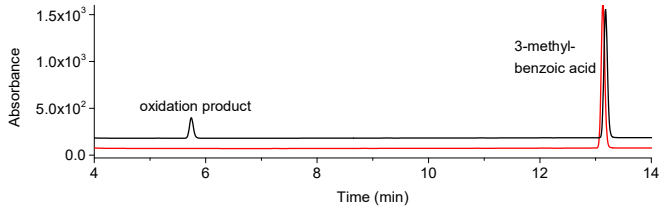

(a) *In vitro* turnover (**black**) and control reaction omitting the P450 (**red**)

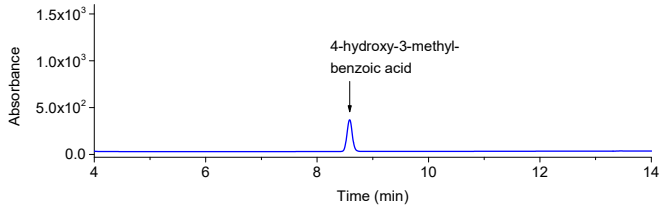

(b) Authentic 4-hydroxy-3-methylbenzoic acid

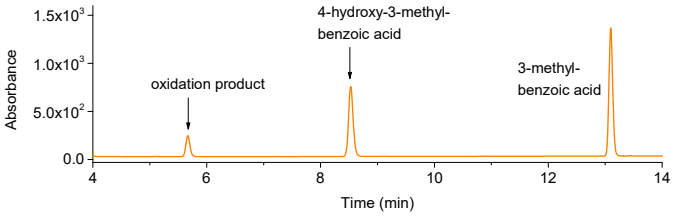

(c) Authentic 4-hydroxy-3-methylbenzoic acid added to the *in vitro* turnover

Figure A9. **(a)** HPLC analysis of the *in vitro* CYP199A4 reaction with 3-methylbenzoic acid. The oxidation product had a retention time of 5.7 min. **(b)** Authentic 4-hydroxy-3-methylbenzoic acid had a retention time of 8.5 min and did not co-elute with the oxidation product **(c)**. Gradient: 20-95% AcCN in H_2O with 0.1% TFA. Detection wavelength: 240 nm.

Note that the retention times of the same compounds differ in Figures A6 and A9 because different HPLC instruments were used.

Chemical synthesis of 3-hydroxymethylbenzoic acid

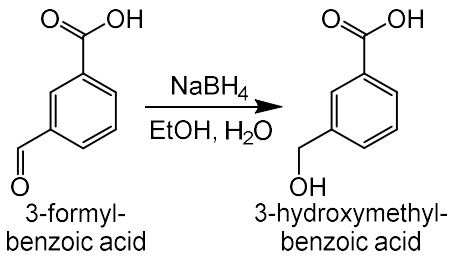

To a stirred solution of 3-formylbenzoic acid (9 mg, 0.06 mmol) in ethanol (1 mL) was added dropwise a solution of sodium borohydride (1.7 mg, 0.045 mmol) in water (1 mL) and the resulting mixture was stirred for 40 min. Water (3 mL) and 50 µL conc. HCl were then added and the reaction was analysed by HPLC (Figure A10).

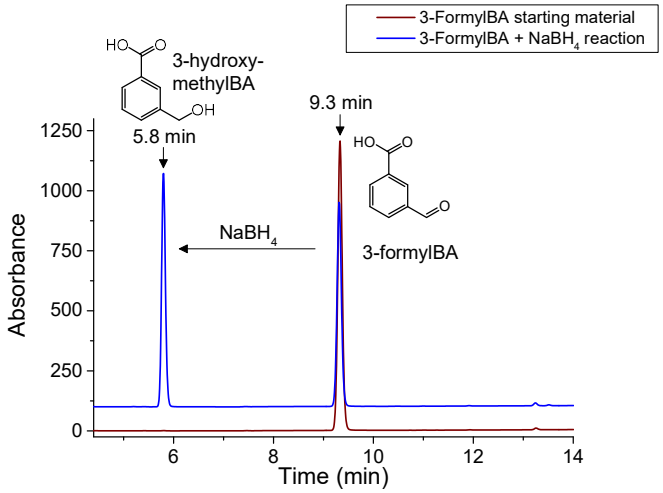

Figure A10. HPLC analysis of the 3-formylbenzoic acid starting material (**wine**, RT = 9.3 min) and the product, 3-hydroxymethylbenzoic acid, arising from reduction of the aldehyde by sodium borohydride (**blue**, RT = 5.8 min). Gradient: 20 → 95% AcCN in H_2O with 0.1% TFA. Detector wavelength: 240 nm.

Co-elution of the synthesised 3-hydroxymethylbenzoic acid with the product of the CYP199A4 reaction with 3-methylbenzoic acid

CYP199A4 converted 3-methylbenzoic acid into a single oxidation product (Figure 3.9). Its mass indicated that it was a hydroxylation product. CYP199A4 does not hydroxylate benzoic acid[162] and hence this product was expected to be 3-hydroxymethylbenzoic acid, not 4-hydroxy-3-methylbenzoic acid which would arise from hydroxylation of the aromatic ring.

To verify that the product was 3-hydroxymethylbenzoic acid, this compound was chemically synthesised via reduction of 3-formylbenzoic acid with $NaBH_4$. The CYP199A4 oxidation product and synthesised 3-hydroxymethylbenzoic acid had identical HPLC retention times (Figure A11).

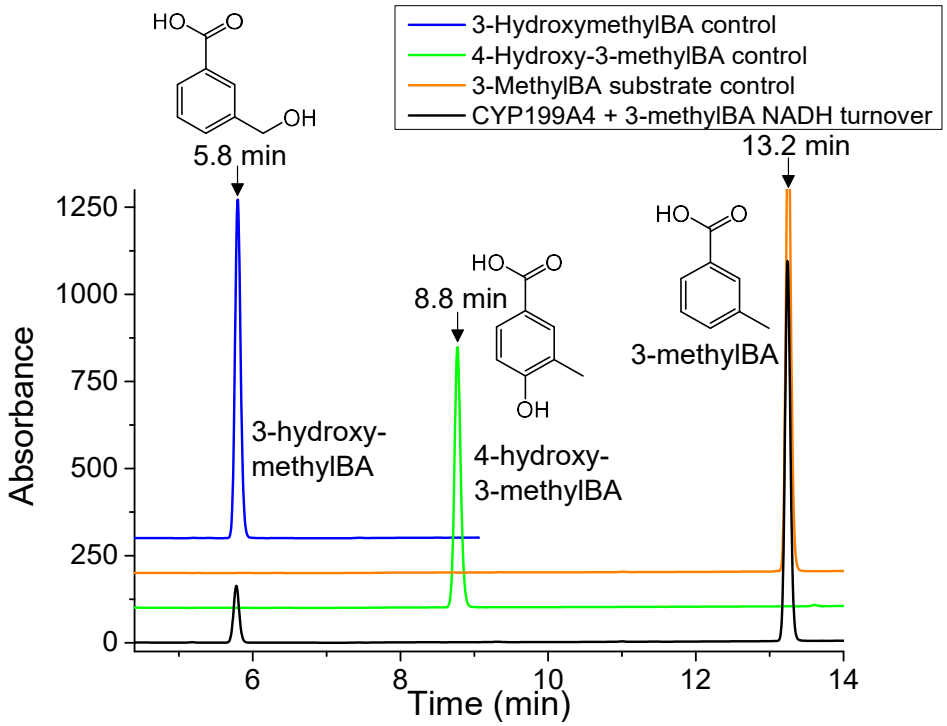

Figure A11. HPLC analysis of the *in vitro* NADH-supported reaction of CYP199A4 with 3-methylbenzoic acid (**black**). In **orange** is the 3-methylbenzoic acid substrate control (RT = 13.2 min), in **blue** is chemically synthesised 3-hydroxymethylbenzoic acid (RT = 5.8 min) and in **green** is authentic 4-hydroxy-3-methylbenzoic acid (RT = 8.8 min). The P450 oxidation product (RT = 5.8 min) co-elutes with 3-hydroxymethylbenzoic acid.

Gradient: 20 → 95% AcCN in H_2O with 0.1% TFA. Detector wavelength: 240 nm.

Binding and turnover data for 2-methylbenzoic acid

Table A2. Binding and *in vitro* turnover data for CYP199A4 with 2-methylbenzoic acid

Substrate	% HS	K_d (μM)	N (min^{-1})	PFR (min^{-1})	C (%)	H_2O_2 (%)
2-methylBA	5%	611 ± 72	13 ± 0.3[a]	–[b]	–[b]	–[c]

[a]The NADH consumption rate reported is the average rate over the first 15 minutes. [b]No product was detected by HPLC or GC analysis. [c]Not measured.

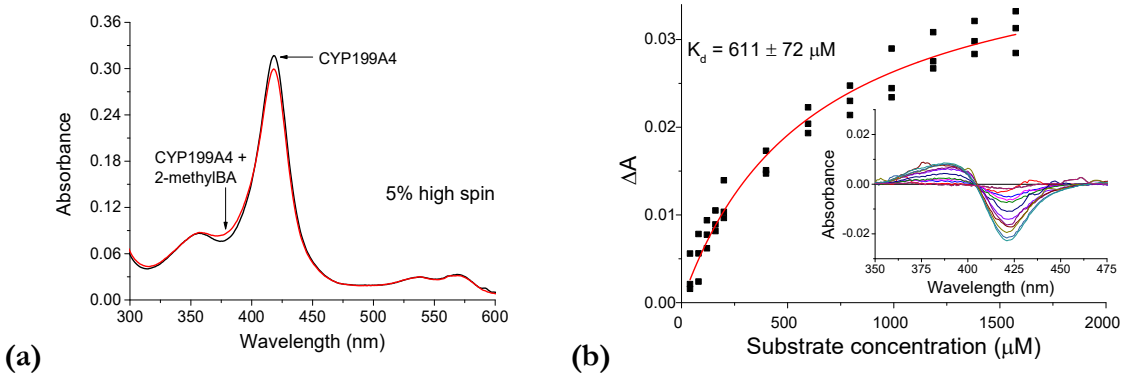

Figure A12. **(a)** Spin-state shift induced by binding of 2-methylbenzoic acid to CYP199A4, and **(b)** determination of the dissociation constant.

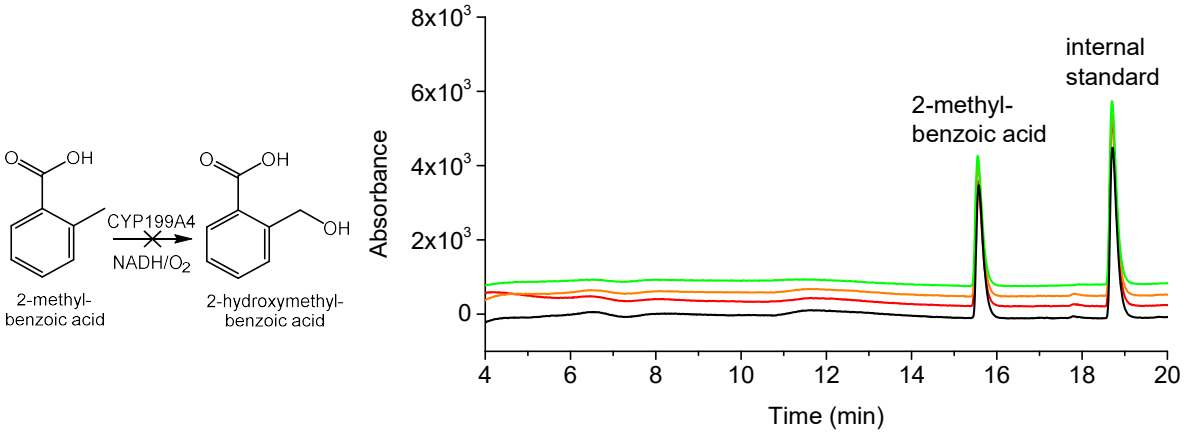

Figure A13. HPLC chromatogram of the CYP199A4 *in vitro* reaction with 2-methylbenzoic acid. No product was detected. In **black** is the *in vitro* turnover, in **red** is a control reaction omitting the P450, in **orange** is a control reaction performed without NADH, and in **green** is the 2-methylbenzoic acid substrate control (RT = 15.6 min). Gradient: 20-95% AcCN in H_2O with 0.1% TFA. Detection wavelength: 254 nm.

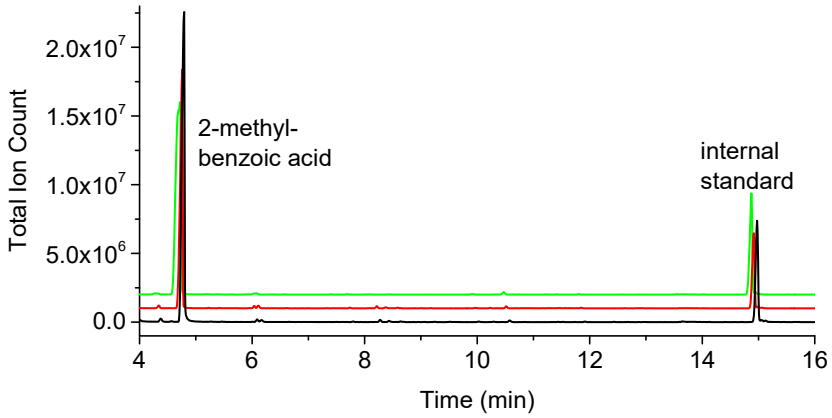

Figure A14. GC-MS analysis of the CYP199A4 *in vitro* reaction with 2-methylbenzoic acid. In **black** is the *in vitro* turnover, in **red** is a control reaction performed without P450 and in **green** is the 2-methylbenzoic acid substrate control (RT = 4.7 min). No oxidation product was detected.

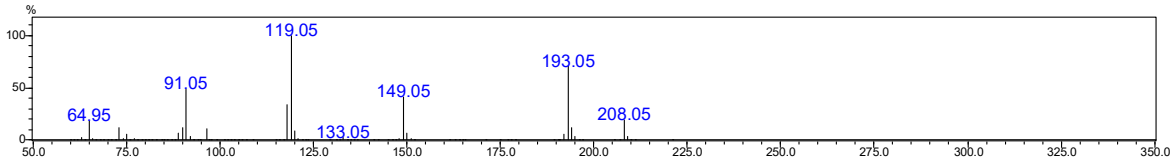

2-Methylbenzoic acid substrate (singly derivatised): m/z = 208.05 (exp. m/z = 208.0920), RT = 4.7 min.

Figure A15. Mass spectral data for the CYP199A4 *in vitro* reaction with 2-methylbenzoic acid. No product was detected.

ICM-Pro docking scores

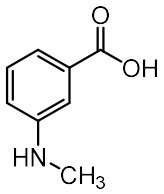

Table A3. Selected distances in Å between 3-methylaminobenzoic acid and active-site residues/heme

Distance (Å)	'Down'	'Up'
Fe - CH_3	4.1	7.4
Fe - N	4.6	7.2
N - nearest heme N	4.0	-
CH_3 - nearest heme N	3.6	-
CH_3 - nearest heme C	3.7	-
CH_3 - closest C of F182	3.8	2.8
CH_3 - closest C of F298	3.8	6.4
CH_3 - closest C of F185	5.5	4.2

Table A4. ICM-Pro scores for **3-methylaminobenzoic acid** docked into CYP199A4 in the 'down' and 'up' orientations

Pose	Score	Vls Score	Strain kcal/mol	Steric	Torsion	Electro	Hbond kcal/mol	Hydroph kcal/mol	Surface
'Down'	-40.19	-43.22	3.028	-13.41	1	-9.149	-10.66	-3.202	6.331
'Up'	-26.73	-36.42	9.698	-6.917	1	-11.1	-10.08	-3.049	6.341

Table A5. ICM-Pro scores for **3-methylthiobenzoic acid** docked into CYP199A4

Pose	Score	Vls Score	Strain kcal/mol	Steric	Torsion	Electro	Hbond kcal/mol	Hydroph kcal/mol	Surface
1	-37.52	-39.79	2.272	-17.83	1	-3.519	-9.179	-3.085	6.74
2	-35.45	-37.55	2.101	-14.09	1	-4.815	-9.431	-3.076	6.728

Table A6. ICM-Pro scores for **3-methylbenzoic acid** docked into CYP199A4 in the 'up' and 'down' orientations

Pose	Score	Vls Score	Strain kcal/mol	Steric	Torsion	Electro	Hbond kcal/mol	Hydroph kcal/mol	Surface
'Down'	-38.05	-39.48	1.425	-16.03	1	-4.867	-8.859	-3.182	4.942
'Up'	-36.88	-39.42	2.535	-8.641	1	-11.47	-10.04	-3.136	4.939

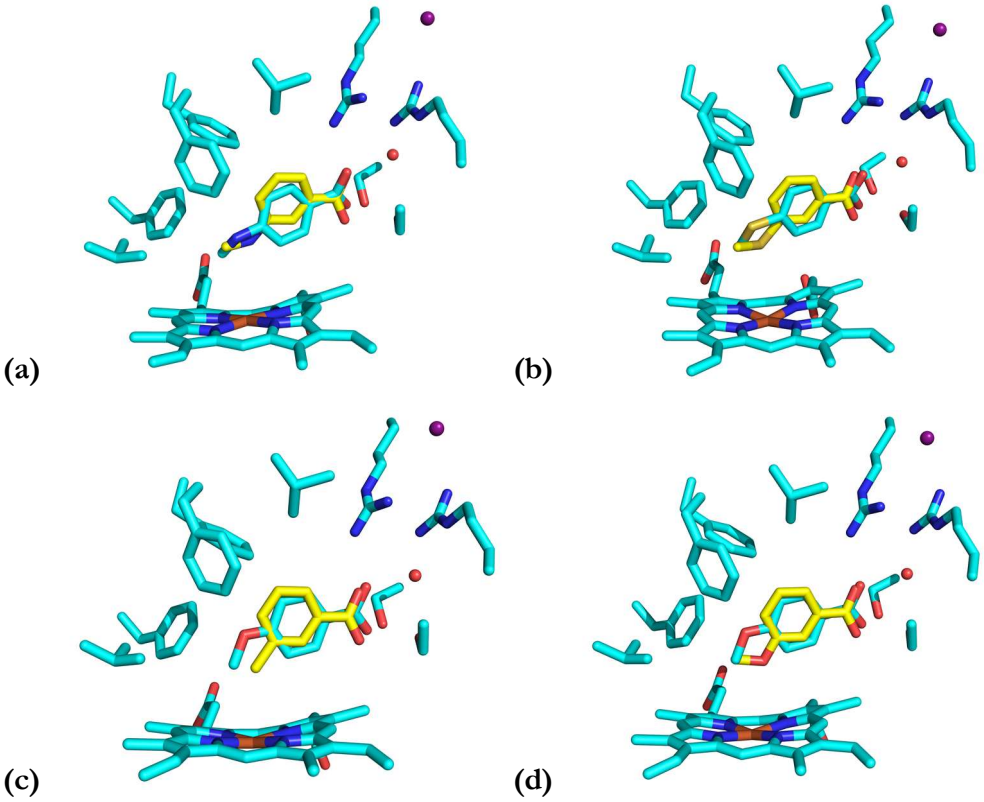

Figure A16. Docked poses of **(a)** 3-methylamino-, **(b)** 3-methylthio-, **(c)** 3-methyl- and **(d)** 3-methoxy-benzoic acid, shown in yellow, are overlaid with the crystal structures of the *para* isomers (cyan). The benzene ring of the *meta* isomers is shifted away from the heme relative to that of the *para* isomers.

Table A7. ICM-Pro scores for **veratric acid** docked into CYP199A4

Pose	**Score**	**Vls Score**	**Strain** kcal/mol	**Steric**	**Torsion**	**Electro**	**Hbond** kcal/mol	**Hydroph** kcal/mol	**Surface**
1	-34.31	-42.1	7.793	-13.86	1	-9.939	-10.17	-3.571	7.777
2	-29.19	-37.54	8.348	-7.206	1	-11.54	-10.48	-3.55	7.439

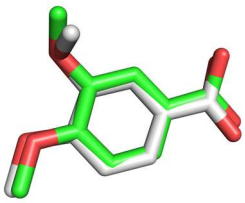

Figure A17. Comparison of the top-scoring docked pose (grey) with the crystal structure pose (green) of veratric acid. ICM-Pro correctly predicted the binding mode. The RMSD between the docked pose and crystallographic pose is 0.326 Å.

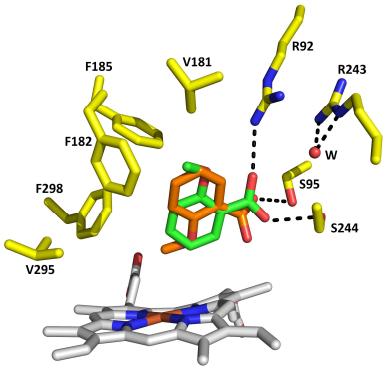

Figure A18. 2-Methoxybenzoic acid docked into CYP199A4 (PDB code: 5U6W). The top-scoring pose (**green**) has the *ortho* methoxy group pointing away from the heme. The alternate pose (**orange**), which has the *ortho* group pointing towards the heme, scored poorly.

Table A8. ICM-Pro scores for **2-methoxybenzoic acid** docked into CYP199A4

Pose	**Score**	**Vls Score**	**Strain** kcal/mol	**Steric**	**Torsion**	**Electro**	**Hbond** kcal/mol	**Hydroph** kcal/mol	**Surface**
'Up'	-22.63	-29.79	7.163	-9.916	1	-4.492	-7.886	-3.275	6.177
'Down'	-5.564	-10.39	4.831	-7.732	1	5.909	-3.796	-3.301	6.205

Table A9. ICM-Pro scores for **3-methoxybenzoic acid** docked into CYP199A4 in the 'up' and 'down' orientations

Pose	**Score**	**Vls Score**	**Strain** kcal/mol	**Steric**	**Torsion**	**Electro**	**Hbond** kcal/mol	**Hydroph** kcal/mol	**Surface**
'Down'	-37.67	-40.63	2.963	-16.55	1	-5.051	-9.507	-3.175	6.446
'Up'	-30.02	-38.16	8.143	-8.934	1	-10.83	-10.07	-3.07	6.483

Data collection and crystal structure refinement statistics

Table A10. Statistics for data collection and refinement of crystal structures of CYP199A4 with 3-methoxy-, 3-methylthio-, 3-methylamino-, 3-methyl- and 4-methyl-benzoic acid bound. Values in parentheses correspond to the highest resolution (outer) shell.

Statistic	3-methoxy	3-methylthio	3-methylamino	3-methyl	4-methyl
PDB code	6PQ6	6PQD	6PRR	6PQW	6PQS
X-ray wavelength	0.9537	0.9537	0.9537	0.9537	0.9537
Unit cell parameters	a = 44.5 b = 51.4 c = 78.9 α = 90.0 β = 92.5 γ = 90.0	a = 44.3 b = 51.3 c = 78.7 α = 90.0 β = 92.6 γ = 90.0	a = 44.4 b = 51.4 c = 79.5 α = 90.0 β = 92.1 γ = 90.0	a = 44.5 b = 51.2 c = 79.0 α = 90.0 β = 92.2 γ = 90.0	a = 44.2 b = 51.3 c = 78.9 α = 90.0 β = 92.1 γ = 90.0
Space group	$P12_11$	$P12_11$	$P12_11$	$P12_11$	$P12_11$
Molecules per asymmetric unit	1	1	1	1	1
Resolution range	43.05 – 1.66 (1.69 – 1.66)	44.25 – 1.89 (1.93 – 1.89)	44.32 – 1.67 (1.70 – 1.67)	44.42 – 1.68 (1.71 – 1.68)	44.19 – 1.60 (1.63 – 1.60)
<I/σ(I)>	12.3 (2.4)	13.6 (4.0)	16.7 (4.1)	14.3 (2.6)	10.3 (1.2)
Unique reflections	41800	28336	40980	40638	45536
Completeness of data	98.9 (94.3)	99.5 (95.1)	98.0 (62.9)	99.8 (97.3)	97.2 (91.8)
Multiplicity	6.3 (5.1)	6.7 (6.1)	6.7 (6.3)	6.9 (6.9)	6.9 (6.8)
R_{merge} (all I+ and I−)	9.5 (66.2)	10.2 (46.2)	6.2 (34.9)	7.4 (56.8)	15.9 (149.2)
R_{pim} (all I+ and I−)	4.0 (30.8)	4.2 (20.2)	2.6 (15.0)	3.0 (23.1)	6.4 (59.7)
$CC_{1/2}$	99.7 (83.2)	99.7 (90.2)	99.9 (91.7)	99.9 (91.5)	99.6 (46.0)
R_{work}	0.1555	0.1540	0.1547	0.1451	0.1598
R_{free} (5% held)	0.1847	0.1999	0.1836	0.1874	0.1939
Ramachandran favoured (%)	98.2	97.95	97.95	98.47	98.21
Ramachandran outliers (%)	0	0	0	0	0
Unusual rotamers (%)	0	0	0	0	0
RMSD bond angles (°)	0.708	0.845	0.903	1.036	0.834
RMSD bond lengths (Å)	0.003	0.006	0.007	0.009	0.004
Omit map type, contour level, carve radius	composite omit map, 1.0 σ, 1.3 Å carve	composite omit map, 1.5 σ, 1.5 Å carve	composite omit map, 1.5 σ, 1.2 Å carve	polder omit map, 2.5 σ, 1.5 Å carve	composite omit map, 1.5 σ, 1.5 Å carve

Three-dimensional fold of CYP199A4 in complex with 3-methoxy-, 3-methylamino-, 3-methylthio-, and 3-methyl-benzoic acid

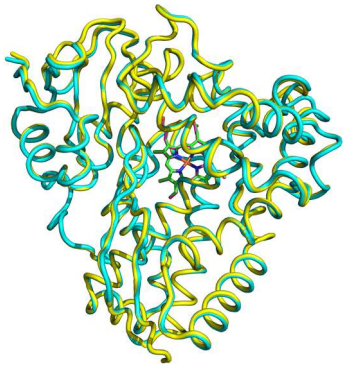

(a) 3- and 4-methoxybenzoic acid (RMSD = 0.588 Å)

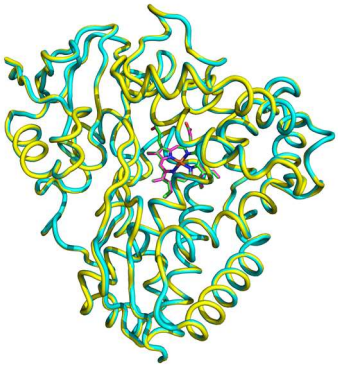

(b) 3- and 4-methylaminobenzoic acid (RMSD = 0.222 Å)

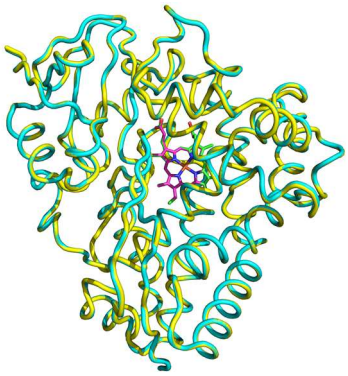

(c) 3- and 4-methylthiobenzoic acid (RMSD = 0.140 Å)

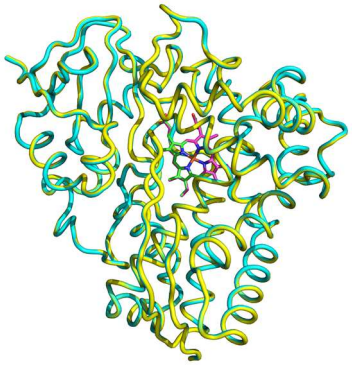

(d) 3- and 4-methylbenzoic acid (RMSD = 0.131 Å)

Figure A19. Overall fold of CYP199A4. In yellow are the crystal structures of CYP199A4 with *meta*-substituted benzoic acids bound. Superimposed with these are the structures of CYP199A4 with the corresponding *para* isomers bound (blue cartoon, green heme). The root-mean-square deviation between the superimposed structures (measured over all 393 pairs of Cα atoms) is given in parentheses under each figure.

4-Methoxybenzoate-bound CYP199A4 (PDB: 4DO1) was crystallised under different conditions than the other crystal structures. This is why the RMSD between the 4- and 3-methoxybenzoic acid structures is higher. If the 3-methoxybenzoic acid structure is superimposed with the 4-methylthiobenzoic acid structure, the RMSD is only 0.155 Å.

Comparison of docked ligand poses and crystallographic poses

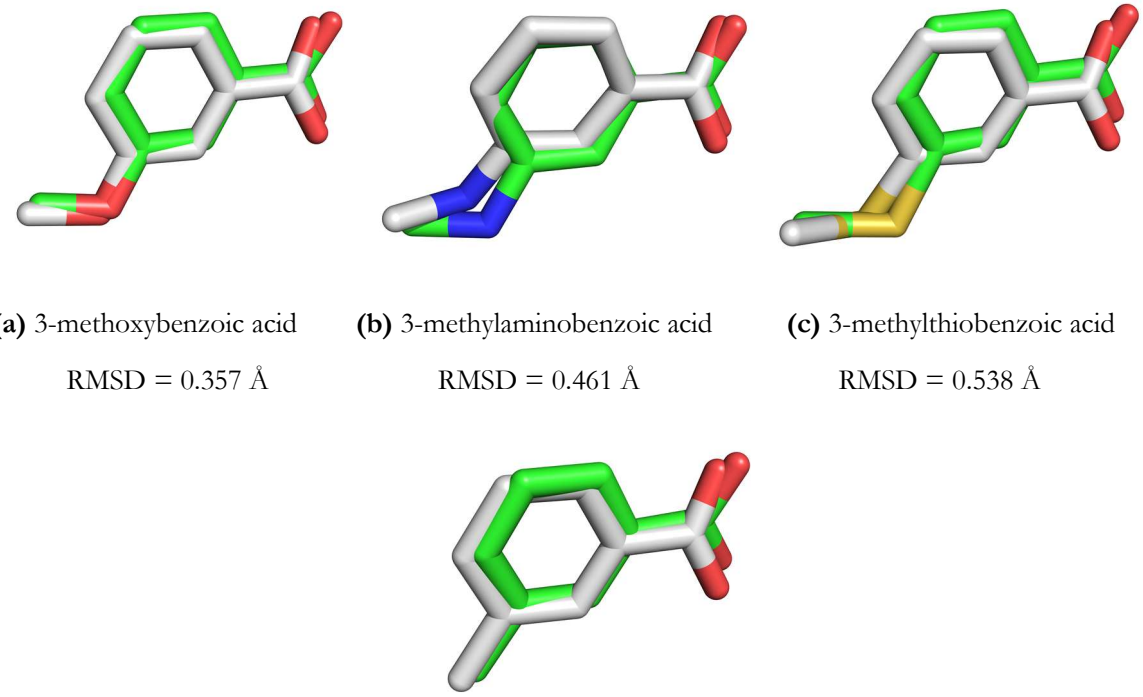

(a) 3-methoxybenzoic acid

RMSD = 0.357 Å

(b) 3-methylaminobenzoic acid

RMSD = 0.461 Å

(c) 3-methylthiobenzoic acid

RMSD = 0.538 Å

(d) 3-methylbenzoic acid

RMSD = 0.423 Å

Figure A20. Comparison of docked ligand poses (grey) and crystallographic poses (green). For each substrate, the top-scoring docked pose agrees well with the crystallographic pose. The RMSD between the predicted pose and crystal structure pose is given beneath each figure. The root-mean-square deviation was calculated using the formula

$$RMSD = \sqrt{\frac{1}{N}\sum_{i=1}^{N} d_i^2}$$

where d_i is the distance between the ith pair of equivalent atoms and N is the number of equivalent atom pairs. A docked pose is commonly considered 'good' if the RMSD is <2 Å.[462-463]

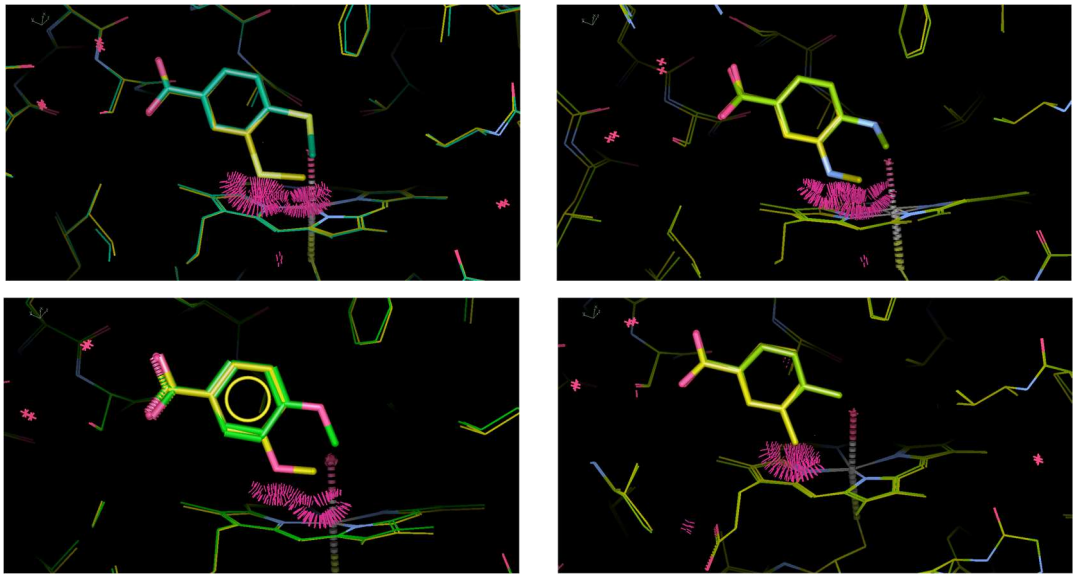

Figure A21. The benzene ring of 3-substituted benzoic acids is held further away from the heme than the benzene ring of 4-substituted benzoic acids. If the *meta*-substituted benzoic acids are repositioned so that their benzene ring is superimposable with that of 4-substituted benzoic acids, as shown above, it results in a steric clash between the *meta* substituent and the heme. *MolProbity*[329] uses hot-pink spikes to represent steric clashes.

Fe-S distances and displacement of the iron out of the heme plane in substrate-bound CYP199A4 crystal structures

Table A11. Displacement of the heme iron below the porphyrin plane in CYP199A4 crystal structures

Ligand bound to wild-type CYP199A4	Water occupancy in crystal structure	Iron displacement below porphyrin plane (Å)	
		Plane defined by the four pyrrole nitrogens	Plane defined by the 24 atoms of the porphyrin macrocycle
3-MethoxyBA	50%	0.222	0.202
3-MethythioBA	77%	0.150	0.151
3-MethylaminoBA	90%	0.121	0.110
3-MethylBA	21%	0.264	0.246
3-EthoxyBA	0	0.255	0.247
4-MethylBA	0	0.309	0.287

Table A12. Iron-sulfur bond distances in CYP199A4 crystal structures

Ligand bound to WT CYP199A4	Iron-sulfur bond length (Å)
3-MethoxyBA	2.35
3-MethythioBA	2.31
3-MethylaminoBA	2.31
3-MethylBA	2.36
3-EthoxyBA	2.35
4-MethylBA	2.34

Table A13. Fe-N(porphyrin) bond distances in WT CYP199A4 crystal structures

WT CYP199A4 crystal structure	Fe-N_A	Fe-N_B	Fe-N_C	Fe-N_D
3-MethoxyBA	2.07	2.05	2.07	2.04
3-MethythioBA	2.04	2.05	2.08	2.02
3-MethylaminoBA	2.02	2.04	2.04	2.05
3-MethylBA	2.06	2.08	2.04	2.02
3-EthoxyBA	2.07	2.05	2.05	2.05
4-MethylBA	2.06	2.06	2.05	2.05

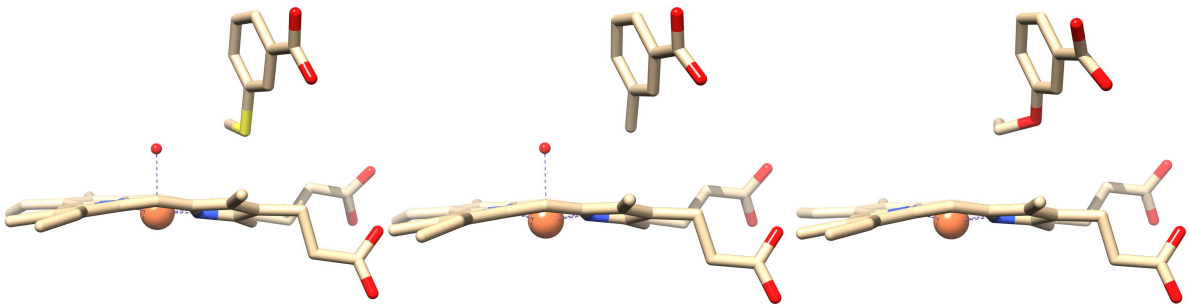

(a) 3-methylthiobenzoic acid **(b)** 3-methylbenzoic acid **(c)** 3-ethoxybenzoic acid

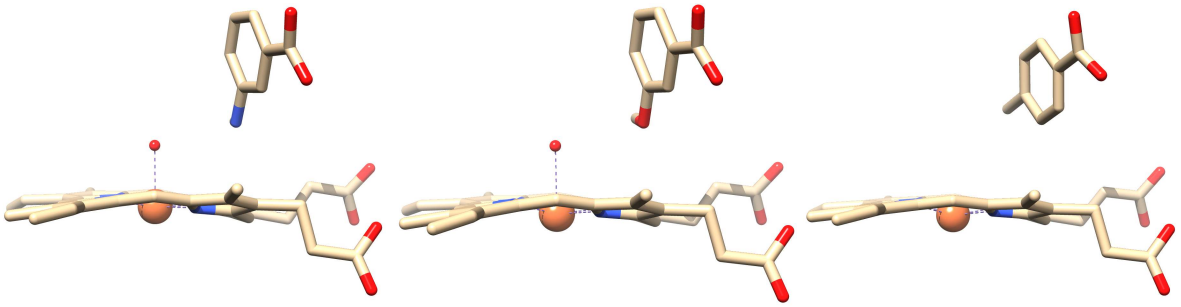

(d) 3-methylaminobenzoic acid **(e)** 3-methoxybenzoic acid **(f)** 4-methylbenzoic acid

Figure A22. Displacement of the iron below the porphyrin plane in substrate-bound CYP199A4 crystal structures.

Bulky *meta*-substituted substrates docked into CYP199A4

Table A14. ICM-Pro scores for **3-ethoxybenzoic acid** docked into CYP199A4

Pose	Score	Vls Score	Strain kcal/mol	Steric	Torsion	Electro	Hbond kcal/mol	Hydroph kcal/mol	Surface
1	-38.79	-42.52	3.727	-16.68	2	-7.03	-9.792	-3.507	6.299
2	-37.55	-41.55	3.997	-15.39	2	-7.129	-9.885	-3.536	6.301

Table A15. ICM-Pro scores for **3-isopropylbenzoic acid** docked into CYP199A4

Pose	Score	Vls Score	Strain kcal/mol	Steric	Torsion	Electro	Hbond kcal/mol	Hydroph kcal/mol	Surface
1	-26.47	-31.12	4.653	-12.03	2	-1.739	-8.031	-3.783	4.937
2	-18.36	-21.66	3.301	-11.68	2	1.207	-5.205	-3.765	4.948

Table A16. ICM-Pro scores for **3-*tert*-butylbenzoic acid** docked into CYP199A4

Pose	Score	Vls Score	Strain kcal/mol	Steric	Torsion	Electro	Hbond kcal/mol	Hydroph kcal/mol	Surface
1	-12.3	-18.14	5.84	4.167	2	-4.464	-8.536	-3.983	4.94

HPLC analysis of the CYP199A4 reaction with 3-isopropylbenzoic acid

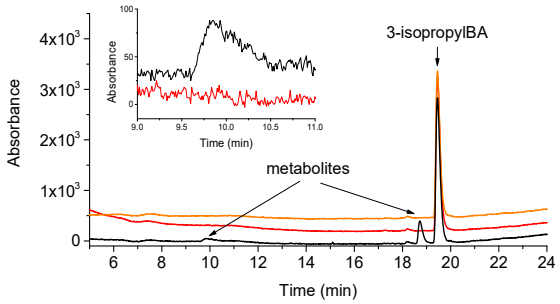

Figure A23. HPLC analysis of the CYP199A4 reaction with 3-isopropylbenzoic acid. In **black** is the *in vitro* turnover and in **red** and **orange** are control reactions omitting the P450 and NADH. The metabolites are expected to be the desaturation product, 3-(prop-1-en-2-yl)benzoic acid, and a hydroxylation product based on the retention times and by analogy to the products of the reaction with 4-isopropylbenzoic acid.

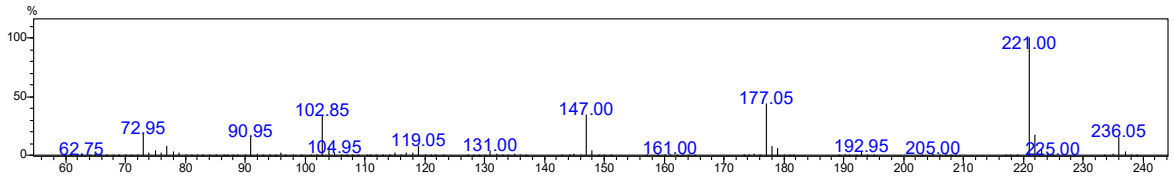

3-Isopropylbenzoic acid substrate (singly derivatised): m/z = 236.05 (expected m/z = 236.12330), RT = 7.9 min

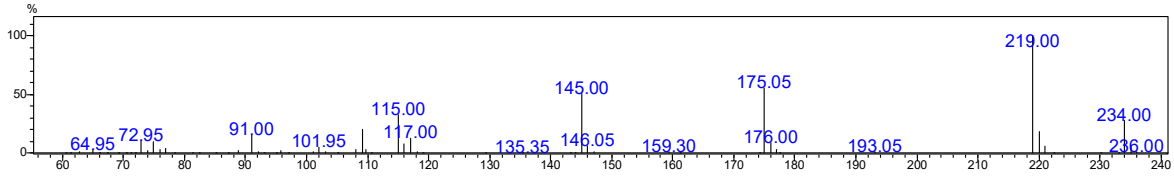

Metabolite assigned as desaturation product (singly derivatised): m/z = 234.00 (expected m/z = 234.1076), RT = 9.0 min

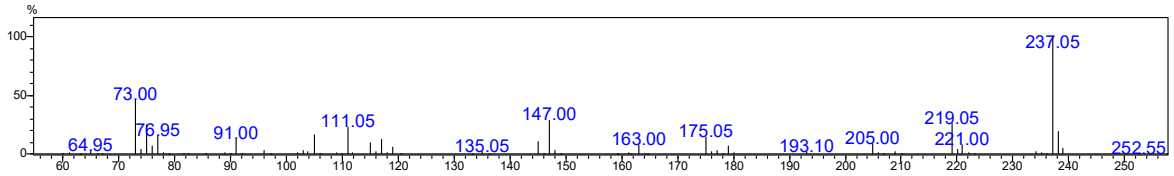

Metabolite assigned as hydroxylation product (singly derivatised): m/z = 252.55 (expected m/z = 252.1182), RT = 11.3 min

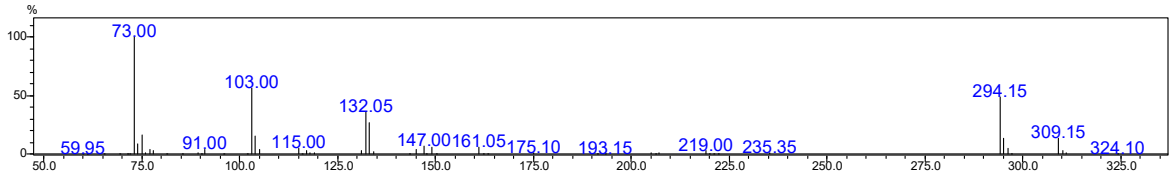

Metabolite assigned as hydroxylation product (doubly derivatised): m/z = 324.10 (expected m/z = 324.1577), RT = 14.2 min

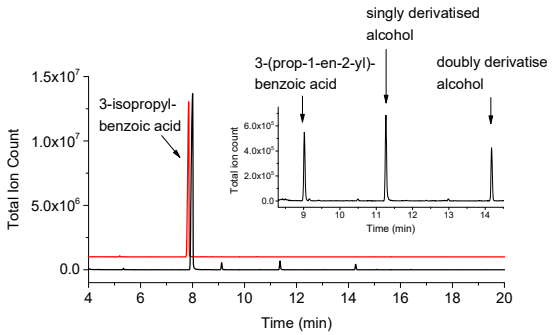

Figure A24. GC-MS analysis of the CYP199A4 *in vitro* reaction with 3-isopropylbenzoic acid. In **black** is the *in vitro* turnover and in **red** is a control reaction omitting the P450.

Data collection and refinement statistics for the crystal structure of 3-ethoxybenzoic acid-bound CYP199A4 and overall fold of the enzyme

Table A17. Statistics for data collection and refinement of the crystal structure of CYP199A4 with **3-ethoxybenzoic acid** bound. Values in parentheses correspond to the highest resolution (outer) shell.

Statistic	
PDB code	6PRS
X-ray wavelength	0.9537
Unit cell parameters	a = 44.6 b = 51.4 c = 79.4 α = 90.0 β = 92.2 γ = 90.0
Space group	$P12_11$
Molecules per asymmetric unit	1
Resolution range	44.56 – 2.37 (2.45 – 2.37)
<I/σ(I)>	5.8 (1.5)
Unique reflections	14637
Completeness of data	98.3 (84.1)
Multiplicity	6.2 (5.2)
R_{merge} (all I+ and I−)	19.2 (75.0)
R_{pim} (all I+ and I−)	8.3 (35.7)
$CC_{1/2}$	98.5 (70.3)
R_{work}	0.1825
R_{free} (5% held)	0.2221
Ramachandran favoured (%)	97.4
Ramachandran outliers (%)	0
Unusual rotamers (%)	0.31
RMSD bond angles (°)	0.612
RMSD bond lengths (Å)	0.002
Omit map type, contour level, carve radius	feature-enhanced map, 1.0 σ, 1.5 Å carve

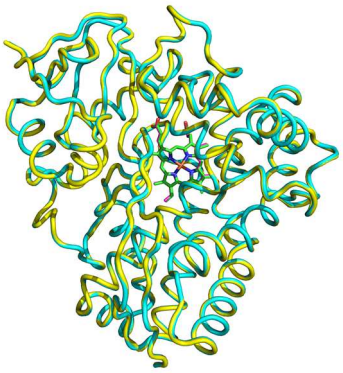

Figure A25. Overlaid structures of 3-ethoxbenzoic acid- (yellow cartoon, magenta heme) and 4-ethoxybenzoic acid-bound (blue cartoon, green heme) CYP199A4. The RMSD between the Cα atoms is 0.182 Å (over all 393 pairs).

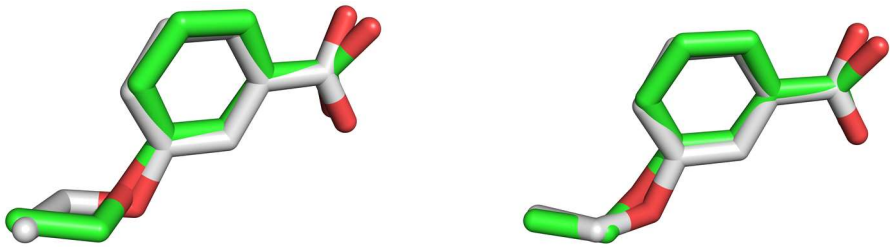

(a) RMSD = 0.536 Å **(b)** RMSD = 0.367 Å

Figure A26. Comparison of the docked ligand poses (grey) with the crystallographic pose of 3-ethoxybenzoic acid (green). In **(a)** the top-scoring docked pose is compared to the crystallographic pose. In **(b)** the second-ranked docked pose is compared to the crystallographic pose. The crystallographic pose is more similar to the second-ranked docked pose shown in **(b)** than the top-ranked docked pose shown in **(a)**.

Crystal structures of 3-methylamino- and 3-methyl-benzoic acid-bound CYP199A4 with modelled hydrogens

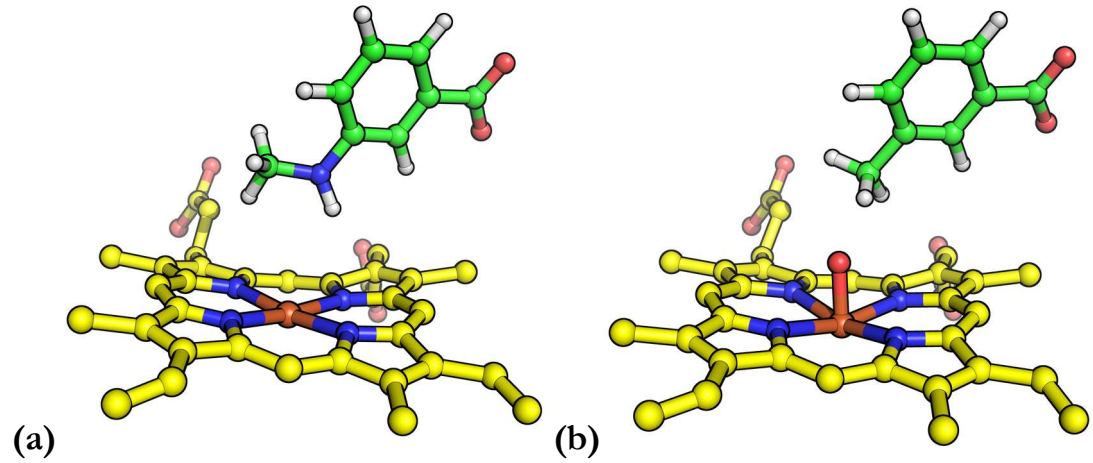

Figure A27. Crystal structures of **(a)** 3-methylamino- and **(b)** 3-methyl-benzoate-bound CYP199A4 with modelled hydrogens. The Cpd I ferryl oxygen is modelled 1.62 Å above the heme iron.

Appendix B: Supplementary Information for Chapter 4

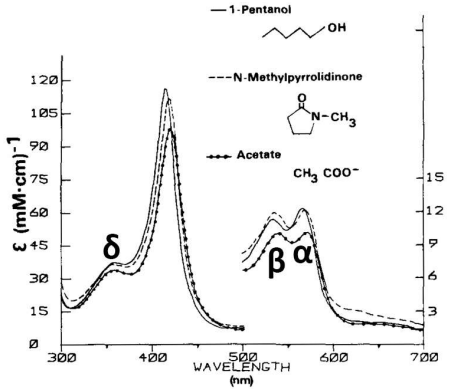

Characteristics of the UV-Vis spectra of P450$_{cam}$ in complex with oxygen donor ligands:

- **Intensity of α-band greater than intensity of β-band**
- **Soret band centred at ~417 nm**

(a) P450$_{cam}$ + oxygen donor ligands

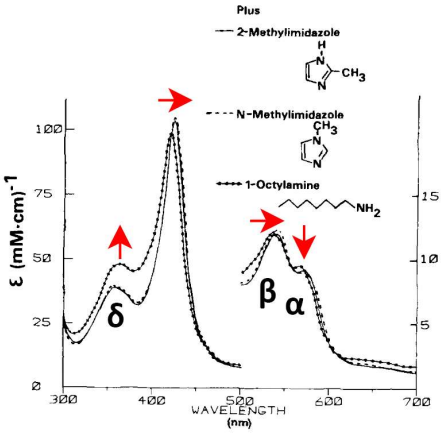

(b) P450$_{cam}$ + 'normal' nitrogen donors

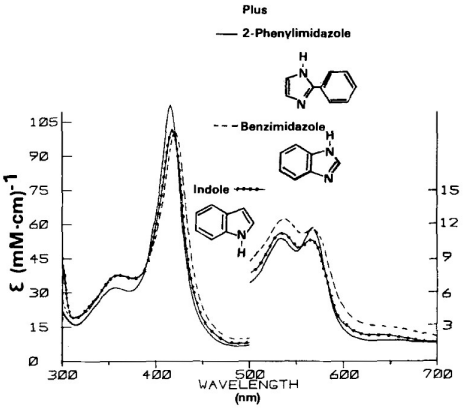

(c) P450$_{cam}$ + 'abnormal' nitrogen donors

Figure B1. UV-Vis spectra of P450$_{cam}$ in complex with **(a)** oxygen donor ligands, **(b)** 'normal' nitrogen donors and **(c)** 'abnormal' nitrogen donors reported by Dawson.[363]

This research was originally published in the Journal of Biological Chemistry. Dawson, J. H.; Andersson, L. A.; Sono, M. Spectroscopic investigations of ferric cytochrome P-450-CAM ligand complexes. Identification of the ligand *trans* to cysteinate in the native enzyme. *J. Biol. Chem.* 1982; 257:3606-17. © the American Society for Biochemistry and Molecular Biology.

Description of the UV-Vis spectra of P450$_{cam}$ with 'normal' and 'abnormal' nitrogen ligands

When 2-methylimidazole, a 'normal' nitrogen donor ligand, binds to P450$_{cam}$, the Soret band is red-shifted from 417 to 424 nm and decreases in intensity (ε = 103 *vs.* 115 mM^{-1} cm^{-1}). The β-band is red-shifted from 536 to 540 nm, while the α-band becomes substantially less intense than the β-band. There is a small red-shift in the position of the δ-band and its intensity is increased (ε = 39 *vs.* 32 mM^{-1} cm^{-1}).

The UV-Vis spectra of P450$_{cam}$ in complex with the 'abnormal' nitrogen donor ligands 2-phenylimidazole, benzimidazole and indole were more resemblant of the spectra of P450$_{cam}$ bound to oxygen donor ligands.

Determination of the extinction coefficients of the Soret band and α, β and δ bands of ferric and ferrous CYP199A4 in complex with 4-pyridin-3-ylBA and 4-pyridin-2-ylBA

Method details

The UV-Vis spectrum of 1000 µL of 7.1 µM WT CYP199A4 in 50 mM Tris-HCl buffer (pH 7.4) was recorded and the extinction coefficients of the α, β, and δ bands were determined. The literature Soret band extinction coefficient (ε_{419} = 119 mM^{-1} cm^{-1})[162] was used to determine the P450 concentration. To form the complex of CYP199A4 with 4-pyridin-3-ylbenzoic acid and 4-pyridin-2-ylbenzoic acid, 20 µL of a 100 mM solution in DMSO was added to the cuvette. To generate the ferrous form, dithionite was added to the cuvette and the UV-Vis spectrum was recorded.

Extinction coefficients of native CYP199A4

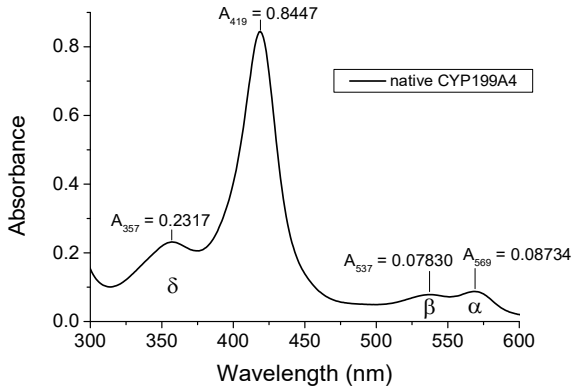

Figure B2. UV-Vis spectrum of ferric substrate-free WT CYP199A4.

The extinction coefficient of CYP199A4 reported in the literature is ε_{419} = **119 mM^{-1} cm^{-1}**.[162]
Concentration of P450 in cuvette: c = $A_{419}/\varepsilon_{419}$ = 0.8447/119 mM^{-1} cm^{-1} = **7.098 µM**

Extinction coefficient of **δ-band** (λ_{max} = 357 nm):
ε_{357} = A_{357}/c = 0.2317/7.098 µM = **32.6 mM^{-1} cm^{-1}**

Extinction coefficient of **β-band** (λ_{max} = 537 nm):
ε_{537} = A_{537}/c = 0.078297/7.098 µM = **11.0 mM^{-1} cm^{-1}**

Extinction coefficient of **α-band** (λ_{max} = 569 nm):
ε_{569} = A_{569}/c = 0.08734/7.098 µM = **12.3 mM^{-1} cm^{-1}**

α:β band ratio: 0.08734/0.07830 = **1.12**

Extinction coefficients of ferric CYP199A4 in complex with 4-pyridin-3-ylbenzoic acid

To form the complex of CYP199A4 with 4-pyridin-3-ylbenzoic acid, 20 µL of a 100 mM solution of 4-pyridin-3-ylbenzoic acid in DMSO was added to the cuvette. The protein solution in the cuvette was therefore diluted from 1000 µL to 1020 µL. Hence, the protein concentration was reduced from 7.098 µM to 6.959 µM.

$c_i v_i = c_f v_f$

c_f = (1000 µL/1020 µL) × 7.098 µM = **6.959 µM**

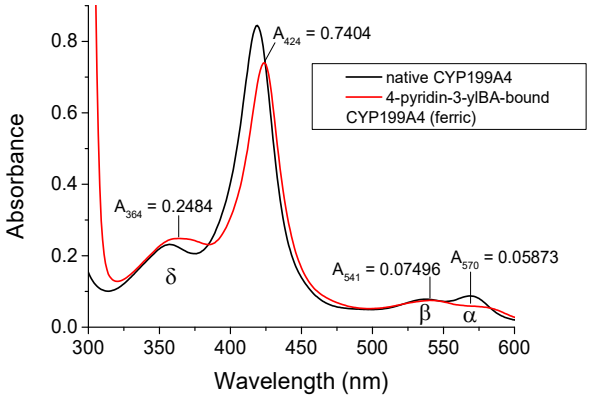

Figure B3. UV-Vis spectrum of ferric CYP199A4 in complex with 4-pyridin-3-ylbenzoic acid (**red**).

Extinction coefficient of **δ-band** (λ_{max} = 364 nm):

$\varepsilon_{364} = A_{364}/c$ = 0.2484/6.959 µM = **35.7 mM^{-1} cm^{-1}**

Extinction coefficient of **Soret band** (λ_{max} = 424 nm):

$\varepsilon_{424} = A_{424}/c$ = 0.7404/6.959 µM = **106 mM^{-1} cm^{-1}**

Extinction coefficient of **β-band** (λ_{max} = 541 nm):

$\varepsilon_{541} = A_{541}/c$ = 0.07496/6.959 µM = **10.8 mM^{-1} cm^{-1}**

Extinction coefficient of **α-band** (shoulder at ~570 nm):

$\varepsilon_{570} = A_{570}/c$ = 0.05873/6.959 µM = **8.4 mM^{-1} cm^{-1}**

α:β band ratio: 0.05873/0.07496 = **0.78**

Extinction coefficients of ferrous CYP199A4 in complex with 4-pyridin-3-ylbenzoic acid

Dithionite was added to the cuvette to reduce the P450 to the ferrous form. The protein concentration was assumed to still be 6.959 μM.

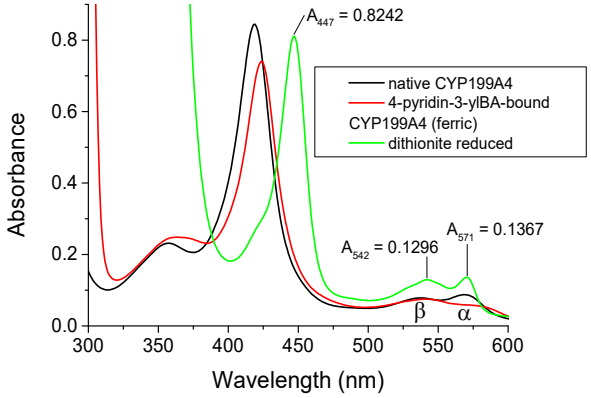

Figure B4. UV-Vis spectrum of ferrous CYP199A4 in complex with 4-pyridin-3-ylbenzoic acid (**green**).

Extinction coefficient of **Soret band** (λ_{max} = 447 nm):

$\varepsilon_{447} = A_{447}/c$ = 0.8242/6.959 μM = **118 mM^{-1} cm^{-1}**

Extinction coefficient of **β-band** (λ_{max} = 542 nm):

$\varepsilon_{542} = A_{542}/c$ = 0.1296/6.959 μM = **18.6 mM^{-1} cm^{-1}**

Extinction coefficient of **α-band** (λ_{max} = 571):

$\varepsilon_{571} = A_{571}/c$ = 0.1367/6.959 μM = **19.6 mM^{-1} cm^{-1}**

α:β band ratio: 0.1367/0.1296 = **1.05**

Extinction coefficients of ferric CYP199A4 in complex with 4-pyridin-2-ylbenzoic acid

Initial concentration of CYP199A4 in cuvette:

A_{419} = 0.8422

$c = A_{419}/\varepsilon_{419}$ = 0.8422/(119 mM^{-1}) = **7.077 µM**

After addition of 20 µL of 100 mM 4-pyridin-2-ylbenzoic acid to 1 mL of 7.077 µM protein solution in the cuvette, the protein concentration was reduced to:

c_f = (1000 µL/1020 µL) × 7.077 µM = **6.938 µM**

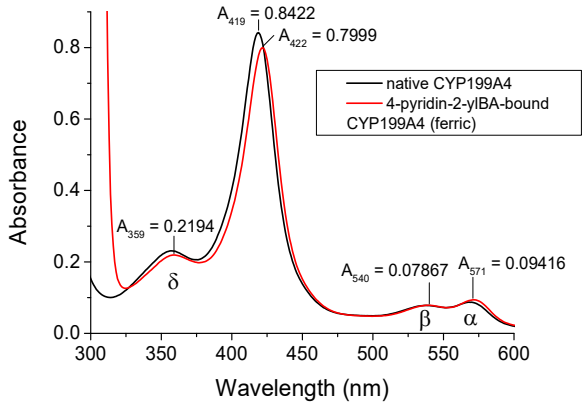

Figure B5. UV-Vis spectrum of ferric CYP199A4 in complex with 4-pyridin-2-ylbenzoic acid (**red**).

Extinction coefficient of **δ-band** (λ_{max} = 359 nm):

$\varepsilon_{359} = A_{359}/c$ = 0.2194/6.938 µM = **31.6 mM^{-1} cm^{-1}**

Extinction coefficient of **Soret band** (λ_{max} = 422 nm):

$\varepsilon_{422} = A_{422}/c$ = 0.7999/6.938 µM = **115 mM^{-1} cm^{-1}**

Extinction coefficient of **β-band** (λ_{max} = 540 nm):

$\varepsilon_{540} = A_{540}/c$ = 0.07867/6.938 µM = **11.3 mM^{-1} cm^{-1}**

Extinction coefficient of **α-band** (λ_{max} = 571 nm):

$\varepsilon_{571} = A_{571}/c$ = 0.09416/6.938 µM = **13.6 mM^{-1} cm^{-1}**

α:β band ratio: 0.09416/0.07867 = **1.20**

Extinction coefficients of CYP199A4 in complex with 4-pyridin-2-ylbenzoic acid after addition of dithionite

Dithionite was added to the cuvette to reduce the P450 to the ferrous form and extinction coefficients were measured. The protein concentration was assumed to still be 6.938 µM.

Note that it became apparent that 4-pyridin-2-ylbenzoic acid-bound CYP199A4 could not be successfully reduced by dithionite. Binding of 4-pyridin-2-ylbenzoic acid to CYP199A4 lowered the reduction potential and prevented reduction, even by the powerful reducing agent dithionite. Consequently, the UV-Vis spectrum that was recorded (Figure B6) is not the spectrum of the ferrous form, and the calculated extinction coefficients (below) are not valid.

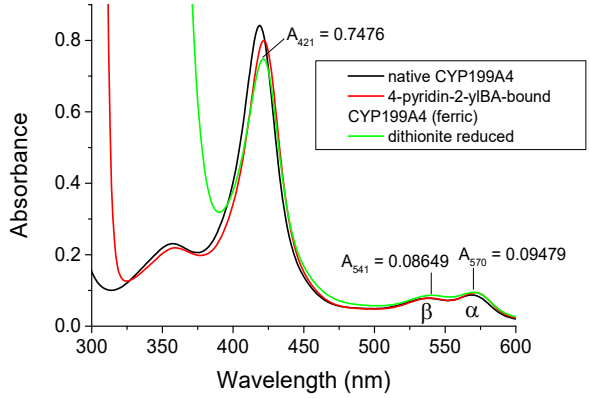

Figure B6. UV-Vis spectrum of CYP199A4 in complex with 4-pyridin-2-ylbenzoic acid (**green**) after addition of dithionite.

Extinction coefficient of **Soret band** (λ_{max} = 421 nm):
$\varepsilon_{421} = A_{421}/c$ = 0.7476/6.938 µM = **108 mM^{-1} cm^{-1}**

Extinction coefficient of **β-band** (λ_{max} = 541 nm):
$\varepsilon_{541} = A_{541}/c$ = 0.08649/6.938 µM = **12.5 mM^{-1} cm^{-1}**

Extinction coefficient of **α-band** (λ_{max} = 570 nm):
$\varepsilon_{570} = A_{570}/c$ = 0.09479/6.938 µM = **13.7 mM^{-1} cm^{-1}**

α:β band ratio: 0.09479/0.08649 = **1.10**

Extinction coefficients of ferric and ferrous CYP199A4 in complex with 4-1*H*-imidazol-1-ylbenzoic acid

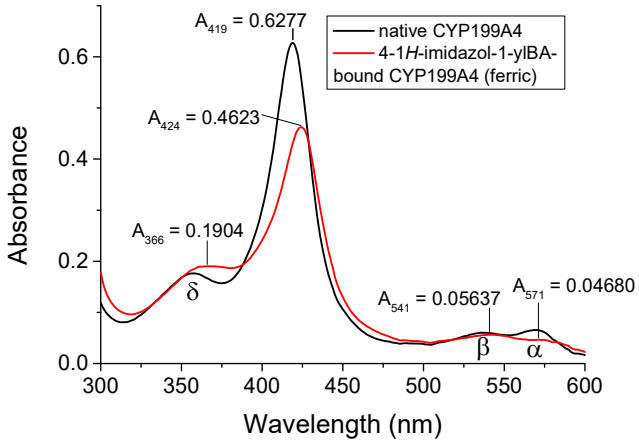

Figure B7. UV-Vis spectrum of ferric CYP199A4 in complex with 4-1*H*-imidazol-1-ylbenzoic acid (**red**). The P450 concentration was 5.3 µM and ligand concentration 1.85 mM.

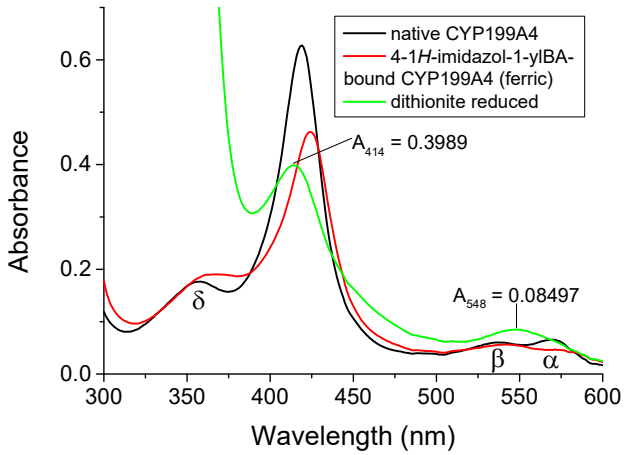

Figure B8. UV-Vis spectrum of ferrous CYP199A4 in complex with 4-1*H*-imidazol-1-ylbenzoic acid (**green**).

Method details

The UV-Vis spectrum of 1000 µL of 5.3 µM WT CYP199A4 in 50 mM Tris-HCl buffer (pH 7.4) was recorded. To form the complex of CYP199A4 with 4-1*H*-imidazol-1-ylbenzoic acid, 80 µL of a 25 mM solution of this ligand in 50 mM Tris buffer (pH 9.5) was added to the cuvette (this reduced the P450 concentration to 4.88 µM). To generate the ferrous form, dithionite was added to the cuvette and the UV-Vis spectrum was recorded.

Ferric CYP199A4 + 4-1*H*-imidazol-1-ylbenzoic acid:

Initial concentration of CYP199A4 in cuvette:
A_{419} = 0.62775
$c = A_{419}/\varepsilon_{419}$ = 0.62775/(119 mM^{-1}) = **5.275 μM**

After addition of 80 μL of 25 mM 4-1*H*-imidazol-1-ylbenzoic acid to 1 mL of 5.275 μM protein solution in the cuvette, the protein concentration was reduced to:
c_f = (1000 μL/1080 μL) × 5.275 μM = **4.884 μM**

Extinction coefficient of **δ-band** (λ_{max} = 366 nm):
$\varepsilon_{366} = A_{366}/c$ = 0.19040/4.8845 μM = **39.0 mM^{-1} cm^{-1}**

Extinction coefficient of **Soret band** (λ_{max} = 424 nm):
$\varepsilon_{424} = A_{424}/c$ = 0.46228/4.8845 μM = **94.6 mM^{-1} cm^{-1}**

Extinction coefficient of **β-band** (λ_{max} = 541 nm):
$\varepsilon_{541} = A_{541}/c$ = 0.056373/4.8845 μM = **11.5 mM^{-1} cm^{-1}**

Extinction coefficient of **α-band** (λ_{max} = 571 nm):
$\varepsilon_{571} = A_{571}/c$ = 0.046799/4.8845 μM = **9.58 mM^{-1} cm^{-1}**

α:β band ratio: 0.046799/0.056373 = **0.83**

Ferrous CYP199A4 + 4-1*H*-imidazol-1-ylbenzoic acid:

Extinction coefficient of **Soret band** (λ_{max} = 414 nm):
$\varepsilon_{414} = A_{414}/c$ = 0.39885/4.8845 μM = **81.7 mM^{-1} cm^{-1}**

Extinction coefficient of **merged α/β band** (λ_{max} = 548 nm):
$\varepsilon_{548} = A_{548}/c$ = 0.084972/4.8845 μM = **17.4 mM^{-1} cm^{-1}**

Spin-state shifts of CYP199A4 induced by binding of imidazole and pyridine

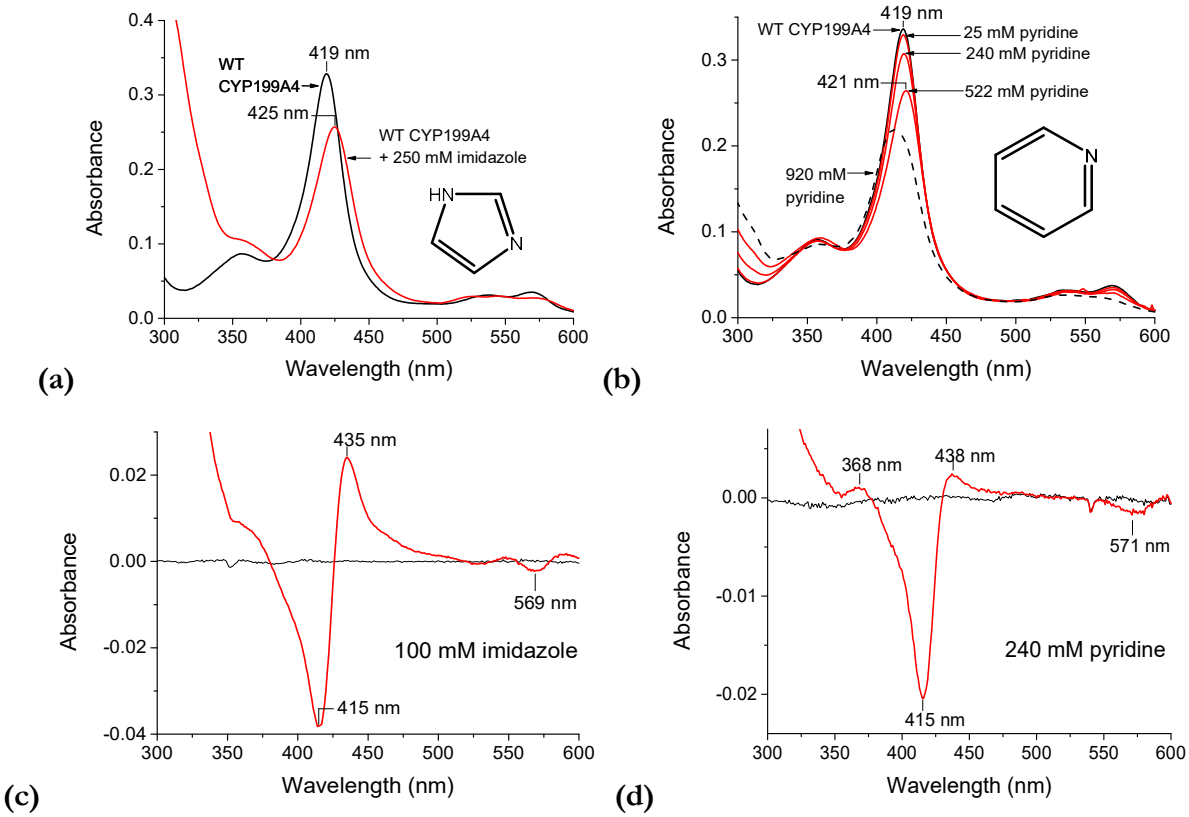

Figure B9. Spin-state shifts induced by addition of **(a)** imidazole and (**b**) pyridine to CYP199A4 and difference spectra of CYP199A4 with **(c)** imidazole and **(d)** pyridine. Addition of a high concentration of either neat pyridine or imidazole (from an 8 M stock in Milli-Q water) to WT CYP199A4 was needed to induce a type II shift. Addition of ~250 mM imidazole shifted the Soret peak to 425 nm (note that the imidazole increased the pH of the Tris-HCl buffer from 7.4 to 8.2). Addition of pyridine to CYP199A4 shifted the Soret band (λ_{max}) to 421 nm, but further addition of pyridine appeared to denature the enzyme (black dashed line).

Calculated mixed type I/type II difference spectra

We considered the possibility that the 'abnormal' UV-Vis spectrum induced by binding of 4-pyridin-2-ylbenzoic acid to CYP199A4 may arise from a mixture of type I and type II binding modes. To assess whether this was the case, we generated mixed type I/type II spectra by summing different proportions of pure type I and type II spectra (Figure B10). (The spectrum of 4-methoxybenzoic acid-bound CYP199A4 was used as the pure type I spectrum and the 4-pyridin-3-ylbenzoic acid-bound CYP199A4 spectrum was used as the pure type II spectrum.) As the proportion of type I binding increases, the peak at 432 nm in the type II difference spectrum disappears, while the intensity of the peak at ~370 nm increases. There is minimal change at 570 nm.

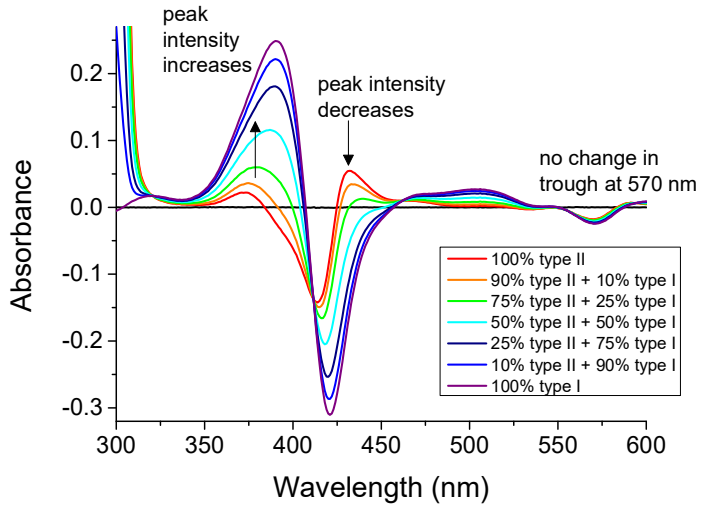

Figure B10. Calculated mixed type I/type II difference spectra generated by summing different proportions of pure type I and type II spectra. The 100% type I spectrum (**purple**) is that of 4-methoxybenzoic acid-bound CYP199A4, while the 100% type II spectrum (**red**) is that of 4-pyridin-3-ylbenzoic acid-bound CYP199A4. The P450 concentration is 4.5 μM. The arrows highlight changes which occur as the proportion of type I binding increases.

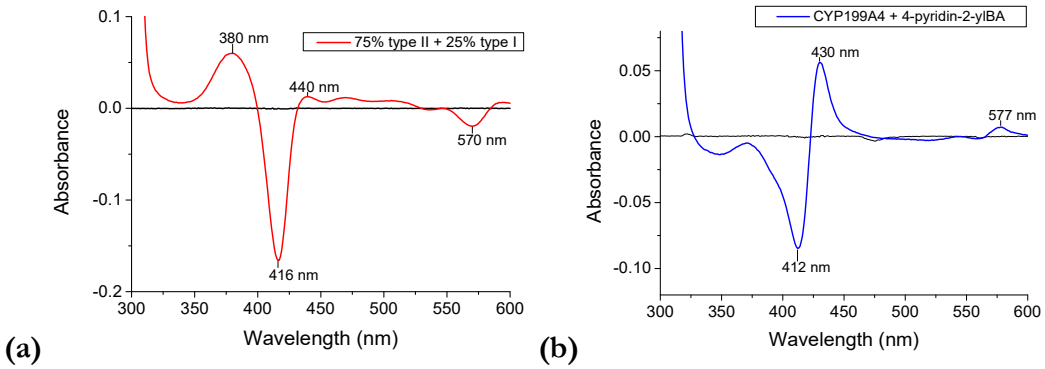

Figure B11. Comparison of **(a)** a calculated mixed type I/type II spectrum (75% type II + 25% type I) (**red**) with **(b)** the 4-pyridin-2-ylbenzoic acid spectrum (**blue**).

We note that the calculated mixed type I/type II spectra (e.g. Figure B11a) do not resemble the 4-pyridin-2-ylbenzoic acid spectrum (Figure B11b). The type I spectrum and 'normal' type II

spectrum both have troughs at 570 nm. Therefore, if the 4-pyridin-2-ylbenzoic acid spectrum arose from a mixture of type I and type II binding modes, we would expect it to also have a trough at 570 nm, which it does not. Additionally, the calculated mixed type I/type II spectra all have clear peaks at ~380 nm, but the 4-pyridin-2-ylbenzoic acid spectrum lacks any peak around 380 nm. Therefore, we do not believe that the spectrum induced by 4-pyridin-2-ylbenzoic acid is a mixed type I/type II spectrum.

Reduction of CYP199A4 in complex with type II ligands using ferredoxin (HaPux), ferredoxin reductase (HaPuR) and NADH

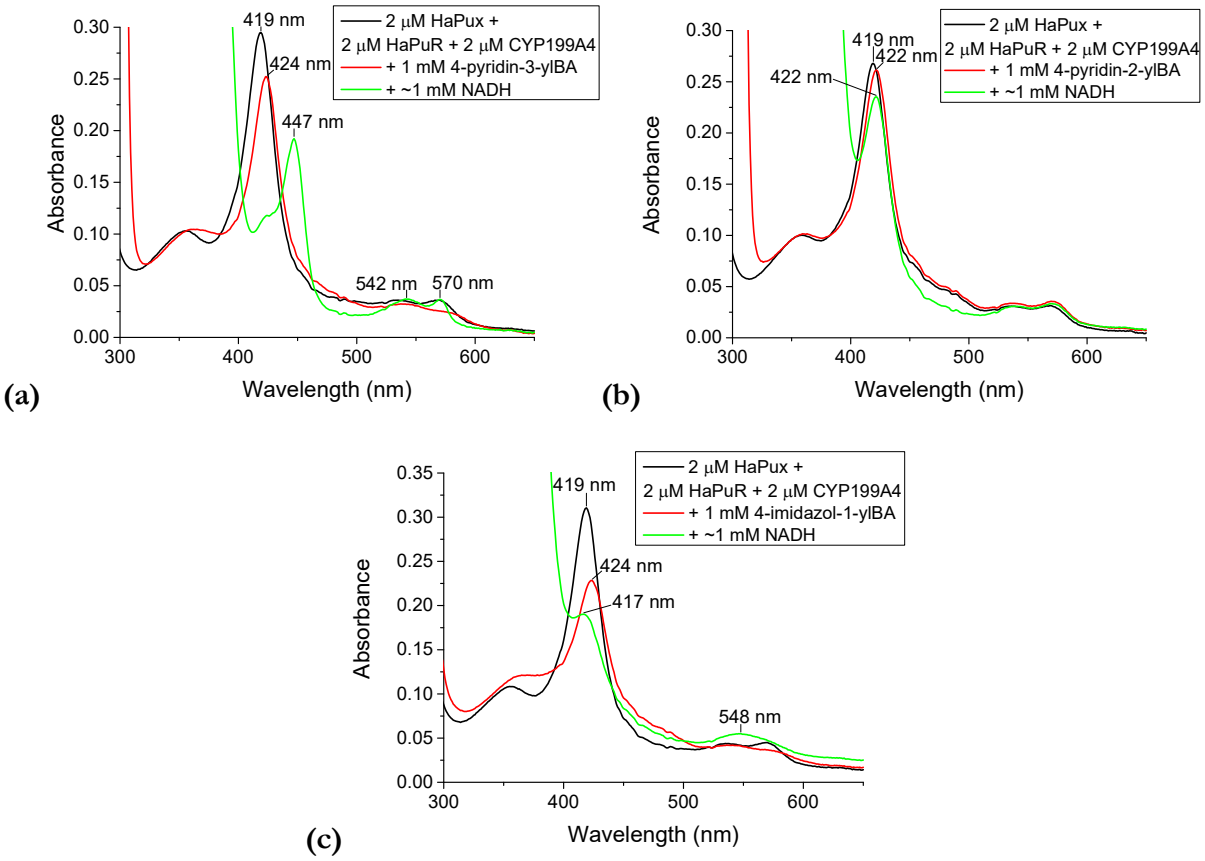

Figure B12. Reduction of **(a)** 4-pyridin-3-ylbenzoic acid-bound CY199A4 by HaPux, HaPuR and NADH. Reduction of the 4-pyridin-3-ylbenzoic acid complex shifted the Soret band to 447 nm. The reaction mixture contained 2 μM CYP199A4, 2 μM HaPux, 2 μM HaPuR and 1 mM inhibitor. NADH was added to a concentration of ~1 mM. The reaction mixture was incubated for ~15 min. **(b)** On the other hand, 4-pyridin-2-ylbenzoic acid-bound CYP199A4 could not be reduced by NADH/HaPux/HaPuR under the same conditions. **(c)** Reduction of 4-imidazol-1-ylbenzoic acid-bound CYP199A4 by HaPux, HaPuR and NADH was evidenced by a shift of λ_{max} from 424 nm to ~417 nm. The reaction mixture was incubated for ~7 min.

UV-Vis spectra of CYP199A4 first reduced with dithionite and then complexed with type II ligands/substrates

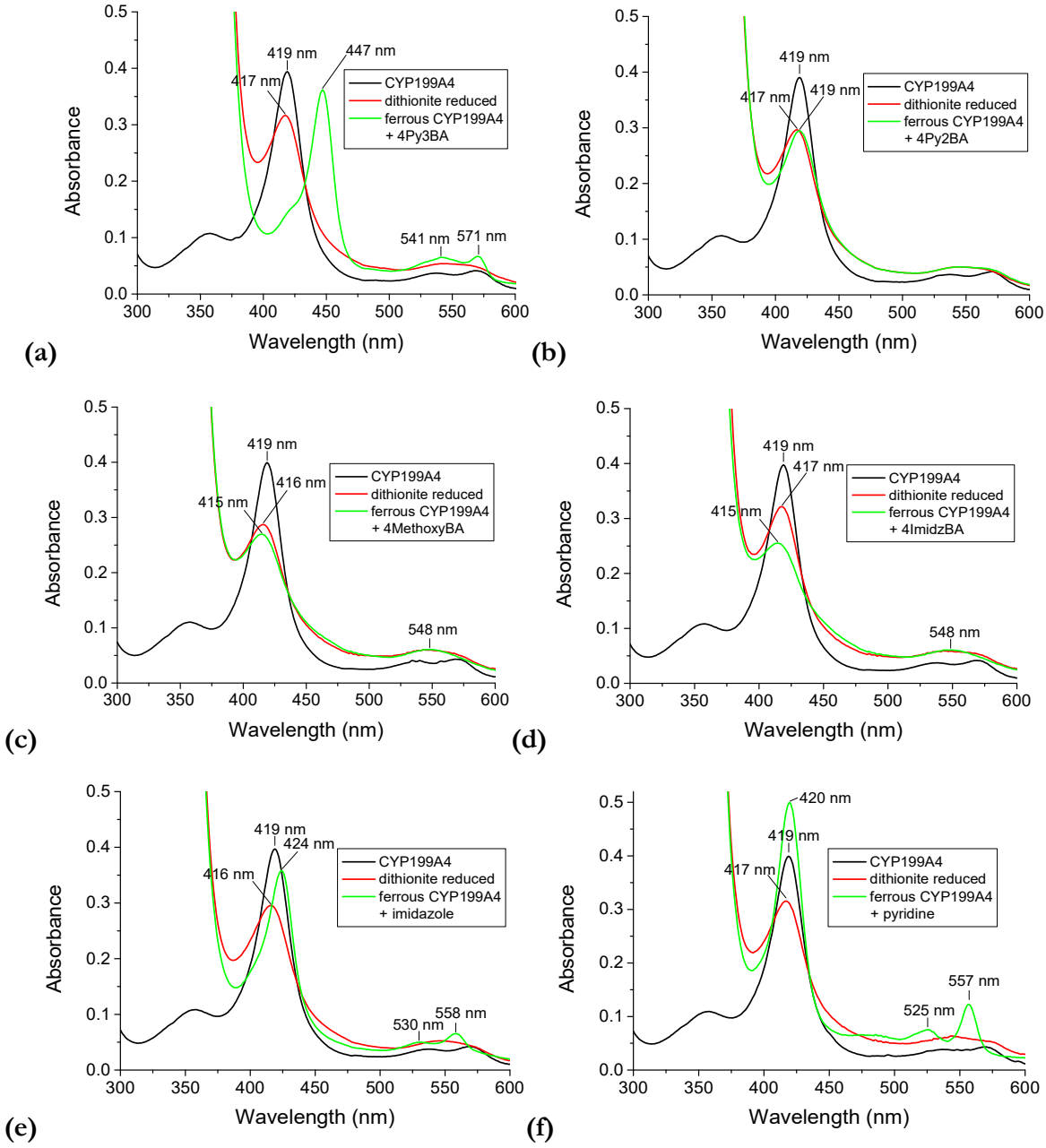

Figure B13. Spectra of ferrous WT CYP199A4 in complex with type II inhibitors/substrates. Substrate-free CYP199A4 was reduced *prior* to addition of the ligands. This experiment was performed because ligation of a nitrogen ligand to the heme iron may hinder reduction of the iron.[359] The ligands are: **(a)** 4-pyridin-3-ylBA, **(b)** 4-pyridin-2-ylBA, **(c)** 4-methoxyBA, **(d)** 4-1*H*-imidazol-1-ylBA, **(e)** imidazole, **(f)** pyridine.

Method

The UV-Vis spectrum of 500 µL of substrate-free WT CYP199A4 in 50 mM Tris-HCl buffer (pH 7.4) was recorded and dithionite was then added to reduce the P450. The reduced P450 was subsequently saturated with ligand (≥1 mM) and the spectrum of the ferrous CYP199A4-ligand complex was recorded. To obtain the spectra of the ferrous CYP199A4-imidazole and CYP199A4-pyridine complexes, 320 mM imidazole or 250 mM pyridine were added to the reduced P450.

UV-Vis spectra of ferrous CYP199A4 in complex with substrates/type II ligands at pH 7.4

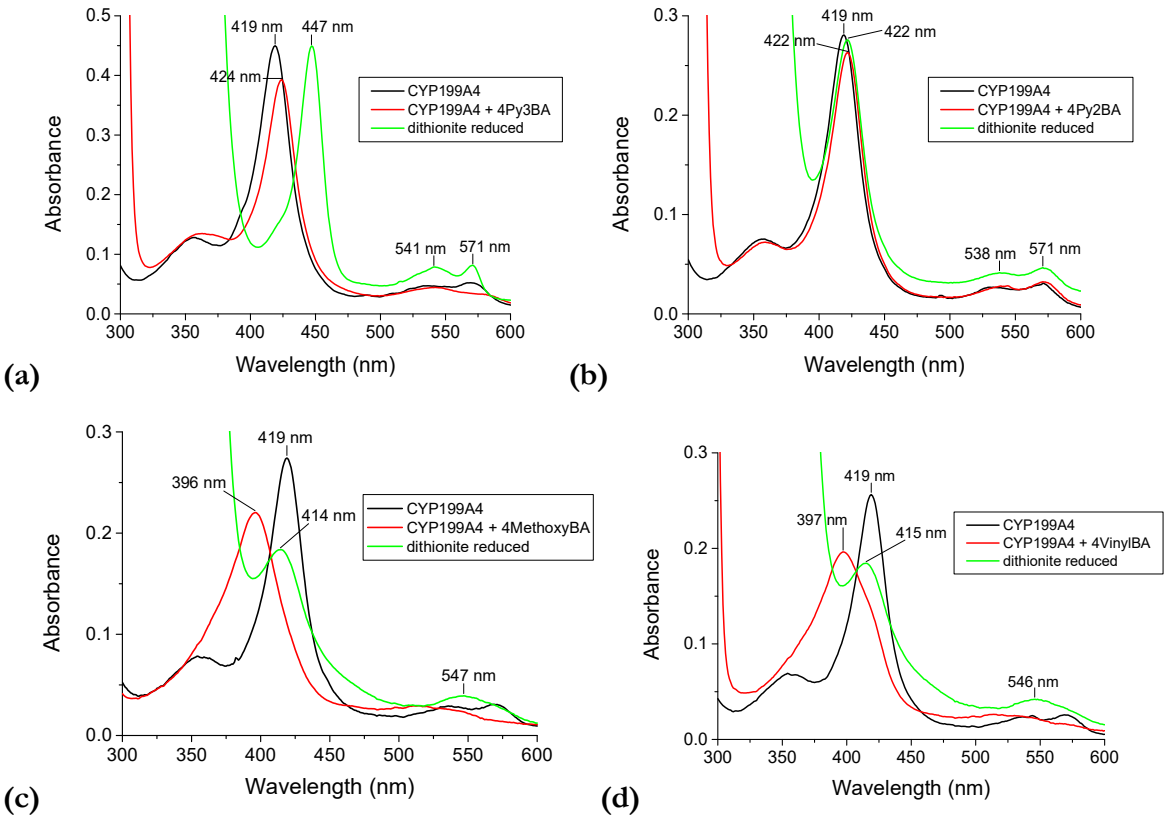

Figure B14. UV-Vis spectra of substrate-free CYP199A4 (**black**), substrate-bound (**red**) and reduced substrate-bound CYP199A4 (**green**). The UV-Vis spectrum of CYP199A4 was recorded (in pH 7.4, 50 mM Tris-HCl buffer) and the protein was then saturated with substrate/inhibitor (≥1 mM). Sodium dithionite was then added and the spectrum of the ferrous P450 complex was recorded. Shown are the spectra of CYP199A4 in complex with **(a)** 4-pyridin-3-ylbenzoic acid (4Py3BA), **(b)** 4-pyridin-2-ylbenzoic acid (4Py2BA), **(c)** 4-methoxybenzoic acid (4MethoxyBA) and **(d)** 4-vinylbenzoic acid (4VinylBA).

UV-Vis spectra of ferrous CYP199A4 in complex with type II ligands at pH 8.5 and 9.3

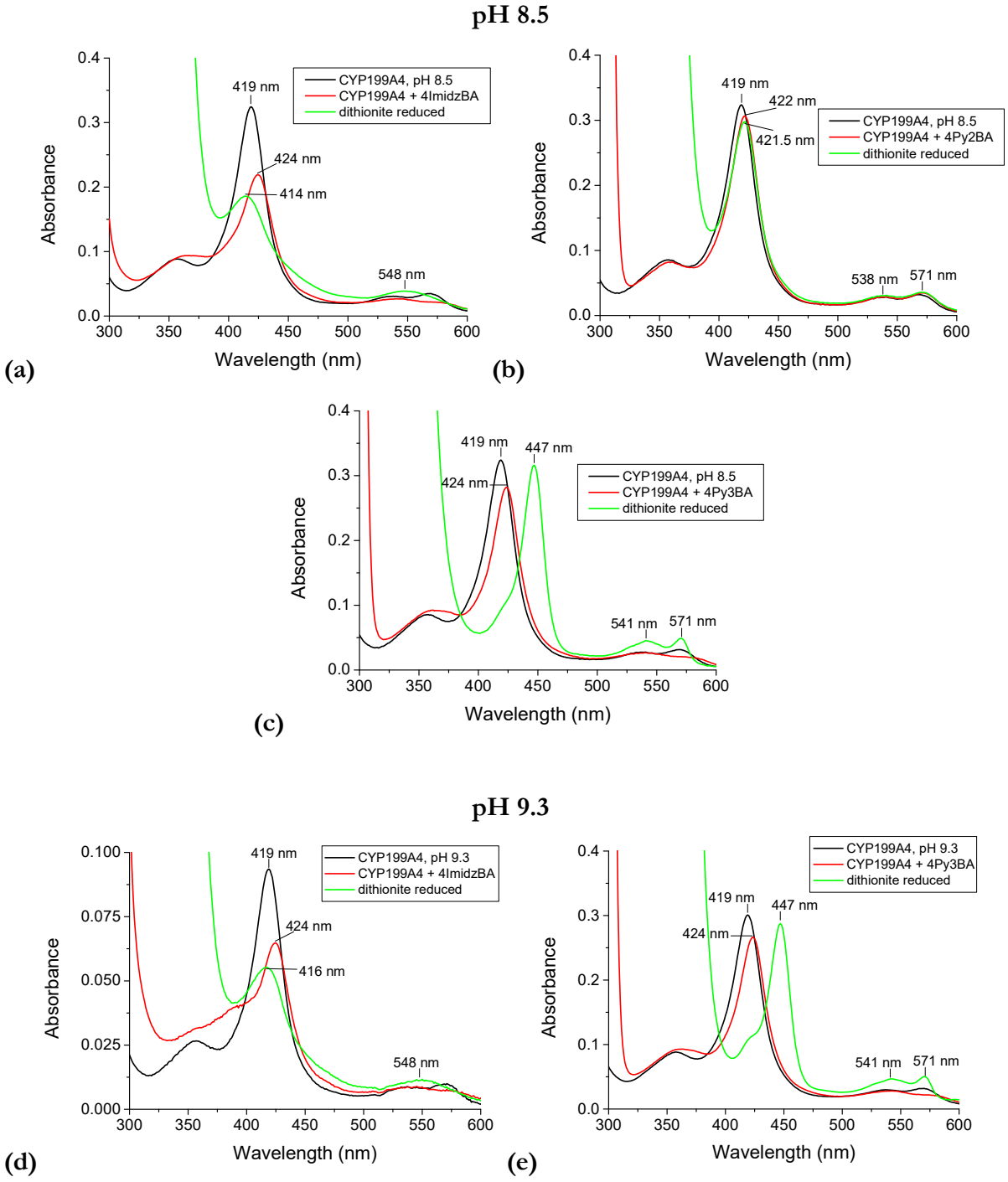

Figure B15. UV-Vis spectra of reduced CYP199A4 in complex with **(a)** 4-1*H*-imidazol-1-yl-, **(b)** 4-pyridin-2-yl-, and **(c)** 4-pyridin-3-yl-benzoic acid measured in **pH 8.5** Tris buffer (50 mM). The experiments were repeated in **pH 9.3** Tris buffer **(d,e)**. In **black** is substrate-free CYP199A4, in **red** is inhibitor-bound CYP199A4 and the reduced complex is in **green**. Abbreviations are: 4Py2BA = 4-pyridin-2-ylbenzoic acid; 4Py3BA = 4-pyridin-3-ylbenzoic acid; 4ImidzBA = 4-1*H*-imidazol-1-ylbenzoic acid.

These spectra were recorded at higher pH to assess whether 4-1*H*-imidazol-1-ylbenzoic acid was being protonated at lower pH, resulting in breakage of the Fe-N bond. However, the spectra at pH 8.5 and 9.3 were identical to those at lower pH (pH 7.4).

UV-Vis spectra of ferrous WT CYP199A4 in complex with pyridine and imidazole at pH 7.4

CYP199A4 was complexed with imidazole/pyridine and then reduced with dithionite (Figure B16). It appeared that the high concentration of imidazole/pyridine required to achieve binding denatured the enzyme, with two molecules of imidazole/pyridine coordinating to the heme in the two axial positions. The reduced CYP199A4-pyridine spectrum is consistent with that of pyridine hemochromogen (reduced heme with two axial pyridine ligands[288]). The reduced CYP199A4-imdiazole spectrum is consistent with the spectrum of reduced cytochrome b_5,[370] which has peaks at 423, 528 and 558 nm. In cytochrome b_5, the heme iron has two histidine (imidazole) ligands in the axial positions. Identical spectra were obtained when the experiment was repeated using enzyme which had been denatured by heating it at 65 °C for 30 min (Figure B18).

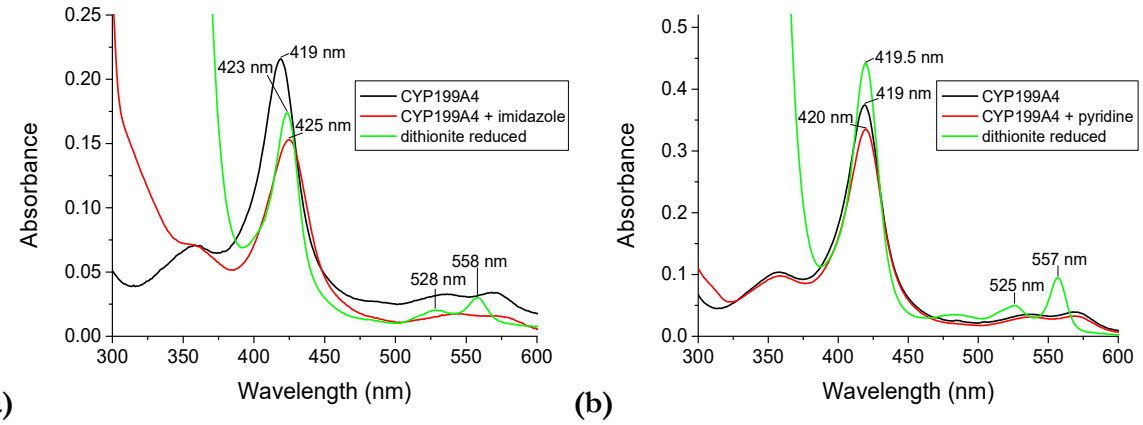

Figure B16. UV-Vis spectra of ferrous CYP199A4 in complex with **(a)** imidazole and **(b)** pyridine. The Soret peak failed to shift to ~447 when dithionite was added to the CYP199A4-ligand complexes.

Method

The UV-Vis spectrum of 1 mL of WT CYP199A4 in 50 mM Tris-HCl buffer (pH 7.4) was recorded and the P450 was then complexed with imidazole (400 mM) or pyridine (370 mM). Dithionite was added to reduce the P450 and the UV-Vis spectrum of the ferrous CYP199A4-ligand complex was recorded. Upon reduction, spectral changes were observed; however, the Soret peak failed to shift to ~447 nm.

An experiment was performed to identify whether the CYP199A4 enzyme was still functional or whether it was partially denatured when a large quantity of imidazole/pyridine was added to induce a type II spectrum.

After addition of pyridine (250 mM) or imidazole (320 mM) to WT CYP199A4 and reduction with dithionite, a saturating concentration of 4-pyridin-3-ylbenzoic acid was added. If the enzyme was still functional, the Soret band should have shifted completely to 447 nm.

The Soret band only partially shifted to 447 nm, indicating that a portion of the enzyme was denatured (Figure 17).

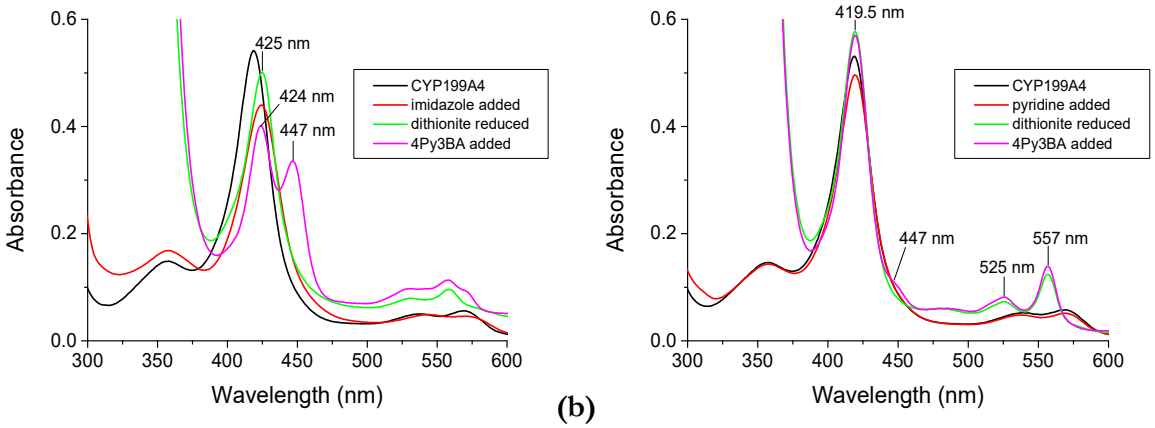

Figure B17. UV-Vis spectra of ferric CYP199A4 complexed with **(a)** imidazole (320 mM) or **(b)** pyridine (250 mM) (**red**) and reduced spectra (**green**). In **magenta** are the spectra after addition of saturating amounts of 4-pyridin-3-ylbenzoic acid (4Py3BA).

Method

To 500 µL of WT CYP199A4 protein was added 10 µL of pyridine (250 mM) or 20 µL of an 8 M imidazole solution in Milli-Q water (320 mM) and dithionite was added to reduce the heme. To this was added 20 µL of 100 mM 4-pyridin-3-ylbenzoic acid in DMSO. The Soret band only partially shifted to 447 nm, indicating that the enzyme was now largely denatured.

UV-Vis spectra of heat-denatured CYP199A4 treated with pyridine/imidazole and reduced with dithionite

We suspected that when large quantities of imidazole/pyridine were added to CYP199A4 to achieve binding, the protein was partially denatured. We expect that the reduced spectra (Figure B16) are those of ferrous heme (from denatured protein) with two pyridine/imidazole ligands in the axial positions. To confirm this, pyridine/imidazole and dithionite were added to heat-denatured CYP199A4. The resulting spectra (Figure B18) were identical to those previously obtained using functional CYP199A4, indicating that the enzyme was being denatured.

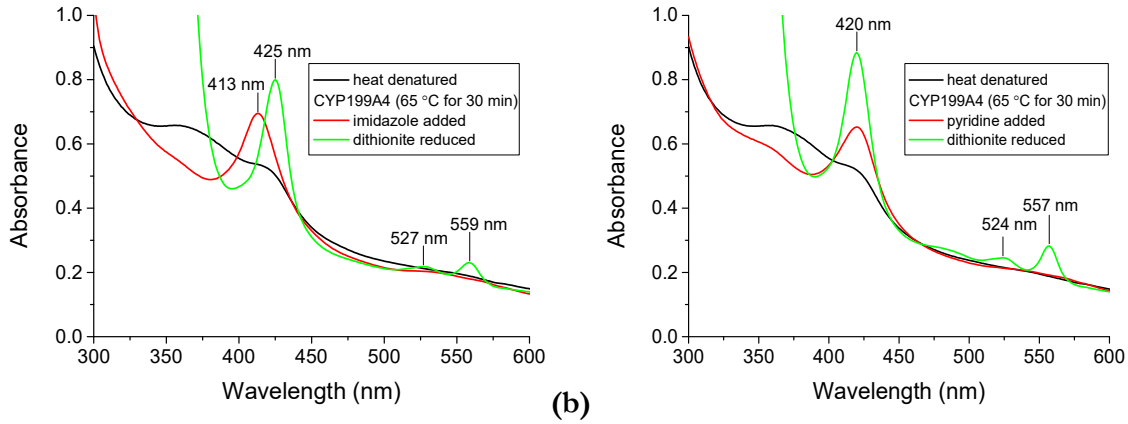

Figure B18. UV-Vis spectra of heat-denatured CYP199A4 which was heated it at 65 °C for 30 min (**black**), and the spectra after addition of **(a)** imidazole (300 mM) or **(b)** pyridine (240 mM) and dithionite (**green**).

Crystallisation method

To form the complex of CYP199A4 with 4-pyridin-2-yl- and 4-pyridin-3-yl-benzoic acid, a co-concentration method was used.[330, 464] To dilute protein (~10 μM) was added 4-pyridin-3-ylbenzoic acid or 4-pyridin-2-ylbenzoic acid (3 mM) from a 100 mM stock solution in 100% DMSO. The mixture was incubated at 4 °C for 2 hours, and the protein-ligand complex was then concentrated to 30-35 mg/mL. Clusters of plate-like crystals appeared within half a day to one week (Figure B19).

Crystals of 4-pyridin-2-yl-, 4-pyridin-3-yl- and 4-1*H*-imidazol-1-yl-benzoate-bound CYP199A4

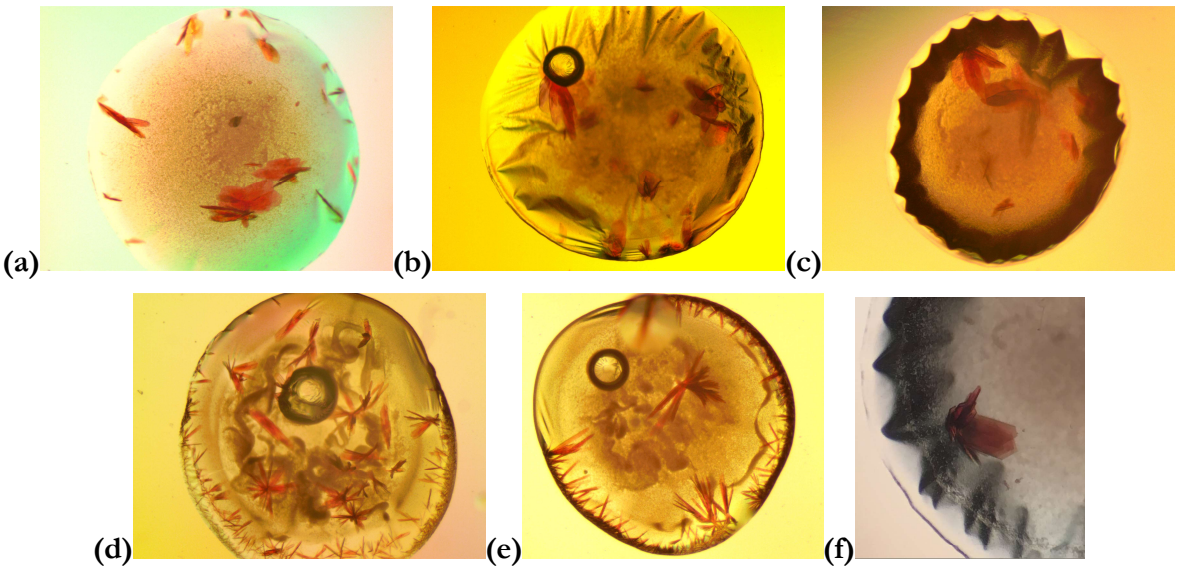

Figure B19. Crystals of (**a, b, c**) 4-pyridin-3-ylbenzoate-, (**d, e**) 4-pyridin-2-ylbenzoate- and (**f**) 4-1*H*-imidazol-1-ylbenzoate-bound CYP199A4 under magnification. Refer to Appendix E for crystal dimensions.

Data collection and crystal structure refinement statistics

Table B1. Statistics for data collection and refinement of crystal structures of WT CYP199A4 in complex with type II ligands. Values in parentheses correspond to the highest resolution (outer) shell.

Statistic	4-pyridin-2-yl	4-pyridin-3-yl	4-1*H*-imidazol-1-yl
PDB code	6U3K	6U30	6U31
X-ray wavelength (Å)	0.9537	0.9537	0.9537
Unit cell parameters (Å/°)	*a* = 44.3 *b* = 51.2 *c* = 79.2 α = 90.0 β = 92.4 γ = 90.0	*a* = 44.4 *b* = 51.5 *c* = 78.8 α = 90.0 β = 92.1 γ = 90.0	*a* = 44.4 *b* = 51.4 *c* = 78.9 α = 90.0 β = 92.3 γ = 90.0
Space group	$P12_11$	$P12_11$	$P12_11$
Molecules per asymmetric unit	1	1	1
Resolution range	44.23 – 1.80 (1.84 – 1.80)	44.36 – 1.66 (1.68 – 1.66)	44.38 – 1.58 (1.60 – 1.58)
<I/σ(I)>	3.0 (0.9)	14.2 (3.4)	18.2 (3.3)
Unique reflections	32441	42402	48847
Completeness of data	98.3 (97.1)	99.7 (96.7)	99.6 (99.0)
Multiplicity	7.2 (7.3)	7.0 (6.0)	7.0 (6.5)
R_{merge} (all I+ and I−)	49.2 (280.7)	9.3 (48.9)	7.7 (57.0)
R_{pim} (all I+ and I−)	19.6 (109.9)	3.8 (21.5)	3.1 (24.0)
$CC_{1/2}$	93.4 (44.6)	99.8 (90.7)	99.9 (87.0)
R_{work}	0.197	0.151	0.143
R_{free} (5% held)	0.241	0.193	0.177
Ramachandran favoured (%)	97.95	98.47	98.72
Ramachandran outliers (%)	0	0	0
Unusual rotamers (%)	0.31	0.62	0.3
RMSD bond angles (°)	0.795	1.02	0.933
RMSD bond lengths (Å)	0.006	0.009	0.007
Omit map type, contour level, carve radius	feature-enhanced map, 1.5 σ, 1.5 Å carve	composite omit map, 1.5 σ, 1.2 Å carve	feature-enhanced map, 1.5 σ, 1.5 Å carve

Overall fold of CYP199A4 in complex with 4-pyridin-3-yl-, 4-pyridin-2-yl- and 4-1*H*-imidazol-1-yl-benzoic acid

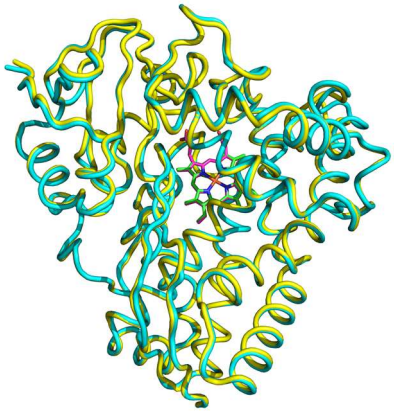

(a) 4-pyridin-2-ylbenzoic acid

(RMSD = 0.622 Å)

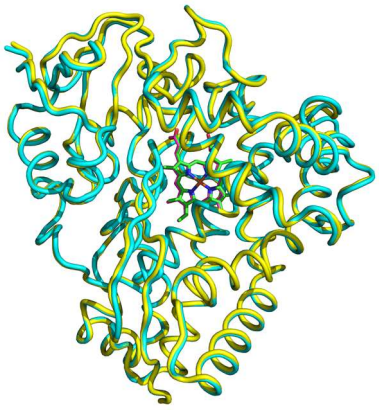

(b) 4-pyridin-3-ylbenzoic acid

(RMSD = 0.604 Å)

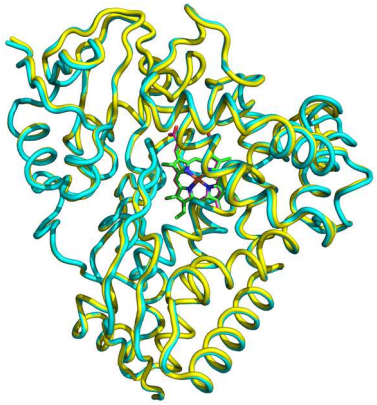

(c) 4-1*H*-imidazol-1-ylbenzoic acid

(RMSD = 0.567 Å)

Figure B20. Overlaid structure of WT CYP199A4 in complex with type II ligands with the structure of 4-methoxybenzoate-bound CYP199A4 (4DO1). In each image, the Cα trace of 4-methoxybenzoic acid-bound CYP199A4 is shown in green (with the heme in blue). The Cα trace of CYP199A4 in complex with each type II ligand is shown in yellow (with the heme in magenta). The RMSD between the Cα atoms is given below each figure (over all 393 pairs).

Chloride binding sites

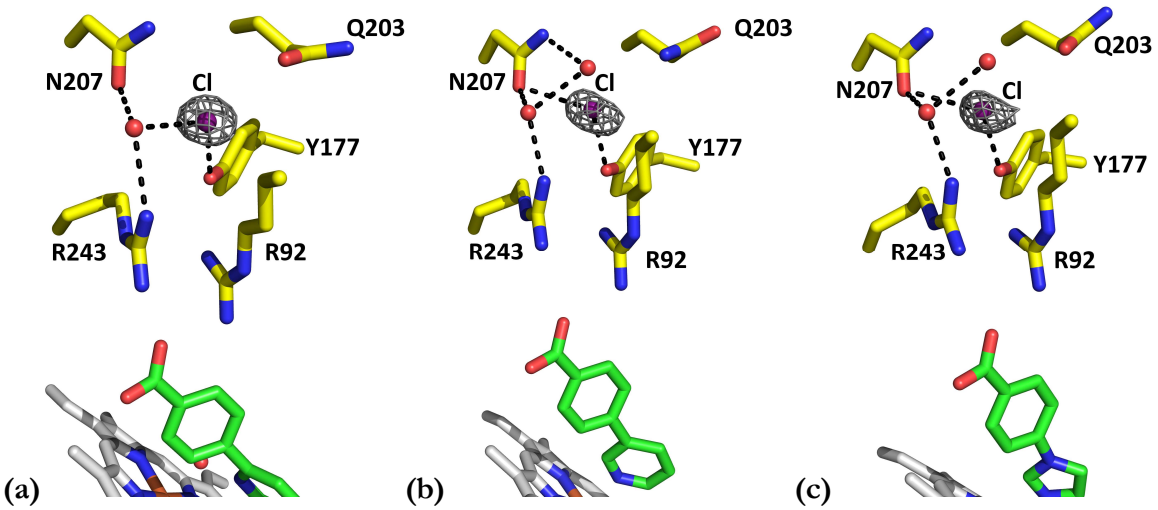

Figure B21. Chloride binding sites of WT CYP199A4 in complex with **(a)** 4-pyridin-2-ylBA, **(b)** 4-pyridin-3-ylBA and **(c)** 4-1*H*-imidazol-1-ylBA. A composite omit map of the chloride anion (purple sphere) is shown as grey mesh contoured at 1.0 σ.

Fe-N bond lengths in crystal structures of inhibitor-bound P450s

The Fe-N bond length in the 4-pyridin-3-ylbenzoic acid-bound $WT_{CYP199A4}$ crystal structure was refined to 2.2 Å. This bond length is longer than the Fe-N bond length in $[Fe(bipy)_3]^{2+}$, which is 1.97 Å.[372] However, it is comparable to the Fe-N bond lengths in crystal structures of other P450s with directly bound pyridine derivatives (Table B2).[359, 364, 373-374]

Table B2. Fe-N bond distances in crystal structures of P450 enzymes with directly coordinated pyridine or imidazole derivatives.

PDB code	Crystal structure description	Fe-N distance (Å)	Resolution (Å)
Pyridine derivatives			
4I4H[359]	CYP3A4 in complex with pyridine-substituted desoxyritonavir	2.14	2.9
3QU8[374]	P450 2B6 (Y226H/K262R) in complex with 4-(4-nitrobenzyl)pyridine	2.37, 2.28, 2.25, 2.34, 2.30	2.8
1W0G[373]	P450 3A4 in complex with metyrapone	2.27	2.73
3QOA[374]	P450 2B6 (Y226H/K262R) in complex with 4-benzylpyridine	2.36	2.1
1PHG[364]	$P450_{cam}$ in complex with metyrapone	2.16	1.6
Imidazole derivatives			
1PHF[364]	$P450_{cam}$ in complex with 4-phenylimidazole	2.22	1.6
1PHD[364]	$P450_{cam}$ in complex with 1-phenylimidazole	2.28	1.6
3MDM[156]	CYP46A1 in complex with thioperamide	2.00	1.6

Overlaid structures of CYP199A4 in complex with 4-pyridin-2-ylbenzoic acid and 4-ethylthiobenzoic acid

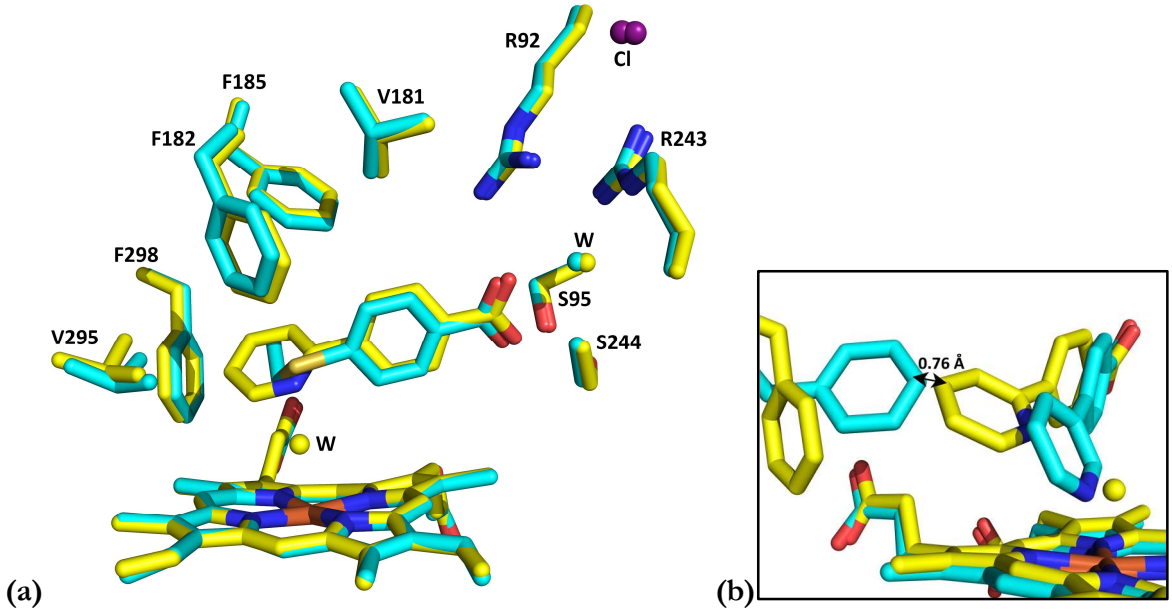

Figure B22. **(a)** 4-Pyridin-2-ylbenzoic acid displaces the phenyl ring of F298, as do bulky substrates such as 4-ethylthiobenzoic acid and 4-thiophen-3-ylbenzoic acid.[277] In cyan is the 4-ethylthiobenzoic acid structure (5U6U) overlaid with that of 4-pyridin-2-ylbenzoic acid (yellow). **(b)** 4-Pyridin-3-ylbenzoic acid (cyan), unlike 4-pyridin-2-ylbenzoic acid (yellow), is not positioned close enough to interfere with F298 and does not displace this residue.

Overlaid structures of CYP199A4 in complex with 4-pyridin-2-ylbenzoic acid and 4-ethylbenzoic acid

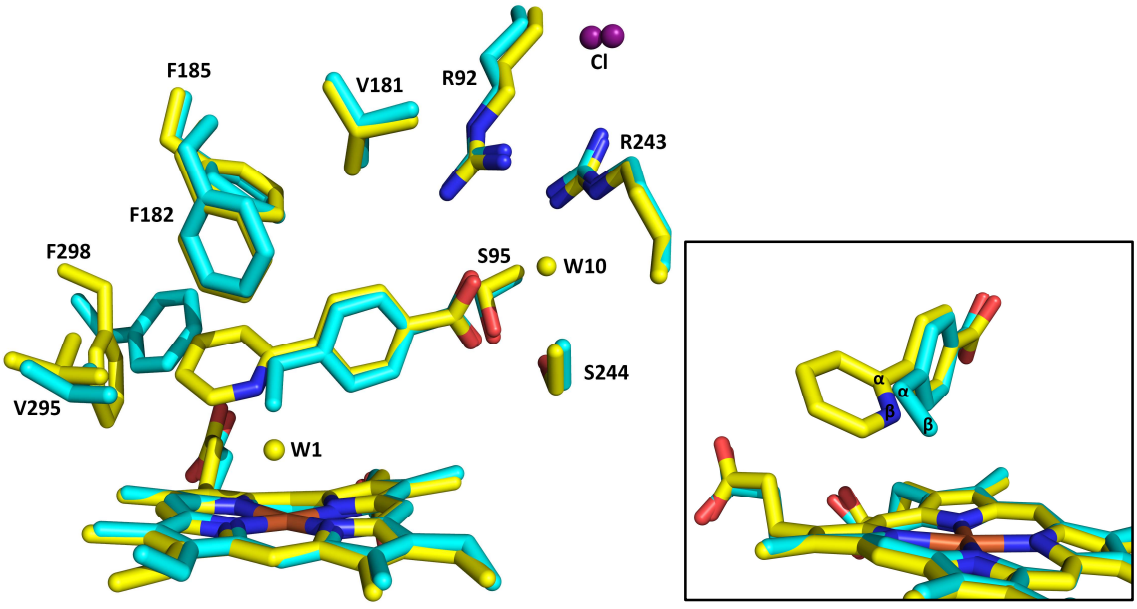

Figure B23. Overlaid structures of 4-pyridin-2-ylbenzoate-bound CYP199A4 (yellow) and 4-ethylbenzoate-bound CYP199A4 (cyan; PDB ID: 4EGM). The α-carbon and β-nitrogen of 4-pyridin-2-ylbenzoic acid are in similar positions to the α- and β-carbons of 4-ethylbenzoic acid.

Distances between equivalent atoms of 4-pyridin-3-ylbenzoic acid and 4-pyridin-2-ylbenzoic acid and displacement of nearby active-site residues in the two CYP199A4 crystal structures

Table B3. Distances between equivalent atoms of 4-pyridin-3-ylbenzoic acid and 4-pyridin-2-ylbenzoic and displacement of nearby active-site residues in the two CYP199A4 crystal structures. The nomenclature used to specify the position of atoms in the amino acid residues is that described by Markley *et al.*[465]

Distances between equivalent atoms of 4Py2BA and 4Py3BA (Å)	
C_1 - C_1	3.1
C_2 - C_2	2.3
C_3 - C_3	1.7
C_4 - N_4	2.1
N_5 - C_5	2.7
C_6 - C_6	3.1
C_7 - C_7	1.2
C_8 - C_8	0.9
C_9 - C_9	0.6
C_{10} - C_{10}	0.4
C_{11} - C_{11}	0.6
C_{12} - C_{12}	1.0
C_{13} - C_{13}	0.3
O_{14} - O_{14}	0.3
O_{15} - O_{15}	0.4

Displacement of F182 phenyl ring (Å)	
C^{γ}	0.8
$C^{\delta 1}$	0.9
$C^{\varepsilon 1}$	0.9
C^{ζ}	0.9
$C^{\varepsilon 2}$	0.9
$C^{\delta 2}$	0.8

Displacement of F298 phenyl ring (Å)	
C^{γ}	1.1
$C^{\delta 1}$	2.9
$C^{\varepsilon 1}$	4.7
C^{ζ}	4.4
$C^{\varepsilon 2}$	2.4
$C^{\delta 2}$	1.4

Displacement of F185 phenyl ring (Å)	
C^{γ}	0.4
$C^{\delta 1}$	0.4
$C^{\varepsilon 1}$	0.5
C^{ζ}	0.4
$C^{\varepsilon 2}$	0.5
$C^{\delta 2}$	0.5

Displacement of bridging water (Å)	
W1 - W10	0.3

Displacement of V295 (Å)	
C^{β}	1.1
$C^{\gamma 1}$	1.3
$C^{\gamma 2}$	1.1

Displacement of A248 (Å)	
C^{α}	0.8
C^{β}	1.0

Displacement of T252 (Å)	
C^{β}	0.9
$C^{\gamma 2}$	1.0
$O^{\gamma 1}$	0.9

Displacement of V181 (Å)	
C^{β}	0.4
$C^{\gamma 1}$	0.4
$C^{\gamma 2}$	0.3

Displacement of L98 (Å)	
C^{γ}	0.4
$C^{\delta 1}$	0.5
$C^{\delta 2}$	0.6

Angle between pyridine/imidazole ring and iron-sulfur axis in inhibitor-bound P450 crystal structures from the PDB

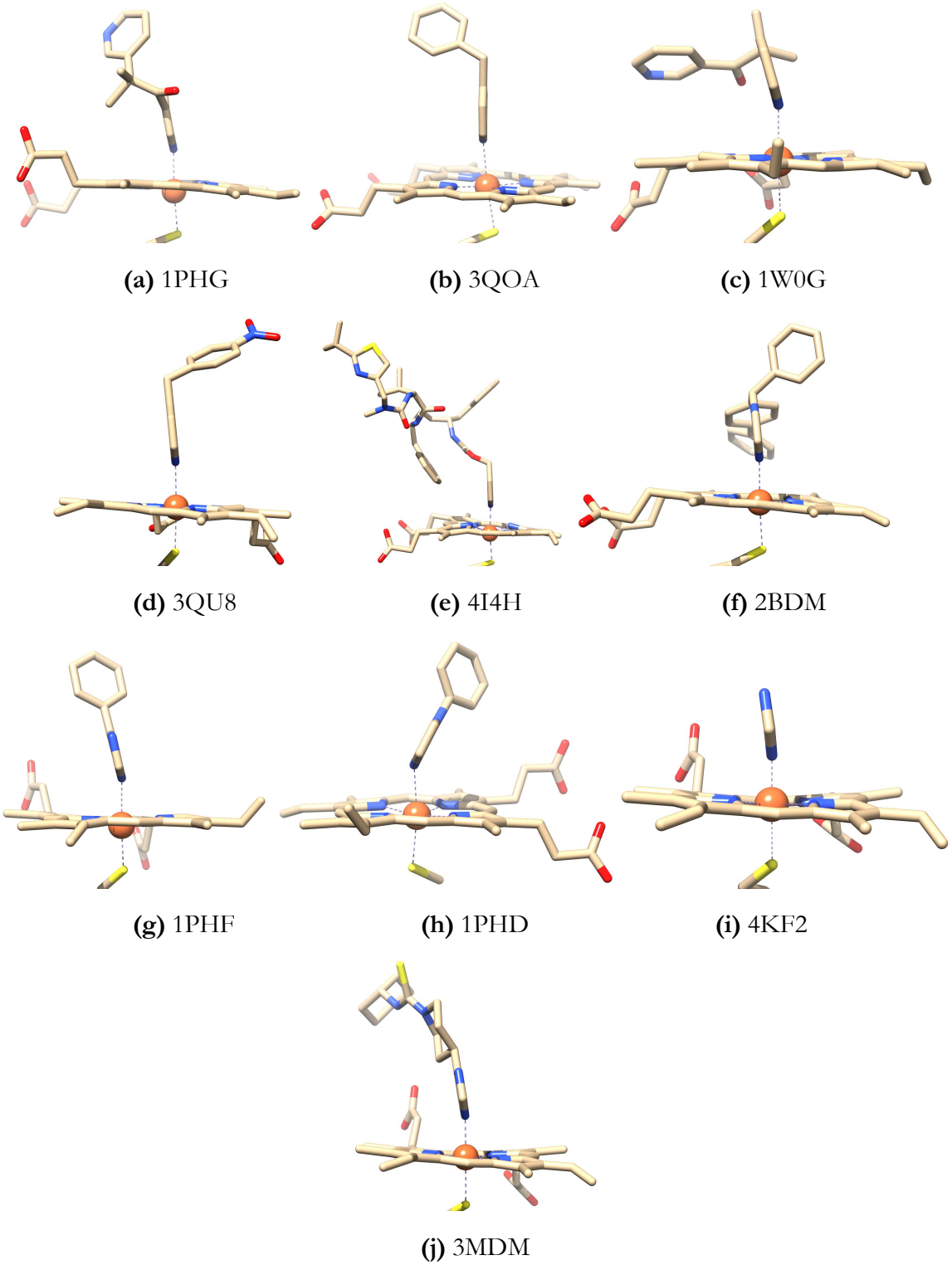

(a) 1PHG **(b)** 3QOA **(c)** 1W0G

(d) 3QU8 **(e)** 4I4H **(f)** 2BDM

(g) 1PHF **(h)** 1PHD **(i)** 4KF2

(j) 3MDM

Figure B24. In many of the crystal structures shown above, the imidazole/pyridine ring of the type II ligand is held approximately perpendicular to the plane of the heme. However, the imidazole ring is noticeably tilted in the structure of $P450_{cam}$ in complex with 1-phenylimidazole (PDB ID: 1PDH) **(h)**.

Table B4. Angle between the pyridine ring and heme in crystal structures of P450 enzymes with directly coordinated pyridine derivatives

PDB code	Description	Angle between pyridine ring and Fe-S bond (˚)	Angle between pyridine ring and plane defined by four heme pyrrole N (˚)
4I4H	CYP3A4 in complex with pyridine-substituted desoxyritonavir	2.0	84.3
3QU8	P450 2B6 (Y226H/K262R) in complex with 4-(4-nitrobenzyl)pyridine	6.6	82.9
1W0G	P450 3A4 in complex with metyrapone	12.9	72.1
3QOA	P450 2B6 (Y226H/K262R) in complex with 4-benzylpyridine	9.4	89.3
1PHG	$P450_{cam}$ in complex with metyrapone	5.1	80.1

Table B5. Angle between the imidazole ring and heme in crystal structures of P450 enzymes with directly coordinated imidazole derivatives

PDB code	Description	Angle between imidazole ring and Fe-S bond (˚)	Angle between imidazole ring and plane defined by four heme pyrrole N (˚)
1PHF	$P450_{cam}$ in complex with 4-phenylimidazole	11.1	76.9
1PHD	$P450_{cam}$ in complex with 1-phenylimidazole	22.6	63.6
4KF2	$P450_{BM3}$ (A82F F87V) in complex with imidazole	6.6	80.8
2BDM	CYP2B4 in complex with bifonazole	2.0	80.7
3MDM	CYP46A1 in complex with thioperamide	9.0	78.8

Table B6. Angle between the imidazole/pyridine ring and heme in crystal structures of CYP199A4 in complex with type II ligands

PDB code	Description	Angle between imidazole/pyridine ring and Fe-S bond (˚)	Angle between imidazole/pyridine ring and plane defined by four heme pyrrole N (˚)
6U3K	4-pyridin-2-ylBA-bound CYP199A4	42.0	40.3
6U30	4-pyridin-3-ylBA-bound CYP199A4	18.0	63.8
6U31	4-1*H*-imidazol-1-ylBA-bound CYP199A4	26.3	56.8

Iron-sulfur and iron-nitrogen bond lengths in hexacoordinate and pentacoordinate CYP199A4 crystal structures

Table B7. Iron-sulfur bond distances in CYP199A4 crystal structures

Ligand bound to wild-type CYP199A4		Iron-sulfur bond length (Å)
4-Pyridin-3-ylBA	Hexacoordinated, low-spin iron	2.30
4-Pyridin-2-ylBA		2.29
4-Imidazol-1-ylBA		2.31
4-MethylBA	Pentacoordianted, high-spin iron	2.34
4-CyclopropylBA (5UVB)		2.36
4-MethoxyBA (4DO1)		2.40
4-EthoxyBA (5U6T)		2.40
4-IsopropylBA (5KDB)		2.40

Table B8. Fe-N(porphyrin) bond distances in CYP199A4 crystal structures

WT CYP199A4 crystal structure	Fe-N_A	Fe-N_B	Fe-N_C	Fe-N_D
4-Pyridin-3-ylBA	2.05	2.04	2.04	2.05
4-Pyridin-2-ylBA	2.02	2.08	2.05	2.04
4-Imidazol-1-ylBA	2.01	2.01	2.03	2.03
4-MethylBA	2.06	2.06	2.05	2.05
4-CyclopropylBA (5UVB)	2.08	2.07	2.05	2.02
4-MethoxyBA (4DO1)	2.13	2.03	2.07	2.13
4-EthoxyBA (5U6T)	2.05	2.05	2.10	2.11
4-IsopropylBA (5KDB)	2.08	2.03	2.08	2.06

CW and HYSCORE EPR data for substrate/inhibitor-bound CYP199A4

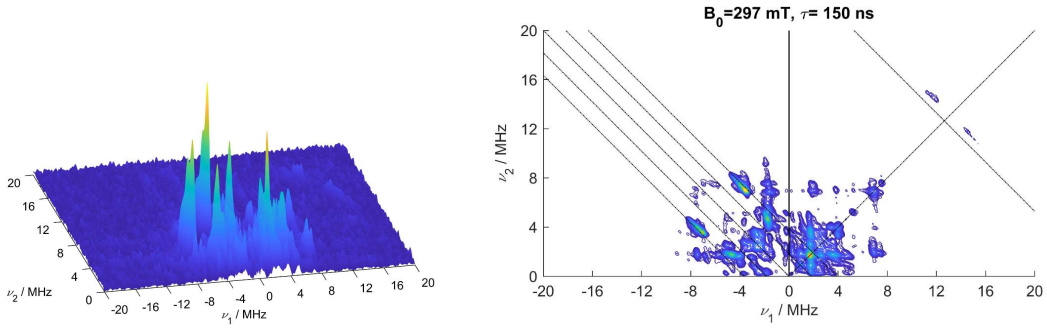

(a) 4-methoxybenzoic acid-bound CYP199A4

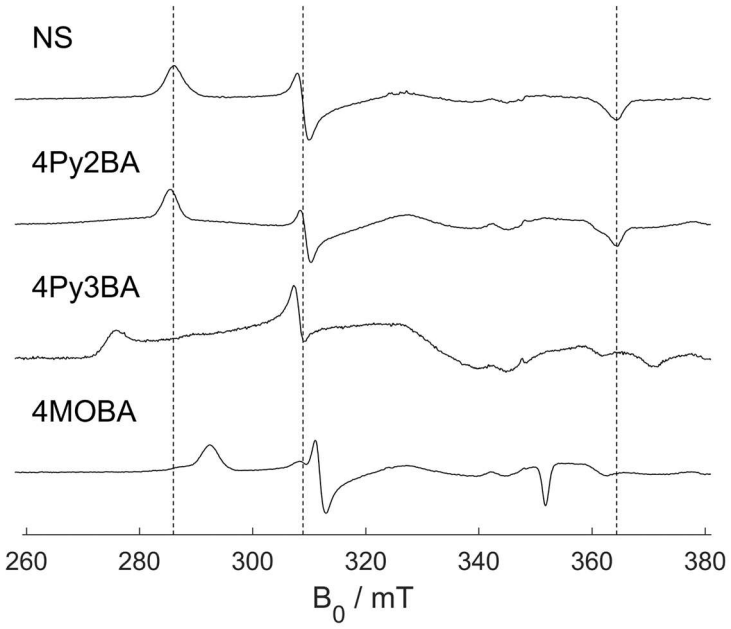

(b) CW EPR spectra

Figure B25. **(a)** HYSCORE spectrum of CYP199A4 with the substrate 4-methoxybenzoic acid, which largely displaces the water ligand. **(b)** CW EPR spectra of CYP199A4 without substrate (NS) and in complex with the type II inhibitors 4-pyridin-2-ylbenzoic acid (4Py2BA) and 4-pyridin-3-ylbenzoic acid (4Py3BA) and the substrate 4-methoxybenzoic acid (4MOBA). **These figures were supplied by Josh Harbort and Jeffrey Harmer at the University of Queensland, who performed the EPR experiments.**

Table B9. CW EPR parameters for CYP199A4 in complex with type I ligands (4-methoxy- and 4-vinyl-benzoic acid) and the type II inhibitors 4-pyridin-2-yl- and 4-pyridin-3-ylbenzoic acid.

This table was supplied by Jeffrey Harmer and Josh Harbort at the University of Queensland, who performed the EPR experiments.

Substrate	Spe-cies	g_z	g_y	g_x	g_z strain[c]	g_y strain[c]	g_x strain[c]	D	E/D	Comp. %	HS (%)
Substrate-free	*1*	2.4332	2.2530	1.9141	0.0308	0.0182	0.0179			100	**0**
4-methoxy benzoic acid	*1*	2.4147	2.2549	1.9216	0.0262	0.0170	0.0151			50.4	**20**
	2	2.4546	2.2561	1.9039	0.0418	0.0195	0.0208			21.1	
	3	2.3851	2.2366	1.9811	0.0279	0.0183	0.0102			8.52	
HS [a]	*4*	8.0990	3.4808	1.6695	0.2337	0.1650	0.0633			19.9	
[b]	"	2	2	2	0.0932	0.0608	0.0501	$\sim 10^8$	~0.108		
4-vinyl benzoic acid	*1*	2.4215	2.2562	1.9165	0.0250	0.0130	0.0223			41.1	**32.6**
	2	2.4447	2.2562	1.9194	0.0208	0.0148	0.0094			12.0	
	3	2.3918	2.2346	1.9794	0.0311	0.0141	0.0086			14.3	
HS [a]	*4*	8.1323	3.4295	1.6515	0.2039	0.1889	0.0699			32.5	
[b]	"	2	2	2	0.1209	0.0643	0.0601	$\sim 10^8$	~0.110		
4-pyridin-2-yl benzoic acid	*1*	2.4388	2.2504	1.9103	0.0246	0.0117	0.0117			100	**0**
4-pyridin-3-yl benzoic acid	*1*	2.5262	2.2583	1.8798	0.0385	0.0156	0.0201			94.4	**0**
	2	2.4112	2.2665	1.9195	0.0299	0.0079	0.0120			5.6 [d]	

[a] Modelled with a $S_{eff} = ½$ spin Hamiltonian. [b] Modelled with a $S = 5/2$ spin Hamiltonian.
[c] g-strain values shown for X-band only. [d] Signal from remaining substrate-free CYP199A4.

Structure of 4-phenylbenzoate-bound CYP199A4 overlaid with the 4-pyridin-2-ylbenzoic acid and 4-pyridin-3-ylbenzoic acid structures

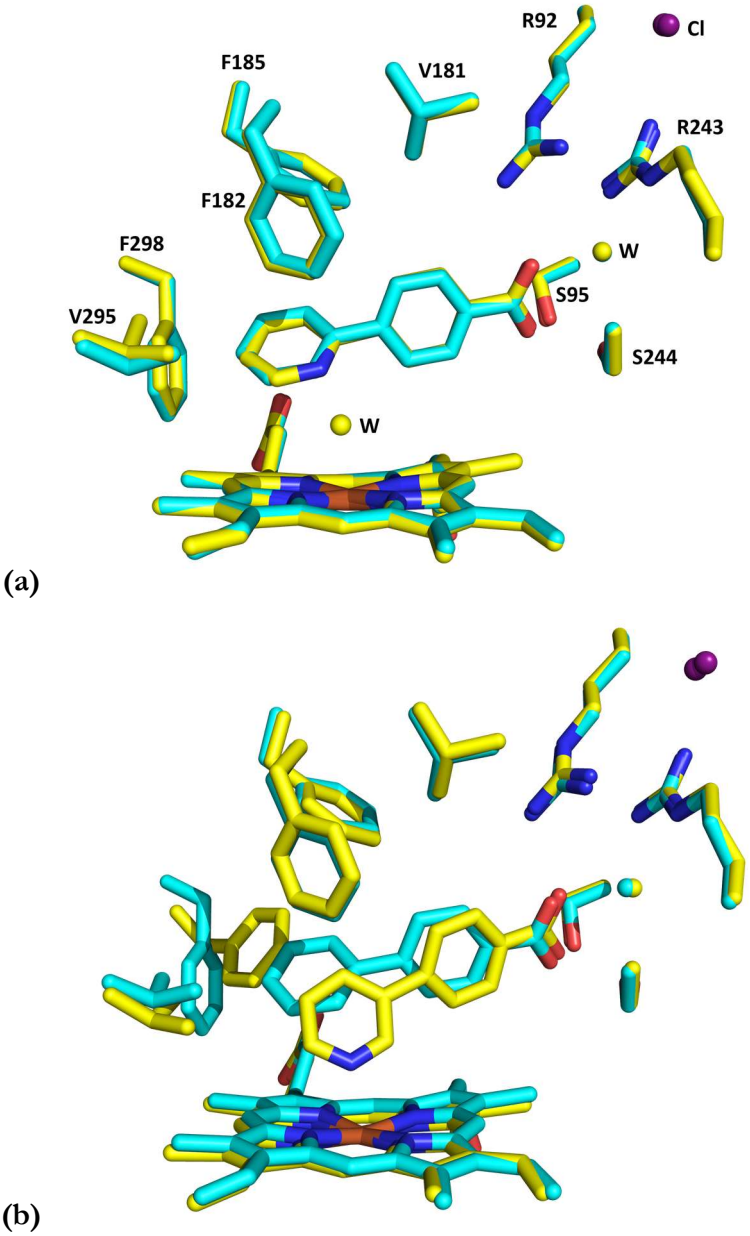

Figure B26. **(a)** Overlaid structures of 4-pyridin-2-ylbenzoate-bound CYP199A4 (yellow) and 4-phenylbenzoate-bound CYP199A4 (cyan). **(b)** Overlaid structures of 4-pyridin-3-ylbenzoate-bound CYP199A4 (yellow) and 4-phenylbenzoate-bound CYP199A4 (cyan). The 4-phenylbenzoic acid structure is unpublished data and was obtained by Joel Lee (PhD student in the Bell Group).

Displacement of 4-pyridin-3-ylbenzoic acid from the CYP199A4 active site by 4-methoxybenzoic acid

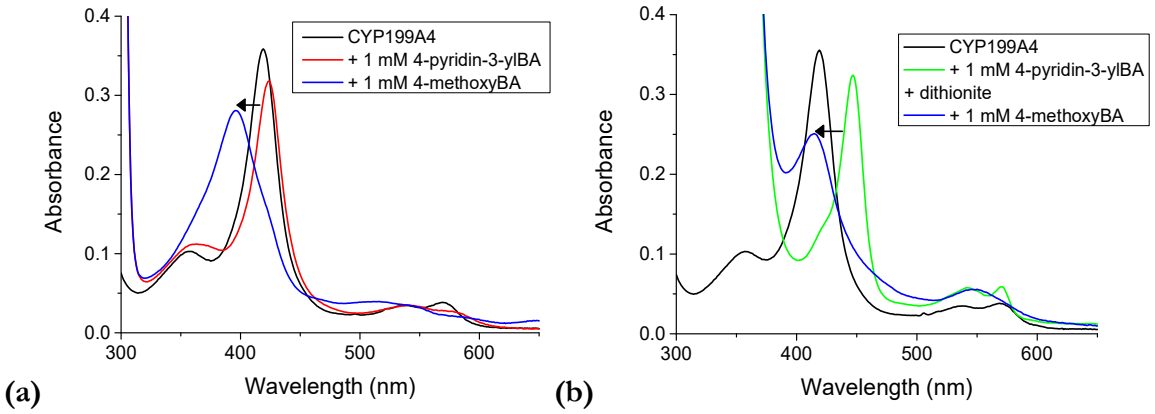

Figure B27. Displacement of 4-pyridin-3-ylbenzoic acid from the active site of **(a)** ferric and **(b)** ferrous CYP199A4 by 4-methoxybenzoic acid.

4-Pyridin-3-ylbenzoic acid could be readily displaced from the active site of CYP199A4 by the tight-binding type I substrate 4-methoxybenzoic acid.

CYP199A4 was first complexed with 4-pyridin-3-ylbenzoic acid (1 mM), which shifted the Soret band to 424 nm. Subsequent addition of 1 mM 4-methoxybenzoic acid almost completely converted the enzyme into the HS form (λ_{max} = 396 nm), indicating that the type I substrate had replaced 4-pyridin-3-ylbenzoic acid in the enzyme active site.

4-Methoxybenzoic acid also readily displaced 4-pyridin-3-ylbenzoic acid from the active site of the dithionite-reduced enzyme. Replacement of 4-pyridin-3-ylbenzoic acid in the active site by 4-methoxybenzoic acid was evidenced by a Soret band shift from 447 nm to 415 nm.

4-Pyridin-3-ylbenzoic acid could also be displaced from the active site of CYP199A4 by 4-pyridin-2-ylbenzoic acid.

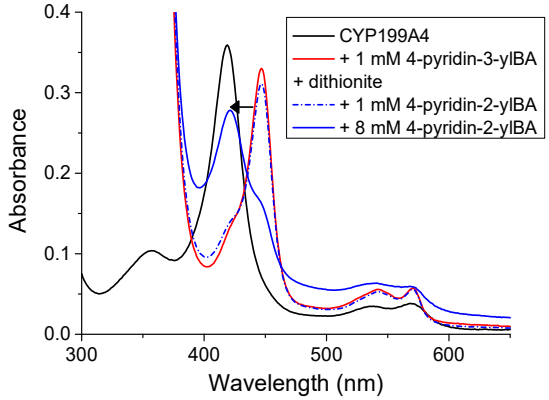

Figure B28. Displacement of 4-pyridin-3-ylbenzoic acid from the active site of ferrous CYP199A4 by 4-pyridin-2-ylbenzoic acid.

Displacement of 4-1*H*-imidazol-1-yl- and 4-pyridin-2-yl-benzoic acid from the CYP199A4 active site by 4-methoxybenzoic acid

The type I substrate 4-methoxybenzoic acid readily displaced the type II ligand 4-1*H*-imidazol-1-ylbenzoic acid from the active site of CYP199A4.

Displacement of the 'pseudo' type II ligand 4-pyridin-2-ylbenzoic acid from the CYP199A4 active site by 4-methoxybenzoic acid was more difficult. A larger concentration of 4-methoxybenzoic acid was required to displace 4-pyridin-2-ylbenzoic acid.

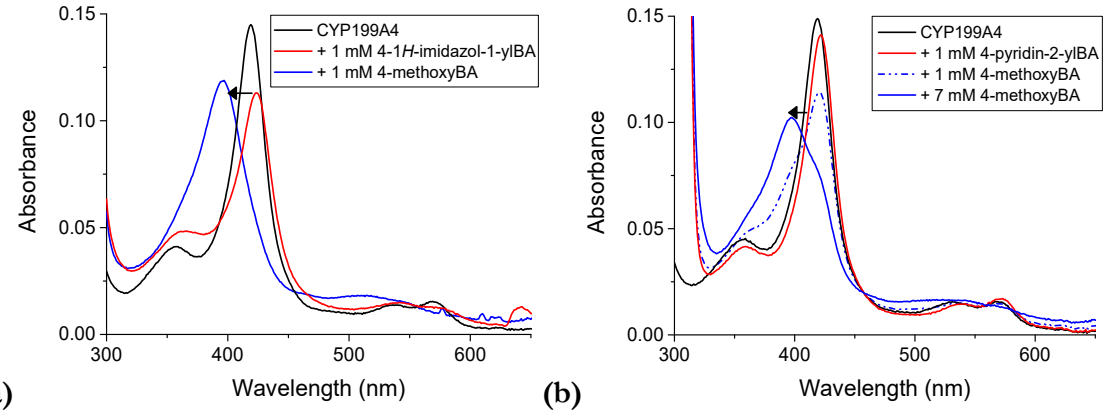

Figure B29. Displacement of **(a)** 4-1*H*-imidazol-1-ylbenzoic acid and **(b)** 4-pyridin-2-ylbenzoic acid from the active site of ferric CYP199A4 by 4-methoxybenzoic acid.

Crystal structure of 2-phenylimidazole-bound $P450_{cam}$ reported by Poulos[364]

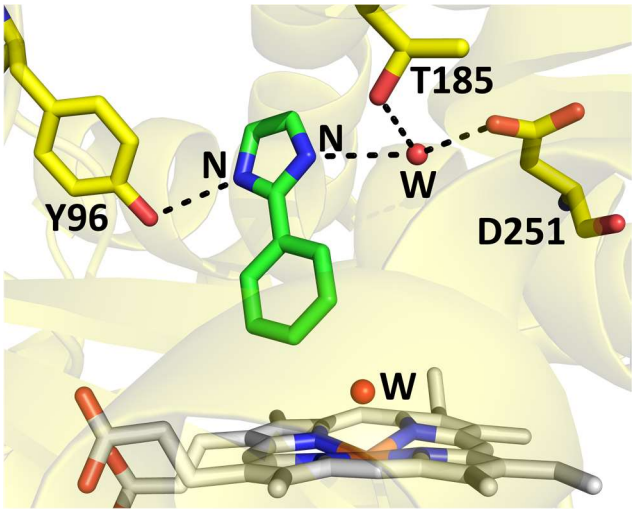

Figure B30. Crystal structure of $P450_{cam}$ in complex with the 'abnormal' nitrogen ligand 2-phenylimidazole reported by Poulos (PDB ID: 1PHE)[364].

Poulos reported that the 'abnormal' nitrogen donor ligand 2-phenylimidazole fails to displace the heme-bound water when it binds to $P450_{cam}$ and does not form a Fe-N bond, explaining the abnormal spectrum. The imidazole moiety of 2-phenylimidazole does not hydrogen-bond to the heme-bound water ligand.[155, 364]

Spectrum of ferrous CYP199A4 in complex with 4-pyridin-2-ylbenzoic acid supplied by Professor Paul V. Bernhardt

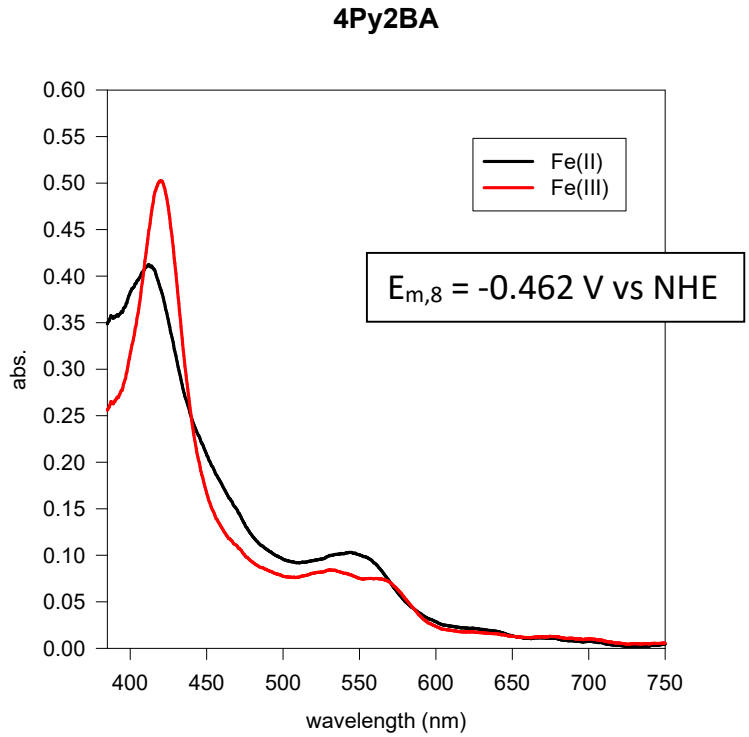

Figure B31. Spectra of ferric 4-pyridin-2-ylbenzoic acid-bound CYP199A4 (**red**) and the reduced form (**black**), with the Soret band shifted to 412 nm and the α/β bands merged into a single peak at 544 nm. **This experiment was performed by Professor Paul V. Bernhardt who supplied the figure.**

Spectra of ferrous CYP199A4 in complex with inhibitors and substrates supplied by Professor Paul V. Bernhardt

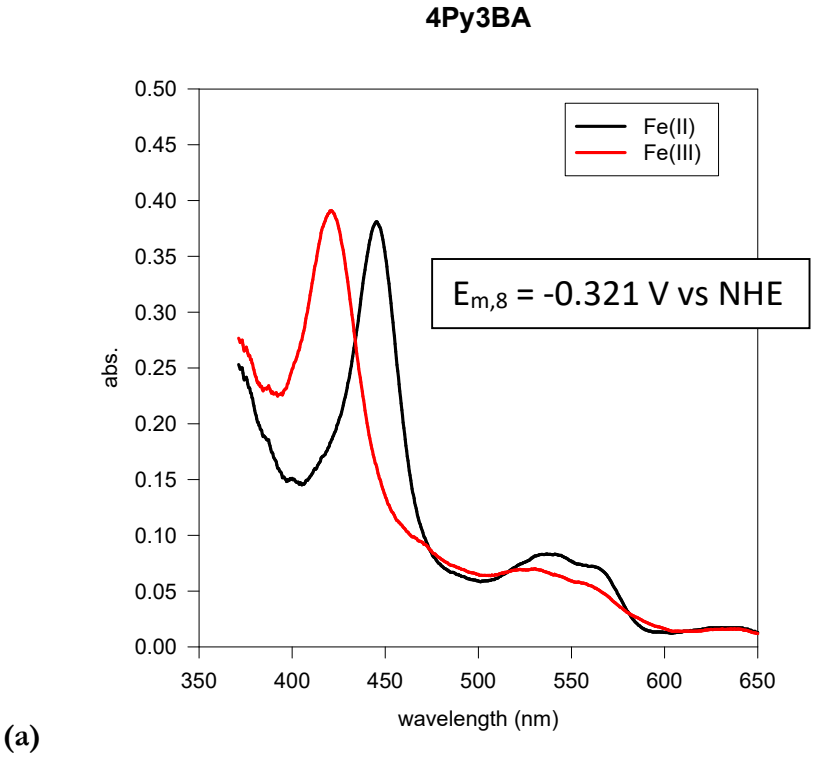

(a)

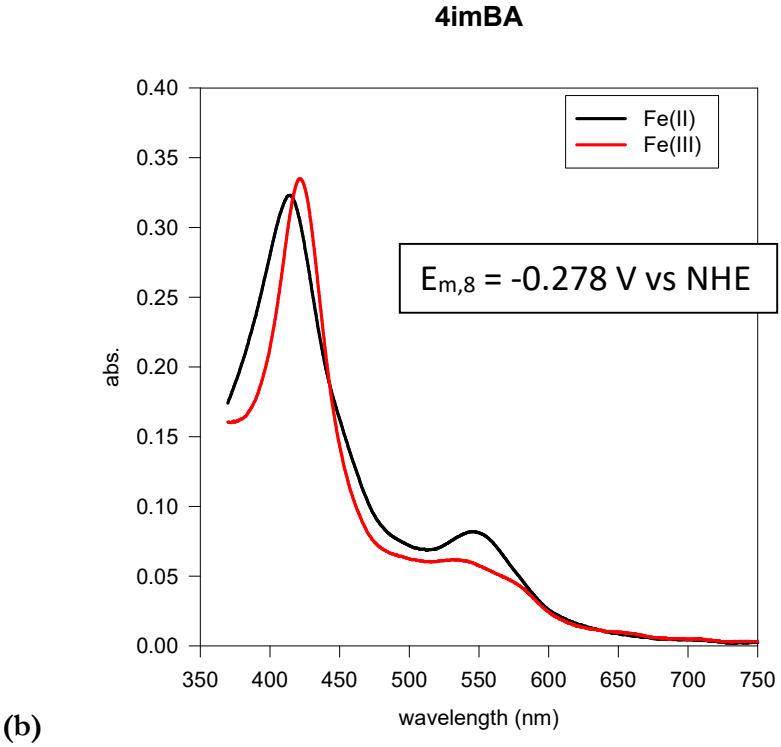

(b)

Figure B32. Spectra of ferric CYP199A4 (**red**) and the reduced form (**black**) in complex with the type II ligands **(a)** 4-pyridin-3-ylBA and **(b)** 4-1*H*-imidazol-1-ylBA. **These experiments were performed by Professor Paul V. Bernhardt who supplied the figures.**

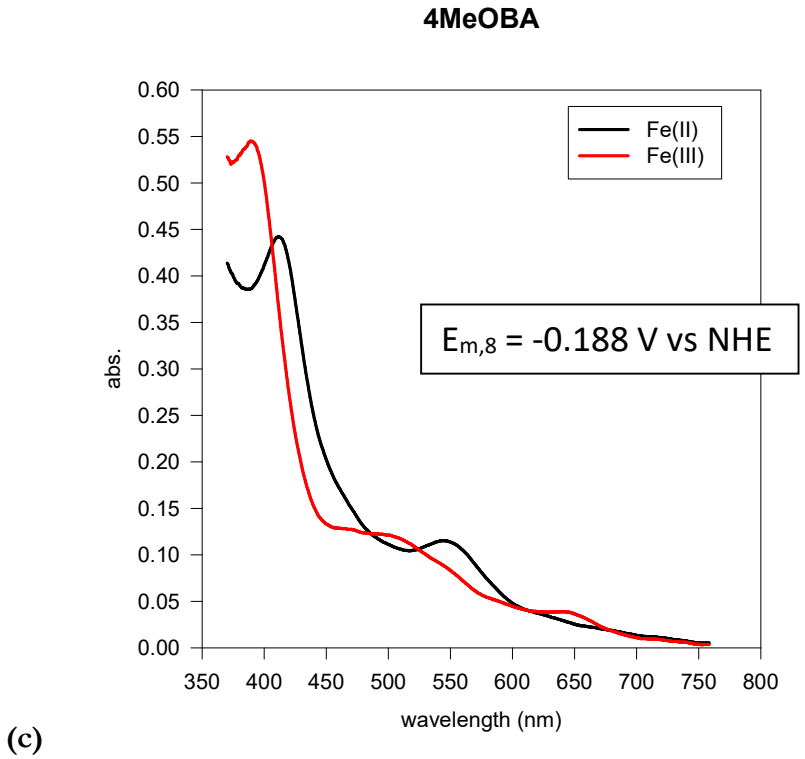

(c)

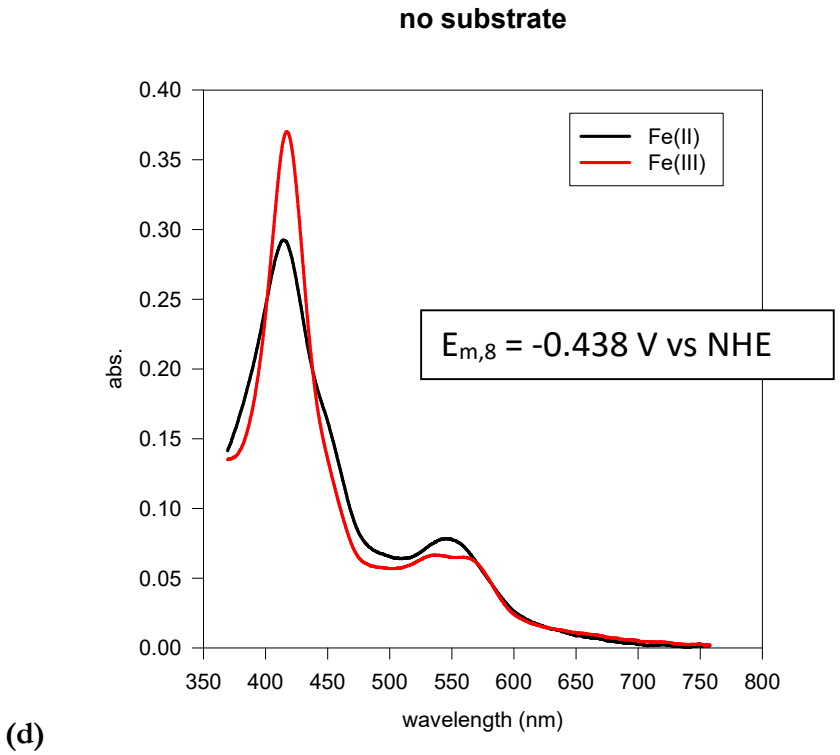

(d)

Figure B32. *(Continued)* Spectra of ferric CYP199A4 (**red**) and the reduced form (**black**) in complex with **(c)** 4-methoxybenzoic acid and **(d)** without substrate. **These experiments were performed by Professor Paul V. Bernhardt who supplied the figures.**

Table B10. Reduction potentials of CYP199A4 in complex with type II inhibitors and substrates supplied by Professor Paul V. Bernhardt at the University of Queensland. The wavelengths of spectra peaks for the ferric and ferrous forms are given.

Substrate	**$E_{m,8}$ (mV vs NHE)**	**Fe(III)**	**Fe(II)**
No substrate	-438	417, 546, 561 nm	414, 548 nm
4-MethoxyBA	-188	390, 500, 645 nm	412, 544 nm
4Py2BA	-462	420, 538, 567 nm	412, 544 nm
4Py3BA	-321	422, 532, 562 nm	447, 540, 567 nm
4-Imidazol-1-ylBA	-278	423, 527 nm	414, 545 nm

Appendix C: Supplementary Information for Chapter 5

Determination of the extinction coefficient of WT CYP199A4 by the CO binding method[284]

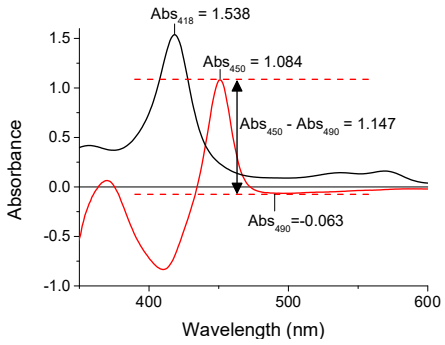

Figure C1. Spectra of native WT CYP199A4 (**black**) and the Fe^{II}–CO versus Fe^{II} difference spectrum (**red**).

Concentration of P450 = $(A_{450} – A_{490})/91$ mM^{-1} cm^{-1} = 12.6 μM

Extinction coefficient for the CYP199A4 Soret band:

$\varepsilon_{418} = A_{418}/(\text{P450 conc.} \times \text{path length})$ = 122 mM^{-1} cm^{-1}

Determination of the extinction coefficient of CYP199A4 isoforms by the pyridine hemochromogen method[288]

Table C1. Calculated Soret band extinction coefficients for WT CYP199A4 and the T252E, D251N and T252A mutants by the pyridine hemochromogen method[288-289]

Trial	Calculated Soret band extinction coefficient (mM^{-1} cm^{-1})			
	WT CYP199A4 $\varepsilon_{419\ nm}$	**T252E mutant** $\varepsilon_{419.5\ nm}$	**D251N mutant** $\varepsilon_{420\ nm}$	**T252A mutant** $\varepsilon_{419\ nm}$
1	122.9	122.5	123.3	120.3
2	120.8	116.0	123.3	118.3
3	121.8	119.5	123.3	116.4
4	123.4	119.7	122.5	126.5
5	126.5	122.0	122.5	
6	128.6	120.2	123.3	
7	123.2	116.7	122.5	
8	129.1	119.0	121.7	
Mean ± SD	**125 ± 3**	**119 ± 2**	**122.8 ± 0.6**	**120 ± 4**

Determination of the extinction coefficient of T252E$_{CYP199A4}$ by the pyridine hemochromogen method

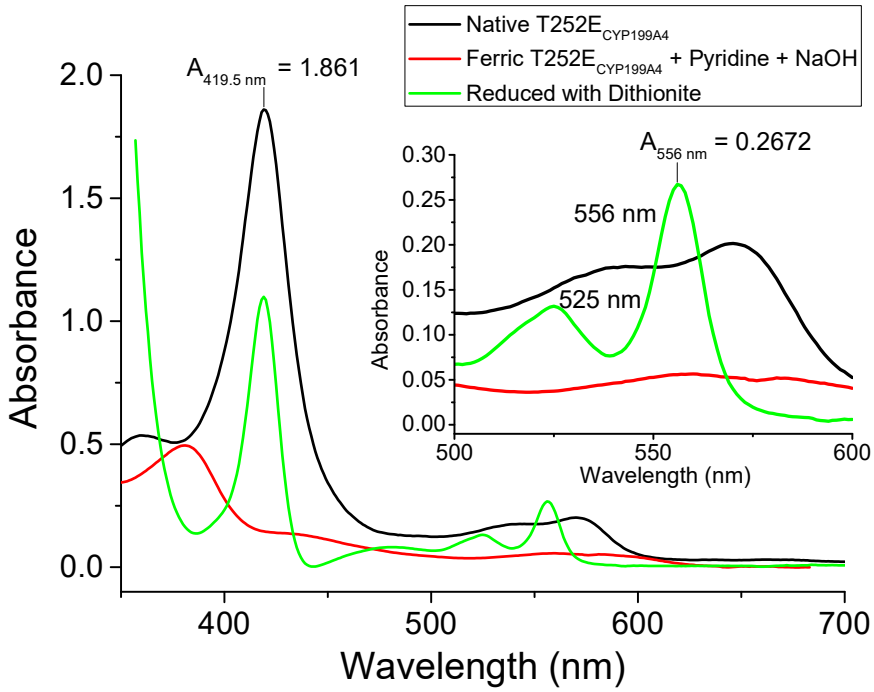

Figure C2. Determination of the Soret band extinction coefficient of native T252E$_{CYP199A4}$ by the pyridine hemochromogen method.[288]

A solution of native T252E$_{CYP199A4}$ was prepared with an absorbance of **1.861** at 419.5 nm.

The T252E$_{CYP199A4}$ solution (0.5 mL) was diluted by addition of 0.5 mL of pyridine/NaOH/$K_3[Fe(CN)_6]$ solution, followed by addition of 10 µL of 0.5 M dithionite solution to reduce the heme. Heme concentration in this sample was determined using ε_{557} = 34.7 mM^{-1} cm^{-1}.

Heme concentration: c = $A_{557}/\varepsilon_{557}$ = 0.2672/34.7 = **7.70 µM heme**

Heme concentration in original (undiluted) P450 solution: 7.70 µM heme × (1.01 mL/0.5 mL) = **15.55 µM heme**

Extinction coefficient of native T252E$_{CYP199A4}$:

$\varepsilon_{419.5\ nm}$ = $A_{419.5\ nm}$/c = 1.861/15.55 µM = **119.7 mM^{-1} cm^{-1}**

Spin-state shifts induced by binding of benzoic acids to $T252E_{CYP199A4}$ with alternative functional groups at the *para* position

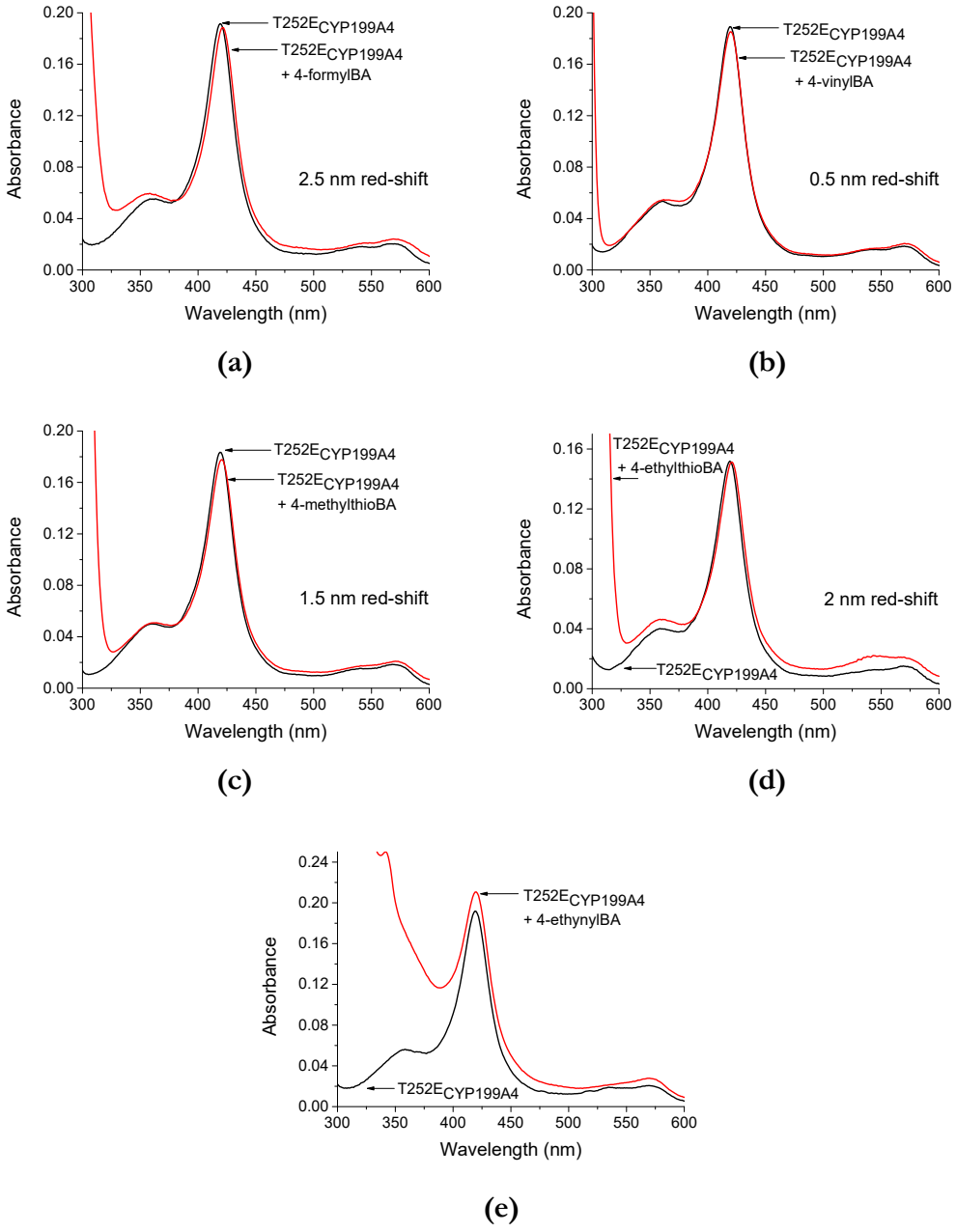

Figure C3. Spin-state shifts of the T252E mutant of CYP199A4 induced by **(a)** 4-formylbenzoic acid, **(b)** 4-vinylbenzoic acid, **(c)** 4-methylthiobenzoic acid, **(d)** 4-ethylthiobenzoic acid and **(e)** 4-ethynylbenzoic acid.

For substrates which induced a red-shift of the Soret band, these red-shifts are shown more clearly in Figure C4.

Red-shifts of the Soret band induced by binding of benzoic acids to T252E$_{CYP199A4}$ with alternative functional groups at the *para* position

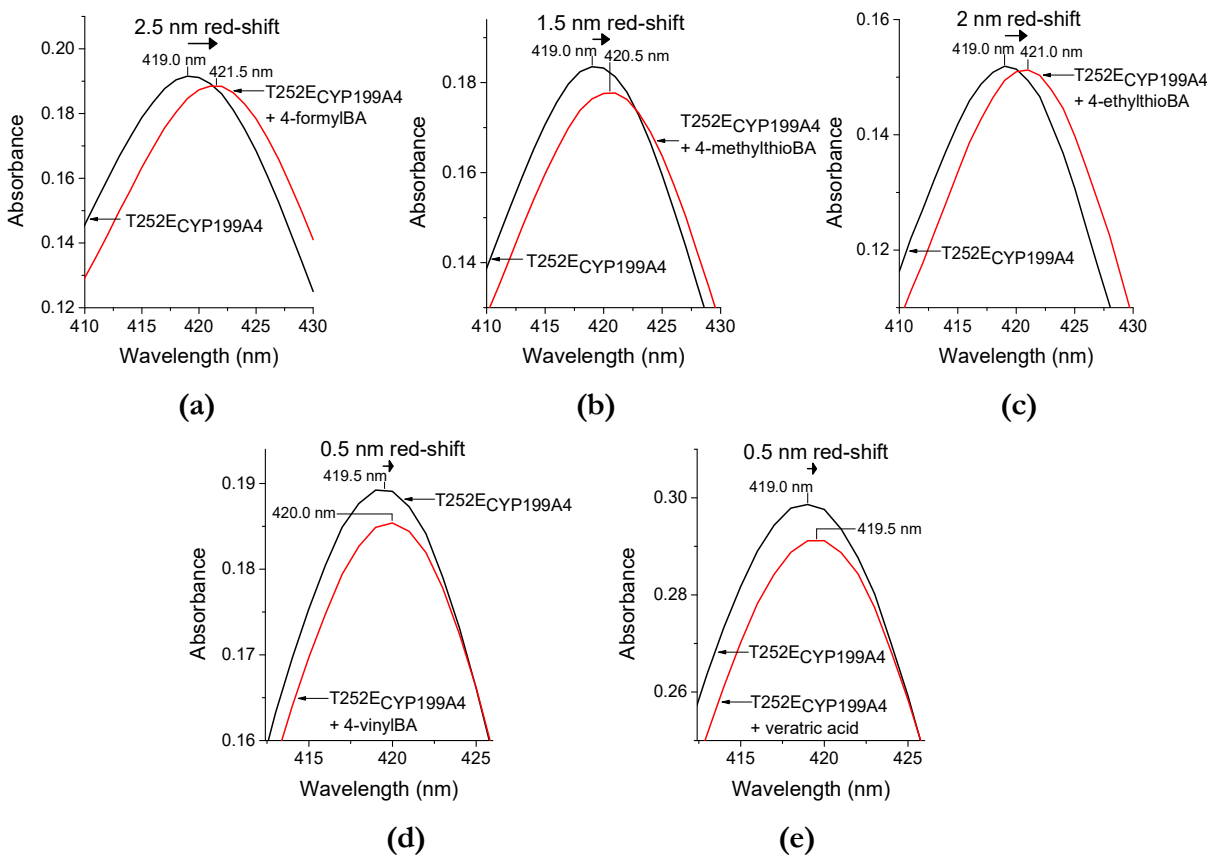

Figure C4. Red-shifts of the Soret band of T252E$_{CYP199A4}$ induced by **(a)** 4-formylbenzoic acid, **(b)** 4-methylthiobenzoic acid, **(c)** 4-ethylthiobenzoic acid and **(d)** 4-vinylbenzoic acid and **(e)** veratric acid.

Dissociation constant analysis of T252E$_{CYP199A4}$ with *para*-substituted benzoic acid substrates

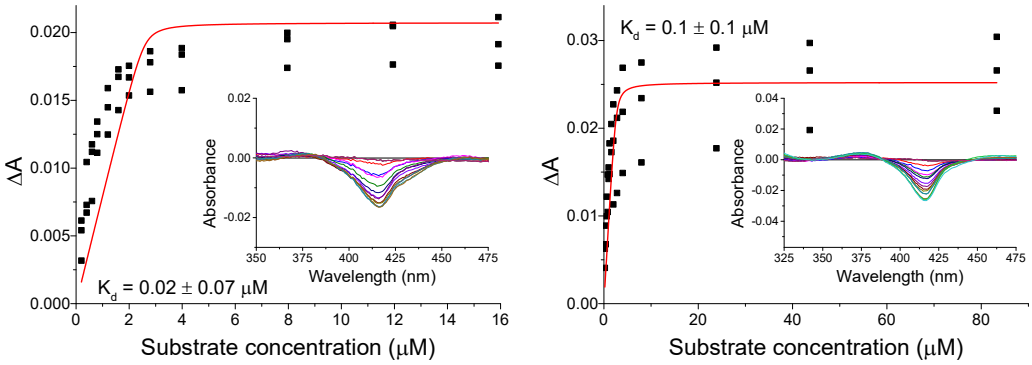

(a) 4-vinylbenzoic acid
(2.6 μM, trough: 416 nm)

(b) 4-methylthiobenzoic acid
(2.6 μM, peak: 376 nm, trough: 416 nm)

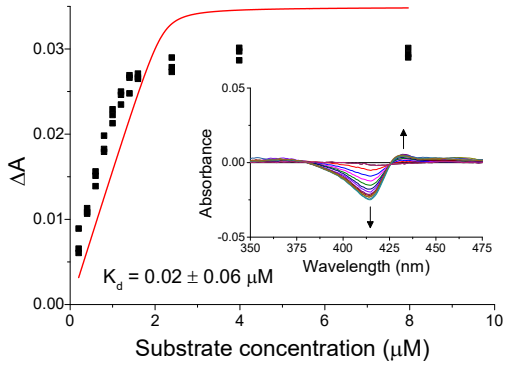

(c) 4-ethylthiobenzoic acid
(2.2 μM, peak: 433 nm, trough: 414 nm)

Figure C5. UV-Vis titrations to determine the dissociation constant of T252E$_{CYP199A4}$ with *para*-substituted benzoic acid substrates. The enzyme concentration used and the peak and trough wavelengths are provided under each graph. The data were fitted to the Morrison tight-binding equation, but the fits are poor. Consequently, the K_d values are not likely to be accurate, but still reveal that the T252E$_{CYP199A4}$ enzyme can tightly bind these substrates.

Co-elution of reaction products with authentic compounds to confirm their identity

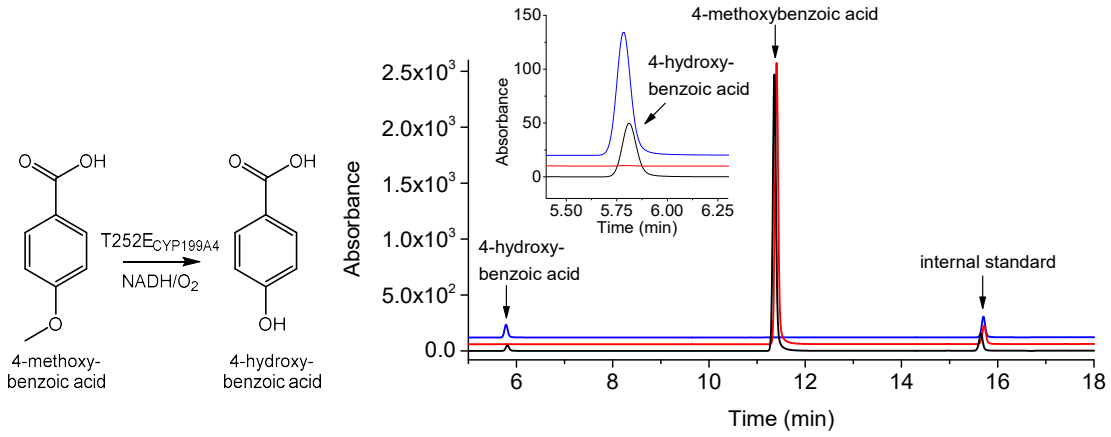

Figure C6. HPLC analysis of the NADH/O_2-driven oxidation of 4-methoxybenzoic acid by T252E$_{CYP199A4}$ (**black**). In **red** is a control reaction omitting the P450, and in **blue** is authentic 4-hydroxybenzoic acid (RT = 5.8 min). The substrate appears at 11.4 min. Gradient: 20-95% AcCN in H_2O with 0.1% TFA. Detection wavelength: 254 nm.

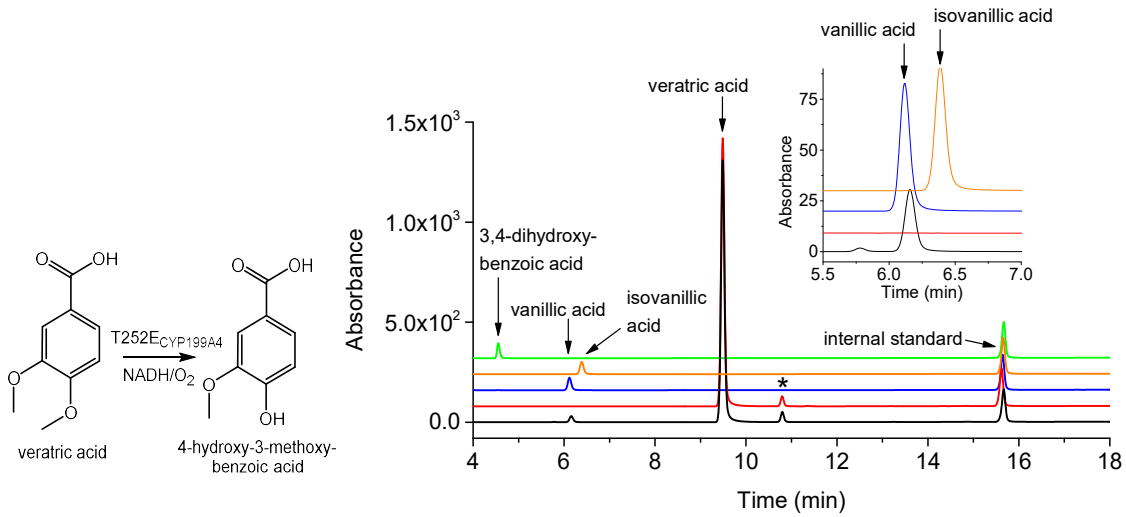

Figure C7. HPLC analysis of the NADH/O_2-driven oxidation of veratric acid by T252E$_{CYP199A4}$ (**black**). In **red** is a control reaction omitting the P450, in **blue** is authentic vanillic acid (RT = 6.1), in **orange** is isovanillic acid (RT = 6.4 min), and in **green** is 3,4-dihydroxybenzoic acid (RT = 4.5 min). The substrate appears at 9.4 min. Gradient: 20-95% AcCN in H_2O with 0.1% TFA. Detection wavelength: 254 nm. * Impurity in substrate.

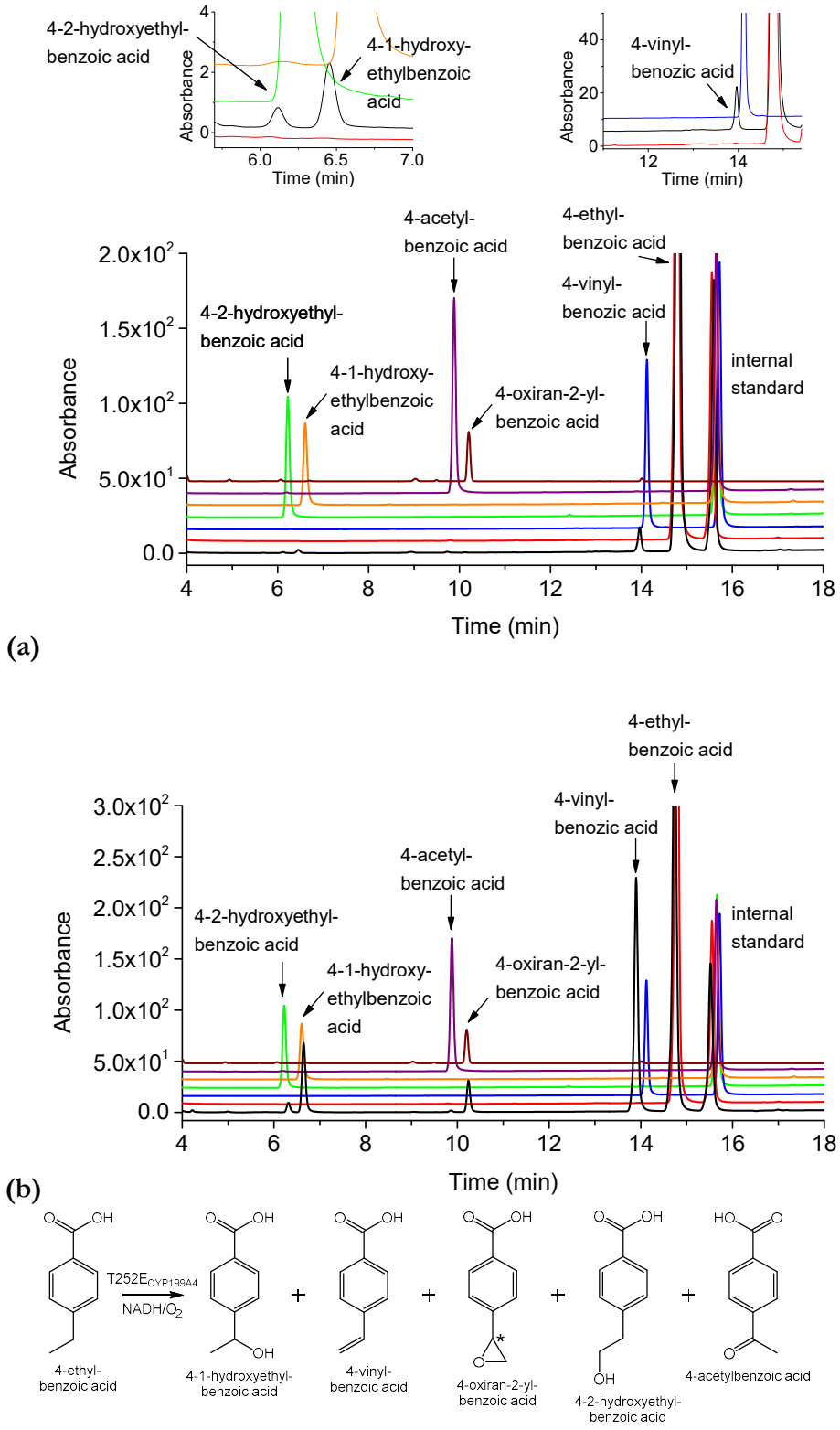

Figure C8. HPLC analysis of the NADH/O_2-driven oxidation of 4-ethylbenzoic acid by **(a)** T252E$_{CYP199A4}$ and **(b)** WT CYP199A4 (**black**). In **red** is a control reaction omitting the P450, in **blue** is authentic 4-vinylbenzoic acid (RT = 14.1 min), in **green** is 4-2-hydroxyethylbenzoic acid (RT = 6.2 min), in **orange** is 4-1-hydroxyethylbenzoic acid (RT = 6.6 min), in **purple** is 4-acetylbenzoic acid (RT = 9.9 min) and in **dark red** is chemically synthesised epoxide (RT = 10.4 min). The substrate appears at 14.9 min. Gradient: 20-95% AcCN in H_2O with 0.1% TFA. Detection wavelength: 254 nm.

Lifetime of the T252E$_{CYP199A4}$ catalyst in the presence of H_2O_2

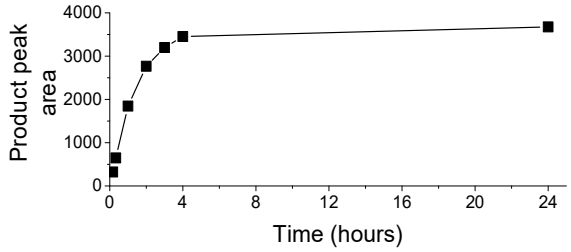

Figure C9. In preliminary experiments, the T252E$_{CYP199A4}$ enzyme was found to be catalytically active for only ~4 hours when exposed to 60 mM H_2O_2. This reaction was performed at room temperature and 4-methoxybenzoic acid was used as the substrate.

Control reactions performed with CYP101B1 and heat-denatured T252E$_{CYP199A4}$

We demonstrated that a Fenton-type reaction was not responsible for the formation of product in the H_2O_2-driven P450 reactions (Figures C10 and C11). In the Fenton reaction, iron reacts with H_2O_2 to generate the potent hydroxyl radical, which is capable of oxidising organic molecules.[411, 451]

Control reactions were performed in which functional T252E enzyme was substituted with CYP101B1, a P450 which does not bind *para*-substituted benzoic acid substrates (Figure C12), or heat-denatured T252E enzyme. In both control reactions, no product was generated. Product was only observed in the presence of functional T252E or WT CYP199A4.

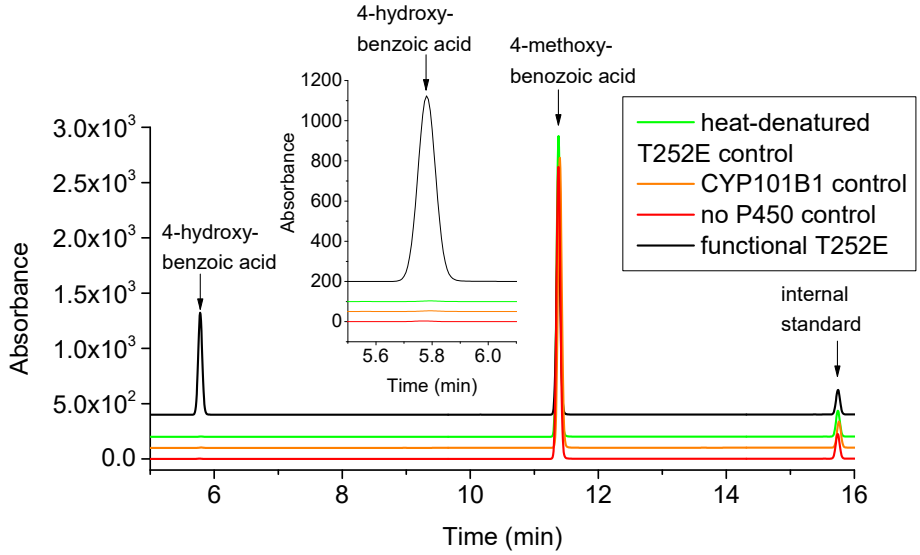

Figure C10. Control reactions performed to demonstrate that a Fenton-type reaction was not responsible for the formation of product in the H_2O_2-driven turnovers. The substrate was 4-methoxybenzoic acid (1 mM), the H_2O_2 concentration was 50 mM and the reaction time was 4 hours. In **red** is a control reaction omitting the P450, in **orange** is a control reaction performed with 3 µM CYP101B1, and in **green** is a control reaction performed with 3 µM heat-denatured T252E$_{CYP199A4}$. These reactions did not generate any product. For comparison, the amount of product (4-hydroxybenzoic acid) generated by functional T252E$_{CYP199A4}$ under the same conditions is shown (**black**).

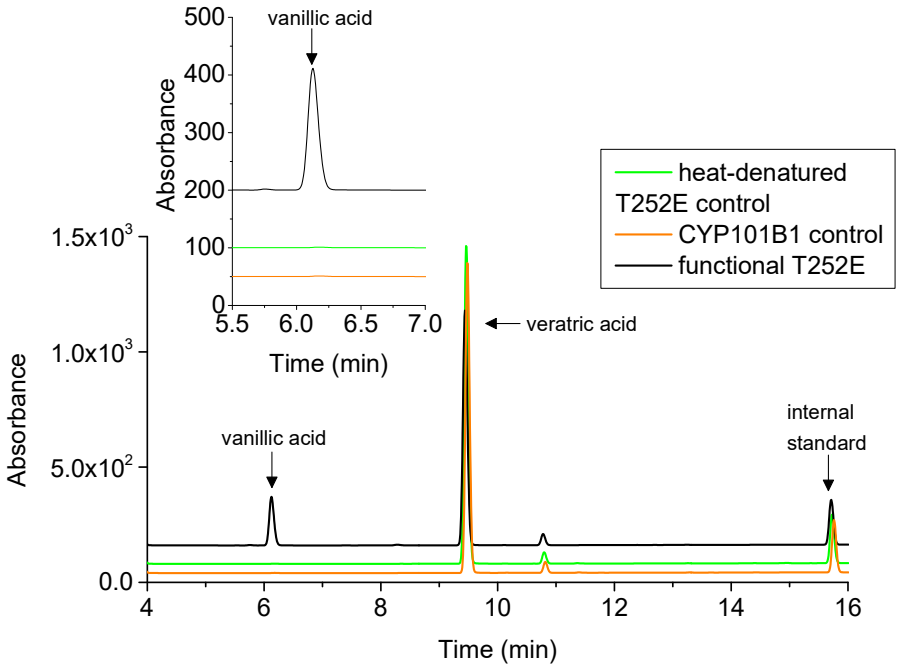

Figure C11. Control reactions performed to demonstrate that a Fenton-type reaction was not responsible for veratric acid demethylation in H_2O_2-driven turnovers.

In **orange** is a control reaction which contained CYP101B1 instead of T252E$_{CYP199A4}$ and in **green** is a control reaction performed with heat-denatured T252E$_{CYP199A4}$. No product was generated in these control reactions. Product was only formed when functional T252E$_{CYP199A4}$ enzyme was present (**black**). The reaction time was 4 hours.

CYP101B1 spin-state shifts

Para-substituted benzoic acids do not bind to CYP101B1 based on the lack of any appreciable spin-state shift to high-spin when these substrates are added to the enzyme. Substrates of CYP101B1 are the norisoprenoids α-ionone, β-ionone and β-damascone.[299, 466]

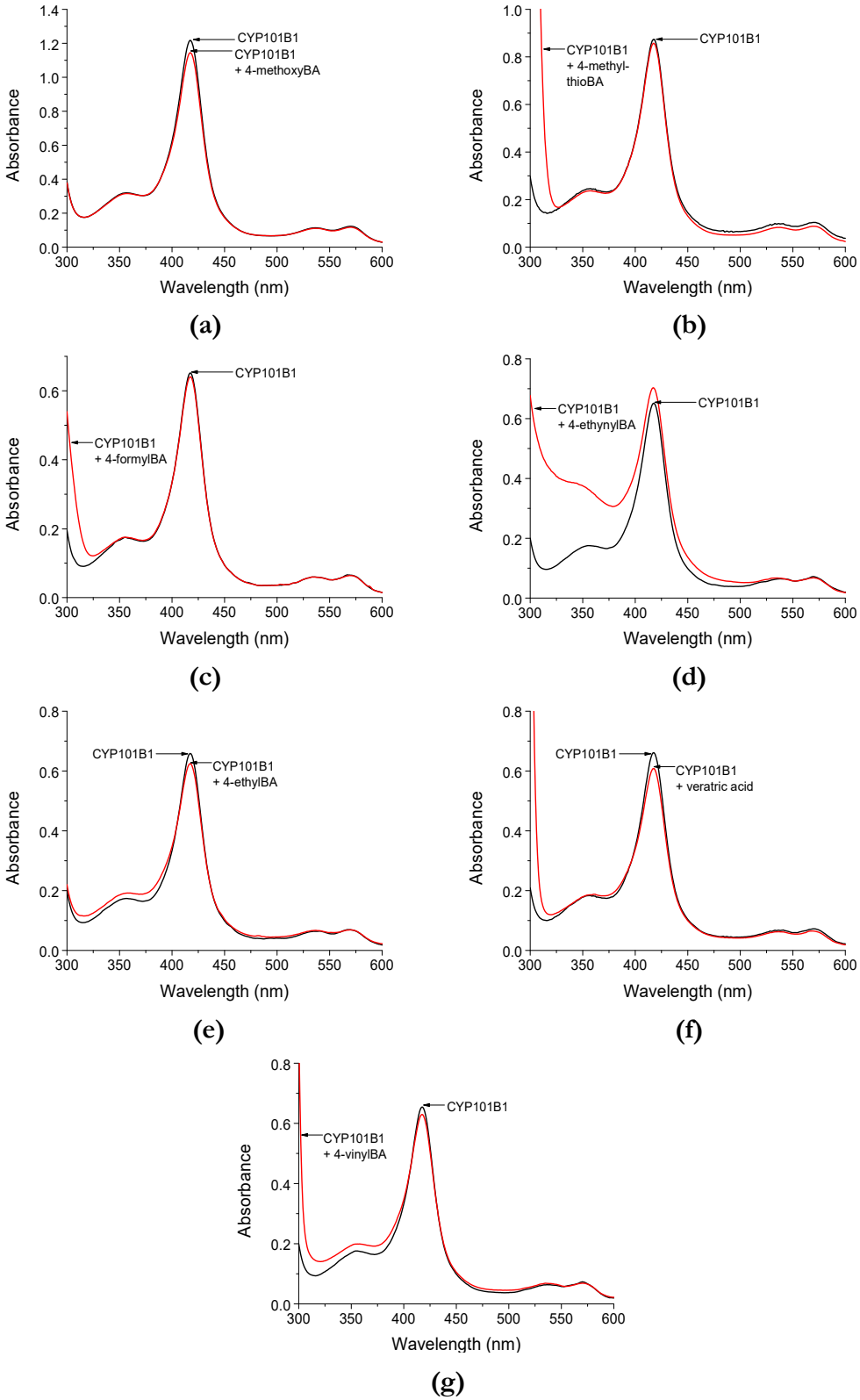

Figure C12. Spin-state shifts of WT CYP101B1 with *para*-substituted benzoic acids: **(a)** 4-methoxybenzoic acid, **(b)** 4-methylthiobenzoic acid, **(c)** 4-formylbenzoic acid, **(d)** 4-ethynylbenzoic acid, **(e)** 4-ethylbenzoic acid, **(f)** veratric acid, and **(g)** 4-vinylbenzoic acid.

Reaction of the T252E$_{CYP199A4}$ enzyme with 4-nitroanisole and 60 mM H_2O_2

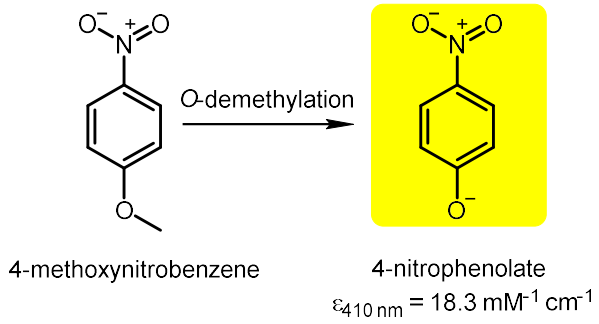

(a)

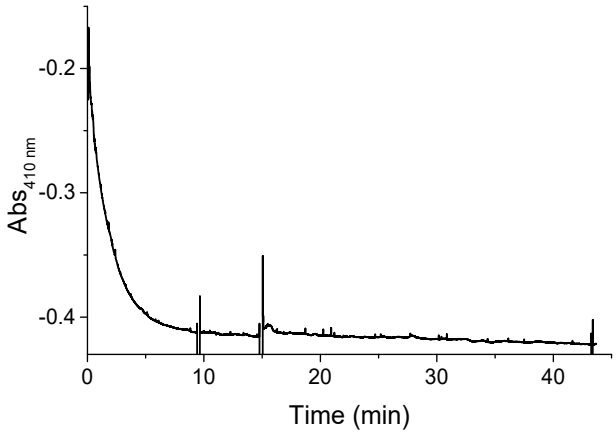

(b)

Figure C13. **(a)** *O*-demethylation of 4-nitroanisole produces a vivid yellow product which absorbs at 410 nm. **(b)** Reaction of 3 μM T252E$_{CYP199A4}$ enzyme with 1 mM 4-nitroanisole and 60 mM H_2O_2 monitored at 410 nm. Instead of observing an increase in absorbance at 410 nm due to 4-nitrophenolate production, a rapid decrease in absorbance occurred due to rapid heme bleaching by H_2O_2.

Heme bleaching by H_2O_2 inactivates the P450

In the absence of substrate, the $T252E_{CYP199A4}$ enzyme was rapidly bleached by H_2O_2. To show that the bleached enzyme was inactive, 3 μM substrate-free $T252E_{CYP199A4}$ was pre-incubated with 50 mM H_2O_2 for 20 minutes before addition of 1 mM 4-methoxybenzoic acid. No product was generated by the bleached enzyme, demonstrating that it was completely inactive (Figure C14).

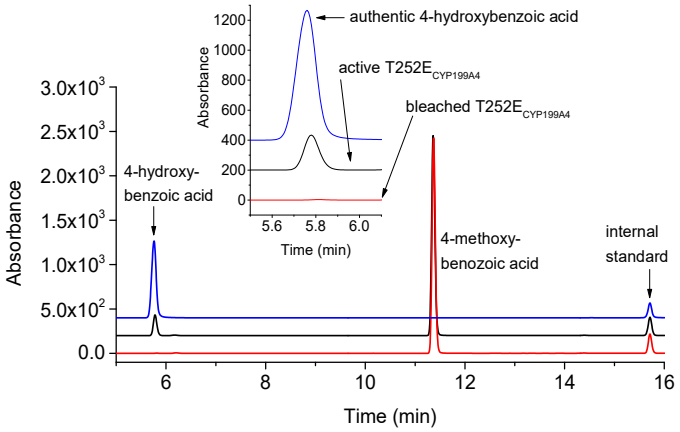

Figure C14. HPLC analysis of a 20-minute reaction of bleached $T252E_{CYP199A4}$ (3 μM) with 4-methoxybenzoic acid (**red**), demonstrating that the bleached enzyme is completely inactive. The T252E enzyme had been bleached by pre-incubation with 50 mM H_2O_2 for 20 minutes before addition of substrate. No 4-hydroxybenzoic acid product was generated by the bleached enzyme.

For comparison, a 20-minute reaction of *active* $T252E_{CYP199A4}$ enzyme (3 μM) with 4-methoxybenzoic acid in the presence of 50 mM H_2O_2 is shown in **black**, which generated product. In **blue** is authentic 4-hydroxybenzoic acid.

Rate of heme bleaching of substrate-free T252E$_{CYP199A4}$ by H_2O_2

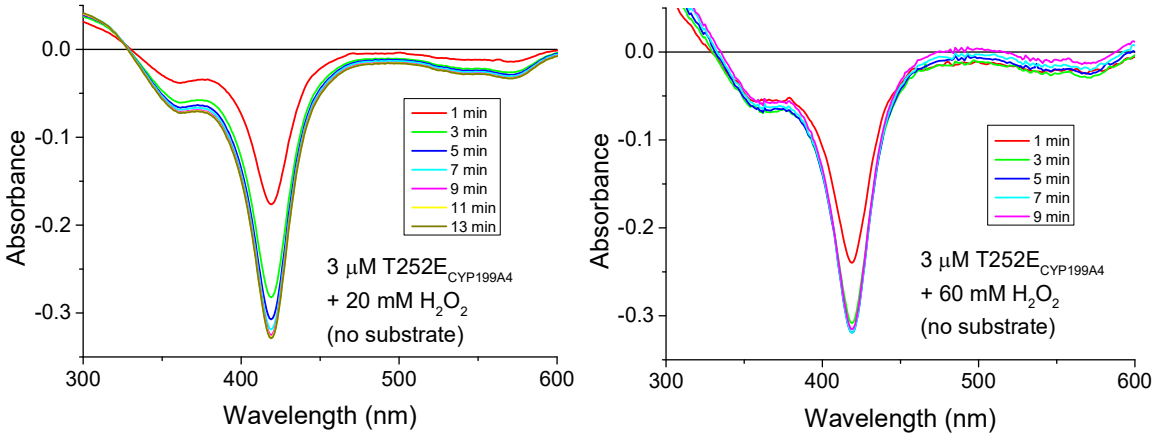

Figure C15. Rate of heme bleaching of **substrate-free T252E$_{CYP199A4}$** (3 μM) when exposed to **20** and **60 mM H_2O_2**. Spectra were recorded at 2 min intervals to monitor the loss of the Soret absorption band. **The heme signal of the substrate-free enzyme was rapidly bleached.**

Substrate protected T252E$_{CYP199A4}$ from rapid heme bleaching by H_2O_2

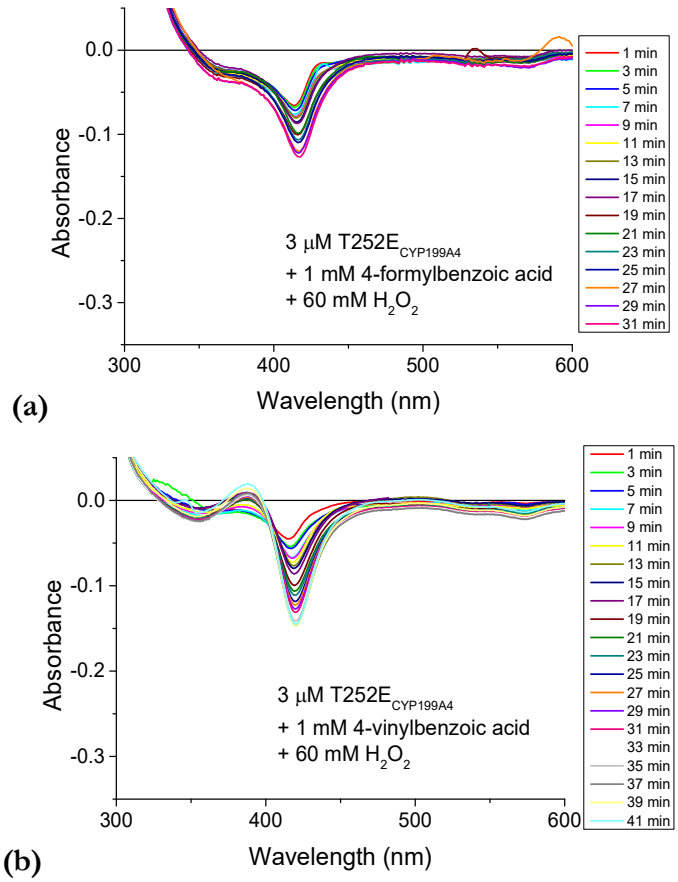

Figure C16. Rate of heme bleaching of 3 μM T252E$_{CYP199A4}$ in the presence of **(a) 1 mM 4-formylbenzoic acid** and **(b) 1 mM 4-vinylbenzoic acid** when exposed to **60 mM H_2O_2**. Spectra were recorded at 2 min intervals to monitor the loss of the Soret absorption band. **Substrate protected the T252E mutant from rapid bleaching**.

Data collection and crystal structure refinement statistics

Table C2. Statistics for data collection and refinement of crystal structures of the T252E mutant of CYP199A4 in complex with benzoic acid substrates. Values in parentheses correspond to the highest resolution (outer) shell.

Statistic	4-methoxy	4-methylthio	4-ethylthio	4-benzyl	4-thiophen-3-yl	4-pyridin-2-yl
X-ray wavelength (Å)	0.71080	0.95370	0.95370	0.95373	0.95373	0.95370
Unit cell parameters (Å/°)	*a* = 41.3 *b* = 51.5 *c* = 79.7 α = 90.0 β = 92.2 γ = 90.0	*a* = 41.1 *b* = 51.8 *c* = 80.0 α = 90.0 β = 92.3 γ = 90.0	*a* = 40.7 *b* = 51.5 *c* = 79.3 α = 90.0 β = 92.3 γ = 90.0	*a* = 44.2 *b* = 51.6 *c* = 79.2 α = 90.0 β = 92.4 γ = 90.0	*a* = 44.1 *b* = 51.6 *c* = 79.5 α = 90.0 β = 92.4 γ = 90.0	*a* = 44.2 *b* = 51.5 *c* = 79.2 α = 90.0 β = 92.3 γ = 90.0
Space group	$P12_11$	$P12_11$	$P12_11$	$P12_11$	$P12_11$	$P12_11$
Molecules per asymmetric unit	1	1	1	1	1	1
Resolution range	43.24 – 1.55 (1.57 – 1.55)	43.46 – 1.66 (1.68 – 1.66)	40.70 – 1.66 (1.68 – 1.66)	44.15 – 1.77 (1.80 – 1.77)	44.08 – 2.02 (2.07 – 2.02)	44.13 – 1.73 (1.76 – 1.73)
<I/σ(I)>	8.5 (2.2)	7.4 (1.6)	9.3 (1.0)	8.7 (1.1)	8.1 (2.1)	13.1 (2.0)
Unique reflections	48517	38747	31873	33739	23380	37249
Completeness of data	98.9 (92.5)	96.3 (90.4)	81.1 (73.3)	96.3 (37.3)	98.8 (89.5)	99.7 (94.3)
Multiplicity	7.2 (6.6)	6.1 (5.1)	5.0 (4.3)	6.2 (3.5)	6.6 (5.7)	7.3 (6.7)
R_{merge} (all I+ and I−)	16.6 (95.1)	16.7 (93.0)	14.5 (152.1)	16.3 (139.1)	13.0 (63.2)	13.0 (87.5)
R_{pim} (all I+ and I−)	6.6 (39.6)	7.1 (44.0)	6.7 (76.3)	7.3 (78.8)	5.4 (28.1)	5.2 (36.1)
$CC_{1/2}$	99.3 (76.4)	99.1 (61.8)	99.4 (37.6)	99.1 (-13.9)	99.5 (87.4)	99.7 (70.0)
R_{work}	0.1707	0.1923	0.1668	0.1709	0.1767	0.1510
R_{free} (5% held)	0.2031	0.2326	0.2045	0.2159	0.2229	0.1852
Ramachandran favoured (%)	97.95	98.21	97.95	97.44	97.19	98.21
Ramachandran outliers (%)	0	0	0	0	0	0
Unusual rotamers (%)	0.30	0.31	0.31	0.31	0	0.31
RMSD bond angles (°)	0.892	0.829	0.736	1.001	0.678	0.674
RMSD bond lengths (Å)	0.007	0.006	0.004	0.009	0.004	0.004
Omit map type, contour level, carve radius	composite omit map, 2.0 σ, 1.5 Å carve	composite omit map, 1.5 σ, 1.5 Å carve	feature-enhanced map, 1.0 σ, 1.5 Å carve	feature-enhanced map, 1.5 σ, 1.5 Å carve	feature-enhanced map, 1.0 σ, 1.5 Å carve	feature-enhanced map, 2.0 σ, 1.5 Å carve

Unidentified ligand bound in the crystal structure of 'substrate-free' T252E$_{CYP199A4}$

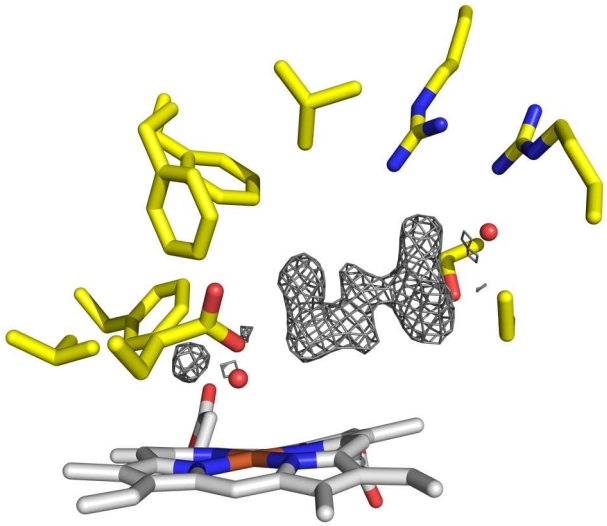

Figure C17. We attempted to obtain a crystal structure of substrate-free T252E$_{CYP199A4}$, but an unidentified ligand was bound in the active site (grey mesh). The electron density map is a *2mFo-DFc* map contoured at 1 σ. The enzyme crystallised in the substrate-bound conformation with a closed substrate-access channel, rather than in a conformation with an open substrate-access channel. When Bell *et al.* previously crystallised WT CYP199A4 in the absence of any intentionally added substrate, they too observed electron density corresponding to an unknown ligand bound in the active site.[29] Bell *et al.* did successfully crystallise CYP199A2, a related enzyme which shares 86% sequence identity with CYP199A4, in the substrate-free form and this had an open substrate-access channel.[29, 467]

T252E$_{CYP199A4}$ chloride binding sites

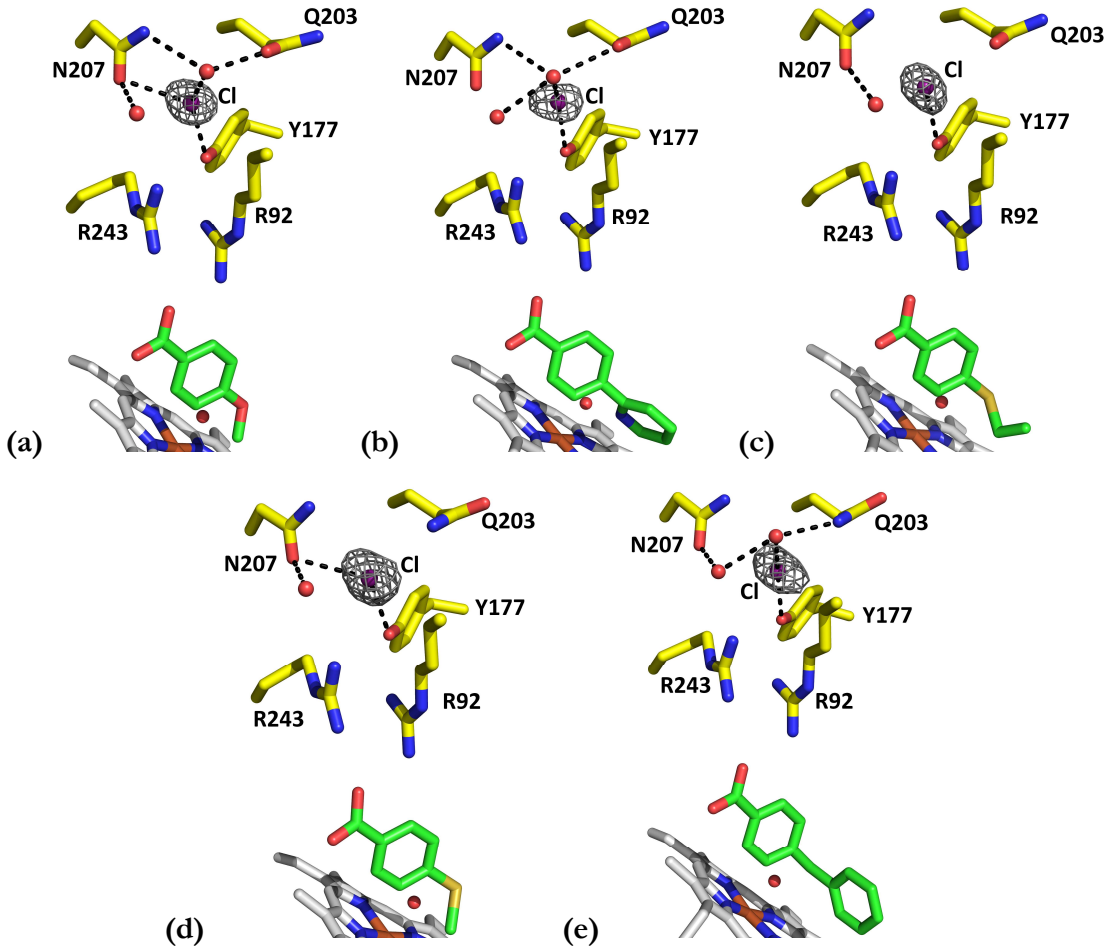

Figure C18. Chloride binding site of the T252E mutant of CYP199A4 in complex with **(a)** 4-methoxyBA, **(b)** 4-pyridin-2-ylBA, **(c)** 4-ethylthioBA, **(d)** 4-methythioBA and **(e)** 4-benzylBA. A composite omit map of the chloride ion (purple sphere) is shown as grey mesh contoured at 1.0 σ (1.5 Å carve).

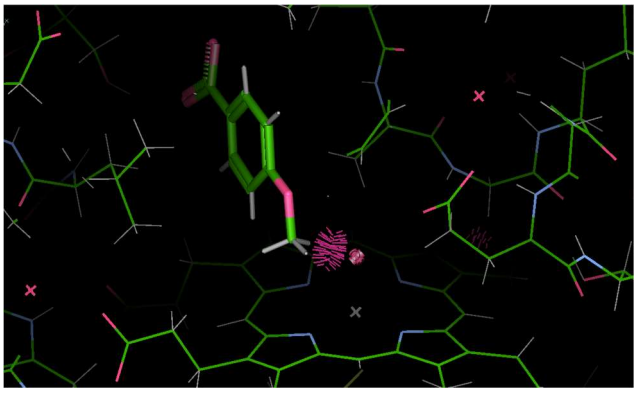

Figure C19. In WT CYP199A4, the *para*-methoxy moiety of 4-methoxybenzoic acid lies in the plane of the benzene ring, whereas in the T252E mutant the *para*-methoxy group is rotated away from the heme by 18°. The methoxy group cannot lie in the same plane as the benzene ring in the T252E mutant because this would result in a steric clash (represented by hot-pink spikes) between the methyl group and the heme-bound H_2O/OH^- ligand, as illustrated by the image above.

Structure of the I-helix in WT CYP199A4 and the T252E mutant

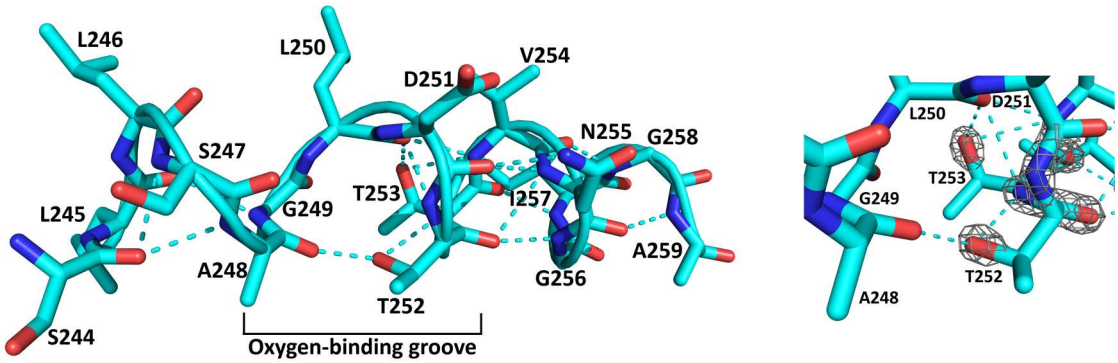

(a) CYP199A4 in complex with 4-methoxybenzoic acid (PDB ID: 4DO1), 2 Å resolution

In WT CYP199A4, the side chain hydroxyl of T253 is hydrogen bonded to the carbonyl of L250 (2.8 Å) and peptide N-H of V254 (3.0 Å). It is 3.9 Å from the carbonyl of G249.

The figure on the right was generated using the crystal structure of 4-pyridin-3-ylbenzoate-bound CYP199A4 (PDB ID: 6U30). The electron density of T252 and T253 is shown as grey mesh contoured at 4 σ to highlight the position of the oxygen atoms. (The map is a *2mFo-DFc* composite omit map.)

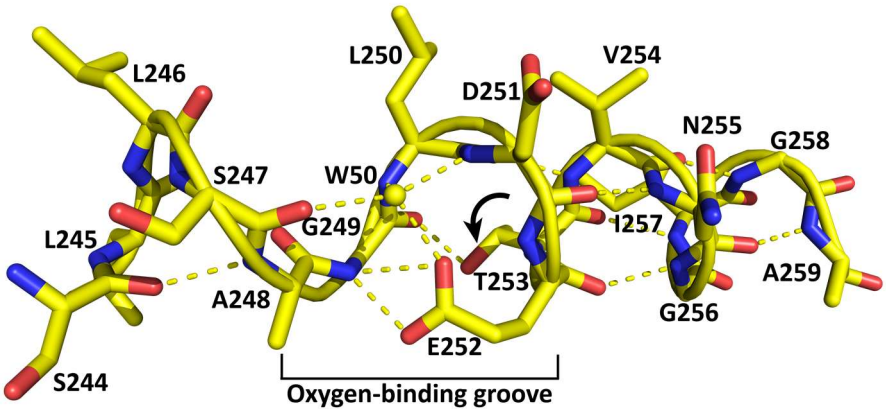

(b) T252E$_{CYP199A4}$ in complex with 4-methoxybenzoic acid, 1.55 Å resolution

Note the altered orientation of T253 (black arrow), which is now H-bonded to the G249 carbonyl (2.7 Å).

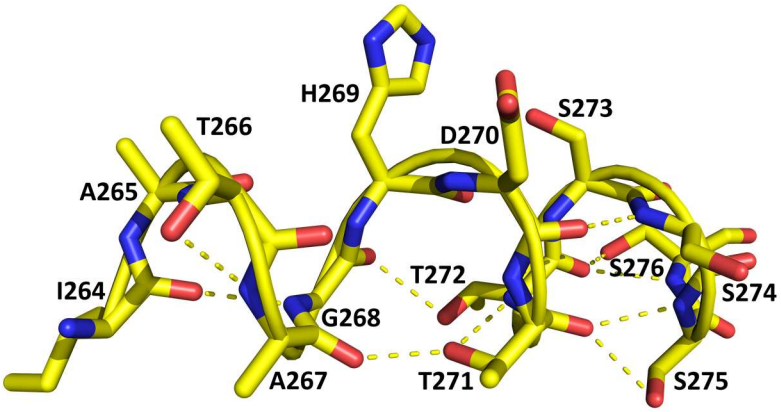

(c) substrate-free P450$_{terp}$ (PDB ID: 1CPT), 2.3 Å resolution

In P450$_{terp}$, the side chain of T272 is hydrogen bonded to the carbonyl of G268 (3.1 Å).

Figure C20. I-helix hydrogen-bonding network of WT CYP199A4, the T252E mutant and P450$_{terp}$. The orientation of T253 in the T252E mutant resembles the orientation of the equivalent threonine in P450$_{terp}$ (T272), P450$_{cin}$ (T243) and P450$_{BM3}$ (T269). Hydrogen bonds with donor-acceptor distances less than 3.2 Å are shown as dashed lines. Hydrogen bonds were identified using Coot.[322]

Overlay of substrate-bound T252E and WT CYP199A4 structures

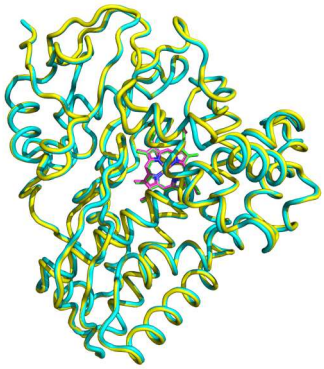

(a) 4-methylthiobenzoic acid
(RMSD = 0.400 Å)

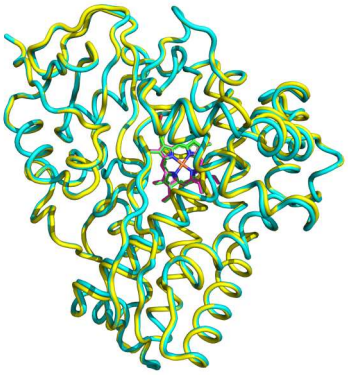

(b) 4-ethylthiobenzoic acid
(RMSD = 0.396 Å)

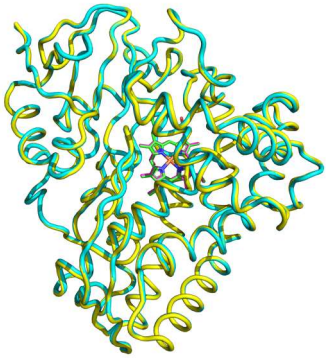

(c) 4-pyridin-2-ylbenzoic acid
(RMSD = 0.257 Å)

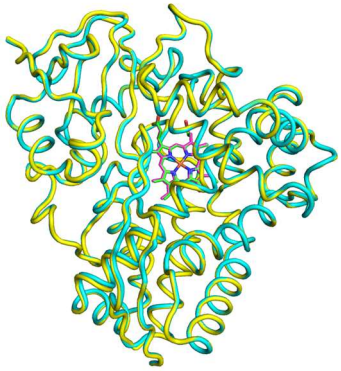

(d) 4-thiophen-3-ylbenzoic acid
(RMSD = 0.256 Å)

Figure C21. Overlaid structures of the T252E mutant (yellow cartoon, magenta heme) and WT CYP199A4 (blue cartoon, green heme) with various ligands bound. The RMSD between the Cα atoms is given below each figure (over all 393 pairs).

Dissociation constant analysis for T252E$_{CYP199A4}$ with bulky ligands

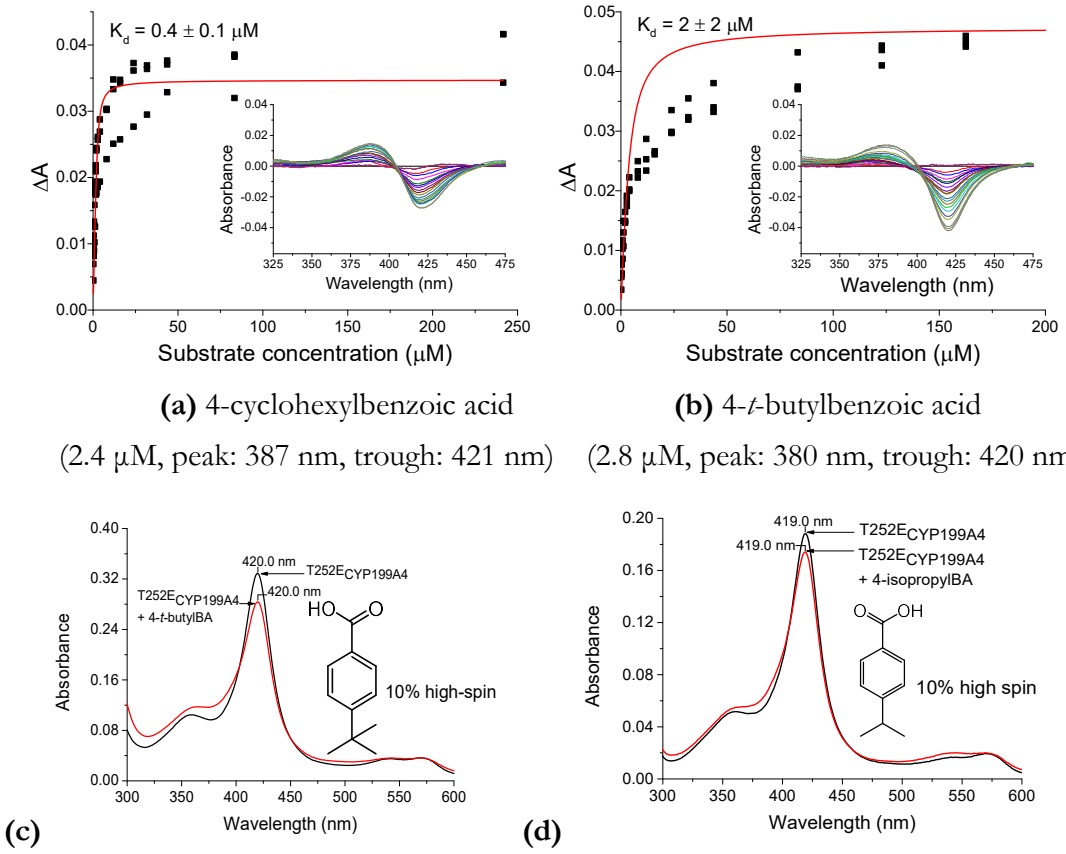

Figure C22. UV-Vis titrations to determine the dissociation constant of T252E$_{CYP199A4}$ with **(a)** 4-cyclohexyl- and **(b)** 4-*t*-butyl-benzoic acid and spin-state shifts induced by **(c)** 4-*t*-butylbenzoic acid and **(d)** 4-isopropylbenzoic acid. The enzyme concentration used and the peak and trough wavelengths are provided under each graph. Note that the fit of the Morrison equation to the 4-*t*-butylbenzoic acid data is poor.

Table C3. Binding affinities of 4-cyclohexyl- and 4-*t*-butyl-benzoic acid to the T252E variant of CYP199A4. Crude values for K_d were determined by performing UV-Vis titrations. More accurate values were obtained by Giang T. H. Nguyen at the University of New South Wales using a mass spectrometry method.[291] Literature K_d values for WT CYP199A4 are provided for comparison.

		T252E		WT
Substrate	**Method**	K_d (µM) UV-Vis titration[a]	K_d (µM) Mass spectrometry	K_d (µM) UV-Vis titration
4-cyclohexylBA		0.4 ± 0.1	1.5 ± 0.1	0.45 ± 0.05[277]
4-*t*-butylBA		2 ± 2	-	39 ± 2[277]

[a]UV-Vis titrations were performed in triplicate.

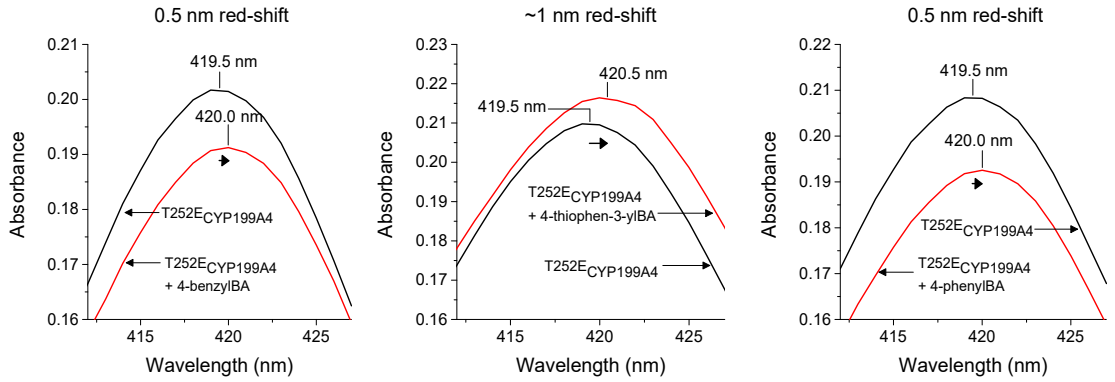

(a) 0.5 nm red-shift **(b)** 1 nm red-shift **(c)** 0.5 nm red-shift

Figure C23. Magnitude of the red-shift induced by binding of **(a)** 4-benzylbenzoic acid, **(b)** 4-thiophen-3-ylbenzoic acid and **(c)** 4-phenylbenzoic acid to T252E$_{CYP199A4}$.

B-factors of 4-benzylbenzoic acid

Table C4. *B*-factors of 4-benzylbenzoic acid in the T252E$_{CYP199A4}$ crystal structure. The benzyl substituent has higher *B*-factors than the benzoic acid moiety, indicating greater mobility.

Atom	*B*-factor (Å^2)
C_1	24
C_2	21
C_3	23
C_4	21
C_5	19
C_6	21
C_7	15
C_8	14
C_9	12
C_{10}	13
C_{11}	13
C_{12}	12
C_{13}	13
C_{14}	13
O_{15}	11
O_{16}	12

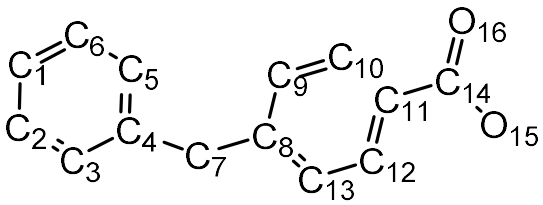

Crystals of 4-cyclohexyl- and 4-pyridin-3-yl-benzoic acid-bound T252E$_{CYP199A4}$

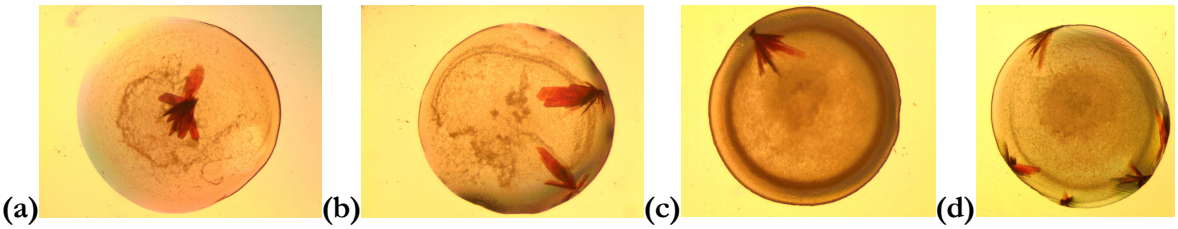

Figure C24. Crystals of T252E$_{CYP199A4}$ in complex with **(a, b)** 4-cyclohexylbenzoic acid and **(c, d)** 4-pyridin-3-ylbenzoic acid. Although crystals were obtained of these complexes, we were unable to solve the structures.

Crystal structure of 4-isopropylbenzoate-bound T252E$_{CYP199A4}$

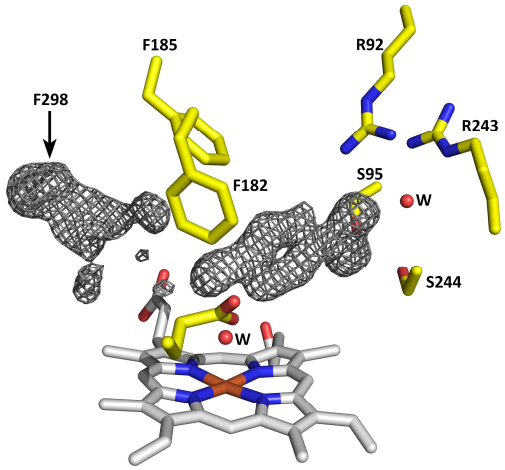

Figure C25. Crystal structure of 4-isopropylbenzoate-bound T252ECYP199A4. A polder omit map of the substrate and F298 is shown as grey mesh contoured at 4 σ (3 Å carve).

We attempted to solve the crystal structure of the T252E mutant in complex with 4-isopropylbenzoic acid. The aim was to identify whether this bulky ligand could displace the heme-bound H_2O/OH^- ligand. A 1.6-Å resolution data set was collected. The crystal structure revealed that the H_2O/OH^- ligand was not displaced. However, the two isopropyl methyl groups were not visible in the electron density map, and residue F298 appeared to be disordered (Figure C25). The structure therefore could not be solved. There may be mobility in the structure; the substrate and F298 side chain may have multiple orientations.

Identification of the position of the sulfur of 4-thiophen-3-ylbenzoic acid in the T252E$_{CYP199A4}$ crystal structure

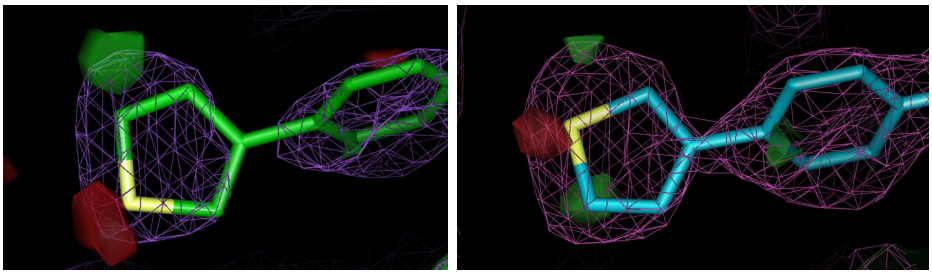

(a) sulfur 'down' **(b) sulfur 'up'**

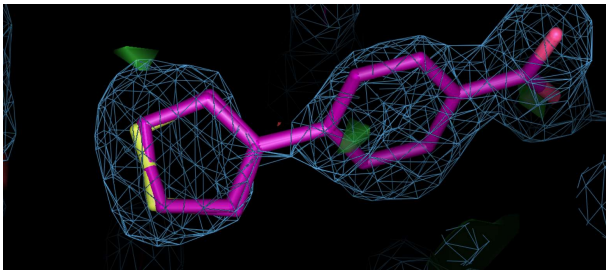

(c) two alternative conformations of substrate modelled

Figure C26. 4-Thiophen-3-ylbenzoic acid positioned with the sulfur pointing **(a)** 'down' towards the heme or **(b)** 'up' away from the heme. The *mFo-DFc* difference map (red and green blobs) is contoured at the ± 3 σ level. **(c)** The difference peaks in the *mFo-DFc* difference map could be removed by modelling both orientations of the substrate.

The thiophene ring of 4-thiophen-3-ylbenzoic acid could either be oriented with the sulfur pointing 'down' towards the heme or 'up' away from the heme (Figure C26a,b). The substrate was initially positioned with the sulfur 'down'. However, negative density (red blobs) in the vicinity of the sulfur in the *mFo-DFc* difference map indicated that the electron density at this position was too high. Positive density (green blobs) opposite the sulfur implied that the electron density at this position was too low. This suggested that the sulfur was inappropriately placed.

When the ring was flipped, placing the sulfur on the opposite side, again negative and positive peaks in the difference map indicated that the sulfur was incorrectly positioned.

The difference peaks in the *mFo-DFc* difference map could be removed by modelling the substrate in both orientations. It appears that the substrate can bind with the sulfur in either position. The occupancies of these alternative conformations were refined to 36% ('down') and 45% ('up') (Table C5).

Table C5. Refined occupancies of the alternative conformations of 4-thiophen-3-ylbenzoic acid

Conformation	Occupancy
Sulfur 'down'	36%
Sulfur 'up'	45%

Table C6. Distances and angles between notable features of the 4-thiophen-3-ylbenzoate-bound T252E$_{CYP199A4}$ crystal structure. Distances are given for the ligand orientation in which the sulfur is pointing 'up' away from the heme.

Distance	**4-thiophen-3-yl-T252E**
Fe - C_{11}	4.3
Fe - C_{10}	5.0
OH_2/OH^- ligand - C_{11}	3.3
OH_2/OH^- ligand - C_{10}	4.1
Angle (°)	
dihedral angle C_{11}-C_7-C_6-C_5	59.1

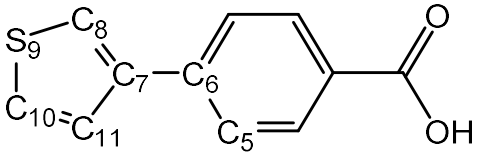

S-Fe-O angle in T252E$_{CYP199A4}$ crystal structures

In the crystal structures of T252E$_{CYP199A4}$ in complex with 4-methoxy-, 4-methylthio-, 4-ethylthio- and 4-pyridin-2-yl-benzoic acid, the S-Fe-O angle is approximately linear. We noticed that when bulky hydrophobic substrates are bound (e.g. 4-benzylbenzoic acid and 4-thiophen-3-ylbenzoic acid), the S-Fe-O angle is bent because the aqua/hydroxo ligand is shifted away from the sterically bulky substrate.

In the 4-thiophen-3-ylbenzoic acid structure, the Fe-O bond is at a 20.7° angle to the Fe-S bond. In the 4-benzylbenzoic acid structure, the Fe-O bond is at a 15.9° angle to the Fe-S bond.

Table C7. S-Fe-O angle in substrate-bound T252E$_{CYP199A4}$ crystal structures

T252E$_{CYP199A4}$ crystal structure	**S-Fe-O angle (°)**
4-methoxyBA	172.7
4-ethylthioBA	174.3
4-methylthioBA	172.8
4-pyridin-2-ylBA	173.3
4-thiophen-3-ylBA	159.3
4-benzylBA	164.1

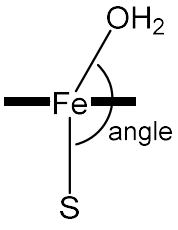

Spin-state shifts of T252E$_{CYP199A4}$ induced by type II ligands

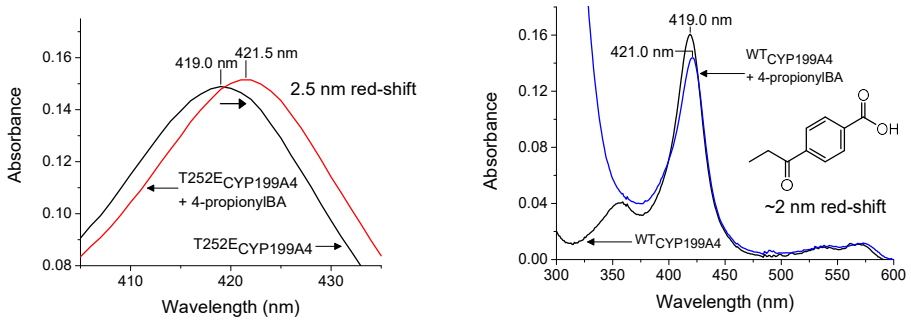

(a) T252E + 4-propionylbenzoic acid **(b)** WT + 4-propionylbenzoic acid

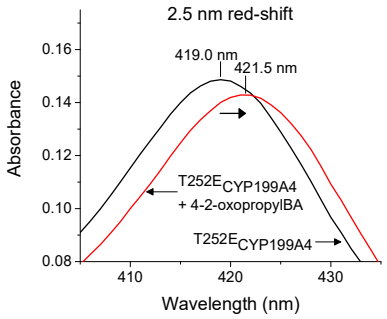

(c) T252E + 4-oxopropylbenzoic acid

Figure C27. Spin-state shifts of T252E$_{CYP199A4}$ induced by the ligands 4-propionylbenzoic acid and 4-oxopropylbenzoic acid (**red**). Spin-state shifts of WT CYP199A4 (**blue**) are shown for comparison.

Table C8. Spin-state shifts of T252E$_{CYP199A4}$ and WT CYP199A4 induced by type II ligands

Substrate	Spin-state shift (% HS)	
	T252E	WT
4-PropionylBA	~2.5 nm red-shift	~2 nm red-shift [277]
4-2-OxopropylBA	~2.5 nm red-shift	50% [277]
4-Pyridin-2-ylBA	~3 nm red-shift	3 nm red-shift[277]
4-Pyridin-3-ylBA	~3.5 nm red-shift	5 nm red-shift[277]

Dissociation constant analysis for T252E$_{CYP199A4}$ with type II ligands

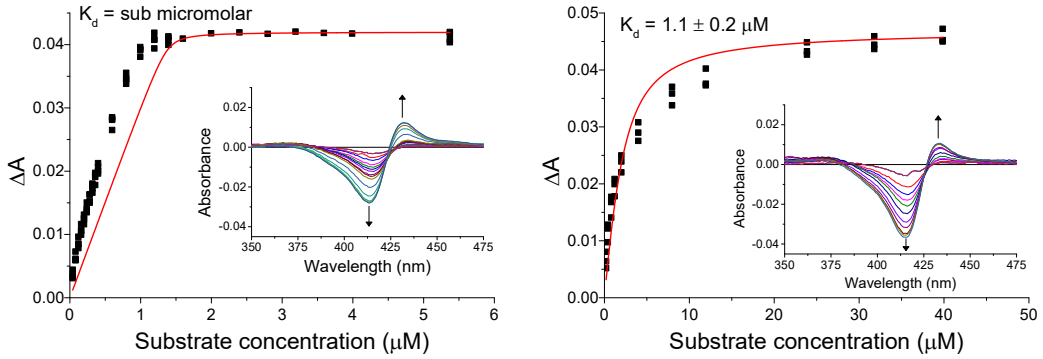

(a) 4-pyridin-2-ylbenzoic acid (1.5 μM)

(b) 4-pyridin-3-ylbenzoic acid (1.8 μM)

Figure C28. UV-Vis titrations to determine the dissociation constant of T252E$_{CYP199A4}$ with **(a)** 4-pyridin-2-yl- and **(b)** 4-pyridin-3-yl-benzoic acid. The enzyme concentration used is provided under each graph.

Table C9. Binding affinities of 4-pyridin-2-yl- and 4-pyridin-3-yl-benzoic acid to the T252E variant of CYP199A4. Crude values for K_d were determined by performing UV-Vis titrations. More accurate values were obtained by Giang T. H. Nguyen at the University of New South Wales using a mass spectrometry method.[291] Literature K_d values for WT CYP199A4 are provided for comparison.

		T252E		WT
Substrate	**Method**	K_d (μM) UV-Vis titration[a]	K_d (μM) Mass spectrometry	K_d (μM) UV-Vis titration
4-pyridin-2-ylBA		Sub micromolar	0.10 ± 0.01	1.0 ± 0.1 [277]
4-pyridin-3-ylBA		1.1 ± 0.2	7.9 ± 0.1	2.3 ± 0.1 [277]

[a]UV-Vis titrations were performed in triplicate.

Determination of the orientation of the pyridine ring in the 4-pyridin-2-ylbenzoate-T252E$_{CYP199A4}$ crystal structure

At resolutions >1.5 Å, carbon and nitrogen can be difficult to distinguish from the electron density map.[468] However, we expect that the pyridine ring must be oriented with the N pointing 'down' towards the heme based on the knowledge that this compound induces a type II spin-state shift, which implies that the N is hydrogen-bonded to the aqua ligand (or coordinated directly to the heme iron). If the pyridine ring were oriented with the N pointing away from the heme, it would instead result in a steric clash between the ring and the aqua ligand (represented by pink spikes in Figure C29b).

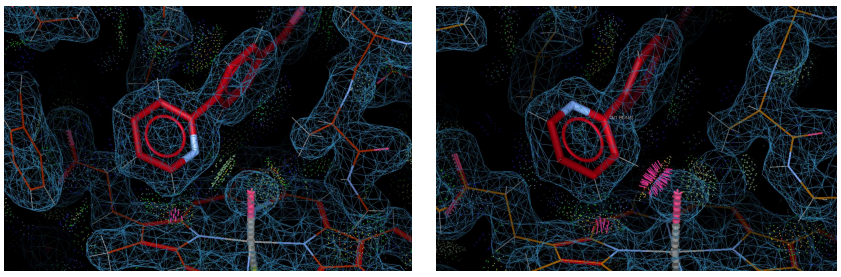

(a) nitrogen 'down' (H-bond between N and aqua ligand)

(b) nitrogen 'up' (steric clash between ring and aqua ligand)

Figure C29. Two possible orientations of the pyridine ring of 4-pyridin-2-ylbenzoic acid in the active site of T252E$_{CYP199A4}$. The ring must be oriented with the nitrogen pointing 'down' towards the heme because this results in a favourable hydrogen bond between the N and aqua ligand. If the ring were oriented with the N pointing away from the heme, it would result in a steric clash between the ring and the aqua ligand (represented by hot-pink spikes).

UV-Vis spectra of T252E$_{CYP199A4}$ in complex with 4-1*H*-imidazol-1-ylbenzoic acid

4-1*H*-Imidazol-1-ylbenzoic acid is another compound that is known to directly coordinate to the heme iron when it binds to WT CYP199A4 (Chapter 4). When added to the T252E mutant, it induced a ~1.5 nm red-shift of the Soret band, which is smaller than the 5 nm red-shift it induces when it binds to WT CYP199A4 (Figure C30a,b). Note that the spectrum of WT CYP199A4 in complex with 4-1*H*-imidazol-1-ylbenzoic acid resembles the spectra of P450$_{cam}$ in complex with 'normal' nitrogen donor ligands reported by Dawson (the α-band intensity is greatly diminished and the δ-band intensity is increased).[363, 365] In contrast, the spectrum of 4-1*H*-imidazol-1-ylbenzoic acid-bound T252E$_{CYP199A4}$ is an 'abnormal' spectrum (the α-band remains more intense than the β-band). The difference spectra of WT$_{CYP199A4}$ and T252E$_{CYP199A4}$ with 4-1*H*-imidazol-1-ylbenzoic acid also differ substantially (Figure C30c,d). This again appears to indicate that the aqua ligand in the T252E mutant is not displaced.

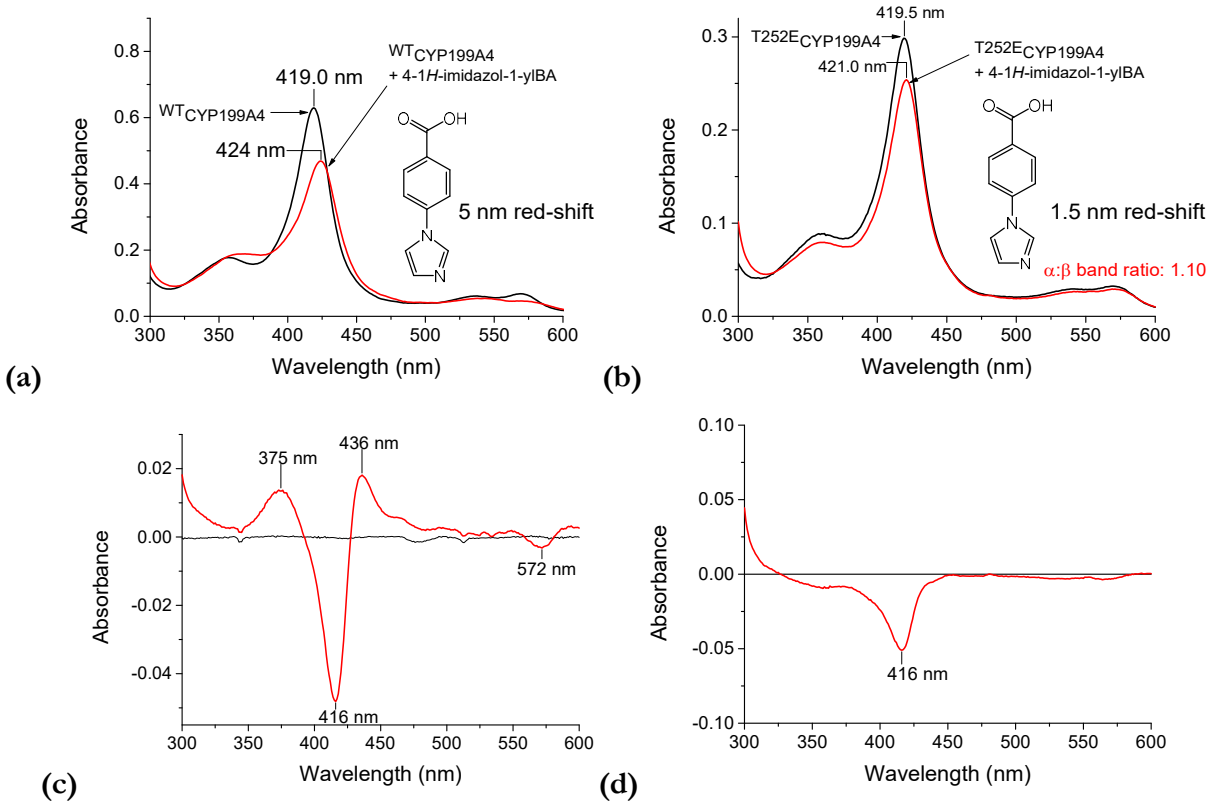

Figure C30. Spin-state shifts of **(a)** WT CYP199A4 and **(b)** the T252E mutant with 4-1*H*-imidazol-1-ylbenzoic acid. Difference spectra of **(c)** WT CYP199A4 and **(d)** T252E$_{CYP199A4}$ with 4-1*H*-imidazol-1-ylbenzoic acid are also given.

Attempts to reduced T252E$_{CYP199A4}$ in complex with type II inhibitors with dithionite

To further investigate whether the distal oxygen ligand in the T252E mutant is displaced by type II ligands, we sought to obtain spectra of the reduced enzyme in complex with 4-pyridin-3-yl-, 4-pyridin-2-yl- and 4-1*H*-imidazol-1-yl-benzoic acid (Figure C31). As discussed in Chapter 4, ferrous P450s with directly bound σ-donor nitrogen ligands display red-shifted Soret peaks at 440-450 nm.[358, 365-366]

Recall that reduced WT CYP199A4 in complex with 4-pyridin-3-ylbenzoic acid exhibits a Soret band at 447 nm. On the other hand, addition of dithionite to the 4-pyridin-3-ylbenzoate-T252E$_{CYP199A4}$ complex did not red-shift the Soret peak (Figure C31a). This is evidence that 4-pyridin-3-ylbenzoic acid is not displacing the aqua ligand in the T252E mutant. The small shoulder which appeared at ~447 nm indicates that only in a minor proportion of enzyme molecules is the nitrogen ligand directly coordinated to the iron. As expected, when dithionite was added to the T252E-4-pyridin-2-ylbenzoic acid complex, the Soret band was again not red-shifted (Figure C31b). This agrees with the crystal structure, which showed that the nitrogen ligand fails to replace the water ligand. We also found that addition of dithionite to the 4-1*H*-imidazol-1-ylbenzoic acid-T252E complex failed to red-shift the Soret band to 440-450 nm (Figure C31c).

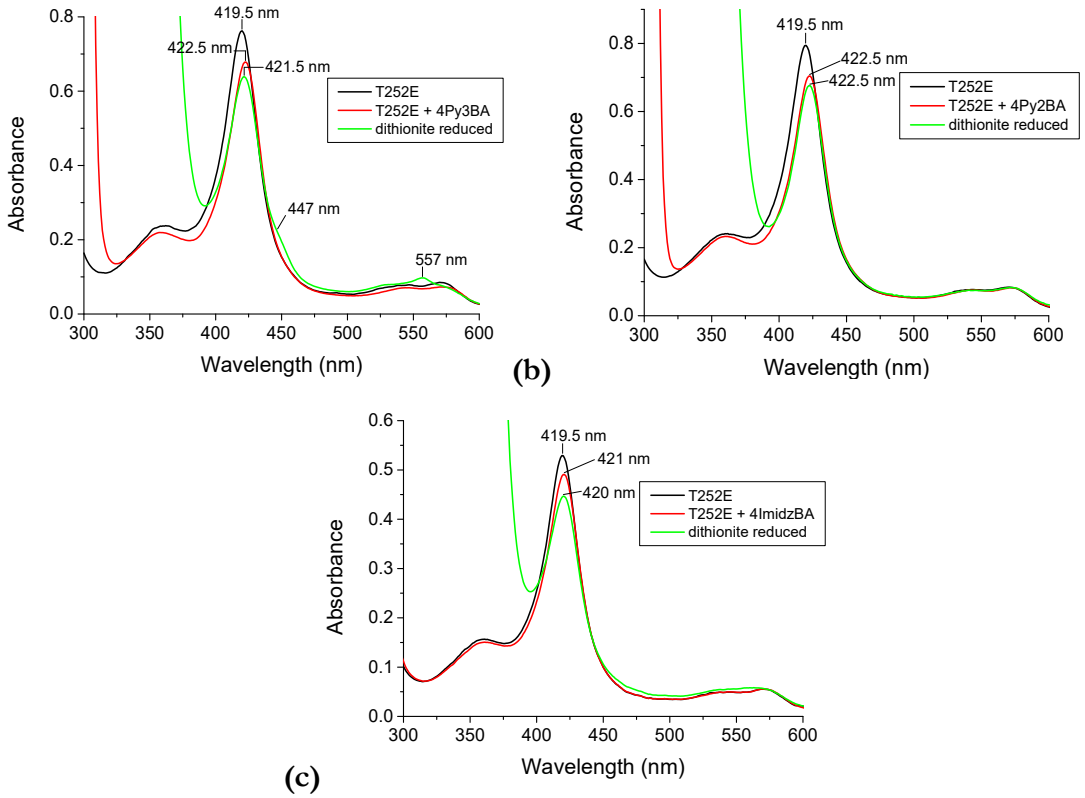

Figure C31. UV-Vis spectra of dithionite-reduced T252E$_{CYP199A4}$ in complex with type II ligands: **(a)** 4-pyridin-3-yl-, **(b)** 4-pyridin-2-yl- and **(c)** 4-1*H*-imidazol-1-yl-benzoic acid. In **black** and **red** are substrate-free and substrate-bound ferric T252E$_{CYP199A4}$. In **green** is the spectrum after addition of dithionite.

For comparison, we added dithionite to the T252E mutant in complex with type I ligands (4-phenylbenzoic acid and 4-methoxybenzoic acid) and recorded UV-Vis spectra (Figure C32). Recall that when we reduced WT CYP199A4 in complex with these type I ligands, the Soret band was blue-shifted to ~414 nm. However, the Soret band of the T252E mutant was not substantially shifted when we added dithionite, which may indicate that the T252E enzyme was not completely reduced under the experimental conditions.

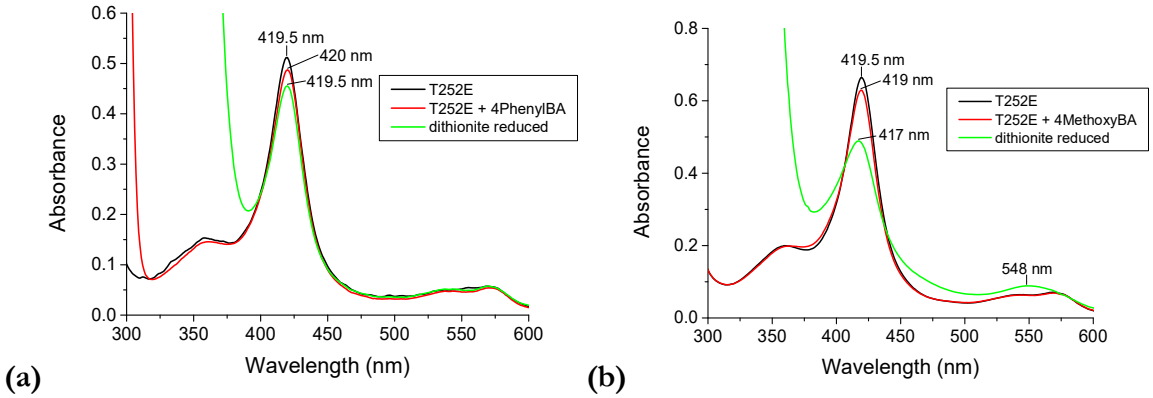

Figure C32. UV-Vis spectra of the T252E enzyme in complex with type I substrates: **(a)** 4-phenyl- and **(b)** 4-methoxy-benzoic acid. In **black** is the substrate-free ferric enzyme, and substrate-bound ferric T252E$_{CYP199A4}$ is in **red**. In **green** is the spectrum after addition of dithionite.

In case the T252E mutant was not being successfully reduced, we attempted to more fully reduce the T252E mutant by incubating it with dithionite on ice for 10-30 minutes before addition of substrate (4-methoxybenzoic acid or 4-pyridin-3-ylbenzoic acid). The resulting spectra were essentially identical to those previously recorded (Figure C33). Thus, the T252E variant appears to be difficult to reduced with dithionite.

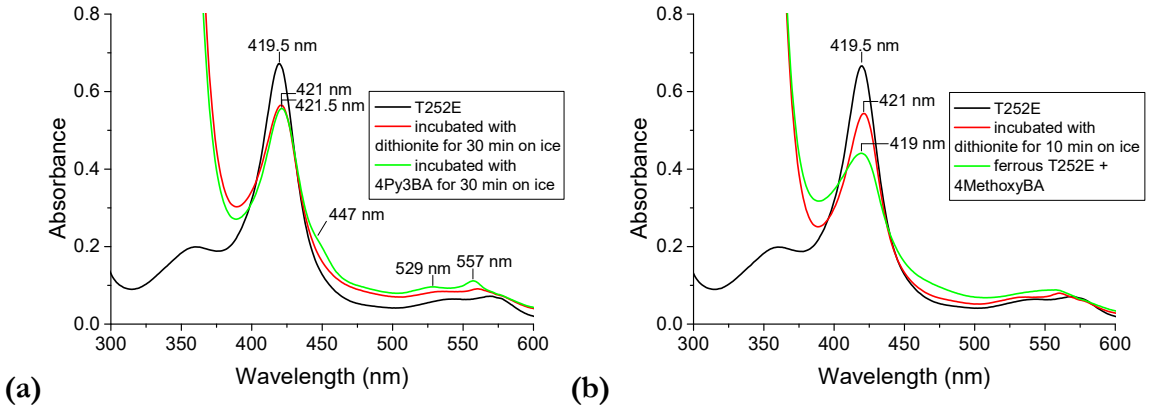

Figure C33. UV-Vis spectra of the T252E mutant incubated with dithionite on ice for 10-30 minutes (**red**) before complexation with **(a)** 4-pyridin-3-ylbenzoic acid or **(b)** 4-methoxybenzoic acid (**green**).

CW EPR spectra of P450st at pH 7 and pH 10 and formate-bound $P450_{cam}$ reported by Dawson *et al.*[164] and Hayakawa *et al.*[418]

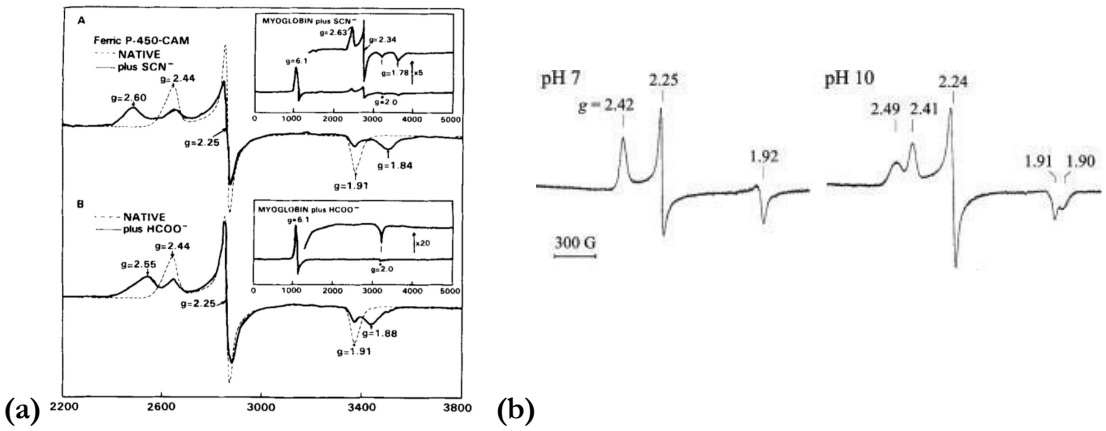

Figure C34. **(a)** EPR spectrum of $P450_{cam}$ with formate ($HCOO^-$) bound reported by Sono and Dawson[164], and **(b)** the EPR spectra of P450st at pH 7 and pH 10 reported by Hayakawa *et al.*[418] Figure **(a)** was originally published in the Journal of Biological Chemistry. Sono, M.; Dawson, J. H. Formation of low spin complexes of ferric cytochrome P-450-CAM with anionic ligands. Spin state and ligand affinity comparison to myoglobin. *J. Biol. Chem.* **1982**, *257* (10), 5496-5502. © the American Society for Biochemistry and Molecular Biology. Figure **(b)** is reproduced with permission from Wiley and the approval of the corresponding author, Prof. Nobuhumi Nakamura. © 2012 Federation of European Biochemical Societies.

Iron displacement out of the porphyrin plane in crystal structures of substrate-bound T252E$_{CYP199A4}$

Table C10. Displacement of the heme iron below the porphyrin plane in crystal structures of substrate-bound T252E CYP199A4

Ligand bound to T252E CYP199A4		Iron displacement below porphyrin plane	
		Plane defined by the four pyrrole nitrogens	Plane defined by the 24 atoms of the porphyrin macrocycle
4-MethoxyBA	Hexacoordinated, low-spin iron	0.156 Å	0.118 Å
4-MethylthioBA		0.161 Å	0.130 Å
4-EthylthioBA		0.077 Å	0.055 Å
4-Pyridin-2-ylBA		0.064 Å	0.053 Å
4-BenzylBA		0.150 Å	0.113 Å
4-Thiophen-3-ylBA		0.113 Å	0.077 Å

Table C11. Displacement of the heme iron below the porphyrin plane in crystal structures of substrate-bound WT CYP199A4 for comparison

Ligand bound to wild-type CYP199A4		Iron displacement below porphyrin plane	
		Plane defined by the four pyrrole nitrogens	Plane defined by the 24 atoms of the porphyrin macrocycle
4-MethoxyBA (4DO1)	Pentacoordinated, high-spin iron	0.204 Å	0.234 Å
4-MethylthioBA (5KT1)		0.223 Å	0.230 Å
4-Thiophen-3-ylBA (6C3J)		0.262 Å	0.221 Å
4-Pyridin-2-ylBA	Hexacoordinated, low-spin iron	0.131 Å	0.096 Å

Table C12. Iron-sulfur bond distances in T252E CYP199A4 crystal structures

Ligand bound to T252E CYP199A4		Iron-sulfur bond length (Å)
4-MethoxyBA	Hexacoordinated, low-spin iron	2.27
4-MethylthioBA		2.31
4-EthylthioBA		2.27
4-Pyridin-2-ylBA		2.28
4-BenzylBA		2.25
4-Thiophen-3-ylBA		2.27

Table C13. Iron-sulfur bond distances in WT CYP199A4 crystal structures for comparison

Ligand bound to wild-type CYP199A4		Iron-sulfur bond length (Å)
4-MethoxyBA (4DO1)	Pentacoordinated, high-spin iron	2.40
4-Thiophen-3-ylBA (6C3J)		2.42
4-MethylthioBA (5KT1)		2.48
4-Pyridin-2-ylBA	Hexacoordinated, low-spin iron	2.29
4-Pyridin-3-ylBA		2.30

Table C14. Fe-N(porphyrin) bond distances (in Å) in T252E CYP199A4 crystal structures

T252E CYP199A4 crystal structure	Fe-N_A	Fe-N_B	Fe-N_C	Fe-N_D
4-MethoxyBA	2.05	1.99	2.01	2.03
4-MethylthioBA	2.08	2.05	2.02	2.05
4-EthylthioBA	2.05	2.04	2.03	2.05
4-Pyridin-2-ylBA	2.02	2.01	2.07	2.04
4-BenzylBA	2.05	2.07	2.00	2.03
4-Thiophen-3-ylBA	2.03	2.05	2.05	2.06

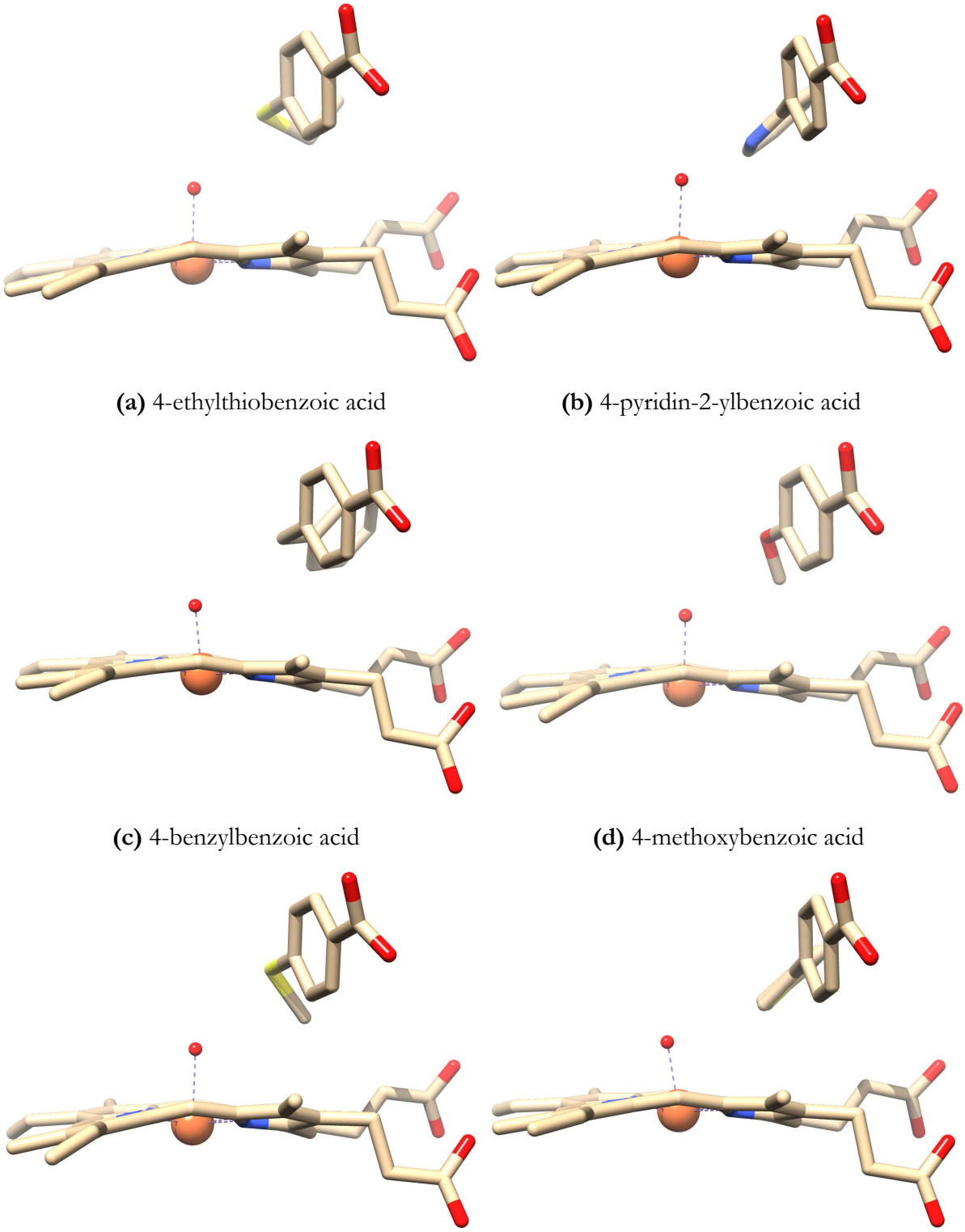

(a) 4-ethylthiobenzoic acid

(b) 4-pyridin-2-ylbenzoic acid

(c) 4-benzylbenzoic acid

(d) 4-methoxybenzoic acid

(e) 4-methylthiobenzoic acid

(f) 4-thiophen-3-ylbenzoic acid

Figure C35. Position of the heme iron in substrate-bound T252E crystal structures. In the substrate-bound T252E$_{CYP199A4}$ crystal structures, in which the iron is six-coordinate and low-spin, the iron is less displaced out of the porphyrin plane than in crystal structures of substrate-bound WT CYP199A4 (where the iron is five-coordinate and high-spin). Note that the S-Fe-O angle is bent when bulky hydrophobic substrates such as 4-benzylbenzoic acid and 4-thiophen-3-ylbenzoic acid are bound.

Appendix D: Supplementary Information for Chapter 6

In vitro NADH turnover data

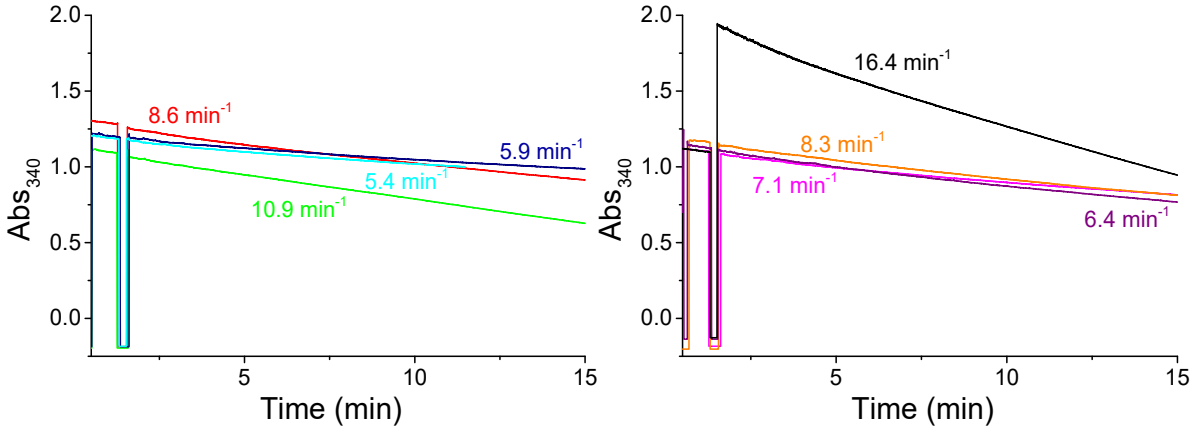

Figure D1. Rates of NADH consumption by the T252E$_{CYP199A4}$ mutant with *para*-substituted benzoic acid substrates: 4-methoxybenzoic acid (**red**), veratric acid (**green**), 4-formylbenzoic acid (**dark blue**), 4-vinylbenzoic acid (**cyan**), 4-methylthiobenzoic acid (**magenta**), 4-ethylbenzoic acid (**orange**), 4-ethylthiobenzoic acid (**purple**), and 4-ethynylbenzoic acid (**black**). 4-Ethynylbenzoic acid absorbs at 340 nm and therefore the absorbance increased when this substrate was added.

HPLC retention times

Table D1. HPLC retention times for *para*-substituted benzoic acid substrates and products. Gradient: 20 → 95% acetonitrile in H_2O with 0.1% TFA over 20 minutes.

Compound	Retention time (min)
4-Methoxybenzoic acid	11.4
4-Hydroxybenzoic acid	5.8
4-Vinylbenzoic acid	14.1
4-Oxiran-2-ylbenzoic acid	10.4
4-Methylthiobenzoic acid	13.6
4-Methylsulfinylbenzoic acid	4.7
4-Mercaptobenzoic acid	12.5
4-Methylsulfonylbenzoic acid (sulfone)	6.9
4-Ethylthiobenzoic acid	15.5
4-Ethylsulfinylbenzoic acid	5.7
4-Ethylbenzoic acid	14.9
4-(1-Hydroxyethyl)benzoic acid	6.6
4-(2-Hydroxyethyl)benzoic acid	6.2
4-Acetylbenzoic acid	9.9
4-Ethynylbenzoic acid	13.2
4-Carboxyphenylacetic acid	6.8
4-Formylbenzoic acid	9.1
Terephthalic acid	6.2
Veratric acid	9.4
Vanillic acid	6.1
Isovanillic acid	6.4
3,4-Dihydroxybenzoic acid	4.5
9-Hydroxyfluorene (internal standard)	15.7

Co-elution of reaction products with authentic compounds to confirm their identity

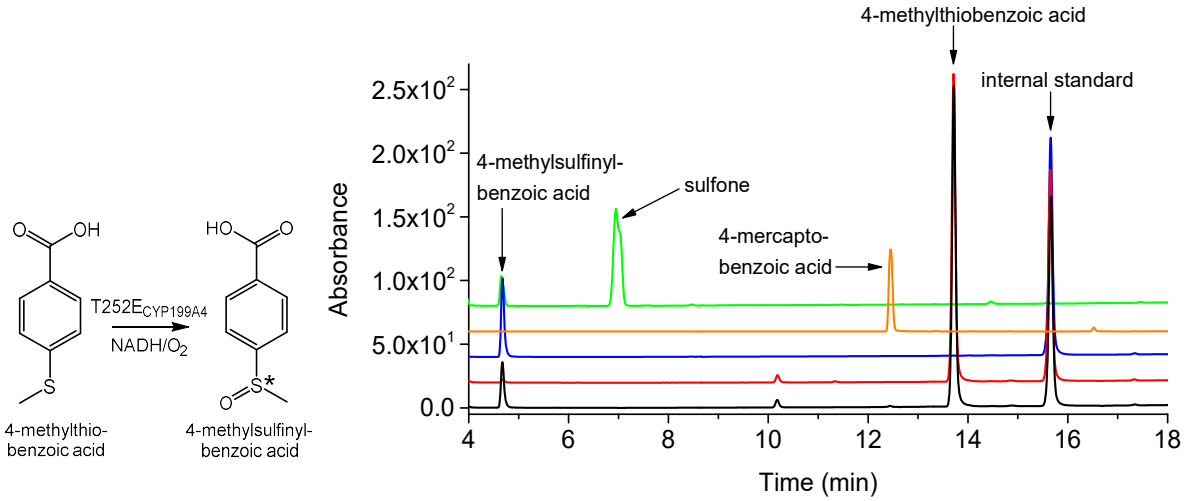

Figure D2. HPLC analysis of the NADH/O_2-driven oxidation of 4-methylthiobenzoic acid by T252E$_{CYP199A4}$ (**black**), which exclusively generated 4-methylsulfinylbenzoic acid. In **red** is a control reaction omitting the P450, and in **blue** is authentic 4-methylsulfinylbenzoic acid (RT = 4.7 min). In **orange** is authentic 4-mercaptobenzoic acid (RT = 12.5 min) and in **green** is authentic 4-methylsulfonylbenzoic acid (RT = 6.9 min); the dealkylation product and sulfone were not formed by the T252E enzyme. No 4-sulfobenzoic acid was detected. The substrate appears at 13.6 min. Gradient: 20-95% AcCN in H_2O with 0.1% TFA. Detection wavelength: 254 nm.

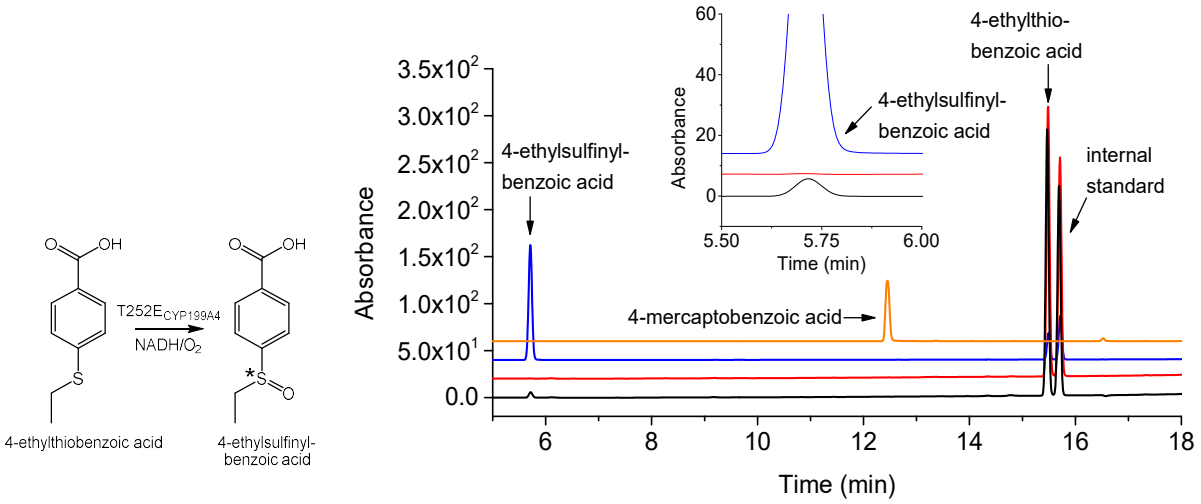

Figure D3. HPLC analysis of the NADH/O_2-driven oxidation of 4-ethylthiobenzoic acid by T252E$_{CYP199A4}$ (**black**). In **red** is a control reaction omitting the P450, and in **blue** is chemically synthesised 4-ethylsulfinylbenzoic acid (RT =5.7 min). The substrate appears at 15.5 min. Gradient: 20-95% AcCN in H_2O with 0.1% TFA. Detection wavelength: 254 nm.

Difference spectra induced by binding of sulfur ligands to $P450_{cam}$ and CYP199A4

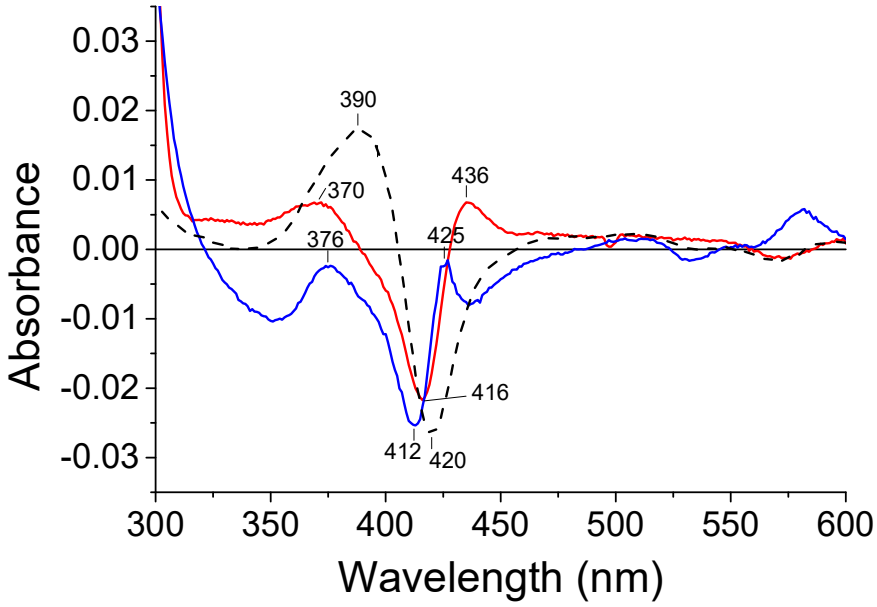

Figure D4. Difference spectra of $P450_{cam}$ with thioanisole (**red**) and $D251N_{CYP199A4}$ with 4-ethylthiobenzoic acid (**blue**). The type I difference spectrum of $T252A_{CYP199A4}$ with 4-ethylthiobenzoic acid is also shown as a **black dashed line** for comparison.

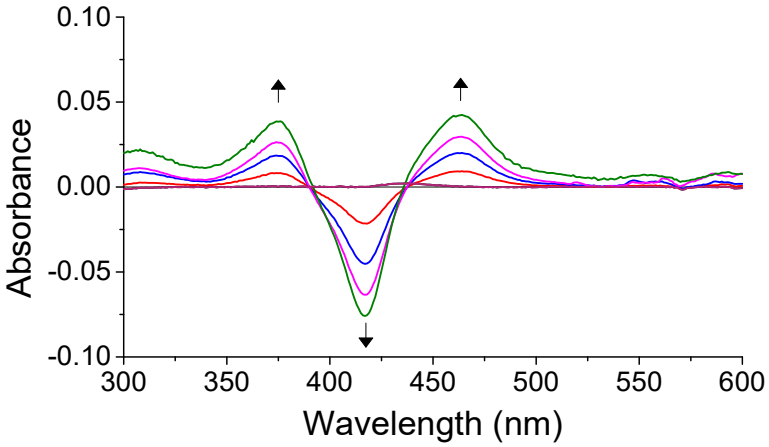

Figure D5. Difference spectra of $P450_{cam}$ with dithiothreitol (DTT).

Table D2. Features of the difference spectra of $P450_{cam}$ with thioanisole and DTT and $D251N_{CYP199A4}$ with 4-ethylthiobenzoic acid

Enzyme / Sulfide	Absorbance maxima (nm)	Absorbance minimum (nm)
$P450_{cam}$ + thioanisole	370, 436	416
$D251N_{CYP199A4}$ + 4-ethylthiobenzoic acid	376, 425	412
$P450_{cam}$ + DTT	375, 464	417

NADH-supported sulfoxidation of 4-ethylthiobenzoic acid by the T252E, D251N, T252A and WT isoforms

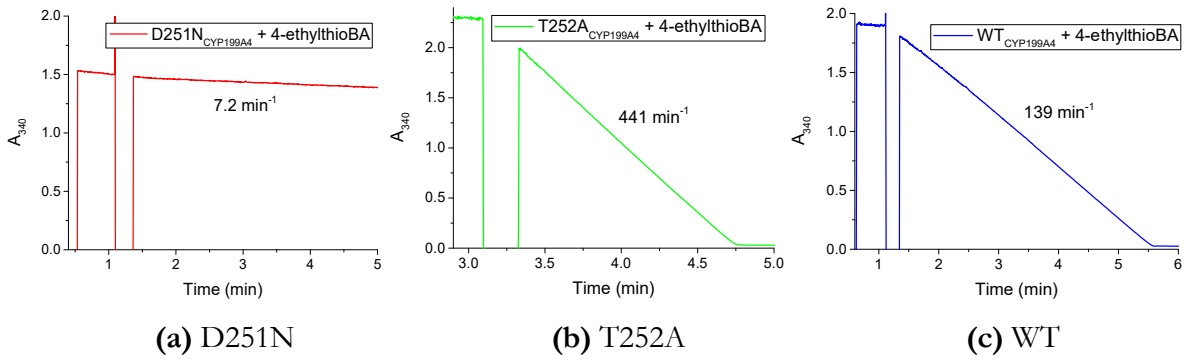

(a) D251N **(b)** T252A **(c)** WT

Figure D6. Comparison of the rates of NADH consumption by **(a)** $D251N_{CYP199A4}$, **(b)** $T252A_{CYP199A4}$ and **(c)** $WT_{CYP199A4}$ with 4-ethylthiobenzoic acid.

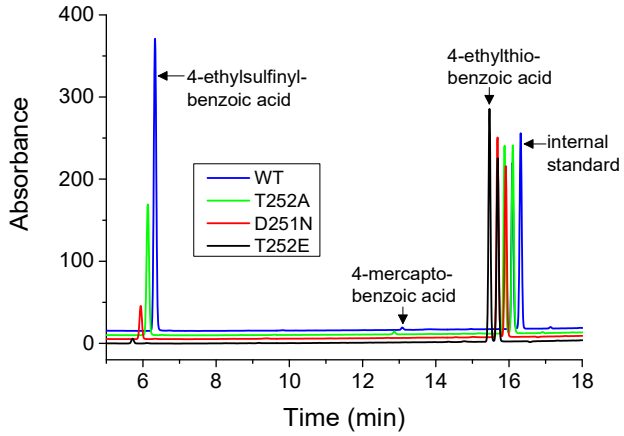

Figure D7. HPLC analysis of the *in vitro* NADH reaction of CYP199A4 variants with 4-ethylthiobenzoic acid. The T252E, D251N, T252A and WT CYP199A4 reactions are shown in **black**, **red**, **green** and **blue**, respectively. Retention times are: 4-ethylsulfinylbenzoic acid, 5.8 min; 4-ethylthiobenzoic acid, 15.5 min; 9-hydroxyfluorene, 15.7 min. Gradient: 20 → 95% AcCN in H_2O (with 0.1% TFA). It has been reported that 4-mercaptobenzoic acid represents ~1% of the product in the WT turnover.[117]

No 4-mercaptobenzoic acid was detected in the T252E or D251N turnovers. In the T252A and WT turnovers, minimal 4-mercaptobenzoic acid was formed. In the T252A turnover, the 4-mercaptobenzoic acid peak was ~2% of the size of the sulfoxide peak. In the WT turnover, it was <1% of the size of the sulfoxide peak.

Co-elution of reaction products with authentic compounds

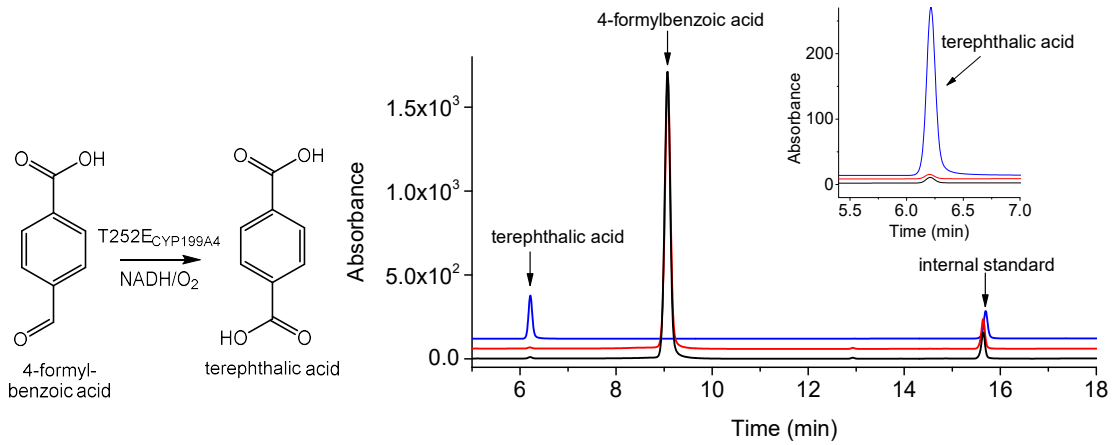

Figure D8. HPLC analysis of the NADH/O_2-driven oxidation of 4-formylbenzoic acid by T252E$_{CYP199A4}$ (**black**). In **red** is a control reaction omitting the P450, and in **blue** is authentic terephthalic acid (RT = 6.2 min). The substrate appears at 9.1 min. Gradient: 20-95% AcCN in H_2O with 0.1% TFA. Detection wavelength: 254 nm.

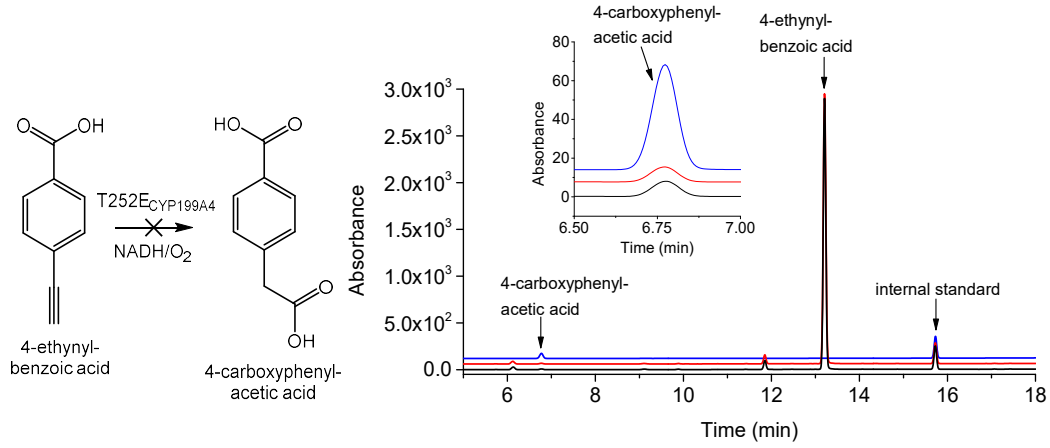

Figure D9. HPLC analysis of the NADH/O_2-driven oxidation of 4-ethynylbenzoic acid by T252E$_{CYP199A4}$ (**black**). In **red** is a control reaction omitting the P450, and in **blue** is authentic 4-carboxyphenylacetic acid (RT = 6.8 min). The substrate appears at 13.2 min. Gradient: 20-95% AcCN in H_2O with 0.1% TFA. Detection wavelength: 254 nm.

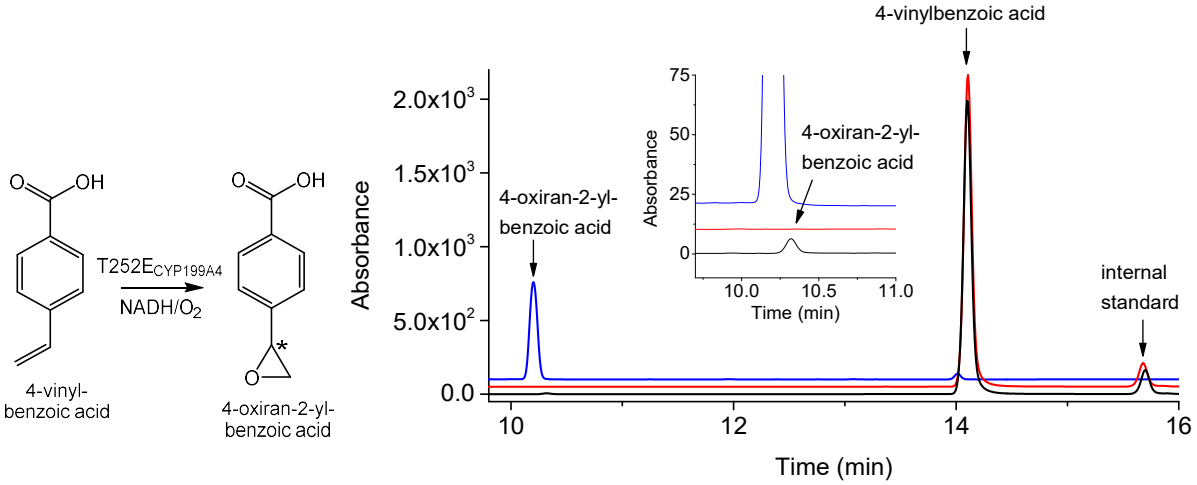

Figure D10. HPLC analysis of the NADH/O_2-driven oxidation of 4-vinylbenzoic acid by T252E$_{CYP199A4}$ (**black**). In **red** is a control reaction omitting the P450, and in **blue** is chemically synthesised 4-oxiran-2-ylbenzoic acid (RT =10.4 min). The substrate appears at 14.1 min. Gradient: 20-95% AcCN in H_2O with 0.1% TFA. Detection wavelength: 254 nm.

WT CYP199A4 converts 4-vinylbenzoic acid into 4-oxiran-2-ylbenzoic acid and the aldehyde rearrangement product (4-(2-oxoethyl)benzoic acid)

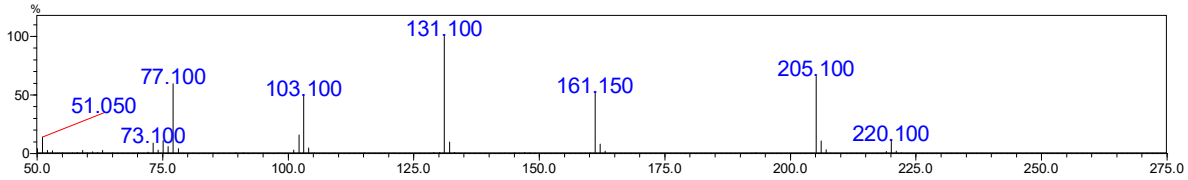

4-Vinylbenzoic acid substrate (singly derivatized), m/z = 220.10 (exp. m/z = 220.0920), RT = 8.3 min

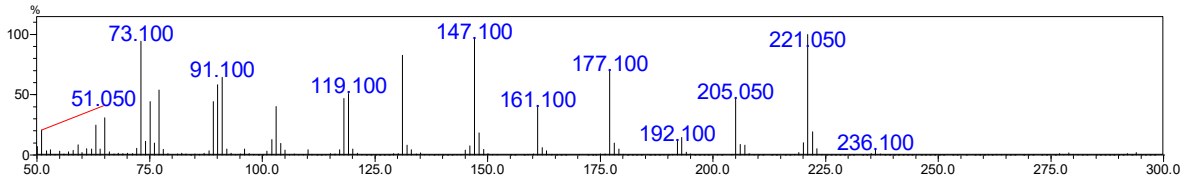

4-Oxiran-2-ylbenzoic acid (singly derivatized), m/z = 236.10 (exp. m/z = 236.0869), RT = 11.2 min

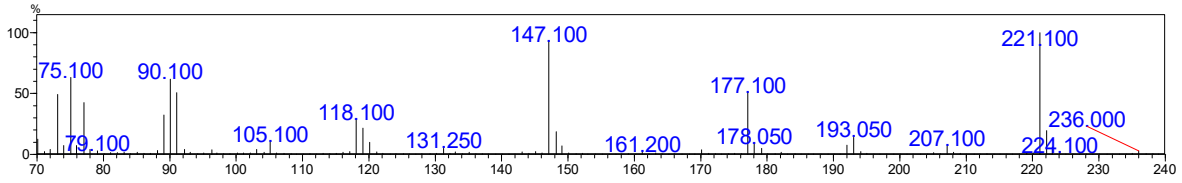

Aldehyde rearrangement product, 4-(2-oxoethyl)benzoic acid (singly derivatized), m/z = 236.00 (exp. m/z = 236.0869), RT = 10.8 min

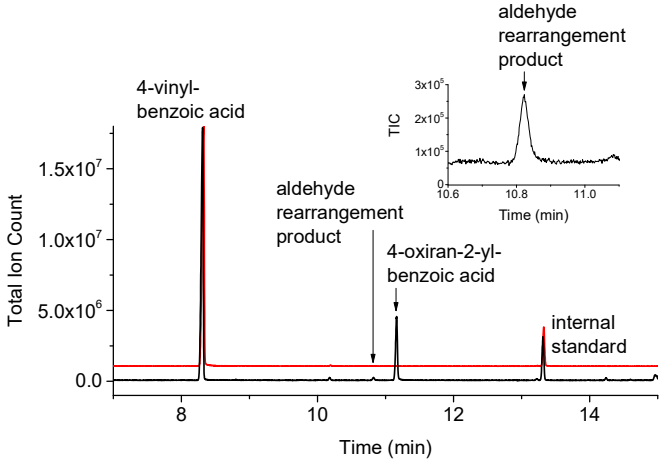

Figure D11. GC-MS analysis of the NADH/O_2-driven oxidation of 4-vinylbenzoic acid by WT CYP199A4. In **black** is the *in vitro* turnover and in **red** is the 4-vinylbenzoic acid substrate control. The substrate appears at 8.3 min, the epoxide product at 11.2 min, and the aldehyde rearrangement product at 10.8 min.

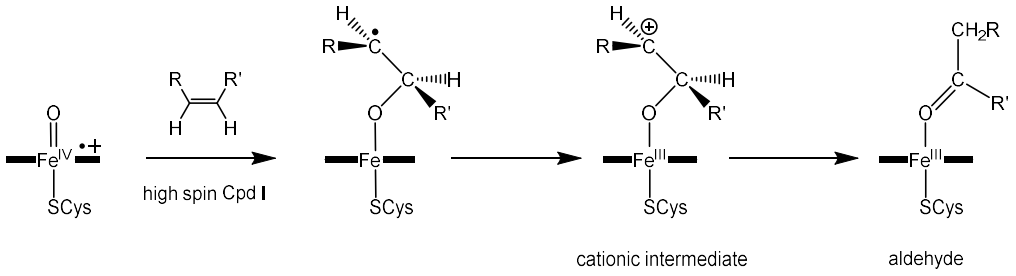

Figure D12. Mechanism of formation of the aldehyde rearrangement product via a cationic intermediate.[437]

NMR spectrum of chemically synthesised 4-oxiran-2-ylbenzoic acid

^{1}H NMR (500 MHz, DMSO): δ_H 2.85 [dd, J = 2.6, 5.4 Hz, 1H, 1 × 7-H], 3.16 [dd, J=4.2, 5.4 Hz, 1H, 1 × 7-H], 4.01 [dd, J = 2.6, 4.2 Hz, 1H, 6-H], 7.40 [d, J=8.4 Hz, 2H, 4-H], 7.92 [d, J=8.4 Hz, 2H, 3-H].

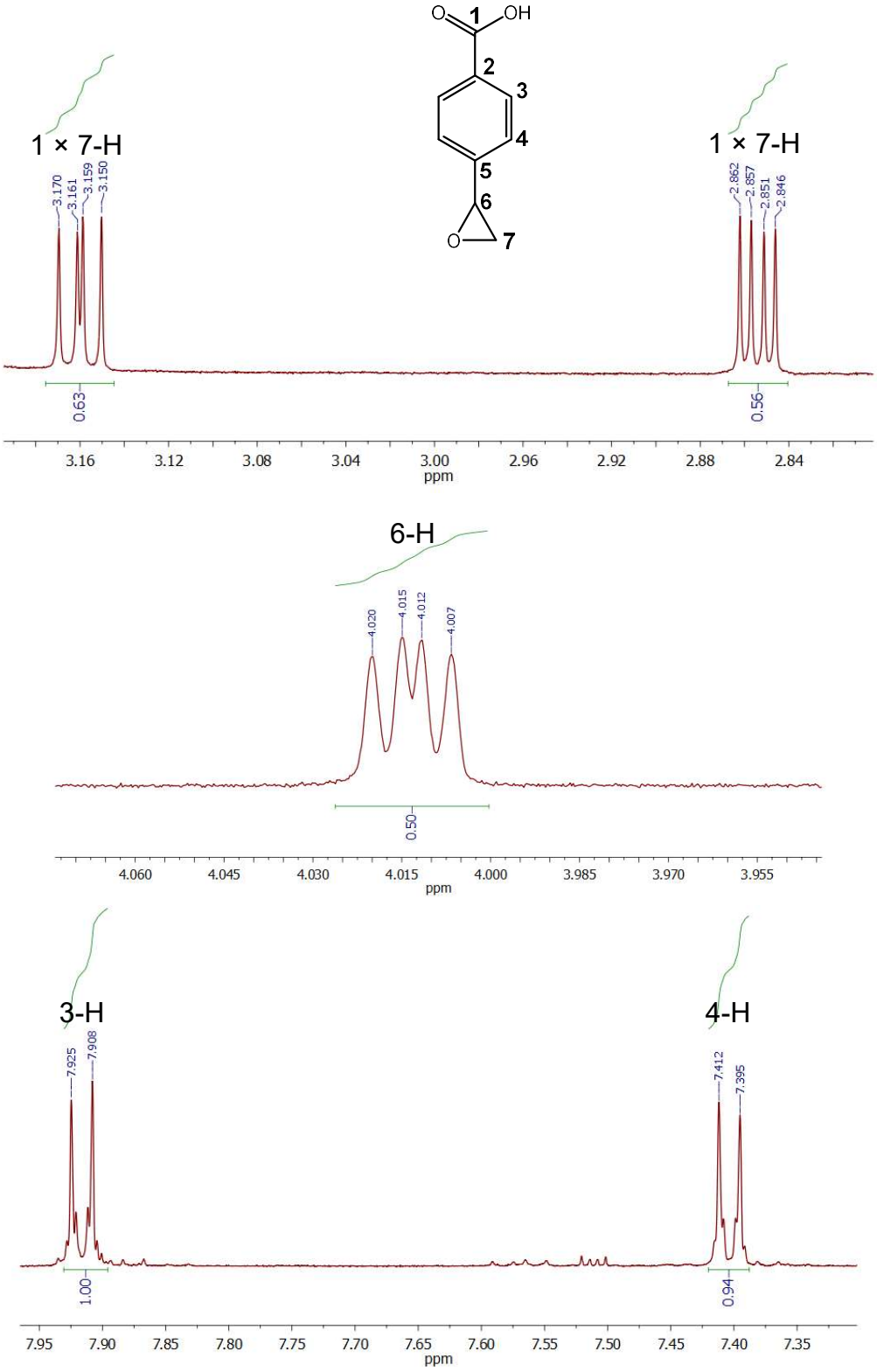

Figure D13. ^{1}H NMR spectrum of chemically synthesised 4-oxiran-2-ylbenzoic acid.

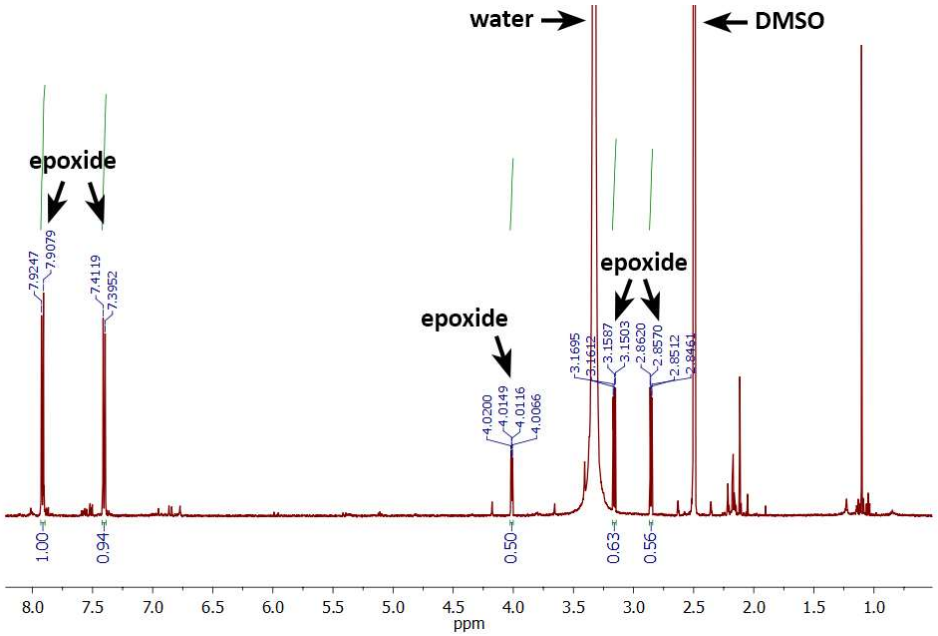

Figure D13 (continued). Full ^{1}H NMR spectrum of chemically synthesised 4-oxiran-2-ylbenzoic acid.

Purification of 4-oxiran-2-ylbenzoic acid by HPLC resulted in ring-opening of the epoxide in the acidic solvent

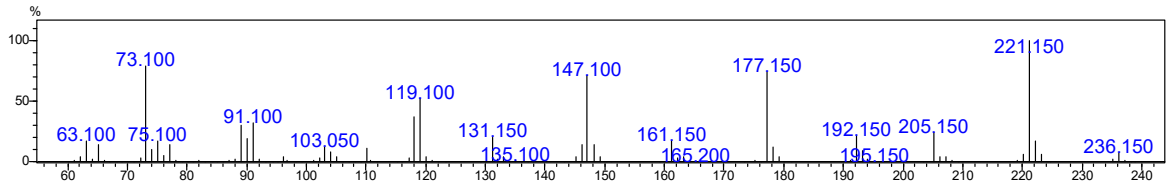

4-Oxiran-2-ylbenzoic acid (singly derivatized): m/z = 236.15 (exp. m/z = 236.0869), RT = 12.4 min

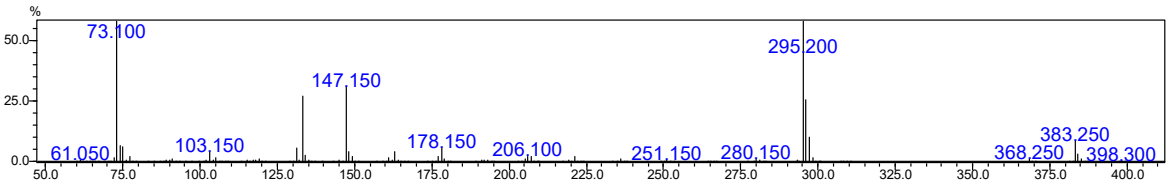

4-(1,2-Dihydroxyethyl)benzoic acid (triply derivatized), m/z = 398.3 (exp. m/z = 398.1765), RT = 18.8 min

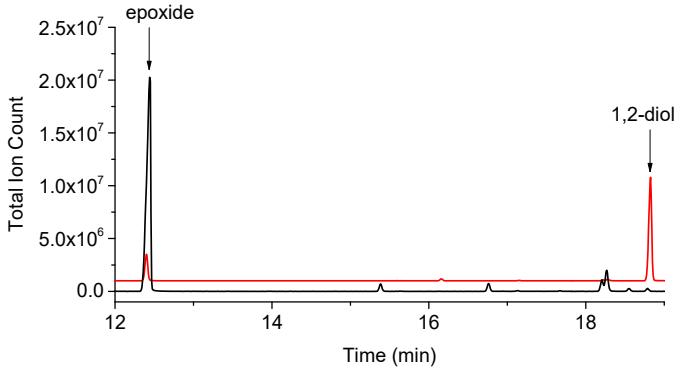

Figure D14. GC-MS data for the chemically synthesised epoxide (4-oxiran-2-ylbenzoic acid) and the 1,2-diol resulting from ring-opening of the epoxide. In **black** is the crude epoxide prior to purification by semi-prep HPLC, and in **red** is the 1,2-diol arising from ring-opening of the epoxide caused by acid in the HPLC solvent.

Product distribution of *in vitro* NADH-supported reactions of D251N, T252A and WT CYP199A4 with 4-vinylbenzoic acid

Table D3. Product distribution of *in vitro* reactions of D251N, T252A and WT CYP199A4 with 4-vinylbenzoic acid. Reactions were supported by NADH. Predominantly the epoxide was formed with minor quantities of the aldehyde rearrangement product. Product was quantified by GC-MS and it was assumed that the epoxide and aldehyde had identical detector responses. The aldehyde rearrangement product had a retention time of 10.8 min; the epoxide had a retention time of 11.2 min. Both products have identical mass (m/z = 236.1).

CYP199A4 isoform	Trial	Product	Peak area	Percentage of total product (%)	Mean ± SD
$\mathbf{WT_{CYP199A4}}$	1	Aldehyde	392488	4.4	96.1 ± 0.7% epoxide, 3.9 ± 0.7% aldehyde
		Epoxide	8576023	95.6	
	2	Aldehyde	181297	3.4	
		Epoxide	5148185	96.6	
$\mathbf{D251N_{CYP199A4}}$	1	Aldehyde	206747	5.1	94.8 ± 0.2% epoxide, 5.2 ± 0.2% aldehyde
		Epoxide	3853117	94.9	
	2	Aldehyde	209936	5.3	
		Epoxide	3730649	94.7	
$\mathbf{T252A_{CYP199A4}}$	1	Aldehyde	65989	5.3	95 ± 1% epoxide, 5 ± 1% aldehyde
		Epoxide	1183118	94.7	
	2	Aldehyde	92369	4.0	
		Epoxide	2209207	96.0	
	3	Aldehyde	126761	6.4	
		Epoxide	1842442	93.6	

20-minute T252E$_{CYP199A4}$ oxidation reactions driven by 50 mM H_2O_2

H_2O_2-driven oxidation of 4-vinylbenzoic acid by T252E$_{CYP199A4}$

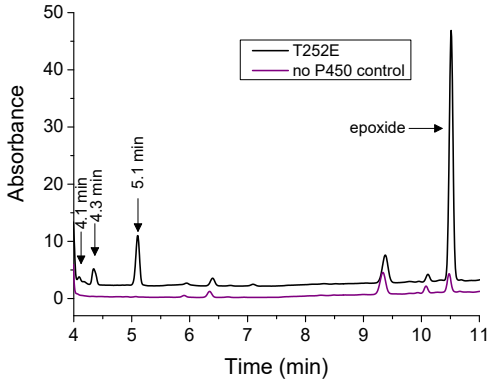

Figure D15. HPLC analysis of the 20-minute T252E$_{CYP199A4}$ reaction (**black**) with 4-vinylbenzoic acid driven by 50 mM H_2O_2 at 30 °C. The T252E mutant converted 4-vinylbenzoic acid predominantly into the corresponding epoxide, 4-oxiran-2-ylbenzoic acid, but additional minor products with retention times of 5.1, 4.3 and 4.1 min were also detected. In **purple** is a control reaction omitting the P450.

Table D4. Estimated product concentration in the 20-min H_2O_2-driven reaction of T252E$_{CYP199A4}$ with 4-vinylbenzoic acid. The H_2O_2 concentration was 50 mM.

Product concentration (μM)			
Epoxide (RT = 10.4 min)	**Aldehyde? (RT = 9.4 min)**	**Unknown product (RT = 5.1 min)**	**Additional products (RT = 6.4, 4.3, 4.1 min)**
54 ± 1 μM	1 ± 0.5 μM	12 ± 0.2 μM	11 ± 0.4 μM
Percentage of total product (%)			
~69%	~2%	~15%	~14%

The epoxide and unidentified minor products were all quantified using the calibration curve for 4-(1-hydroxyethyl)benzoic acid.

H_2O_2-driven oxidation of 4-methylthiobenzoic acid by T252E$_{CYP199A4}$

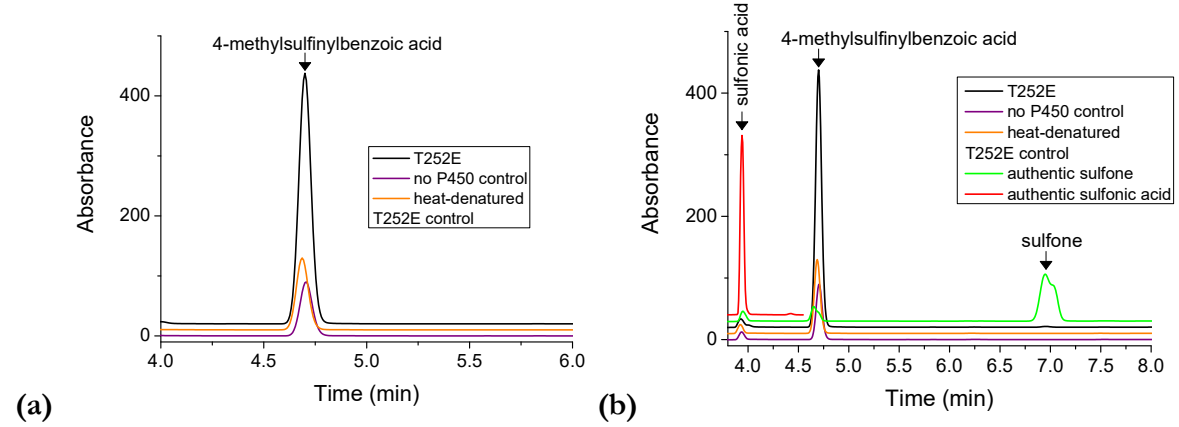

Figure D16. **(a)** Sulfoxidation of 4-methylthiobenzoic acid by the T252E mutant over a 20-minute period. H_2O_2 (**50 mM**) was used as the oxygen donor. The **black line** is the T252E turnover. In **orange** is the heat-denatured T252E control, and in **purple** is the no P450 control. **(b)** In **red** and **green** are authentic 4-sulfobenzoic acid and 4-methylsulfonylbenzoic acid; these products were not formed by the T252E enzyme.

Table D5. Sulfoxide concentration in the T252E turnover, no P450 control and heat-denatured T252E control reactions. H_2O_2 (50 mM) was used as the oxygen donor and the reaction time was 20 minutes.

Substrate	**Product concentration (μM)**		
	T252E turnover	**no P450 control**	**heat-denatured T252E**
4-methylthioBA	311 ± 2	66 ± 1	86

Control reactions to assess whether a Fenton-type reaction is responsible for the formation of product in the H_2O_2-driven reactions

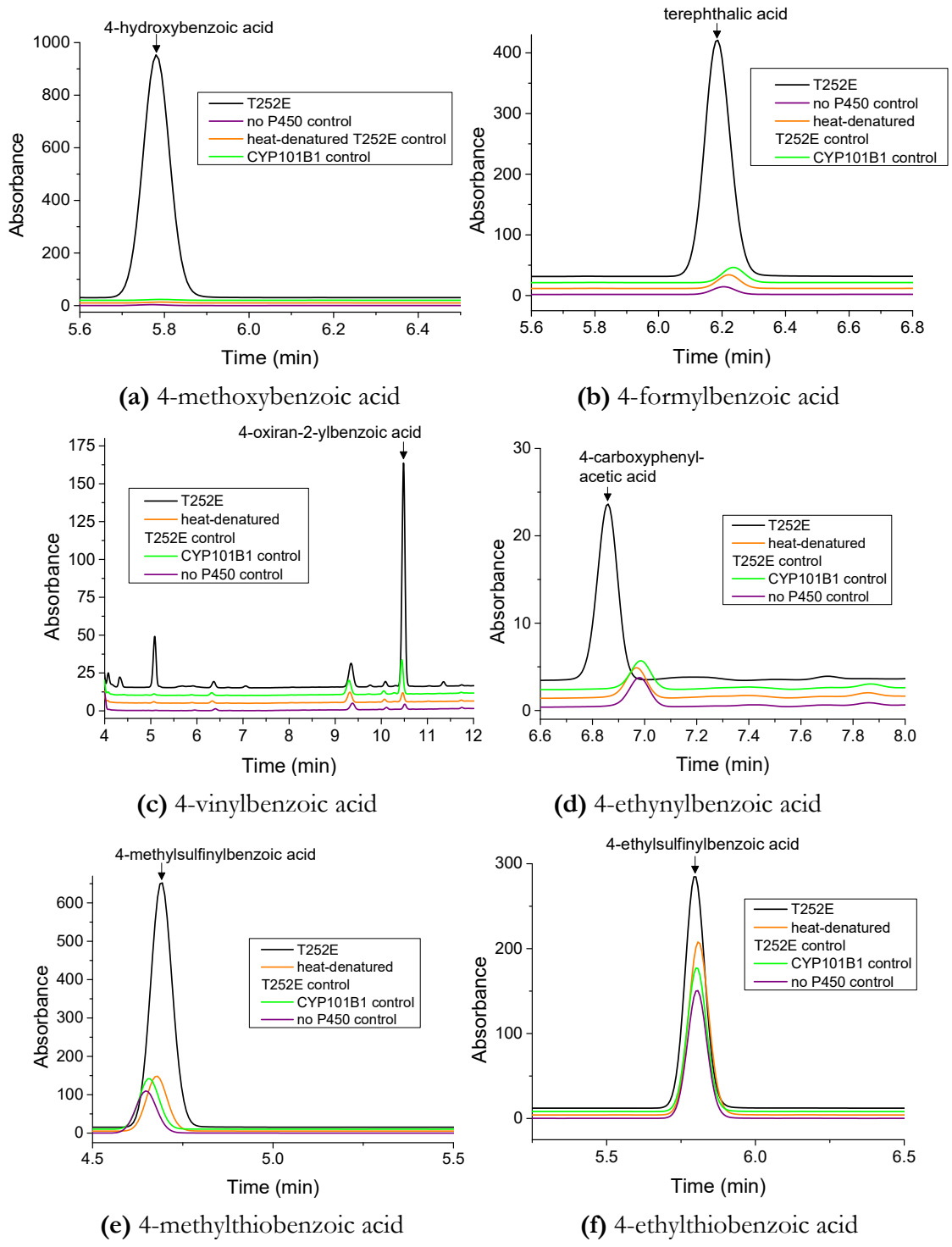

Figure D17. Comparison of the amount of product generated in the H_2O_2-driven T252E reactions (**black**) to the amount of product detected in the no P450 control (**purple**), CYP101B1 control (**green**) and heat-denatured T252E control (**orange**) reactions. **The reaction time was 240 min.** The H_2O_2 concentration was 6 mM for the sulfide substrates but 50 mM for all other substrates.

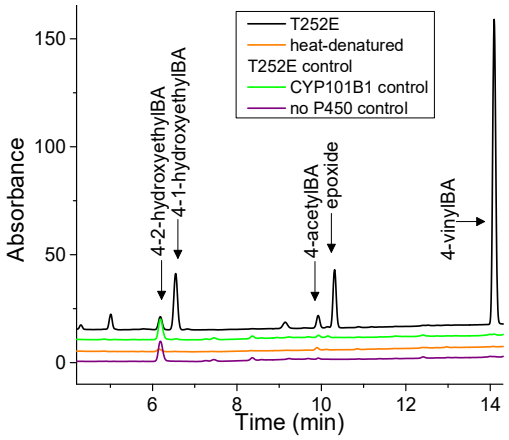

(g) 4-ethylbenzoic acid

Figure D17. (*Continued*) Comparison of the amount of product generated in the H_2O_2-driven oxidation of 4-ethylbenzoic acid by the T252E mutant (**black**) to the amount of product detected in the no P450 control (**purple**), CYP101B1 control (**green**) and heat-denatured T252E control (**orange**) reactions. The reaction time was 240 min. Note that in the no P450 control reaction and CYP101B1 control reaction (but not in the heat-denatured T252E control), there is a peak at 6.2 min which elutes at the same time as 4-2-hydroxyethylbenzoic acid. This may be due to a contaminant in these control reactions.

Table D6. Amount of product detected in the no P450 control, CYP101B1 control and heat-denatured T252E control reactions **after 240-min reactions**. *For the thioether reactions, 6 mM H_2O_2 was used instead of 50 mM H_2O_2.

Substrate	Product concentration (μM)		
	no P450 control	CYP101B1 control	heat-denatured T252E
4-methoxyBA	1	1	1
4-formylBA	8	15	14
4-vinylBA	5	29	8
4-methylthioBA *	91	92	107
4-ethylthioBA *	115	130	161
4-ethylBA	~0	~0	~0
4-ethynylBA	6	7	7

HPLC analysis of product formation by CYP199A4 isoforms driven by H_2O_2

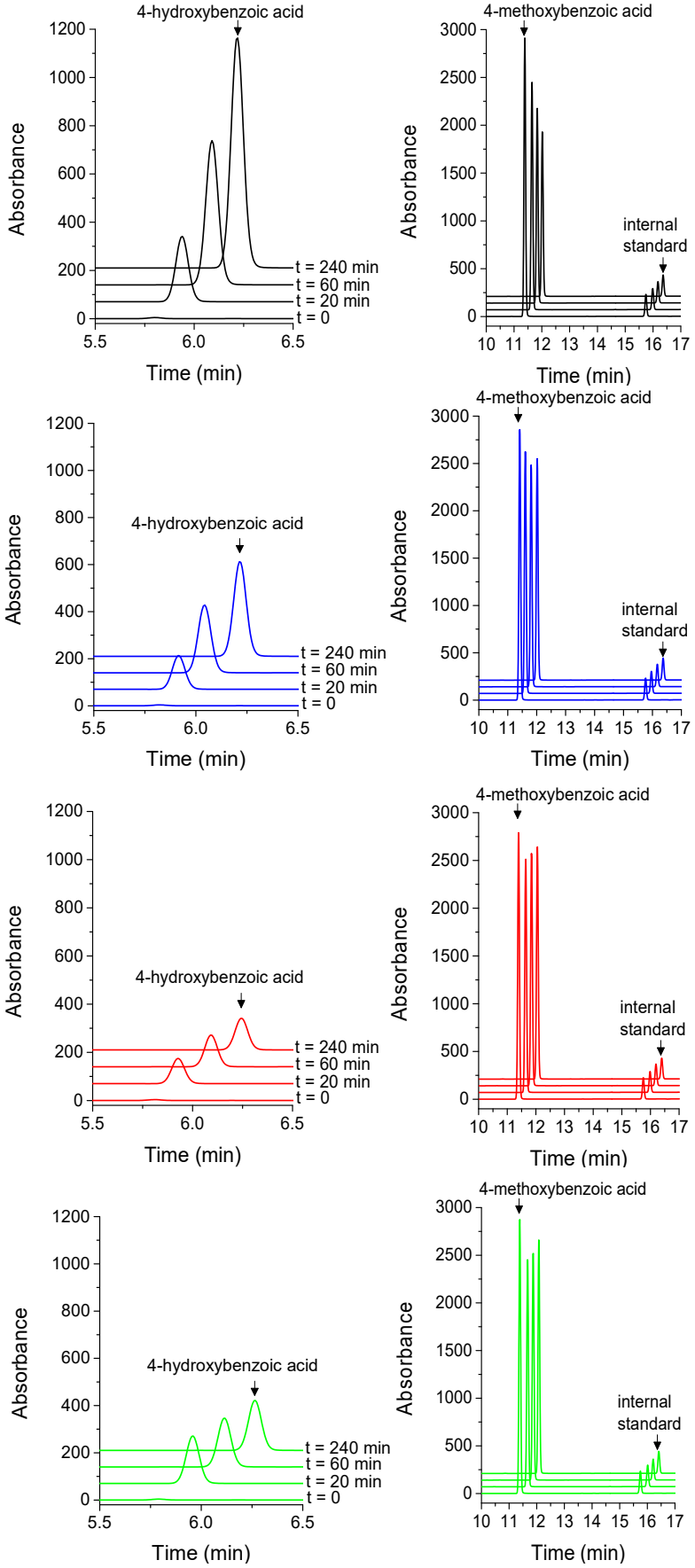

Figure D18. Conversion of 4-methoxybenzoic acid into 4-hydroxybenzoic acid by WT CP199A4 (**blue**) and the T252E (**black**), D251N (**red**) and T252A (**green**) mutants over a 4-hour period. H_2O_2 (50 mM) was used as the oxygen donor.

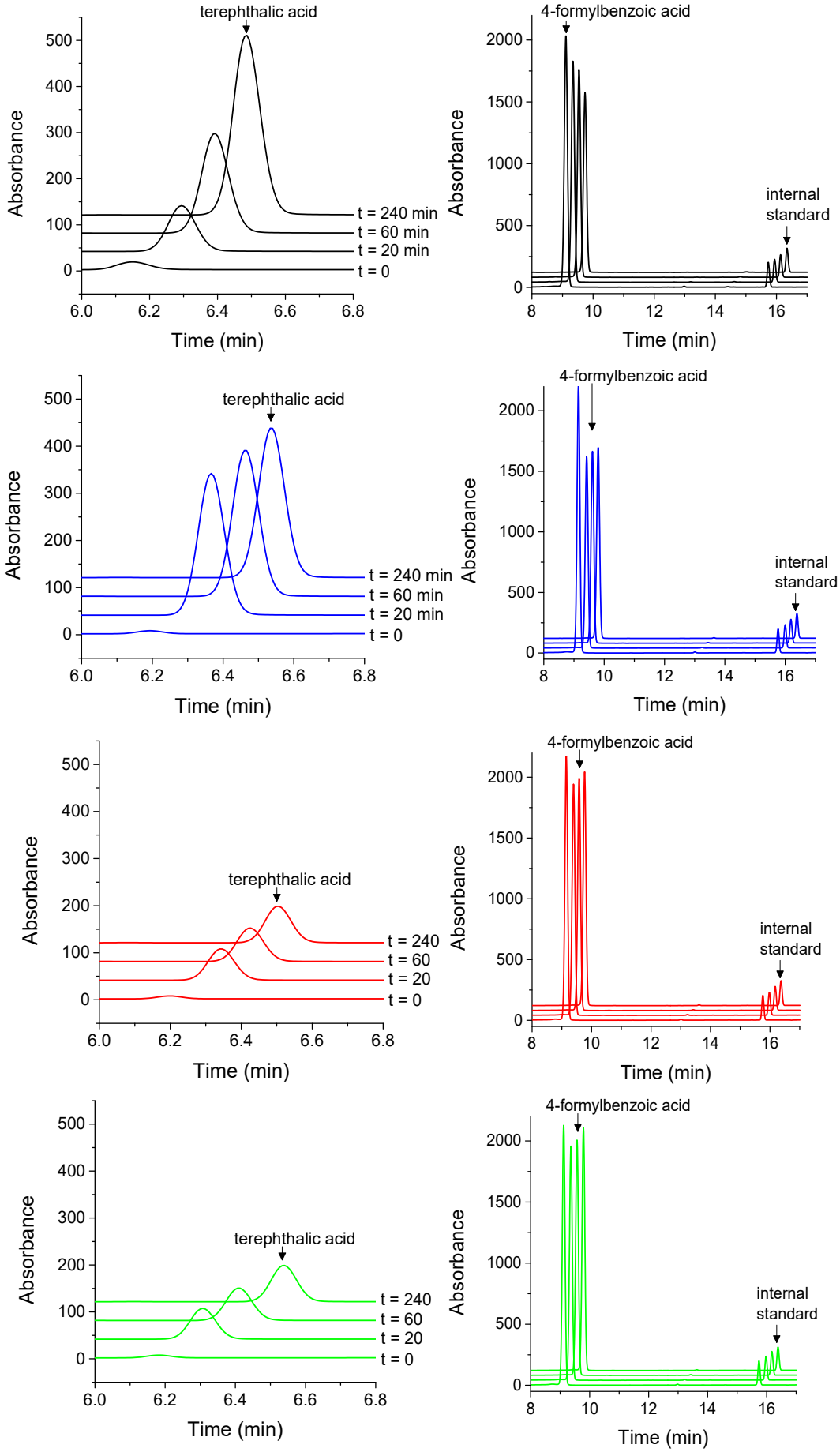

Figure D19. Conversion of 4-formylbenzoic acid into terephthalic acid by WT CP199A4 (**blue**) and the T252E (**black**), D251N (**red**) and T252A (**green**) mutants over a 4-hour period. H_2O_2 (50 mM) was used as the oxygen donor.

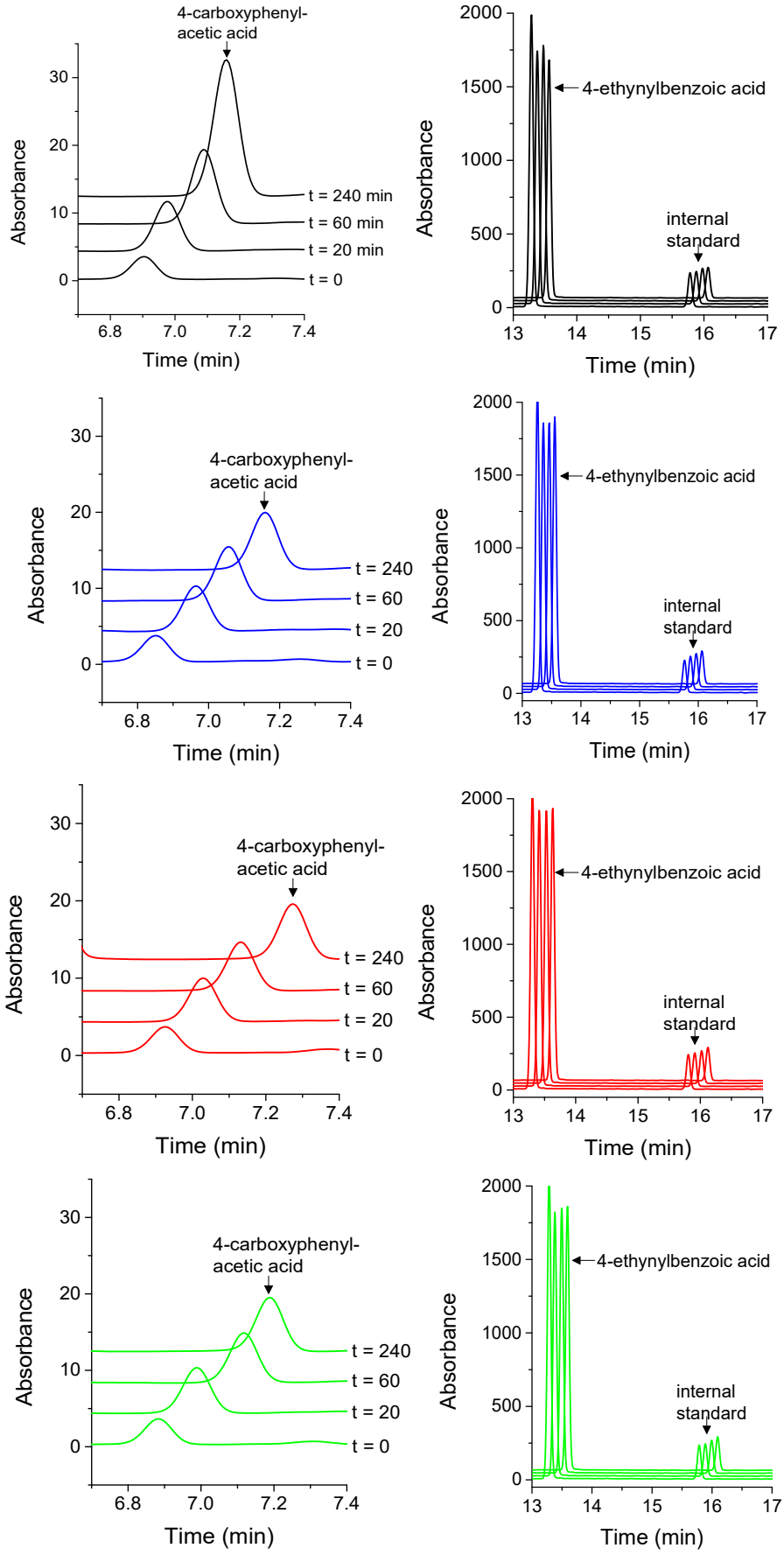

Figure D20. Oxidation of 4-ethynylbenzoic acid to 4-carboxyphenylacetic acid by WT CYP199A4 (**blue**) and the T252E (**black**), D251N (**red**) and T252A (**green**) mutants over a 4-hour period. H_2O_2 (50 mM) was used as the oxygen donor.

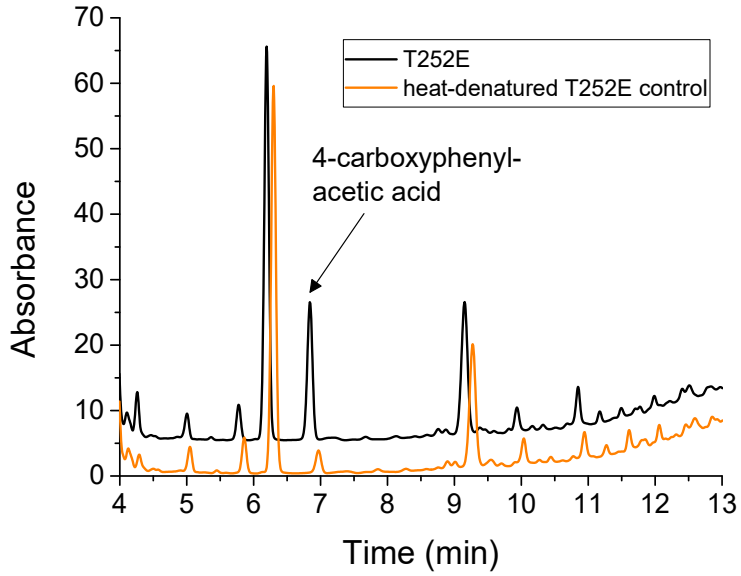

Figure D21. HPLC analysis of the 240-min, H_2O_2-driven reaction of $T252E_{CYP199A4}$ with 4-ethynylbenzoic acid (**black**) and a control reaction performed with heat-denatured $T252E_{CYP199A4}$ (**orange**).

A single product, 4-carboxyphenylacetic acid, was generated by $T252E_{CYP199A4}$. Notice that the HPLC chromatogram contains multiple other peaks, but these peaks also appear in the control reactions.

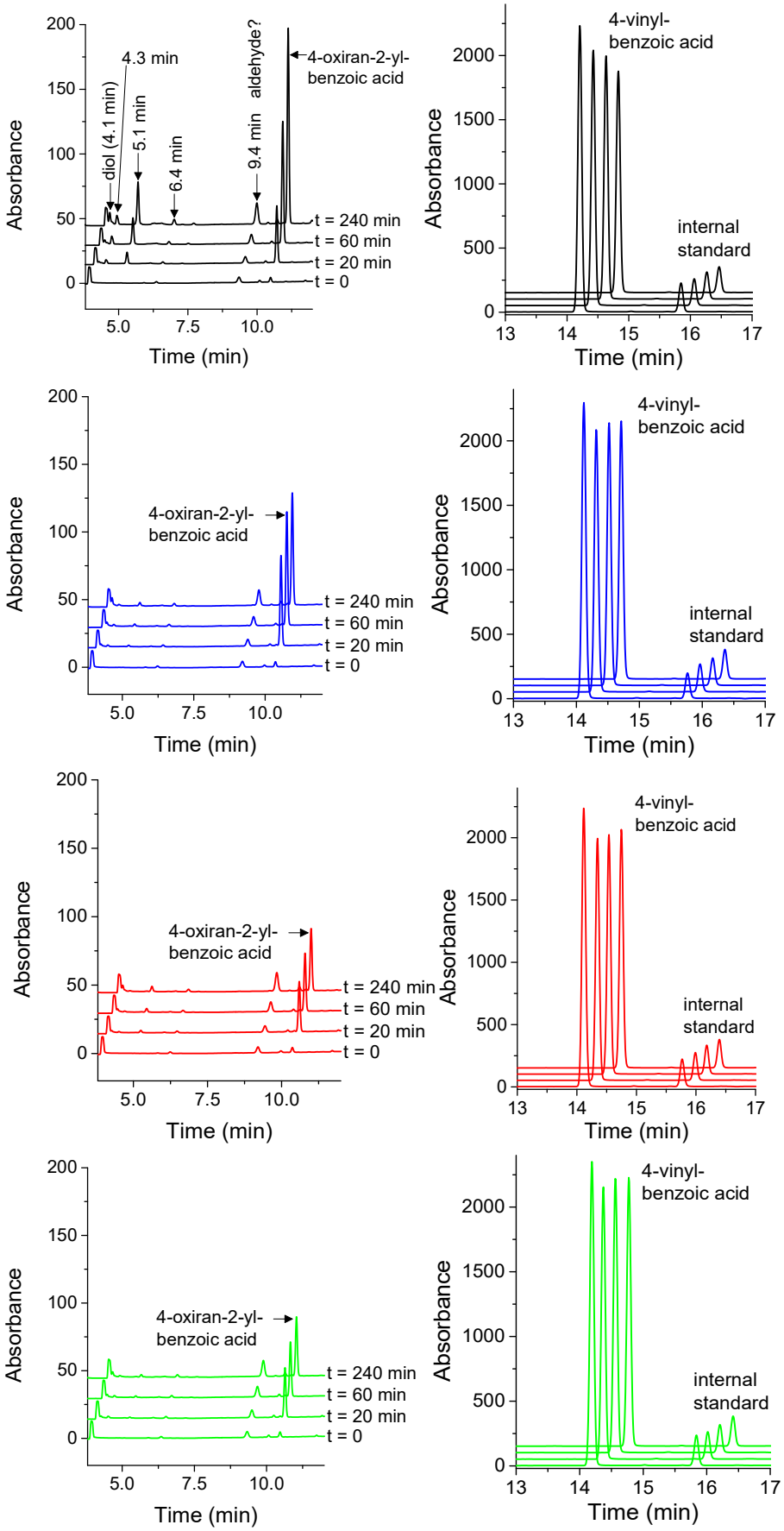

Figure D22. Oxidation of 4-vinylbenzoic acid to the corresponding epoxide by WT CYP199A4 (**blue**) and the T252E (**black**), D251N (**red**) and T252A (**green**) mutants over a 4-hour period. H_2O_2 (50 mM) was used as the oxygen donor.

Table D7. Product distribution for the H_2O_2-driven oxidation of 4-vinylbenzoic acid by CYP199A4 isoforms. The percentage of each product was determined by assuming that the detector response was identical for all products. Authentic samples of the products were not available for calibration.

CYP199A4 isoform	Product distribution (%)			
	Epoxide (RT 10.4 = min)	Aldehyde? (RT = 9.4 min)	Unknown product (RT = 5.1 min)	Additional products (RT = 6.4, 4.3, 4.1 min)
T252E	~66%	~8%	~15.5%	~10.5%
WT	~82%	~10%	~3%	~5%
D251N	~67%	~23%	~6%	~4%
T252A	~71%	~19.5%	~3.5%	~6%

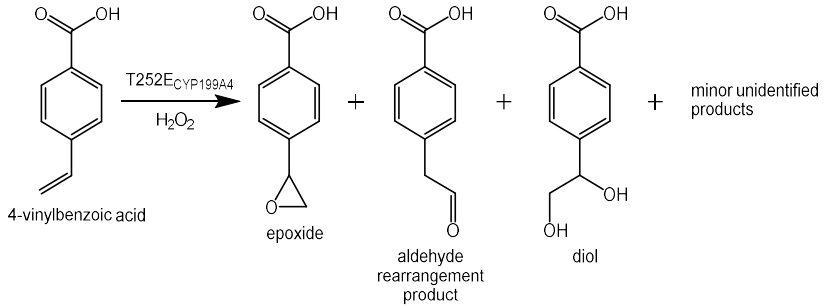

HPLC retention time of the diol (4-1,2-dihydroxyethylbenzoic acid)

The diol, 4-(1,2-dihydroxyethyl)benzoic acid, which could arise from ring opening of the epoxide, was chemically synthesised by Luke Churchman and James de Voss at the University of Queensland. This diol had a HPLC retention time of 4.1 min (Figure D23).

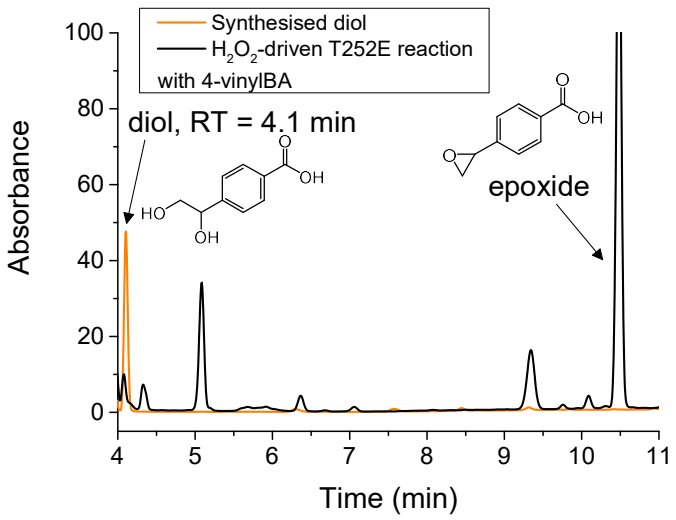

Figure D23. HPLC analysis of chemically synthesised 4-(1,2-dihydroxyethyl)benzoic acid, which was synthesised by Luke Churchman at the University of Queensland. The diol eluted at 4.1 min.

In **black** is the H_2O_2-driven $T252E_{CYP199A4}$ reaction with 4-vinylbenzoic acid, which generated multiple unidentified products, including minor quantities of this diol. Gradient: 20-95% AcCN in H_2O_2 with 0.1% TFA.

HPLC retention time of 4-hydroxymethylbenzoic acid

We also considered the possibility that the product at 5.1 min in the T252E reaction with 4-vinylbenzoic acid was 4-hydroxymethylbenzoic acid, arising from a cleavage reaction. We speculated that the aldehyde rearrangement product may undergo Baeyer-Villiger oxidation, followed by hydrolysis of the ester (Figure D24a). However, the retention time of the enzyme product different from that of authentic 4-hydroxymethylbenzoic acid (Figure D24b).

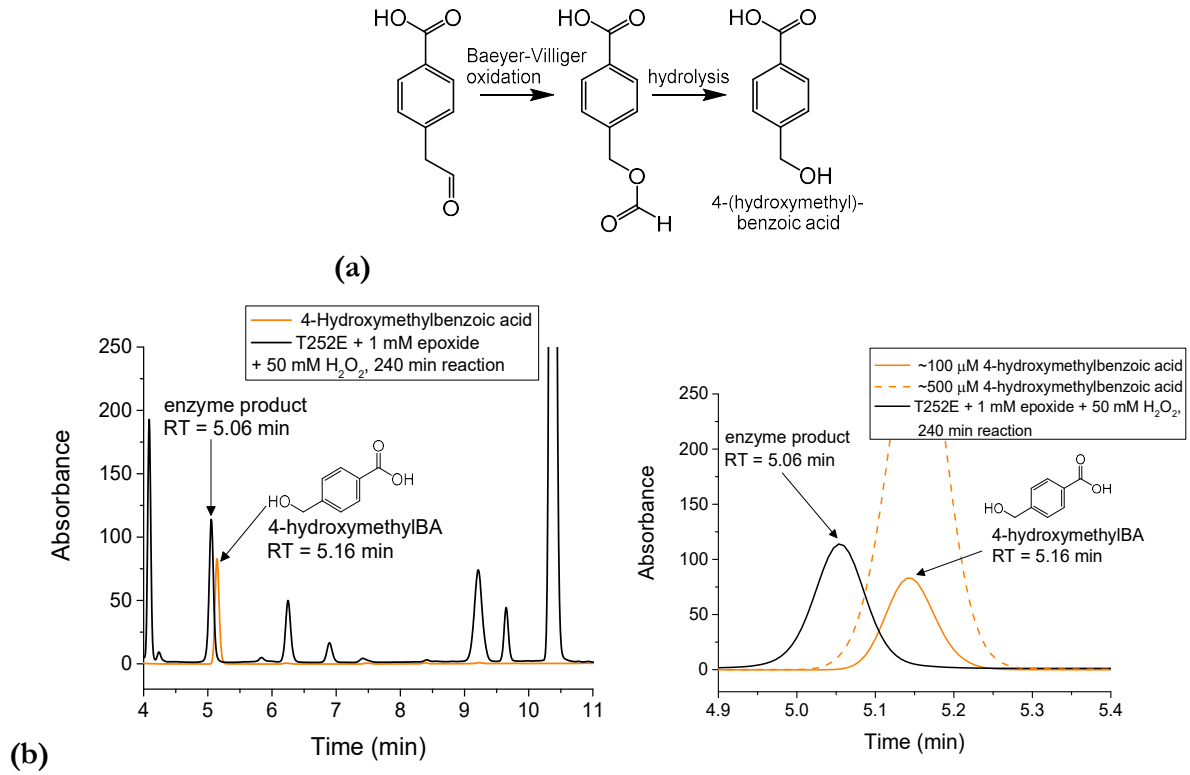

Figure D24. **(a)** We speculated that the aldehyde rearrangement product may be undergoing Baeyer-Villiger oxidation, followed by ester hydrolysis to give 4-hydroxymethylbenzoic acid. **(b)** However, 4-hydroxymethylbenzoic acid did not co-elute with the enzyme product at 5.06 min. Authentic 4-hydroxymethylbenzoic acid had a retention time of 5.16 min. These samples were analysed by HPLC on the same day.

The 4-vinylbenzoic acid epoxide is further metabolised by T252E$_{CYP199A4}$ to yield an additional product with a retention time of 5.1 min

We performed reactions to assess whether the peak seen at 5.1 min in the T252E reaction with 4-vinylbenzoic acid arises from further oxidation of the epoxide product by the T252E mutant. A 120-minute, H_2O_2-driven reaction of the T252E mutant (3 µM) with chemically synthesised epoxide as the substrate was performed (Figure D25, **black**). The reaction was performed at 30 °C and was driven by 50 mM H_2O_2. The concentration of the epoxide substrate was 50 µM.

In this reaction, the T252E$_{CYP199A4}$ enzyme converted the epoxide into an unknown product with a retention time of 5.1 min. This confirms that the product observed at 5.1 min arises from further metabolism of the epoxide by the T252E$_{CYP199A4}$ enzyme.

H_2O_2 alone failed to convert the epoxide into this product (Figure D25, **red**).

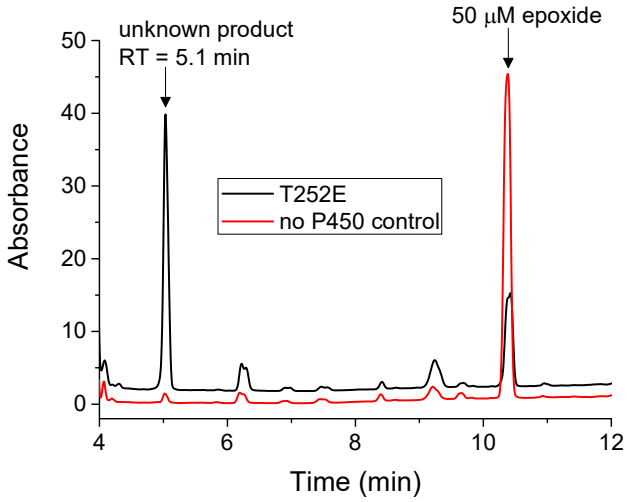

Figure D25. HPLC analysis of a 120-minute, H_2O_2-driven reaction of the T252E mutant (3 µM) with chemically synthesised epoxide (4-oxiran-2-ylbenzoic acid) as the substrate (50 µM) (**black**). The reaction was performed at 30 °C and was driven by 50 mM H_2O_2. In **red** is a control reaction omitting the P450. Gradient: 20-95% AcCN in H_2O_2 with 0.1% TFA. The T252E mutant generated an unknown product with a retention time of 5.1 min.

We aimed to determine the mass of this unidentified product by GC-MS. After quenching the reaction mixture (1 mL) by adding 20 µL of catalase solution, 3 µL of 3 M HCl was added and the reaction mixture extracted with EtOAc (3 × 400 µL). The organic extracts were dried over anhydrous MgSO4 and the solvent evaporated under N_2. The residue was redissolved in anhydrous AcCN (150 µL) and derivatised with 15 µL BSTFA + TMCS (99:1). The reaction was left for 2 hours prior to analysis by GC-MS. The unidentified product was not detected by GC-MS.

We repeated this experiment using a higher concentration of the epoxide substrate and a longer reaction time with the aim of producing more of the unknown product so that it could be detected by GC-MS. The reactions contained 50 mM H_2O_2, 3 μM T252E$_{CYP199A4}$ enzyme and 1 mM chemically synthesised 4-oxiran-2-ylbenzoic acid as the substrate; the reaction time was 4 hours.

The H_2O_2-driven reaction of T252E$_{CYP199A4}$ with the epoxide generated the unidentified product with a retention time of 5.1 min. Control reactions omitting the P450 or H_2O_2 did not generate this product (Figure D26). As the T252E$_{CYP199A4}$ enzyme produced only minor quantities of this product, we again expected that we would be unable to detect it by GC-MS.

A peak at 4.1 min increased substantially in size over the 4-hour period in both the T252E reaction and the no P450 and no H_2O_2 control reactions. This peak is the diol resulting from ring-opening of the epoxide over time.

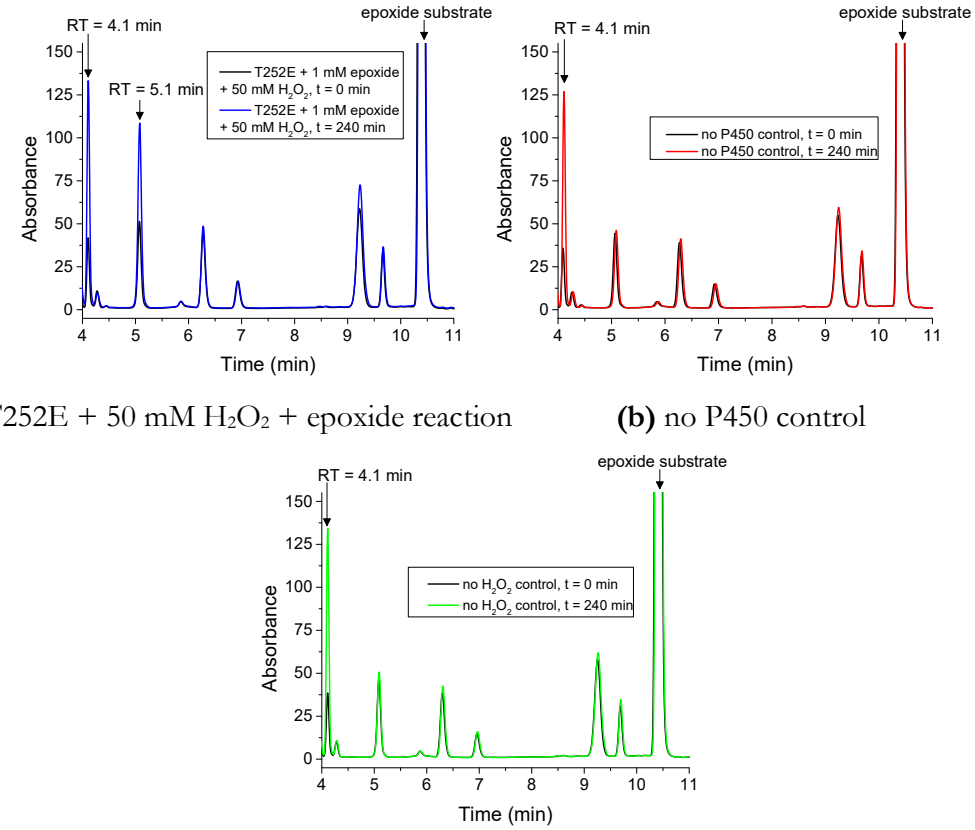

(a) T252E + 50 mM H_2O_2 + epoxide reaction **(b)** no P450 control

(c) no H_2O_2 control

Figure D26. **(a)** HPLC analysis of the H_2O_2-driven reaction of the T252E mutant with chemically synthesised 4-oxiran-2-ylbenzoic acid over a 240-min period. In **(b)** and **(c)**, control reactions omitting the P450 or H_2O_2 are shown. In both the T252E reaction and control reactions, a peak at 4.1 min increased substantially in size over time. The peak at 5.1 min increased in size only in the T252E reaction, not in the control reactions. Note that the epoxide substrate was impure so there are multiple impurity peaks which appear in the control reactions.

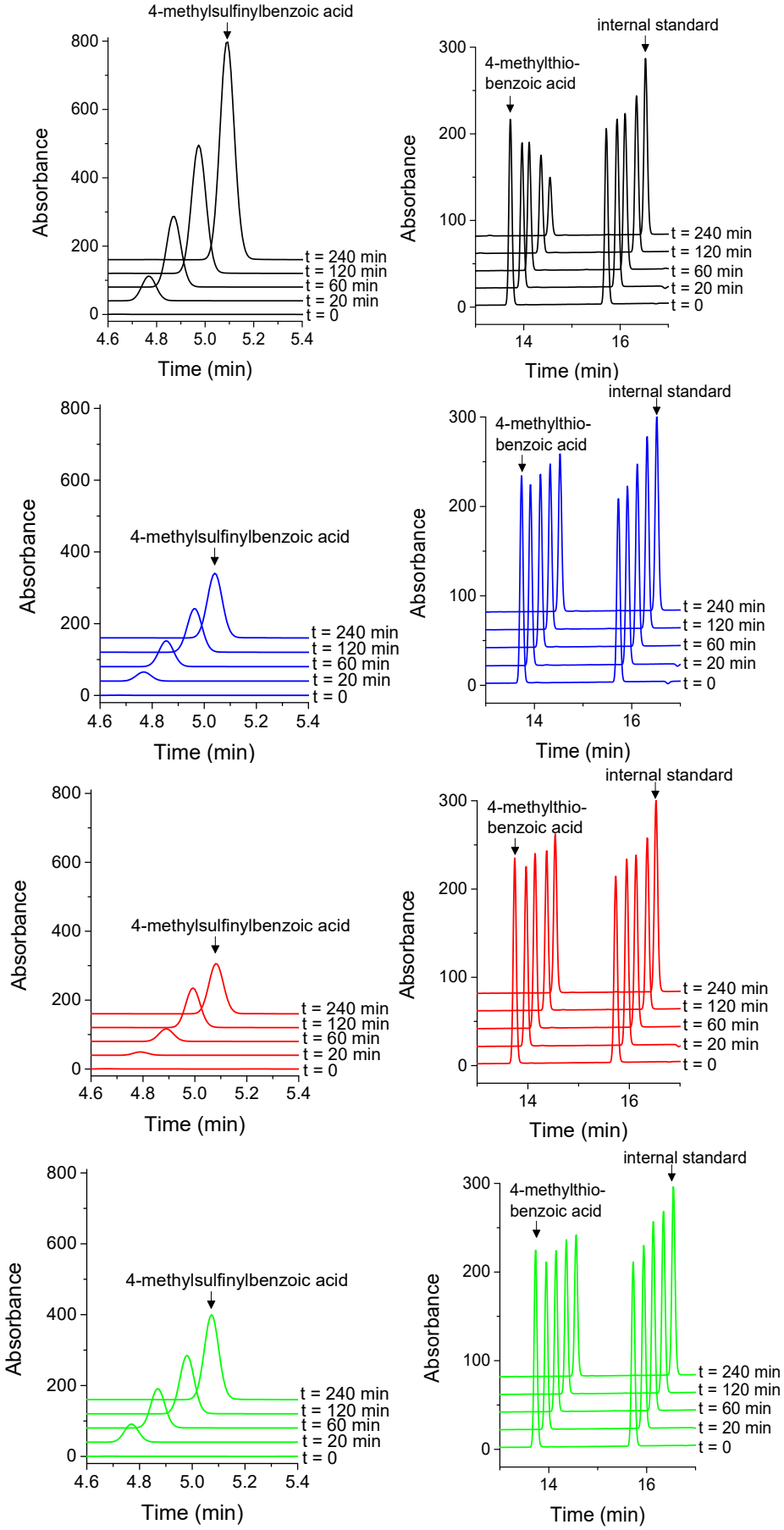

Figure D27. Conversion of 4-methylthiobenzoic acid into 4-methylsulfinylbenzoic acid by WT CP199A4 (**blue**) and the T252E (**black**), D251N (**red**) and T252A (**green**) mutants over a 4-hour period. H_2O_2 (6 mM) was used as the oxygen donor.

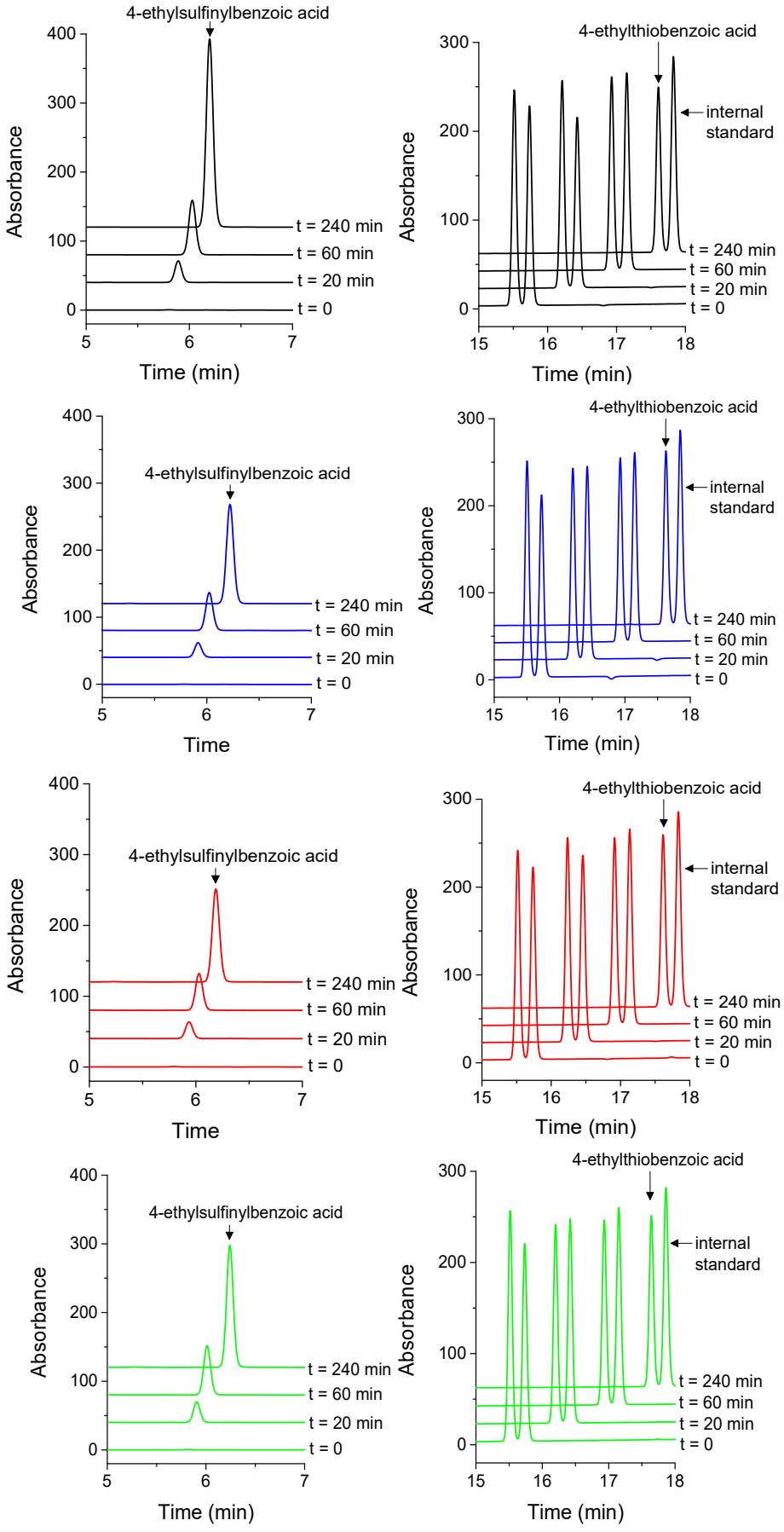

Figure D28. Conversion of 4-ethylthiobenzoic acid into 4-ethylsulfinylbenzoic acid by WT CP199A4 (**blue**) and the T252E (**black**), D251N (**red**) and T252A (**green**) mutants over a 4-hour period. H_2O_2 (6 mM) was used as the oxygen donor. No 4-mercaptobenzoic acid was detected.

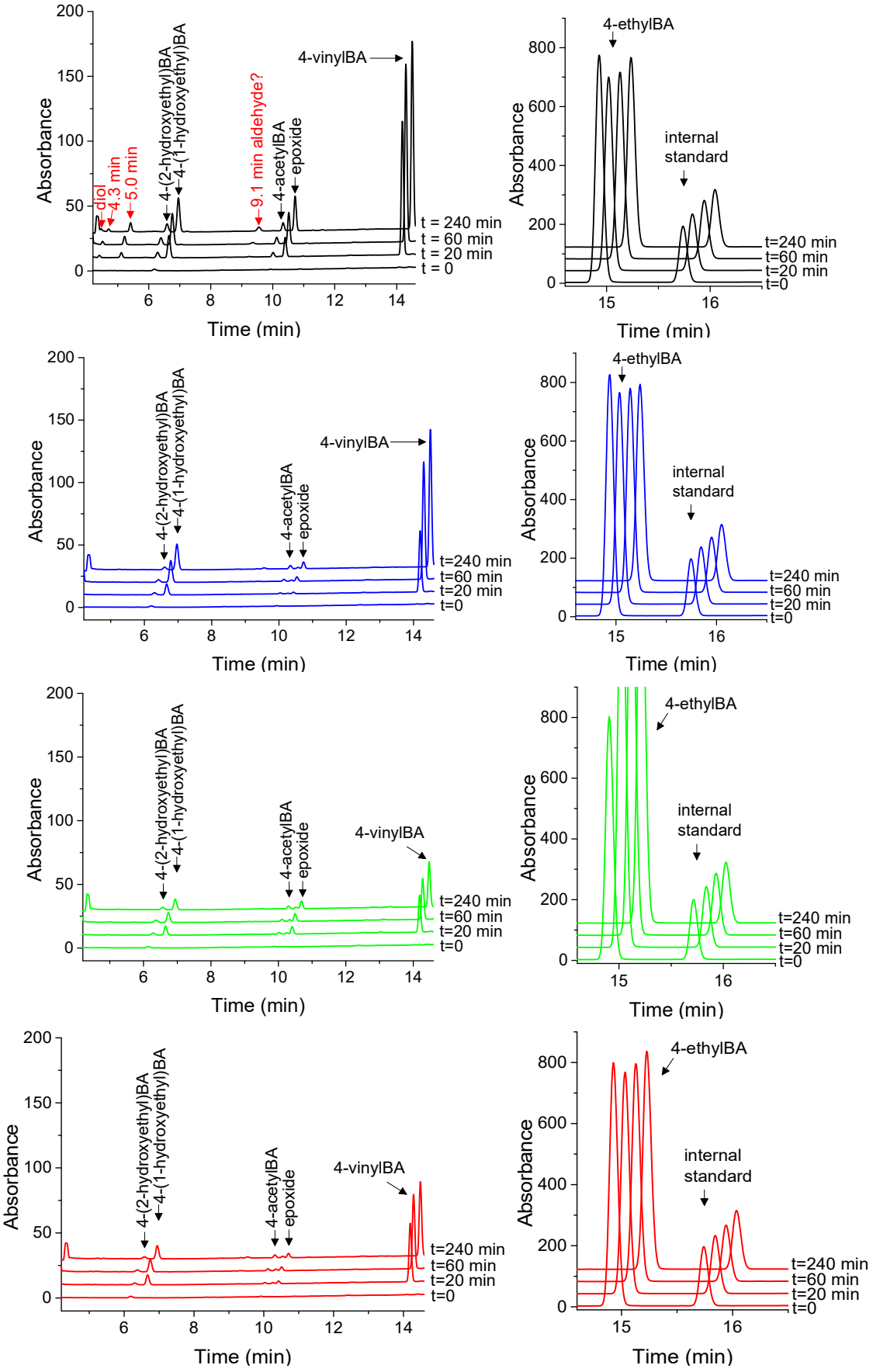

Figure D29. Oxidation of 4-ethylbenzoic acid by WT CYP199A4 (**blue**) and the T252E (**black**), D251N (**red**) and T252A (**green**) mutants over a 4-hour period. H_2O_2 (50 mM) was used as the oxygen donor.

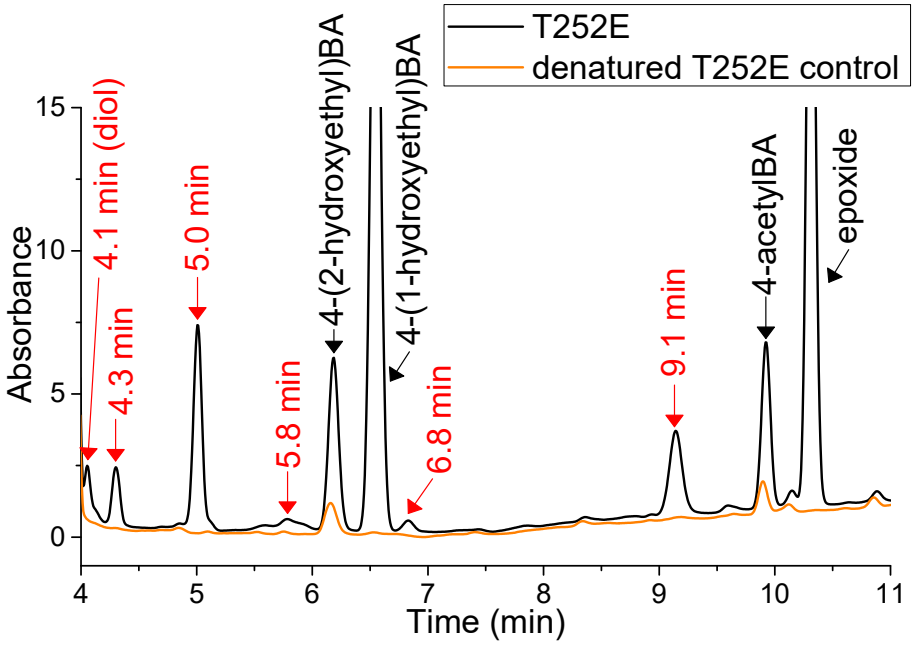

Figure D30. Enlarged view of the HPLC chromatogram of the H_2O_2-driven reaction of $T252E_{CYP199A4}$ with 4-ethylbenzoic acid. There are multiple peaks corresponding to minor products that were not generated by the other CYP199A4 isoforms (indicated by red arrows). One of the additional products is the diol arising from ring opening of the epoxide (RT = 4.1 min), but the other metabolites are yet to be identified.

Table D8. Estimated concentration of additional products formed in the H_2O_2-driven T252E reaction with 4-ethylbenzoic acid. The calibration curve for 4-1-hydroxyethylbenzoic acid was used to estimate the concentration of these unknown metabolites.

	Concentration of unidentified products (μM)				
Retention time	**4.1 min**	**4.3 min**	**5.0 min**	**9.1 min**	**Total concentration**
	2.2	2.6	14.2	7.8	~27

The active-site structure of CYP199A4 is largely unaffected by the T252 → A, D251 → N and T252 → E mutations

Mutation of T252 to alanine or glutamate, or D251 to asparagine, did not appreciably alter the geometry of the active site of CYP199A4 nor the binding mode of 4-methoxybenzoic acid (Figure D31).[277]

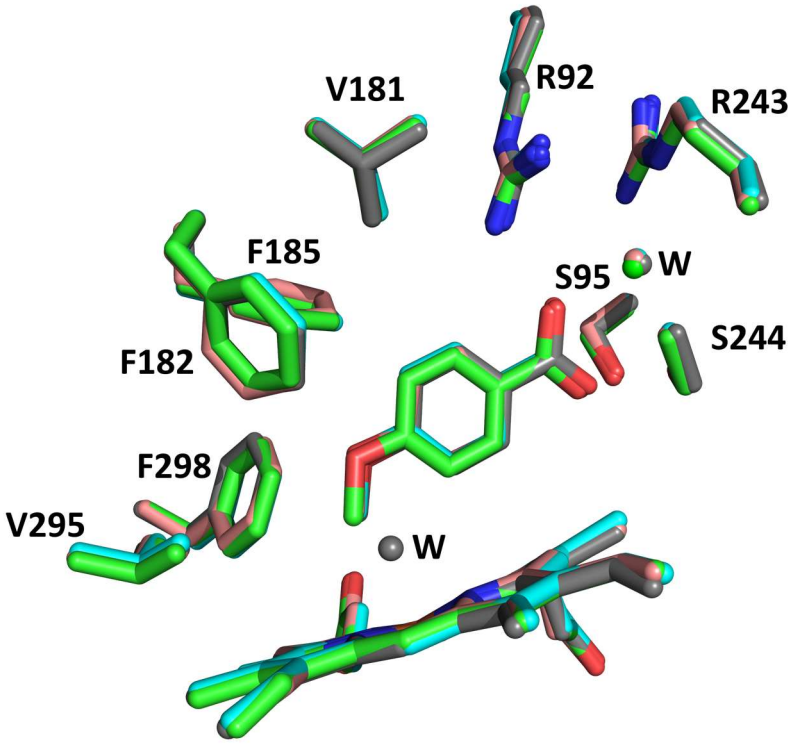

Figure D31. Active-site structure of WT CYP199A4 (cyan) and the T252E (grey), D251N (salmon) and T252A (green) isoforms in complex with 4-methoxybenzoic acid. These mutations do not appreciably alter the geometry of the active site nor the substrate binding mode. The D251N and T252A structures were reported by Coleman[277] (PDB codes: 5KDY and 5KDZ).

Enantioselectivity of NADH- or H_2O_2-driven epoxidation of 4-vinylbenzoic acid catalysed by CYP199A4 isoforms

Table D9. Enantioselectivity of NADH- or H_2O_2-driven epoxidation of 4-vinylbenzoic acid catalysed by CYP199A4 isoforms. In all cases, the major enantiomer is the (*S*)-enantiomer, which was first to elute.

CYP199A4 isoform	Trial	Peak area		Average % ee	Ratio of enantiomers (*S* : *R*)
		(*S*)-epoxide	(*R*)-epoxide		
WT-NADH	1	4400427	21392	98.9 ± 0.2	99.4 : 0.6
	2	3842471	24143		
D251N-NADH	1	2197733	69220	93.7 ± 0.3	96.8 : 3.2
	2	2095310	71196		
T252A-NADH	1	1852366	8752	98.9 ± 0.1	99.5 : 0.5
	2	1094290	6676		
	3	572697	3099		
T252E-NADH	1	120210	1507	~97.5	98.8 : 1.2
T252E-60 mM H_2O_2 (60-min reaction)	1	541523	17608	~93.7	96.9 : 3.1
WT-60 mM H_2O_2 (60-min reaction)	1	43971	1883	93 ± 1	96 : 4
	2	43351	1274		
	3	44092	1816		
Racemic epoxide		23538662	23490290	0.1	50.05 : 49.95

Enantioselectivity of H_2O_2-driven epoxidation of 4-vinylbenzoic acid by WT CYP199A4

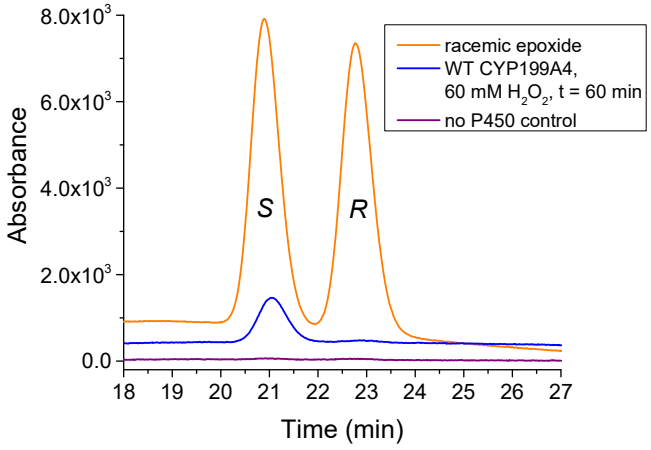

Figure D32. In H_2O_2-driven reactions, WT CYP199A4 converted 4-vinylbenzoic acid into predominantly the (*S*)-epoxide; the enantiomeric excess was 93 ± 1%. (The ratio of enantiomers was 96% (*S*)-epoxide and 4% (*R*)-epoxide.)

Assignment of the absolute configuration of the 4-vinylbenzoic acid epoxide generated by CYP199A4 isoforms

CYP199A4 converted 4-vinylbenzoic acid into predominantly the (*S*)-epoxide. The absolute configuration of the epoxide was identified by HPLC co-elution of the major enantiomer with an authentic sample of the (*S*)-epoxide synthesised by Luke Churchman and James de Voss at the University of Queensland (Figure D33).

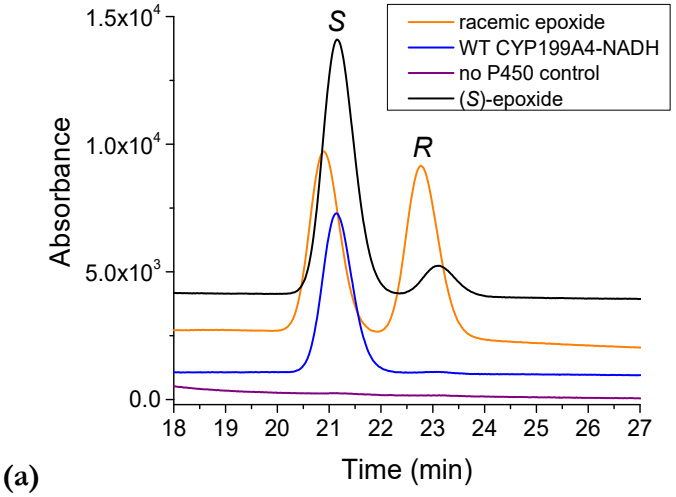

(a)

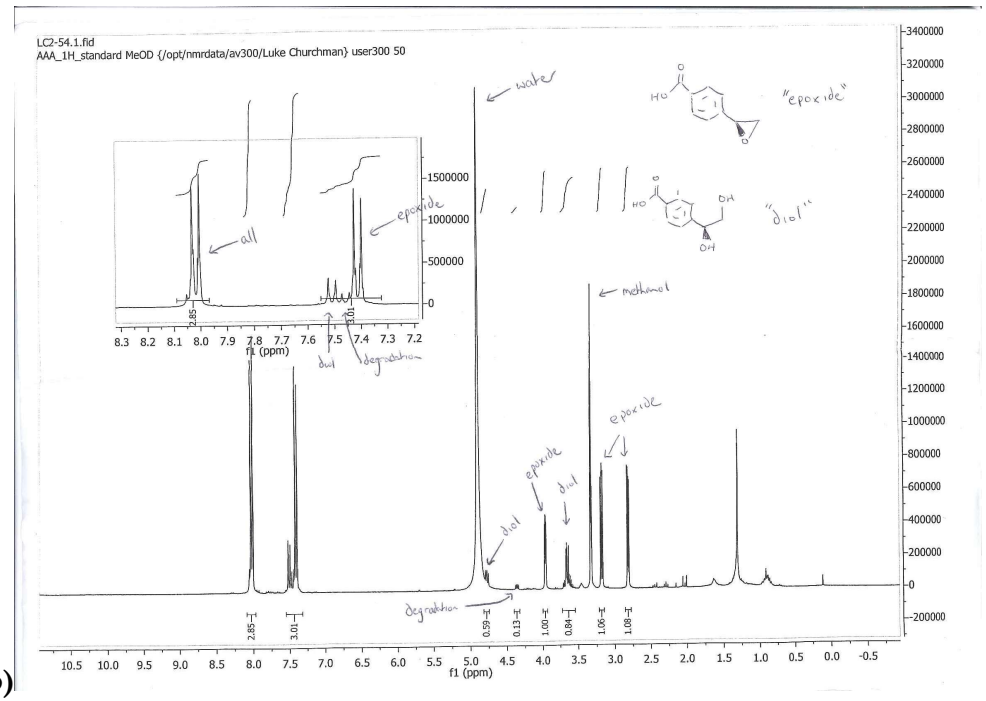

(b)

Figure D33. **(a)** CYP199A4 converts 4-vinylbenzoic acid almost exclusively into the (*S*)-epoxide. In **black** is the (*S*)-enantiomer synthesised by Luke Churchman and James de Voss at the University of Queensland. In **orange** is the racemic epoxide. In **blue** is the epoxide generated by WT CYP199A4 in an NADH-supported reaction and in **purple** is a reaction omitting the P450. **(b)** ^{1}H NMR spectrum of the (*S*)-epoxide supplied by Luke Churchman at the University of Queensland.

Enantioselectivity of NADH- and H_2O_2-driven α-hydroxylation of 4-ethylbenzoic acid catalysed by WT CYP199A4

In NADH-supported reactions, WT CYP199A4 and the D251N and T252A mutants catalysed the α-hydroxylation of 4-ethylbenzoic acid with high enantioselectivity (≥60% ee) (Table D10). These isoforms predominantly gave the (*S*)-enantiomer. In H_2O_2-driven reactions, WT CYP199A4 also gave the (*S*)-enantiomer as the major enantiomer (Figure D34).

In contrast, the T252E mutant displayed low enantioselectivity (~6% ee) and had a small preference for the (*R*)-enantiomer. In H_2O_2-driven reactions, the T252E mutant also had low enantioselectivity (~13% ee) and again favoured the (*R*)-enantiomer.

Table D10. Enantioselectivity of NADH- or H_2O_2-driven α-hydroxylation of 4-ethylbenzoic acid catalysed by CYP199A4 isoforms. The (*S*)-enantiomer eluted at 9.4 min, while the (*R*)-enantiomer eluted at 10.3 min. It has previously been reported that WT CYP199A4 predominantly gives the (*S*)-enantiomer of 4-1-hydroxyethylbenzoic acid in NADH-supported reactions and our ee value for this reaction (76% ee) agrees with the previously published value.[117]

CYP199A4 isoform	Trial	Peak area		Average % ee	Ratio of enantiomers (*S* : *R*)
		(*S*)-enantiomer	(*R*)-enantiomer		
WT-NADH	1	951885	136447	76 ± 1	88 : 12
	2	936077	121132		
	3	299501	43077		
	4	136431	18832		
D251N-NADH	1	417003	27383	87.5 ± 0.4	93.7 : 6.3
	2	388445	26926		
	3	415355	27173		
T252A-NADH	1	213019	52422	60.2 ± 0.4	80.1 : 19.9
	2	211414	53064		
T252E-NADH[a]	1	7160	8229	6 ± 5	47 : 53
	2	7841	8051		
	3	5404	6700		
T252E-60 mM H_2O_2 (60-min reaction)	1	57761	75219	~13	43.4 : 56.6
WT-60 mM H_2O_2 (60-min reaction)	1	5580	1163	59 ± 7	79 : 21
	2	5636	1427		
	3	5616	1810		
Racemic 4-1-hydroxyethyl-benzoic acid		1099642	1100786	0.05	49.97 : 50.03

[a] Note that minor amounts of 4-1-hydroxyethylbenzoic acid were detected in control reactions omitting the P450. The product peak areas in the control reaction were subtracted from the product peak areas in the NADH-driven T252E reaction when calculating the enantioselectivity of the T252E reaction.

Enantioselectivity of H_2O_2-driven α-hydroxylation of 4-ethylbenzoic acid catalysed by WT CYP199A4

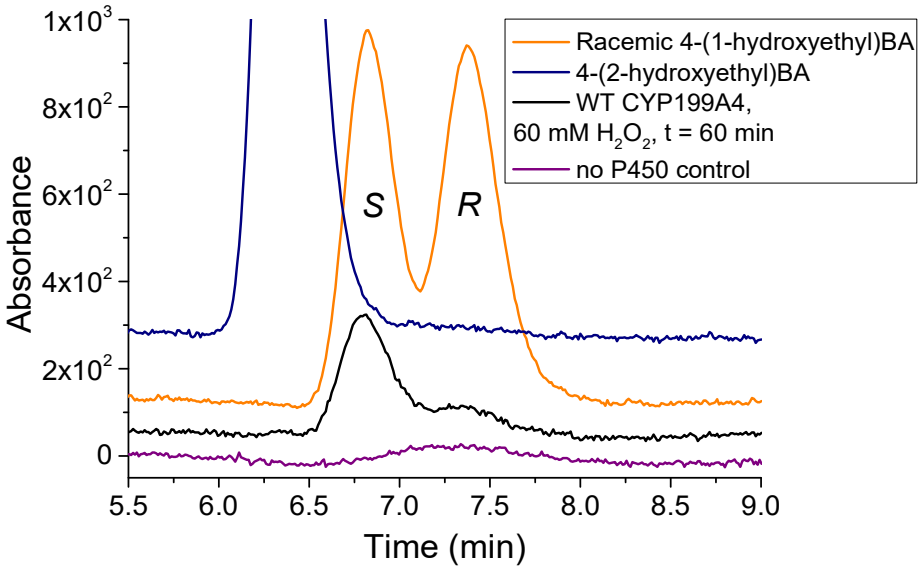

Figure D34. In H_2O_2-driven reactions, WT CYP199A4 performed enantioselective α-hydroxylation of 4-ethylbenzoic acid, giving predominantly the (*S*)-enantiomer. The enantiomeric excess was 59 ± 7%. (The ratio of enantiomers was 79% (*S*)-enantiomer and 21% (*R*)-enantiomer.

Enantioselectivity of 4-ethylthiobenzoic acid sulfoxidation by CYP199A4 isoforms

Table D11. Enantioselectivity of NADH- and H_2O_2-supported sulfoxidation of 4-ethylthiobenzoic acid catalysed by CYP199A4 isoforms. I performed these NADH- and H_2O_2-driven CYP199A4 reactions and synthesised racemic 4-ethylsulfinylbenzoic acid. These reactions were then extracted and sent to the University of Queensland, where the enantioselectivity was measured by Professor James de Voss. The table and figures below were supplied by the University of Queensland.

	Substrate	Enantiomer 1	Enantiomer 2	1:2 ratio	% ee
Racemic sulfoxide	563.703	685.168	699.066	0.98	-
WT_NADH	431.497	390.919	36.872	10.60	83%
T252A_NADH	221.069	112.907	11.17	10.11	82%
T252E_NADH	790.379	35.652	6.839	5.21	68%
D251N_NADH	755.839	44.594	19.958	2.23	38%
WT_6 mM H_2O_2	621.171	56.754	32.382	1.75	27%
T252A_6 mM H_2O_2	3169.367	178.883	124.751	1.43	18%
T252E_6 mM H_2O_2	1850.834	79.859	55.354	1.44	18%
D251N_6 mM H_2O_2	2719.882	145.148	106.376	1.36	15%

Enantiomer numbering based on elution order.

Note that the true enantioselectivity of the H_2O_2-driven sulfoxidation reactions catalysed by the CYP199A4 isoforms could not be determined. H_2O_2 alone can convert sulfides into sulfoxides. In the presence of H_2O_2, formation of racemic sulfoxide through uncatalysed background oxidation of the sulfide would have occurred alongside the P450 reaction (Figure D35).

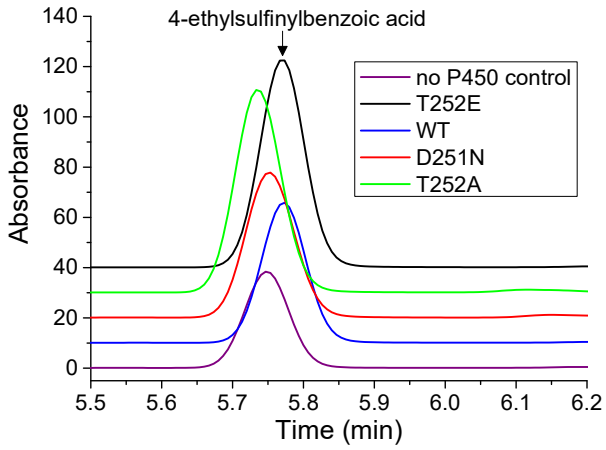

Figure D35. Amount of sulfoxidation of 4-ethylthiobenzoic acid that occurred over a 2-hour period in the presence of 6 mM H_2O_2, with or without P450 present. A substantial amount of sulfoxidation occurred when no P450 was present due to uncatalysed oxidation by H_2O_2 (**purple**).
A considerable portion of the sulfoxide in the T252E (**black**), WT (**blue**), D251N (**red**) and T252A (**green**) reactions would therefore be racemic sulfoxide resulting from background oxidation of the sulfide by H_2O_2.

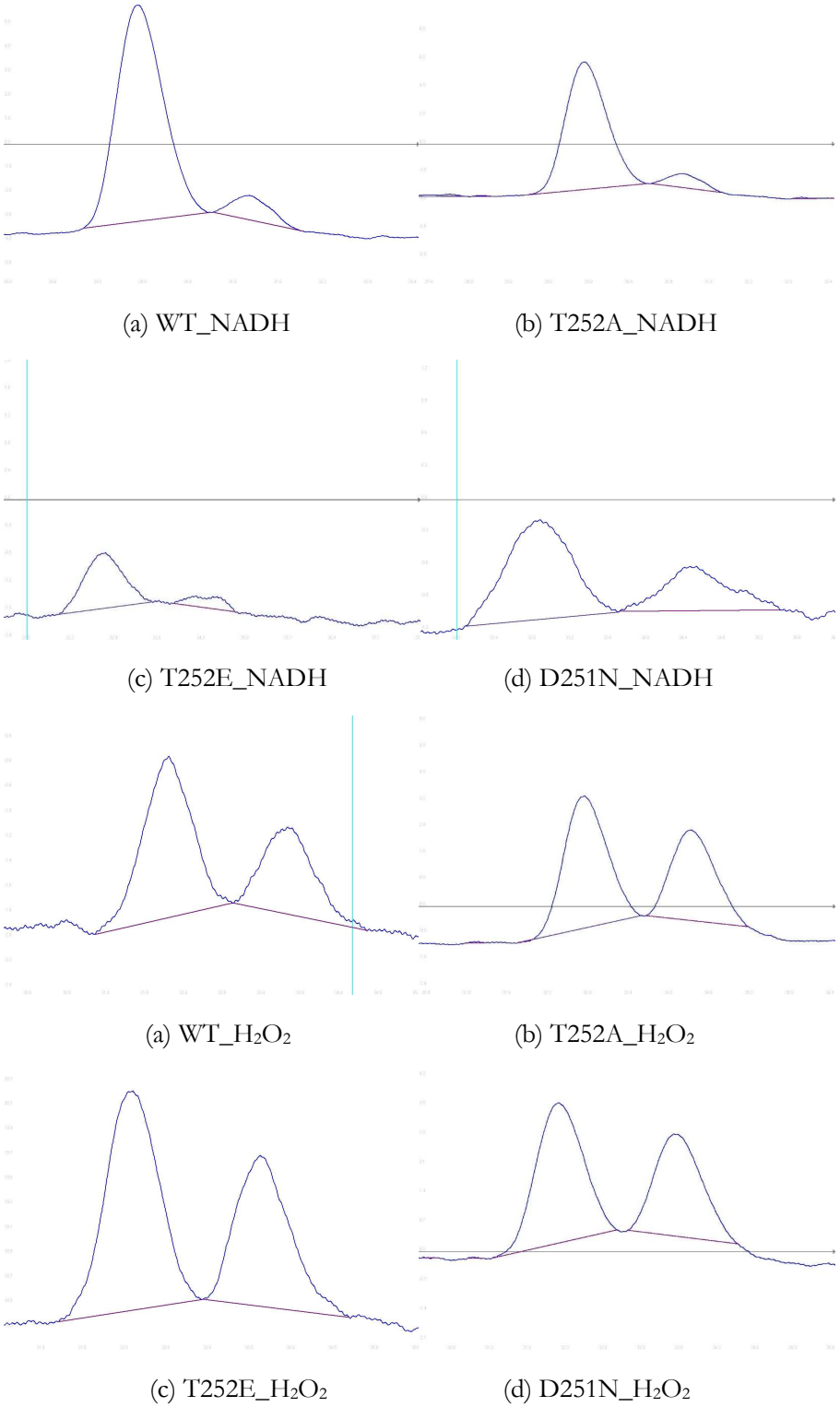

Figure D36. Chiral HPLC analysis of NADH- and H_2O_2-driven sulfoxidation of 4-ethylthiobenzoic acid catalysed by CYP199A4 isoforms. Chiral analysis was performed by Professor James de Voss at the University of Queensland, who supplied the figures. In all cases, the major enantiomer was the first to elute.

Note that the measured enantioselectivity of the reactions is low for the H_2O_2-driven reactions. In the presence of H_2O_2, uncatalysed conversion of 4-ethylthiobenzoic acid into racemic sulfoxide would have occurred alongside the P450 reaction. Because of this background oxidation, we could not determine the true enantioselectivity of the CYP199A4-catalysed reactions.

Use of *t*-BuOOH as a surrogate oxygen donor to drive CYP199A4 reactions

Table D12. Product generated by $T252E_{CYP199A4}$, WT CYP199A4 or the D251N or T252A mutants utilising *t*-BuOOH as the oxygen donor during **60-min** reactions. The values given are mean ± SD, with $n \geq 2$. Reaction volumes were 990 µL and contained 1 mM substrate, 3 µM P450 and **50 mM *t*-BuOOH** in 50 mM Tris-HCl buffer (pH 7.4). Reactions were performed at **30 °C** and were quenched after **60 min**.

Substrate / CYP199A4 isoform	Product concentration (µM)
4-methoxyBA$_{T252E}$	~1
4-methoxyBA$_{WT}$	~0
4-methoxyBA$_{D251N}$	~0
4-methoxyBA$_{T252A}$	~0
4-formylBA$_{T252E}$	11 ± 1
4-vinylBA$_{T252E}$	6 ± 1

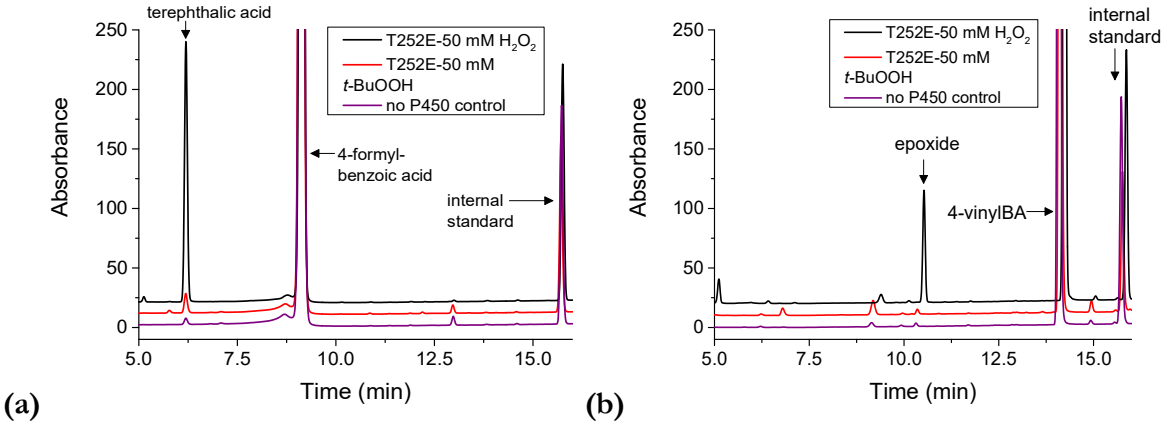

Figure D37. Comparison of the amount of product generated in 1 hour by $T252E_{CYP199A4}$ using either H_2O_2 (**black**) or *t*-BuOOH (**red**) as the surrogate oxygen donor. The oxidant concentration was 50 mM. The substrate was **(a)** 4-formylbenzoic acid or **(b)** 4-vinylbenzoic acid. In **purple** is a control reaction that contained substrate and 50 mM *t*-BuOOH but omitted the P450.

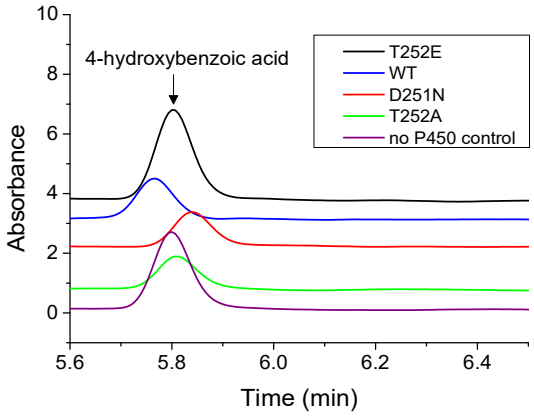

Figure D38. Amount of 4-methoxybenzoic acid converted into 4-hydroxybenzoic acid in 1 hour by CYP199A4 isoforms using 50 mM *t*-BuOOH. In **black** is the T252E reaction, in **blue** the WT reaction, in **red** the D251N reaction and in **green** the T252A reaction. In **purple** is a control reaction omitting the P450.

Appendix E: Dimensions of CYP199A4-ligand crystals

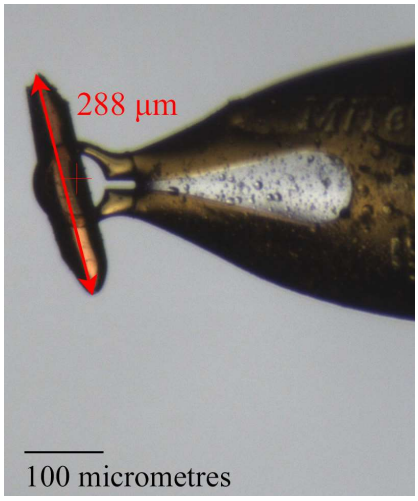

3-MethylthioBA-bound $WT_{CYP199A4}$

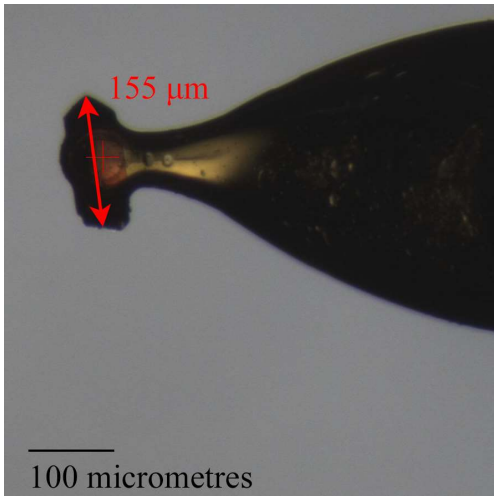

4-*tert*-ButylBA-bound $T252E_{CYP199A4}$

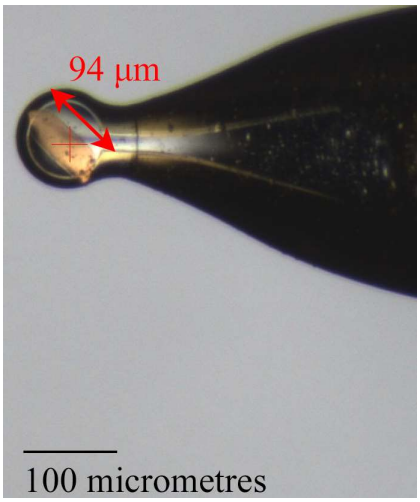

4-Pyridin-2-ylBA-bound $T252E_{CYP199A4}$

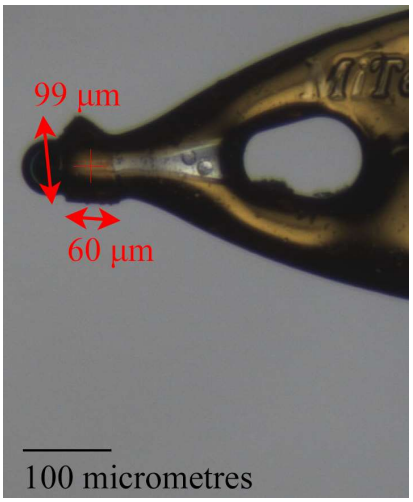

4-Pyridin-3-ylBA-bound $WT_{CYP199A4}$

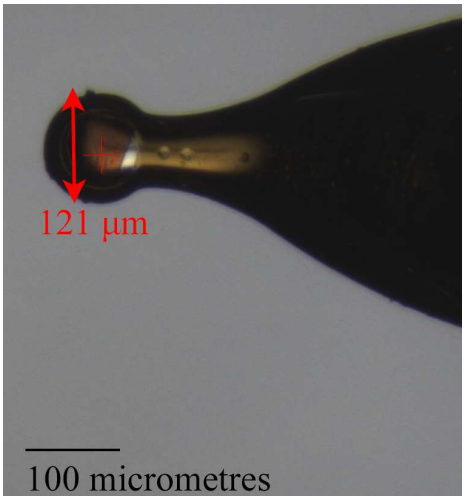

3-MethoxyBA-bound $WT_{CYP199A4}$

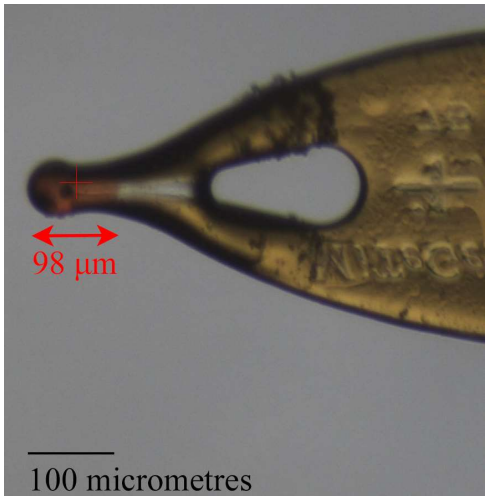

4-EthylthioBA-bound $T252E_{CYP199A4}$

Figure E1. Dimensions of mounted crystals of WT and T252E CYP199A4. Diffraction data were collected from these crystals at the Australian Synchrotron.

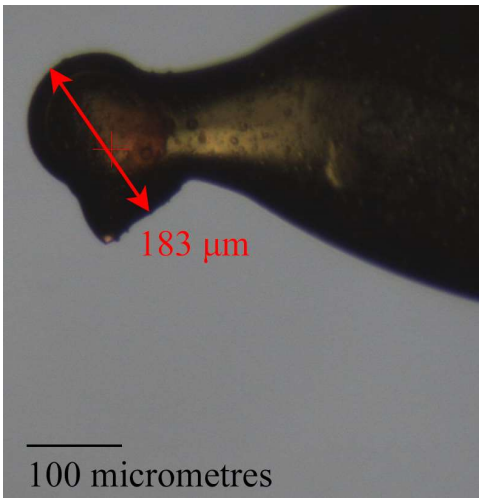

4-Pyridin-3-ylBA-bound $WT_{CYP199A4}$

Figure E1. *(Continued)* Dimensions of mounted crystals of WT and T252E CYP199A4. Diffraction data were collected from these crystals at the Australian Synchrotron.

Reference List

1. Klingenberg, M. Pigments of rat liver microsomes. *Arch. Biochem. Biophys.* **1958**, *75* (2), 376-386.
2. Garfinkel, D. Studies on pig liver microsomes. I. Enzymic and pigment composition of different microsomal fractions. *Arch. Biochem. Biophys.* **1958**, *77* (2), 493-509.
3. Werck-Reichhart, D.; Feyereisen, R. Cytochromes P450: a success story. *Genome Biol.* **2000**, *1* (6), reviews3003.1.
4. Nelson, D. R. The cytochrome P450 homepage. *Human Genomics* **2009**, *4* (1), 59-65.
5. Omura, T.; Sato, R. A New Cytochrome in Liver Microsomes. *J. Biol. Chem.* **1962**, *237* (4), PC1375-PC1376.
6. Omura, T. Pioneers in the Early Years of Cytochrome P450 Research. In *Fifty Years of Cytochrome P450 Research*; Yamazaki, H., Ed.; Springer Japan: Tokyo, 2014; pp 3-16.
7. Ortiz de Montellano, P. R.; De Voss, J. J. Substrate Oxidation by Cytochrome P450 Enzymes. In *Cytochrome P450: Structure, Mechanism, and Biochemistry*; Ortiz de Montellano, P. R., Ed.; Springer US: Boston, MA, 2005; pp 183-245.
8. Coelho, P. S.; Wang, Z. J.; Ener, M. E.; Baril, S. A.; Kannan, A.; Arnold, F. H.; Brustad, E. M. A serine-substituted P450 catalyzes highly efficient carbene transfer to olefins in vivo. *Nat. Chem. Biol.* **2013**, *9*, 485.
9. Yoshioka, S.; Takahashi, S.; Hori, H.; Ishimori, K.; Morishima, I. Proximal cysteine residue is essential for the enzymatic activities of cytochrome $P450_{cam}$. *Eur. J. Biochem.* **2001**, *268* (2), 252-259.
10. Perera, R.; Sono, M.; Voegtle, H. L.; Dawson, J. H. Molecular basis for the inability of an oxygen atom donor ligand to replace the natural sulfur donor heme axial ligand in cytochrome P450 catalysis. Spectroscopic characterization of the Cys436Ser CYP2B4 mutant. *Arch. Biochem. Biophys.* **2011**, *507* (1), 119-125.
11. Murugan, R.; Mazumdar, S. Structure and Redox Properties of the Haem Centre in the C357M Mutant of Cytochrome P450cam. *ChemBioChem* **2005**, *6* (7), 1204-1211.
12. Vatsis, K. P.; Peng, H.-M.; Coon, M. J. Replacement of active-site cysteine-436 by serine converts cytochrome P450 2B4 into an NADPH oxidase with negligible monooxygenase activity. *J. Inorg. Biochem.* **2002**, *91* (4), 542-553.
13. Ortiz de Montellano, P. R. Hydrocarbon Hydroxylation by Cytochrome P450 Enzymes. *Chem. Rev.* **2010**, *110* (2), 932-948.
14. Coelho, P. S.; Brustad, E. M.; Kannan, A.; Arnold, F. H. Olefin Cyclopropanation via Carbene Transfer Catalyzed by Engineered Cytochrome P450 Enzymes. *Science* **2013**, *339* (6117), 307-310.
15. Prier, C. K.; Zhang, R. K.; Buller, A. R.; Brinkmann-Chen, S.; Arnold, F. H. Enantioselective, intermolecular benzylic C–H amination catalysed by an engineered iron-haem enzyme. *Nat. Chem.* **2017**, *9*, 629.
16. Farwell, C. C.; McIntosh, J. A.; Hyster, T. K.; Wang, Z. J.; Arnold, F. H. Enantioselective Imidation of Sulfides via Enzyme-Catalyzed Intermolecular Nitrogen-Atom Transfer. *J. Am. Chem. Soc.* **2014**, *136* (24), 8766-8771.
17. Farwell, C. C.; Zhang, R. K.; McIntosh, J. A.; Hyster, T. K.; Arnold, F. H. Enantioselective Enzyme-Catalyzed Aziridination Enabled by Active-Site Evolution of a Cytochrome P450. *ACS Cent. Sci.* **2015**, *1* (2), 89-93.
18. Guengerich, F. P. Common and Uncommon Cytochrome P450 Reactions Related to Metabolism and Chemical Toxicity. *Chem. Res. Toxicol.* **2001**, *14* (6), 611-650.
19. Oshima, R.; Fushinobu, S.; Su, F.; Zhang, L.; Takaya, N.; Shoun, H. Structural Evidence for Direct Hydride Transfer from NADH to Cytochrome P450nor. *J. Mol. Biol.* **2004**, *342* (1), 207-217.
20. Zhang, X.; Li, S. Expansion of chemical space for natural products by uncommon P450 reactions. *Nat. Prod. Rep.* **2017**, *34* (9), 1061-1089.

21. Lamb, D. C.; Lei, L.; Warrilow, A. G. S.; Lepesheva, G. I.; Mullins, J. G. L.; Waterman, M. R.; Kelly, S. L. The First Virally Encoded Cytochrome P450. *J. Virol.* **2009**, *83* (16), 8266-8269.
22. Nelson, D. R. Cytochrome P450 diversity in the tree of life. *Biochim. Biophys. Acta Proteins Proteom.* **2018**, *1866* (1), 141-154.
23. Schuler, M. A.; Sligar, S. G. Diversities and Similarities in P450 Systems: An Introduction. In *The Ubiquitous Roles of Cytochrome P450 Proteins*; Sigel, A., Sigel, H., Sigel, R. K., Eds.; John Wiley & Sons Ltd: Chichester, 2007.
24. Nelson, D. R.; Schuler, M. A.; Paquette, S. M.; Werck-Reichhart, D.; Bak, S. Comparative Genomics of Rice and Arabidopsis. Analysis of 727 Cytochrome P450 Genes and Pseudogenes from a Monocot and a Dicot. *Plant Physiol.* **2004**, *135* (2), 756-772.
25. Child, S. A.; Naumann, E. F.; Bruning, J. B.; Bell, S. G. Structural and functional characterisation of the cytochrome P450 enzyme CYP268A2 from *Mycobacterium marinum*. *Biochem. J* **2018**, *475* (4), 705-722.
26. Nelson, D. R. Cytochrome P450 Nomenclature, 2004. In *Cytochrome P450 Protocols*; Phillips, I. R., Shephard, E. A., Eds.; Humana Press: Totowa, NJ, 2006; pp 1-10.
27. Plettner, E. Preface: Cytochrome P450. *Biochim. Biophys. Acta Proteins Proteom.* **2018**, *1866* (1), 1.
28. Nelson, D. R.; Kamataki, T.; Waxman, D. J.; Guengerich, F. P.; Estabrook, R. W.; Feyereisen, R.; Gonzalez, F. J.; Coon, M. J.; Gunsalus, I. C.; Gotoh, O.; Okuda, K.; Nebert, D. W. The P450 Superfamily: Update on New Sequences, Gene Mapping, Accession Numbers, Early Trivial Names of Enzymes, and Nomenclature. *DNA Cell Biol.* **1993**, *12* (1), 1-51.
29. Bell, S. G.; Yang, W.; Tan, A. B. H.; Zhou, R.; Johnson, E. O. D.; Zhang, A.; Zhou, W.; Rao, Z.; Wong, L.-L. The crystal structures of 4-methoxybenzoate bound CYP199A2 and CYP199A4: structural changes on substrate binding and the identification of an anion binding site. *Dalton Trans.* **2012**, *41* (28), 8703-8714.
30. Lepesheva, G. I.; Hargrove, T. Y.; Ott, R. D.; Nes, W. D.; Waterman, M. R. Biodiversity of CYP51 in trypanosomes. *Biochem. Soc. Trans.* **2006**, *34* (6), 1161-1164.
31. Bellamine, A.; Lepesheva, G. I.; Waterman, M. R. Fluconazole binding and sterol demethylation in three CYP51 isoforms indicate differences in active site topology. *J. Lipid Res.* **2004**, *45* (11), 2000-2007.
32. Zhang, S.; Zhao, L.; Liu, D.; Wan, J.; Zhang, Q.; Xiao, W. Expression and homology modeling of sterol 14α-demethylase from Penicillium digitatum. *FEMS Microbiol. Lett.* **2007**, *277* (1), 37-43.
33. Jin, S.; Makris, T. M.; Bryson, T. A.; Sligar, S. G.; Dawson, J. H. Epoxidation of Olefins by Hydroperoxo−Ferric Cytochrome P450. *J. Am. Chem. Soc.* **2003**, *125* (12), 3406-3407.
34. Katagiri, M.; Ganguli, B. N.; Gunsalus, I. C. A Soluble Cytochrome P-450 Functional in Methylene Hydroxylation. *J. Biol. Chem.* **1968**, *243* (12), 3543-3546.
35. Poulos, T. L.; Johnson, E. F. Structures of Cytochrome P450 Enzymes. In *Cytochrome P450: Structure, Mechanism, and Biochemistry*; Ortiz de Montellano, P. R., Ed.; Springer International Publishing: Cham, 2015; pp 3-32.
36. Munro, A. W.; Girvan, H. M.; McLean, K. J. Variations on a (t)heme-novel mechanisms, redox partners and catalytic functions in the cytochrome P450 superfamily. *Nat. Prod. Rep.* **2007**, *24* (3), 585-609.
37. Poulos, T. L.; Finzel, B. C.; Howard, A. J. High-resolution crystal structure of cytochrome P450cam. *J. Mol. Biol.* **1987**, *195* (3), 687-700.
38. Nelson, D. R. A world of cytochrome P450s. *Philos. Trans. R. Soc. Lond., B, Biol. Sci. 368* (1612), 20120430-20120430.
39. Structure and Dynamics of Human Drug-Metabolizing Cytochrome P450 Enzymes. In *Drug Metabolism Prediction*.
40. Shaik, S.; Cohen, S.; Wang, Y.; Chen, H.; Kumar, D.; Thiel, W. P450 Enzymes: Their Structure, Reactivity, and Selectivity—Modeled by QM/MM Calculations. *Chem. Rev.* **2010**, *110* (2), 949-1017.
41. Ingelman-Sundberg, M. Genetic polymorphisms of cytochrome P450 2D6 (CYP2D6): clinical consequences, evolutionary aspects and functional diversity. *Pharmacogenomics J.* **2004**, *5*, 6.

42. Vevelstad, M.; Pettersen, S.; Tallaksen, C.; Brørs, O. O-demethylation of codeine to morphine inhibited by low-dose levomepromazine. *Eur. J. Clin. Pharmacol.* **2009**, *65* (8), 795.
43. Carver, P. L. Cytochrome P450 Enzymes: Observations from the Clinic. In *The Ubiquitous Roles of Cytochrome P450 Proteins*; Sigel, A., Sigel, H., Sigel, R. K., Eds.; John Wiley & Sons Ltd: Chichester, 2007.
44. O'Reilly, E.; Kohler, V.; Flitsch, S. L.; Turner, N. J. Cytochromes P450 as useful biocatalysts: addressing the limitations. *Chem. Commun.* **2011**, *47* (9), 2490-2501.
45. Guengerich, F. P. Cytochrome P450 enzymes in the generation of commercial products. *Nat. Rev. Drug Discov.* **2002**, *1* (5), 359.
46. Hrycay, E. G.; Bandiera, S. M. Chapter Two - Involvement of Cytochrome P450 in Reactive Oxygen Species Formation and Cancer. In *Advances in Pharmacology*; Hardwick, J. P., Ed.; Academic Press: 2015; Vol. 74, pp 35-84.
47. Fasan, R. Tuning P450 Enzymes as Oxidation Catalysts. *ACS Catal.* **2012**, *2* (4), 647-666.
48. Kumar, S.; Jin, M.; Weemhoff, J. L. Cytochrome P450-Mediated Phytoremediation using Transgenic Plants: A Need for Engineered Cytochrome P450 Enzymes. *J. Pet. Environ. Biotechnol.* **2012**, *3* (5), 1000127.
49. Kumar, S. Engineering cytochrome P450 biocatalysts for biotechnology, medicine and bioremediation. *Expert Opin. Drug Metab. Toxicol.* **2010**, *6* (2), 115-131.
50. Bell, S. G.; Hoskins, N.; Whitehouse, C. J. C.; Wong, L. L. Design and Engineering of Cytochrome P450 Systems. In *The Ubiquitous Roles of Cytochrome P450 Proteins*; Sigel, A., Sigel, H., Sigel, R. K., Eds.; John Wiley & Sons Ltd: Chichester, 2007.
51. Schulz, S.; Girhard, M.; Gaßmeyer, S. K.; Jäger Vera, D.; Schwarze, D.; Vogel, A.; Urlacher, V. B. Selective Enzymatic Synthesis of the Grapefruit Flavor (+)-Nootkatone. *ChemCatChem* **2015**, *7* (4), 601-604.
52. Bang, L. M.; Goa, K. L. Pravastatin. *Drugs & Aging* **2003**, *20* (14), 1061-1082.
53. Jung, S. T.; Lauchli, R.; Arnold, F. H. Cytochrome P450: taming a wild type enzyme. *Curr. Opin. Biotechnol.* **2011**, *22* (6), 809-817.
54. Joo, H.; Lin, Z.; Arnold, F. H. Laboratory evolution of peroxide-mediated cytochrome P450 hydroxylation. *Nature* **1999**, *399* (6737), 670.
55. Sowden, R. J.; Yasmin, S.; Rees, N. H.; Bell, S. G.; Wong, L.-L. Biotransformation of the sesquiterpene (+)-valencene by cytochrome $P450_{cam}$ and $P450_{BM-3}$. *Org. Biomol. Chem.* **2005**, *3* (1), 57-64.
56. Xu, F.; Bell, S. G.; Lednik, J.; Insley, A.; Rao, Z.; Wong, L. L. The Heme Monooxygenase Cytochrome $P450_{cam}$ Can Be Engineered to Oxidize Ethane to Ethanol. *Angew. Chem. Int. Ed.* **2005**, *44* (26), 4029-4032.
57. Arnold, F. H. Directed Evolution: Bringing New Chemistry to Life. *Angew. Chem. Int. Ed.* **2018**, *57* (16), 4143-4148.
58. O'Driscoll, C. Designer biology. *Chemistry & Industry* **2017**, *81* (3), 30-35.
59. Fraatz, M. A.; Berger, R. G.; Zorn, H. Nootkatone—a biotechnological challenge. *Appl. Microbiol. Biotechnol.* **2009**, *83* (1), 35-41.
60. Tanaka, Y.; Brugliera, F. Flower colour and cytochromes P450. *Philos. Trans. R. Soc. Lond., B, Biol. Sci. 368* (1612), 20120432-20120432.
61. Lilac—the new blue? *Nat. Biotechnol.* **2009**, *27*, 1069.
62. Bernhardt, R.; Urlacher, V. B. Cytochromes P450 as promising catalysts for biotechnological application: chances and limitations. *Appl. Microbiol. Biotechnol.* **2014**, *98* (14), 6185-6203.
63. Nanjaraj Urs, A. N.; Hu, Y.; Li, P.; Yuchi, Z.; Chen, Y.; Zhang, Y. Cloning and Expression of a Nonribosomal Peptide Synthetase to Generate Blue Rose. *ACS Synth. Biol.* **2018**.
64. Rylott, E. L.; Jackson, R. G.; Sabbadin, F.; Seth-Smith, H. M. B.; Edwards, J.; Chong, C. S.; Strand, S. E.; Grogan, G.; Bruce, N. C. The explosive-degrading cytochrome P450 XplA: Biochemistry, structural features and prospects for bioremediation. *Biochim. Biophys. Acta Proteins Proteom.* **2011**, *1814* (1), 230-236.

65. Girhard, M.; Bakkes, P. J.; Mahmoud, O.; Urlacher, V. B. P450 Biotechnology. In *Cytochrome P450: Structure, Mechanism, and Biochemistry*; Ortiz de Montellano, P. R., Ed.; Springer International Publishing: Cham, 2015; pp 451-520.
66. Wong, L.-L.; Westlake, A. C. G.; Nickerson, D. P. Protein engineering of cytochrome $P450_{cam}$. In *Metal Sites in Proteins and Models: Iron Centres*; Hill, H. A. O., Sadler, P. J., Thomson, A. J., Eds.; Springer Berlin Heidelberg: Berlin, Heidelberg, 1997; pp 175-207.
67. Musshoff, F.; Stamer, U. M.; Madea, B. Pharmacogenetics and forensic toxicology. *Forensic Sci. Int.* **2010**, *203* (1), 53-62.
68. Bell-Parikh, L. C.; Guengerich, F. P. Kinetics of Cytochrome P450 2E1-Catalyzed Oxidation of Ethanol to Acetic Acid via Acetaldehyde. *J. Biol. Chem.* **1999**, *274* (34), 23833-23840.
69. Bui, P. H.; Hsu, E. L.; Hankinson, O. Fatty Acid Hydroperoxides Support Cytochrome P450 2S1-Mediated Bioactivation of Benzo[*a*]pyrene-7,8-dihydrodiol. *Mol. Pharmacol.* **2009**, *76* (5), 1044-1052.
70. Denisov, I. G.; Sligar, S. G. Activation of Molecular Oxygen in Cytochromes P450. In *Cytochrome P450: Structure, Mechanism, and Biochemistry*; Ortiz de Montellano, P. R., Ed.; Springer International Publishing: Cham, 2015; pp 69-109.
71. Alexandrov, K.; Rojas, M.; Rolando, C. DNA Damage by Benzo(a)pyrene in Human Cells Is Increased by Cigarette Smoke and Decreased by a Filter Containing Rosemary Extract, Which Lowers Free Radicals. *Cancer Res.* **2006**, *66* (24), 11938-11945.
72. Sadeque, A. J. M.; Fisher, M. B.; Korzekwa, K. R.; Gonzalez, F. J.; Rettie, A. E. Human CYP2C9 and CYP2A6 Mediate Formation of the Hepatotoxin 4-Ene-Valproic Acid. *J. Pharmacol. Exp. Ther.* **1997**, *283* (2), 698-703.
73. Rettie, A. E.; Rettenmeier, A. W.; Howald, W. N.; Baillie, T. A. Cytochrome P-450-Catalyzed Formation of Δ^4-VPA, a Toxic Metabolite of Valproic Acid. *Science* **1987**, *235* (4791), 890-893.
74. Pochapsky, T. C.; Wong, N.; Zhuang, Y.; Futcher, J.; Pandelia, M.-E.; Teitz, D. R.; Colthart, A. M. NADH reduction of nitroaromatics as a probe for residual ferric form high-spin in a cytochrome P450. *Biochim. Biophys. Acta Proteins Proteom.* **2018**, *1866* (1), 126-133.
75. Ciaramella, A.; Minerdi, D.; Gilardi, G. Catalytically self-sufficient cytochromes P450 for green production of fine chemicals. *Rend. Fis. Acc. Lincei* **2017**, *28* (1), 169-181.
76. McLean, K. J.; Luciakova, D.; Belcher, J.; Tee, K. L.; Munro, A. W. Biological Diversity of Cytochrome P450 Redox Partner Systems. In *Monooxygenase, Peroxidase and Peroxygenase Properties and Mechanisms of Cytochrome P450*; Hrycay, E. G., Bandiera, S. M., Eds.; Springer International Publishing: Cham, 2015; pp 299-317.
77. Cryle, M. J.; De Voss, J. J. Carbon–carbon bond cleavage by cytochrome $P450_{BioI}$ (CYP107H1). *Chem. Commun.* **2004**, (1), 86-87.
78. Cryle, Max J. Selectivity in a barren landscape: the $P450_{BioI}$–ACP complex. *Biochem. Soc. Trans.* **2010**, *38* (4), 934-939.
79. Ortiz de Montellano, P. R. Substrate Oxidation by Cytochrome P450 Enzymes. In *Cytochrome P450: Structure, Mechanism, and Biochemistry*; Ortiz de Montellano, P. R., Ed.; Springer International Publishing: Cham, 2015; pp 111-176.
80. Kanhai, W.; Koob, M.; Dekant, W.; Henschler, D. Metabolism of 14C-dichloroethyne in rats. *Xenobiotica* **1991**, *21* (7), 905-916.
81. McMahon, R. E.; Turner, J. C.; Whitaker, G. W.; Sullivan, H. R. Deuterium-isotope effect in the biotransformation of 4-ethynylbiphenyls to 4-biphenylylacetic acids by rat hepatic microsomes. *Biochem. Biophys. Res. Commun.* **1981**, *99* (2), 662-667.
82. Watanabe, Y.; Numata, T.; Iyanagi, T.; Oae, S. Enzymatic Oxidation of Alkyl Sulfides by Cytochrome P-450 and Hydroxyl Radical. *Bull. Chem. Soc. Jpn.* **1981**, *54* (4), 1163-1170.
83. Bu, H. Z. A Literature Review of Enzyme Kinetic Parameters for CYP3A4-Mediated Metabolic Reactions of 113 Drugs in Human Liver Microsomes: Structure- Kinetics Relationship Assessment. *Curr. Drug Metab.* **2006**, *7* (3), 231-249.

84. Shiraga, T.; Kaneko, H.; Iwasaki, K.; Tozuka, Z.; Suzuki, A.; Hata, T. Identification of cytochrome P450 enzymes involved in the metabolism of zotepine, an antipsychotic drug, in human liver microsomes. *Xenobiotica* **1999**, *29* (3), 217-229.
85. Pohl, L. R.; Nelson, S. D.; Krishna, G. Investigation of the mechanism of the metabolic activation of chloramphenicol by rat liver microsomes: Identification of a new metabolite. *Biochem. Pharmacol.* **1978**, *27* (4), 491-496.
86. Oguri, K.; Tanimoto, Y.; Mishima, M.; Yoshimura, H. Metabolic fate of strychnine in rats. *Xenobiotica* **1989**, *19* (2), 171-178.
87. Ladona, M. G.; Gonzalez, M. L.; Rane, A.; Peter, R. M.; de la Torre, R. Cocaine metabolism in human fetal and adult liver microsomes is related to cytochrome P450 3A expression. *Life Sci.* **2000**, *68* (4), 431-443.
88. Biooxidation with Cytochrome P450 Monooxygenases. In *Modern Oxidation Methods*.
89. Barry, S. M.; Kers, J. A.; Johnson, E. G.; Song, L.; Aston, P. R.; Patel, B.; Krasnoff, S. B.; Crane, B. R.; Gibson, D. M.; Loria, R.; Challis, G. L. Cytochrome P450–catalyzed L-tryptophan nitration in thaxtomin phytotoxin biosynthesis. *Nat. Chem. Biol.* **2012**, *8*, 814.
90. Dodani, S. C.; Cahn, J. K. B.; Heinisch, T.; Brinkmann-Chen, S.; McIntosh, J. A.; Arnold, F. H. Structural, Functional, and Spectroscopic Characterization of the Substrate Scope of the Novel Nitrating Cytochrome P450 TxtE. *ChemBioChem* **2014**, *15* (15), 2259-2267.
91. Spracklin, D. K.; Thummel, K. E.; Kharasch, E. D. Human reductive halothane metabolism in vitro is catalyzed by cytochrome P450 2A6 and 3A4. *Drug Metab. Dispos.* **1996**, *24* (9), 976-983.
92. Arnold, F. H. The nature of chemical innovation: new enzymes by evolution. *Q. Rev. Biophys.* **2015**, *48* (4), 404-410.
93. Wang, Z. J.; Renata, H.; Peck, N. E.; Farwell, C. C.; Coelho, P. S.; Arnold, F. H. Improved Cyclopropanation Activity of Histidine-Ligated Cytochrome P450 Enables the Enantioselective Formal Synthesis of Levomilnacipran. *Angew. Chem. Int. Ed.* **2014**, *53* (26), 6810-6813.
94. Modi, A. R.; Dawson, J. H. Oxidizing Intermediates in P450 Catalysis: A Case for Multiple Oxidants. In *Monooxygenase, Peroxidase and Peroxygenase Properties and Mechanisms of Cytochrome P450*; Hrycay, E. G., Bandiera, S. M., Eds.; Springer International Publishing: Cham, 2015; pp 63-81.
95. Barry, S. M.; Challis, G. L. Chapter Nine - Tailoring Reactions Catalyzed by Heme-Dependent Enzymes: Spectroscopic Characterization of the L-Tryptophan-Nitrating Cytochrome P450 TxtE. In *Methods Enzymol.*; Hopwood, D. A., Ed.; Academic Press: 2012; Vol. 516, pp 171-194.
96. Groves, J. T. Key elements of the chemistry of cytochrome P-450: The oxygen rebound mechanism. *J. Chem. Educ.* **1985**, *62* (11), 928.
97. Poulos, T. L.; Raag, R. Cytochrome $P450_{cam}$: crystallography, oxygen activation, and electron transfer. *FASEB J.* **1992**, *6* (2), 674-679.
98. Schlichting, I.; Berendzen, J.; Chu, K.; Stock, A. M.; Maves, S. A.; Benson, D. E.; Sweet, R. M.; Ringe, D.; Petsko, G. A.; Sligar, S. G. The Catalytic Pathway of Cytochrome P450cam at Atomic Resolution. *Science* **2000**, *287* (5458), 1615-1622.
99. Poulos, T. L.; Finzel, B. C.; Gunsalus, I. C.; Wagner, G. C.; Kraut, J. The 2.6-Å crystal structure of Pseudomonas putida cytochrome P-450. *J. Biol. Chem.* **1985**, *260* (30), 16122-30.
100. Honeychurch, M. J.; Hill, H. A. O.; Wong, L.-L. The thermodynamics and kinetics of electron transfer in the cytochrome $P450_{cam}$ enzyme system. *FEBS Lett.* **1999**, *451* (3), 351-353.
101. Conner, K. P.; Woods, C. M.; Atkins, W. M. Interactions of cytochrome P450s with their ligands. *Arch. Biochem. Biophys.* **2011**, *507* (1), 56-65.
102. Correia, M. A.; Ortiz de Montellano, P. R. Inhibition of Cytochrome P450 Enzymes. In *Cytochrome P450: Structure, Mechanism, and Biochemistry*; Ortiz de Montellano, P. R., Ed.; Springer US: Boston, MA, 2005; pp 247-322.
103. Rittle, J.; Green, M. T. Cytochrome P450 Compound I: Capture, Characterization, and C-H Bond Activation Kinetics. *Science* **2010**, *330* (6006), 933-937.
104. Yosca, T. H.; Green, M. T. Preparation of Compound I in $P450_{cam}$: The Prototypical P450. *Isr. J. Chem.* **2016**, *56* (9-10), 834-840.

105. Blanksby, S. J.; Ellison, G. B. Bond Dissociation Energies of Organic Molecules. *Acc. Chem. Res.* **2003**, *36* (4), 255-263.
106. Hrycay, E. G.; Bandiera, S. M. Monooxygenase, Peroxidase and Peroxygenase Properties and Reaction Mechanisms of Cytochrome P450 Enzymes. In *Monooxygenase, Peroxidase and Peroxygenase Properties and Mechanisms of Cytochrome P450*; Hrycay, E. G., Bandiera, S. M., Eds.; Springer International Publishing: Cham, 2015; pp 1-61.
107. Perera, R.; Jin, S.; Sono, M.; Dawson, J. H. Cytochrome P450-Catalyzed Hydroxylations and Epoxidations. In *The Ubiquitous Roles of Cytochrome P450 Proteins*; Sigel, A., Sigel, H., Sigel, R. K., Eds.; John Wiley & Sons Ltd: Chichester, 2007.
108. Hayakawa, S.; Matsumura, H.; Nakamura, N.; Yohda, M.; Ohno, H. Identification of the rate-limiting step of the peroxygenase reactions catalyzed by the thermophilic cytochrome P450 from *Sulfolobus tokodaii* strain 7. *FEBS J.* **2014**, *281* (5), 1409-1416.
109. Crowell, R. A.; Lian, R.; Sauer, M. C.; Oulianov, D. A.; Shkrob, I. A. Geminate recombination of hydroxyl radicals generated in 200 nm photodissociation of aqueous hydrogen peroxide. *Chem. Phys. Lett.* **2004**, *383* (5), 481-485.
110. Poulos, T. L. Heme Enzyme Structure and Function. *Chem. Rev.* **2014**, *114* (7), 3919-3962.
111. Raimund, N.; J., P. R. Diverging Mechanisms: Cytochrome-P450-Catalyzed Demethylation and γ-Lactone Formation in Bacterial Gibberellin Biosynthesis. *Angew. Chem. Int. Ed.* **2018**, *57* (21), 6082-6085.
112. C., C. P.; H., A. F. A Self-Sufficient Peroxide-Driven Hydroxylation Biocatalyst. *Angew. Chem. Int. Ed.* **2003**, *42* (28), 3299-3301.
113. Ma, N.; Chen, Z.; Chen, J.; Chen, J.; Wang, C.; Zhou, H.; Yao, L.; Shoji, O.; Watanabe, Y.; Cong, Z. Dual-Functional Small Molecules for Generating an Efficient Cytochrome P450BM3 Peroxygenase. *Angew. Chem. Int. Ed.* **2018**, *57* (26), 7628-7633.
114. Whitehouse, C. J. C.; Bell, S. G.; Wong, L.-L. P450BM3 (CYP102A1): connecting the dots. *Chem. Soc. Rev.* **2012**, *41* (3), 1218-1260.
115. Makris, T. M.; Denisov, I.; Schlichting, I.; Sligar, S. G. Activation of Molecular Oxygen by Cytochrome P450. In *Cytochrome P450: Structure, Mechanism, and Biochemistry*; Ortiz de Montellano, P. R., Ed.; Springer US: Boston, MA, 2005; pp 149-182.
116. Kadkhodayan, S.; Coulter, E. D.; Maryniak, D. M.; Bryson, T. A.; Dawson, J. H. Uncoupling Oxygen Transfer and Electron Transfer in the Oxygenation of Camphor Analogues by Cytochrome P450-CAM: Direct Observation of an Intermolecular Isotope Effect for Substrate C-H Activation. *J. Biol. Chem.* **1995**, *270* (47), 28042-28048.
117. Coleman, T.; Wong, S. H.; Podgorski, M. N.; Bruning, J. B.; De Voss, J. J.; Bell, S. G. Cytochrome P450 CYP199A4 from *Rhodopseudomonas palustris* Catalyzes Heteroatom Dealkylations, Sulfoxidation, and Amide and Cyclic Hemiacetal Formation. *ACS Catal.* **2018**, 5915-5927.
118. Wang, B.; Li, C.; Cho, K.-B.; Nam, W.; Shaik, S. The $Fe^{III}(H_2O_2)$ Complex as a Highly Efficient Oxidant in Sulfoxidation Reactions: Revival of an Underrated Oxidant in Cytochrome P450. *J. Chem. Theory Comput.* **2013**, *9* (6), 2519-2525.
119. Litzenburger, M.; Izzo, R. L.; Bernhardt, R.; Khatri, Y. Investigating the roles of T224 and T232 in the oxidation of cinnamaldehyde catalyzed by myxobacterial CYP260B1. *FEBS Lett.* **2016**, *591* (1), 39-46.
120. Vaz, A. D.; Pernecky, S. J.; Raner, G. M.; Coon, M. J. Peroxo-iron and oxenoid-iron species as alternative oxygenating agents in cytochrome P450-catalyzed reactions: switching by threonine-302 to alanine mutagenesis of cytochrome P450 2B4. *Proc. Natl. Acad. Sci. U.S.A.* **1996**, *93* (10), 4644-4648.
121. Vaz, A. D. N.; McGinnity, D. F.; Coon, M. J. Epoxidation of olefins by cytochrome P450: Evidence from site-specific mutagenesis for hydroperoxo-iron as an electrophilic oxidant. *Proc. Natl. Acad. Sci. U.S.A.* **1998**, *95* (7), 3555-3560.
122. Kells, P. M.; Ouellet, H.; Santos-Aberturas, J.; Aparicio, J. F.; Podust, L. M. Structure of Cytochrome P450 PimD Suggests Epoxidation of the Polyene Macrolide Pimaricin Occurs via a Hydroperoxoferric Intermediate. *Chemistry & Biology* **2010**, *17* (8), 841-851.

123. Cryle, M. J.; Voss, J. J. D. Is the Ferric Hydroperoxy Species Responsible for Sulfur Oxidation in Cytochrome P450s? *Angew. Chem. Int. Ed.* **2006**, *45* (48), 8221-8223.
124. Volz, T. J.; Rock, D. A.; Jones, J. P. Evidence for Two Different Active Oxygen Species in Cytochrome P450 BM3 Mediated Sulfoxidation and N-Dealkylation Reactions. *J. Am. Chem. Soc.* **2002**, *124* (33), 9724-9725.
125. Newcomb, M.; Toy, P. H. Hypersensitive Radical Probes and the Mechanisms of Cytochrome P450-Catalyzed Hydroxylation Reactions. *Acc. Chem. Res.* **2000**, *33* (7), 449-455.
126. Sharma, P. K.; de Visser, S. P.; Shaik, S. Can a Single Oxidant with Two Spin States Masquerade as Two Different Oxidants? A Study of the Sulfoxidation Mechanism by Cytochrome P450. *J. Am. Chem. Soc.* **2003**, *125* (29), 8698-8699.
127. Munro, A. W.; McLean, K. J.; Grant, J. L.; Makris, T. M. Structure and function of the cytochrome P450 peroxygenase enzymes. *Biochem. Soc. Trans.* **2018**.
128. Nagano, S. Structural and Functional Diversity of Cytochrome P450. In *Fifty Years of Cytochrome P450 Research*; Yamazaki, H., Ed.; Springer Japan: Tokyo, 2014; pp 95-106.
129. Nagano, S.; Poulos, T. L. Crystallographic Study on the Dioxygen Complex of Wild-type and Mutant Cytochrome P450cam: Implications for the Dioxygen Activation Mechanism. *J. Biol. Chem.* **2005**, *280* (36), 31659-31663.
130. Imai, M.; Shimada, H.; Watanabe, Y.; Matsushima-Hibiya, Y.; Makino, R.; Koga, H.; Horiuchi, T.; Ishimura, Y. Uncoupling of the cytochrome P-450cam monooxygenase reaction by a single mutation, threonine-252 to alanine or valine: possible role of the hydroxy amino acid in oxygen activation. *Proc. Natl. Acad. Sci. U.S.A.* **1989**, *86* (20), 7823-7827.
131. Kimata, Y.; Shimada, H.; Hirose, T.; Ishimura, Y. Role of THR-252 in Cytochrome $P450_{CAM}$: A Study with Unnatural Amino Acid Mutagenesis. *Biochem. Biophys. Res. Commun.* **1995**, *208* (1), 96-102.
132. Raag, R.; Martinis, S. A.; Sligar, S. G.; Poulos, T. L. Crystal structure of the cytochrome $P-450_{CAM}$ active site mutant Thr252Ala. *Biochemistry* **1991**, *30* (48), 11420-11429.
133. Vidakovic, M.; Sligar, S. G.; Li, H.; Poulos, T. L. Understanding the Role of the Essential Asp251 in Cytochrome P450cam Using Site-Directed Mutagenesis, Crystallography, and Kinetic Solvent Isotope Effect. *Biochemistry* **1998**, *37* (26), 9211-9219.
134. Dubey, K. D.; Wang, B.; Vajpai, M.; Shaik, S. MD simulations and QM/MM calculations show that single-site mutations of cytochrome P450BM3 alter the active site's complexity and the chemoselectivity of oxidation without changing the active species. *Chem. Sci.* **2017**, *8* (8), 5335-5344.
135. Hannemann, F.; Bichet, A.; Ewen, K. M.; Bernhardt, R. Cytochrome P450 systems—biological variations of electron transport chains. *Biochim. Biophys. Acta Gen. Subj.* **2007**, *1770* (3), 330-344.
136. Cook, D. J.; Finnigan, J. D.; Cook, K.; Black, G. W.; Charnock, S. J. Chapter Five - Cytochromes P450: History, Classes, Catalytic Mechanism, and Industrial Application. In *Advances in Protein Chemistry and Structural Biology*; Christov, C. Z., Ed.; Academic Press: 2016; Vol. 105, pp 105-126.
137. Bell, S. G.; Tan, A. B. H.; Johnson, E. O. D.; Wong, L.-L. Selective oxidative demethylation of veratric acid to vanillic acid by CYP199A4 from *Rhodopseudomonas palustris* HaA2. *Mol. BioSyst.* **2009**, *6* (1), 206-214.
138. Zhang, T.; Zhang, A.; Bell, S. G.; Wong, L. L.; Zhou, W. The structure of a novel electron-transfer ferredoxin from Rhodopseudomonas palustris HaA2 which contains a histidine residue in its iron–sulfur cluster-binding motif. *Acta Crystallogr. Sect. D. Biol. Crystallogr.* **2014**, *70* (5), 1453-1464.
139. Schiffler, B.; Bernhardt, R. Bacterial (CYP101) and mitochondrial P450 systems—how comparable are they? *Biochem. Biophys. Res. Commun.* **2003**, *312* (1), 223-228.
140. Bernhardt, R.; Waterman, M. R. Cytochrome P450 and Steroid Hormone Biosynthesis. In *The Ubiquitous Roles of Cytochrome P450 Proteins*; Sigel, A., Sigel, H., Sigel, R. K., Eds.; John Wiley & Sons Ltd: Chichester, 2007.

141. Lamb, D. C.; Waterman, M. R. Fifty Years of Cytochrome P450 Research: Examples of What We Know and Do Not Know. In *Fifty Years of Cytochrome P450 Research*; Yamazaki, H., Ed.; Springer Japan: Tokyo, 2014; pp 43-71.
142. McLean, K. J.; Sabri, M.; Marshall, K. R.; Lawson, R. J.; Lewis, D. G.; Clift, D.; Balding, P. R.; Dunford, A. J.; Warman, A. J.; McVey, J. P.; Quinn, A.-M.; Sutcliffe, M. J.; Scrutton, N. S.; Munro, A. W. Biodiversity of cytochrome P450 redox systems. *Biochem. Soc. Trans.* **2005**, *33* (4), 796-801.
143. Waskell, L.; Kim, J.-J. P. Electron Transfer Partners of Cytochrome P450. In *Cytochrome P450: Structure, Mechanism, and Biochemistry*; Ortiz de Montellano, P. R., Ed.; Springer International Publishing: Cham, 2015; pp 33-68.
144. Puchkaev, A. V.; Wakagi, T.; Ortiz de Montellano, P. R. CYP119 Plus a Sulfolobus tokodaii Strain 7 Ferredoxin and 2-Oxoacid:Ferredoxin Oxidoreductase Constitute a High-Temperature Cytochrome P450 Catalytic System. *J. Am. Chem. Soc.* **2002**, *124* (43), 12682-12683.
145. Narhi, L. O.; Fulco, A. J. Identification and characterization of two functional domains in cytochrome P-450BM-3, a catalytically self-sufficient monooxygenase induced by barbiturates in Bacillus megaterium. *J. Biol. Chem.* **1987**, *262* (14), 6683-6690.
146. Guengerich, F. P.; Munro, A. W. Unusual Cytochrome P450 Enzymes and Reactions. *J. Biol. Chem.* **2013**, *288* (24), 17065-17073.
147. Noble, M. A.; Miles, C. S.; Chapman, S. K.; Lysek, D. A.; Mackay, A. C.; Reid, G. A.; Hanzlik, R. P.; Munro, A. W. Roles of key active-site residues in flavocytochrome P450 BM3. *Biochem. J.* **1999**, *339 (Pt 2)*, 371.
148. Nakayama, N.; Takemae, A.; Shoun, H. Cytochrome P450foxy, a Catalytically Self-Sufficient Fatty Acid Hydroxylase of the Fungus *Fusarium oxysporum*. *J. Biochem.* **1996**, *119* (3), 435-440.
149. Lamb, D. C.; Waterman, M. R. Unusual properties of the cytochrome P450 superfamily. *Philos. Trans. R. Soc. Lond., B, Biol. Sci.* **2013**, *368* (1612), 1-13.
150. Brash, A. R. Mechanistic aspects of CYP74 allene oxide synthases and related cytochrome P450 enzymes. *Phytochemistry* **2009**, *70* (13), 1522-1531.
151. Aguey-Zinsou, K.-F.; Bernhardt, P. V.; De Voss, J. J.; Slessor, K. E. Electrochemistry of P450cin: new insights into P450 electron transfer. *Chem. Commun.* **2003**, (3), 418-419.
152. Daff, S. N.; Chapman, S. K.; Holt, R. A.; Govindaraj, S.; Poulos, T. L.; Munro, A. W. Redox Control of the Catalytic Cycle of Flavocytochrome P-450 BM3. *Biochemistry* **1997**, *36* (45), 13816-13823.
153. Harbort, J. S.; De Voss, J. J.; Stok, J. E.; Bell, S. G.; Harmer, J. R. CW and Pulse EPR of Cytochrome P450 to Determine Structure and Function. In *Future Directions in Metalloprotein and Metalloenzyme Research*; Hanson, G., Berliner, L., Eds.; Springer International Publishing: Cham, 2017; pp 103-142.
154. Conner, K. P.; Vennam, P.; Woods, C. M.; Krzyaniak, M. D.; Bowman, M. K.; Atkins, W. M. 1,2,3-Triazole–Heme Interactions in Cytochrome P450: Functionally Competent Triazole–Water–Heme Complexes. *Biochemistry* **2012**, *51* (32), 6441-6457.
155. Conner, K. P.; Cruce, A. A.; Krzyaniak, M. D.; Schimpf, A. M.; Frank, D. J.; Ortiz de Montellano, P.; Atkins, W. M.; Bowman, M. K. Drug Modulation of Water–Heme Interactions in Low-Spin P450 Complexes of CYP2C9d and CYP125A1. *Biochemistry* **2015**, *54* (5), 1198-1207.
156. Mast, N.; Charvet, C.; Pikuleva, I. A.; Stout, C. D. Structural Basis of Drug Binding to CYP46A1, an Enzyme That Controls Cholesterol Turnover in the Brain. *J. Biol. Chem.* **2010**, *285* (41), 31783-31795.
157. Locuson, C. W.; Hutzler, J. M.; Tracy, T. S. Visible Spectra of Type II Cytochrome P450-Drug Complexes: Evidence that "Incomplete" Heme Coordination Is Common. *Drug Metab. Dispos.* **2007**, *35* (4), 614-622.
158. Lockart, M. M.; Rodriguez, C. A.; Atkins, W. M.; Bowman, M. K. CW EPR parameters reveal cytochrome P450 ligand binding modes. *J. Inorg. Biochem.* **2018**, *183*, 157-164.
159. Seward, H. E.; Roujeinikova, A.; McLean, K. J.; Munro, A. W.; Leys, D. Crystal Structure of the *Mycobacterium tuberculosis* P450 CYP121-Fluconazole Complex Reveals New Azole Drug-P450 Binding Mode. *J. Biol. Chem.* **2006**, *281* (51), 39437-39443.

160. Correia, M. A.; Hollenberg, P. F. Inhibition of Cytochrome P450 Enzymes. In *Cytochrome P450: Structure, Mechanism, and Biochemistry*; Ortiz de Montellano, P. R., Ed.; Springer International Publishing: Cham, 2015; pp 177-259.
161. Ouellet, H.; Kells, P. M.; Ortiz de Montellano, P. R.; Podust, L. M. Reverse type I inhibitor of *Mycobacterium tuberculosis* CYP125A1. *Bioorg. Med. Chem. Lett.* **2011**, *21* (1), 332-337.
162. Coleman, T.; Chao, R. R.; Bruning, J. B.; De Voss, J. J.; Bell, S. G. CYP199A4 catalyses the efficient demethylation and demethenylation of *para*-substituted benzoic acid derivatives. *RSC Adv.* **2015**, *5* (64), 52007-52018.
163. Suzuki, H.; Inabe, K.; Shirakawa, Y.; Umezawa, N.; Kato, N.; Higuchi, T. Role of Thiolate Ligand in Spin State and Redox Switching in the Cytochrome P450 Catalytic Cycle. *Inorg. Chem.* **2017**, *56* (8), 4245-4248.
164. Sono, M.; Dawson, J. H. Formation of low spin complexes of ferric cytochrome P-450-CAM with anionic ligands. Spin state and ligand affinity comparison to myoglobin. *J. Biol. Chem.* **1982**, *257* (10), 5496-5502.
165. Colthart, A. M.; Tietz, D. R.; Ni, Y.; Friedman, J. L.; Dang, M.; Pochapsky, T. C. Detection of substrate-dependent conformational changes in the P450 fold by nuclear magnetic resonance. *Sci. Rep.* **2016**, *6*, 22035.
166. Raag, R.; Poulos, T. L. Crystal structures of cytochrome P-450CAM complexed with camphane, thiocamphor, and adamantane: factors controlling P-450 substrate hydroxylation. *Biochemistry* **1991**, *30* (10), 2674-2684.
167. Raag, R.; Poulos, T. L. The structural basis for substrate-induced changes in redox potential and spin equilibrium in cytochrome P-450$_{CAM}$. *Biochemistry* **1989**, *28* (2), 917-922.
168. Lochner, M.; Mu, L.; Woggon, W. D. Remote Effects Modulating the Spin Equilibrium of the Resting State of Cytochrome P450$_{cam}$ – An Investigation Using Active Site Analogues. *Adv. Synth. Catal.* **2003**, *345* (6-7), 743-765.
169. Lochner, M.; Meuwly, M.; Woggon, W.-D. The origin of the low-spin character of the resting state of cytochrome P450cam investigated by means of active site analogues. *Chem. Commun.* **2003**, (12), 1330-1332.
170. Aissaoui, H.; Bachmann, R.; Schweiger, A.; Woggon, W.-D. On the Origin of the Low-Spin Character of Cytochrome P450cam in the Resting State—Investigations of Enzyme Models with Pulse EPR and ENDOR Spectroscopy. *Angew. Chem. Int. Ed.* **1998**, *37* (21), 2998-3002.
171. Thomann, H.; Bernardo, M.; Goldfarb, D.; Kroneck, P. M. H.; Ullrich, V. Evidence for Water Binding to the Fe Center in Cytochrome P450cam Obtained by ^{17}O Electron Spin-Echo Envelope Modulation Spectroscopy. *J. Am. Chem. Soc.* **1995**, *117* (31), 8243-8251.
172. Goldfarb, D.; Bernardo, M.; Thomann, H.; Kroneck, P. M. H.; Ullrich, V. Study of Water Binding to Low-Spin Fe(III) in Cytochrome P450 by Pulsed ENDOR and Four-Pulse ESEEM Spectroscopies. *J. Am. Chem. Soc.* **1996**, *118* (11), 2686-2693.
173. Luthra, A.; Denisov, I. G.; Sligar, S. G. Spectroscopic features of cytochrome P450 reaction intermediates. *Arch. Biochem. Biophys.* **2011**, *507* (1), 26-35.
174. Harford-Cross, C. F.; Carmichael, A. B.; Allan, F. K.; England, P. A.; Rouch, D. A.; Wong, L.-L. Protein engineering of cytochrome P450cam (CYP101) for the oxidation of polycyclic aromatic hydrocarbons. *Protein Eng. Des. Sel.* **2000**, *13* (2), 121-128.
175. Blanck, J.; Rein, H.; Sommer, M.; Ristau, O.; Smettan, G.; Ruckpaul, K. Correlations between spin equilibrium shift, reduction rate, and N-demethylation activity in liver microsomal cytochrome P-450 and a series of benzphetamine analogues as substrates. *Biochem. Pharmacol.* **1983**, *32* (11), 1683-1688.
176. Atkins, W. M.; Sligar, S. G. The roles of active site hydrogen bonding in cytochrome P-450cam as revealed by site-directed mutagenesis. *J. Biol. Chem.* **1988**, *263* (35), 18842-9.
177. Bell, S. G.; Chen, X.; Sowden, R. J.; Xu, F.; Williams, J. N.; Wong, L.-L.; Rao, Z. Molecular Recognition in (+)-α-Pinene Oxidation by Cytochrome P450cam. *J. Am. Chem. Soc.* **2003**, *125* (3), 705-714.
178. Sibbesen, O.; Zhang, Z.; Ortiz de Montellano, P. R. Cytochrome P450$_{cam}$ Substrate Specificity: Relationship between Structure and Catalytic Oxidation of Alkylbenzenes. *Arch. Biochem. Biophys.* **1998**, *353* (2), 285-296.

179. Fisher, M. T.; Sligar, S. G. Control of heme protein redox potential and reduction rate: linear free energy relation between potential and ferric spin state equilibrium. *J. Am. Chem. Soc.* **1985**, *107* (17), 5018-5019.
180. Bell, S. G.; Yang, W.; Yorke, J. A.; Zhou, W.; Wang, H.; Harmer, J.; Copley, R.; Zhang, A.; Zhou, R.; Bartlam, M.; Rao, Z.; Wong, L. L. Structure and function of CYP108D1 from Novosphingobium aromaticivorans DSM12444: an aromatic hydrocarbon-binding P450 enzyme. *Acta Crystallogr. Sect. D. Biol. Crystallogr.* **2012**, *68* (3), 277-291.
181. Coleman, T.; Chao, R. R.; De Voss, J. J.; Bell, S. G. The importance of the benzoic acid carboxylate moiety for substrate recognition by CYP199A4 from *Rhodopseudomonas palustris* HaA2. *Biochim. Biophys. Acta Proteins Proteom.* **2016**, *1864* (6), 667-675.
182. Wong, L.-L.; Bell, S. G. Iron: Heme Proteins, Mono- & Dioxygenases Based in part on the article Iron: Heme Proteins, Mono- & Dioxygenases by Masanori Sono & John H. Dawson which appeared in the Encyclopedia of Inorganic Chemistry, First Edition. *Encyclopedia of Inorganic Chemistry* **2006**.
183. Ortiz de Montellano, P. R.; Stearns, R. A. Timing of the radical recombination step in cytochrome P-450 catalysis with ring-strained probes. *J. Am. Chem. Soc.* **1987**, *109* (11), 3415-3420.
184. Auclair, K.; Hu, Z.; Little, D. M.; Ortiz de Montellano, P. R.; Groves, J. T. Revisiting the Mechanism of P450 Enzymes with the Radical Clocks Norcarane and Spiro[2,5]octane. *J. Am. Chem. Soc.* **2002**, *124* (21), 6020-6027.
185. Newcomb, M.; Shen, R.; Choi, S.-Y.; Toy, P. H.; Hollenberg, P. F.; Vaz, A. D. N.; Coon, M. J. Cytochrome P450-catalyzed hydroxylation of mechanistic probes that distinguish between radicals and cations. Evidence for cationic but not for radical intermediates. *J. Am. Chem. Soc.* **2000**, *122* (12), 2677-2686.
186. Visser, S.; S. Porro, C.; Quesne, M.; Sainna, M.; Munro, A. Overview on Theoretical Studies Discriminating the Two-Oxidant Versus Two-State-Reactivity Models for Substrate Monoxygenation by Cytochrome P450 Enzymes. *Curr. Top. Med. Chem.* **2013**, *13*, 2218-2232.
187. Shaik, S.; Hirao, H.; Kumar, D. Reactivity patterns of cytochrome P450 enzymes: multifunctionality of the active species, and the two states–two oxidants conundrum. *Nat. Prod. Rep.* **2007**, *24* (3), 533-552.
188. Jin, S.; Bryson, T. A.; Dawson, J. H. Hydroperoxoferric heme intermediate as a second electrophilic oxidant in cytochrome P450-catalyzed reactions. *J. Biol. Inorg. Chem.* **2004**, *9* (6), 644-653.
189. Shaik, S.; Cohen, S.; de Visser, Samuël P.; Sharma, Pankaz K.; Kumar, D.; Kozuch, S.; Ogliaro, F.; Danovich, D. The "Rebound Controversy": An Overview and Theoretical Modeling of the Rebound Step in C−H Hydroxylation by Cytochrome P450. *Eur. J. Inorg. Chem.* **2004**, *2004* (2), 207-226.
190. Shaik, S.; de Visser, S. P.; Ogliaro, F.; Schwarz, H.; Schröder, D. Two-state reactivity mechanisms of hydroxylation and epoxidation by cytochrome P-450 revealed by theory. *Curr. Opin. Chem. Biol.* **2002**, *6* (5), 556-567.
191. Meunier, B.; de Visser, S. P.; Shaik, S. Mechanism of Oxidation Reactions Catalyzed by Cytochrome P450 Enzymes. *Chem. Rev.* **2004**, *104* (9), 3947-3980.
192. Ortiz de Montellano, P. R.; De Voss, J. J. Oxidizing species in the mechanism of cytochrome P450. *Nat. Prod. Rep.* **2002**, *19* (4), 477-493.
193. Kumar, D. Chapter 9 Drug Metabolism by Cytochrome P450: A Tale of Multistate Reactivity. In *Iron-Containing Enzymes: Versatile Catalysts of Hydroxylation Reactions in Nature*; The Royal Society of Chemistry: 2011; pp 281-329.
194. Wang, Y.; Kumar, D.; Yang, C.; Han, K.; Shaik, S. Theoretical Study of N-Demethylation of Substituted N,N-Dimethylanilines by Cytochrome P450: The Mechanistic Significance of Kinetic Isotope Effect Profiles. *J. Phys. Chem. B* **2007**, *111* (26), 7700-7710.
195. Guengerich, F. P.; Yun, C.-H.; Macdonald, T. L. Evidence for a 1-Electron Oxidation Mechanism in N-Dealkylation of N,N-Dialkylanilines by Cytochrome P450 2B1: Kinetic Hydrogen Isotope Effect, Linear Free Energy Relationships, Comparisons With Horseradish Peroxidase, and Studies with Oxygen Surrogates. *J. Biol. Chem.* **1996**, *271* (44), 27321-27329.

196. Hutzler, J. M.; Powers, F. J.; Wynalda, M. A.; Wienkers, L. C. Effect of carbonate anion on cytochrome P450 2D6-mediated metabolism in vitro: the potential role of multiple oxygenating species. *Arch. Biochem. Biophys.* **2003**, *417* (2), 165-175.
197. Rydberg, P.; Ryde, U.; Olsen, L. Sulfoxide, Sulfur, and Nitrogen Oxidation and Dealkylation by Cytochrome P450. *J. Chem. Theory Comput.* **2008**, *4* (8), 1369-1377.
198. Loew, G. H.; Chang, Y. T. Theoretical studies of the oxidation of N- and S-containing compounds by cytochrome P450. *Int. J. Quantum Chem* **1993**, *48* (S27), 815-826.
199. Shaik, S.; Wang, Y.; Chen, H.; Song, J.; Meir, R. Valence bond modelling and density functional theory calculations of reactivity and mechanism of cytochrome P450 enzymes: thioether sulfoxidation. *Faraday Discuss.* **2010**, *145* (0), 49-70.
200. Li, C.; Zhang, L.; Zhang, C.; Hirao, H.; Wu, W.; Shaik, S. Which Oxidant Is Really Responsible for Sulfur Oxidation by Cytochrome P450? *Angew. Chem. Int. Ed.* **2007**, *46* (43), 8168-8170.
201. Li, C.; Wu, W.; Kumar, D.; Shaik, S. Kinetic Isotope Effect is a Sensitive Probe of Spin State Reactivity in C−H Hydroxylation of N,N-Dimethylaniline by Cytochrome P450. *J. Am. Chem. Soc.* **2006**, *128* (2), 394-395.
202. Dubey, K. D.; Shaik, S. Cytochrome P450—The Wonderful Nanomachine Revealed through Dynamic Simulations of the Catalytic Cycle. *Acc. Chem. Res.* **2019**.
203. Park, M. J.; Lee, J.; Suh, Y.; Kim, J.; Nam, W. Reactivities of Mononuclear Non-Heme Iron Intermediates Including Evidence that Iron(III)−Hydroperoxo Species Is a Sluggish Oxidant. *J. Am. Chem. Soc.* **2006**, *128* (8), 2630-2634.
204. Kerber, W. D.; Ramdhanie, B.; Goldberg, D. P. H_2O_2 Oxidations Catalyzed by an Iron(III) Corrolazine: Avoiding High-Valent Iron–Oxido Species? *Angew. Chem. Int. Ed.* **2007**, *46* (20), 3718-3721.
205. Davis, S. C.; Sui, Z.; Peterson, J. A.; de Montellano, P. R. O. Oxidation of ω-Oxo Fatty Acids by Cytochrome P450BM-3(CYP102). *Arch. Biochem. Biophys.* **1996**, *328* (1), 35-42.
206. Guengerich, F. P.; Sohl, C. D.; Chowdhury, G. Multi-step oxidations catalyzed by cytochrome P450 enzymes: Processive vs. distributive kinetics and the issue of carbonyl oxidation in chemical mechanisms. *Arch. Biochem. Biophys.* **2011**, *507* (1), 126-134.
207. Liu, X.; Wang, Y.; Han, K. Systematic study on the mechanism of aldehyde oxidation to carboxylic acid by cytochrome P450. *J. Biol. Inorg. Chem.* **2007**, *12* (7), 1073-1081.
208. Watanabe, Y.; Takehira, K.; Shimizu, M.; Hayakawa, T.; Orita, H. Oxidation of aldehydes by an iron(III) porphyrin complex–m-chloroperbenzoic acid system. *J. Chem. Soc., Chem. Commun.* **1990**, (13), 927-928.
209. Wang, Y.; Wang, H.; Wang, Y.; Yang, C.; Yang, L.; Han, K. Theoretical Study of the Mechanism of Acetaldehyde Hydroxylation by Compound I of CYP2E1. *J. Phys. Chem. B* **2006**, *110* (12), 6154-6159.
210. Raner, G. M.; Chiang, E. W.; Vaz, A. D. N.; Coon, M. J. Mechanism-Based Inactivation of Cytochrome P450 2B4 by Aldehydes: Relationship to Aldehyde Deformylation via a Peroxyhemiacetal Intermediate. *Biochemistry* **1997**, *36* (16), 4895-4902.
211. Vaz, A. D. N.; Roberts, E. A.; Coon, M. J. Olefin formation in the oxidative deformylation of aldehydes by cytochrome P-450. Mechanistic implications for catalysis by oxygen-derived peroxide. *J. Am. Chem. Soc.* **1991**, *113* (15), 5886-5887.
212. Ogliaro, F.; de Visser, S. P.; Cohen, S.; Sharma, P. K.; Shaik, S. Searching for the Second Oxidant in the Catalytic Cycle of Cytochrome P450: A Theoretical Investigation of the Iron(III)-Hydroperoxo Species and Its Epoxidation Pathways. *J. Am. Chem. Soc.* **2002**, *124* (11), 2806-2817.
213. Wang, B.; Li, C.; Dubey, K. D.; Shaik, S. Quantum Mechanical/Molecular Mechanical Calculated Reactivity Networks Reveal How Cytochrome P450cam and Its T252A Mutant Select Their Oxidation Pathways. *J. Am. Chem. Soc.* **2015**, *137* (23), 7379-7390.
214. Kamel, A.; Harriman, S. Inhibition of cytochrome P450 enzymes and biochemical aspects of mechanism-based inactivation (MBI). *Drug Discovery Today: Technologies* **2013**, *10* (1), e177-e189.
215. Ortiz de Montellano, P. R. Acetylenes: cytochrome P450 oxidation and mechanism-based enzyme inactivation. *Drug Metab. Rev.* **2019**, *51* (2), 162-177.

216. Rettie, A. E.; Boberg, M.; Rettenmeier, A. W.; Baillie, T. A. Cytochrome P-450-catalyzed desaturation of valproic acid in vitro. Species differences, induction effects, and mechanistic studies. *J. Biol. Chem.* **1988**, *263* (27), 13733-8.
217. Wong Siew, H.; Bell Stephen, G.; De Voss James, J., P450 catalysed dehydrogenation. In *Pure Appl. Chem.*, 2017; Vol. 89, p 841.
218. Fisher, M. B.; Thompson, S. J.; Ribeiro, V.; Lechner, M. C.; Rettie, A. E. P450-Catalyzed In-Chain Desaturation of Valproic Acid: Isoform Selectivity and Mechanism of Formation of Δ3-Valproic Acid Generated by Baculovirus- Expressed CYP3A1. *Arch. Biochem. Biophys.* **1998**, *356* (1), 63-70.
219. Bell, S. G.; Zhou, R.; Yang, W.; Tan, A. B. H.; Gentleman, A. S.; Wong, L.-L.; Zhou, W. Investigation of the Substrate Range of CYP199A4: Modification of the Partition between Hydroxylation and Desaturation Activities by Substrate and Protein Engineering. *Chem. Eur. J.* **2012**, *18*, 16677-16688.
220. Wang, X.; Saba, T.; Yiu, H. H. P.; Howe, R. F.; Anderson, J. A.; Shi, J. Cofactor NAD(P)H Regeneration Inspired by Heterogeneous Pathways. *Chem* **2017**, *2* (5), 621-654.
221. Walt, D. R.; Findeis, M. A.; Rios-Mercadillo, V. M.; Auge, J.; Whitesides, G. M. An efficient chemical and enzymic synthesis of nicotinamide adenine dinucleotide (NAD+). *J. Am. Chem. Soc.* **1984**, *106* (1), 234-239.
222. Urlacher, V. B. Catalysis with Cytochrome P450 Monooxygenases. In *Handbook of Green Chemistry*; Anastas, P., T., Ed.; 2010.
223. Urlacher, V. B.; Eiben, S. Cytochrome P450 monooxygenases: perspectives for synthetic application. *Trends Biotechnol.* **2006**, *24* (7), 324-330.
224. Schallmey, A.; Domínguez de María, P.; Bracco, P. Biocatalytic Asymmetric Oxidations in Stereoselective Synthesis. In *Stereoselective Synthesis of Drugs and Natural Products*; Andrushko, V., Andrushko, N., Eds.; John Wiley & Sons, Inc.: 2013.
225. Wu, H.; Tian, C.; Song, X.; Liu, C.; Yang, D.; Jiang, Z. Methods for the regeneration of nicotinamide coenzymes. *Green Chemistry* **2013**, *15* (7), 1773-1789.
226. Song, K.; Zhou, X.; Liu, Y.; Gong, Y.; Zhou, B.; Wang, D.; Wang, Q. Role of oxidants in enhancing dewaterability of anaerobically digested sludge through Fe (II) activated oxidation processes: hydrogen peroxide versus persulfate. *Sci. Rep.* **2016**, *6*, 24800.
227. Shoji, O.; Fujishiro, T.; Nishio, K.; Kano, Y.; Kimoto, H.; Chien, S.-C.; Onoda, H.; Muramatsu, A.; Tanaka, S.; Hori, A.; Sugimoto, H.; Shiro, Y.; Watanabe, Y. A substrate-binding-state mimic of H_2O_2-dependent cytochrome P450 produced by one-point mutagenesis and peroxygenation of non-native substrates. *Catal. Sci. Technol.* **2016**, *6* (15), 5806-5811.
228. Albertolle, M. E.; Song, H. D.; Wilkey, C. J.; Segrest, J. P.; Guengerich, F. P. Glutamine-451 Confers Sensitivity to Oxidative Inhibition and Heme-Thiolate Sulfenylation of Cytochrome P450 4B1. *Chem. Res. Toxicol.* **2019**, *32* (3), 484-492.
229. Li, Q.-S.; Ogawa, J.; Shimizu, S. Critical Role of the Residue Size at Position 87 in H_2O_2-Dependent Substrate Hydroxylation Activity and H_2O_2 Inactivation of Cytochrome P450BM-3. *Biochem. Biophys. Res. Commun.* **2001**, *280* (5), 1258-1261.
230. Cirino, P. C.; Arnold, F. H. Regioselectivity and Activity of Cytochrome P450 BM-3 and Mutant F87A in Reactions Driven by Hydrogen Peroxide. *Adv. Synth. Catal.* **2002**, *344* (9), 932-937.
231. Salazar, O.; Cirino, P. C.; Arnold, F. H. Thermostabilization of a Cytochrome P450 Peroxygenase. *ChemBioChem* **2003**, *4* (9), 891-893.
232. Cirino, P. C.; Tang, Y.; Takahashi, K.; Tirrell, D. A.; Arnold, F. H. Global incorporation of norleucine in place of methionine in cytochrome P450 BM-3 heme domain increases peroxygenase activity. *Biotechnol. Bioeng.* **2003**, *83* (6), 729-734.
233. Matsuura, K.; Tosha, T.; Yoshioka, S.; Takahashi, S.; Ishimori, K.; Morishima, I. Structural and functional characterization of "laboratory evolved" cytochrome P450cam mutants showing enhanced naphthalene oxygenation activity. *Biochem. Biophys. Res. Commun.* **2004**, *323* (4), 1209-1215.
234. Shoji, O.; Watanabe, Y. Peroxygenase reactions catalyzed by cytochromes P450. *J. Biol. Inorg. Chem.* **2014**, *19* (4), 529-539.

235. Huang, X.; Groves, J. T. Oxygen Activation and Radical Transformations in Heme Proteins and Metalloporphyrins. *Chem. Rev.* **2018**, *118* (5), 2491-2553.
236. Erman, J. E.; Vitello, L. B.; Miller, M. A.; Shaw, A.; Brown, K. A.; Kraut, J. Histidine 52 is a critical residue for rapid formation of cytochrome c peroxidase compound I. *Biochemistry* **1993**, *32* (37), 9798-9806.
237. Newmyer, S. L.; de Montellano, P. R. O. Horseradish Peroxidase His-42 → Ala, His-42 → Val, and Phe-41 → Ala Mutants: Histidine Catalysis and Control of Substrate Access to the Heme Iron. *J. Biol. Chem.* **1995**, *270* (33), 19430-19438.
238. Tanaka, M.; Ishimori, K.; Morishima, I. The Distal Glutamic Acid as an Acid-Base Catalyst in the Distal Site of Horseradish Peroxidase. *Biochem. Biophys. Res. Commun.* **1996**, *227* (2), 393-399.
239. Tanaka, M.; Ishimori, K.; Mukai, M.; Kitagawa, T.; Morishima, I. Catalytic Activities and Structural Properties of Horseradish Peroxidase Distal His42 → Glu or Gln Mutant. *Biochemistry* **1997**, *36* (32), 9889-9898.
240. Poulos, T. L.; Kraut, J. The stereochemistry of peroxidase catalysis. *J. Biol. Chem.* **1980**, *255* (17), 8199-8205.
241. Jones, P.; Dunford, H. B. The mechanism of Compound I formation revisited. *J. Inorg. Biochem.* **2005**, *99* (12), 2292-2298.
242. Derat, E.; Shaik, S. The Poulos−Kraut Mechanism of Compound I Formation in Horseradish Peroxidase: A QM/MM Study. *J. Phys. Chem. B* **2006**, *110* (21), 10526-10533.
243. Strittmatter, E.; Liers, C.; Ullrich, R.; Wachter, S.; Hofrichter, M.; Plattner, D. A.; Piontek, K. First Crystal Structure of a Fungal High-redox Potential Dye-decolorizing Peroxidase: Substrate Interaction Sites And Long-Range Electron Transfer. *J. Biol. Chem.* **2013**, *288* (6), 4095-4102.
244. Girhard, M.; Schuster, S.; Dietrich, M.; Dürre, P.; Urlacher, V. B. Cytochrome P450 monooxygenase from Clostridium acetobutylicum: A new α-fatty acid hydroxylase. *Biochem. Biophys. Res. Commun.* **2007**, *362* (1), 114-119.
245. Onoda, H.; Shoji, O.; Suzuki, K.; Sugimoto, H.; Shiro, Y.; Watanabe, Y. α-Oxidative decarboxylation of fatty acids catalysed by cytochrome P450 peroxygenases yielding shorter-alkyl-chain fatty acids. *Catal. Sci. Technol.* **2018**, *8* (2), 434-442.
246. Girvan, H. M.; Poddar, H.; McLean, K. J.; Nelson, D. R.; Hollywood, K. A.; Levy, C. W.; Leys, D.; Munro, A. W. Structural and catalytic properties of the peroxygenase P450 enzyme CYP152K6 from Bacillus methanolicus. *J. Inorg. Biochem.* **2018**, *188*, 18-28.
247. Fujishiro, T.; Shoji, O.; Nagano, S.; Sugimoto, H.; Shiro, Y.; Watanabe, Y. Crystal Structure of H_2O_2-dependent Cytochrome $P450_{SP\alpha}$ with Its Bound Fatty Acid Substrate: Insight into the Regioselective Hydroxylation of Fatty Acids at the α Position. *J. Biol. Chem.* **2011**, *286* (34), 29941-29950.
248. Liu, Y.; Wang, C.; Yan, J.; Zhang, W.; Guan, W.; Lu, X.; Li, S. Hydrogen peroxide-independent production of alpha-alkenes by OleTJE P450 fatty acid decarboxylase. *Biotechnol. Biofuels* **2014**, *7* (1), 28.
249. Matthews, S.; Belcher, J. D.; Tee, K. L.; Girvan, H. M.; McLean, K. J.; Rigby, S. E. J.; Levy, C. W.; Leys, D.; Parker, D. A.; Blankley, R. T.; Munro, A. W. Catalytic Determinants of Alkene Production by the Cytochrome P450 Peroxygenase OleTJE. *J. Biol. Chem.* **2017**, *292* (12), 5128-5143.
250. Lee, D.-S.; Yamada, A.; Sugimoto, H.; Matsunaga, I.; Ogura, H.; Ichihara, K.; Adachi, S.-i.; Park, S.-Y.; Shiro, Y. Substrate Recognition and Molecular Mechanism of Fatty Acid Hydroxylation by Cytochrome P450 from Bacillus subtilis : Crystallographic, Spectroscopic, and Mutational Studies. *J. Biol. Chem.* **2003**, *278* (11), 9761-9767.
251. Belcher, J.; McLean, K. J.; Matthews, S.; Woodward, L. S.; Fisher, K.; Rigby, S. E. J.; Nelson, D. R.; Potts, D.; Baynham, M. T.; Parker, D. A.; Leys, D.; Munro, A. W. Structure and Biochemical Properties of the Alkene Producing Cytochrome P450 OleTJE (CYP152L1) from the Jeotgalicoccus sp. 8456 Bacterium. *J. Biol. Chem.* **2014**, *289* (10), 6535-6550.
252. Matsunaga, I.; Ueda, A.; Sumimoto, T.; Ichihara, K.; Ayata, M.; Ogura, H. Site-Directed Mutagenesis of the Putative Distal Helix of Peroxygenase Cytochrome P450. *Arch. Biochem. Biophys.* **2001**, *394* (1), 45-53.

253. Grant, J. L.; Mitchell, M. E.; Makris, T. M. Catalytic strategy for carbon−carbon bond scission by the cytochrome P450 OleT. *Proc. Natl. Acad. Sci. U.S.A.* **2016**, *113* (36), 10049-10054.
254. Hsieh, C. H.; Huang, X.; Amaya, J. A.; Rutland, C. D.; Keys, C. L.; Groves, J. T.; Austin, R. N.; Makris, T. M. The Enigmatic P450 Decarboxylase OleT Is Capable of, but Evolved To Frustrate, Oxygen Rebound Chemistry. *Biochemistry* **2017**, *56* (26), 3347-3357.
255. Shoji, O.; Fujishiro, T.; Nagano, S.; Tanaka, S.; Hirose, T.; Shiro, Y.; Watanabe, Y. Understanding substrate misrecognition of hydrogen peroxide dependent cytochrome P450 from Bacillus subtilis. *J. Biol. Inorg. Chem.* **2010**, *15* (8), 1331-1339.
256. Ramanan, R.; Dubey, K. D.; Wang, B.; Mandal, D.; Shaik, S. Emergence of Function in P450-Proteins: A Combined Quantum Mechanical/Molecular Mechanical and Molecular Dynamics Study of the Reactive Species in the H_2O_2-Dependent Cytochrome $P450_{SP\alpha}$ and Its Regio- and Enantioselective Hydroxylation of Fatty Acids. *J. Am. Chem. Soc.* **2016**, *138* (21), 6786-6797.
257. Shoji, O.; Fujishiro, T.; Nakajima, H.; Kim, M.; Nagano, S.; Shiro, Y.; Watanabe, Y. Hydrogen Peroxide Dependent Monooxygenations by Tricking the Substrate Recognition of Cytochrome $P450_{BS\beta}$. *Angew. Chem. Int. Ed.* **2007**, *46* (20), 3656-3659.
258. Shoji, O.; Watanabe, Y. Design of H_2O_2-dependent oxidation catalyzed by hemoproteins. *Metallomics* **2011**, *3* (4), 379-388.
259. Shoji, O.; Watanabe, Y. Oxygenation of Nonnative Substrates Using a Malfunction State of Cytochrome P450s. In *Fifty Years of Cytochrome P450 Research*; Yamazaki, H., Ed.; Springer Japan: Tokyo, 2014; pp 107-124.
260. Fujishiro, T.; Shoji, O.; Kawakami, N.; Watanabe, T.; Sugimoto, H.; Shiro, Y.; Watanabe, Y. Chiral-Substrate-Assisted Stereoselective Epoxidation Catalyzed by H_2O_2-Dependent Cytochrome P450SPα. *Chem. Asian J.* **2012**, *7* (10), 2286-2293.
261. Onoda, H.; Shoji, O.; Watanabe, Y. Acetate anion-triggered peroxygenation of non-native substrates by wild-type cytochrome P450s. *Dalton Trans.* **2015**, *44* (34), 15316-15323.
262. Cherry, J. R.; Lamsa, M. H.; Schneider, P.; Vind, J.; Svendsen, A.; Jones, A.; Pedersen, A. H. Directed evolution of a fungal peroxidase. *Nat. Biotechnol.* **1999**, *17*, 379.
263. Zhang, W.; Fernández-Fueyo, E.; Ni, Y.; van Schie, M.; Gacs, J.; Renirie, R.; Wever, R.; Mutti, F. G.; Rother, D.; Alcalde, M.; Hollmann, F. Selective aerobic oxidation reactions using a combination of photocatalytic water oxidation and enzymatic oxyfunctionalisations. *Nat. Catal.* **2018**, *1* (1), 55.
264. Matthews, S.; Tee, K. L.; Rattray, N. J.; McLean, K. J.; Leys, D.; Parker, D. A.; Blankley, R. T.; Munro, A. W. Production of alkenes and novel secondary products by P450 $OleT_{JE}$ using novel H_2O_2-generating fusion protein systems. *FEBS Lett.* **2017**, *591* (5), 737-750.
265. Gandomkar, S.; Dennig, A.; Dordic, A.; Hammerer, L.; Pickl, M.; Haas, T.; Hall, M.; Faber, K. Biocatalytic Oxidative Cascade for the Conversion of Fatty Acids into α-Ketoacids via Internal H_2O_2 Recycling. *Angew. Chem. Int. Ed.* **2018**, *57* (2), 427-430.
266. van de Velde, F.; Lourenço, N. D.; Bakker, M.; van Rantwijk, F.; Sheldon, R. A. Improved operational stability of peroxidases by coimmobilization with glucose oxidase. *Biotechnol. Bioeng.* **2000**, *69* (3), 286-291.
267. van Rantwijk, F.; Sheldon, R. A. Selective oxygen transfer catalysed by heme peroxidases: synthetic and mechanistic aspects. *Curr. Opin. Biotechnol.* **2000**, *11* (6), 554-564.
268. Seelbach, K.; van Deurzen, M. P. J.; van Rantwijk, F.; Sheldon, R. A.; Kragl, U. Improvement of the total turnover number and space-time yield for chloroperoxidase catalyzed oxidation. *Biotechnol. Bioeng.* **1997**, *55* (2), 283-288.
269. Deurzen, M. P. J. v.; Groen, B. W.; van Rantwijk, F.; Sheldon, R. A. A Simple Purification Method for Chloroperoxidase and Its Use in Organic Media. *Biocatalysis* **1994**, *10* (1-4), 247-255.
270. Paul, C. E.; Churakova, E.; Maurits, E.; Girhard, M.; Urlacher, V. B.; Hollmann, F. In situ formation of H_2O_2 for P450 peroxygenases. *Biorg. Med. Chem.* **2014**, *22* (20), 5692-5696.
271. Van Deurzen, M. P. J.; Seelbach, K.; van Rantwijk, F.; Kragl, U.; Sheldon, R. A. Chloroperoxidase: Use of a Hydrogen Peroxide-Stat for Controlling Reactions and Improving Enzyme Performance. *Biocatal. Biotransform.* **1997**, *15* (1), 1-16.

272. Girhard, M.; Kunigk, E.; Tihovsky, S.; Shumyantseva, V. V.; Urlacher, V. B. Light-driven biocatalysis with cytochrome P450 peroxygenases. *Biotechnol. Appl. Biochem.* **2013**, *60* (1), 111-118.
273. Perez, D. I.; Grau, M. M.; Arends, I. W. C. E.; Hollmann, F. Visible light-driven and chloroperoxidase-catalyzed oxygenation reactions. *Chem. Commun.* **2009**, (44), 6848-6850.
274. Xu, F.; Bell, S. G.; Peng, Y.; Johnson, E. O. D.; Bartlam, M.; Rao, Z.; Wong, L. L. Crystal structure of a ferredoxin reductase for the CYP199A2 system from *Rhodopseudomonas palustris*. *Proteins: Structure, Function, and Bioinformatics* **2009**, *77* (4), 867-880.
275. Chao, R. R.; De Voss, J. J.; Bell, S. G. The efficient and selective catalytic oxidation of *para*-substituted cinnamic acid derivatives by the cytochrome P450 monooxygenase, CYP199A4. *RSC Adv.* **2016**, *6* (60), 55286-55297.
276. Chao, R. R. Utilising CYP199A4 from *Rhodopseudomonas palustris* HaA2 for Biocatalysis and Mechanistic Studies. M.Phil Thesis, The University of Adelaide, July 2016.
277. Coleman, T. Utilising CYP199A4 from *Rhodopseudomonas palustris* HaA2 for investigation of the mechanism of cytochrome P450-catalysed oxidations. PhD Thesis, The University of Adelaide, Adelaide, March 2018.
278. Lessard, J. C. Chapter Eleven - Growth Media for E. coli. In *Methods Enzymol.*; Lorsch, J., Ed.; Academic Press: 2013; Vol. 533, pp 181-189.
279. Sudhamsu, J.; Kabir, M.; Airola, M. V.; Patel, B. A.; Yeh, S.-R.; Rousseau, D. L.; Crane, B. R. Co-expression of ferrochelatase allows for complete heme incorporation into recombinant proteins produced in E. coli. *Protein Expr. Purif.* **2010**, *73* (1), 78-82.
280. Johnson, E. O.; Wong, L.-L. Partial fusion of a cytochrome P450 system by carboxy-terminal attachment of putidaredoxin reductase to P450cam (CYP101A1). *Catal. Sci. Technol.* **2016**, *6* (20), 7549-7560.
281. de Marco, A. Recombinant polypeptide production in E. coli: towards a rational approach to improve the yields of functional proteins. *Microbial Cell Factories* **2013**, *12* (1), 101.
282. de Marco, A.; Vigh, L.; Diamant, S.; Goloubinoff, P. Native folding of aggregation-prone recombinant proteins in Escherichia coli by osmolytes, plasmid- or benzyl alcohol–overexpressed molecular chaperones. *Cell Stress & Chaperones* **2005**, *10* (4), 329-339.
283. Jeffreys, L. N.; Girvan, H. M.; McLean, K. J.; Munro, A. W. Chapter Eight - Characterization of Cytochrome P450 Enzymes and Their Applications in Synthetic Biology. In *Methods Enzymol.*; Scrutton, N., Ed.; Academic Press: 2018; Vol. 608, pp 189-261.
284. Guengerich, F. P.; Martha, V. M.; Christal, D. S.; Qian, C. Measurement of cytochrome P450 and NADPH–cytochrome P450 reductase. *Nature Protocols* **2009**, *4* (9), 1245.
285. Otey, C. R. High-Throughput Carbon Monoxide Binding Assay for Cytochromes P450. In *Directed Enzyme Evolution: Screening and Selection Methods*; Arnold, F. H., Georgiou, G., Eds.; Humana Press: Totowa, NJ, 2003; pp 137-139.
286. Omura, T.; Sato, R. The Carbon Monoxide-binding Pigment of Liver Microsomes: I. Evidence for its hemoprotein nature. *J. Biol. Chem.* **1964**, *239* (7), 2370-2378.
287. Ogura, H.; Nishida, C. R.; Hoch, U. R.; Perera, R.; Dawson, J. H.; Ortiz de Montellano, P. R. EpoK, a Cytochrome P450 Involved in Biosynthesis of the Anticancer Agents Epothilones A and B. Substrate-Mediated Rescue of a P450 Enzyme. *Biochemistry* **2004**, *43* (46), 14712-14721.
288. Barr, I.; Guo, F. Pyridine Hemochromagen Assay for Determining the Concentration of Heme in Purified Protein Solutions. *Bio-protocol* **2015**, *5* (18), e1594.
289. Berry, E. A.; Trumpower, B. L. Simultaneous determination of hemes *a*, *b*, and *c* from pyridine hemochrome spectra. *Anal. Biochem.* **1987**, *161* (1), 1-15.
290. Williams, J. W.; Morrison, J. F. [17] The kinetics of reversible tight-binding inhibition. In *Methods Enzymol.*; Academic Press: 1979; Vol. 63, pp 437-467.
291. Nguyen, G. T. H.; Tran, T. N.; Podgorski, M. N.; Bell, S. G.; Supuran, C. T.; Donald, W. A. Nanoscale Ion Emitters in Native Mass Spectrometry for Measuring Ligand–Protein Binding Affinities. *ACS Cent. Sci.* **2019**, *5* (2), 308-318.
292. Fruetel, J. A.; Mackman, R. L.; Peterson, J. A.; Ortiz de Montellano, P. R. Relationship of active site topology to substrate specificity for cytochrome P450terp (CYP108). *J. Biol. Chem.* **1994**, *269* (46), 28815-28821.

293. Glieder, A.; Meinhold, P. High-Throughput Screens Based on NAD(P)H Depletion. In *Directed Enzyme Evolution: Screening and Selection Methods*; Arnold, F. H., Georgiou, G., Eds.; Humana Press: Totowa, NJ, 2003; pp 157-170.
294. Bruckner, R.; Harmata, M.; Wender, P. A.; Harmata, D. M. *Organic Mechanisms : Reactions, Stereochemistry and Synthesis*; Berlin/Heidelberg: Springer Berlin Heidelberg: Berlin/Heidelberg, 2010.
295. Hildebrandt, A. G.; Roots, I. Reduced nicotinamide adenine dinucleotide phosphate (NADPH)-dependent formation and breakdown of hydrogen peroxide during mixed function oxidation reactions in liver microsomes. *Arch. Biochem. Biophys.* **1975**, *171* (2), 385-397.
296. Chelikani, P.; Fita, I.; Loewen, P. C. Diversity of structures and properties among catalases. *Cellular and Molecular Life Sciences CMLS* **2004**, *61* (2), 192-208.
297. Heck, D. E.; Shakarjian, M.; Kim, H. D.; Laskin, J. D.; Vetrano, A. M. Mechanisms of oxidant generation by catalase. *Ann. N.Y. Acad. Sci.* **2010**, *1203* (1), 120-125.
298. Yao, H.; Richardson, D. E. Epoxidation of Alkenes with Bicarbonate-Activated Hydrogen Peroxide. *J. Am. Chem. Soc.* **2000**, *122* (13), 3220-3221.
299. Hall, E. A.; Bell, S. G. The efficient and selective biocatalytic oxidation of norisoprenoid and aromatic substrates by CYP101B1 from *Novosphingobium aromaticivorans* DSM12444. *RSC Adv.* **2015**, *5* (8), 5762-5773.
300. Moldoveanu, S.; David, V. Chapter 10 - Chemical Reactions Used in Derivatizations. In *Modern Sample Preparation for Chromatography*; Moldoveanu, S., David, V., Eds.; Elsevier: Amsterdam, 2015; pp 333-391.
301. Moldoveanu, S.; David, V. Chapter 9 - The Role of Derivatization in Chromatography. In *Modern Sample Preparation for Chromatography*; Moldoveanu, S., David, V., Eds.; Elsevier: Amsterdam, 2015; pp 307-331.
302. Rontani, J.-F.; Aubert, C. Hydrogen and trimethylsilyl transfers during EI mass spectral fragmentation of hydroxycarboxylic and oxocarboxylic acid trimethylsilyl derivatives. *J. Am. Soc. Mass. Spectrom.* **2008**, *19* (1), 66-75.
303. Hanukoglu, I. Antioxidant Protective Mechanisms against Reactive Oxygen Species (ROS) Generated by Mitochondrial P450 Systems in Steroidogenic Cells. *Drug Metab. Rev.* **2006**, *38* (1-2), 171-196.
304. Xu, F.; Bell, S. G.; Rao, Z.; Wong, L.-L. Structure-activity correlations in pentachlorobenzene oxidation by engineered cytochrome P450cam1. *Protein Eng. Des. Sel.* **2007**, *20* (10), 473-480.
305. Pincus, M. R.; Bock, J. L.; Rossi, R.; Cai, D. Chemical Basis for Analyte Assays and Common Interferences. In *Henry's Clinical Diagnosis and Management by Laboratory Methods*; McPherson, R. A., Pincus, M. R., Eds.; 2017; pp 428-440.e1.
306. Weiß, M. S.; Pavlidis, I. V.; Vickers, C.; Höhne, M.; Bornscheuer, U. T. Glycine Oxidase Based High-Throughput Solid-Phase Assay for Substrate Profiling and Directed Evolution of (R)- and (S)-Selective Amine Transaminases. *Anal. Chem.* **2014**, *86* (23), 11847-11853.
307. Lane, B. S.; Burgess, K. A Cheap, Catalytic, Scalable, and Environmentally Benign Method for Alkene Epoxidations. *J. Am. Chem. Soc.* **2001**, *123* (12), 2933-2934.
308. Keating, C. S.; McClure, B. A.; Rack, J. J.; Rubtsov, I. V. Sulfoxide stretching mode as a structural reporter via dual-frequency two-dimensional infrared spectroscopy. *The Journal of Chemical Physics* **2010**, *133* (14), 144513.
309. Abagyan, R.; Totrov, M.; Kuznetsov, D. ICM—A new method for protein modeling and design: Applications to docking and structure prediction from the distorted native conformation. *J. Comput. Chem.* **1994**, *15* (5), 488-506.
310. Orry, A. J. W.; Abagyan, R. Preparation and Refinement of Model Protein–Ligand Complexes. In *Homology Modeling: Methods and Protocols*; Orry, A. J. W., Abagyan, R., Eds.; Humana Press: Totowa, NJ, 2012; pp 351-373.
311. Abagyan, R.; Orry, A. J. W.; Raush, E.; Totrov, M. ICM User's Guide: 5.1 Convert to ICM Object. http://www.molsoft.com/gui/icm-object.html (accessed Jan 26, 2018).
312. Abagyan, R.; Orry, A. J. W.; Raush, E.; Totrov, M. ICM User's Guide: 15.9 Dock or Minimize Ligand. http://www.molsoft.com/gui/re-dock-ligand.html (accessed Jan 26, 2018).

313. Abagyan, R.; Orry, A. J. W.; Raush, E.; Totrov, M. ICM User's Guide: 21.5 FAQ-Docking. http://www.molsoft.com/icmpro/faq-docking.html#faq-thoroughness (accessed March 30, 2018).
314. Rondeau, J.-M.; Schreuder, H. Protein Crystallography and Drug Discovery. In *The Practice of Medicinal Chemistry (Third Edition)*; Academic Press: New York, 2008; pp 605-634.
315. Aragão, D.; Aishima, J.; Cherukuvada, H.; Clarken, R.; Clift, M.; Cowieson, N. P.; Ericsson, D. J.; Gee, C. L.; Macedo, S.; Mudie, N.; Panjikar, S.; Price, J. R.; Riboldi-Tunnicliffe, A.; Rostan, R.; Williamson, R.; Caradoc-Davies, T. T. MX2: a high-flux undulator microfocus beamline serving both the chemical and macromolecular crystallography communities at the Australian Synchrotron. *Journal of Synchrotron Radiation* **2018**, *25* (3), 885-891.
316. Cowieson, N. P.; Aragao, D.; Clift, M.; Ericsson, D. J.; Gee, C.; Harrop, S. J.; Mudie, N.; Panjikar, S.; Price, J. R.; Riboldi-Tunnicliffe, A.; Williamson, R.; Caradoc-Davies, T. MX1: a bending-magnet crystallography beamline serving both chemical and macromolecular crystallography communities at the Australian Synchrotron. *Journal of Synchrotron Radiation* **2015**, *22* (1), 187-190.
317. Battye, T. G. G.; Kontogiannis, L.; Johnson, O.; Powell, H. R.; Leslie, A. G. W. iMOSFLM: a new graphical interface for diffraction-image processing with MOSFLM. *Acta Crystallographica Section D* **2011**, *67* (4), 271-281.
318. Evans, P. R.; Murshudov, G. N. How good are my data and what is the resolution? *Acta Crystallographica Section D* **2013**, *69* (7), 1204-1214.
319. Winn, M. D.; Ballard, C. C.; Cowtan, K. D.; Dodson, E. J.; Emsley, P.; Evans, P. R.; Keegan, R. M.; Krissinel, E. B.; Leslie, A. G. W.; McCoy, A.; McNicholas, S. J.; Murshudov, G. N.; Pannu, N. S.; Potterton, E. A.; Powell, H. R.; Read, R. J.; Vagin, A.; Wilson, K. S. Overview of the CCP4 suite and current developments. *Acta Crystallographica Section D* **2011**, *67* (4), 235-242.
320. McCoy, A. J.; Grosse-Kunstleve, R. W.; Adams, P. D.; Winn, M. D.; Storoni, L. C.; Read, R. J. Phaser crystallographic software. *J. Appl. Crystallogr.* **2007**, *40* (4), 658-674.
321. Moriarty, N. W.; Grosse-Kunstleve, R. W.; Adams, P. D. electronic Ligand Builder and Optimization Workbench (eLBOW): a tool for ligand coordinate and restraint generation. *Acta Crystallographica Section D* **2009**, *65* (10), 1074-1080.
322. Emsley, P.; Lohkamp, B.; Scott, W. G.; Cowtan, K. Features and development of Coot. *Acta Crystallographica Section D* **2010**, *66* (4), 486-501.
323. Afonine, P. V.; Grosse-Kunstleve, R. W.; Echols, N.; Headd, J. J.; Moriarty, N. W.; Mustyakimov, M.; Terwilliger, T. C.; Urzhumtsev, A.; Zwart, P. H.; Adams, P. D. Towards automated crystallographic structure refinement with phenix.refine. *Acta Crystallographica Section D* **2012**, *68* (4), 352-367.
324. Adams, P. D.; Afonine, P. V.; Bunkoczi, G.; Chen, V. B.; Davis, I. W.; Echols, N.; Headd, J. J.; Hung, L.-W.; Kapral, G. J.; Grosse-Kunstleve, R. W.; McCoy, A. J.; Moriarty, N. W.; Oeffner, R.; Read, R. J.; Richardson, D. C.; Richardson, J. S.; Terwilliger, T. C.; Zwart, P. H. PHENIX: a comprehensive Python-based system for macromolecular structure solution. *Acta Crystallographica Section D* **2010**, *66* (2), 213-221.
325. Wlodawer, A.; Minor, W.; Dauter, Z.; Jaskolski, M. Protein crystallography for aspiring crystallographers or how to avoid pitfalls and traps in macromolecular structure determination. *The FEBS Journal* **2013**, *280* (22), 5705-5736.
326. Rhodes, G. *Crystallography Made Crystal Clear : A Guide for Users of Macromolecular Models*; Elsevier Science & Technology: Burlington, MA, 2014.
327. Terwilliger, T. C.; Grosse-Kunstleve, R. W.; Afonine, P. V.; Moriarty, N. W.; Adams, P. D.; Read, R. J.; Zwart, P. H.; Hung, L.-W. Iterative-build OMIT maps: map improvement by iterative model building and refinement without model bias. *Acta Crystallographica Section D* **2008**, *64* (5), 515-524.
328. Afonine, P. V.; Moriarty, N. W.; Mustyakimov, M.; Sobolev, O. V.; Terwilliger, T. C.; Turk, D.; Urzhumtsev, A.; Adams, P. D. FEM: feature-enhanced map. *Acta Crystallographica Section D* **2015**, *71* (3), 646-666.

329. Chen, V. B.; Arendall, W. B., III; Headd, J. J.; Keedy, D. A.; Immormino, R. M.; Kapral, G. J.; Murray, L. W.; Richardson, J. S.; Richardson, D. C. MolProbity: all-atom structure validation for macromolecular crystallography. *Acta Crystallographica Section D* **2010**, *66* (1), 12-21.
330. Rondeau, J.-M.; Schreuder, H. Chapter 22 - Protein Crystallography and Drug Discovery. In *The Practice of Medicinal Chemistry (Fourth Edition)*; Wermuth, C. G., Aldous, D., Raboisson, P., Rognan, D., Eds.; Academic Press: San Diego, 2015; pp 511-537.
331. Acharya, K. R.; Lloyd, M. D. The advantages and limitations of protein crystal structures. *Trends in Pharmacological Sciences* **2005**, *26* (1), 10-14.
332. Schrodinger, LLC, The PyMOL Molecular Graphics System, Version 1.4.1. 2015.
333. Chao, R. R.; Lau, I. C. K.; Voss, J. J. D.; Bell, S. G. Modification of an Enzyme Biocatalyst for the Efficient and Selective Oxidative Demethylation of *para*-Substituted Benzene Derivatives. *ChemCatChem* **2016**, *8* (23), 3626-3635.
334. Oostenbrink, C. Structure-Based Methods for Predicting the Sites and Products of Metabolism. In *Drug Metabolism Prediction*; Kirchmair, J., Ed.; Wiley-VCH: Weinheim, Germany, 2014.
335. de Graaf, C.; Oostenbrink, C.; Keizers, P. H. J.; van der Wijst, T.; Jongejan, A.; Vermeulen, N. P. E. Catalytic Site Prediction and Virtual Screening of Cytochrome P450 2D6 Substrates by Consideration of Water and Rescoring in Automated Docking. *J. Med. Chem.* **2006**, *49* (8), 2417-2430.
336. Bell, S. G.; Hoskins, N.; Xu, F.; Caprotti, D.; Rao, Z.; Wong, L.-L. Cytochrome P450 enzymes from the metabolically diverse bacterium *Rhodopseudomonas palustris*. *Biochem. Biophys. Res. Commun.* **2006**, *342* (1), 191-196.
337. Sligar, S. G. Coupling of spin, substrate, and redox equilibria in cytochrome P450. *Biochemistry* **1976**, *15* (24), 5399-5406.
338. Vanoye, L.; Favre-Réguillon, A.; Aloui, A.; Philippe, R.; de Bellefon, C. Insights in the aerobic oxidation of aldehydes. *RSC Adv.* **2013**, *3* (41), 18931-18937.
339. Zhang, Y.; Cheng, Y.; Cai, H.; He, S.; Shan, Q.; Zhao, H.; Chen, Y.; Wang, B. Catalyst-free aerobic oxidation of aldehydes into acids in water under mild conditions. *Green Chemistry* **2017**, *19* (23), 5708-5713.
340. Liebschner, D.; Afonine, P. V.; Moriarty, N. W.; Poon, B. K.; Sobolev, O. V.; Terwilliger, T. C.; Adams, P. D. Polder maps: improving OMIT maps by excluding bulk solvent. *Acta Crystallographica Section D* **2017**, *73* (2), 148-157.
341. Lonsdale, R.; Oláh, J.; Mulholland, A. J.; Harvey, J. N. Does Compound I Vary Significantly between Isoforms of Cytochrome P450? *J. Am. Chem. Soc.* **2011**, *133* (39), 15464-15474.
342. Schöneboom, J. C.; Lin, H.; Reuter, N.; Thiel, W.; Cohen, S.; Ogliaro, F.; Shaik, S. The Elusive Oxidant Species of Cytochrome P450 Enzymes: Characterization by Combined Quantum Mechanical/Molecular Mechanical (QM/MM) Calculations. *J. Am. Chem. Soc.* **2002**, *124* (27), 8142-8151.
343. Krest, C. M.; Silakov, A.; Rittle, J.; Yosca, T. H.; Onderko, E. L.; Calixto, J. C.; Green, M. T. Significantly shorter Fe–S bond in cytochrome P450-I is consistent with greater reactivity relative to chloroperoxidase. *Nat. Chem.* **2015**, *7*, 696.
344. Hanukoglu, I.; Rapoport, R.; Weiner, L.; Sklan, D. Electron Leakage from the Mitochondrial NADPH-Adrenodoxin Reductase-Adrenodoxin-P450scc (Cholesterol Side Chain Cleavage) System. *Arch. Biochem. Biophys.* **1993**, *305* (2), 489-498.
345. Luo, Y.-R. *Handbook of bond dissociation energies in organic compounds*; CRC Press: Boca Raton, FL, 2002.
346. Alfassi, Z. B.; Golden, D. M. Bond dissociation energy of the carbon-hydrogen bond in ethanol. Kinetic study of the reaction iodine + ethanol. *The Journal of Physical Chemistry* **1972**, *76* (23), 3314-3319.
347. Oyeyemi, V. B.; Keith, J. A.; Carter, E. A. Trends in Bond Dissociation Energies of Alcohols and Aldehydes Computed with Multireference Averaged Coupled-Pair Functional Theory. *J. Phys. Chem. A* **2014**, *118* (17), 3039-3050.

348. Lonsdale, R.; Houghton, K. T.; Żurek, J.; Bathelt, C. M.; Foloppe, N.; de Groot, M. J.; Harvey, J. N.; Mulholland, A. J. Quantum Mechanics/Molecular Mechanics Modeling of Regioselectivity of Drug Metabolism in Cytochrome P450 2C9. *J. Am. Chem. Soc.* **2013**, *135* (21), 8001-8015.
349. Paulsen, M. D.; Ornstein, R. L. Predicting the product specificity and coupling of cytochrome P450cam. *J. Comput. Aided Mol. Des.* **1992**, *6* (5), 449-460.
350. Schöneboom, J. C.; Cohen, S.; Lin, H.; Shaik, S.; Thiel, W. Quantum Mechanical/Molecular Mechanical Investigation of the Mechanism of C−H Hydroxylation of Camphor by Cytochrome P450cam: Theory Supports a Two-State Rebound Mechanism. *J. Am. Chem. Soc.* **2004**, *126* (12), 4017-4034.
351. Loida, P. J.; Sligar, S. G.; Paulsen, M. D.; Arnold, G. E.; Ornstein, R. L. Stereoselective Hydroxylation of Norcamphor by Cytochrome $P450_{cam}$: Experimental Verification of Molecular Dynamics Simulations. *J. Biol. Chem.* **1995**, *270* (10), 5326-5330.
352. Kuhn, B.; Jacobsen, W.; Christians, U.; Benet, L. Z.; Kollman, P. A. Metabolism of Sirolimus and Its Derivative Everolimus by Cytochrome P450 3A4: Insights from Docking, Molecular Dynamics, and Quantum Chemical Calculations. *J. Med. Chem.* **2001**, *44* (12), 2027-2034.
353. Peng, C.-C.; Pearson, J. T.; Rock, D. A.; Joswig-Jones, C. A.; Jones, J. P. The effects of type II binding on metabolic stability and binding affinity in cytochrome P450 CYP3A4. *Arch. Biochem. Biophys.* **2010**, *497* (1), 68-81.
354. Dahal, U. P.; Joswig-Jones, C.; Jones, J. P. Comparative Study of the Affinity and Metabolism of Type I and Type II Binding Quinoline Carboxamide Analogues by Cytochrome P450 3A4. *J. Med. Chem.* **2012**, *55* (1), 280-290.
355. Podust, L. M.; von Kries, J. P.; Eddine, A. N.; Kim, Y.; Yermalitskaya, L. V.; Kuehne, R.; Ouellet, H.; Warrier, T.; Altekös ter, M.; Lee, J.-S.; Rademann, J.; Oschkinat, H.; Kaufmann, S. H. E.; Waterman, M. R. Small-Molecule Scaffolds for CYP51 Inhibitors Identified by High-Throughput Screening and Defined by X-Ray Crystallography. *Antimicrob. Agents Chemother.* **2007**, *51* (11), 3915-3923.
356. Balding, P. R.; Porro, C. S.; McLean, K. J.; Sutcliffe, M. J.; Maréchal, J.-D.; Munro, A. W.; Visser, S. P. d. How Do Azoles Inhibit Cytochrome P450 Enzymes? A Density Functional Study. *J. Phys. Chem. A* **2008**, *112* (50), 12911-12918.
357. Sagatova, A. A.; Keniya, M. V.; Wilson, R. K.; Monk, B. C.; Tyndall, J. D. A. Structural Insights into Binding of the Antifungal Drug Fluconazole to *Saccharomyces cerevisiae* Lanosterol 14α-Demethylase. *Antimicrob. Agents Chemother.* **2015**, *59* (8), 4982-4989.
358. Sevrioukova, I. F.; Poulos, T. L. Structure and mechanism of the complex between cytochrome P4503A4 and ritonavir. *Proc. Natl. Acad. Sci. U.S.A.* **2010**, *107* (43), 18422-18427.
359. Sevrioukova, I. F.; Poulos, T. L. Pyridine-Substituted Desoxyritonavir Is a More Potent Inhibitor of Cytochrome P450 3A4 than Ritonavir. *J. Med. Chem.* **2013**, *56* (9), 3733-3741.
360. Cruce, A. A.; Lockart, M.; Bowman, M. K. Chapter Twelve - Pulsed EPR in the Study of Drug Binding in Cytochrome P450 and NOS. In *Methods Enzymol.*; Qin, P. Z., Warncke, K., Eds.; Academic Press: 2015; Vol. 563, pp 311-340.
361. Pearson, J.; Dahal, U. P.; Rock, D.; Peng, C.-C.; Schenk, J. O.; Joswig-Jones, C.; Jones, J. P. The kinetic mechanism for cytochrome P450 metabolism of Type II binding compounds: Evidence supporting direct reduction. *Arch. Biochem. Biophys.* **2011**, *511* (1), 69-79.
362. Zamora, A.; Denning, C. A.; Heidary, D. K.; Wachter, E.; Nease, L. A.; Ruiz, J.; Glazer, E. C. Ruthenium-containing P450 inhibitors for dual enzyme inhibition and DNA damage. *Dalton Trans.* **2017**, *46* (7), 2165-2173.
363. Dawson, J. H.; Andersson, L. A.; Sono, M. Spectroscopic investigations of ferric cytochrome P-450-CAM ligand complexes. Identification of the ligand *trans* to cysteinate in the native enzyme. *J. Biol. Chem.* **1982**, *257* (7), 3606-17.
364. Poulos, T. L.; Howard, A. J. Crystal structures of metyrapone- and phenylimidazole-inhibited complexes of cytochrome $P\text{-}450_{cam}$. *Biochemistry* **1987**, *26* (25), 8165-8174.
365. Yoshida, Y.; Aoyama, Y.; Nishino, T.; Katsuki, H.; Maitra, U. S.; Mohan, V. P.; Sprinson, D. B. Spectral properties of a novel cytochrome P-450 of a *Saccharomyces cerevisiae* mutant SG1. A

cytochrome P-450 species having a nitrogenous ligand *trans* to thiolate. *Biochem. Biophys. Res. Commun.* **1985**, *127* (2), 623-628.
366. Dawson, J. H.; Andersson, L. A.; Sono, M. The diverse spectroscopic properties of ferrous cytochrome P-450-CAM ligand complexes. *J. Biol. Chem.* **1983**, *258* (22), 13637-45.
367. Denisov, I. G.; Makris, T. M.; Sligar, S. G.; Schlichting, I. Structure and Chemistry of Cytochrome P450. *Chem. Rev.* **2005**, *105* (6), 2253-2278.
368. Wilker, J. J.; Dmochowski, I. J.; Dawson, J. H.; Winkler, J. R.; Gray, H. B. Substrates for Rapid Delivery of Electrons and Holes to Buried Active Sites in Proteins. *Angew. Chem. Int. Ed.* **1999**, *38* (1-2), 89-92.
369. Hirst, J.; Wilcox, S. K.; Williams, P. A.; Blankenship, J.; McRee, D. E.; Goodin, D. B. Replacement of the Axial Histidine Ligand with Imidazole in Cytochrome c Peroxidase. 1. Effects on Structure. *Biochemistry* **2001**, *40* (5), 1265-1273.
370. Alam, S.; Yee, J.; Couture, M.; Takayama, S.-i. J.; Tseng, W.-H.; Mauk, A. G.; Rafferty, S. Cytochrome b_5 from *Giardia lamblia*. *Metallomics* **2012**, *4* (12), 1255-1261.
371. Karunakaran, V.; Sun, Y.; Benabbas, A.; Champion, P. M. Investigations of the Low Frequency Modes of Ferric Cytochrome c Using Vibrational Coherence Spectroscopy. *J. Phys. Chem. B* **2014**, *118* (23), 6062-6070.
372. Dick, S., Crystal structure of tris(2,2'-bipyridine)iron(II) bis(hexafluorophosphate), $(C_{10}H_8N_2)_3Fe(PF_6)_2$. In *Zeitschrift für Kristallographie - New Crystal Structures*, 1998; Vol. 213, p 370.
373. Williams, P. A.; Cosme, J.; Vinković, D. M.; Ward, A.; Angove, H. C.; Day, P. J.; Vonrhein, C.; Tickle, I. J.; Jhoti, H. Crystal Structures of Human Cytochrome P450 3A4 Bound to Metyrapone and Progesterone. *Science* **2004**, *305* (5684), 683-686.
374. Shah, M. B.; Pascual, J.; Zhang, Q.; Stout, C. D.; Halpert, J. R. Structures of Cytochrome P450 2B6 Bound to 4-Benzylpyridine and 4-(4-Nitrobenzyl)pyridine: Insight into Inhibitor Binding and Rearrangement of Active Site Side Chains. *Mol. Pharmacol.* **2011**, *80* (6), 1047-1055.
375. Pettersen, E. F.; Goddard, T. D.; Huang, C. C.; Couch, G. S.; Greenblatt, D. M.; Meng, E. C.; Ferrin, T. E. UCSF Chimera—A visualization system for exploratory research and analysis. *J. Comput. Chem.* **2004**, *25* (13), 1605-1612.
376. Beitlich, T.; Kühnel, K.; Schulze-Briese, C.; Shoeman, R. L.; Schlichting, I. Cryoradiolytic reduction of crystalline heme proteins: analysis by UV-Vis spectroscopy and X-ray crystallography. *Journal of Synchrotron Radiation* **2007**, *14* (1), 11-23.
377. Egawa, T.; Hishiki, T.; Ichikawa, Y.; Kanamori, Y.; Shimada, H.; Takahashi, S.; Kitagawa, T.; Ishimura, Y. Refolding Processes of Cytochrome $P450_{cam}$ from Ferric and Ferrous Acid Forms to the Native Conformation: Formations of Folding Intermediates with Non-Native Heme Coordination State. *J. Biol. Chem.* **2004**, *279* (31), 32008-32017.
378. Prusakov, V. E.; Stukan, R. A.; Davidov, R. M.; Gersonde, K. Non-equilibrium state of a monomeric insect haemoglobin induced by γ-irradiation and detected by Mössbauer spectroscopy. *FEBS Lett.* **1985**, *186* (2), 158-162.
379. Trofimov, A. A.; Polyakov, K. M.; Lazarenko, V. A.; Popov, A. N.; Tikhonova, T. V.; Tikhonov, A. V.; Popov, V. O. Structural study of the X-ray-induced enzymatic reaction of octahaem cytochrome c nitrite reductase. *Acta Crystallographica Section D Biological Crystallography* **2015**, *71* (5), 1087-1094.
380. Verras, A.; Alian, A.; Montellano, P. R. O. d. Cytochrome P450 active site plasticity: attenuation of imidazole binding in cytochrome $P450_{cam}$ by an L244A mutation. *Protein Eng. Des. Sel.* **2006**, *19* (11), 491-496.
381. Shaik, S.; Kumar, D.; de Visser, S. P.; Altun, A.; Thiel, W. Theoretical Perspective on the Structure and Mechanism of Cytochrome P450 Enzymes. *Chem. Rev.* **2005**, *105* (6), 2279-2328.
382. Lewis, D. F. V.; Ito, Y. Chapter 1 Cytochrome P450 Structure and Function: An Evolutionary Perspective. In *Cytochromes P450: Role in the Metabolism and Toxicity of Drugs and other Xenobiotics*; The Royal Society of Chemistry: 2008; pp 3-45.
383. Amaya, J. A.; Rutland, C. D.; Makris, T. M. Mixed regiospecificity compromises alkene synthesis by a cytochrome P450 peroxygenase from *Methylobacterium populi*. *J. Inorg. Biochem.* **2016**, *158*, 11-16.

384. Peng, C.-C.; Cape, J. L.; Rushmore, T.; Crouch, G. J.; Jones, J. P. Cytochrome P450 2C9 Type II Binding Studies on Quinoline-4-Carboxamide Analogues. *J. Med. Chem.* **2008**, *51* (24), 8000-8011.
385. Sharrock, M.; Muenck, E.; Debrunner, P. G.; Marshall, V.; Lipscomb, J. D.; Gunsalus, I. C. Mössbauer studies of cytochrome P-450$_{cam}$. *Biochemistry* **1973**, *12* (2), 258-265.
386. Dawson, J. H.; Andersson, L. A.; Sono, M. Systematic Trends in the Spectroscopic Properties of Low-Spin Ferric Ligand Adducts of Cytochrome P-450 and Chloroperoxidase: the Transition from Normal to Hyper Spectra. *New J. Chem.* **1992**, *16*, 577-582.
387. Viola, F.; Aime, S.; Coletta, M.; Desideri, A.; Fasano, M.; Paoletti, S.; Tarricone, C.; Ascenzi, P. Azide, cyanide, fluoride, imidazole and pyridine binding to ferric and ferrous native horse heart cytochrome c and to its carboxymethylated derivative: A comparative study. *J. Inorg. Biochem.* **1996**, *62* (3), 213-222.
388. Harbury, H. A.; Loach, P. A. Interaction of Nitrogenous Ligands with Heme Peptides from Mammalian Cytochrome c. *J. Biol. Chem.* **1960**, *235* (12), 3646-3653.
389. Vashi, P. R.; Marques, H. M. The coordination of imidazole and substituted pyridines by the hemeoctapeptide *N*-acetyl-ferromicroperoxidase-8 (Fe^{II}NAcMP8). *J. Inorg. Biochem.* **2004**, *98* (9), 1471-1482.
390. Ishida, N.; Aoyama, Y.; Hatanaka, R.; Oyama, Y.; Imajo, S.; Ishiguro, M.; Oshima, T.; Nakazato, H.; Noguchi, T.; Maitra, U. S.; Mohan, V. P.; Sprinson, D. B.; Yoshida, Y. A single amino acid substitution converts cytochrome P450$_{14DM}$ to an inactive form, cytochrome P450$_{SG1}$: Complete primary structures deduced from cloned DNAs. *Biochem. Biophys. Res. Commun.* **1988**, *155* (1), 317-323.
391. Haines, D. C.; Chen, B.; Tomchick, D. R.; Bondlela, M.; Hegde, A.; Machius, M.; Peterson, J. A. Crystal Structure of Inhibitor-Bound P450BM-3 Reveals Open Conformation of Substrate Access Channel. *Biochemistry* **2008**, *47* (12), 3662-3670.
392. Prusakov, V. E.; Steyer, J.; Parak, F. G. Mössbauer spectroscopy on nonequilibrium states of myoglobin: a study of r-t relaxation. *Biophys. J.* **1995**, *68* (6), 2524-2530.
393. Dawson, J. H.; Andersson, L. A.; Sono, M.; Gadecki, S. E.; Davis, I. M.; Nardo, J. V.; Svastits, E. W. Magnetic Circular Dichroism Spectroscopy as a Probe of Ferric Cytochrome P-450 and its Ligand Complexes. In *The Coordination Chemistry of Metalloenzymes: The Role of Metals in Reactions Involving Water, Dioxygen and Related Species Proceedings of the NATO Advanced Study Institute held at San Miniato, Pisa, Italy, May 28 – June 8, 1982*; Bertini, I., Drago, R. S., Luchinat, C., Eds.; Springer Netherlands: Dordrecht, 1983; pp 369-376.
394. Udit, A. K.; Hagen, K. D.; Goldman, P. J.; Star, A.; Gillan, J. M.; Gray, H. B.; Hill, M. G. Spectroscopy and Electrochemistry of Cytochrome P450 BM3-Surfactant Film Assemblies. *J. Am. Chem. Soc.* **2006**, *128* (31), 10320-10325.
395. Mayhew, S. G. The Redox Potential of Dithionite and SO_2^- from Equilibrium Reactions with Flavodoxins, Methyl Viologen and Hydrogen plus Hydrogenase. *Eur. J. Biochem.* **1978**, *85* (2), 535-547.
396. Driscoll, M. D.; McLean, K. J.; Levy, C.; Mast, N.; Pikuleva, I. A.; Lafite, P.; Rigby, S. E. J.; Leys, D.; Munro, A. W. Structural and Biochemical Characterization of *Mycobacterium tuberculosis* CYP142: Evidence for Multiple Cholesterol 27-Hydroxylase Activities in a Human Pathogen. *J. Biol. Chem.* **2010**, *285* (49), 38270-38282.
397. Dunford, A. J.; McLean, K. J.; Sabri, M.; Seward, H. E.; Heyes, D. J.; Scrutton, N. S.; Munro, A. W. Rapid P450 Heme Iron Reduction by Laser Photoexcitation of *Mycobacterium tuberculosis* CYP121 and CYP51B1: Analysis Of Co Complexation Reactions and Reversibility of the P450/P420 Equilibrium. *J. Biol. Chem.* **2007**, *282* (34), 24816-24824.
398. Sun, Y.; Zeng, W.; Benabbas, A.; Ye, X.; Denisov, I.; Sligar, S. G.; Du, J.; Dawson, J. H.; Champion, P. M. Investigations of Heme Ligation and Ligand Switching in Cytochromes P450 and P420. *Biochemistry* **2013**, *52* (34), 5941-5951.
399. Hui Bon Hoa, G.; Di Primo, C.; Dondaine, I.; Sligar, S. G.; Gunsalus, I. C.; Douzou, P. Conformational changes of cytochromes P-450$_{cam}$ and P-450$_{lin}$ induced by high pressure. *Biochemistry* **1989**, *28* (2), 651-656.

400. Sun, L.; Wang, Z.; Jiang, H.; Tan, X.; Huang, Z. Novel Conformational Transitions of Human Cytochrome P450 2C8 during Thermal and Acid-induced Unfolding. *Chin. J. Chem* . **2010**, *28* (8), 1491-1502.
401. Yu, X.-C.; Shen, S.; Strobel, H. W. Denaturation of Cytochrome P450 2B1 by Guanidine Hydrochloride and Urea: Evidence for a Metastable Intermediate State of the Active Site. *Biochemistry* **1995**, *34* (16), 5511-5517.
402. Champion, P. M.; Gunsalus, I. C.; Wagner, G. C. Resonance Raman investigations of cytochrome $P450_{CAM}$ from *Pseudomonas putida*. *J. Am. Chem. Soc.* **1978**, *100* (12), 3743-3751.
403. Nagel, R.; Peters, R. J. Probing the specificity of CYP112 in bacterial gibberellin biosynthesis. *Biochem. J* **2018**, *475* (13), 2167-2177.
404. Waterman, M. R.; Ullrich, V.; Estabrook, R. W. Effect of substrate on the spin state of cytochrome P-450 in hepatic microsomes. *Arch. Biochem. Biophys.* **1973**, *155* (2), 355-360.
405. Girvan, H. M.; Seward, H. E.; Toogood, H. S.; Cheesman, M. R.; Leys, D.; Munro, A. W. Structural and Spectroscopic Characterization of P450 BM3 Mutants with Unprecedented P450 Heme Iron Ligand Sets: New Heme Ligation States Influence Conformational Equilibria in P450 BM3. *J. Biol. Chem.* **2007**, *282* (1), 564-572.
406. Joyce, M. G.; Girvan, H. M.; Munro, A. W.; Leys, D. A Single Mutation in Cytochrome P450 BM3 Induces the Conformational Rearrangement Seen upon Substrate Binding in the Wild-type Enzyme. *J. Biol. Chem.* **2004**, *279* (22), 23287-23293.
407. Walling, C. Fenton's reagent revisited. *Acc. Chem. Res.* **1975**, *8* (4), 125-131.
408. García Einschlag, F. S.; Braun, A. M.; Oliveros, E. Fundamentals and Applications of the Photo-Fenton Process to Water Treatment. In *Environmental Photochemistry Part III*; Bahnemann, D. W., Robertson, P. K. J., Eds.; Springer Berlin Heidelberg: Berlin, Heidelberg, 2015; pp 301-342.
409. Luehrs, D. C.; Roher, A. E.; Stephen, W. W. Demonstration of the Fenton Reaction. *J. Chem. Educ.* **2007**, *84* (8), 1290.
410. Pignatello, J. J.; Oliveros, E.; MacKay, A. Advanced Oxidation Processes for Organic Contaminant Destruction Based on the Fenton Reaction and Related Chemistry. *Critical Reviews in Environmental Science and Technology* **2006**, *36* (1), 1-84.
411. Fenton, H. J. H. LXXIII.—Oxidation of tartaric acid in presence of iron. *Journal of the Chemical Society, Transactions* **1894**, *65* (0), 899-910.
412. Wang, H.-Y.; Hu, Y.-N.; Cao, G.-P.; Yuan, W.-K. Degradation of propylene glycol wastewater by Fenton's reagent in a semi-continuous reactor. *Chem. Eng. J.* **2011**, *170* (1), 75-81.
413. Smith, J. R. L.; Norman, R. O. C. 539. Hydroxylation. Part I. The oxidation of benzene and toluene by Fenton's reagent. *Journal of the Chemical Society (Resumed)* **1963**, (0), 2897-2905.
414. Walling, C.; Johnson, R. A. Fenton's reagent. V. Hydroxylation and side-chain cleavage of aromatics. *J. Am. Chem. Soc.* **1975**, *97* (2), 363-367.
415. Xu, X.; John, V. T.; McPherson, G. L.; Grimm, D. A.; Akkara, J. A.; Kaplan, D. L. A combined chemical-enzymatic method to remove selected aromatics from aqueous streams. *Appl. Biochem. Biotechnol.* **1995**, *51* (1), 649-660.
416. Cirino, P. C. Laboratory Evolution of Cytochrome P450 Peroxygenase Activity California Institute of Technology, Pasadena, California 2004.
417. Wlodawer, A.; Minor, W.; Dauter, Z.; Jaskolski, M. Protein crystallography for non-crystallographers, or how to get the best (but not more) from published macromolecular structures. *The FEBS Journal* **2008**, *275* (1), 1-21.
418. Hayakawa, S.; Matsumura, H.; Nakamura, N.; Yohda, M.; Ohno, H. Spectroscopic characterization of the acid–alkaline transition of a thermophilic cytochrome P450. *FEBS Lett.* **2013**, *587* (1), 94-97.
419. Isom, D. G.; Castañeda, C. A.; Cannon, B. R.; Velu, P. D.; García-Moreno E., B. Charges in the hydrophobic interior of proteins. *Proc. Natl. Acad. Sci. U.S.A.* **2010**, *107* (37), 16096-16100.
420. Brunori, M.; Amiconi, G.; Antonini, E.; Wyman, J.; Zito, R.; Rossi Fanelli, A. The transition between 'acid' and 'alkaline' ferric heme proteins. *Biochimica et Biophysica Acta (BBA) - Protein Structure* **1968**, *154* (2), 315-322.

421. Koppenol, W. H. Oxygen Activation by Cytochrome P450: A Thermodynamic Analysis. *J. Am. Chem. Soc.* **2007**, *129* (31), 9686-9690.
422. Song, Y.; Mao, J.; Gunner, M. R. Electrostatic Environment of Hemes in Proteins: pK_as of Hydroxyl Ligands. *Biochemistry* **2006**, *45* (26), 7949-7958.
423. Karich, A.; Scheibner, K.; Ullrich, R.; Hofrichter, M. Exploring the catalase activity of unspecific peroxygenases and the mechanism of peroxide-dependent heme destruction. *J. Mol. Catal. B: Enzym.* **2016**, *134*, 238-246.
424. Burek, B. O. O.; Bormann, S.; Hollmann, F.; Bloh, J.; Holtmann, D. Hydrogen peroxide driven biocatalysis. *Green Chemistry* **2019**.
425. Albertolle, M. E.; Kim, D.; Nagy, L. D.; Yun, C.-H.; Pozzi, A.; Savas, Ü.; Johnson, E. F.; Guengerich, F. P. Heme–thiolate sulfenylation of human cytochrome P450 4A11 functions as a redox switch for catalytic inhibition. *J. Biol. Chem.* **2017**, *292* (27), 11230-11242.
426. Freakley, S. J.; Kochius, S.; van Marwijk, J.; Fenner, C.; Lewis, R. J.; Baldenius, K.; Marais, S. S.; Opperman, D. J.; Harrison, S. T. L.; Alcalde, M.; Smit, M. S.; Hutchings, G. J. A chemo-enzymatic oxidation cascade to activate C–H bonds with in situ generated H_2O_2. *Nature Communications* **2019**, *10* (1), 4178.
427. Hollmann, F.; Tieves, F.; Willot, S. J.-P.; van Schie, M. M. C. H.; Rauch, M. C. R.; Younes, S. H. H.; Zhang, W.; de Santos, P. G.; Robbins, J. M.; Bommarius, B.; Alcalde, M.; Bommarius, A. Formate oxidase (FOx) from *Aspergillus oryzae*: one catalyst to promote H_2O_2-dependent biocatalytic oxidation reactions. *Angew. Chem. Int. Ed. 58*, 7873-7877.
428. Choi, D. S.; Ni, Y.; Fernández-Fueyo, E.; Lee, M.; Hollmann, F.; Park, C. B. Photoelectroenzymatic Oxyfunctionalization on Flavin-Hybridized Carbon Nanotube Electrode Platform. *ACS Catal.* **2017**, *7* (3), 1563-1567.
429. Dezvarei, S.; Shoji, O.; Watanabe, Y.; Bell, S. G. The effect of decoy molecules on the activity of the P450Bm3 holoenzyme and a heme domain peroxygenase variant. *Catal. Commun.* **2019**.
430. Stok, J. E.; Yamada, S.; Farlow, A. J.; Slessor, K. E.; De Voss, J. J. Cytochrome P450cin (CYP176A1) D241N: Investigating the role of the conserved acid in the active site of cytochrome P450s. *Biochim. Biophys. Acta Proteins Proteom.* **2013**, *1834* (3), 688-696.
431. Benson, D. E.; Suslick, K. S.; Sligar, S. G. Reduced Oxy Intermediate Observed in D251N Cytochrome P450cam. *Biochemistry* **1997**, *36* (17), 5104-5107.
432. Davydov, R.; Macdonald, I. D. G.; Makris, T. M.; Sligar, S. G.; Hoffman, B. M. EPR and ENDOR of Catalytic Intermediates in Cryoreduced Native and Mutant Oxy-Cytochromes P450cam: Mutation-Induced Changes in the Proton Delivery System. *J. Am. Chem. Soc.* **1999**, *121* (45), 10654-10655.
433. Derat, E.; Kumar, D.; Hirao, H.; Shaik, S. Gauging the Relative Oxidative Powers of Compound I, Ferric-Hydroperoxide, and the Ferric-Hydrogen Peroxide Species of Cytochrome P450 Toward C−H Hydroxylation of a Radical Clock Substrate. *J. Am. Chem. Soc.* **2006**, *128* (2), 473-484.
434. Chandrasena, R. E. P.; Vatsis, K. P.; Coon, M. J.; Hollenberg, P. F.; Newcomb, M. Hydroxylation by the Hydroperoxy-Iron Species in Cytochrome P450 Enzymes. *J. Am. Chem. Soc.* **2004**, *126* (1), 115-126.
435. Nastainzcyk, W.; Ruf, H. H.; Ullrich, V. Ligand Binding of Organic Sulfides to Microsomal Cytochrome P-450. *Eur. J. Biochem.* **1975**, *60* (2), 615-620.
436. Yeom, H.; Sligar, S. G. Oxygen Activation by Cytochrome $P450_{BM-3}$: Effects of Mutating an Active Site Acidic Residue. *Arch. Biochem. Biophys.* **1997**, *337* (2), 209-216.
437. de Visser, S. P.; Kumar, D.; Shaik, S. How do aldehyde side products occur during alkene epoxidation by cytochrome P450? Theory reveals a state-specific multi-state scenario where the high-spin component leads to all side products. *J. Inorg. Biochem.* **2004**, *98* (7), 1183-1193.
438. Kuo, C.-L.; Raner, G. M.; Vaz, A. D. N.; Coon, M. J. Discrete Species of Activated Oxygen Yield Different Cytochrome P450 Heme Adducts from Aldehydes. *Biochemistry* **1999**, *38* (32), 10511-10518.

439. Kuo, C.-L.; Vaz, A. D. N.; Coon, M. J. Metabolic Activation of *trans*-4-Hydroxy-2-nonenal, a Toxic Product of Membrane Lipid Peroxidation and Inhibitor of P450 Cytochromes. *J. Biol. Chem.* **1997**, *272* (36), 22611-22616.
440. Palucki, M.; McCormick, G. J.; Jacobsen, E. N. Low temperature asymmetric epoxidation of unfunctionalized olefins catalyzed by (salen)Mn(III) complexes. *Tetrahedron Lett.* **1995**, *36* (31), 5457-5460.
441. Hrycay, E. G.; Bandiera, S. M. The monooxygenase, peroxidase, and peroxygenase properties of cytochrome P450. *Arch. Biochem. Biophys.* **2012**, *522* (2), 71-89.
442. Keizers, P. H. J.; Schraven, L. H. M.; de Graaf, C.; Hidestrand, M.; Ingelman-Sundberg, M.; van Dijk, B. R.; Vermeulen, N. P. E.; Commandeur, J. N. M. Role of the conserved threonine 309 in mechanism of oxidation by cytochrome P450 2D6. *Biochem. Biophys. Res. Commun.* **2005**, *338* (2), 1065-1074.
443. Davydov, R.; Perera, R.; Jin, S.; Yang, T.-C.; Bryson, T. A.; Sono, M.; Dawson, J. H.; Hoffman, B. M. Substrate Modulation of the Properties and Reactivity of the Oxy-Ferrous and Hydroperoxo-Ferric Intermediates of Cytochrome P450cam As Shown by Cryoreduction-EPR/ENDOR Spectroscopy. *J. Am. Chem. Soc.* **2005**, *127* (5), 1403-1413.
444. Hlavica, P. Models and mechanisms of O-O bond activation by cytochrome P450. *Eur. J. Biochem.* **2004**, *271* (22), 4335-4360.
445. Quiñonero, D.; Morokuma, K.; Musaev, D. G.; Mas-Ballesté, R.; Que, L. Metal−Peroxo versus Metal−Oxo Oxidants in Non-Heme Iron-Catalyzed Olefin Oxidations: Computational and Experimental Studies on the Effect of Water. *J. Am. Chem. Soc.* **2005**, *127* (18), 6548-6549.
446. Martinis, S. A.; Atkins, W. M.; Stayton, P. S.; Sligar, S. G. A conserved residue of cytochrome P-450 is involved in heme-oxygen stability and activation. *J. Am. Chem. Soc.* **1989**, *111* (26), 9252-9253.
447. Chen, J.; Kong, F.; Ma, N.; Zhao, P.; Liu, C.; Wang, X.; Cong, Z. Peroxide-Driven Hydroxylation of Small Alkanes Catalyzed by an Artificial P450BM3 Peroxygenase System. *ACS Catal.* **2019**, *9* (8), 7350-7355.
448. Batabyal, D.; Poulos, T. L. Crystal Structures and Functional Characterization of Wild-Type CYP101D1 and Its Active Site Mutants. *Biochemistry* **2013**, *52* (49), 8898-8906.
449. Silverman, R. B.; Holladay, M. W. Chapter 8 - Drug Metabolism. In *The Organic Chemistry of Drug Design and Drug Action (Third Edition)*; Silverman, R. B., Holladay, M. W., Eds.; Academic Press: Boston, 2014; pp 357-422.
450. Mason, R. P.; Holtzman, J. L. The role of catalytic superoxide formation in the O_2 inhibition of nitroreductase. *Biochem. Biophys. Res. Commun.* **1975**, *67* (4), 1267-1274.
451. Albertolle, M. E.; Peter Guengerich, F. The relationships between cytochromes P450 and H_2O_2: Production, reaction, and inhibition. *J. Inorg. Biochem.* **2018**, *186*, 228-234.
452. Liang, K.; Ricco, R.; Doherty, C. M.; Styles, M. J.; Bell, S.; Kirby, N.; Mudie, S.; Haylock, D.; Hill, A. J.; Doonan, C. J.; Falcaro, P. Biomimetic mineralization of metal-organic frameworks as protective coatings for biomacromolecules. *Nature Communications* **2015**, *6*, 7240.
453. Liang, W.; Carraro, F.; Solomon, M. B.; Bell, S. G.; Amenitsch, H.; Sumby, C. J.; White, N. G.; Falcaro, P.; Doonan, C. J. Enzyme Encapsulation in a Porous Hydrogen-Bonded Organic Framework. *J. Am. Chem. Soc.* **2019**, *141* (36), 14298-14305.
454. Romero, E.; Gadda, G., Alcohol oxidation by flavoenzymes. In *Biomolecular Concepts*, 2014; Vol. 5, p 299.
455. Forneris, F.; Heuts, D. P. H. M.; Delvecchio, M.; Rovida, S.; Fraaije, M. W.; Mattevi, A. Structural Analysis of the Catalytic Mechanism and Stereoselectivity in Streptomyces coelicolor Alditol Oxidase. *Biochemistry* **2008**, *47* (3), 978-985.
456. Ener, M. E.; Lee, Y.-T.; Winkler, J. R.; Gray, H. B.; Cheruzel, L. Photooxidation of cytochrome P450-BM3. *Proc. Natl. Acad. Sci. U.S.A.* **2010**, *107* (44), 18783-18786.
457. Low, D. W.; Winkler, J. R.; Gray, H. B. Photoinduced Oxidation of Microperoxidase-8: Generation of Ferryl and Cation-Radical Porphyrins. *J. Am. Chem. Soc.* **1996**, *118* (1), 117-120.
458. Berglund, J.; Pascher, T.; Winkler, J. R.; Gray, H. B. Photoinduced Oxidation of Horseradish Peroxidase. *J. Am. Chem. Soc.* **1997**, *119* (10), 2464-2469.

459. Ener, M. E. Electron Flow through Cytochrome P450 California Institute of Technology, 2014.
460. Boisvert, L.; Denney, M. C.; Hanson, S. K.; Goldberg, K. I. Insertion of Molecular Oxygen into a Palladium(II) Methyl Bond: A Radical Chain Mechanism Involving Palladium(III) Intermediates. *J. Am. Chem. Soc.* **2009**, *131* (43), 15802-15814.
461. Blanksby, S. J.; Ramond, T. M.; Davico, G. E.; Nimlos, M. R.; Kato, S.; Bierbaum, V. M.; Lineberger, W. C.; Ellison, G. B.; Okumura, M. Negative-Ion Photoelectron Spectroscopy, Gas-Phase Acidity, and Thermochemistry of the Peroxyl Radicals CH_3OO and CH_3CH_2OO. *J. Am. Chem. Soc.* **2001**, *123* (39), 9585-9596.
462. Ramírez, D.; Caballero, J. Is It Reliable to Take the Molecular Docking Top Scoring Position as the Best Solution without Considering Available Structural Data? *Molecules* **2018**, *23* (5), 1038.
463. Ding, Y.; Fang, Y.; Moreno, J.; Ramanujam, J.; Jarrell, M.; Brylinski, M. Assessing the similarity of ligand binding conformations with the Contact Mode Score. *Computational Biology and Chemistry* **2016**, *64*, 403-413.
464. Hampton Research. Crystallization of (insoluble) ligand protein complexes https://www.hamptonresearch.com/tip_detail.aspx?id=124 (accessed 6 Feb 2018).
465. Markley, J. L.; Bax, A.; Arata, Y.; Hilbers, C. W.; Kaptein, R.; Sykes, B. D.; Wright, P. E.; Wüthrich, K. Recommendations for the presentation of NMR structures of proteins and nucleic acids – IUPAC-IUBMB-IUPAB Inter-Union Task Group on the Standardization of Data Bases of Protein and Nucleic Acid Structures Determined by NMR Spectroscopy. *J. Biomol. NMR* **1998**, *12* (1), 1-23.
466. Hall, E. A.; Sarkar, M. R.; Lee, J. H. Z.; Munday, S. D.; Bell, S. G. Improving the Monooxygenase Activity and the Regio- and Stereoselectivity of Terpenoid Hydroxylation Using Ester Directing Groups. *ACS Catal.* **2016**, *6* (9), 6306-6317.
467. Bell, S. G.; Xu, F.; Forward, I.; Bartlam, M.; Rao, Z.; Wong, L.-L. Crystal Structure of CYP199A2, a *Para*-Substituted Benzoic Acid Oxidizing Cytochrome P450 from *Rhodopseudomonas palustris*. *J. Mol. Biol.* **2008**, *383* (3), 561-574.
468. McDonald, I. K.; Thornton, J. M. The application of hydrogen bonding analysis in X-ray crystallography to help orientate asparagine, glutamine and histidine side chains. *Protein Eng. Des. Sel.* **1995**, *8* (3), 217-224.